Errata

Page 2	Line 19: ‘O^{2-} ads’ should read ‘O^{2-}_{ads}’
Page 5	Line 10: ‘exists’ should read ‘exist’
Page 6	Line 3: ‘[n^2]’ should read ‘n^2’; ‘[$pO^{1/2}$]’ should read ‘$pO_2^{1/2}$’
Page 6	Line 6: ‘$n = pO_2^{-1/4}$’ should read ‘$n \propto pO_2^{-1/4}$’
Page 6	Line 14: ‘$p = pO_2^{1/4}$’ should read ‘$p \propto pO_2^{1/4}$’
Page 7	Line 1: ‘there is negligible’ should read ‘there are negligible’
Page 12	Line 21: ‘criteria’ should read ‘criterion’
Page 30	Line 5: ‘Equation 1.2’ should read ‘Equation 1.12’, and subsequent numbering for following equations.
Page 31	Line 3: ‘Rr’ should read ‘R_R’
Page 38	Line 6: C. Balanchandran
Page 39	Line 14: ‘#rd’ should read ‘3rd’
Page 39	Line 37: ‘Uion’ should read ‘Ion’; ‘Editors:5’ should read ‘Editors:’
Page 42	Line 3: ‘Mathey’ should read ‘Matthey’
Page 50	Line13: ’Electron Dispersive X-Ray Analysis’ should read ‘Energy Dispersive X-Ray Analysis’
Page 52	Figure Caption: ‘H2O’ should read ‘H_2O’
Page 53	Line 8: ‘Q’ should read ‘Y_o’; ‘(П/2n)’ should read ‘(nП/2)’
Page 53	Line 10: ‘n=1’ should read ‘n=-1’
Page 92	Line 19: ’20 Ω’ should read ‘3 Ω’
Page 137	Line 9: ‘high’ should read ‘low’

Fabrication and Characterisation of Nickel/Yttria Stabilised Zirconia Cermet Anodes for Solid Oxide Fuel Cells

A thesis
submitted in partial fulfillment of
the requirements for the degree
of
Doctor of Philosophy
in Technology
at the
University of Waikato
By

Michael Steven Brown

University of Waikato
September, 1998

Abstract

The primary objective of this thesis was to study the Ni/YSZ system from powder preparation to electrochemical and morphological characterisation.

Nickel/yttria stabilised zirconia (YSZ) cermet systems are employed as anode materials in high temperature solid oxide fuel cell (SOFC) applications. The ionically conducting YSZ powder was modified, by sintering and milling to vary the particle distribution. This allowed the fabrication of cermet powders with varying particle sizes and therefore microstructures. Bimodal particle distributions were present for the milled YSZ, which indicated two particle sizes. The finest particles were individual YSZ particles of approximately 0.4 µm, and represented the grinding limit, which was independent of calcining temperature. The agglomerate size decreased and the amount of fine YSZ increased as milling times were extended.

A 'paint' consisting of the cermet powder (NiO/YSZ), a solvent, and a binder was developed in order to use a wet powder spraying (WPS®) technique, to apply the electrode layer to the electrolyte substrate. By this method, reproducible anodes with good morphological properties were produced. The slurry was prepared with ethanol as the solvent and a PVP binder, to form a stable suspension.

Anode sintering temperature was studied with results indicating that a temperature of 1300 °C provided the optimum sintering effect. Anodes sintered at 1300 °C showed no agglomeration of NiO. There was no discernable increase of Ni particle size after reducing in hydrogen.

A number of Ni/YSZ cermet anodes consisting of 40 vol% nickel and 60 vol% YSZ were fabricated with varying thickness of the active layer. The anode materials were milled to the appropriate particle sizes, air-sprayed onto YSZ substrates and subsequently sintered to produce the anode component. The thicknesses ranged from 3.5 µm to 54 µm in order to find the minimum thickness of active layer for a high performance anode using the least material. The anodes were studied in an atmosphere of hydrogen, water and nitrogen in a 3-electrode setup. Impedance spectroscopy was carried out at a temperature of 1000 °C.

It was found that approximately 12 μm was the limiting thickness for a low polarisation resistance. Below a thickness of 12 μm, the polarisation resistance increased in an erratic manner as the reaction zone was reduced.

Ni/YSZ cermet anodes consisting of 90 vol% Ni and 10 vol% YSZ were fabricated in order to create an anode with significantly higher polarisation resistance. Hereby a structure-related impedance arc at high frequencies could be examined in detail. The anode was studied in mixtures of hydrogen, water and nitrogen in a 3-electrode setup. Impedance measurements were carried out at temperatures ranging between 700°C and 1000°C. The present work confirmed that a high frequency arc from impedance spectroscopy data was indeed related to the structure of the cermet.

Four types of Ni/YSZ anodes were characterised and compared to illustrate similarities and differences from state-of-the-art cermet anodes to coarse structure cermets to two-dimensional Ni anodes with significantly higher polarization resistance. The anode structure-dependent high frequency section of the impedance spectrum was studied.

The thesis concludes with recommendations for further investigations.

Acknowledgements

I would like to thank my supervisor, Professor Nigel Sammes for providing the opportunity to study in New Zealand and for furthering my knowledge in the field of solid oxide fuel cells. I appreciate all the advice and guidance, and helpful discussions throughout the course of this research.

I would also like to thank Dr Mogens Mogensen for the opportunity to study at the Materials Research Laboratory in Denmark.

I would especially like to thank the members of my family, for their emotional (and financial) support during the many years I have endured the student life. Thank you to my Grandmother for her superior English grammar skills when proofreading this thesis.

Of the various people who aided and assisted me during this work, thanks are due to the following:

Søren Primdahl and the team at Risø National Laboratory, who encouraged this research and led me onto the more challenging aspects of solid oxide fuel cells. Thank you for the opportunity to work, and expand my knowledge at your institute.

Mr A.Harris and Mr D.Wild for their assistance with the scanning electron microscope, and its various accessories.

My fellow research students, Dr Mike (Battler) Phillipps, Dr Geoff (Homer) Tompsett, Basil (Family Man) Fenton, Charlie (Farley-Felicity Ferret) Hatchwell, Roslyn (the Snoz) Phillips, Matthew (Mattress) Henderson, Russell (da Muss) Cross, John (Skatey Boyee) Davidson, Clive-O Desouza, Tracey (the Ace) Murray and Yuanji (the Flange) Zhang for their helpful advice on aspects of this work. Last, but not least, thanks to Sue (Poo) Mends for the macadamia cookies and shoulder rubs...

This research was carried out under FoRST contract UOW 402, in collaboration with the Danish SOFC program, Risø National Laboratory, Denmark.

Contents

1. INTRODUCTION AND LITERATURE REVIEW 1

1.1 INTRODUCTION 1

1.2 INTRODUCTION TO THE SOLID OXIDE FUEL CELL 2

1.3 SOLID OXIDE FUEL CELL COMPONENTS 3

1.3.1 Requirements 3

1.3.2 Electrolyte 4

1.3.3 Cathode 7

1.3.4 Interconnect 8

1.4 ANODE SYSTEMS 10

1.4.1 Introduction 10

1.4.1.1 Materials 11

1.4.1.1.1 Cermet Anodes 11

1.4.1.1.2 Mixed Ionic/Electronic Conducting Anodes 12

1.4.2 Anode Requirements 13

1.4.3 Structure/Morphology 15

1.4.4 Fabrication 18

1.4.4.1 Slurry Coating 18

1.4.4.2 Wet Powder Spraying (WPS®) 19

1.4.4.3 Electrochemical Vapour Deposition 20

1.4.4.4 Plasma Spraying 21

1.4.4.5 Tape Casting 22

1.4.5 Electrical Conductivity 23

1.4.6 Thermal Expansion 26

1.4.7 Stability 27

1.4.8 Kinetics and Mechanisms 28

1.4.9 Fuels 33

1.4.9.1 Types of Fuels 33

1.4.9.2 Fuel Reformation 35

1.5 SCOPE OF THE RESEARCH 36

1.6 REFERENCES 37

2. METHODS AND EXPERIMENTAL APPARATUS 41

2.1 INTRODUCTION 41

2.2 POWDER PREPARATION 41

2.2.1 Materials *41*

2.2.2 Milling *42*

2.2.3 Sintering *44*

2.2.4 Pressing *45*

2.3 PARTICLE SIZE/DISTRIBUTION 46

2.4 ANODE FABRICATION 46

2.4.1 Mixture preparation *46*

2.4.2 Ceramic Slurry Application *47*

2.4.3 Drying *47*

2.4.4 Sintering *48*

2.5 MICROSCOPY 49

2.5.1 Optical Microscopy *49*

2.5.2 Scanning Electron Microscopy *50*

2.6 ELECTRON DISPERSIVE X-RAY ANALYSIS 50

2.7 ELECTROCHEMICAL TECHNIQUES 51

2.7.1 Theory *51*

2.7.1.1 Impedance Spectroscopy 51

2.7.1.2 Chronoamperometry 55

2.7.1.3 Cyclic Voltammetry 56

2.7.2 Experimental *56*

2.7.2.1 Single Atmosphere Electrode Testing Setup 58

2.7.2.2 Dual Atmosphere Electrode Testing Setup 60

3. FABRICATION, STRUCTURE AND CONDUCTIVITY OF Ni/YSZ CERMET ANODES 63

3.1 INTRODUCTION 63

3.2 METHODS AND MATERIALS 65

3.2.1 Anode Materials *65*

3.2.2 Experimental Apparatus *65*
3.2.3 Anode Fabrication *66*
3.2.3.1 Method 66
3.2.3.2 Technique 67
3.3 RESULTS 67
3.3.1 YSZ Calcining Temperature *67*
3.3.2 Milling *69*
3.3.2.1 Ball Milling 69
3.3.2.2 Centrifugal Milling 77
3.3.3 Wet Powder Spraying® *82*
3.3.4 Sintering Temperature *84*
3.3.5 Fabricated Anodes *87*
3.4 DISCUSSION 89
3.4.1 YSZ Calcining Temperature *89*
3.4.2 Milling *90*
3.4.3 Wet Powder Spraying *91*
3.4.4 Sintering Temperature *92*
3.4.5 Anode Fabrication *93*
3.4.5.1 Anode 1 91
3.4.5.2 Anodes 2 to 7 94
3.4.5.3 Anodes 8 to 11 94
3.4.5.4 Anodes 12 and 13 95
3.4.5.5 Anode 14 95
3.4.5.6 Anodes 15 to 19 95
3.5 CONCLUSIONS 96
3.6 REFERENCES 97

4. Ni/YSZ ACTIVE LAYER THICKNESS 99

4.1 INTRODUCTION 99
4.2 METHODS AND MATERIALS 102
4.2.1 Test Setup Design *102*
4.2.2 Electrochemical Testing *103*

4.3 RESULTS AND DISCUSSION 103
4.4 CONCLUSIONS 118
4.5 ACKNOWLEDGEMENTS 118
4.6 REFERENCES 118

5. H_2 OXIDATION AT THE Ni/YSZ INTERFACE 120

5.1 INTRODUCTION 120
5.2 METHODS AND MATERIALS 122
  5.2.1 Test Setup Design 122
  5.2.2 Sample Preparation 123
    5.2.2.1 Anode Paste Preparation 123
  5.2.3 Electrochemical Testing 124
  5.2.4 Experimental Design 125
5.3 RESULTS 125
  5.3.1 Interpretation of Impedance Spectra 125
  5.3.2 Anode Structure 127
  5.3.3 Thermal Activation 129
  5.3.4 Gas Composition 130
  5.3.5 Polarisation 132
5.4 DISCUSSION 134
  5.4.1 Thermal Activation 134
  5.4.2 Hydrogen Partial Pressure 135
  5.4.3 Steam Partial Pressure 136
  5.4.4 Polarisation 136
5.5 CONCLUSIONS 138
5.6 ACKNOWLEDGEMENTS 138
5.6 REFERENCES 138

6. CHARACTERISATION OF TYPES OF Ni/YSZ ANODES 141

6.1 INTRODUCTION 141
6.2 EXPERIMENTAL 145
  6.2.1 Sample Preparation 145

6.2.2 Electrochemical Testing *146*
6.3 RESULTS 147
6.3.1 Anode Structure *147*
6.3.2 Impedance Spectra *150*
6.3.3 Thickness *155*
6.3.4 Thermal Activation *156*
6.3.5 Gas Composition *159*
6.4 DISCUSSION 164
6.4.1 Active Thickness *164*
6.4.2 Thermal Activation *164*
6.4.3 Hydrogen Partial Pressure *165*
6.4.4 Steam Partial Pressure *166*
6.4.5 Possible Limiting Processes *167*
6.5 CONCLUSIONS 168
6.6 ACKNOWLEDGEMENTS 169
6.6 REFERENCES 169

7. CONCLUSIONS AND RECOMMENDATIONS 172

7.1 CONCLUSIONS 172
7.2 RECOMMENDATIONS FOR FUTURE WORK 176
7.2.1 General Comments *176*
7.2.2 Experimental Parameters *177*
7.2.2.1 Ni/YSZ Anodes 178
7.2.2.2 Experimental Matrix 178
7.2.2.3 Fabrication 178
7.2.2.4 Electrochemical Characterisation 179
7.2.2.5 Microstructural Characterisation 179

APPENDIX 1 180

KRÖGER-VINK NOTATION 180

APPENDIX 2 181

PARTICLE SIZE STUDY 181

APPENDIX 3 217

SCANNING ELECTRON MICROSCOPY STUDY 217

APPENDIX 4 223

OPTICAL MICROSCOPY STUDY 223

List of Figures

Chapter One

Figure 1.1. Schematic diagram showing the mass transport processes involved in a SOFC. 3

Figure 1.2 Diagram of the crystal structure of a fluorite type electrolyte. 5

Figure 1.3 Variation of electrical conductivity as a function of oxygen partial pressure for a MO_2-B_2O_3 system. 7

Figure 1.4 Perovskite structure of $LaMnO_3$. 8

Figure 1.5 Flat-plate SOFC design showing the design of the interconnect. 9

Figure 1.6 Schematic diagram of (a) the standard electronically conducting anode and (b) the mixed ionic/electronic conducting anode. 11

Figure 1.7 Microstructure of a sintered Ni/YSZ cermet anode illustrating intra-particle connection and porosity. 14

Figure 1.8 Schematic diagram of the electronic and ionic pathways in a Ni/YSZ cermet showing the triple phase boundary points (TPB). 16

Figure 1.9 Principle of electrochemical vapour deposition. 20

Figure 1.10 Typical plasma spray gun. 22

Figure 1.11 Schematic diagram of a tape casting system. 23

Figure 1.12 Conductivity of a Ni/YSZ cermet at 1000 °C as a function of nickel content. 24

Figure 1.13 Secondary electron image (SEI) of a Ni/YSZ cermet showing the elemental distribution of the two sizes of white YSZ particles and dark NiO particles. 25

Figure 1.14 Thermal expansion coefficient of the cermet anode as a function of NiO (or Ni) content. 26

Figure 1.15 Micrograph of 90% Ni/YSZ cermet illustrating the prevention of Ni agglomeration by the pinning effect of the fine YSZ particles. 27

Figure 1.16 Semi-log plot of the polarisation resistance as a function of the log partial pressure of oxygen. 30

FIGURE 1.17 TYPICAL IMPEDANCE PLOT OBSERVED FOR A NI/YSZ CERMET AT 1000 °C BY MEANS OF IMPEDANCE SPECTROSCOPY. 31
FIGURE 1.18 IMPEDANCE PLOT OF A NI/YSZ CERMET AT 1000 °C IN H_2 AT OCV SHOWING THE THREE ARCS RELATING TO THE ANODE REACTION. 32

Chapter Two

FIGURE 2.1 BALL MILL USED FOR MILLING ALL MATERIALS INCLUDING NIO AND YSZ, AND FOR MIXING THE CERMET POWDERS. 43
FIGURE 2.2 CENTRIFUGAL MILL USED FOR HIGH ENERGY MILLING OF THE 44
FIGURE 2.3 CERAMIC ENGINEERING HT05/18 HIGH TEMPERATURE FURNACE, CAPABLE OF TEMPERATURES UP TO 1700 °C, USED PRIMARILY FOR SINTERING YSZ AGGLOMERATES 45
FIGURE 2.4 WET POWDER SPRAYING TECHNIQUE USED TO APPLY THE CERMET SLURRIES ONTO THE YSZ SUBSTRATES. THIS TECHNIQUE WAS ALSO USED HORIZONTALLY TO INHIBIT RUNNING OF THE PAINT. 49
FIGURE 2.5 (A), (B) ELECTROCHEMICAL IMPEDANCE SPECTRA OF SOFC NI/YSZ 52
FIGURE 2.6 THE SIMPLEST POSSIBLE EQUIVALENT CIRCUIT FOR IMPEDANCE SPECTRA 53
FIGURE 2.7 ERROR PLOTS OF THE FITS OF THE SPECTRA OF FIGURE 2.5 USING THE EQUIVALENT CIRCUIT OF FIGURE 2.6 AND FIXED N-VALUES (N_1, N_2, N_3) = (0.8, 0.75, 1). EACH POINT GIVES THE DIFFERENCE 54
FIGURE 2.8 SINGLE ATMOSPHERE ELECTRODE TESTING SETUP USED TO PROVIDE A ... 58
FIGURE 2.9 INTERNAL STRUCTURE OF THE SINGLE ATMOSPHERE ELECTRODE TESTING SETUP 59
FIGURE 2.10 DUAL ATMOSPHERE ELECTRODE TESTING SETUP. 61

Chapter Three

FIGURE 3.1(A) MICROGRAPH OF YTTRIA STABILISED ZIRCONIA (YSZ) SINTERED AT 1100 °C 68

FIGURE 3.1(B) MICROGRAPH OF YSZ SINTERED AT 1400 °C. 69
FIGURE 3.2(A) PARTICLE SIZE DISTRIBUTION OF YSZ SINTERED AT 1100 °C AFTER 26 HOURS OF BALL MILLING. 70
FIGURE 3.2(B) PARTICLE SIZE DISTRIBUTION OF YSZ SINTERED AT 1400 °C AFTER 4.5 HOURS OF BALL MILLING. 70
FIGURE 3.3(A) MICROGRAPH OF YSZ SINTERED AT 1100 °C AFTER MILLING FOR 26 HOURS. 71
FIGURE 3.3(B) MICROGRAPH OF YSZ SINTERED AT 1400 °C AFTER MILLING FOR 4.5 HOURS. 72
FIGURE 3.4(A) BIMODAL PARTICLE SIZE DISTRIBUTION OF YSZ SINTERED AT 1400 °C OBSERVED AFTER 9 HOURS OF BALL MILLING. 73
FIGURE 3.4(B) BIMODAL PARTICLE SIZE DISTRIBUTION OF YSZ SINTERED AT 1400 °C OBSERVED AFTER 267 HOURS OF BALL MILLING. 74
FIGURE 3.5 PARTICLE SIZE DISTRIBUTION OF NIO AS RECEIVED. 75
FIGURE 3.6 PARTICLE SIZE DISTRIBUTION OF NIO AFTER 52 HOURS OF BALL MILLING. 76
FIGURE 3.7 PARTICLE SIZE DISTRIBUTION OF THE YSZ AGGLOMERATES AFTER SINTERING AT 1400 °C. 77
FIGURE 3.8 PARTICLE SIZE DISTRIBUTION OF THE YSZ SINTERED AT 1400 °C AFTER 7 HOURS OF CENTRIFUGAL MILLING. 78
FIGURE 3.9 MICROGRAPH OF YSZ SINTERED AT 1100 °C AFTER 45 MINUTES OF MILLING. 79
FIGURE 3.10(A) BIMODAL PARTICLE SIZE DISTRIBUTION OF NIO BEFORE MILLING, INCLUDING A THIRD PEAK OF AGGLOMERATED NIO. 80
FIGURE 3.10(B) BIMODAL PARTICLE SIZE DISTRIBUTION OF NIO AFTER 30 MINUTES OF CENTRIFUGAL MILLING. 80
FIGURE 3.11(A) MICROGRAPH OF NIO BEFORE CENTRIFUGAL MILLING. 81
FIGURE 3.11(B) MICROGRAPH OF NIO AFTER CENTRIFUGAL MILLING FOR 30 MINUTES. 81
FIGURE 3.12 MICROGRAPH OF A SINTERED ANODE FABRICATED WITH A WET POWDER SPRAYING® TECHNIQUE. 82

FIGURE 3.13 FLOWCHART OF THE STEPS INVOLVED IN THE FABRICATION OF NI/YSZ CERMET ANODES. 83
FIGURE 3.14(A) OPTICAL MICROGRAPH OF A NIO/YSZ ANODE AFTER SINTERING AT 1300 °C SHOWING HOMOGENEOUS MICROSTRUCTURE. 84
FIGURE 3.14(B) OPTICAL MICROGRAPH OF A NI/YSZ ANODE AFTER REDUCTION IN H_2 AT 700 °C SHOWING HOMOGENEOUS MICROSTRUCTURE. 85
FIGURE 3.15(A) OPTICAL MICROGRAPH OF A NIO/YSZ ANODE AFTER SINTERING AT 1450 °C SHOWING AGGLOMERATION OF NIO. 86
FIGURE 3.15(B) OPTICAL MICROGRAPH OF A NI/YSZ ANODE AFTER REDUCTION IN H_2 AT 700 °C SHOWING AGGLOMERATION OF NI INTO NON-CONNECTING 'ISLANDS'. 87
FIGURE 3.16 POLARISATION RESISTANCE AS A FUNCTION OF SINTERING TEMPERATURE FOR ANODES AT 1000 °C IN H_2 + 3% H_2O AT OCV 93

Chapter Four

FIGURE 4.1 SCHEMATIC DIAGRAM OF THE ANODE STRUCTURE SHOWING 100
FIGURE 4.2 SCHEMATIC DIAGRAM OF THE ANODE STRUCTURE SHOWING 101
FIGURE 4.3(A) STRUCTURE OF POLISHED CROSS-SECTION OF THE CURRENT COLLECTING NI 104
FIGURE 4.3(B) STRUCTURE OF A 3.5µM NI/YSZ ANODE LAYER WITH OVERLYING CURRENT COLLECTION LAYER(A697). 105
FIGURE 4.3(C) STRUCTURE OF A 4µM NI/YSZ ANODE LAYER WITH OVERLYING CURRENT COLLECTION LAYER(A696). 105
FIGURE 4.3(D) STRUCTURE OF A 5.5µM NI/YSZ ANODE LAYER WITH OVERLYING CURRENT COLLECTION LAYER(A698). 106
FIGURE 4.3(E) STRUCTURE OF A 11µM NI/YSZ ANODE LAYER WITH OVERLYING CURRENT COLLECTION LAYER(A515). 106
FIGURE 4.3(F) STRUCTURE OF A 12µM NI/YSZ ANODE LAYER WITH OVERLYING CURRENT COLLECTION LAYER(A516). 107

FIGURE 4.3(G) STRUCTURE OF A 12µM NI/YSZ ANODE LAYER WITH OVERLYING CURRENT COLLECTION LAYER(A518). 107

FIGURE 4.3(H) STRUCTURE OF A 22µM NI/YSZ ANODE LAYER WITH OVERLYING CURRENT COLLECTION LAYER(A520). 108

FIGURE 4.3(I) STRUCTURE OF A STANDARD ANODE (54µM) WITH OVERLYING CURRENT COLLECTION LAYER(A588). 108

FIGURE 4.4 EQUIVALENT CIRCUIT USED FOR THE FITTING PROCEDURE OF THE IMPEDANCE DATA. L IS AN INDUCTANCE ORIGINATING FROM THE TESTING EQUIPMENT, R_S IS THE SERIES RESISTANCE ORIGINATING FROM THE ELECTROLYTE AND THE LEADS, AND R_1Q_1, R_2Q_2, R_3Q_3 DESCRIBE THE ELECTRODE RESPONSE. 109

FIGURE 4.5 TYPICAL IMPEDANCE DIAGRAM FOR A NI/YSZ CERMET ANODE AT 1000°C IN 110

FIGURE 4.6(A) IMPEDANCE SPECTRUM OBTAINED FOR CURRENT COLLECTING LAYER (ACC). 111

FIGURE 4.6(B) IMPEDANCE SPECTRUM OBTAINED FOR 3.5 µM ANODE LAYER (A697). 111

FIGURE 4.6(C) IMPEDANCE SPECTRUM OBTAINED FOR 4 µM ANODE LAYER (A696). 112

FIGURE 4.6(D) IMPEDANCE SPECTRUM OBTAINED FOR 5.5 µM ANODE LAYER (A698). 112

FIGURE 4.6(E) IMPEDANCE SPECTRUM OBTAINED FOR 11 µM ANODE LAYER (A515). 113

FIGURE 4.6(F) IMPEDANCE SPECTRUM OBTAINED FOR 12 µM ANODE LAYER (A516). 113

FIGURE 4.6(G) IMPEDANCE SPECTRUM OBTAINED FOR 12 µM ANODE LAYER (A518). 114

FIGURE 4.6(H) IMPEDANCE SPECTRUM OBTAINED FOR 22 µM ANODE LAYER (A520). 114

FIGURE 4.6(I) IMPEDANCE SPECTRUM OBTAINED FOR 54 µM ANODE LAYER (A588). 115

FIGURE 4.7 GRAPH OF THE STRUCTURE RELATED IMPEDANCE ARC RESISTANCE AS A FUNCTION OF ANODE THICKNESS 116

Chapter Five

FIGURE 5.1 IMPEDANCE SPECTRA OF STANDARD RISØ ANODE AND A HIGH NI ANODE AT 1000 °C, AT OCV IN WET H_2, CORRECTED FOR ANODE AREA AND R_S SUBTRACTED. 126

FIGURE 5.2 MICROSTRUCTURE OF ANODE ACTIVE LAYER, ILLUSTRATING NI BALLS PRODUCED FROM THE DECOMPOSITION OF $Ni(NO_3)_2$ AT 1420 °C IN WET H_2. 127

FIGURE 5.3 SURFACE OF THE CURRENT COLLECTING LAYER CONTAINING 90 VOL% NI AND 10 VOL% YSZ AS OBSERVED BY SEM, ILLUSTRATING THE DEGREE OF NI SINTERING. 128

FIGURE 5.4 SEM IMAGE OF THE CURRENT COLLECTING LAYER SURFACE, INDICATING THE PURPOSE OF THE FINE YSZ PARTICLES TO INHIBIT THE HIGH DEGREE OF NI PARTICLE SINTERING. 128

FIGURE 5.5 STRUCTURE OF POLISHED CROSS-SECTION OF THE CURRENT COLLECTING LAYER AS OBSERVED BY SEM. 129

FIGURE 5.6 THERMAL ACTIVATION OF PROCESSES IN THE RANGE OF 700 °C TO 1000 °C. 130

FIGURE 5.7 INVERSE RESISTANCE OF R_I AS A FUNCTION OF STEAM PARTIAL PRESSURE SHOWING A DEPENDENCE UP TO 0.2 ATM. 131

FIGURE 5.8 INVERSE RESISTANCE OF R_I AS A FUNCTION OF H_2 PARTIAL PRESSURE SHOWING A DEPENDENCE OF R PROPORTIONAL TO $pH_2^{-0.16}$, UP TO 0.2 ATM. 132

FIGURE 5.9 CONTRIBUTIONS TO THE POLARISATION RESISTANCE RP AND THE DEPENDENCY ON ANODIC OVERPOTENTIAL AT 1000 °C IN H_2 + 3% H_2O. 133

FIGURE 5.10. I-η CHARACTERISTICS AFTER CORRECTION FOR IR LOSSES. T=1000 °C IN AN ATMOSPHERE OF 97% H_2 + 3% H_2O. THE HYSTERESIS IS INDUCTIVE. 133

FIGURE 5.11 TAFEL TYPE PLOT OF ELECTRODE OVERPOTENTIAL AS A FUNCTION OF LOG CURRENT. T=1000 °C IN AN ATMOSPHERE OF 97% H_2 + 3% H_2O. ONLY INCREASING CURRENTS FROM OCV ARE GIVEN. 134

Chapter Six

FIGURE 6.1 SEM MICROGRAPH SHOWING STRUCTURE OF A FINE CERMET ANODE AS OBSERVED BY BACKSCATTERED ELECTRONS ON A POLISHED CROSS SECTION... 148

FIGURE 6.2 SEM MICROGRAPH SHOWING STRUCTURE OF A NI-PASTE ANODE AS OBSERVED BY BACKSCATTERED ELECTRONS ON A POLISHED CROSS SECTION... 149

FIGURE 6.3 SEM MICROGRAPH SHOWING STRUCTURE OF A NI-PASTE ANODE AS OBSERVED BY BACKSCATTERED ELECTRONS ON THE SURFACE. 149

FIGURE 6.4 SEM MICROGRAPH SHOWING STRUCTURE OF A COARSE CERMET ANODE AS OBSERVED BY BACKSCATTERED ELECTRONS ON A POLISHED CROSS SECTION... 150

FIGURE 6.5 AREA SPECIFIC IMPEDANCE SPECTRA OBTAINED AT OCV AT 1000°C IN H_2 + 3% H_2O ON A FINE CERMET ANODE. POINTS ARE EXPERIMENTAL DATA, SOLID LINES ARE TOTAL FIT DATA AND DASHED LINES INDICATE EACH IMPEDANCE ARC IN THE FIT. 151

FIGURE 6.6 AREA SPECIFIC IMPEDANCE SPECTRA OBTAINED AT OCV AT 1000°C IN H_2 + 3% H_2O ON A NI-PASTE ANODE A528,. POINTS ARE EXPERIMENTAL DATA, SOLID LINES ARE TOTAL FIT DATA AND DASHED LINES INDICATE EACH IMPEDANCE ARC IN THE FIT. 152

FIGURE 6.7 AREA SPECIFIC IMPEDANCE SPECTRA OBTAINED AT OCV AT 1000°C IN H_2 + 3% H_2O ON A COARSE CERMET ANODE X133. POINTS ARE EXPERIMENTAL DATA, SOLID LINES ARE TOTAL FIT DATA AND DASHED LINES INDICATE EACH IMPEDANCE ARC IN THE FIT. 152

FIGURE 6.8 AREA SPECIFIC IMPEDANCE SPECTRA OBTAINED AT OCV AT 1000°C IN H_2 + 3% H_2O ON A NI-FELT ANODE X73 POINTS ARE EXPERIMENTAL DATA, SOLID LINES ARE TOTAL FIT DATA AND DASHED LINES INDICATE EACH IMPEDANCE ARC IN THE FIT. 153

FIGURE 6.9 DEPENDENCE OF ANODE THICKNESS FOR CONTRIBUTIONS TO THE POLARISATION RESISTANCE FOR FINE CERMET ANODES AT 1000°C IN 97% H_2 + 3% H_2O AT OCV. 156

FIGURE 6.10 ARRHENIUS TYPE PLOT WHEREFROM THE APPARENT ACTIVATION ENERGY OF $R_{1\alpha}$, $R_{1\beta}$, AND R_1 CAN BE ESTIMATED. DATA OBTAINED BY FITTING IMPEDANCE

SPECTRA OBTAINED AT 700°C TO 1000°C IN H_2 + 3% H_2O AT OCV. NI-SLURRY ANODE ,A528, IN H_2 (OPEN) AND IN 50/50 N_2/H_2. 157

FIGURE 6.11 ARRHENIUS TYPE PLOT WHERE THE APPARENT ACTIVATION ENERGY OF $R_{1\alpha}$, $R_{1\beta}$, AND R_1 CAN BE ESTIMATED. DATA OBTAINED BY FITTING IMPEDANCE SPECTRA OBTAINED AT 700°C TO 1000°C IN H_2 + 3% H_2O AT OCV. NI-FELT X73 (SQUARES) AND X76 (BULLETS). 157

FIGURE 6.12 ARRHENIUS TYPE PLOT WHERE THE APPARENT ACTIVATION ENERGY OF $R_{1\alpha}$, $R_{1\beta}$, AND R_1 CAN BE ESTIMATED. DATA OBTAINED BY FITTING IMPEDANCE SPECTRA OBTAINED AT 700 °C TO 1000 °C IN H_2 + 3% H_2O AT OCV. COARSE CERMET ANODE, X133. 158

FIGURE 6.13 DEPENDENCE OF $R_{1\alpha}$, $R_{1\beta}$ AND R_1 ON pH_2 AT 1000°C IN 3% H_2O AT OCV, NI-PASTE ANODE. 159

FIGURE 6.14 DEPENDENCE OF $R_{1\alpha}$, $R_{1\beta}$ AND R_1 ON pH_2 AT 1000°C IN 3% H_2O AT OCV. X134, NI-FELT X76. 160

FIGURE 6.15 DEPENDENCE OF $R_{1\alpha}$, $R_{1\beta}$ AND R_1 ON pH_2 AT 1000°C IN 3% H_2O AT OCV.A528, COARSE CERMET. 160

FIGURE 6.16 DEPENDENCE OF $R_{1\alpha}$, $R_{1\beta}$ AND R_1 ON pH_2O AT 1000°C IN H_2 AT OCV, NI-PASTE ANODE A528, 50% H_2 (SQUARES) AND 25% H_2 (BULLETS). 162

FIGURE 6.17 DEPENDENCE OF $R_{1\alpha}$, $R_{1\beta}$ AND R_1 ON pH_2O AT 1000°C IN H_2 AT OCV, NI-FELT ANODE X76 IN 96-99.9% H_2. 162

FIGURE 6.18 DEPENDENCE OF $R_{1\alpha}$, $R_{1\beta}$ AND R_1 ON pH_2O AT 1000°C IN H_2 AT OCV, COARSE CERMET ANODE X134 IN 96-99.9% H_2. 163

List of Tables

TABLE 2.1 MATERIALS USED AND THEIR RESPECTIVE MANUFACTURERS..........42

TABLE 2.2 TABLE OF MILLS USED TO BREAK DOWN YSZ AND NiO PARTICLES TO CONTROL PARTICLE SIZE..........43

TABLE 3.1 PARTICLE SIZES OBTAINED WITH THE SPECIFIC MILLING TIMES, USING THE BALL MILLING TECHNIQUE FOR YSZ SINTERED AT 1100 °C..........72

TABLE 3.2 PARTICLE SIZES OBTAINED WITH THE SPECIFIC MILLING TIMES, USING THE BALL MILLING TECHNIQUE FOR YSZ SINTERED AT 1400 °C..........74

TABLE 3.3 PARTICLE SIZES OBTAINED WITH THE SPECIFIC MILLING TIMES, USING THE BALL MILLING TECHNIQUE FOR NiO..........76

TABLE 3.4 PARTICLE SIZES OBTAINED WITH THE SPECIFIC MILLING TIMES, USING THE CENTRIFUGAL MILLING TECHNIQUE FOR YSZ SINTERED AT 1400 °C...79

TABLE 4.1 ACTIVE THICKNESS ANODES WITH ASSOCIATED RESISTANCES..........109

TABLE 6.1 APPEARANCE OF THE ANODE STRUCTURE DEPENDENT SECTION OF THE IMPEDANCE SPECTRA AND EQUIVALENT CIRCUITS AND SELECTED N-VALUESFOR EACH ARC. α DENOTES THE HIGH FREQUENCY ARC, WHERE TWO ARCS ARE REQUIRED TO OBTAIN ACCEPTABLE FITS..........155

TABLE 6.2 THERMAL ACTIVATION ENERGY,E, AS EVALUATED FROM LINEAR REGRESSION IN AN ARRHENIUS PLOT, E_l, CORRESPONDING TO R_l, WHEREAS E_α AND E_β CORRESPOND TO THE α AND β ARC, RESPECTIVELY..........158

TABLE 6.3 HYDROGEN PARTIAL PRESSURE DEPENDENCE AS EVALUATED FROM LINEAR REGRESSION OF DOUBLE LOGARITHMIC PLOTS, FIGURES 6.13, 6.14 AND 6.15. M_l CORRESPONDS TO R_l, WHEREAS M_α AND M_β CORRESPOND TO THE α AND β ARC, RESPECTIVELY..........161

TABLE 6.4 STEAM PARTIAL PRESSURE DEPENDENCE AS EVALUATED FROM LINEAR REGRESSION OF DOUBLE LOGARITHMIC PLOTS, FIGURES 6.16, 6.17 AND 6.18. M_l CORRESPONDS TO R_l, WHEREAS M_α AND M_β CORRESPOND TO THE α AND β ARC, RESPECTIVELY..........163

TABLE 7.1 TABLE OF THE EXPERIMENTAL MATRIX SHOWING ANODE SAMPLES TO BE FABRICATED..........178

Chapter One

1. Introduction and Literature Review

1.1 Introduction

A fuel cell is a device for converting the chemical energy of a fuel such as H_2, CO, CH_4 directly into electrical energy[1]. The fuel cell operates with greater efficiency than that of conventional electric power generators, with the added advantage of lower polluting emissions.

All fuel cells use a fuel and an oxidiser which are consumed during their operation to produce exhaust products with the creation of electrical energy. The fuel is consumed at the anode and the oxidant is consumed at the cathode.

Over the last 25 years, a number of different fuel cell concepts have been developed[2]. They are categorised according to the type of electrolyte used in the cell. There are five main types of fuel cells listed in order of operating temperature:

(1) Polymer Electrolyte Fuel Cell (SPFC) 80 °C,
(2) Alkali Fuel Cell (AFC) 100 °C,
(3) Phosphoric Acid Fuel Cell (PAFC) 200 °C,
(4) Molten Carbonate Fuel Cell (MCFC) 650 °C,
(5) Solid Oxide Fuel Cell (SOFC) 1000 °C.

1.2 Introduction to the Solid Oxide Fuel Cell

The solid oxide fuel cell is an all solid-state (fuel) cell consisting of two porous ceramic electrodes separated by a dense oxide ion conducting ceramic electrolyte. The cell, which usually operates at 1000 °C, combines fuel gas with oxygen to produce a voltage of approximately 0.5-1.0 V. In order to utilise such small voltages, many cells are put together to produce stacks, with common fuel and air manifolds. The stack can then be coupled to a fuel processor to control fuel gas composition, DC-AC converters, heat exchangers and equipment for controlling gas flow, temperature and electrical load; forming a SOFC system. The hot exhaust from a SOFC stack may be used in a 'bottoming cycle', such as a gas or steam turbine or in co-generation applications. The working principles of the SOFC are shown in figure 1.1.

In SOFCs, the oxidant[3] is passed through the cathode where it gains electrons forming oxygen ions, O^{2-}. These ions are transported through the electrolyte, to the anode, where the oxygen ions react with hydrogen to produce water (exhaust product) and release two electrons per molecule of water.

There are six fundamental processes involving mass transport in the SOFC:

(1) An oxidant gas (O_2, air or similar) is diffused into the cathode of the SOFC.
(2) Charge transfer occurs at the cathode/electrolyte interface. O_2 is adsorbed onto the interface in the form of oxygen ions, O^{2-}ads.
(3) Diffusion of the O^{2-}_{ads} occurs through the electrolyte via a vacancy mechanism towards the anode, due to the lower partial pressure of oxygen on the anode side of the fuel cell.
(4) Diffusion of the fuel gas (H_2, CO, CH_4) occurs through the anode to the triple phase boundary (TPB-anode/electrolyte/fuel)
(5) Oxidation reaction of the fuel gas at the TPB to yield exhaust products.
(6) Diffusion of the exhaust products through the anode to waste.

The main advantages of SOFC technology are the potential for high electrical efficiencies and low emissions of SO_2 and NO_x. To date, only demonstration systems have been constructed, although a 100 kW stack has been produced[4]. This means that a significant amount of materials research and development is still needed before multi-megawatt SOFC power plants can be built by mass production in a manner which is competitive with other power plant technologies.

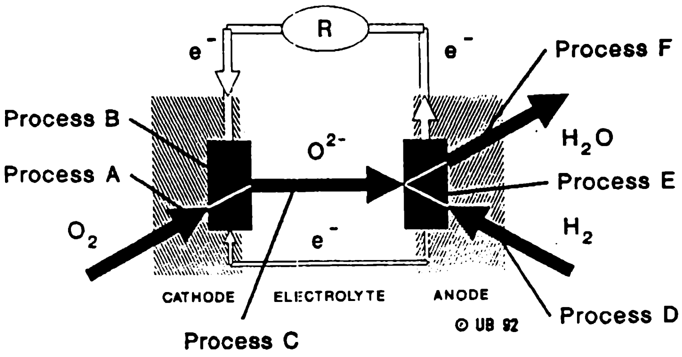

Figure 1.1. Schematic diagram showing the mass transport processes involved in a SOFC[3].

1.3 Solid Oxide Fuel Cell Components

1.3.1 Requirements

A SOFC is comprised of four essential components: the electrolyte, the anode, the cathode and the interconnect. Each of these components has a different function to perform, but some properties of the materials must be similar to ensure compatibility.

Each material must be stable over the entire temperature range from room temperature to sintering temperature. This is especially relevant for monolithic designs where all the fuel cell components are co-sintered. Thus, a phase transformation from one crystal structure to another cannot be tolerated if the transition involves a change in volume, since the SOFC would be destroyed. It is necessary for each material to have a similar coefficient of expansion in order to avoid cracking of the ceramic materials when increasing from room temperature to operating temperature, up to 1000 °C. Also, the components in direct contact with each other should not react chemically and the electrical conductivity of the electrodes and interconnect should be as high as possible, while the electrolyte needs high oxygen ion conduction and negligible electronic conduction[5].

Economically, easily fabricated, low cost materials with relatively simple manufacturing processes must be used to provide a commercially viable energy production option.

1.3.2 Electrolyte

A SOFC electrolyte must be a good ionic conductor and a good electronic insulator. It must be chemically stable over a wide temperature range from room temperature to the sintering temperature used in its manufacture, and also over a wide range of oxygen partial pressures; one atmosphere on the cathode side to 10^{-24} atmospheres on the anode side[5].

Most SOFC systems have been developed using yttria stabilised zirconia (YSZ), a solid solution of Y_2O_3 (8-9 mol%) in ZrO_2. The addition of the yttria stabilises the cubic structure of ZrO_2 from room temperature to its melting point and also considerably increases the ionic conductivity[5]. Figure 1.2 illustrates the fluorite (cubic) structure of stabilised YSZ.

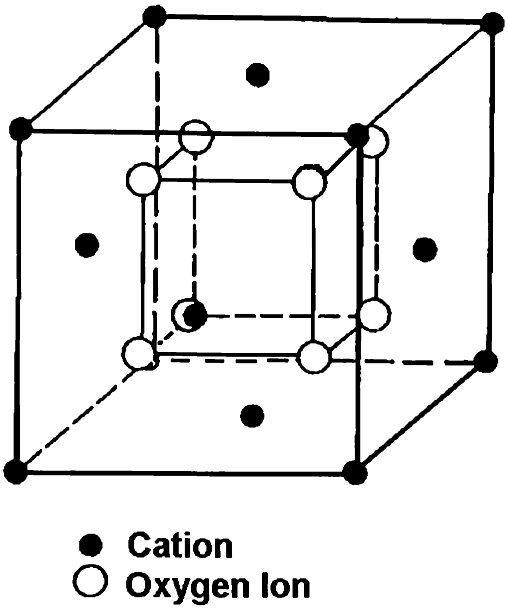

Figure 1.2 Diagram of the crystal structure of a fluorite type electrolyte[6].

Addition of an aliovalent ion into the ZrO_2 generates a high oxygen ion vacancy concentration, which is conducive to high ionic conductivity. This is shown in Kröger-Vink notation[7](see Appendix 1):

$$Y_2O_3 \rightarrow ZrO_2 + 2Y_{Zr}^{-} + V_o^{\cdot\cdot} + 3O_o^{x} \qquad \textbf{Equation 1.1}$$

where Y_{zr}^{-} is a Y^{3+} on a Zr^{4+} site, $V_o^{\cdot\cdot}$ is an oxygen vacancy and O_o^{x} is an occupied oxygen vacancy. The migration of the oxygen ion defects (interstitial or vacancy) provide the mechanism for oxygen ion transport. For the YSZ system, the ionic conductivity over a wide range, is independent of oxygen partial pressure (pO_2) over several orders of magnitude. Varying the oxygen partial pressure varies the type of conductivity. At low pO_2 the following defect equilibria exists:

$$O_o^x \rightarrow V_o^{\cdot\cdot} + \frac{1}{2}O_{2(g)} + 2e^-$$

Equation 1.2

and the equilibrium constant,

$$k = [V_o^{\cdot\cdot}][n^2][pO^{\frac{1}{2}}]$$

Equation 1.3

where n = concentration of electrons. If $[V_o^{\cdot\cdot}]$ is large and constant, then equation 1.3 becomes:

$$n = pO_2^{\frac{-1}{4}}$$

Equation 1.4

that is, electronic conduction (n-type) dominates. At high pO_2, the defect equilibria exists as:

$$\frac{1}{2}O_2 \rightarrow O_i^{=} + 2h^{\cdot}$$

Equation 1.5

and the equilibrium constant

$$k = [O_i^{=}]p^2 / pO_2$$

Equation 1.6

where $h^{\cdot}$ signifies an electron hole, p is the concentration of electron holes and $O_i^{=}$ is an oxygen interstitial. If $[O_i^{=}]$ is large and constant, then equation1.6 becomes:

$$p = pO_2^{\frac{1}{4}}$$

Equation 1.7

that is, electron hole (p-type) conductivity dominates. At an intermediate pO_2 there is negligible n or p effects and conduction is predominantly ionic[8]. One of the criteria for the electrolyte is that the ionic transport number must be greater than 0.99, which means that greater than 99% of the electrical conduction of the electrolyte material is ionic. This is shown in figure 1.3 as the horizontal region in the graph.

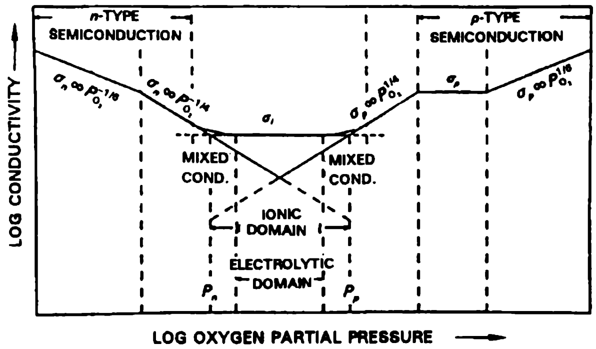

Figure 1.3 Variation of electrical conductivity as a function of oxygen partial pressure for a MO_2-B_2O_3 system[6].

1.3.3 Cathode

The cathode, or air electrode, must be stable in oxygen at temperatures up to 1000 °C, and be chemically and dimensionally stable during fabrication. Performance requirements include high electronic conductivity, a suitable thermal expansion, moderate cost, simple manufacture and good catalytic activity towards oxygen reduction[9].

The cathode is usually based upon the $LaMnO_3$ perovskite structure doped with M typically Sr or Ca, of the general formula $La_{1-x}M_xMnO_3$ where x is typically 0.1 to

0.3. The cathode is a p-type electronic semiconductor and is usually approximately 70 % theoretical density structure to permit rapid diffusion of the air or oxygen to the TPB. Figure 1.4 shows the structure of the $LaMnO_3$ perovskite.

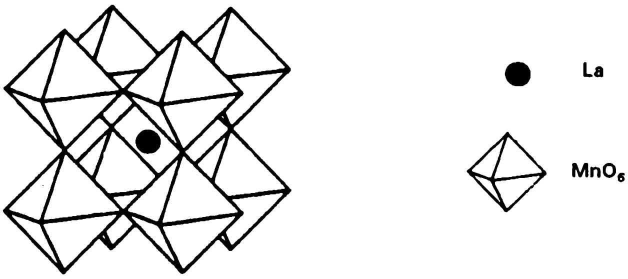

Figure 1.4 Perovskite structure of $LaMnO_3$[6].

The primary design problems of the SOFC system lie with the cathode. Much of the cell resistance and high electrode overpotential occur at the cathode. The electronic conductivity of doped $LaMnO_3$ is rather low at 100-200 Scm^{-1} [5]. However, doped $LaCoO_3$ is also being tested as a cathode material and its advantages include a higher electronic conductivity (1000 Scm^{-1} at 1000 °C), higher ionic conduction (0.8 Scm^{-1} at 900 °C) and very good electrocatalytic activity towards oxygen reduction. The disadvantages are a much higher coefficient of expansion and a high reactivity with YSZ[5].

1.3.4 Interconnect

The purpose of the interconnect or bipolar plate is to separate two adjacent cells, thereby separating the oxidant gas and the fuel gas, and also to act as a current collector. The individual cells can then be stacked in series or parallel (or a combination of both) to produce a workable voltage. The special requirements of the interconnect are that it should be a good electronic conductor and a good ionic insulator. It must be stable in both oxidising and reducing atmospheres at the operating temperature of the SOFC, and have a thermal expansion coefficient that closely matches the other components of the cell. It must also be chemically non-reactive with other cell components and be produceable as a thin gas-impervious layer. Figure 1.5 shows the interconnect in a fuel cell stack.

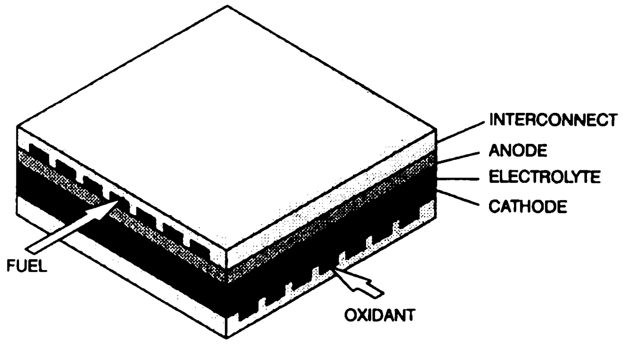

Figure 1.5 Flat-plate SOFC design showing the design of the interconnect[6].

The most satisfactory material developed to date is based upon the electronically conducting lanthanum chromite perovskite structure doped with either calcium or strontium on the A-site. Several researchers are working to produce metallic interconnects[10]. The disadvantage with metallic interconnects is that besides some precious metals, only expensive, high melting point Inconel materials could be used. If the operating temperature could be lowered to about 850 °C, stainless steels could be used, which develop a passive layer of Cr_2O_3, which is stable in air[5].

1.4 Anode Systems

1.4.1 Introduction

Currently there are two types of anode being investigated. These are a two-phase composite anode and a single phase mixed ionic/electronic conducting anode[11]. The former type usually consists of a ceramic phase (YSZ) and a metallic phase. The ceramic component ensures a similar thermal expansion coefficient to the electrolyte to reduce thermal mismatch at the operating temperature of 1000 °C. The ceramic phase also increases the triple phase boundary (TPB) between the YSZ and the metallic phase, thus increasing the performance of the cell. The metallic component has the function of providing the electronic pathways, and high catalytic activity towards fuel oxidation.

The mixed ionic/electronic conducting anodes usually have a perovskite-based structure with a general formula ABO_3. The advantage of the mixed conductors is that the anode oxidation reaction can occur over the entire surface of the material, instead of just at the TPB, as shown by the cermet anodes. This greatly increases the active reaction area thereby increasing anode performance. Figure 1.6 illustrates the concept of the active reaction area of the TPB, for a cermet anode (a), as opposed to the active reaction area for a mixed ionic/electronic conducting anode material (b).

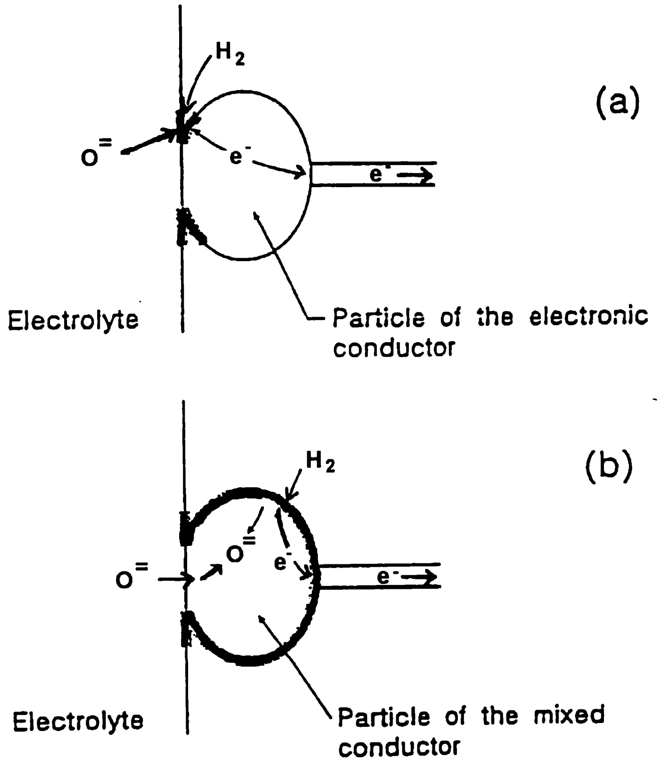

Figure 1.6 Schematic diagram of (a) the standard electronically conducting anode and (b) the mixed ionic/electronic conducting anode[11].

1.4.1.1 Materials

1.4.1.1.1 Cermet Anodes

Due to the reducing conditions of the fuel gas, metals can be used as SOFC anode materials. Since the composition of the fuel changes during the operation of the cell, suitable metals must be non-oxidised not only at the fuel inlet conditions, but also at the more oxidising conditions of the fuel outlet.

At the 1000 °C operating temperature of the YSZ-based SOFCs, suitable metals are limited mainly to nickel, cobalt and noble metals. Nickel is most commonly used due to its high electrocatalytic activity towards hydrogen oxidation and low cost when compared to cobalt, palladium and platinum for example. The SOFC anode is commonly made from YSZ and NiO powders. The NiO is reduced *in-situ* to nickel metal when exposed to the fuel in the cell.

Cobalt is another suitable anode material that has been used in SOFCs, since the metal can withstand the fuel environment and can remain non-oxidised. Compared with nickel, cobalt has the advantage of high sulphur tolerance; however, it is not commonly used due to its higher cost. Also, the oxidation potential of cobalt is higher than that of nickel, thus producing a less complete fuel combustion[8].

Recently, ruthenium/YSZ cermets have been tested as promising anode materials. Ruthenium has the advantage of better resistance to sintering and higher reforming activity. Sasaki *et al.*[12] reported that for a ruthenium anode, a maximum power density of 1550 W/cm^2 was achieved, which is about 8 times that of a standard cell.

1.4.1.1.2 Mixed Ionic/Electronic Conducting Anodes

Other materials such as conducting oxides have been used as anode materials[13,14]. Their ability to maintain their structure in the presence of a large concentration of defects makes them attractive since they can possess high ionic and/or electronic conductivity. By doping the perovskite structure, the degree of mixed conduction may be varied and the total conductivity increased. The main criteria for a perovskite-based anode is the ability to maintain considerable conductivity at very low oxygen partial pressures.

One particular system ($CaFe_xTi_{1-x}O_{3-\delta}$) has been studied with a view towards using it as a SOFC anode. George and Grace[15] studied point defects in a single crystal of $CaTiO_3$ and Balanchandran *et al.*[16] measured conductivities in undoped, donor-doped (La) and acceptor-doped (Al,Cr) polycrystalline $CaTiO_3$. Another ceramic material for the replacement of the Ni/YSZ system is CeO_2.

More than 30 years ago Takahashi[17] demonstrated the superior anodic kinetics associated with reduced CeO_2 due to the presence of relatively high electronic and ionic conductivity. Steele *et al.*[18] reported that cells incorporating CeO_2 anodes could directly, electrochemically, oxidise dry methane, as the presence of mobile lattice oxygen reduced the rate of carbon deposition. However, CeO_2 anodes have not replaced Ni/YSZ based anodes because of the relatively low levels of electronic conductivity and the large lattice expansion associated with the loss of oxygen under anodic conditions which can lead to the anode spalling off the substrate.

Complete oxidation of dry methane has been attempted by Baker *et al.*[19] using a perovskite-based material, $La_{0.8}Ca_{0.2}CrO_{3-x}$. It was discovered that both complete oxidation of methane and surface methane dissociation occur at temperatures above 500 °C with negligible carbon deposition.

Other attempts have been made with materials such as $Ti_{0.97}Nb_{0.03}O_2$, $Mg_{0.3}Nb_{0.1}Ti_{2.6}O_5$, $Sm_2Ti_{1.9}Nb_{0.1}O_7$ and $CrTi_2O_5$[20,21,22,23]. Unfortunately, no materials have performed satisfactorily over the entire oxygen partial pressure range that the anode is subjected to, with adequate electronic conductivity.

1.4.2 Anode Requirements

The anode material is employed as a catalyst not only for the oxidation of fuels but also for steam reforming of hydrocarbons, and as a current collector. In addition to these properties, the anodic materials are required to possess an appropriate thermal expansion coefficient and be inert towards the YSZ electrolyte. As such, nickel has been the most popular anode material. The material of choice at this stage is the Ni/YSZ cermet anode. Figure 1.7 illustrates the microstructure of a sintered Ni/YSZ anode, showing the intimate contact between particles necessary for good anode performance.

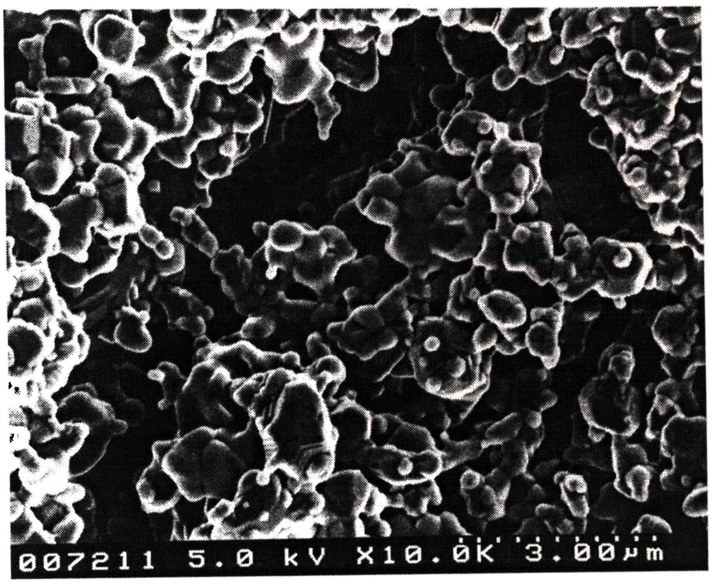

Figure 1.7 Microstructure of a sintered Ni/YSZ cermet anode illustrating intra-particle connection and porosity.

At present, a mixture of 40-50 vol% Ni in a matrix of YSZ is used, having particle sizes in the range of 1 µm[24]. This produces a long triple phase boundary (TPB) per unit area and also adequate percolation for electronic conductivity through the Ni phase. Ni is a good electrocatalyst for the oxidation of H_2 and CO but not for CH_4. If CH_4 is oxidised with a Ni catalyst, carbon deposits are formed on the catalyst, thus destroying it. However, nickel is an excellent catalyst for steam reforming according to the equation:

$$CH_4 + H_2O \rightarrow CO + 3H_2 \qquad \textbf{Equation 1.8}$$

Thus, internal reforming can be carried out directly on the anode using steam[25].

1.4.3 Structure/Morphology

The morphological requirements for the anode are:

(1) Large triple phase boundary (reaction area),
(2) Good contact between the anode layer and the electrolyte,
(3) Correct metal/ceramic particle size ratio,
(4) Correct porosity,
(5) High ionic and electronic conductivity (percolation of both phases),
(6) Long term stability of the microstructure.

The composite Ni/YSZ cermet anode has been widely studied as an anode component for the SOFC. It consists of an intimate mixture of NiO and YSZ particles with a specific microstructure, optimised to enhance the TPB and percolation of the two phases. Figure 1.8 shows a schematic diagram of the ionic and electronic pathways in a Ni/YSZ cermet, including the TPB points.

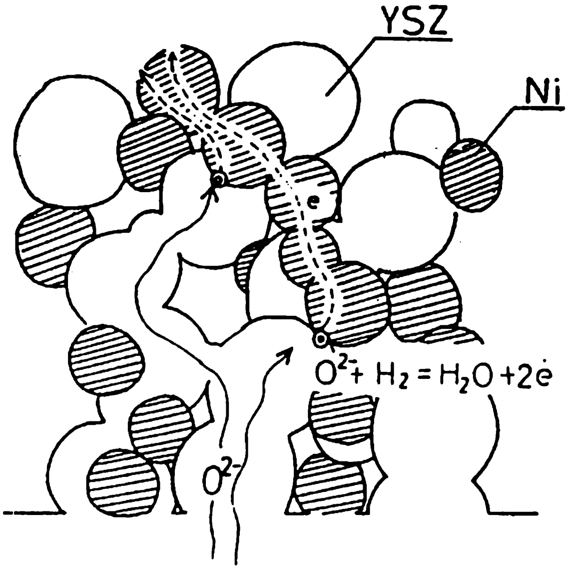

Figure 1.8 Schematic diagram of the electronic and ionic pathways in a Ni/YSZ cermet showing the triple phase boundary points (TPB)[29].

The percolation threshold for the conductivity is approximately 30 vol% Ni[26]. This percolation behaviour is explained by the presence of two conduction mechanisms through the cermet: an electronic path throught the Ni phase, and an ionic path through the YSZ phase. Below 30 vol% Ni, the conductivity of the cermet is similar to that of YSZ, indicating an ionic conduction phase through the YSZ. Above 30 vol% Ni, the conductivity is approximately three orders of magnitude higher, corresponding to a change in mechanism to electronic conduction through the nickel phase.

For optimum performance and long term stability, it is necessary to strictly control the anode morphology, which reduces the effects of Ni particle agglomeration and hence the loss of electron percolation[27]. It has been shown by Saito[28], Kawada *et al.*[29,30] and Bagger[31] that the particle size and particle size ratio of Ni/YSZ is very important for the performance of a SOFC anode.

Using a computer model, Costamagna *et al*[32], have shown that an optimum performance is obtained for a composition near to the percolation limit of the electronic conducting phase and that the ratio of particle diameters strongly influences the electrode resistance. Saito[28] suggests that a YSZ particle size of 0.5 µm was suitable for maintaining electrode structure and ionic conductivity. The small particle size of the YSZ inhibited the agglomeration of the Ni particles at the operating temperature of 1000 °C, thus maintaining a high Ni surface area and good electronic percolation. A high surface area also reduces the anode interfacial resistance and therefore increases the TPB length, which is essential for high performance.

Dees *et al.*[33] and Kawada *et al.*[29] determined that increasing the YSZ particle size, while maintaining a constant Ni particle size, increased the conductivity because as the YSZ particle size is increased, the Ni-Ni particle contact becomes more intimate. Bagger[31] explained that pre-calcining a certain percentage of the YSZ component could provide for a broader particle size distribution. Thus an improved packing efficiency, and hence an increase in conductivity of the anode, would occur.

The improved packing of the cermet particles inhibited Ni particle agglomeration and thus reduced the loss of percolation in low Ni vol% anodes.

It has been suggested[34] that a good cermet anode should consist of a matrix of small YSZ particles (<1 µm) with Ni particles of a similar size to ensure a large TPB, combined with a significant volume of larger YSZ particles (5-10 µm) to form major pathways for ionic transport. It is then assumed that the electrochemically active layer of the anode will have a significant thickness. Work of this nature has been performed by Itoh *et al.*[35] to increase the long-term stability of the anode. This anode had a coarse structure of YSZ (27 µm), sintered together with fine YSZ (0.6 µm).

It has been stipulated by Bossel[3], that an electrode must contain more than 30% porosity. A range of porosities were used by Saito[28] to investigate the effect of porosity on anode efficiency. Porosity values from 15 % to 35 % were examined and it was concluded that the anode interface resistance was unaffected by the variation.

1.4.4 Fabrication

There are many techniques for fabricating a suitable electrode. Typical processes include, but are not limited to: slurry coating, wet powder spraying (WPS®), EVD, plasma spraying, tape casting and electroless deposition.

The physical properties of the raw materials and the applied manufacturing technique, have a strong influence on the electrochemical properties of the electrode in the final cell composition. Parameters including the particle morphology of the powder, and porosity of the sintered electrode, influence the electrical conductivity of the electrode structure. Other parameters such as sintering temperature, and the sintering time of the electrode, have an effect on the adherence of the electrode to the electrolyte.

1.4.4.1 Slurry Coating

Slurry coating is probably the most simple method of producing an anode for a SOFC. It is an economically favourable method that has been shown to give reproducible results in terms of porosity and layer thickness[36]. A slurry of the cermet powder is produced, and the sample to be coated is dipped into the cermet slurry. A thin layer of the slurry adheres to the sample, thus forming the electrode. It is imperative that the rheological properties of the slurry are monitored closely. Particle size, binder quantity, dispersant and viscosity must all be optimised to produce a satisfactory slurry, capable of performing the rheological requirements necessary to deposit the desired cermet structure.

Chou *et al.*[36] produced a slurry from Ni powder (60 wt%), YSZ powder and a polyvinylacetate (PVA) solution. The slurry was poured over the electrolyte and allowed to run off, leaving a thin layer of the slurry adhering to the electrolyte surface. This was then dried and sintered at 1100 °C for 17 hours under an atmosphere of N_2 with 2 $\%H_2$, followed by natural cooling under an atmosphere of 5 $\%H_2$ in N_2. At the end of the sintering step, a porous layer of Ni adhering to the electrolyte was obtained. The electrolyte/electrode was then introduced into a vacuum infiltration chamber which was maintained at a pressure of 5 torr and a YSZ slurry containing 30 vol% water and 3 mL of (4 N) nitric acid was introduced in order to completely immerse the zirconia in the slurry. The vacuum was then released and the YSZ slurry was allowed to infiltrate into the pores of the Ni structure. The sample was then sintered at 1200 °C for 7 hours to produce the cermet.

1.4.4.2 Wet Powder Spraying (WPS®)

Wet Powder Spraying involves mixing a slurry of the appropriate components (powder, solvent binder) with a specific viscosity, and incorporating this mixture into a spray gun or similar appliance, and applying an even coat of the anode powder onto the surface of the electrolyte. It is a relatively simple process, nevertheless it can be applied to a variety of materials to produce thin coatings.

Bagger *et al.*[31] used this method to produce anodes posessing firm adherence to the electrolyte and high electronic conductivities at room temperature, after sintering at 1300 °C. Impedance spectroscopy measurements on the anodes showed excellent electrochemical performance. It was also noted that milling/mixing techniques, and the selection of organic constituents (binders), were important in controlling dispersion and packing of the green powder, on the surface of the electrolyte, prior to sintering.

1.4.4.3 Electrochemical Vapour Deposition

The electrochemical vapour deposition (EVD) process is used extensively in the manufacture of Westinghouse seamless tubular design SOFC[8]. The anode is applied by dipping the cell in a Ni slurry. The anode covers the entire electrolyte surface, except around the interconnect, to avoid short-circuiting. The anode is then infiltrated with YSZ into the Ni matrix, using the EVD technique. The YSZ acts as a sintering inhibitor and maintains a porous, structurally stable anode. The principle of the process is shown schematically in figure 1.9.

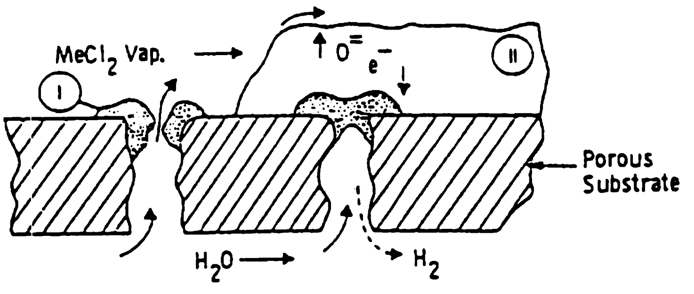

PHASE I PORE CLOSURE BY CVD

$MeCl_2 + H_2O = MeO + 2\,HCl$

PHASE II SCALE GROWTH BY EVD

$MeCl_2 + O^{2-} = MeO + Cl_2 + 2e^-$

$H_2O + 2e^- = H_2 + O^{2-}$

Figure 1.9 Principle of electrochemical vapour deposition[6].

The process involves growing a dense oxide layer on a porous substrate at elevated temperatures and reduced pressures[37]. In the EVD of components for tubular SOFCs, steam and/or oxygen is fed into the interior of the support tube, while metal chloride vapour, hydrogen and argon are fed to the outside. Hydrogen is used to remove the chlorine formed and argon is used as the carrier gas. The growth of the oxide layer occurs in two stages at temperatures of 1200 °C to 1350 °C and at pressures of 53 to 267 Pa.

Stage (1) The chemical vapour deposition (CVD) process, involving the formation of the oxide compound, takes place according to the following reactions:

$$2MeCl_y + \frac{1}{2}O_2 + yH_2 \rightarrow 2MeO_{\frac{y}{2}} + 2yHCl$$ **Equation 1.9**

This oxide formation closes the pores of the substrate.

Stage (2) The EVD process involves the growth of the oxide scale by reaction of metal chloride with oxygen ions in the oxide. Oxygen ions are transported to the reaction sites by diffusion across the scale.

$$MeCl_y + \frac{1}{2}O^{2-} \rightarrow MeO_{\frac{y}{2}} + \frac{1}{2}Cl_2 + ye^-$$ **Equation 1.10**

$$H_2O + ye^- \rightarrow \frac{1}{2}H_2 + \frac{1}{2}O^{2-}$$ **Equation 1.11**

The scale growth-rate of the EVD material can be varied by temperature, pressure and chloride concentration, and can deposit between 0.5 and 2 µm/min.

1.4.4.4 Plasma Spraying

Plasma spraying is a process in which the desired coating material, in powder or rod form, is heated above its melting point while being accelerated by a carrier gas stream through an electric arc. The molten powder is directed at the substrate, and on impact, forms a coating on the substrate surface.

The cathode, electrolyte and the anode[38] can all be deposited using the plasma spray method. The anode powder (NiO/YSZ) is fed into the plasma arc producing a layer 50 to 100 µm thick, utilising an acetylene-flame-spraying process. Figure 1.10 shows a schematic representation of a typical plasma spray gun.

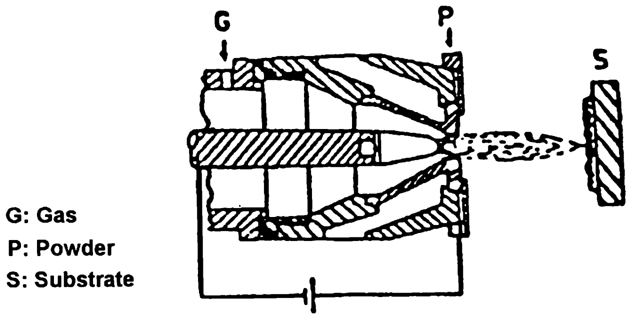

Figure 1.10 Typical plasma spray gun[6].

1.4.4.5 Tape Casting

Tape casting[39] has been developed for forming large-area, thin, flat ceramic layers for SOFCs. Figure 1.11 is a schematic diagram of a tape casting system.

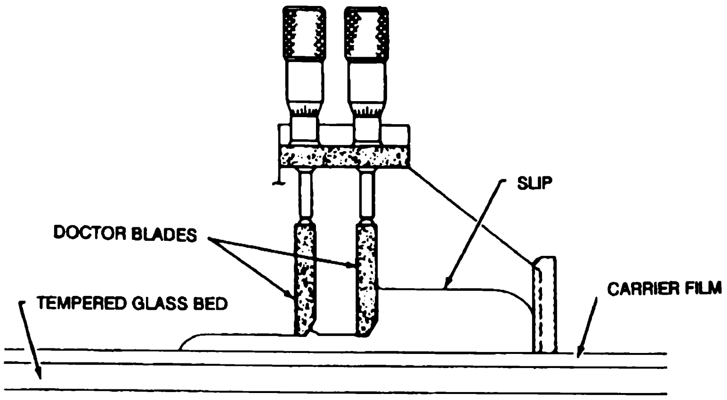

Figure 1.11 Schematic diagram of a tape casting system[6].

The tape casting process begins with a slip of ceramic materials dispersed in a liquid. The liquid contains dissolved organic binders (polyvinylbutyral, methyl cellulose, butylmethacrylate) and plasticisers (ethylene glycol, dibutyl phthalate, diethyloxalate). The slip is spread onto a flat surface and the thickness is controlled by a doctor blade system; the solvents are then allowed to evaporate. Multi-layer tapes are fabricated by sequentially casting one layer on top of another. The resulting tape, which is flexible, can be stripped from the casting surface, cut to size and formed prior to sintering.

1.4.5 Electrical Conductivity

The electrical conductivity of the Ni/YSZ cermet is dependent on the content of Ni. This Ni content dependency has been described by percolation theory and is shown in figure 1.12.

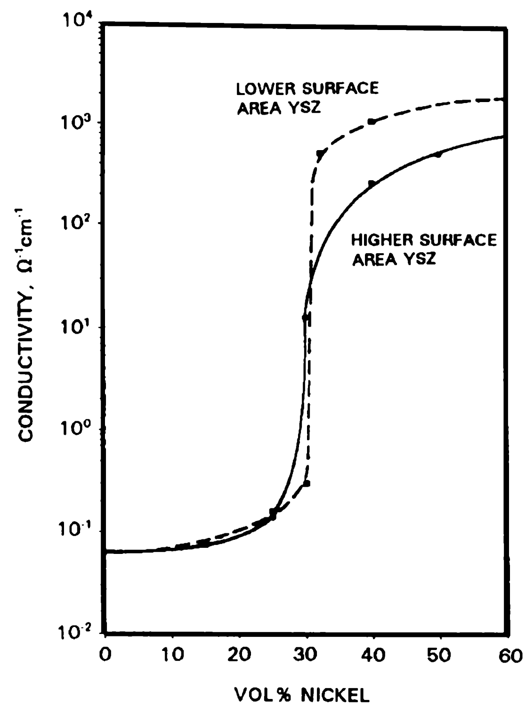

Figure 1.12 Conductivity of a Ni/YSZ cermet at 1000 °C as a function of nickel content[6].

There is an abrupt increase in conductivity at approximately 30 vol% Ni. This can be explained by the presence of the two conduction mechanisms inherent in the cermet. Below 30 vol% Ni, the predominant conduction mechanism is ionic, which occurs through the YSZ phase. Above 30 vol% Ni, percolation of the Ni phase exists and therefore the predominant conductivity is electronic and increases by three orders of magnitude.

The electrical conductivity of the cermet is also dependent on the microstructure. High electronic conductivity is relatively easy to achieve if the YSZ phase is coarse or a high volume percentage of Ni is used. Coarse YSZ can form a stable matrix to increase long-term stability and can also allow an increase in Ni-Ni particle contact and therefore a higher degree of electronic conduction. However, a coarse YSZ phase can lead to an increased rate of anode degradation when there is no fine YSZ present to inhibit Ni sintering and agglomeration.

A high Ni content can create problems with respect to adhesion. Since Ni does not wet YSZ, adhesion to the electrolyte is entirely dependent on the YSZ in the cermet. If there is insufficient contact between the YSZ in the cermet and the electrolyte, caused by a high Ni content, then spalling of the anode layer can occur.

As the Ni content is increased to provide better electronic conduction, a problem can arise concerning the thermal expansion coefficient. The thermal expansion coefficient increases with increasing Ni content and over a certain volume percentage of Ni, the thermal mismatch between the anode layer and the electrolyte will be too great and the cell will crack under thermal gradients. This suggests that the optimum anode would consist of a minimum amount of Ni to allow electronic conductivity, together with a certain amount of fine YSZ to inhibit sintering/agglomeration of the Ni and a stable matrix of coarse YSZ for long term stability. Figure 1.13 clearly illustrates the two YSZ particle sizes present in the anode layer.

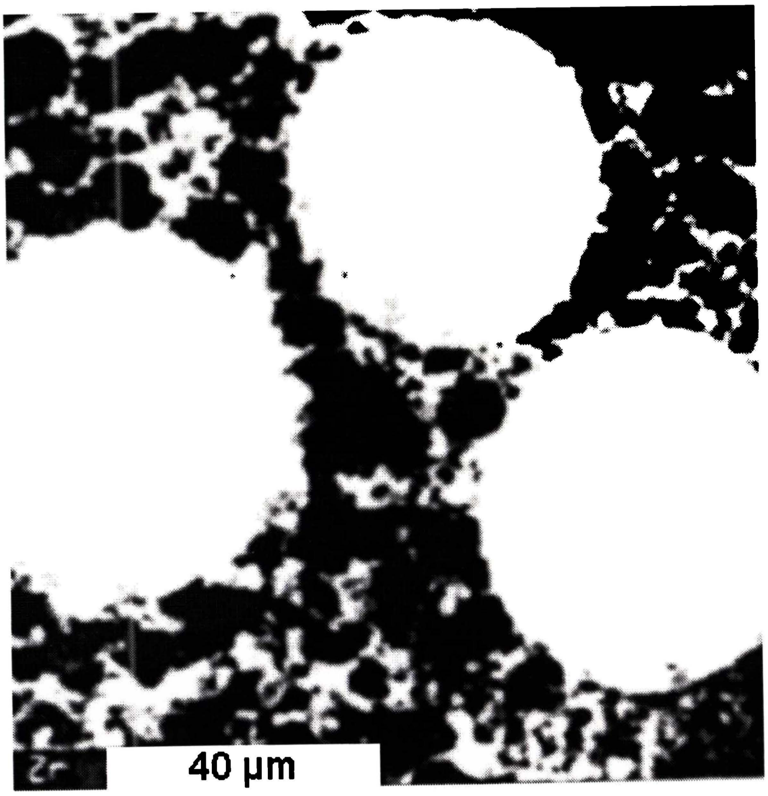

Figure 1.13 Secondary electron image (SEI) of a Ni/YSZ cermet showing the elemental distribution of the two sizes of white YSZ particles and dark NiO particles[44].

1.4.6 Thermal Expansion

The thermal expansion of the anode must be similar to that of the other components to avoid cracking and spalling during operation and thermal cycling. The anode has a higher thermal expansion coefficient compared to the other components of the fuel cell due to the metallic (Ni) content. The thermal expansion of the Ni/YSZ cermet increases with increasing Ni content as shown in figure 1.14.

The electrolyte (8 mol% YSZ) has a thermal expansion coefficient of approximately 10.8 x 10^{-6} cm/cm.K[40], whereas pure Ni has a thermal expansion coefficient of approximately 13 x 10^{-6} cm/cm.K[41]. An anode with 40 vol% Ni has a thermal expansion coefficient of approximately 12 x 10^{-6} cm/cm.K[42].

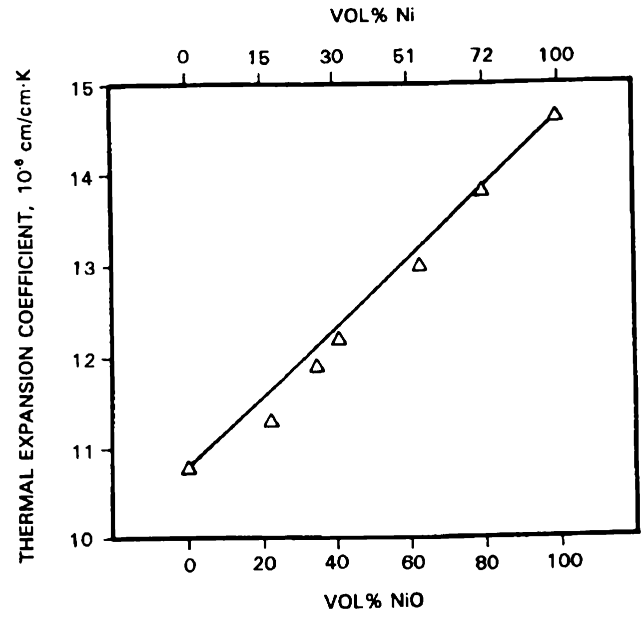

Figure 1.14 Thermal expansion coefficient of the cermet anode as a function of NiO (or Ni) content[6].

1.4.7 Stability

Ni and YSZ are known to be chemically stable in the reducing environment of the anode. There is negligible chemical reactivity towards each other or toward the interconnect at 1000 °C[43]. However, at higher temperatures, NiO can react with $LaCrO_3$ to form phases such as $NiCrO_4$, which is a poor electronic conductor[42].

The major problem with anode stability is the degradation of the cermet structure with time. This is due to Ni sintering at the operating temperature, causing an agglomeration of the fine Ni particles and thus a loss of a percolating metallic phase. This causes a loss of active TPB and leads to a degradation of performance[44,45].

It has been shown that fabricating an anode with a three-dimensional YSZ network greatly supports the anode structure and reduces this sintering effect. A small percentage of fine (<1 μm) YSZ incorporated in the anode has also been shown to reduce the tendency for the Ni particles to agglomerate[45]. The fine YSZ particles inhibit the sintering of the Ni by coming between two Ni particles, thus hindering the bonding (figure 1.15).

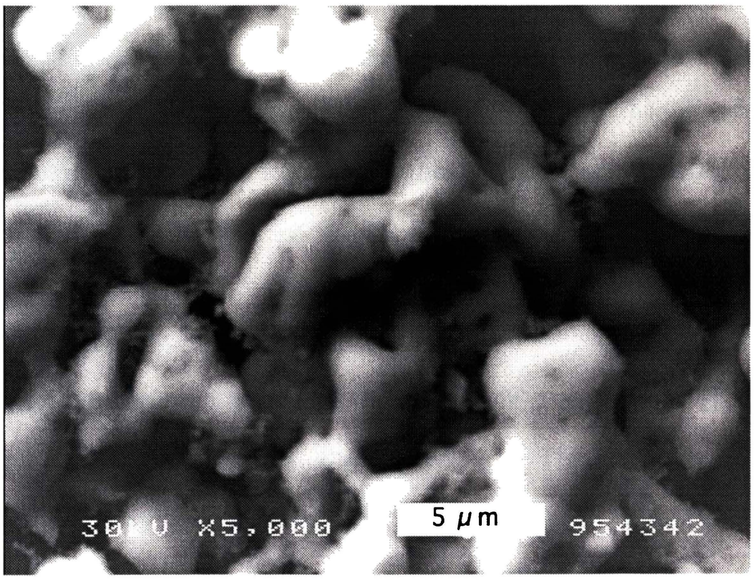

Figure 1.15 Micrograph of 90% Ni/YSZ cermet illustrating the prevention of Ni agglomeration by the pinning effect of the fine YSZ particles.

Ohara *et al.*[46]developed a spray pyrolysis method for producing Ni/YSZ powders. The morphology of the obtained powder consisted of fine YSZ particles dispersed on the surface of NiO particles. It was observed in the final cermet that YSZ particles surrounded the NiO particles, providing a high degree of long-term stability by suppressing the sintering action of the Ni.

Long term stability was improved with a novel anode structure fabricated by Itoh *et al.*[45]. Coarse YSZ particles were described to be essential for the formation of a YSZ frame to reduce volume changes, and alterations in porosity, in the cermet structure during sintering. The addition of fine YSZ was effective in sintering the coarse YSZ particles together to form a rigid matrix. It was stated that the conductivity of the anode depends not only on the Ni content but also on the particle size of the YSZ, and the YSZ mixture ratio (ratio of coarse to fine YSZ).

1.4.8 Kinetics and Mechanisms

At present, the Ni/YSZ cermet is the material known to show the best performance as an anode in a SOFC fuelled by H_2. Intensive work has been carried out to optimise the electrical and structural properties of this material. Most of the work is concerned with increasing the TPB within the cermet, which in turn increases its overall performance as an anode. However, the kinetics and mechanisms involved in the oxidation reaction are still not fully understood.

At the operating temperature of the SOFC (1000 °C), nearly all H_2 molecules are bound to the Ni surface and dissociated into two H_{ads}. The H atoms are bound to the Ni by strong covalent bonds (radius of approximately18 pm). Reaction on the surface of the Ni takes place with other species (OH^-) to reform H_2.

Both Ni atoms, and the adsorbed species associated with the oxidation reaction, are mobile. The high mobility of the Ni particles means that a significant modification of the microstructure can take place at the operating temperature of 1000 °C. This problem becomes even more severe with a very fine particle size, due to the higher degree of agglomeration prevalent with small particle sizes, and therefore long-term stability can be compromised. The high mobility of H_{ads} and large coverage of H_{ads} on the Ni, make it unlikely that this process (H adsorption or H_{ads} diffusion) will be the rate-determining step.

Saito[28] studied the performance of anodes with varying YSZ and Ni particle sizes. The results indicated that it was possible to improve the anode performance by optimising the particle sizes and weight ratios. It was found that YSZ particle size should be less than 1 μm, whereas Ni particle size was less critical. This is evidence to suggest that a fine matrix of YSZ plays an important part in the anode microstructure and would produce a high performance anode as long as the Ni content was sufficient to allow a low electronic resistance.

Van Berkel *et al.*[47] attempted to optimise the anode structure with a large YSZ particle size (10.4 μm) and small Ni (1.2 μm). This was explained by the fact that a high performance anode needs a fine YSZ matrix for high TPB length and also a relatively coarse YSZ structure for efficient, (short path length) ionic conduction. Anodes of this nature have been studied by Itoh *et al.*[45] for the express purpose of pinning the Ni/YSZ structure for long term stability.

Eguchi *et al.*[48] studied the polarisation resistance, Rp, of a Ni/YSZ cermet in a wide range of oxygen partial pressures (10^{-12} - 10^{-20} atm of O_2). The results are shown in figure 1.16 in a semi-log plot.

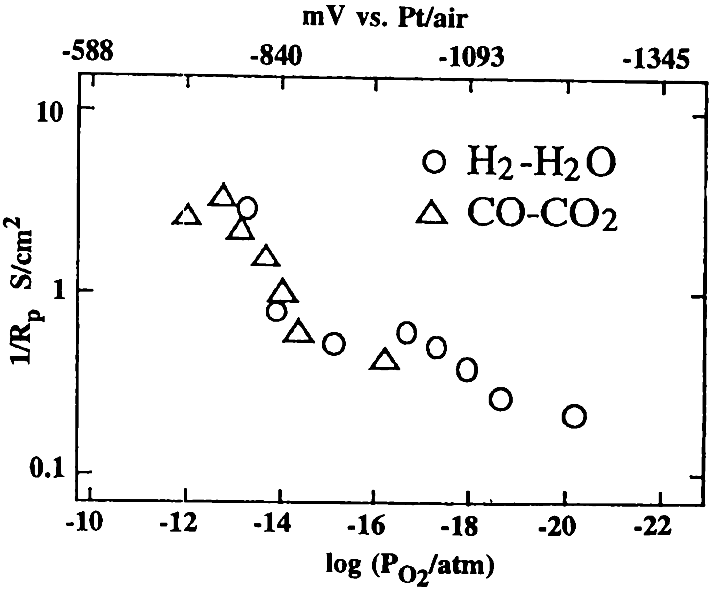

Figure 1.16 Semi-log plot of the polarisation resistance as a function of the log partial pressure of oxygen[49].

The curve revealed two different slopes, which corresponded to two different mechanisms operating at different oxygen partial pressures. In the high partial pressure range, Kawada *et al.*[39] also studied Ni/YSZ cermet anodes in H_2 + H_2O and proposed the following mechanism:

$$O^{2-}_{YSZ} \leftrightarrow O_{ads,Ni} \leftrightarrow +2e^{-} \qquad \text{Equation 1.2}$$

$$H_{2(g)} + O_{ads,Ni} \leftrightarrow H_2O_{(g)} \qquad \text{Equation 1.3}$$

In the low oxygen partial pressure range (10^{-17} - 10^{-20} atm.) Guindet *et al.*[50] found, using a ball shaped electrode, that the current density/potential relationship followed a Tafel type law which was in agreement with Kawada *et al.*[29]. Mogensen and Lindegaard[51] have also investigated the H_2/H_2O electrode reaction on a Ni/YSZ cermet at 1000 °C by means of impedance spectroscopy. Within the range of pH_2 to

pH_2O ratios investigated, two impedance arcs were observed. Figure 1.17 illustrates the typical impedance plot observed.

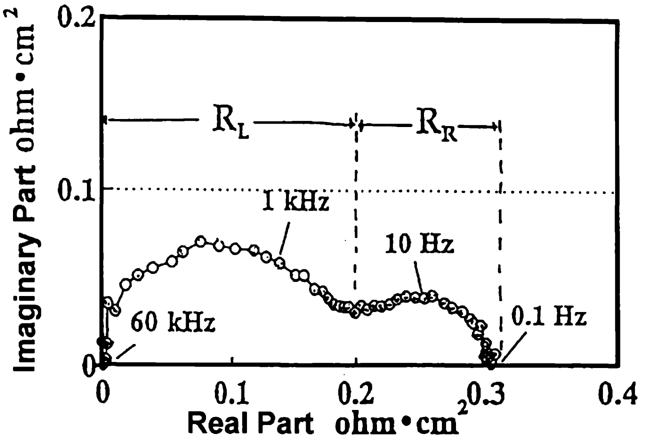

Figure 1.17 Typical impedance plot observed for a Ni/YSZ cermet at 1000 °C by means of impedance spectroscopy[49].

It was determined that Rr was due to a pure chemical reaction; its rate being proportional to a reactant activity involving two electrons. At low pH_2, a reaction order of 1 was observed and at higher pH_2 a reaction order of 2 was observed. A reaction mechanism for the hydrogen oxidation, in the low pO_2 range, was proposed by Mogensen and Lindegaard[51] as given below:

$$H_2 \leftrightarrow 2H_{ads,Ni}$$ **Equation 1.4**

$$2\times(H_{ads,Ni} \leftrightarrow H^{+}_{ads,Ni} + e^{-})$$ **Equation 1.5**

diffusion of $H^{+}_{ads,Ni}$ to Ni/YSZ boundary **Equation 1.6**

$$2\times(H^{+}_{ads,Ni}+O^{2-}_{YSZ}\leftrightarrow OH^{-}_{YSZ})$$ **Equation 1.7**

$$2OH^{-}_{YSZ}\leftrightarrow H_2O+O^{2-}_{YSZ}$$ **Equation 1.8**

R_L is assumed to be due to the proton transfer from the Ni to the YSZ and R_R is taken to be the reaction resistance.

Recently, Mogensen *et al.*[52]studied a number of different Ni/YSZ cermet anode structures in H_2/H_2O in the temperature range 800-1000 °C using impedance spectroscopy and DC electrochemical methods. The electrode performance was correlated to the structure of the cermet as revealed by optical microscopy. Experiments were carried out on both very fine and coarse structures including the limiting case of a Ni point electrode. Three arcs were observed in the impedance spectra. The dependence of the three associated polarisation resistance components on structure, temperature and overpotential was reported and a tentative model for the Ni/YSZ-H_2/H_2O electrode was described (figure 1.18).

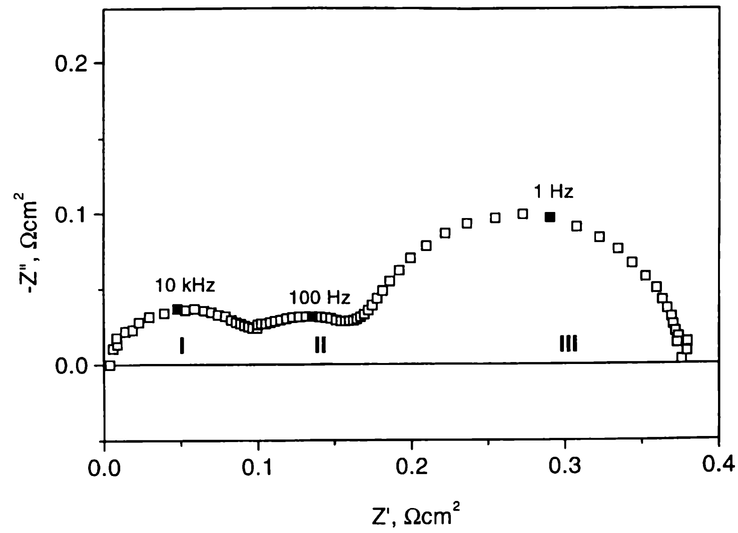

Figure 1.18 Impedance plot of a Ni/YSZ cermet at 1000 °C in H_2 at OCV showing the three arcs relating to the anode reaction.

The results indicated that the high frequency resistance, R_L, was closely related to the structure. This probably reflects the resistance of proton transfer from the nickel surface to the YSZ surface, which should be in inverse proportion to the TPB. For example, a short TPB gives rise to a high R_L. The reaction mechanism proposed by Mogensen and Lindegaard[51] previously, is still valid in light of this new work.

Overall, Mogensen *et al.*[52] have concluded that at least three processes contribute to the polarisation resistance. Those responding at high frequency are dependent on the structure, whereas the low frequency response shows a clear dependence on electrical potential.

Recently, Primdahl and Mogensen[53] studied the low frequency impedance arc obtained for Ni/YSZ anodes. It has been recognised that the magnitude of the low frequency arc is dependent on the test setup geometry and whether the working and reference electrodes are placed in separate or the same atmospheres. When two nominally identical anodes are tested in the two different atmospheric setups (see section 2.10.2), the impedance spectra differ considerably. It has been shown that an impedance spectrum obtained from a two-atmosphere system exhibits three impedance arcs whereas only two arcs appear when a single atmosphere system is used. A comparison of two structurally different anodes, tested in a two-atmosphere setup, exhibited identical arcs at low frequency. Thus the authors concluded that the setup geometry was the cause of the discrepancy in the impedance spectra.

1.4.9 Fuels

1.4.9.1 Types of Fuels

A SOFC can convert several types of fuels to oxidation products and electricity. Besides H_2, CO, CH_4, NH_3 and SO_2 fuels have also been used[8]. In cases where NH_3

or SO_2 fuels are used, the main purpose is to generate HNO_3 and H_2SO_4 products, electricity being the secondary product. In these cases the SOFC is often called an electrochemical reactor[54]. H_2 and CO are fuels which can be directly oxidised in SOFCs with a Ni/YSZ anode.

The main advantage of the fuels H_2 and CO is the low polarisation losses, particularly for H_2 oxidation. However, the opposite is observed for methane, which reacts slowly. This gives rise to high polarisation losses and furthermore CH_4 will precipitate carbon as graphite on the cermet electrode, very quickly destroying it. This means that Ni/YSZ cermets cannot be used for oxidising dry CH_4. Most SOFC developers plan to steam reform CH_4 into CO and H_2, either in an external reformer or *in-situ* inside the stack.

CH_4 has the advantage of being very abundant (natural gas) and there is no loss of entropy during oxidation, due to the fact that the number of molecules before and after oxidation is the same. This can be seen via the following equations:

$$2H_2 + O_2 \rightarrow 2H_2O$$ **Equation 1.9**

$$2CO + O_2 \rightarrow 2CO_2$$ **Equation 1.10**

$$CH_4 + 2O_2 \rightarrow CO_2 + 2H_2O$$ **Equation 1.11**

As the direct electrochemical oxidation of CH_4 seems to be very advantageous, research efforts for finding an alternative anode material are under away. So far, CeO_2 anodes have proved capable of direct oxidation of CH_4 on a small laboratory scale[55].

1.4.9.2 Fuel Reformation

With the present state of SOFC technology, it is not possible to produce commercial quantities (megawatts) of electricity by the direct oxidation of hydrocarbons. The hydrocarbons must first be converted into hydrogen, which can then be utilised by the fuel cell. This conversion can be carried out by steam reforming according to the following reaction:

$$CH_4 + H_2O \leftrightarrow CO + 3H_2 \qquad \textbf{Equation 1.12}$$

Steam reforming of methane is a reversible and endothermic reaction, favoured by a high temperature and low pressure for maximum conversion. At 1000 °C, full conversion of methane is reached at atmospheric pressure.

External reforming is usually necessary if higher hydrocarbons ($>C_2$) are to be used as the SOFC fuel. When external reforming is used, it is necessary to integrate the fuel processing system, and the fuel, in order to utilise the excess heat generated in the fuel cell itself. For SOFC purposes, the obvious way to heat the external reformer is by using the exhaust gas at the anode outlet. A reforming system uses a nickel based catalyst.

Sulphur, in the form of H_2S, is the most common poison for nickel catalysts and must be removed otherwise severe loss of performance will result at the anode. Even low levels (ppm) can result in performance losses, which can only be partially recoverable. The tolerance limit for H_2S in the fuel, for SOFCs, has not been firmly established[8].

Because of the high operating temperature of the SOFC, internal reformation of hydrocarbons is possible. The feasibility of internal reformation in SOFCs has been demonstrated[56]. The heat from the electrochemical reaction is utilised directly thus minimising extra external cooling. By performing internal reforming in the anode chamber, the chemical equilibrium is also adjusted by the consumption of hydrogen, thereby producing a higher conversion of methane. As the reforming reaction is endothermic, steep temperature gradients can form, thus inducing thermal stresses on the stack and shortening stack life.

1.5 Scope of the Research

The research performed in this thesis covers the fabrication and electrochemical testing of Ni/YSZ cermet anodes for solid oxide fuel cells.

Chapter three describes the preparation of the raw materials, including milling and sintering schedules, and particle size studies. Also covered is the fabrication of the anode layers using a wet powder spraying (WPS®) process. A novel microstructure is studied, consisting of coarse and fine YSZ together with NiO for the purpose of producing an anode layer with high electronic and ionic conductivity, and long term stability. The coarse YSZ forms a continuous matrix for the purpose of providing a stable structure for ionic conduction. The fine component of the YSZ provides the sintering ability to bond the YSZ matrix together.

Chapter four concentrates on the electrochemical properties of a number of fabricated Ni/YSZ cermets. The aim of this research was to demonstrate the electrochemically active thickness of a state-of-the-art cermet anode. The anodes were fabricated with varying thicknesses from 3.5 µm to 54 µm and studied using impedance spectroscopy, chronoamperometry and cyclic voltammetry, including polarisation measurements.

Chapter five attempts to relate structure and performance together, to determine what microstructural aspects affect the electrochemical performance. Elements studied include particle size of Ni and YSZ, anode thickness, dependence of partial pressure of hydrogen and partial pressure of steam, thermal activation, microstructure and porosity and polarisation resistance.

Chapter six discusses four types of Ni/YSZ anodes, which were characterised and compared to illustrate similarities and differences, from state-of-the-art cermet anodes to coarse structured cermets to two-dimensional Ni anodes with significantly higher polarisation resistances. The anode structure dependent high frequency part of the impedance spectrum was studied.

1.6 References

---

[1] N.Sammes, R.Ratnaraj, M.Phillipps. *The Institute of Professional Engineers New Zealand, Transactions.* **20** 1/EMCh, Nov. 1993.

[2] B.J.Riley. *Journal of Power Sources*, **29** 233 (1990)

[3] U.G.Bossel. Final Report on SOFC Data, Facts and Figures. Program of R,D and D on Advanced Fuel Cells. Annex II: Modelling and Evaluation of Advanced SOFC. Swiss Federal Office of Energy Operating Agent Task II, International Energy Agency, Bern, April 1992.

[4] M.C.Williams. Status and Market Applications for the Solid Oxide Fuel Cell in the U.S. Proceedings of the 3rd European Solid Oxide Fuel Cell Forum. Edited by Philippe Stevens. 2-5 June, Nantes, France. 1998.

[5] B.C.H.Steele. Oxygen Ion Conductors. *High Conductivity Solid Ionic Conductors*, Edited by T.Takahashi. World Scientific Publication, 1988.

[6] N.Q.Minh, T.Takahashi. Science and Technology of Ceramic Fuel Cells. Elsevier Publishing. Amsterdam, Netherlands, 1995.

[7] F.A.Kröger, H.J.Vink. *Solid State Ionics.* **11** 317 (1956)

[8] N.Q.Minh. *Journal of the American Ceramic Society,* **76** 3, 563 (1993)

[9] L.S.Wang, S.A.Barnett. *Journal of the Electrochemical Society.* **139** 4 (1992)

[10] T.Kadowaki, T.Shiomitsu, E.Matsuda, H.Nakagawa, H.Tsuneizumi, T.Maruyama. *Solid State Ionics.* **67** 65 (1993)

[11] M.Mogensen. Electrode Kinetics of SOFC anodes and cathodes. High Temperature Electrochemical Behaviour of Fast Ion and Mixed Conductors. 14th Risø International Symposium on Materials Science. Edited by F.W.Poulsen, J.J.Bentzen, T.Jacobsen, E.Skou, M.J.L.Østergård. 1993.

[12] H.Sasaki, M.Suzuki, S.Otoshi, A.Kajimura, M.Ippommatsu. *Journal of the Electrochemical Society,* **139** 1 (1992)

---

[13] M.Dokiya. New Materials for SOFC Technology. 9th International Conference on SOFC in Solid State Ionics, Extended Abstracts, Edited by B.A.Boukamp, A.J.Burgraaf and J.Schoonman. Sept. 12-17, The Hague, The Netherlands, 1993.

[14] M.A.Panhans, R.N.Blumenthal. *Solid State Ionics.* **60** 29 (1993)

[15] W.L.George, R.E.Grace. *J.Phys. Sol.* **30** 881 (1969)

[16] Balanchandran, B.Odekirk, N.G.Eror. *J.Solid State Chemistry,* **41** 185 (1982)

[17] T.Takahashi. *Physics of Electrolytes.* **2** Edited by J.Hladik (Academic Press).

[18] B.C.H.Steele, I.E.Kelly, P.H.Middleton, R.A.Rudkin. *Solid State Ionics.* **28/30** 1547 (1988)

[19] R.T.Baker, I.S.Metcalfe, P.H.Middleton, B.C.H.Steele. *Solis State Ionics* **72** 328-333 (1994)

[20] B.C.H.Steele, P.H.Middleton, R.A.Rudkin. *Solid State Ionic*s 40/41 810 (1990)

[21] P.H.Middleton, H.J.Steiner, G.M.Christie, R.Baker, I.S.Metcalfe, B.C.H.Steele. Proceedings of the 4th International Symposium on Solid Oxide Fuel Cells. Electrochemical Society, New Jersey, USA, 1995.

[22] H.J.Steiner, P.H.Middleton, B.C.H.Steele. *Journal of Alloys and Compounds.* **190,** 279 (1993)

[23] R.T.Baker, I.S.Metcalfe. . Proceedings of the 4th International Symposium on Solid Oxide Fuel Cells. Electrochemical Society, New Jersey, USA, 1995.

[24] D.W.Dees, T.D.Claar, T.E.Easler, D.C.Fee, F.C.Mrazek. *Soild State Ionics.* **137** 2141 (1987)

[25] A.L.Dicks, K.D.Pointon, A.Swann. Proceedings of the 3rd European SOFC Conference. p249. Edited by Philippe Stevens. 2-5 June, Nantes, France. 1998.

[26] T.Kawashima, M.Hishinuma. *Materials Transactions.* **37** 7 (1996)

[27] N.M.Sammes, M.B.Phillipps. Selection and Fabrication and Properties of Electrodes used in High Temperature Fuel Cells. Pp 742-751. The Science and Technology of Zirconia V. Edited by S.P.S.Badwal, M.J.Bannister, R.H.J.Hannik, Technomics, 1993.

[28] T.Saito. Effect of Ni and ZrO_2 on Anode Performance. SOFC Micromodelling. Edited by L.Dubal. Swiss Federal Office of Energy, Berne. p21, 1992.

[29] T.Kawada, N.Sakai, H.Yokokawa, M.Dokiya, M.Mori, T.Iwata. *Solid State Ionics.* **40-41** 402 (1990)

[30] T.Kawada, N.Sakai, H.Yokokawa, M.Dokiya, M.Mori, T.Iwata. *Journal of the Electrochemical Society,* **137** 10, 3042 (1990)

[31] C.Bagger. Improved Production Methods for YSZ Electrolyte and Ni/YSZ Anodes for SOFC. 1992 Fuel Cell Seminar, Program and Abstracts. November 29-December 2, Tucson, Arizona, USA. 1992.

[32] P.Costamagna, P.Costa, V.Antonucci. *Electrochimica Acta.* **43** 3, 375 (1998)

[33] D.W.Dees, T.D.Claar, T.E.Easler, D.C.Fee, F.C.Mrazek. *Solid State Ionics.* **134** 2141 (1987)

[34] M.Mogensen, S.Skaarup. *Solid State Ionics,* **86-88** 1151 (1996)

[35] H.Itoh, T.Yamamoto, M.Mori, T.Watanabe, T.Abe. *Denki Kagaku,* **64** 6 (1996)

[36] K.C.Chou, S.Yuan, U.Pal. Deposition, Electrical Properties and Direct Porosity Measurements of Ni/YSZ Cermet Anodes. Proceeding of the Third International Symposium on SOFC. Edited by S.C.Singhal, H.Iwahara. **PV 93-4**, Electrochemical Socociety Inc., 1993.

---

[37] A.O.Isenberg. Growth of Refractory Oxide Layers by EVD at Elevated Temperatures. pp 572. Proceeding of the Third International Symposium on SOFC. Edited by S.C.Singhal, H.Iwahara. **PV 93-4**, Electrochem Soc. Inc. 1993.

[38] R.Pattabiraman, R.Chandrasekaran, S.Muzhumathi, I.Arul Raj, S.Dheenadayalan, D.Bhatt, M.Mohan Rao. *Bulletin of Electrochemistry*. **9(5-7)** 360 (1993)

[39] T.Kawada, N.Sakai, H.Yokokawa, M.Dokiya, I.Anzai. Polarisation of a Ni/YSZ Anode with H_2, CO and CH_4 fuels in a SOFC. Proceedings on High Temperature Electrode Materials and Characterisation. Edited by D.D MacDonald, A.C.Khandkar. Proc. Vol 91-6, Electrochem. Soc., p165, (1991).

[40] S.P.S.Badwal, A.E.Hughes. Proceedings of the Second International Symposium on SOFC. Edited by F.Grosz, P.Zegers, S.C.Singhal, O.Yamamoto. Commission of the European Communities, Luxembourg, p445, 1991.

[41] Kirk-Othmer, Encyclopedia of Chemical Technology. Edited by M.Grayson, D.Eckroth, H.Mark, D.Othmer, C.Overberger, G.Seaborg. #rd Edition, Volume 15. John Wiley and Sons, 1981.

[42] S.Majumdar, T.Claar, B.Flandermeyer. *Journal of the American Ceramics Society*. **69** 628 (1986)

[43] T.R.Armstrong, L.A.Chick, J.L.Bates. Proceedings of the Third International Symposium on Solid Oxide Fuel Cells, May 16-21, 1993, Honolulu, Hawaii. Edited by S.C.Singhal, H.Iwahara. Electrochemical Society, Pennington, NJ, 1993, p714.

[44] H.Itoh, T.Yamamoto, M.Mori, T.abe. Proceedings of the Fourth Symposium on Solid Oxide Fuel Cells. Edited by M.Dokiya, O.Yamamoto, H.Tagawa, S.C.Singhal. Proceedings Volume 95-1, p639. The Electrochemical Society Proceedings Series, Pennington, NJ (1995).

[45] H.Itoh, T.Yamamoto, M.Mori, T.Horita, N.Sakai, H.Yokokawa, M.Dokiya. *Journal of the Electrochemical Society,* **144** 2, 641 (1997)

[46] S.Ohara, T.Fukui, K.Mukai, K.Kodera, Y.Kubo. Microstructure and Long-Term Stability on Ni-YSZ Anode. Proceedings of the 5th International Symposium on SOFC. June 2-5, 1997, Aachen, Germany.

[47] F.P.F.van Berkel, F.H.van Heuveln, J.P.P.Huijsmans. *Solid State Ionics*. **72** 240 (1994)

[48] K.Eguchi, T.Setoguchi, K.R.Okamoto, H.Arai. Catalytic and Electrochemical Properties of Anodes for SOFCs. Proceedings of the International Fuel Cell Conference, Feb. 3-6, Makuhare, Japan, p373-376, 1992.

[49] M.Mogensen. Electrode Kinetics of SOFC Anodes and Cathodes. Proceedings of the 14th Risø International Symposium on Mayterial Science: High Temperature Electrochemical Behaviour of Fast Uion Conductors. Editors:5 F.W.Poulsen, J.J.Bentzen, T.Jacobsen, E.Skou, M.J.L.Østergård. Risø National Laboratory, Roskilde, Denmark, 1993.

[50] J.Guindet, C.Roux, A.Hammou. Hydrogen Oxidation at the Ni/YSZ Electrode. Proceeding of the Second International Symposium on SOFC, 2-5 July, Athens, Greece, 1991.

[51] M.Mogensen, T.Lindegaard. The Kinetics of Hydrogen Oxidation on a Ni/YSZ SOFC Electrode at 1000°C. Proceeding of the Third International Symposium on SOFC. Edited by S.C.Singhal, H.Iwahara. Proceedings Vol. 93-94. Electrochem Soc., p484-493, 1993.

---

[52] M.Mogensen, S.Primdahl, J.T.Rheinlander, S.Gormsen, S.Linderoth, M.Brown. Relations Between Performance and Structure of Ni-YSZ Cermet SOFC Anodes. 4th International Symposium on Solid Oxide Fuel Cells, June 18-23. 1995, Japan

[52] T.Kawada, N.Sakai, H.Yokokawa, M.Dokiya, M.Mori, T.Iwata. *Solid State Ionics*, **40/41**, 402, (1990)

[53] S.Primdahl, M.Mogensen. Gas Conversion Impedance, a Test Geometry Effect in Characterisation of Solid Oxide Fuel Cell anodes. Submitted to Journal of the Electrochem. Soc. Dec. 1997.

[54] A.Baiker, P.E.Marti, P.Keusch, E.Fritsch, A.Reller. *Journal of Catalysis*. **146** 268, (1994)

[55] M.Mogensen. Properties of CeO_2 Based SOFC Anode Materials. Proceeding of the Second International Symposium on SOFC, 2-5 July, Athens, Greece, 1991.

[56] R.Ødegård, I.R.Theodorsen, T.Sigvartsen, T.Monsen, H.Løvåsen. Proceedings of the 14th International Symposium on Materials Science, High Temperature Electrochemical Behaviour of Fast Ion and Mixed Conductors, September 6-10, 1993, Roskilde, Denmark. Edited by F.W.Poulsen, J.J.Bentzen, T.Jacobsen, E.Skou, M.J.L. Østergård. Risø National Laboratory, Roskilde, Denmark, 1993, p117.

Chapter Two

2. Methods and Experimental Apparatus

2.1 Introduction

Outlined in this chapter are the methods utilised for preparation and analysis of the cermet anodes fabricated in this thesis. Also included in this chapter are the details of some of the experimental setups employed in studying the performance of the anodes. Each subsection will explain a method used to perform a specific task.

2.2 Powder Preparation

2.2.1 Materials

Materials used for powder preparation and their purities, as assayed by the manufacturer are shown in Table 2.1.

Table 2.1 Materials used and their respective manufacturers.

Chemicals	Manufacturer
Nickel Oxide	Ajax Chemicals
Nickel Oxide	Johnson Mathey
Yttria stabilised Zirconia (YSZ)	Tosoh TZ-8Y
Polyvinylbutyral	Aldrich Chemical Co.
Polyvinylpyrrolidone Molec. Weight: 700,000	BDH
Polyvinylpyrrolidone Molec. Weight: 10,000	Sigma
Methlyethylketone	Merck
Ethanol	BDH
Hypermer KD1	ICI Americas

2.2.2 Milling

Simple ball mills were used for most milling and mixing procedures, using polyethylene milling containers and 10 mm diameter yttria partially stabilised zirconia (PSZ) grinding media.

The milling procedure consisted of grinding NiO in ethanol, with the addition of a binder, for approximately 48 hours, in order to obtain the appropriate particle size. The yttria stabilised zirconia (YSZ) was then added and milling continued until the cermet mixture obtained the correct particle size distribution as measured by a Mastersizer Particle Size Analyser described in section 2.3. The anode slurry was milled for a specific time and examined with the particle size analyser, comparing the particle size distribution with standards and remilling if necessary. The correct particle size distribution was based on standards derived from experimentation and fabrication methods developed at Risø National Laboratory, Denmark[1].

Table 2.2 Table of mills used to break down YSZ and NiO particles for controlling the particle size.

Mill Type	Speed	Sample Vessel	Milling Media	Milling Fluid
Ball Mill 1	57 rpm	30mL polyethylene container	Partially stabilised zirconia (PSZ)	Ethanol
Ball Mill 2	22 rpm	70mL polyethylene container	PSZ	Ethanol
Ball Mill 3	0-400 rpm	250 ml to 5000 mL	PSZ	Ethanol
Centrifugal Mill	0-500 rpm	250ml porcelain	PSZ	Ethanol

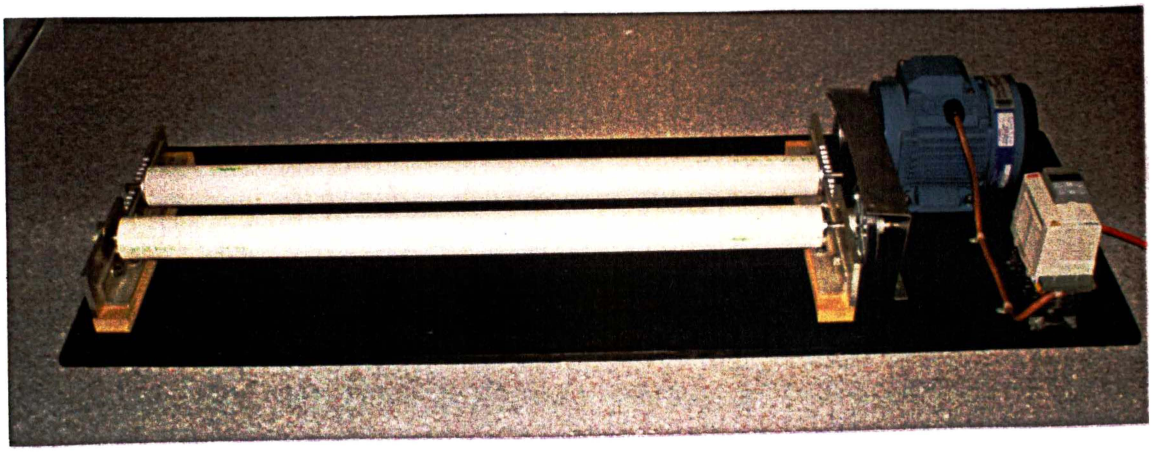

Figure 2.1 Ball mill used for milling all materials including NiO and YSZ, and for mixing the cermet powders.

Figure 2.2 Centrifugal mill used for high energy milling of the highly sintered YSZ powders in order to control particle size.

2.2.3 Sintering

Sintering and high temperature firing was performed in a Ceramic Engineering HT05/18 high temperature furnace, capable of temperatures up to 1700 °C. The role of the furnace included full sintering of YSZ agglomerates, producing dense compacts for milling to specific particle sizes. Binder burnout was carried out in a Carbolite RHF 17/3 Rapid Heating Furnace with 'Super Kanthal 33' heating elements and a Eurotherm temperature controller. Tube furnaces were used for cell testing and these were fabricated *in-house*.

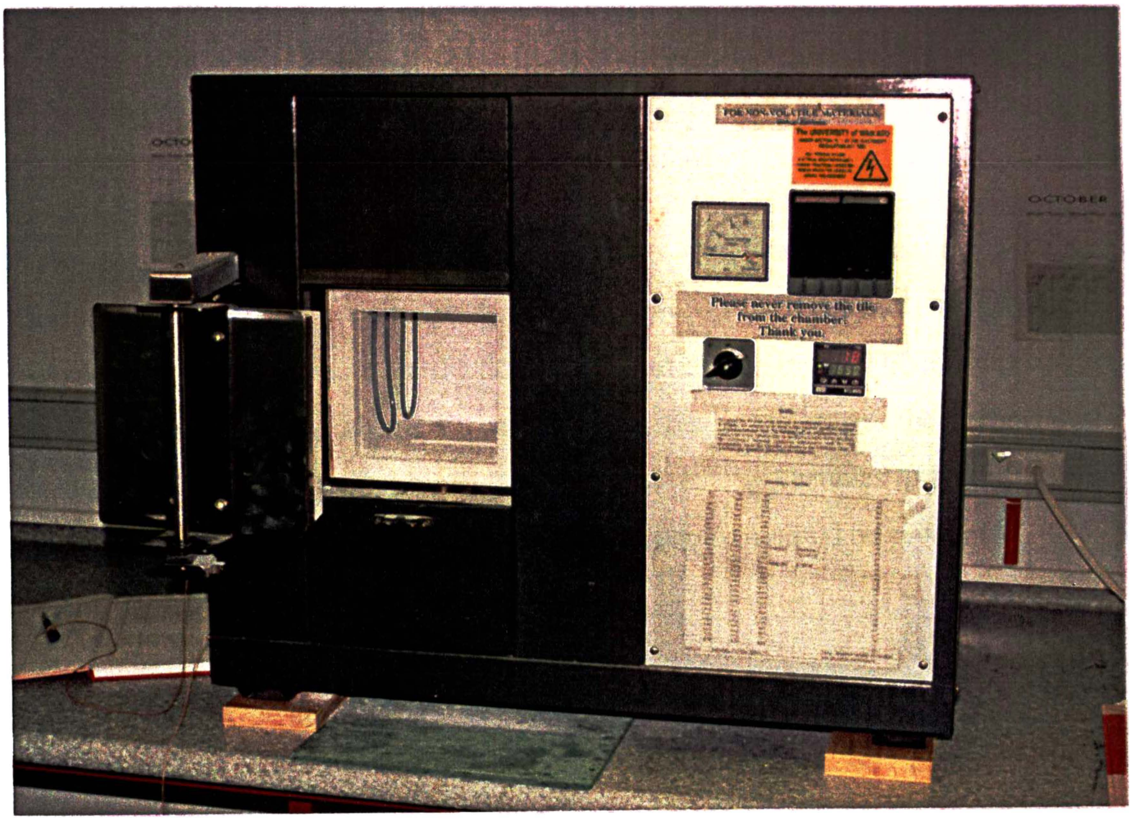

Figure 2.3 Ceramic Engineering HT05/18 high temperature furnace, capable of temperatures up to 1700°C used primarily for sintering YSZ agglomerates.

2.2.4 Pressing

Electrolyte pellets and dense Ni/YSZ cermets were prepared using an uniaxial hydraulic press with a 30 mm diameter die at a pressure of 30 MPa. The YSZ electrolyte powder consisted of 5 wt% oleic acid to aid in the compaction process and pellet integrity before firing. Uniaxial pressing was followed by cold isostatic pressing, using a Stansted Fluid Power Isostatic Press at 200 MPa. The pellets were dried in an oven to remove the oleic acid, and then placed in a furnace and heated to 1600 °C for 17 hours to ensure densification.

2.3 Particle Size/Distribution

A selection of anode powders and raw materials were analysed using a Malvern Mastersizer E laser diffraction system. This system was used primarily to determine particle size and particle size distribution of the starting powders. The technique was also used during milling procedures on anode slurries to determine the particle size change as a function of milling time. This allowed milling schedules to be created, in which anode slurries with specific particle size distributions could be produced.

2.4 Anode Fabrication

Anodes were fabricated using a wet powder spraying (WPS®) technique. This involved four principle steps[2] as described below.

2.4.1 Mixture Preparation

The NiO powder, binder (PVP, polyvinylpyrrholidone, molecular weight=10,000) and solvent (Ethanol, 100 %) were milled, with yttria partially stabilised zirconia (YSZ) grinding media, for approximately 48 hours until the appropriate particle size was obtained. This was measured using a Malvern Particle Size analyser. The volume ratio between the binder and the solvent was adjusted so that the volume fraction of the binder within the powder was approximately 5 wt%. This was the optimum volume for the lowest viscosity, providing a more fluid ceramic slurry[3]. After 48 hours, YSZ and the binder were added and the mixture was milled for another 24 hours. This was to ensure the two ceramic phases were thoroughly mixed and also to ensure the appropriate particle size distribution was obtained.

2.4.2 Ceramic Slurry Application

A spraygun (ECCO 30, ECCO Finishing AB, Skara, Sweden; Badger Air Brush system) was used to apply the ceramic powder. The slurry consisted of mixtures of NiO (40-50 vol%) and YSZ dispersed within ethanol and PVP. The rate, and quality of the deposited coating is basically controlled by the spray velocity and the distance between the spray nozzle and the substrate. Viscosity is an important parameter to control to ensure the slurry will be sufficiently fluid within the spray gun and also to allow densification of the NiO and YSZ particles after the mixture has been deposited on the substrate.

The slurry was applied in three layers, the first layer being in the order of 10 µm thick. The two subsequent layers were approximately 20 µm in thickness, to give a total thickness of 50 µm. Sintering was carried out after the first and third layers were applied.

2.4.3 Drying

The drying step begins with the evaporation of the solvent during spraying from the spray gun nozzle. It is preferable that the mixture arrives at the substrate in a semi-dry state so that no dripping or running can occur. The semi-dry state also reduces the chance of demixing or layering within the cermet powder due to varying particle sizes settling at different times. The deposited layer must be sufficiently wet to allow densification and thus control of porosity.

The spray gun was designed with two trigger settings. The first trigger setting allowed the passage of air with no application of the ceramic slurry. The second trigger setting applied the ceramic slurry to the substrate. The first trigger setting was used to dry the anode layer immediately after spraying to ensure the very fine (0.4 µm) YSZ did not settle to the top as an electronically insulating layer.

2.4.4 Sintering

The binder was removed by using a slow heating rate of 100 K/hour. This allowed controlled binder burnout, permitting the vapours of the disintegrating binder to migrate out through the porous structure, without causing disruption of the anode microstructure. At approximately 400-500 °C, the binder had been removed and a more aggressive heating rate of 180-300 K/hour could be employed to allow sintering of the bulk layer to take place. The sintering temperature and time were adjusted according to the properties required of the final anode microstructure.

Sintering of an anode was performed at a heating rate of 100 K/hour up to 1573 K where it was held for 2 hours and then ramped down at approximately 100 K/hour to room temperature.

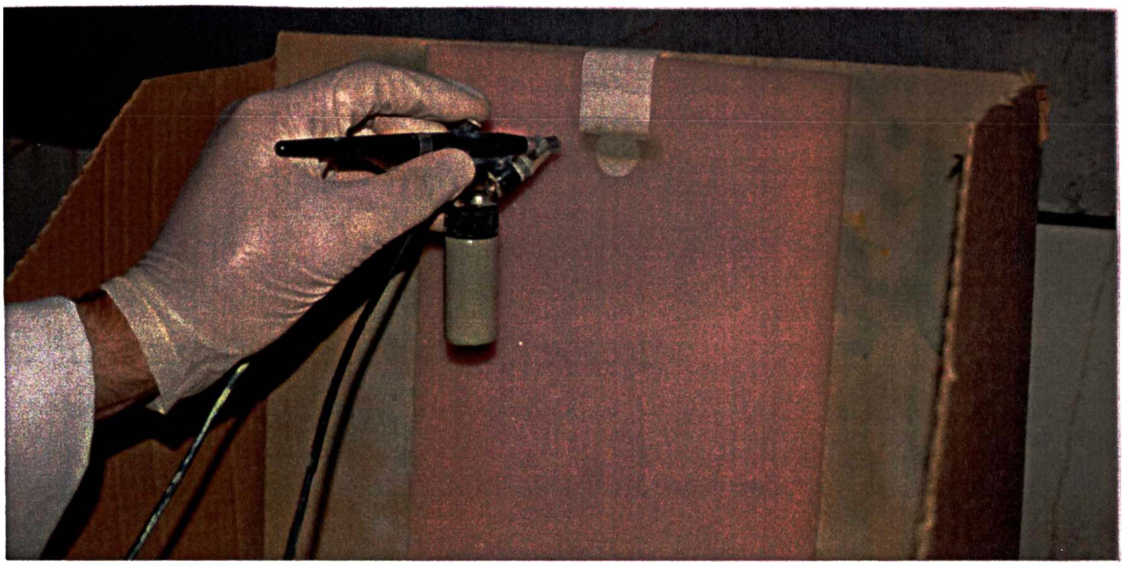

Figure 2.4 Wet Powder Spraying technique used to apply the cermet slurries onto the YSZ substrates. This technique was also used horizontally to inhibit running of the paint.

2.5 Microscopy

2.5.1 Optical Microscopy

Optical Microscopy was the technique of choice for the observation of the microstructure of the anodes. This was due to the ease of identification of the individual materials in the anode.

Completed (or tested) anodes were embedded in epoxy resin (Struers Epofix EPOF 1) using a vacuum technique, specifically for permeable materials, to allow the epoxy to fully penetrate the porosity of the layer. Metallurgical polishing was performed with a Struers RotoPol-21 and Struers RotoForce-4 sample holding attachment.

Anode samples were ground with SiC papers ranging from 500 grit to 4000 grit and then polished to a finish of 3 µm using Struers DP-Suspension diamond polishing solution. The samples were viewed using an Olympus BX 60 microscope with an Olympus SC 35 type 12 camera attachment.

2.5.2 Scanning Electron Microscopy

Scanning Electron Microscopy (SEM) was performed using a Hitachi S4000 SEM. Fracture surfaces, coating thickness', particle sizes, sintering effects, particle distribution and porosity were all observed using this technique. Except for metallic samples, all samples were coated with gold/palladium, using radio frequency (R.F.) sputtering.

2.6 Electron Dispersive X-Ray Analysis

Electron dispersive X-ray analysis (EDX) was performed using a Kevex Microanalyser attached to the SEM system. This technique was used only qualitatively to determine the elements present in a sample.

2.7 Electrochemical Techniques

Various electrochemical techniques were used to determine the reactions occurring at the SOFC anode. Both AC and DC methods were employed.

To elucidate an electrode mechanism it is necessary to measure the current density while varying the concentrations (partial pressures) of the reactants and products, and the overpotential over wide ranges. It is also a good idea to vary the temperature to provide data for activation energy calculation, the flow rate for the possible determination of diffusion controlled processes, and the electrode geometry. The measured electrode potential of an electrode must be corrected for the potential drop across the electrolyte due to the relatively low conductivity of the ionic conductor. This is achieved by combining potentiostatic DC measurements with AC measurements in order to counteract the changing series resistance, which can vary with applied overpotential.

2.7.1 Theory

2.7.1.1 Impedance Spectroscopy

Impedance Spectroscopy (IS) is a relatively new and powerful method of characterising the electrical properties of a variety of materials and the interfacial reactions between electrolytes and electrodes. It may be used to investigate the kinetics and mechanisms of many materials, both liquid and solid: ionic, semi-conducting, mixed ionic/electronic and dielectrics.

For fuel cell research, impedance spectroscopy is definitely an important method, backed up by various DC techniques, to describe electrode processes occurring, and is necessary in order to see whether the electrode kinetics are limited by one or more processes. Figure 2.5(a), (b) show examples of what impedance spectra of a SOFC anode may look like[4].

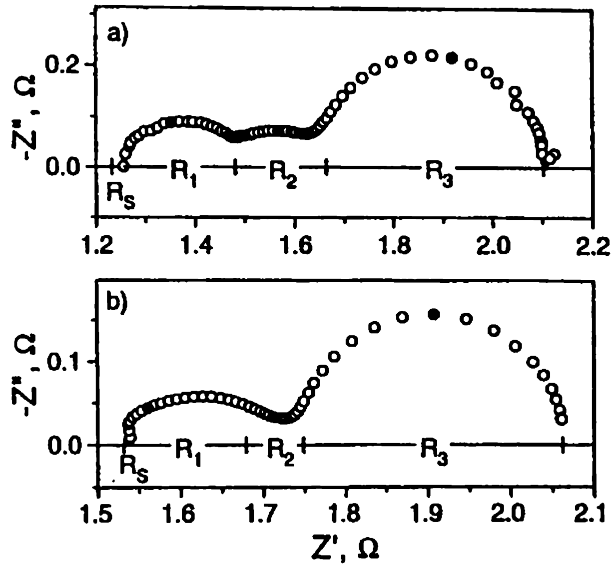

Figure 2.5(a), (b) Electrochemical impedance spectra of SOFC Ni/YSZ anodes measured at 1000°C in H_2 with 3% H2O at OCV[4].

The standard way of treating impedance data is to fit the impedance spectra to the simplest equivalent circuit. Fitting the impedance spectra to equivalent circuits, is performed using a type of non-linear least squares analysis software package such as those developed by Boukamp[5] or Macdonald[6]. The process of finding a useful equivalent circuit is determined by the experimental data obtained and the proposed reaction taking place in the system. Usually, the equivalent circuit is modified to accommodate new experimental data as the mechanism is elucidated. Ultimately, the equivalent circuit chosen to represent the experimental data must reflect the physical and chemical information contained in the measured impedance spectra.

For a Ni/YSZ cermet anode consisting of an impedance spectra with three semicircles as shown in figure 2.5(a), (b), the simplest possible equivalent circuit is shown in figure 2.6.

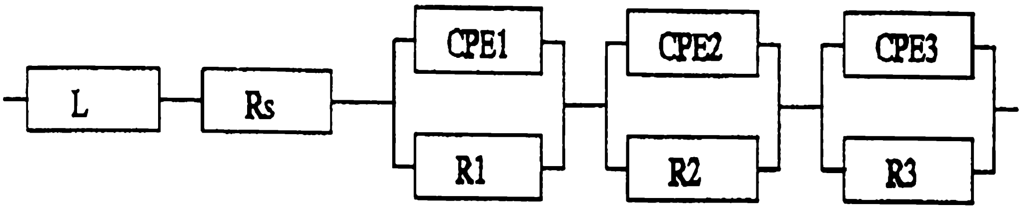

Figure 2.6 The simplest possible equivalent circuit for impedance spectra with three semicircles. L is an inductance originating from the testing equipment, R_s is the series resistance originating from the electrolyte and the leads, and R_1Q_1, R_2Q_2, R_3Q_3 describe the electrode response[4].

An inductance, L, originates from the leads of the experimental apparatus. The series resistance, R_S, is due to resistance in the electrolyte and in the lead to the working electrode. The three parallel RQs in series describe the electrode impedance which are the rate limiting processes. Q is a constant phase element (CPE) with the admittance:

$$Q = Y_o(j\omega)^n \qquad \textbf{Equation 2.1}$$

therefore the impedance can be described by:

$$Z = \frac{1}{Q(j\omega)^n} = \frac{1}{Q\omega^n[\cos(\frac{\pi}{2n}) + j\sin(\frac{\pi}{2n})]} \qquad \textbf{Equation 2.2}$$

where ω is the angular frequency and j=√-1. The CPE has two constants Q and n. If n=1, the CPE is an inductance with $L=Q^{-1}$; if n=0, the CPE is a resistance with $R=Q^{-1}$; if n=0.5, the CPE is a Warburg diffusion, and if n=1, the CPE is a capacitance with C=Q. The units of the CPE are variable depending on the value of n:

$$Q = Fs^{-n}$$ **Equation 2.3**

It is necessary to compare the n-values for a number of spectra obtained and decide on a representative set of n-values for each impedance semicircle, covering all experimental conditions such as temperature, gas composition and anode microstructure. n-values must be constant when comparing the R and Q values directly from spectra to spectra. All spectra are fitted with the same set of n-values and if the fitting error is small as described in figure 2.7 the average n-values are taken as valid and R and Q can be compared across numerous sample anodes.

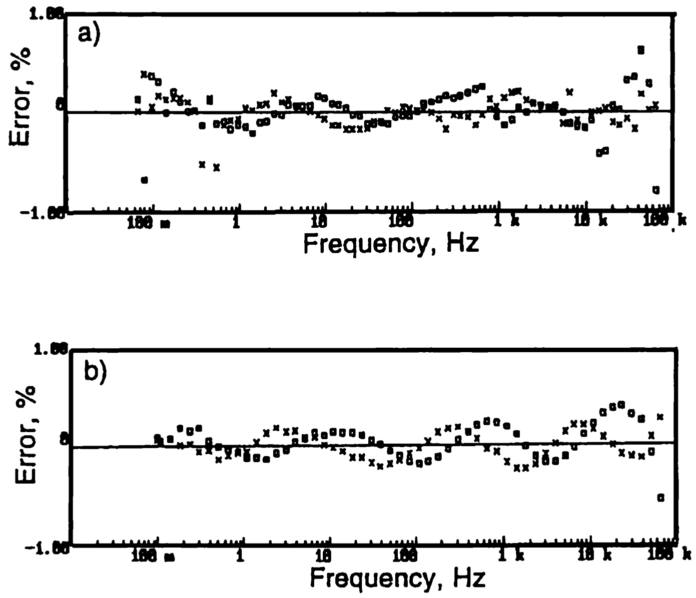

Figure 2.7 Error plots of the fits of the spectra of figure 2.5 using the equivalent circuit of figure 2.6 and fixed n-values (n_1, n_2, n_3) = (0.8, 0.75, 1). Each point gives the difference between the measured and the equivalent circuit value in percent of the measured[4].

Using this procedure it has been found[7] for the H_2/H_2O-Ni-YSZ anode that all spectra obtained in the temperature range from 850-1000 °C for a wide variety of conditions may be fitted with little error using $(n_1, n_2, n_3) = (0.8, 0.75, 1)$, ($n_3 = 1$ indicates that Q_3 is a capacitance). It has been shown that R_1Q_1 is closely related to the cermet structure[8] and R_3Q_3 is due to gas conversion impedance[9], which was a physical process dependent on the test setup geometry, gas flow rate and partial pressures.

In order to study the structure related process (R_1Q_1) in detail, the anode microstructure was modified to enhance this impedance semicircle by fabricating anodes with 90% Ni/10% YSZ to reduce the performance and thereby increase the high frequency and structure related arc resistance. Each of the elements was then characterised by varying the experimental parameters.

2.7.1.2 Chronoamperometry

Chronoamperometry is the main DC method used for testing the anode. It consists of measuring the current density as a function of time. It can also be used to measure the current density after a potential step and thus polarised data can be obtained, after a steady state is achieved. When using chronoamperometry to measure current density versus overpotential, a correction for the IR_s drop must be employed to ensure what is being studied is actually being measured. It is also important to check that R_s (electrolyte resistance) is constant over the polarisation range under study. A variable R_s can be caused by a change in the temperature of the electrolyte, caused by high current flow, or possibly a change in electrode contact area.

2.7.1.3 Cyclic Voltammetry

DC polarisation is evaluated by cyclic voltammetry and by impedance spectroscopy. Cyclic voltammograms are taken at a rate of 5 mV/s (applied) and are corrected for IR loss. Anodic and cathodic sweeps are taken from OCV and usually give inductive hysteresis in both directions. A Tafel type representation can be produced from this sweep data, from which mechanistic data can be elucidated.

2.7.2 Experimental

Impedance spectroscopy was the main technique combined with chronoamperometry and cyclic voltammetry to provide electrochemical data relevant to the anode reactions. Polarisation measurements were also undertaken to provide valuable data on the performance of the anode under loading conditions.

The equipment used for impedance spectroscopy was a Solartron 1260 frequency response analyser interfaced to a Solartron 1287 electrochemical interface. Impedance spectroscopy was conducted using an applied amplitude of 20-30 mV. The frequency range used was 500 kHz to 0.01 Hz and at least 20 minutes was allowed for stabilisation before recording each impedance spectrum. The current measurement resistors used were 1 Ω for polarised and 10 Ω for unpolarised measurements.

Anodes were heated to 1000 °C in 9% H_2 + 3% H_2O before switching to an atmosphere of 97% H_2 + 3% H_2O with an open circuit voltage (OCV) against Pt in air of approximately -1070 mV ($pO_2 \sim 2 \times 10^{-18}$ atm). A total of 100 mL/min (at 25 °C) moist gas was passed over the anodes. Fuel composition was controlled by mixing nitrogen and hydrogen through thermal mass flowmeters (Brooks massflow meters TR5850) and saturating this mixture with water at a controlled temperature.

PO_2 was determined by the Nernst expression from OCV vs. Pt/air. The accurate partial pressure pH_2O is determined from pO_2 and pH_2 by the following algorithm valid for 1000 K<T<1300 K[10]:

$$pH_2O = 10^{-(2.958-13022/T)}.pH_2.\sqrt{pO_2} \qquad \textbf{Equation 2.4}$$

The experimental procedure used to manage the electrochemical tests was run by FCL, which is a software package designed to control impedance spectroscopy, chronoamperometry, cyclic voltammetry, gas flows, and to monitor furnace temperature. A typical experiment consisted of placing the test anode into the anode testing rig and heating up to 1000 °C in an atmosphere of 9% H_2 + 3% H_2O (25 °C) with the balance being N_2. At 1000 °C, the atmosphere was changed typically to 97% H_2 + 3% H_2O. After stabilisation in the new atmosphere, a potential reading was taken to ensure an adequate open circuit voltage (OCV), in order to determine if there were any leaks in the system. FCL[11] was then programmed to perform the chronoamperometry, polarisation, cyclic voltammetry and impedance spectroscopy experiments.

Usually, an experiment would begin with chronoamperometry and impedance spectroscopy at OCV. Then an anodic potential sweep would be performed from OCV down to -650 mV, followed by a potential step experiment consisting of chronoamperometry and impedance spectroscopy at OCV, -950 mV, -850 mV, -750 mV and -650 mV. A cathodic potential sweep was then performed from OCV up to -1450 mV, followed by a potential step experiment consisting of chronoamperometry and impedance spectroscopy at OCV, -1150 mV, -1250 mV, -1350 mV and -1450 mV.

Finally, another set of chronoamperometry and impedance spectroscopy measurements were performed for the purpose of determining if the former electrochemical experiments had modified the behavior of the anode, or the anode itself had changed within the time of the measurements taking place.

2.7.2.1 Single Atmosphere Electrode Testing Setup

A single atmosphere testing setup was built to provide a means of testing anodes[12]. It consisted of a large alumina beaker (3 litre) with a water cooled, sealed lid which houses the gas inlet and outlet for the fuel gas, a thermocouple, an oxygen sensor and various wires for connection to the anode under test inside the beaker (Figure 2.8).

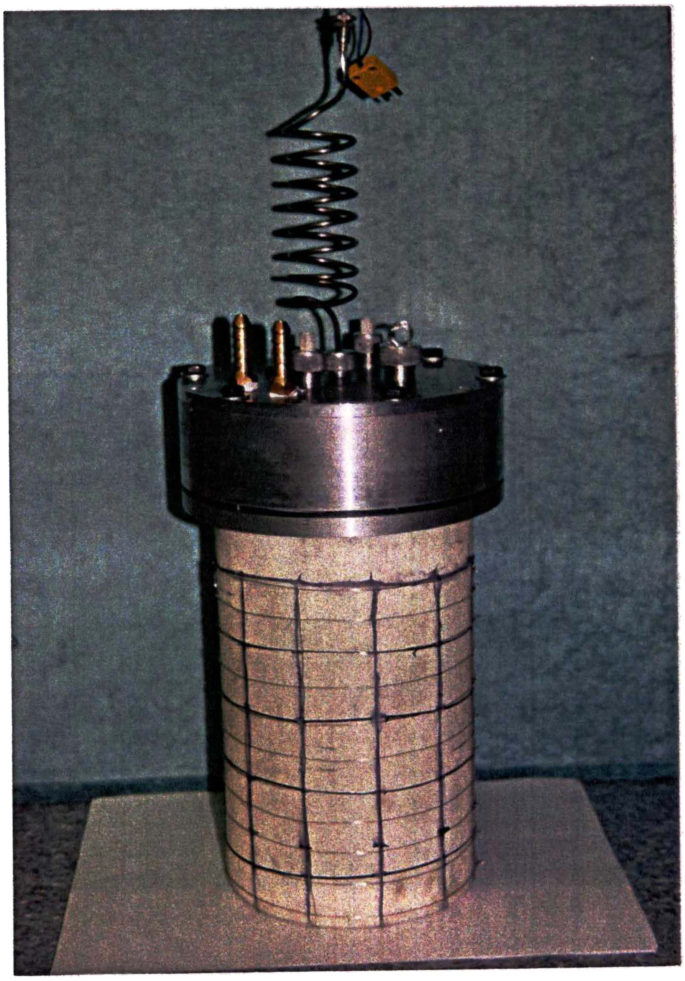

Figure 2.8 Single atmosphere electrode testing setup used to provide a reducing atmosphere within which electrochemical testing could take place.

Inside the beaker is an alumina supporting frame suspended from the lid. This provides support for the alumina insulation and a platform for the anode to be tested on. (Figure 2.9). The fuel gas atmosphere was varied from 9% H_2 + 3% H_2O to 97% H_2 + 3% H_2O.

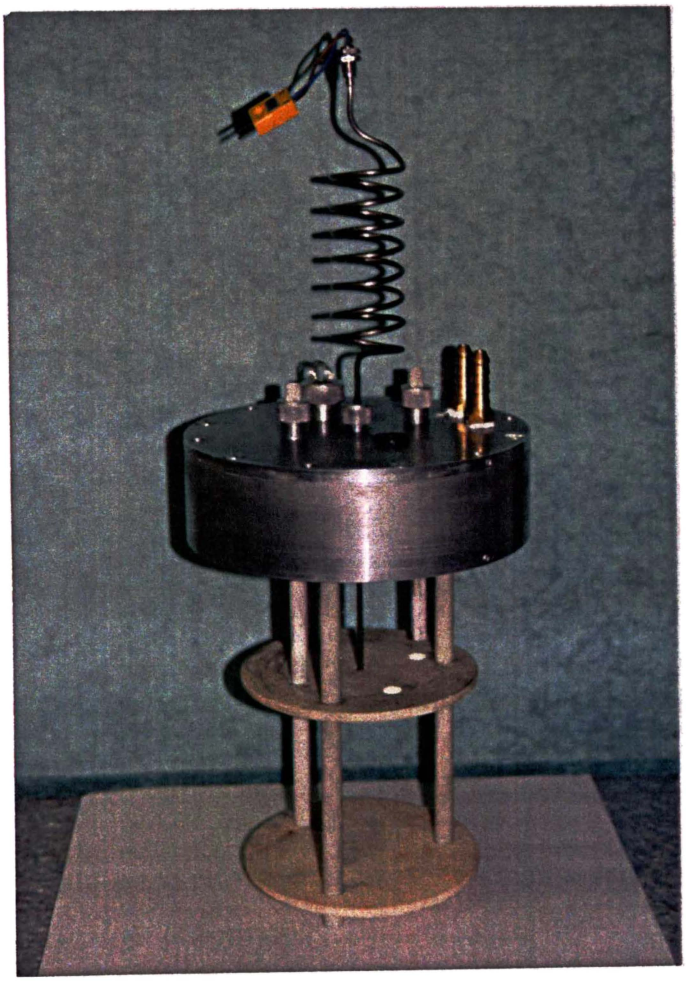

Figure 2.9 Internal structure of the single atmosphere electrode testing setup showing alumina platform used for suspending the anodes while testing.

2.7.2.2 Dual Atmosphere Electrode Testing Setup

The electrochemical testing rig consisted of a vertical tube furnace capable of temperatures up to 1100 °C[12]. Within the furnace were two alumina tubes, which connected end-on to the electrolyte pellet to allow the passage of the oxidant and fuel gases to either side of the electrolyte pellet. The oxidant gas used was air at atmospheric pressure and the fuel gas was varied from a mixture of 9% H_2 + 3% H_2O in N_2 to 97% H_2 + 3% H_2O. Around the cell, a flush-gas flowed (N_2) to ensure no contaminant gases could enter, thus disrupting the operating conditions. This also avoided a buildup of H_2 in the surrounding area in case of a leak in the cell. The fuel-gas flow was metered by variable computer controlled mass-flow valves. The software for this control (FCL) also controlled the potentiostat/galvanostat, the impedance analyser and the furnace temperature controller.

Electrochemical tests were carried out on a three-electrode pellet made from YSZ (Tosoh, TZ-8Y) of the geometry given in figure 2.10. The YSZ three-electrode pellets with circular working electrodes of approximately 0.44 cm^2 were fabricated with a Pt-paste counter electrode, a Pt ball reference electrode (see figure 2.10) in the centre bore and two leads in contact with the working electrode. The electrolyte geometry used here was verified by finite element analysis[13] to have a stable, homogeneous current distribution, causing less than 3% error on a polarisation area specific resistance of 0.3 Ωcm^2.

The whole experimental setup provided the basis for the basic research concerning the evaluation and performance of both anodes and cathodes.

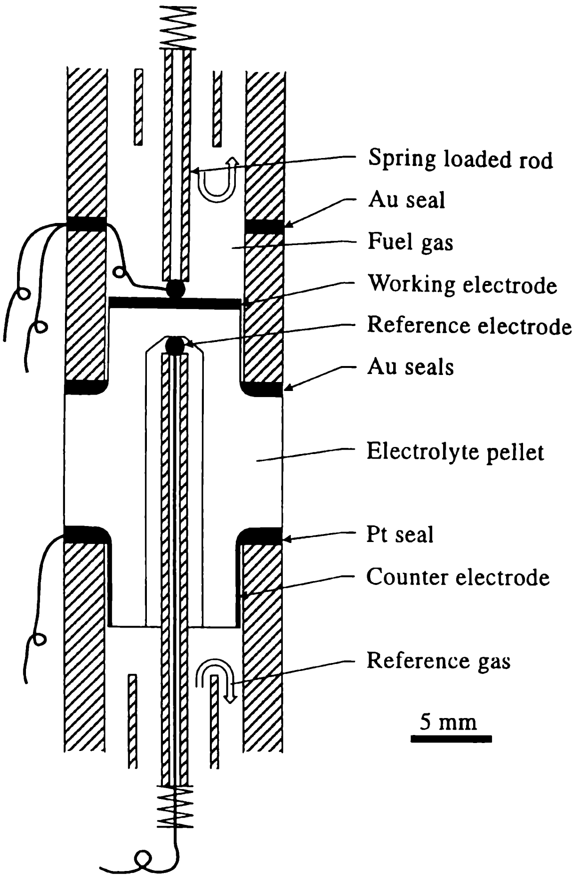

Figure 2.10 Dual atmosphere electrode testing setup[12].

References

---

[1] C.Bagger. Improved production Methods for YSZ Electrolyte and Ni-YSZ anode for SOFC. 1992 Fuel Cell Seminar. Program and Abstracts. November 29-December 2, 1992, Tuscon, Arizona.

[2] A.Ruder, H.P.Buchkremer, H.Jansen, W.Mallèner, D.Stöver. *Surface and Coatings Technology*. **53** 71-74 (1992)

[3] C.B.Manon. Dispersion of Anode Materials. Internal Report, Risø National Laboratory, Roskilde, Denmark.

[4] M.Mogensen, S.Primdahl, M.Juhl. Revealing the Mechanisms of SOFC Electrodes Using a Combination of AC and DC Methods. Proceedings of the 5th International Symposium on Solid Oxide Fuel Cells, SOFC5, June 2-5, 1997. Aachen, Germany.

[5] B.A. Boukamp. *Solid State Ionics*. **20** 31 (1986)

---

[6] J.R. Macdonald. Complex Nonlinear Least Squares Immitance Fitting Program, Version 8/16/90. University of North Carolina, Chapel Hill (1990).

[7] M.Mogensen, S.Primdahl, J.T.Rheinlander, S.Gormsen, S.Linderoth, M.Brown. Relations Between Performance and Structure of Ni-YSZ Cermet SOFC Anodes. Proceedings of the 4th International Symposium on Solid Oxide Fuel Cells, June 18-23, 1995. Yokohama, Japan.

[8] M.Mogensen, S.Skaarup. *Solid State Ionics* **86-88** 1151-1160 (1996)

[9] S.Primdahl, M.Mogensen. Gas Comversion Impedance: SOFC Anodes in H_2/H_2O Atmospheres. Proceedings of the 5th International Symposium on Solid Oxide Fuel Cells, SOFC5, June 2-5, 1997. Aachen, Germany.

[10] R.Hartung, H.H.Möbius. *Chemie-Ing. Techn.*, **40** 12 (1968)

[11] B.Malmgren-Hansen: User manual for FCL Software, Materials Department, Risø, Denmark, 1991.

[12] S.Primdahl, M.Mogensen. Gas Conversion Impedance: A Test Geometry Effect in Characterisation of SOFC Anodes. *Journal of the Electrochemical Society,* **145** 2431 (1998)

[13] J.Winkler, P.V.Hendriksen, N.Bonanos, M.Mogensen. *Journal of the Electrochemical Society.* **145** 4, 1184 (1998)

Chapter Three

Paper to be submitted to The Journal of the American Ceramics Society.

3. Fabrication, Structure and Conductivity of Ni/YSZ Cermet Anodes

3.1 Introduction

The Ni/yttria stabilised zirconia (YSZ) cermet is one of the most favourable anode materials for the solid oxide fuel cell (SOFC)[1]. Intensive work concerned with the optimisation of the electrical and structural properties of this material is being carried out in many laboratories[2,3,4,5,6,7]. The bulk of this work is concerned with fabrication techniques ensuring continuous Ni and YSZ networks throughout the anode structure and adequate adhesion of the anode layer to the electrolyte. There are a number of programmes dedicated to long term stability studies and the prevention of Ni agglomeration under the operating conditions of the SOFC[5,8,9,10,11,12].

It has been shown by Kawada *et al.*[13] that the particle size ratio of Ni/YSZ was very important for the performance of a cermet anode. Murakami *et al.*[14] suggested that a YSZ particle size of 0.5 μm was suitable for maintaining electrode structure and electronic conductivity. The small particle size of the YSZ inhibited the agglomeration of the nickel particles at the operating temperature of 1000 °C, thus maintaining a high nickel surface area. This gave increased nickel-nickel particle contact, and therefore increased conduction. A high surface area also reduces interfacial resistance, thus concluding that the reaction area in the anode is related to the nickel surface area, which implies that a long triple phase boundary (TPB) is essential for high performance.

Itoh *et al.*[6] suggested that the optimum anode consisted of a minimum amount of Ni to allow electronic conductivity, together with a certain amount of fine YSZ to inhibit sintering/agglomeration of the Ni, and a stable matrix of coarse YSZ for long term stability.

Dees *et al.*[15] determined that increasing the YSZ particle size, while maintaining a constant nickel particle size, increased the conductivity. As the YSZ particle size increased, the nickel-nickel particle contact becomes more intimate, and thus the nickel phase is able to thoroughly cover the surface of the YSZ matrix.

Bagger *et al.*[16] explained that by pre-calcining a certain percentage of the YSZ component, thereby changing its particle size, a broader particle size distribution and thus improved packing efficiency, and hence conductivity, of the anode was observed. A range of particle sizes was also used by Murakami *et al.*[14] to investigate the effect of porosity on anode efficiency. Porosity values from 65% to 85% were examined, and it was concluded that the anode interface was unaffected by this variation.

Since electrochemical characteristics of the electrode are strongly affected by its morphology, it is necessary to investigate the relations between fabrication procedures and the microstructure. In the present study, Ni/YSZ cermet anodes have been fabricated to examine structural and conduction properties. Calcining temperatures, particle sizes and slurry compositions were varied in order to determine their effect on the anode microstructure and in-plane electronic conductivity.

3.2 Methods and Materials

(see chapter 2 for complete experimental procedures)

3.2.1 Anode Materials

8 mol% yttria stabilised zirconia (YSZ) (Tosoh TZ8Y) pellets (30 mm diameter) were pressed using an uniaxial die-press, at 7 MPa and sintered at 1600 °C for 6 hours, to produce a dense substrate suitable for the application of the anode system.

The anode materials were modified, by calcining and milling to produce the appropriate particle sizes. The YSZ powder was in the form of 40 to 50 μm porous agglomerates, which were calcined at 1100 °C and 1400 °C. After sintering, the YSZ was milled, using a ball mill and a centrifugal mill (Retsch) to break-up the agglomerates. A study relating particle size to milling time was performed to determine particle size distributions, depending on the type of mill used and the sintering temperature of the YSZ. A similar study was performed with the NiO in order to modify particle size and particle size distribution.

3.2.2 Experimental Apparatus

50 mL polyethylene milling containers with 25 mL of ethanol and 10 partially stabilised zirconia (PSZ) grinding balls (10 mm diameter), were used for ball milling the YSZ calcined at 1100 °C. 250 mL polyethylene milling containers, with 10 g of YSZ and 20 mL of ethanol at a speed of 200 rpm, and 200 g PSZ milling balls, were used for ball milling the YSZ, previously calcined at 1400 °C. Centrifugal milling was performed using a 100 mL porcelain container, 50 mL of ethanol, with 30 PSZ grinding balls, at a speed of 310 rpm.

Ball milling of the NiO was performed in 250 mL polyethylene milling containers, with 10 g of NiO and 20 mL of ethanol at a speed of 200 rpm, and 200 g PSZ milling balls. Centrifugal milling of the NiO was performed using the same parameters as the YSZ. NiO was crushed in the centrifugal mill to produce a large particle distribution from 0.2 μm to 1 μm.

Scanning electron microscopy was used to determine the shape of the particles after milling. This proved to be an excellent technique for an approximate determination of particle size and particle size distribution. A particle size analyser was used to determine particle size and particle distribution.

3.2.3 Anode Fabrication

3.2.3.1 Method

The anode powders were fabricated from YSZ and NiO with a 50 vol% Ni ratio, mixed with a solvent, methyl ethyl ketone (MEK) or ethanol and a binder, polyvinyl pyrrolidone (PVP), polyvinyl butral (PVB) or Hypermer KD1® (ICI Americas) to produce a slurry for wet powder spraying.

NiO and 5 wt% binder were mixed with ethanol or MEK and milled for 48 hours in a ball mill. After the first 48 hours, the YSZ powder and 5 wt% binder were added to the already milled NiO and further milled for another 24 hours. This was the basic technique used, with various modifications performed as new anodes were fabricated.

3.2.3.2 Technique

Wet powder spraying[17] was the method of choice for applying the anode to the YSZ substrate. The spraying system consisted of a Badger air powered spray gun, which drew the anode slurry into the air stream, propelling it towards the target. The slurry was sprayed onto the YSZ pellets in three layers, the first being approximately 10 µm in thickness, and subsequent layers with a total of 50 µm in thickness. This method was performed to eliminate the mud-cracking effect when only one thick layer is applied. Each layer was sintered before applying the next, and temperatures ranging from 1300 °C to 1450 °C were used for sintering, in order to determine the effect of sintering temperature on YSZ and NiO agglomeration.

Reduction of the NiO was performed in a 100% hydrogen atmosphere tube furnace at 700 °C for 1 hour. The resulting anode layers were then prepared for optical microscopy by vacuum impregnation of epoxy resin (Struers Epofix) and subsequent polishing to a 3 µm finish using a Struers diamond polishing paste. Magnification of up to 1500x was used to observe the microstructure using an Olympus BO71 optical microscope with a C-35DA-2 camera attachment.

3.3 Results

3.3.1 YSZ Calcining Temperature

The YSZ agglomerates were pre-sintered at 1100 °C and 1400 °C to vary the degree of agglomeration[18]. This was performed as a way of varying the particle size distribution after milling. It was postulated that the least sintered YSZ powder (sintered at 1100 °C) would break down into the individual particles more readily. Therefore producing a powder with a wider particle size distribution and a larger amount of fine YSZ, which was necessary to produce a stable YSZ matrix in the anode layer.

Scanning electron micrographs of the YSZ particles showed two very different agglomerates, as seen in Figures 3.1(a) and 3.1(b). The fine particles of agglomerated YSZ, calcined at 1100 °C, had partially sintered together forming porous spherical structures from the original agglomerates present in the standard Tosoh TZ-8Y. The YSZ calcined at 1400 °C showed highly sintered spherical structures with no porosity present. Each fine YSZ grain had sintered to the adjacent grains forming a very dense particle, which needed a significant amount of milling to granulate.

Figure 3.1(a) Micrograph of yttria stabilised zirconia (YSZ) sintered at 1100 °C

Figure 3.1(b) Micrograph of YSZ sintered at 1400 °C.

3.3.2 Milling

3.3.2.1 Ball Milling

Ball milling was used to crush the YSZ agglomerates sintered at 1100 °C to the appropriate sizes. The YSZ was ball milled for varying amounts of time, and particle size analyses were performed. A bimodal distribution was present in the milled samples. This can be explained by the presence of the semi-crushed agglomerates, and the individual YSZ (0.4 μm) grains. A smaller peak located between the fine YSZ (0.4 μm) and the semi-crushed agglomerates was present. This could be accounted for by presuming a particular fragment size had fractured off in the milling process. Figures 3.2(a) and 3.2(b) show the two particle size distributions obtained from each of the sintering temperatures used (see Appendix 2 for complete particle size results).

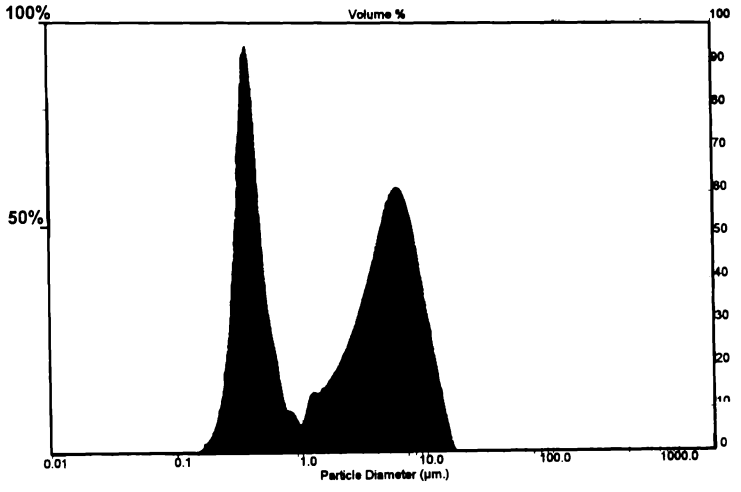

Figure 3.2(a) Particle size distribution of YSZ sintered at 1100 °C after 26 hours of ball milling.

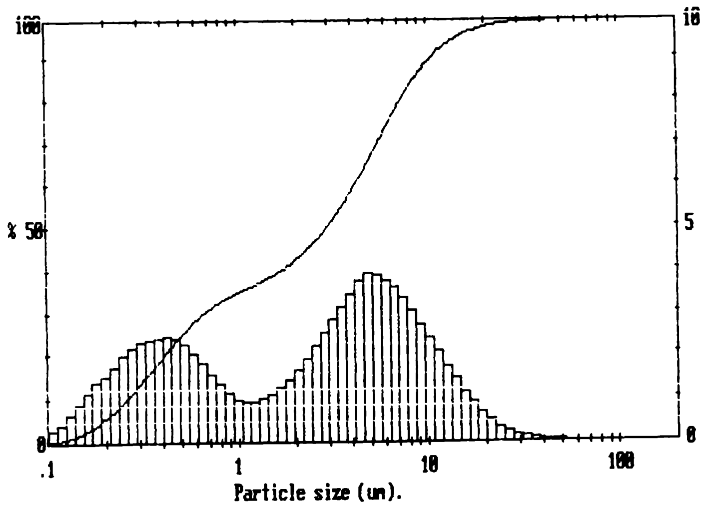

Figure 3.2(b) Particle size distribution of YSZ sintered at 1400 °C after 4.5 hours of ball milling.

Figures 3.3(a) and 3.3(b) show micrographs of the milled particles after the milling procedure. After ball milling for 26 hours, the particle size had reduced to 5 µm, with a very large amount of the fine YSZ grains (0.4 µm) also present. The scanning electron microscopy (SEM) images clearly show an increase of fine YSZ with an increased milling time (see Appendix 3 for complete SEM analysis). Table 3.1 lists the particle sizes obtained with the specific milling times using the ball milling technique for YSZ sintered at 1100 °C.

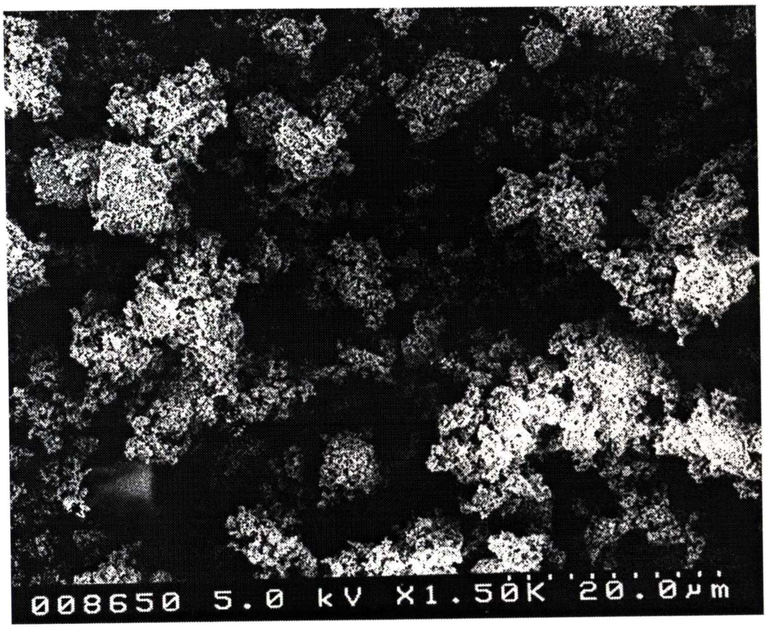

Figure 3.3(a) Micrograph of YSZ sintered at 1100 °C after milling for 26 hours.

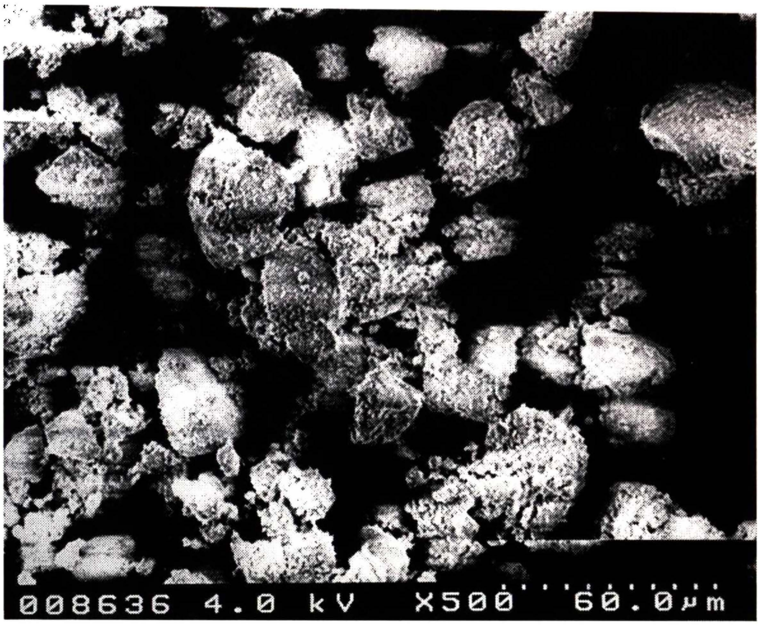

Figure 3.3(b) Micrograph of YSZ sintered at 1400 °C after milling for 4.5 hours.

Table 3.1 Particle sizes obtained with the specific milling times, using the ball milling technique for YSZ sintered at 1100 °C.

Time (hours)	Particle Size (µm)
0	45
10	0.4/12
15	0.4/9
26	0.4/6

Ball milling was also performed on the YSZ sintered at 1400 °C. The results indicated a significantly longer amount of milling time was necessary to complete the same degree of milling, when comparing the milling times to that of the YSZ sintered at 1100 °C. This is, of course, due to the increased sintering effect and the subsequent increased density and cohesion of the YSZ particles.

After 9 hours of milling, a bimodal distribution was observed (figure 3.4(a)). Again present were the crushed agglomerates and the fine YSZ particles (0.4 µm). As the milling continued, the agglomerate size was reduced and more fine YSZ was evident. After 176 hours of ball milling, a trimodal particle size distribution was evident. A very small and broad peak at approximately 8 µm particle size appeared, along with peaks at 0.4 and 2 µm. At 267 hours of milling, the middle (2 µm) peak had disappeared and a bimodal distribution remained (figure 3.4(b)); a peak at 0.4 µm and a broad peak at 8 µm (see Appendix 2 for the full particle size results). Table 3.2 lists the particle sizes obtained with the specific milling times using the ball milling technique for YSZ sintered at 1400 °C.

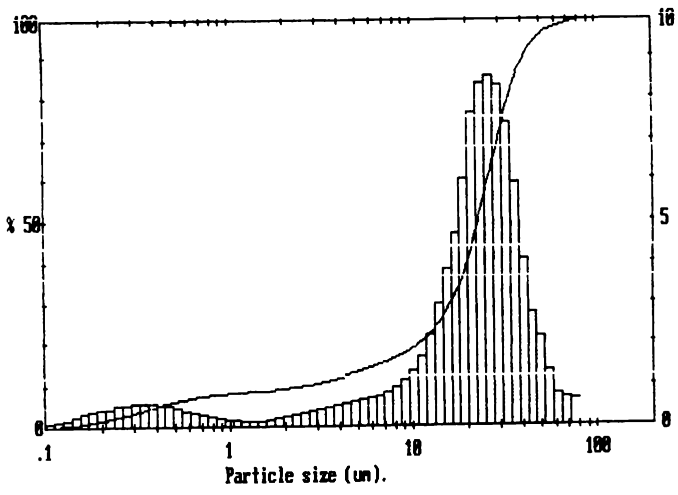

Figure 3.4(a) Bimodal particle size distribution of YSZ sintered at 1400 °C observed after 9 hours of ball milling.

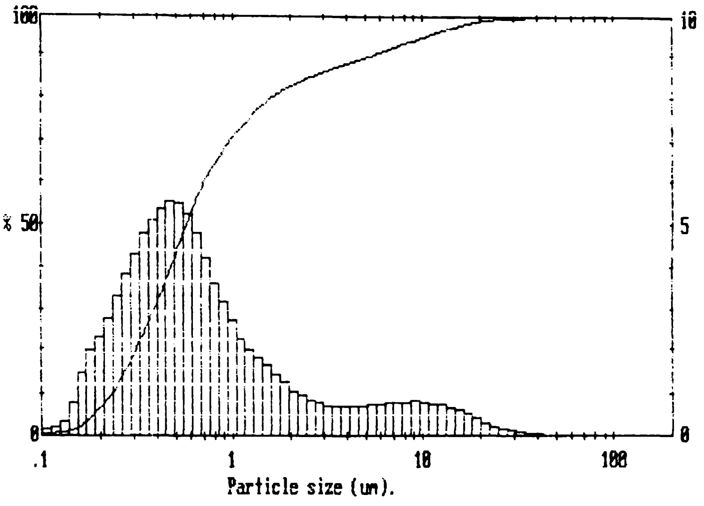

Figure 3.4(b) Bimodal particle size distribution of YSZ sintered at 1400 °C observed after 267 hours of ball milling.

Table 3.2 Particle sizes obtained with the specific milling times using the ball milling technique for YSZ sintered at 1400 °C.

Time (hours)	Particle Size (μm)	Time (hours)	Particle Size (μm)
0	45	104	3/0.4
1	40	128	2.5/0.4
2	38	152	2/0.4
9	30/0.4	176	8/2/0.4
21	17/0.4	197	8/1.5/0.4
33	12/0.4	230	8/0.4
44	9/0.4	267	8/0.4
56	5.5/0.4	291	8/0.4
80	4/0.4		

NiO was ball milled to reduce the size of the raw material. The standard particle size was approximately 18 μm, which was deemed too large for anode use (see figure 3.5). A particle size/milling study was performed to determine the time taken to reduce the particle size to the appropriate dimensions.

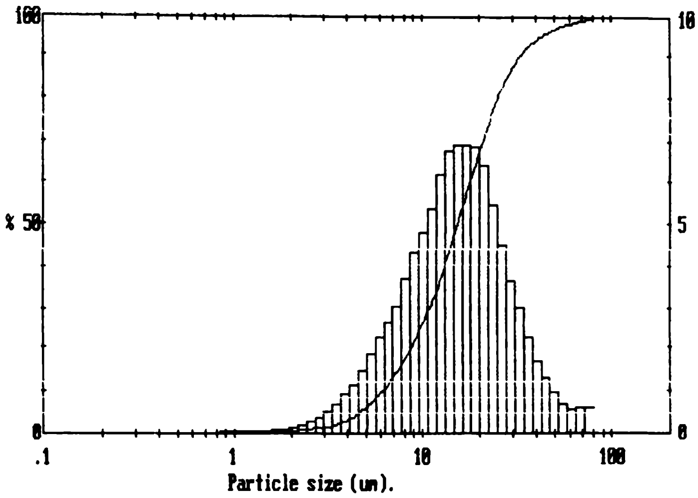

Figure 3.5 Particle size distribution of NiO as received.

After approximately 45 minutes of ball milling, a bimodal particle size distribution was observed with a peak at 7 μm and a broad peak at 0.5 μm. The broad peak grew as more fine NiO was milled and the other peak slowly moved towards a smaller particle size. At approximately 52 hours of ball milling, the two peaks merged giving a monomodal particle size distribution at 0.6 μm (see figure 3.6). Further milling to a maximum of 64 hours was undertaken, with no significant change in particle size. Table 3.3 lists the particle sizes obtained with the specific milling times using the ball milling technique for NiO.

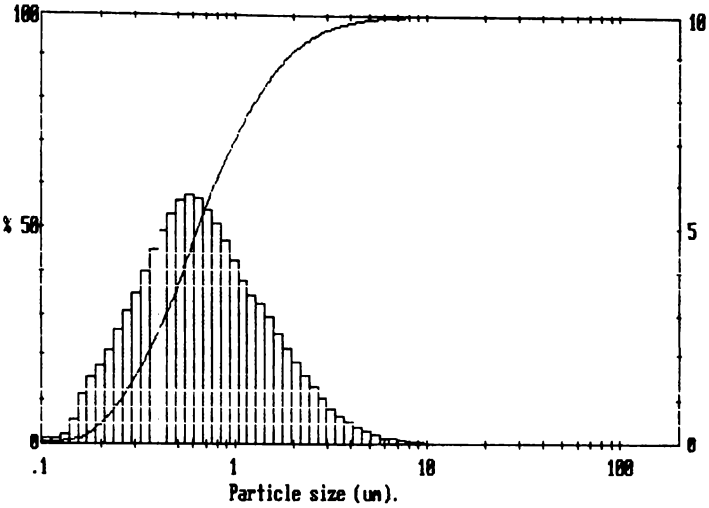

Figure 3.6 Particle size distribution of NiO after 52 hours of ball milling.

Table 3.3 Particle sizes obtained with the specific milling times using the ball milling technique for NiO.

Time (hours)	Particle Size (μm)
0	18
45 minutes	8/0.6
1	7/0.4
2	7/0.4
6	5/0.4
11	4/0.4
16	3/0.4
23	2.5/0.4
40	1.8/0.4
52	0.65
64	0.60

3.3.2.2 Centrifugal Milling

The standard size of the YSZ agglomerates after sintering at 1400 °C was approximately 33 μm (figure 3.7). Centrifugal milling of the YSZ calcined at 1400 °C produced a smaller particle size distribution as shown by the steep peaks on the particle size graph. After 45 minutes of centrifugal milling a bimodal particle size distribution was observed with particle sizes of 0.3 and 15 μm. Figure 3.8 shows the particle size at the maximum milling time of 7 hours, at which time the particles attained a size of 0.3 and 5 μm.

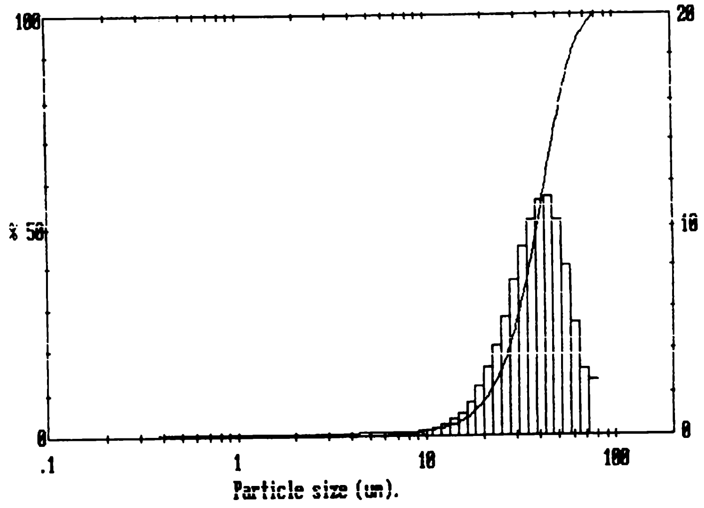

Figure 3.7 Particle size distribution of the YSZ agglomerates after sintering at 1400 °C.

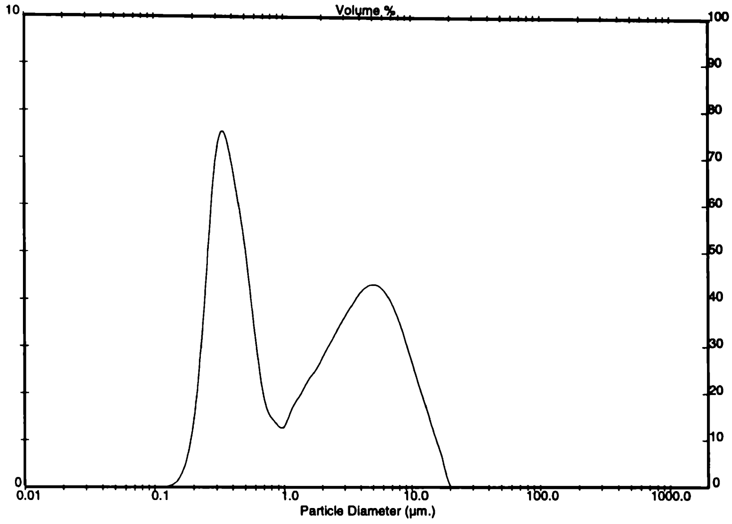

Figure 3.8 Particle size distribution of the YSZ sintered at 1400 °C after 7 hours of centrifugal milling.

The SEM micrograph (figure 3.9) of the YSZ agglomerates after 45 minutes of milling, shows the mode of fracture occurring. The YSZ sintered at 1100 °C produced a large amount of very fine YSZ (0.4 µm) as well as the fractured agglomerates which had broken off individual YSZ particles. The YSZ agglomerates sintered at 1400 °C had been fractured into pieces rather than fine particles, due to the high degree of sintering, and thus a smaller proportion of the fine YSZ was present. The resulting particles produced from the centrifugal mill were very irregular in shape and had a large surface area, and therefore a larger reaction area in the final anode would be expected (see Appendix 3 for a complete record of the SEM study). Table 3.4 lists the particle sizes obtained with the specific milling times using the centrifugal milling technique for YSZ sintered at 1400 °C.

Figure 3.9 Micrograph of YSZ sintered at 1100 °C after 45 minutes of milling.

Table 3.4 Particle sizes obtained with the specific milling times using the centrifugal milling technique for YSZ sintered at 1400 °C.

Time (hours)	Particle Size (µm)
0	35
45 minutes	12/0.3
1	10/0.3
3	9/0.3
5	5/0.3
7	4.9/0.3

Centrifugal milling of the NiO was also performed for the express purpose of modifying the particle size. It can be seen from figure 3.10(a) that a bimodal particle size distribution was present before milling had commenced, with a third peak consisting of agglomerated NiO. After 30 minutes of milling, most of the agglomerated NiO had been dispersed and two peaks were observed at approximately 0.3 μm and 2 μm (figure 3.10(b)).

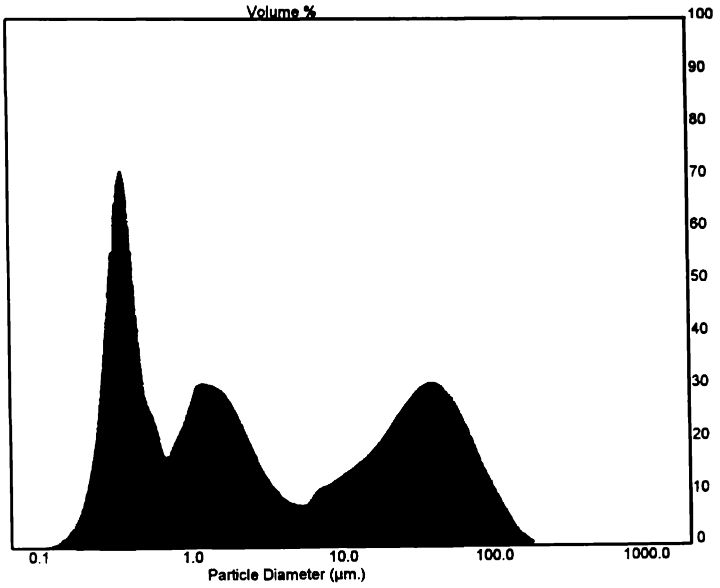

Figure 3.10(a) Bimodal particle size distribution of NiO before milling, including a third peak of agglomerated NiO.

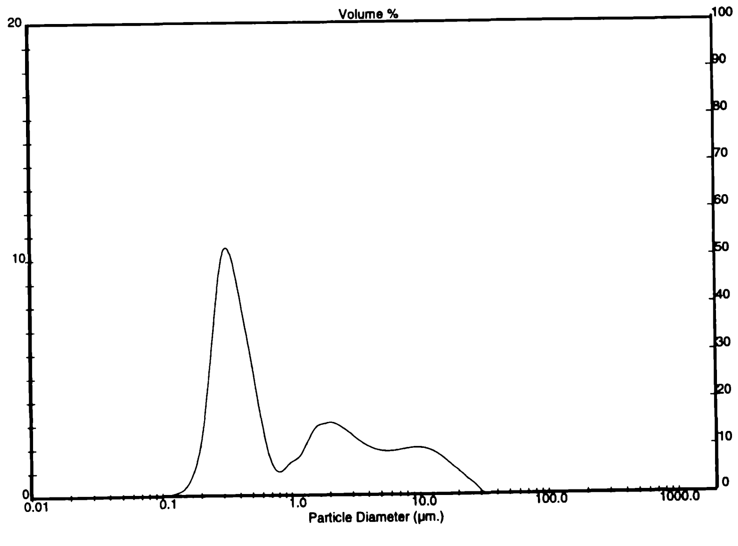

Figure 3.10(b) Bimodal particle size distribution of NiO after 30 minutes of centrifugal milling.

The SEM images (figure 3.11(a) and 3.11(b)) clearly show the decreased particle size of the NiO after the centrifugal milling had taken place. It is obvious that a wider particle size distribution has been produced, ranging from approximately 0.1 µm to 2 µm.

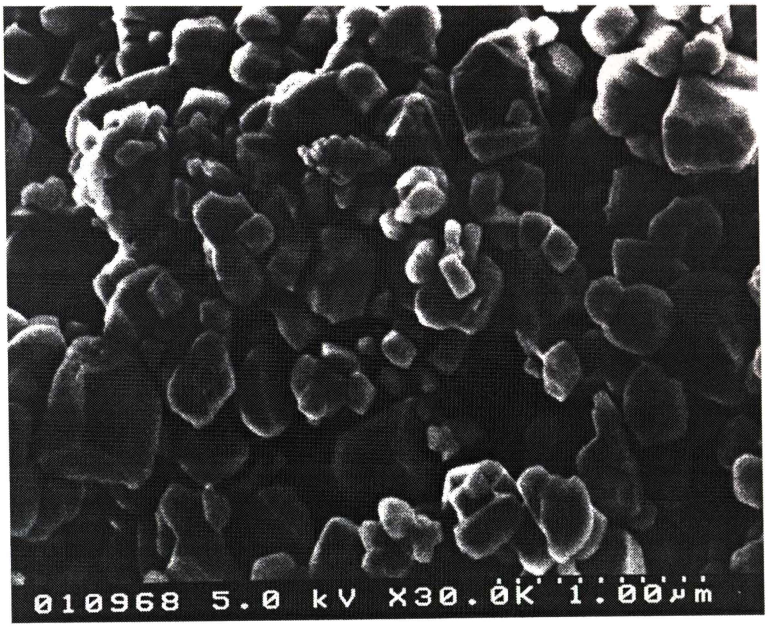

Figure 3.11(a) Micrograph of NiO before centrifugal milling.

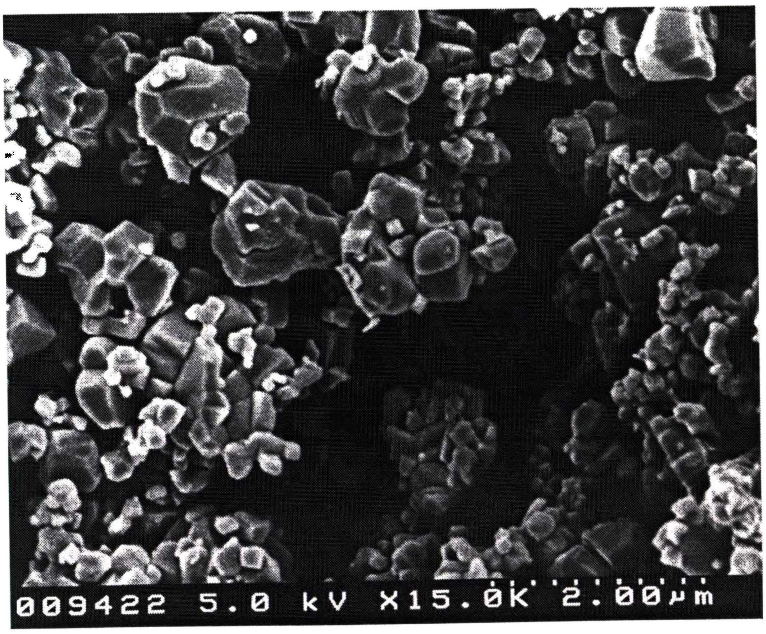

Figure 3.11(b) Micrograph of NiO after centrifugal milling for 30 minutes.

3.3.3 Wet Powder Spraying®

Different paint formulae were tested, using varying the type of solvent and binders. Methyl ethyl ketone was mixed with Hypermer KD1® dispersant, and the anode powder, and applied onto the YSZ substrate. It was discovered that the MEK evaporated immediately after leaving the spray gun and thus the anode powder arrived at the substrate in a dry state, and therefore could not pack down sufficiently to produce a working anode. Figure 3.12 shows a micrograph of a sprayed anode after sintering using the MEK based paint. The porosity of the anode was considered too high and therefore no electronic conduction was evident.

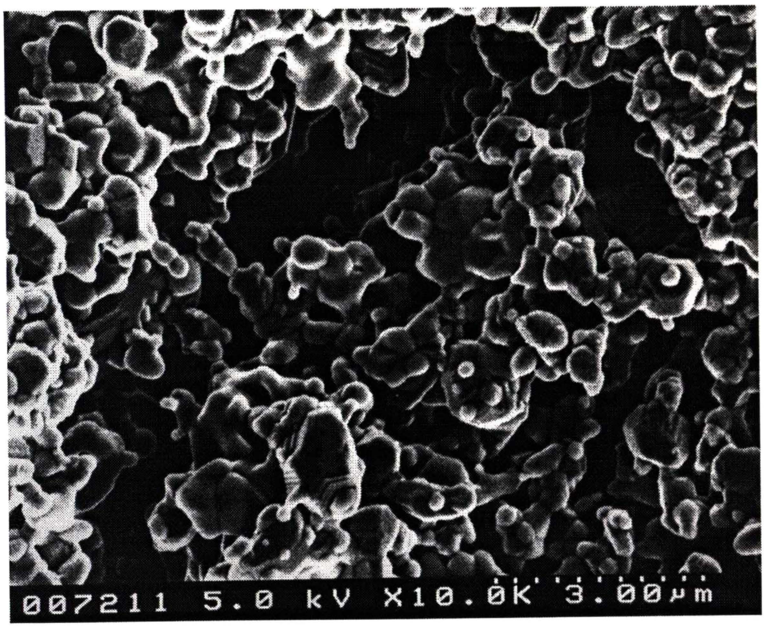

Figure 3.12 Micrograph of a sintered anode fabricated with a Wet Powder Spraying® technique.

The paint solvent was changed to ethanol and the binder/dispersant changed to PVP which produced a slurry with no visible settling-out in the time taken to spray an anode layer. This procedure was based on a method developed by Bagger[17] and worked satisfactorily with the modified setup used for this research. Figure 3.13 shows a flowchart of the steps involved in the fabrication of the anode layer.

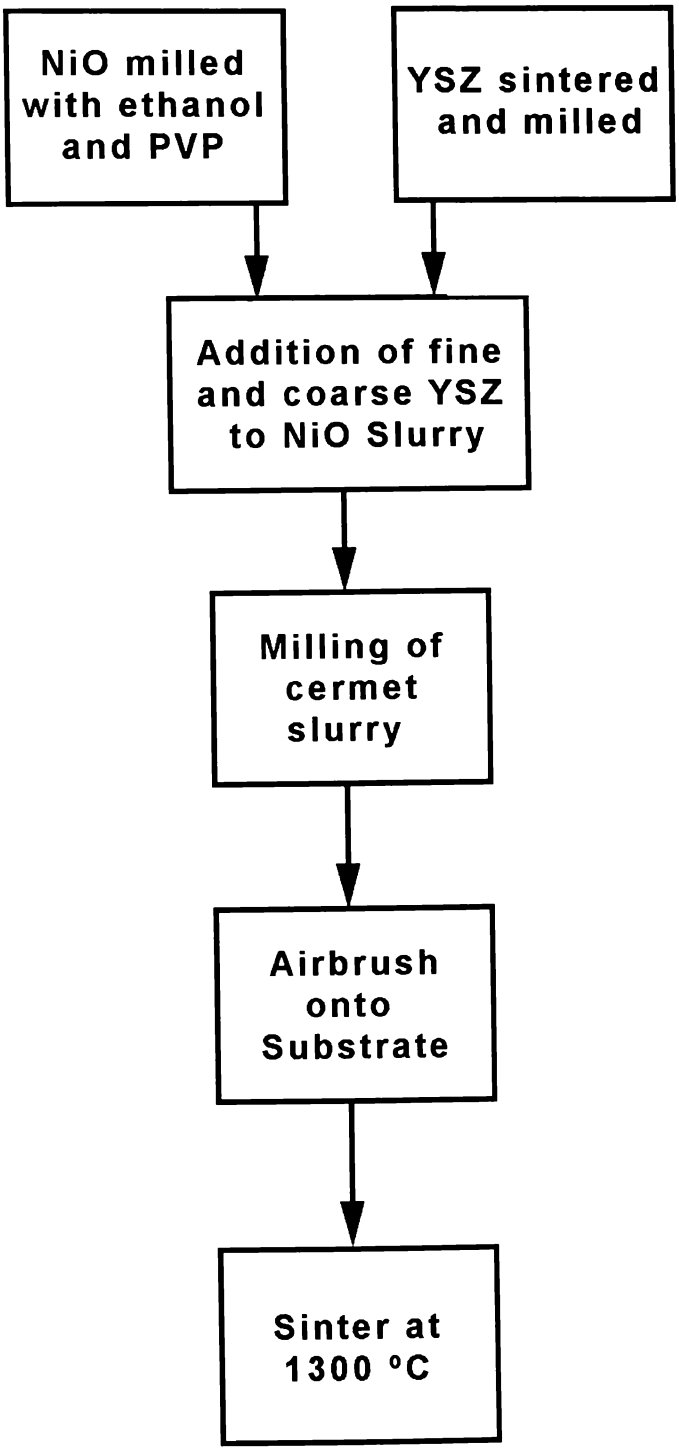

Figure 3.13 Flowchart of the steps involved in the fabrication of Ni/YSZ cermet anodes.

3.3.4 Sintering Temperature

Three sintering temperatures were tested, these being 1300 °C, 1400 °C and 1450 °C. At the sintering temperature of 1400 °C, the NiO agglomeration was not obvious, but proved high enough to impede electronic conduction in the reduced anode. The 1300 °C sintering temperature was sufficient to sinter the active YSZ, producing an adhering anode layer in the samples, with no agglomeration of the NiO observed. Figures 3.14(a) and 3.14(b) show the particle size of the Ni after sintering and after reduction, with no significant increase. In-plane resistance for the anode sintered at 1300 °C, with a distance of 1 cm between the contacts gave a value of 3 Ω. This was due to the reduced Ni agglomeration and higher density of the anode structure, creating the continuous Ni phase essential for electronic conduction.

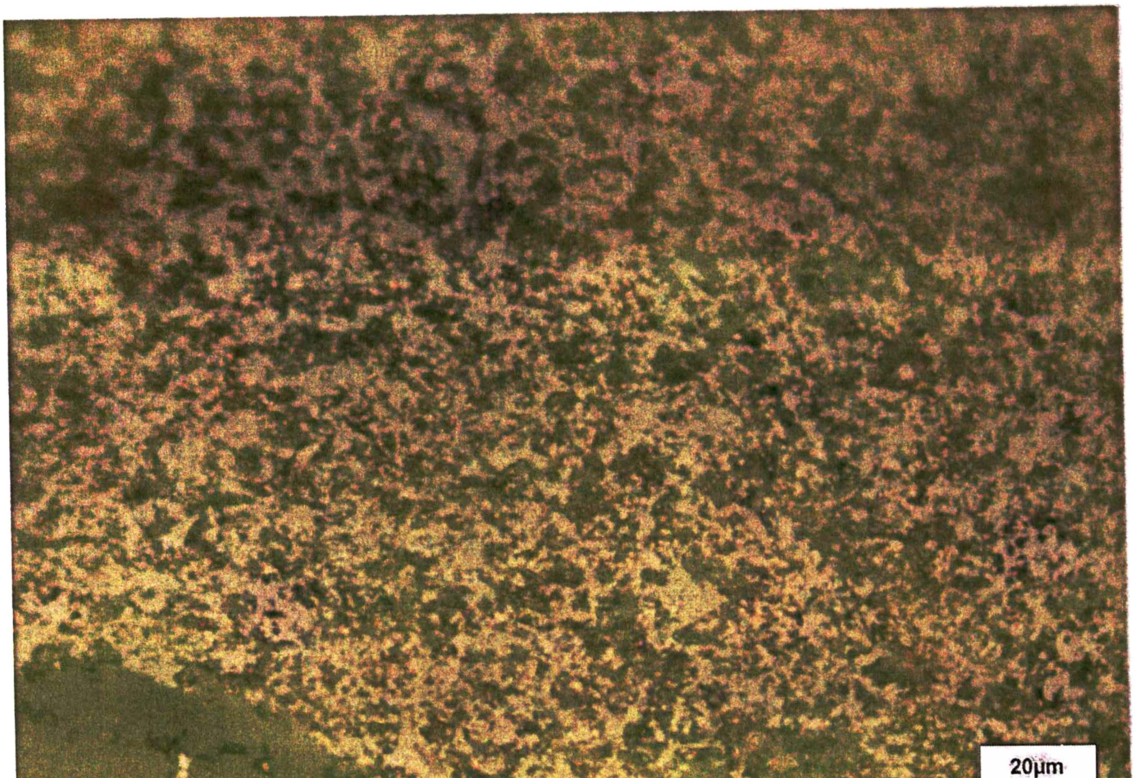

Figure 3.14(a) Optical micrograph of a NiO/YSZ anode after sintering at 1300 °C showing homogeneous microstructure.

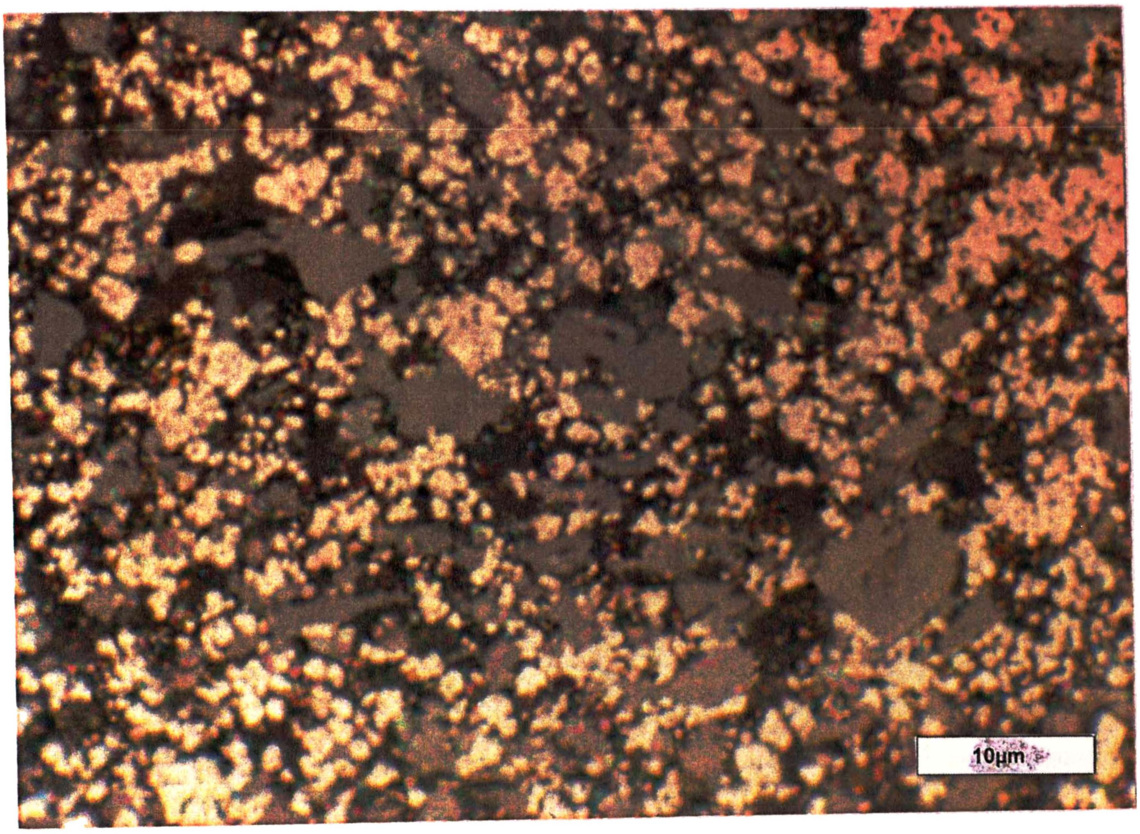

Figure 3.14(b) Optical micrograph of a Ni/YSZ anode after reduction in H_2 at 700 °C showing homogeneous microstructure.

It was found that at 1450 °C there was significant agglomeration of the NiO causing a very high resistance in the final anode after reduction. Fig 3.15(a) shows the particle size of the NiO (4-5 μm) after sintering, compared to the original particle size of 0.5 μm-1μm.

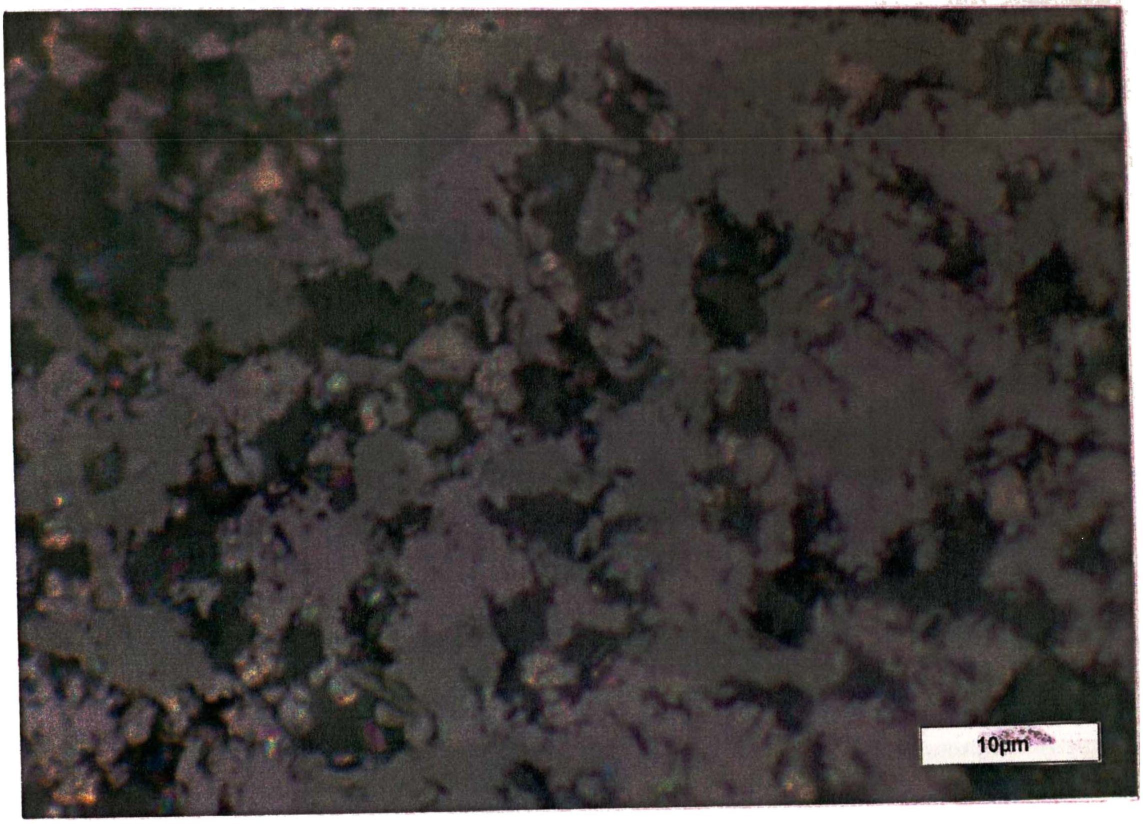

Figure 3.15(a) Optical micrograph of a NiO/YSZ anode after sintering at 1450 °C showing agglomeration of NiO.

Fig 3.15(b) illustrates the same anode after reduction in hydrogen. The porosity of the anode is very high, and all the fine Ni has agglomerated into 4 µm particles, therefore no continuous Ni paths are present.

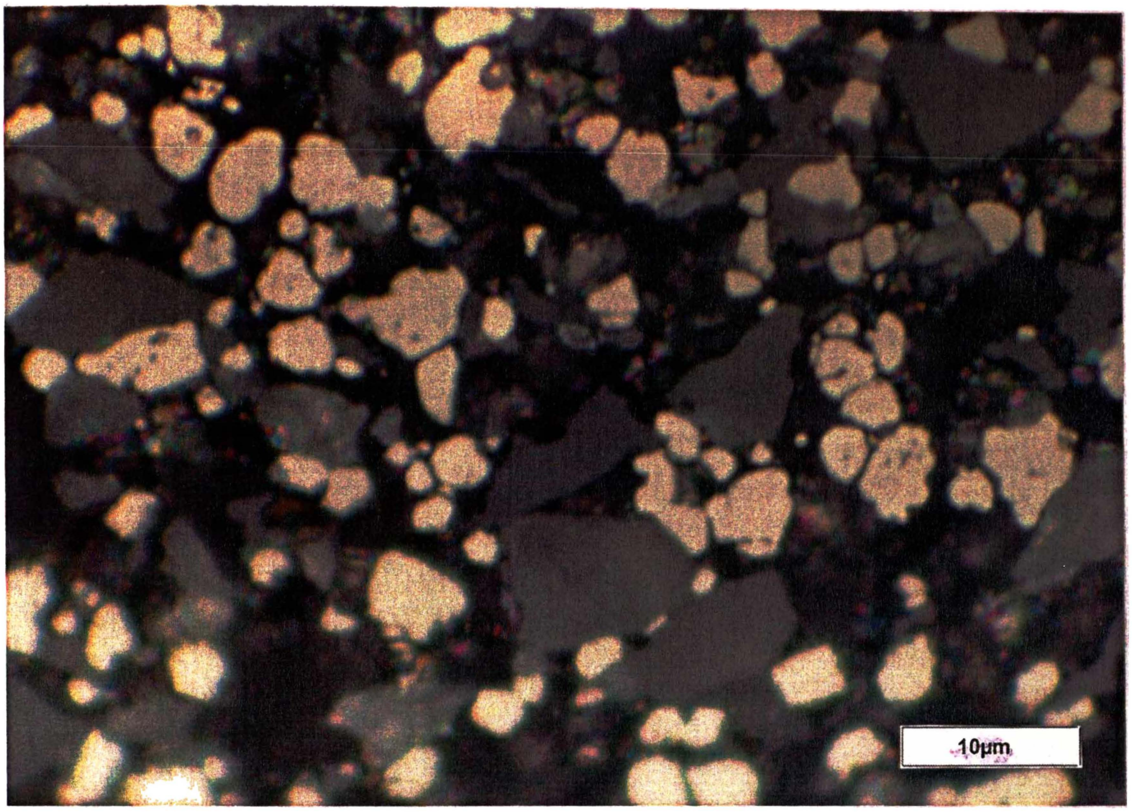

Figure 3.15(b) Optical micrograph of a Ni/YSZ anode after reduction in H_2 at 700 °C showing agglomeration of Ni into non-connecting'islands'.

3.3.5 Fabricated Anodes

This section describes the anodes fabricated, including the materials (and modifications to those materials), the procedures involved and a brief summary of the results. All the anodes have 50 vol% Ni, unless otherwise stated (see Appendix 4 for optical micrographs of all anodes fabricated).

Anode #	Materials							Methodology							Methodology	Results
	YSZ Particle Size (micron)	Calcining Temperature (degrees C/hours)	Mill Type	Milling Time (hours)	NiO Particle Size (micron)	Mill Type	Milling Time (hours)	Slurry Binder	Slurry Solvent	Anode Layers	Sintering Temperature (degree C/hours)	Mill Type	Milling Time (hours)	Anode Reduction (Temp/gas)		
1	45	1100/2			0.5-1micron	Centrifugal	30 mins	KD1	MEK	1	1250/2	Ball Mill	1	700/H2	NiO milled for 30 minutes in the centrifugal mill in ethanol and 5 wt% KD1. YSZ sintered at 1100 deg. for 2 hours. YSZ added to NiO and mixed for 1 hour in the centrifugal mill.	After reduction the whole anode spalled off theYSZ pellet. Conduction of 0.4 W/cm. Optical microscopy shows large YSZ agglomerates surrounded by continuous paths of Ni particles. Very high porosity and no matrix of fine YSZ to form a rigid structure therefore no adhesion of anode layer.
2	80 wt%/45 20 wt%/0.4	1100/2			0.5-1micron	Centrifugal	2	PVP	Ethanol	1	1400/2	Ball Mill	24	700/H2	NiO milled for 24hours with 5wt% PVP in 70ml milling vessel with 5 PSZ milling balls in 30ml ethanol at 57rpm. YSZ and 5wt% PVP was mixed with the NiO and milled for another 24hrs. 1 layer sprayed onto YSZ substrate and sintered at 1400°C for 2 hrs.	No conduction and no adhesion. Optical microscopy showed 3-5mm Ni particles, but no fine YSZ present. All the YSZ was in the form of agglomerates and therefore no adhesion of the anode to the substrate. Very porous microstructure.
3	60 wt%/45 40 wt%/0.4	1100/2			0.5-1micron	Centrifugal	2	PVP	Ethanol	1	1400/2	Ball Mill	24	700/H2	NiO milled (mill#2) for 24hrs. with 5wt% PVP and then YSZ added with a further 5wt% PVP. 1 layer sprayer and sintered at 1400°C for 2 hrs.	No conduction and no adhesion. Optical microscopy showed 3-5mm Ni particles, but no fine YSZ present. All the YSZ was in the form of agglomerates and therefore no adhesion of the anode to the substrate. Very porous microstructure.
4	80 wt%/40 20 wt%/0.4	1400/17			0.5-1micron	Centrifugal	2	PVP	Ethanol	1	1400/2	Ball Mill	24	700/H2	NiO milled (mill#2) for 24hrs. with 5wt% PVP and then YSZ added with a further 5wt% PVP. 1 layer sprayed and sintered at 1400°C for 2 hrs.	No conduction and no adhesion. Optical microscopy showed 3-5mm Ni particles, but no fine YSZ present. All the YSZ was in the form of agglomerates and therefore no adhesion of the anode to the substrate. Very porous microstructure.
5	60 wt%/40 40 wt%/0.4	1400/17			0.5-1micron	Centrifugal	2	PVP	Ethanol	1	1400/2	Ball Mill	24	700/H2	NiO milled (mill#2) for 24hrs. with 5wt% PVP and then YSZ added with a further 5wt% PVP. 1 layer sprayer and sintered at 1400°C for 2 hrs.	No conduction and no adhesion. Optical microscopy showed 3-5mm Ni particles, but no fine YSZ present. All the YSZ was in the form of agglomerates and therefore no adhesion of the anode to the substrate. Very porous microstructure.
6	50 wt%/40 50 wt%/0.4	1100/2			0.5-1micron	Centrifugal	2	PVP	Ethanol	3	1400/2	Ball Mill	24	700/H2	Using Riso method. NiO milled with 5wt% PVP for 24 hours and then YSZ added with another 5wt% PVP and milled for 24 hours. 3 layers sprayed onto YSZ substrate and sintered at 1400°C for 2 hours. Sintering performed between layers.	No conduction and no adhesion. Optical microsopy showed a slightly denser structure than the previous anodes. Large voids in the first layer and still complete agglomerates present. Porosity high.
7	50 wt%/45 50 wt%/0.4	1100/2			0.5-1micron	Centrifugal	2	PVP	Ethanol	1	1400/2	Ball Mill	24	700/H2	NiO and YSZ was mixed together for 20 mins. using an ultrasonic bath. The mix was sprayed onto a YSZ substrate and sintered at 1400°C for 2 hrs.	No adhesion and no conduction. Optical microscopy showed a homogeneous microstructure (no large YSZ agglomerates) but still high porosity.
8	80 wt%/14 20 wt%/0.4	1400/17	Centrifugal	45 mins	0.5-1micron	Centrifugal	2	PVP	Ethanol	2	1450/2	Ball Mill	24	700/H2	NiO and 5wt% PVP milled for 24hrs. YSZ and PVP milled with NiO for 24hrs. No milling media added for the second 24 hrs milling due to the fact that the raw materials have the correct particle sizes already. Fine anode layer applied to the substrate and fired at 1450 deg for 5 hrs. One thick layer applied and fired again.	Good adhesion but no conduction. Optical microscopy showed agglomeration of the Ni caused by a too high firing temp. agglomerating the NiO. Very high porosity.
9	80 wt%/14 20 wt%/0.4	1400/17	Centrifugal	45 mins	0.5-1micron	Centrifugal	2	PVP	Ethanol	2	1450/2	Ball Mill	24	700/H2	NiO and 5wt% PVP milled for 24hrs. YSZ and PVP milled with NiO for 24hrs. No milling media added for the second 24 hrs milling due to the fact that the raw materials have the correct particle sizes already. Fine anode layer applied to the substrate and fired at 1450 deg for 5 hrs. One thick layer applied and fired again.	Good adhesion and spot-wise conduction of about 1.5 ohms/5mm. Optical microscopy showed a denser structure. Continuous pathways of Ni and YSZ are evident with varying amounts of Ni throughout the anode.
10	14	1400/17	Centrifugal	45 mins	0.5-1micron	Centrifugal	2	PVP	Ethanol	2	1450/5	Ball Mill	24	700/H2	NiO and 5wt% PVP milled for 24hrs. YSZ and PVP milled with NiO for 24hrs. No milling media added for the second 24 hrs milling due to the fact that the raw materials have the correct particle sizes already. Fine layer applied and sintered at 1450°C for 5hrs. Another thicker layer applied and sintered at the same temp.	Good adhesion but no conduction. Optical microscopy showed agglomeration of the Ni due to agglomeration of the NiO because of high sintering temp. Very high porosity.
11	80 wt%/14 20 wt%/0.4	1400/17	Centrifugal	45 mins	0.5-1micron	Centrifugal	2	PVP	Ethanol	2	1450/5	Ball Mill	24	700/H2	NiO and 5wt% PVP milled for 24hrs. YSZ and PVP milled with NiO for 24hrs. This time the milling media was left in for the last 24hrs of milling. . Fine layer applied and sintered at 1450°C for 5hrs. Another thicker layer applied and sintered at the same temp.	Good adhesion, no conduction. Large agglomerates present, slightly less porosity, no fine sintered particles of YSZ present (only the agglomerates). Agglomeration of the Ni due to the high sintering temp.
12	5	1400/17	Centrifugal	5	100nm-1micron	Centrifugal	2	PVP	Ethanol	1	1450/5	Ball Mill	24	700/H2	NiO and YSZ milled together for 24hrs with 5wt% PVP and 1 layer sprayed on to YSZ substrate.	Good adhesion, no conduction. Optical microscopy shows lower porosity but not as low as anode 16a. Evenly sized YSZ and Ni of about 4-5mm. Ni agglomerated due to high sintering temp.
13 60 vol% Ni	5	1400/17	Centrifugal	5	100nm-1micron	Centrifugal	2	PVP	Ethanol	1	1450/5	Ball Mill	24	700/H2	NiO and YSZ milled together without milling media for 24hrs with 5wt% PVP. Single layer applied and sintered at 1450°C for 5 hrs.	Slightly less adhesion and more porosity than anode 12, perhaps due to extra Ni content. No conduction. Ni agglomeration due to high sintering temp.
14	5	1400/17	Centrifugal	5	1 micron			PVP	Ethanol	1	1300/2	Ball Mill	24	700/H2	NiO milled for 24hrs with 10wt% PVP. YSZ added and milled for a further 24hrs. 1 layer sprayed on to a YSZ substrate and sintered at 1300°C for 2hrs.	Good adhesion. Resistance of <20 ohms/cm over parts of the anode. Optical microscopy shows finely dispersed Ni particles. Lower porosity, but still not low enough.
15	50 wt%/5 50 wt%/0.4	1400/17	Centrifugal	5	100nm-1micron	Centrifugal	5	PVP	Ethanol	3	1300/2	Ball Mill	24	700/H2	NiO and 5wt% PVP milled for 24hrs and then YSZ added with 5wt% PVP and milled for another 24hrs. Three layers sprayed onto YSZ substrate beginning with a thin (10mm) layer. Sintered at 1300°C for 2 hrs and reduced in hydrogen at 700°C for 1hr.	No conduction, good adhesion. Optical microscopy showed a homogeneous microstructure after sintering with continuous paths of YSZ particles and NiO particles. After reduction, individual particles of Ni were present and very high porosity perhaps indicating agglomeration of the Ni particles.
16	75 wt%/5 25 wt%/0.4	1400/17	Centrifugal	5	100nm-1micron	Centrifugal	5	PVP	Ethanol	3	1300/2	Ball Mill	24	700/H2	NiO and 5wt% PVP milled for 24hrs and then YSZ added with 5wt% PVP and milled for another 24hrs. Three layers sprayed onto YSZ substrate beginning with a thin (10mm) layer. Sintered at 1300°C for 2 hrs and reduced in hydrogen at 700°C for 1hr.	No conduction, good adhesion. Optical microscopy showed a homogeneous microstructure after sintering with continuous paths of YSZ particles and NiO particles. After reduction, individual particles of Ni were present and very high porosity perhaps indicating agglomeration of the Ni particles.
17	50 wt%/4 50 wt%/0.4	1400/17	Centrifugal	7	100nm-1micron	Centrifugal	5	PVP	Ethanol	3	1300/2	Ball Mill	24	700/H2	NiO and 5wt% PVP milled for 24hrs and then YSZ added with 5wt% PVP and milled for another 24hrs. Three layers sprayed onto YSZ substrate beginning with a thin (10mm) layer. Sintered at 1300°C for 2 hrs and reduced in hydrogen at 700°C for 1hr.	No conduction, good adhesion. Optical microscopy showed a homogeneous microstructure after sintering with continuous paths of YSZ particles and NiO particles. After reduction, individual particles of Ni were present and very high porosity perhaps indicating agglomeration of the Ni particles.
18	75 wt%/4 25 wt%/0.4	1400/17	Centrifugal	7	100nm-1micron	Centrifugal	5	PVP	Ethanol	3	1300/2	Ball Mill	24	700/H2	NiO and 5wt% PVP milled for 24hrs and then YSZ added with 5wt% PVP and milled for another 24hrs. Three layers sprayed onto YSZ substrate beginning with a thin (10mm) layer. Sintered at 1300°C for 2 hrs and reduced in hydrogen at 700°C for 1hr.	No conduction, good adhesion. Optical microscopy showed a homogeneous microstructure after sintering with continuous paths of YSZ particles and NiO particles. After reduction, individual particles of Ni were present and very high porosity perhaps indicating agglomeration of the Ni particles.
19	4	1400/17	Centrifugal	7	100nm-1micron	Centrifugal	5	PVP	Ethanol	3	1300/2	Ball Mill	24	700/H2	NiO and 5wt% PVP milled for 24hrs and then YSZ added with 5wt% PVP and milled for another 24hrs. Three layers sprayed onto YSZ substrate beginning with a thin (10mm) layer. Sintered at 1300°C for 2 hrs and reduced in hydrogen at 700°C for 1hr.	No conduction, good adhesion. Optical microscopy showed a homogeneous microstructure after sintering with continuous paths of YSZ particles and NiO particles. After reduction, individual particles of Ni were present and very high porosity perhaps indicating agglomeration of the Ni particles.

3.4 Discussion

3.4.1 YSZ Calcining Temperature

This section of research was performed to show there was a large dependence on the milling time and particle size distribution, as a function of initial sintering temperature of the YSZ. An increase in sintering temperature coarsens the powder through diffusional processes by increasing the bond area at the point of contact between particles. The calcination process accelerated grain growth and strengthens intragranular bonds[19].

At a sintering temperature of 1100 °C, the YSZ was only partially sintered. The structure of the agglomerates showed YSZ balls (approximately 45-50 μm in diameter) made up of fine particles of YSZ. The structure was porous with partial sintering, indicating a weak structure, which was easily milled into fine YSZ (0.4 μm) and fractured agglomerates.

At a sintering temperature of 1400 °C, no porosity within the agglomerates was present. The average size (35-40 μm) of the agglomerates was smaller than the YSZ sintered at 1100 °C, indicating a more dense structure. Figure 3.1(b) clearly shows the higher density of the structure as each particle is completely bonded to its surrounding particles.

The higher sintering temperature allowed more intragrain interaction and higher reactivity of the YSZ thereby enhancing the individual YSZ particles to bond, forming agglomerates with increased density. The difference in sintering temperature of the YSZ allowed the variations in particle size distribution to be produced, to study the effects of particle size on anode performance.

It has been shown[16] that precalcining a portion of the YSZ for the anode slurry at 1000-1100 °C, and the addition of uncalcined YSZ, can enhance adhesion. Presumably, this can be accounted for by the high sinterability of the uncalcined (fine) YSZ. Increasing the particle size distribution also allows the anode to be sintered at 1300 °C with good adhesion.

3.4.2 Milling

Since milling of the YSZ can be performed before adding it to the anode slurry, additional control of the slurry particle properties can be obtained. Ball milling and centrifugal milling of the YSZ sintered at 1100 °C and 1400 °C were used to modify the particle size and particle size distribution of the YSZ and the NiO.

Overall, bimodal particle distributions were present for the YSZ, which indicated two particle sizes. The finest particles were individual YSZ particles of approximately 0.4 µm, which represented the grinding limit, and was independent of calcining temperature. The larger particles in the bimodal distribution data consisted of fractured agglomerates. The agglomerate size decreased and the amount of fine YSZ increased as milling times were extended. This indicated that the agglomerates were being milled into finer agglomerates, but also a substantial amount of fine YSZ was being produced.

Centrifugal milling was the more energetic of the two milling processes and therefore less time was needed to produce a given particle size. Centrifugal milling of the YSZ calcined at 1100 °C was so efficient that this avenue was not pursued due to the very short milling times encountered, which caused inhomogeneous milling.

The grinding limit of the NiO (approximately 0.5 µm) was reached at approximately 52 hours with the ball milling technique, whereas the YSZ sintered at 1400 °C was milled for 291 hours and still retained a very broad peak at approximately 8-9 μm. The grinding limit of the YSZ sintered at 1100 °C was not reached after 26 hours.

3.4.3 Wet Powder Spraying

The technique used to deposit the anode slurry onto the YSZ substrate was wet powder spraying (WPS®). In the present series of experiments, the method used was air spraying an ethanol-based slurry onto the substrate. During the early stages of experimentation, a methylethylketone (MEK) based slurry with Hypermer KD1® dispersant/binder was used to form the stable slurry. It was found that the ceramic powders would arrive at the substrate in a semi-dry condition, thus allowing minimum densification on the substrate. The anodes produced with this slurry proved to be very porous and it is suggested that this is a contributing factor to the very low electronic conductivity of these anodes.

The slurry was modified, by using ethanol as the solvent and a PVP binder to form the stable suspension. The ethanol reduced the rapid evaporation rate of the slurry and allowed the ceramic powders more time to settle before evaporation was complete. It also came clear that too much of the liquid phase on the substrate allowed separation of the NiO and YSZ to occur, causing a layering effect. The large particles descended to the electrolyte/electrode layer interface and the fine YSZ floated to the surface. This caused very low in-plane electronic conduction. Adhesion was also compromised due to too little of the fine, highly sinterable YSZ being present at the electrolyte/electrode interface to form the bonding of the cermet layer.

It was also observed that the application of a thin (5-10 μm) primary layer of anode slurry was beneficial, as determined by Bagger *et al.*[16]. The limited thickness gave a good anchoring effect for the subsequent layers and also inhibited a mud-cracking effect encountered when one thick anode layer was applied.

3.4.4 Sintering Temperature

The importance of the sintering temperature on conductivity and performance of Ni/YSZ anodes was examined by sintering anodes at 1300, 1400 and 1450 °C. From figures 3.15(a) and 3.15(b) it can be seen that a significant amount of NiO agglomeration has occurred at the sintering temperature of 1450 °C. It was also present to a much lesser degree in the anodes sintered at 1400 °C.

Agglomeration of the NiO had occurred at the high sintering temperature of 1450 °C. At this temperature the NiO was mobile enough to agglomerate from a particle size of approximately 1 μm to an average particle size of 4 μm. Upon reduction in hydrogen, the Ni formed 'islands' within the YSZ matrix and thus little percolation existed, causing very low electronic conduction. This implied that the sintering temperature was too high and must be reduced to fabricate satisfactory anodes.

Anodes sintered at 1300 °C showed none of the agglomeration of NiO present in the samples sintered at higher temperatures. It can be seen in figures 3.14(a) and 3.14(b) that there was no discernable increase of Ni particle size after sintering and reduction in hydrogen. This allowed for increased percolation of the metallic phase and therefore a higher electronic conduction. An in-plane resistance of 20 Ω was achieved over a distance of 1 cm.

Ni/YSZ anodes fabricated by Primdahl *et al.*[19] were sintered between 1100 and 1500 °C. Figure 3.16 shows that with sintering temperatures from 1300 to 1400 °C the anode polarisation resistance was 0.12-0.14 Ωcm^2, measured in a symmetrical electrode geometry at 1000 °C in wet hydrogen. At 1250 and 1500 °C the polarisation resistance was higher by a factor of two, and below a sintering temperature of 1250 °C, no in-plane conductivity was established after reduction.

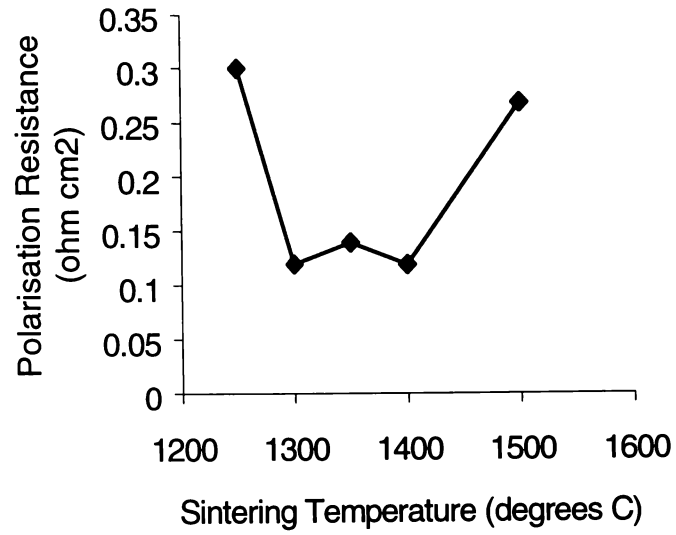

Figure 3.16 Polarisation resistance as a function of sintering temperature for anodes at 1000 °C in H_2 + 3% H_2O at OCV.

3.4.5 Anode Fabrication

3.4.5.1 Anode 1

Optical microscopy showed an anode fabricated with agglomerated YSZ (approximately 40 µm in diameter) and fine Ni (approximately 1 µm). No fine YSZ was present in the anode layer and thus a low degree of sintering occurred. This caused the anode to spall off the YSZ substrate, since there was no YSZ matrix present. Very good conduction was observed due to the continuous paths of Ni present. Long term performance of this anode would be very poor due to agglomeration of the Ni, reducing the electronic conduction.

3.4.5.2 Anodes 2 to 7

Optical microscopy showed good adhesion of the anode layer to the YSZ substrate after sintering, but major spalling occurred after the reduction process. This suggests that the fine YSZ present in the cermet did not sinter together to form the YSZ matrix needed for a stable anode layer. All five anodes showed a high porosity which is detrimental to anode adhesion and electronic conductivity. Anodes four and five exhibited layering of the coarse and fine YSZ. The coarse YSZ collected at the electrode/electrolyte interface, whereas the fine YSZ occupied the top of the layer. This caused a lack of adhesion to the YSZ substrate and also produced high porosity.

3.4.5.3 Anodes 8 to 11

Optical microscopy showed severe agglomeration of the NiO after sintering, which indicated a sintering temperature of 1450 °C was too high. The particle size of the Ni grew from approximately 1 µm to an average of 4 µm. This resulted in a 'Ni island' effect after reduction, and therefore very low electronic conduction. Adhesion was good, probably due to the higher sintering temperature causing more YSZ agglomeration to occur, forming a dense YSZ matrix to stabilise the anode layer. Anode nine exhibited spot-wise resistance of 3 Ωcm^{-1}. Optical microscopy showed a denser structure when comparing to the other anodes and therefore more continuity of the Ni phase was present, resulting in a higher electronic conduction. An inhomogeneous Ni distribution was also observed for anode nine (see figure A4.33, Appendix 4). Less Ni was present towards the edges of the YSZ substrate, hence the spotwise conduction.

3.4.5.4 Anodes 12 and 13

Due to the high sintering temperature used (1450 °C), agglomeration of the NiO had taken place resulting in very low electronic conduction. Anode 13 had 60 vol% Ni in order to increase the possibility of electronic conduction. This increased Ni content had weakened the adhesion by reducing the amount of YSZ available to form the YSZ stabilising matrix. There were large (20 µm diameter) holes present in the anode, possibly due to air bubbles trapped in the layer during spray painting.

3.4.5.5 Anode 14

Anode 14 had very good adhesion due to the lower Ni content (50 vol%) when compared to anode 13. The sintering temperature was lowered to 1300 °C to avoid NiO agglomeration. This anode had an in-plane resistance of <20 Ωcm^{-1}, which was due to the finely dispersed Ni particles with an average size of approximately 1 µm. The porosity was also low which enhanced the Ni-Ni particle contact and increased percolation.

3.4.5.6 Anodes 15 to 19

A sintering temperature of 1300 °C reduced the level of NiO agglomeration and ensured most of the reduced anodes had a finely dispersed Ni phase present in the cermet layer. Each of the anodes had a homogeneous structure with obvious connecting paths of NiO and YSZ throughout the thickness of the anode layer. Porosity was very high and was the reason for the lack of electronic conductivity. Anodes 18 and 19 showed slight agglomeration of the Ni phase due to a reduced amount of fine YSZ present. This lack of fine YSZ reduced the 'pinning' effect between the Ni particles and thus allowed Ni agglomeration to proceed.

3.5 Conclusions

At a sintering temperature of 1100 °C, the YSZ was only partially sintered. The structure of the agglomerates showed YSZ balls (approximately 45-50 µm in diameter) made up of fine particles of YSZ, which were easily milled. At a sintering temperature of 1400 °C, no porosity within the agglomerates was present. The average size (35-40 µm) of the agglomerates was smaller than the YSZ sintered at 1100 °C, indicating a more dense structure.

Bimodal particle distributions were present for the milled YSZ, which indicated two particle sizes. The finest particles were individual YSZ particles of approximately 0.4 µm, and represented the grinding limit, which was independent of calcining temperature. The agglomerate size decreased and the amount of fine YSZ increased as milling times were extended. The grinding limit of the NiO (approximately 0.5 µm) was reached at approximately 52 hours with the ball milling technique. The YSZ sintered at 1400 °C was milled for 291 hours and retained a very broad peak at approximately 8-9 µm. The resulting particles after centrifugal milling were very irregular in shape, and therefore had a large surface area, which could give a larger reaction area (TPB) in the completed anode. The grinding limit of the YSZ sintered at 1100 °C was not reached after 26 hours.

The slurry was modified, by using ethanol as the solvent and a PVP binder to form a stable suspension. The ethanol reduced the rapid evaporation rate of the slurry and allowed the ceramic powders more time to settle before evaporation was complete. It also became clear that too much of a liquid phase on the substrate allowed separation of the NiO and YSZ to occur, causing a layering effect.

Agglomeration of the NiO in the anodes had occurred at the high sintering temperature of 1450 °C. At this temperature the NiO was mobile enough to agglomerate from a particle size of approximately 1 µm to an average particle size of 4 µm. Upon reduction in hydrogen, the Ni formed 'islands' within the YSZ matrix and thus little percolation existed, causing very low electronic conduction

Anodes sintered at 1300 °C showed none of the agglomeration of NiO present in the samples sintered at higher temperatures. There was no discernable increase of Ni particle size after sintering and reducing in hydrogen.

The anodes fabricated for this research have followed some distinct trends. It has become evident that the anode slurry must contain fine (0.4 µm) YSZ in order to produce an easily sintered YSZ matrix to form the anode structure. It is also possible that a certain amount of coarse (5-10 µm) YSZ would be beneficial to shorten the ionically conducting paths, and also to stabilise the YSZ structure. The Ni must have a small particle size (approximately 1 µm) to ensure a large triple phase boundary (TPB), but only a sufficient quantity (40-50 vol%) to ensure the percolation of electrons. Electronic conductivity was improved with the increase in density of the anode.

3.6 References

---

[1] N.Minh, Journal of the American Ceramic Society, **76**, 563 (1993)

[2] M.Mogensen, S.Primdahl. J.Rheinlander, S.Gormsen, S.Linderoth, M.Brown. Relations Between Performance and Structure of Ni-YSZ Cermet SOFC Anodes. 4th International Symposium on Solid Oxide Fuel Cells, June 18-23. 1995, Japan

[3] T.Kawada, N.Sakai, H.Yokokawa, M.Dokiya, M.Mori, T.Iwata. Solid State Ionics, **40/41**, 402 (1990)

[4] R.J.Aaberg, R.Tunold, F.W.Poulsen, N.Bonanos. Short Term Structural Changes in NiO/YSZ Electrodes upon Reduction. Proceedings of the 5th International Symposium on Solid Oxide Fuel Cells, SOFC V, June 2-5, 1997. Aachen, Germany.

[5] S.Ohara, T.Fului, K.Kodera, Y.Kubo. Microstructure and Long-Term Stability on Ni-YSZ Anode. Proceedings of the 5th International Symposium on Solid Oxide Fuel Cells, SOFC V, June 2-5, 1997. Aachen, Germany.

---

[6] H.Itoh, T.Yamamoto, M.Mori, T.Watanabe, T.Abe. *Denki Kagaku.* **64** 6 (1996)

[7] T.Saito. Effect of Ni and ZrO_2 on Anode Performance. SOFC Micromodelling. Edited by L.Dubal. Swiss Federal Office of Energy, Bern, pp21, 1992.

[8] A.Gubner, H.Landes, J.Metzger, H.Seeg, R.StÜbner. Investigations into the Degradation of the Cermet Anode of a Solid Oxide Fuel Cell. Proceedings of the 5th International Symposium on Solid Oxide Fuel Cells, SOFC V, June 2-5, 1997. Aachen, Germany.

[9] R.Wilkenhöner, Th.Kloidt, W.Malléner. Improved Initial Stability of SOFC Anode by Microstructural Optimisation. Proceedings of the 5th International Symposium on Solid Oxide Fuel Cells, SOFC V, June 2-5, 1997. Aachen, Germany.

[10] F.P.F.van Berkel, B. de Boer, G.S.Schipper, G.M.Christie. Optimisation of Anode Materials for use in a SOFC System. Proceedings of the 5th International Symposium on Solid Oxide Fuel Cells, SOFC V, June 2-5, 1997. Aachen, Germany.

[11] T.Iwata. *J.Electrochem.Soc.* **143** 5 (1996)

[12] A.Ioselevich, A.A.Kornyshev, W.Lehnert. *Journal of the Electrochemical Society.* **144** 9 (1997)

[13] T.Kawada, N.Sakai, H.Yokokawa, M.Dokiya, M.Mori and T.Iwata, *Journal of the Electrochemical Society*, **137**, 3042 (1990)

[14] S.Murakami, Y.Akiyama, N.Ishida, T.Yasuo, T.Saito, N.Furukawa. Development of a Solid Oxide Fuel Cell with Composite Anodes. Proceedings of the Second International Symposium on SOFC, July, 1991, Athens, Greece.

[15] D.W.Dees, T.D.Claar, T.E.Easler, D.C.Fee and F.C.Mrazek, *Journal of the Electrochemical Society*, **134**, 2141 (1987)

[16] C.Bagger; Improved Production Methods for YSZ Electrolyte and Ni/YSZ Anodes for SOFC. 1992 Fuel Cell Seminar, Tucson, Az., Nov., 1992.

[17] A.Ruder, H.Buchkremer, H.Jansen, W.Mallener and D.Stover. *Surface Coating Technology*, **53**, 71 (1992)

[18] C.Manon. Tailoring the Cathode Layer Through Ball Milling. Risø Internal Report, Material Science Department, Roskilde, Denmark. Nov. 1995.

[19] S.Primdahl. Anode Sintering Temperature. Risø Internal Report. BC-322, March 1997. Materials Research Department, Risø National Laboratory, Denmark.

Chapter Four

Paper submitted to The 18th Australasian Ceramics Conference. Proceedings to be published in a special issue of The Journal of the Australasian Ceramics Society.

4. Ni/YSZ Active Layer Thickness

4.1 Introduction

A porous cermet of Ni/yttria stabilised zirconia (YSZ) is generally accepted as a high performance anode for a solid oxide fuel cell[1]. The performance of the anode is strongly dependent on the fabrication methods and resulting microstructure of the cermet[2].

A structure consisting of three percolating phases (Ni, YSZ, porosity) is considered to be an efficient anode with a long triple phase boundary (TPB). The TPB is the reaction area where hydrogen oxidation takes place and is present wherever YSZ, Ni and the fuel gas meet.

For efficient percolation, it is very important that the composition and particle size of the anode materials are accurately chosen. Particles of the same type (electronic or ionic conductors) must contact each other to form a continuous matrix throughout the anode layer. Moreover, there must be adequate contact between the electronic and ionic phases to ensure that a large active TPB is formed (Figure 4.1).

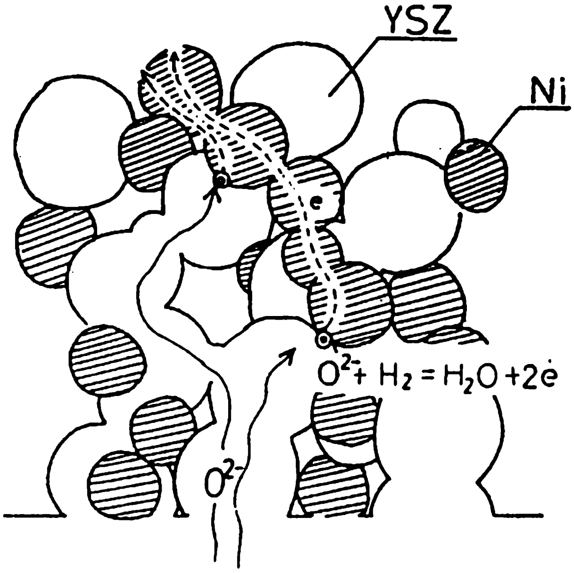

Figure 4.1 Schematic diagram of the anode structure showing percolating paths of electronic and ionic conduction and the TPB[3].

In order to explain the morphology of the anode, a system is used whereby different types of paths of connecting particles are given labels. This is used in order to successfully describe the optimum microstructure of a cermet anode.

A-clusters[4] (Figure 4.2) are completely connected from the electrolyte to the current collection layer and represent a continuous network of either ionic or electronic conduction. This type of cluster adds to the overall performance of the anode, to produce an optimum high performance structure. B-clusters are shorter chains connected only to the electrolyte or the current collector. They therefore contribute to the anode reaction for only a limited thickness of the anode layer. C-clusters are insulated from either end of the anode layer. They cannot therefore add to the transportation of electrons or oxygen ion conduction and represent a loss in performance.

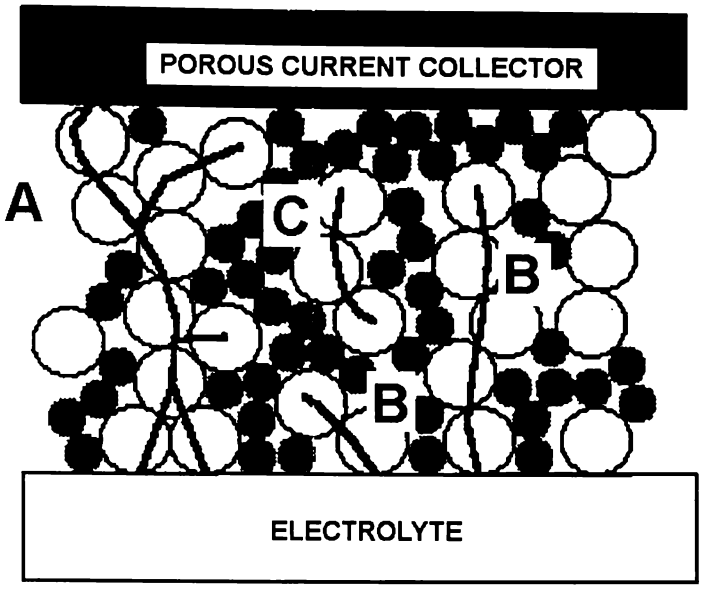

Figure 4.2 Schematic diagram of the anode structure showing the types of clusters present, relating to the electrolyte[4].

It has also been noted[4,5] that there exist percolation thresholds, which depend on the ratio between the dimensions of the particles in the anode. If the ratio between particle dimensions and anode thickness is not within the appropriate region, the percolation limit can change drastically, causing loss of conduction.

It has been illustrated by Primdahl *et al.*[6] that no significant dependance of polarisation resistance on anode thickness has been found within a range of 20-70 μm, for standard anodes. Impedance spectra, recorded at 1000°C at OCV in wet hydrogen on anodes of 20 μm and 70 μm, were very similar. Anode layers thinner than 20 μm were tested, but were unable to sustain sufficient current collection over the sample surface, causing an increasing and unstable polarisation resistance.

A new current collection layer was employed to solve this problem, consisting of a slurry of 90% Ni and 10% YSZ. This anode layer was intended to have no active reaction sites due to the low YSZ content, and to function solely as a current collecting layer. The 10% YSZ is added only to restrain Ni agglomeration by sintering and is not believed to percolate.

The research described in this chapter aims to give insight into a minimum thickness of active anode material for efficient hydrogen oxidation, while retaining a high performance.

4.2 Methods and Materials

4.2.1 Test Setup Design

All electrochemical tests were carried out on a three-electrode pellet (produced from ZrO_2 with 8 mol% Y_2O_3, Tosoh corporation). This setup provided a reference atmosphere (air) and a sealed cylindrical anode compartment for exposing the anode to a reducing fuel gas. The fuel gas was fed through a concentric tube in the anode chamber. The height from the anode surface to the feed tube was approximately 1 cm. The reference electrode was placed in air (reference gas), and a Nernst potential was measured, as described in section 1.2. The working electrode of ~0.44 cm^2 was contacted with several mm of 0.3 mm diameter Pt wire pressed against the center. The pellets were prepared with a Pt-paste counter electrode, a Pt-ball reference electrode in the centre bore, and two Pt leads in contact with the working electrode. The contacts for the working electrode and the reference electrode were pressed onto the surface of the electrolyte by means of a spring system providing a constant pressure to ensure adequate electrical contact. The two alumina tubes for supplying the fuel and oxidising gases were sealed to the YSZ electrolyte by means of gold and platinum seals. Gold and platinum were used because of the malleability and good sealing properties at the 1000 °C operating temperature of the fuel cell.

4.2.2 Electrochemical Testing

Anodes were heated to 1000 °C in N_2 + 9% H_2 + 3% H_2O and then changed to a standard measurement atmosphere: 97% H_2 + 3% H_2O with an open circuit voltage (OCV) against Pt in air of approximately -1070 mV ($pO_2 \sim 2\times10^{-18}$ atm.). A total of 100 ml/min (at 1000°C) of wet hydrogen was passed over the anodes. Atmospheric control was performed, by mixing an inert gas (N_2) with hydrogen, through thermal massflow meters. This was then saturated with water, at a controlled temperature. pO_2 was determined by the Nernst expression from OCV vs. Pt/air. The partial pressure pH_2O was determined from pO_2 and pH_2 by the following algorithm valid for 1000K<T<1300K[7]:

$$pH_2O = 10^{-(2.958-13022/T)}.pH_2.\sqrt{pO_2} \qquad \textbf{Equation 4.1}$$

Impedance spectroscopy was conducted with an applied amplitude of 20-30 mV. The frequency range used was 500 kHz to 0.01 Hz. At least 20 minutes was allowed for stabilization before recording each impedance spectrum.

The equipment used for impedance spectroscopy was a Solartron 1260 frequency response analyzer with a Solartron 1287 electrochemical interface.

4.3 Results and Discussion

Standard anodes[8] have been fabricated with varying thickness' ranging from 3.5 µm to 54 µm with an overlying current collection layer. A blank sample consisting of only the current collecting layer deposited on an electrolyte pellet was assigned a thickness of 0 µm.

Impedance spectra recorded at 1000 °C at OCV in wet hydrogen on anodes of 20 μm and 70 μm were very similar. Anode layers of less than 20 μm were tested, but were unable to sustain sufficient current collection over the sample surface, causing an increasing and unstable polarisation resistance. Due to the new current collection method, anode samples with thickness' of 3.5 μm to 54 μm have been successfully tested, as shown in figures 4.3(a) to 4.3(i).

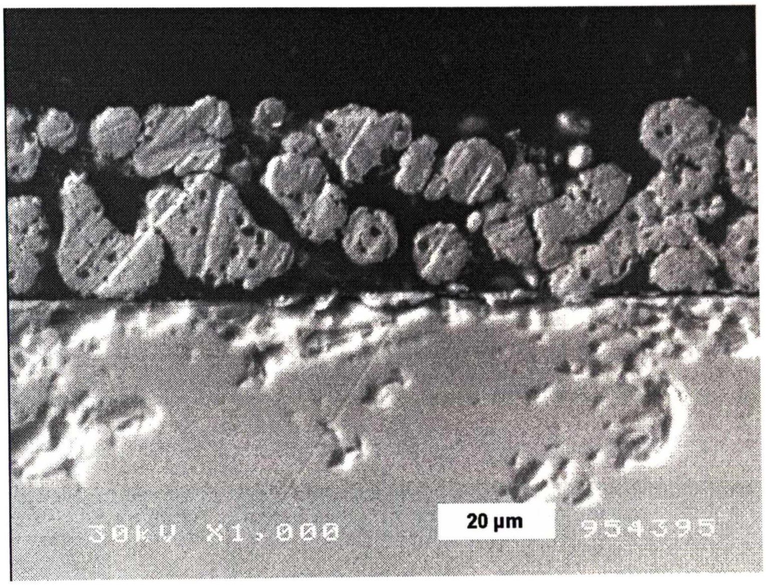

Figure 4.3(a): Structure of the polished cross-section of the current collecting Ni layer, deposited on a YSZ substrate; as observed by SEM (ACC).

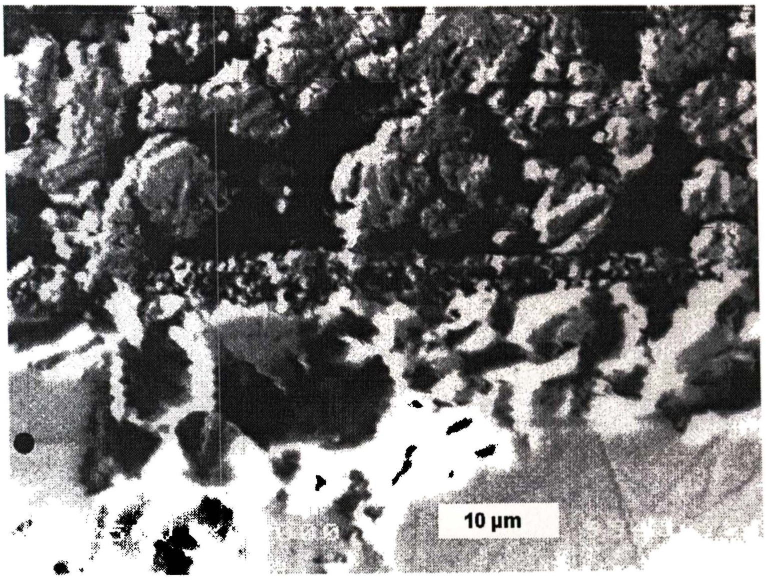

Figure 4.3(b): Structure of a 3.5µm thick Ni/YSZ anode layer with overlying current collection layer(A697).

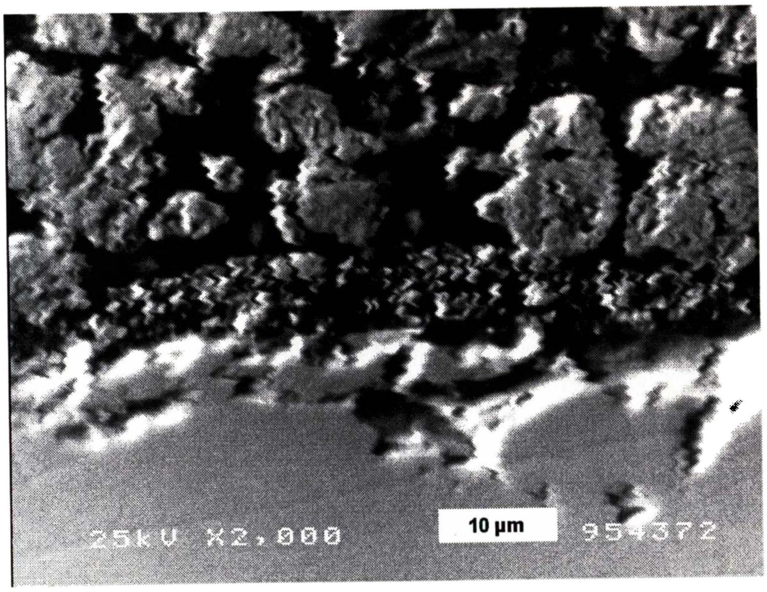

Figure 4.3(c): Structure of a 4µm thick Ni/YSZ anode layer with overlying current collection layer(A696).

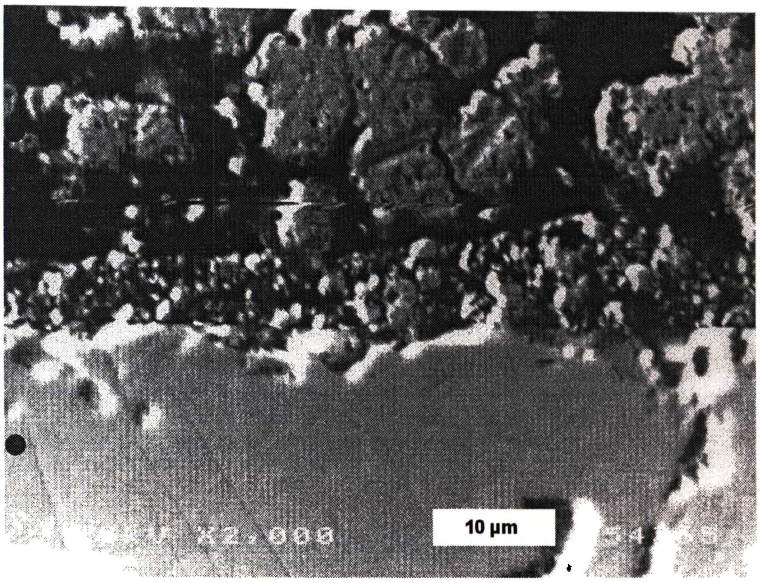

Figure 4.3(d): Structure of a 5.5µm thick Ni/YSZ anode layer with overlying current collection layer(A698).

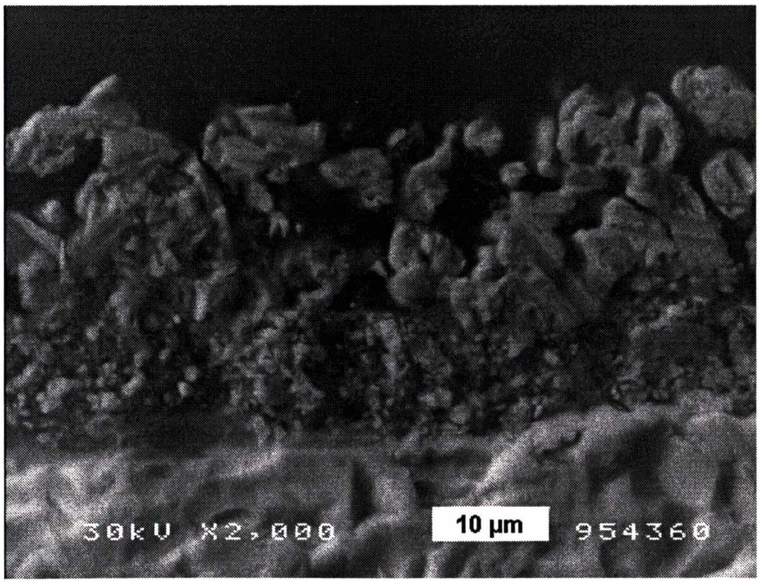

Figure 4.3(e): Structure of a 11µm thick Ni/YSZ anode layer with overlying current collection layer(A515).

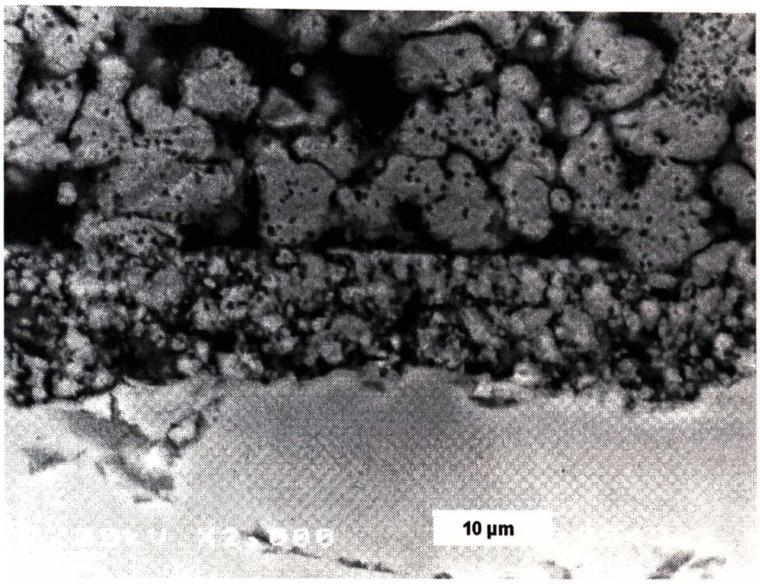

Figure 4.3(f): Structure of a 12μm thick Ni/YSZ anode layer with overlying current collection layer(A516).

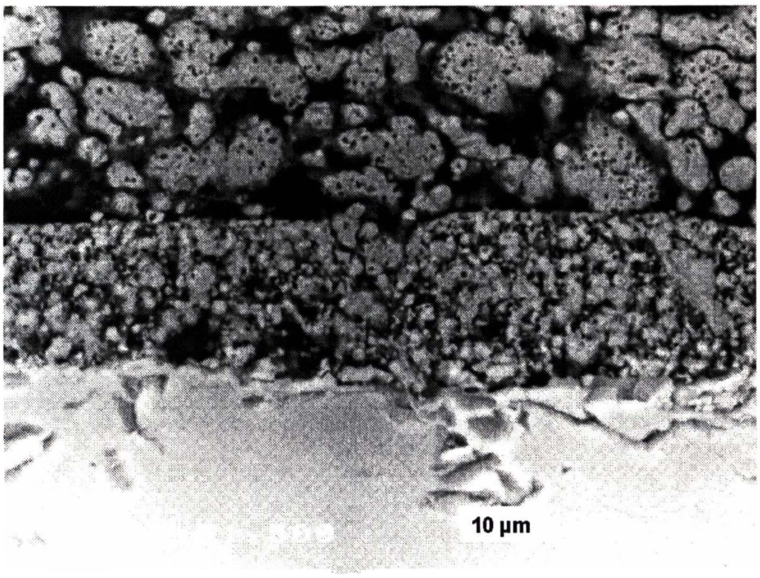

Figure 4.3(g): Structure of a 12μm thick Ni/YSZ anode layer with overlying current collection layer(A518).

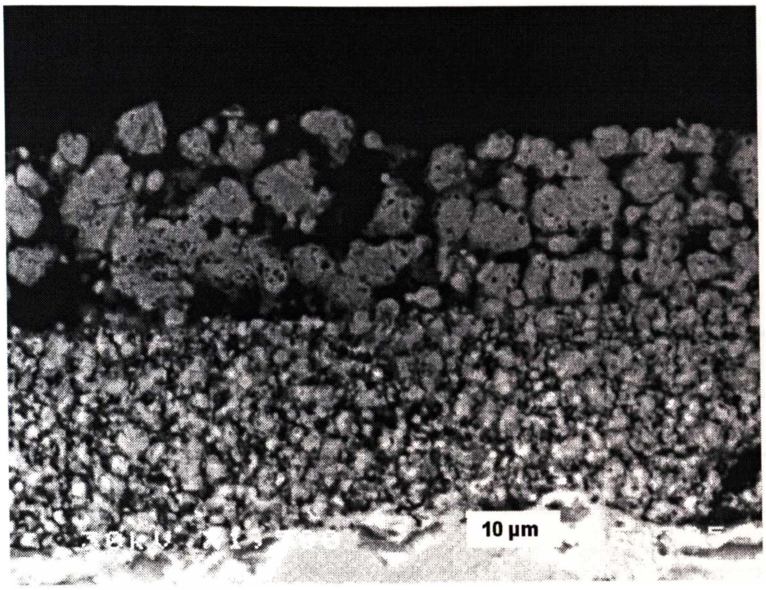

Figure 4.3(h): Structure of a 22µm thick Ni/YSZ anode layer with overlying current collection layer(A520).

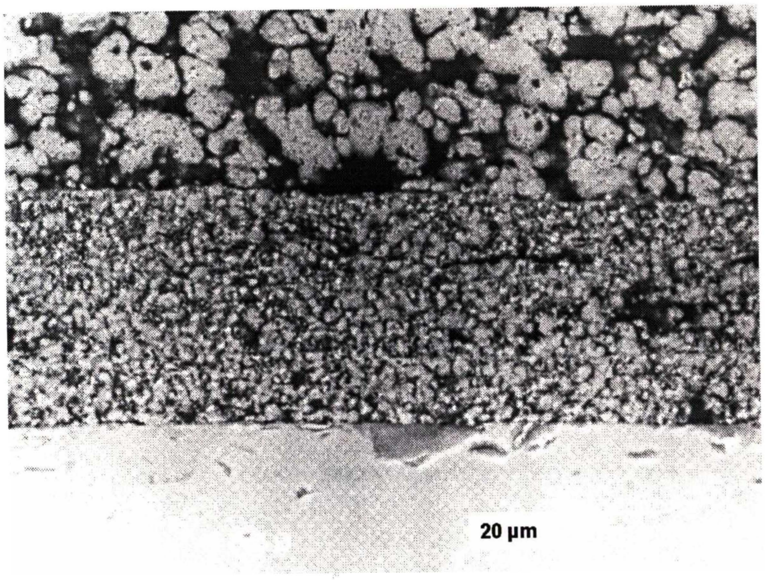

Figure 4.3(i): Structure of a standard anode (54µm) with overlying current collection layer(A588).

The samples and associated anode thickness' are given in Table 4.1. Anode A588 is considered to be a standard anode fabricated at Risø National Laboratory, Denmark. The other anodes are based upon the same fabrication method, the only difference being the thickness and the number of layers applied to form the completed cermet.

Table 4.1: Active thickness anodes with associated resistances.

Sample Number	Resistance (ohm cm^2)	Thickness (μm)
A588	0.06	54
A520	0.07	22
A518	0.05	12
A516	0.09	12
A515	0.64	11
A698	0.75	5.5
A696	0.78	4
A697	0.78	3.5
ACC	0.78	0

The anodes were tested at 1000°C in 97% H_2 + 3% H_2O, and with impedance spectroscopy were fitted to the appropriate equivalence circuit (figure 4.4).

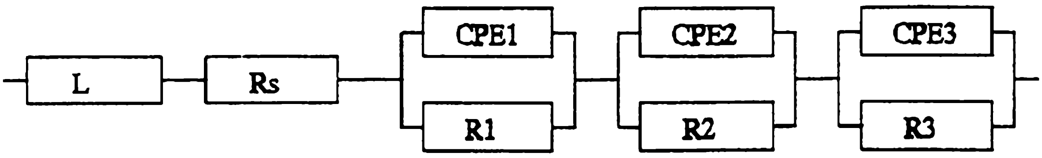

Figure 4.4 Equivalent circuit used for the fitting procedure of the impedance data. L is an inductance originating from the testing equipment, R_s is the series resistance originating from the electrolyte and the leads, and R_1Q_1, R_2Q_2, R_3Q_3 describe the electrode response.

A typical impedance spectra is shown in figure 4.5. The spectra consists of 3 arcs relating to the anode reaction and describes a typical impedance spectrum obtained from a state-of-the-art anode fabricated at Risø National Laboratory, Roskilde, Denmark. Marked on the graph are the three impedance arcs observed under the experimental conditions noted. The high frequency arc (I) is purported to be structure related, arc II is a diffusion related process and the third arc (III) is explained by a gas diffusion impedance based upon the geometry of the electrode testing facility.

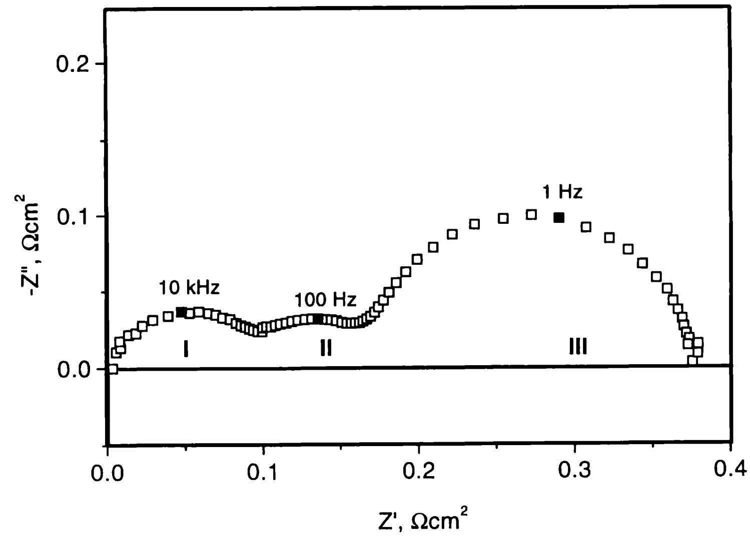

Figure 4.5: Typical impedance diagram for a Ni/YSZ cermet anode at 1000°C in 97%H_2+ 3%H_2O at OCV, showing three arcs present for the anode reaction.

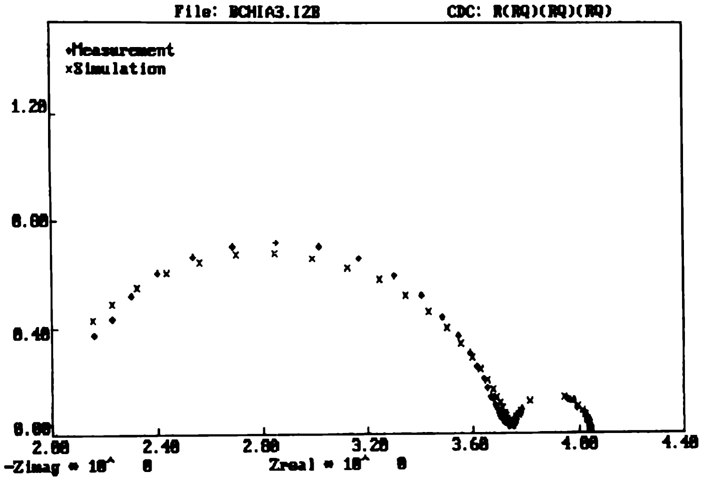

Figure 4.6(a). Impedance spectrum obtained for current collecting layer (ACC).

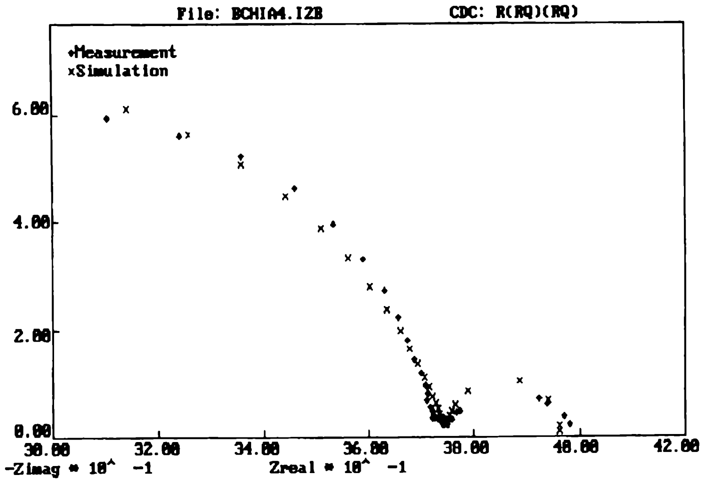

Figure 4.6(b). Impedance spectrum obtained for 3.5 µm thick anode layer (A697).

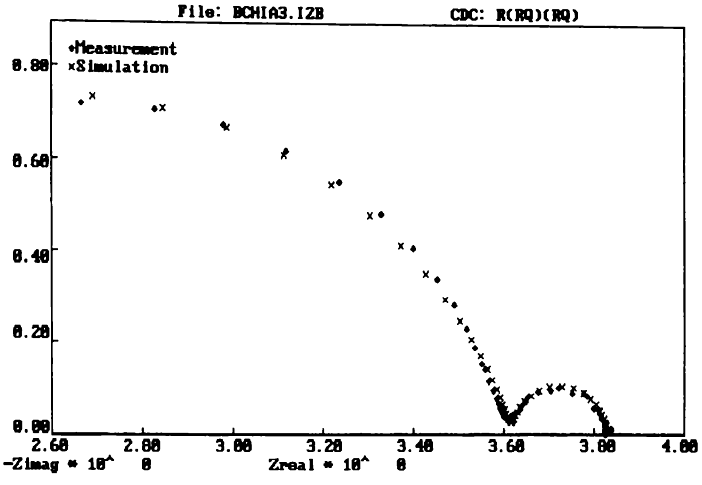

Figure 4.6(c). Impedance spectrum obtained for 4 µm thick anode layer (A696).

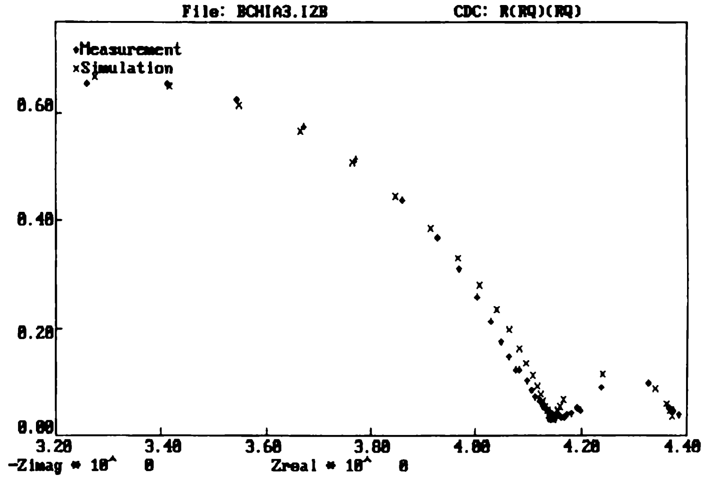

Figure 4.6(d). Impedance spectrum obtained for 5.5 µm thick anode layer (A698).

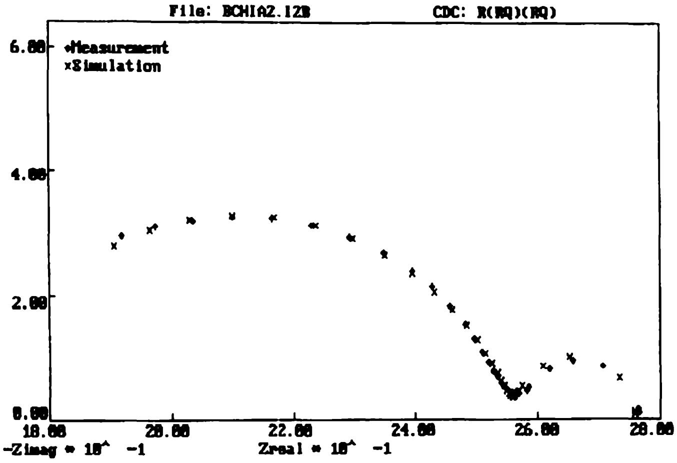

Figure 4.6(e). Impedance spectrum obtained for 11 µm thick anode layer (A515).

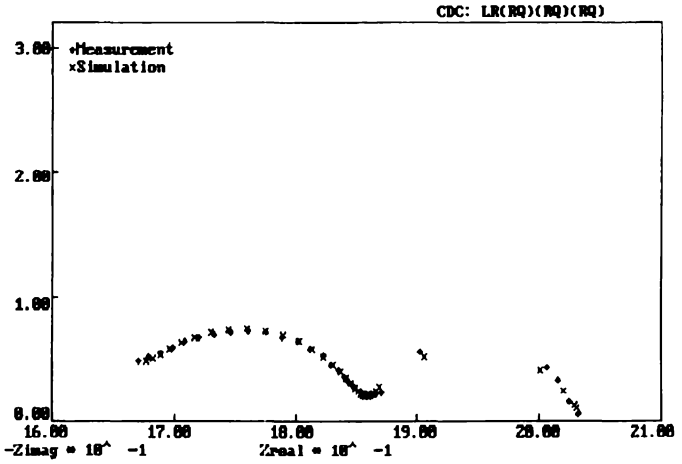

Figure 4.6(f). Impedance spectrum obtained for 12 µm thick anode layer (A516).

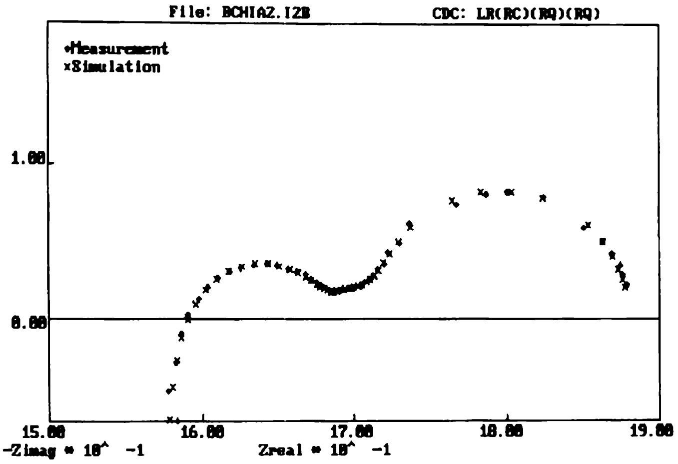

Figure 4.6(g). Impedance spectrum obtained for 12 µm thick anode layer (A518).

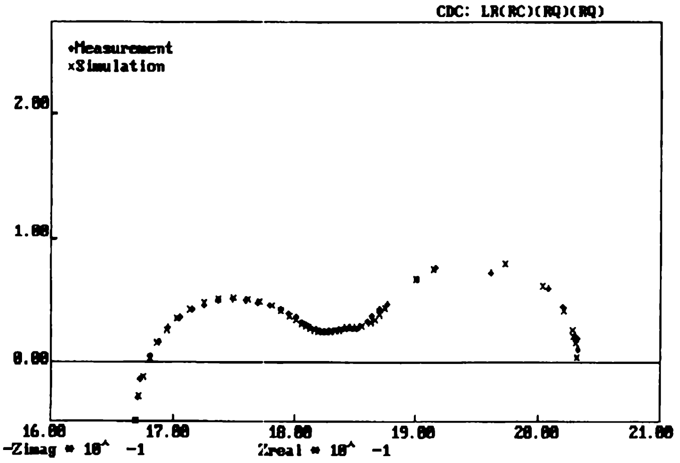

Figure 4.6(h). Impedance spectrum obtained for 22 µm thick anode layer (A520).

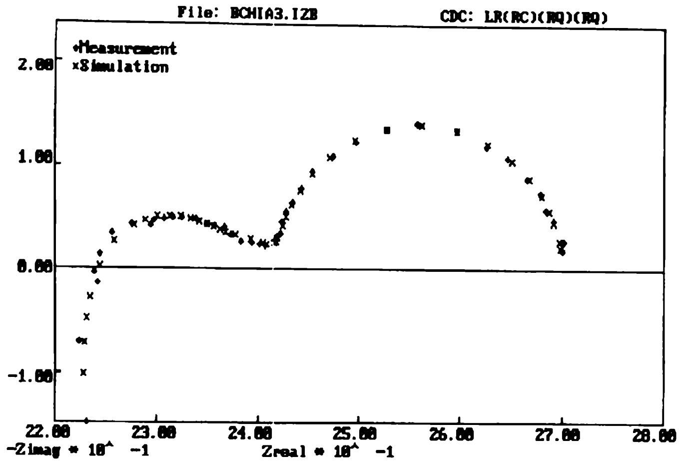

Figure 4.6(i). Impedance spectrum obtained for 54 µm thick anode layer (A588).

At an anode thickness of approximately 12 µm, a pronounced change in R_l (the resistance of the structure-related arc) was observed. At lower thickness', the values were approximately 0.8 Ωcm^2 which were greater than those observed for the 12 µm sample; the values were a factor of 10 lower. The series resistance was scattered between 1 and 3 Ω which was expected for the electrolyte pellet of this geometry and thickness, at this temperature. This indicated good in-plane conductivity in the current collector. R_l is given in figure 4.7 as a function of anode thickness.

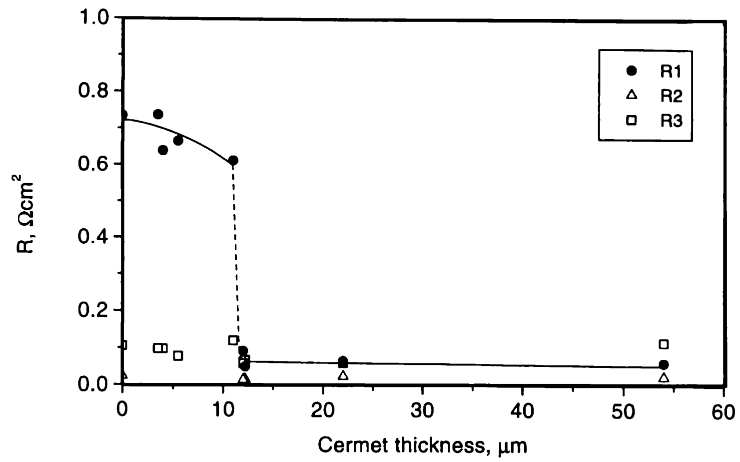

Figure 4.7 Graph of the structure related impedance arc resistance as a function of anode thickness.

This result suggests that a maximum thickness of 12 µm is all that is needed to produce the performance necessary for an efficient anode. However, if an anode with a greater active thickness could be fabricated, it could be suggested that an even higher performance could be obtained.

An extensive study was performed by Juhl *et al.*[9] to correlate the performance and structure of composite (lanthanum strontium manganite, LSM/YSZ) cathodes. It was suggested that increasing the layer thickness of a composite cathode had a net positive effect on the electrode performance. This implied that the bulk of the LSM/YSZ composite cathode was active with respect to the oxygen reduction reaction. These results could imply that with precise control of the microstructure, a significant thickness could be made active, thus improving the overall performance of the electrodes (anode and cathode).

To reinforce this statement, Abudula *et al.*[10], using dry CH_4 and H_2 for power generation experiments, found a dependence of anode overpotential on anode thickness. It was concluded that the effective TPB extended through the anodic layer to a depth of 120 μm for pure H_2, and to 70 μm for 4.2% CH_4 fuel.

Nakagawa *et al.*[11] fabricated anodes with various thickness', capping them with a porous ceramic layer. The electrode impedance was found to be dependent on the thickness of the ceramic porous layer and not on that of the Ni film. Their results suggested that the oxidation reaction took place on a very thin zone of the Ni film within 1μm of the electrode/electrolyte interface.

This phenomena has been independently observed by Mizusaki *et al.*[12] who examined Ni film electrodes. The authors showed, by studies at the porous Pt/YSZ as well as at the porous oxide/YSZ interfaces, that the reaction rate is almost independent of the thickness of the electrode layer when the electrode layer is in the order of several microns thick. These results suggest that the sites, which determine the electrode reaction rate, lie at the TPB, very close to the electrode/electrolyte interface, in the order of 1μm in thickness.

To produce an optimised anode structure with superior performance, it is suggested that a particle size of approximately 1 μm for the nickel phase is essential. A nickel particle size any smaller than 1 μm promotes excessive nickel agglomeration at the fuel cell operating temperature of 1000 °C, and subsequent loss of percolation. This, in conjunction with fine YSZ (approximately 1 μm), would produce the required microstructure with a large reaction area. The fine YSZ would also inhibit nickel agglomeration. In order to stabilise the whole structure, a matrix of larger YSZ particles (approximately 5-10 μm) is possibly required. This would increase the ionic conduction by producing relatively short conducting paths, and so make ionic conduction more efficient.

4.4 Conclusions

It was found that 12 μm was the limiting thickness for a low polarisation resistance, for the type of anode structure fabricated. Below a thickness of 12 μm, the polarisation resistance increased in an erratic manner as the reaction zone (effective TPB) was reduced. Above this threshold, the polarisation resistance was at a minimum of approximately 0.05 Ωcm^2 for a 12 μm thick Ni-YSZ cermet (sample A518) and no significant change was observed up to a thickness of 54 μm (sample A588).

4.5 Acknowledgements

Research performed in collaboration with Søren Primdahl from Risø National Laboratory, Roskilde, Denmark.

4.6 References

---

[1] N.Q.Minh. *Journal of the American Ceramic Society*, **76** 3, 563 (1993)
[2] M.Brown, S.Primdahl, M.Mogensen. "Structural Effects on Performance of Ni/YSZ Anodes for SOFC". To be published in the Journal of the Electrochemical Society.
[3] T.Kawada, N.Sakai, H.Yokokawa, M.Dokiya. *Solid State Ionics*. **40/41** 402 (1990)
[4] P.Costamagna, P.Costa, V.Antonucci. *Electrochimica Acta*. **43** 3-4, 375 (1998)
[5] T.Kawashima, M.Hishinuma. *Materials Transactions*. JIM, **37** 7 (1996)
[6] S.Primdahl, M.Mogensen. *Journal of the Electrochemical Society*. Submitted for publication, November 15, (1996)
[7] R.Hartung, H.-H.Mobius. *Chemie-Ing. Techn.*, **40** 12 (1968)
[8] C.Bagger. "Improved Production Methods for YSZ Electrolyte and Ni-YSZ Anode for SOFC. 1992 Fuel Cell Seminar. Program and Abstracts. Nov.29-Dec.2, Tuscon, Arizona, 1992.
[9] M.Juhl, S.Primdahl, C.Manon, M.Mogensen. *Journal of Power Sources*. **61** 173 (1996)
[10] A.Abudula, M.Ihara, H.Komiyama, K.Yamada. *Solid State Ionics*. **86-88** 1203-1209 (1996)

---

[11] N.Nakagawa, H.Sakurai, K.Kondo, T.Morimoto, K.Hatanaka, K.Kato. *Journal of the Electrochemical Society*, **142** 10 (1995)

[12] J.Mizusaki, H.Tagawa, T.Saito, K.Kamitana, T.Yamamura, K.Hirano, S.Ehara, T.Takagi, T.Hikita, M.Ippommatsu, S.Nakagawa, K.Hashimoto. "Preparation of Nickel Pattern Electrodes on YSZ and their Electrochemical Properties in H_2-H_2O Atmospheres". Proceedings of the Third International Symposium on SOFC. Edited by S.C.Singhal and H.Iwahara. The Electrochemical Society, INC. Vol. 93-4. P533. 1993.

Chapter Five

To be submitted as part of a paper to The Journal of the Electrochemical Society.

5. H_2 Oxidation at the Ni/YSZ Interface

5.1 Introduction

The Ni/YSZ cermet is the most common and most studied anode for the oxidation of hydrogen in a SOFC. The cermet consists of an intimate mixture of fine NiO and YSZ particles which is deposited onto the electrolyte by, for example, spray painting or screen printing. After firing in air to obtain a porous and rigid YSZ structure, the NiO is reduced to Ni in the fuel cell prior to operation.

The oxidation of hydrogen on Ni/YSZ cermets has been studied by several groups using: AC techniques (impedance spectroscopy), DC techniques or a combination of these. Both technological anodes with high current densities and anodes with a simple geometry have been studied and reported[1,2,3,4,5,6,7,8].

It should be noted that not all measured impedance arcs contribute to the electrochemical performance of the anodes. Processes such as gas conversion[9,10] (changes in the Nernst potential by passing current when the reference electrode is separated from the working electrode) and diffusion over the anode surface[7] bear no relation to the electrochemical performance of the anode. They are linked to the rig design, placement of reference electrode and gas exchange rates. These processes have only recently been recognised to contribute arcs in the impedance spectra. Such contributions, which can be very different for different test geometries, have added to the confusion, and jeopardised simple comparisons of data obtained in different equipment, between different researchers.

It has been recognised that in previous impedance studies[8,11] the resolution of data on the high frequency structure-related arc is unsatisfactory due to the presence of these secondary arcs. On separating these secondary arcs, there are several indications that one or two arcs in the impedance spectra are related to the true anode overpotential.

Impedance measurements on micro-electrodes (point shaped contacts) are reported to give one[6] or two[12,13] arcs. Measurements on Ni pattern electrodes are also reported to yield one[14] or two[15] arcs. Measurements on cermets have been reported to contain: one arc[16], or one arc plus an arc from diffusion above the active anode'[17], or finally one arc plus two arcs relating to diffusion over the anode and gas conversion[9,10,11].

A summary of the literature has suggested that Ni/YSZ anodes operated in H_2/H_2O atmospheres at 700-1000 °C exhibit only one arc representing only one significant rate limiting process, but in several cases a second arc has been shown to appear[18]. The nature of this second arc is at present unclear. The inherent arc appears at high frequencies, and is linked to the double layer capacitance and the Ni surface near the TPB. This arc can be studied in detail on:

i) simple geometry anodes, or

ii) state-of-the-art cermet anodes of complex structure in a test geometry that minimizes other contributing, and often confusing, processes.

Work was conducted with Ni/YSZ cermet anodes consisting of 90 vol% Ni and 10 vol% YSZ. These were fabricated in order to create a cermet anode with significantly higher polarization resistance than state-of-the-art cermets[a]. It was decided to investigate a cermet resembling state-of-the-art anodes but with considerably lower performance in order to obtain a larger structure related arc. Hereby, a structure-related impedance arc at high frequencies could be examined in detail.

The aim of this research was to provide a detailed description of the impedance arcs associated with the limiting anode process in terms of thermal activation, dependency on partial pressures of H_2 and H_2O, and electrochemical behavior under DC load. The anodes were studied in mixtures of hydrogen, water and nitrogen in a 3-electrode setup. AC and DC measurements were carried out at temperatures between 700 °C and 1000 °C

5.2 Methods and Materials

5.2.1 Test Setup Design

All electrochemical tests were carried out on a three-electrode produced from YSZ (ZrO_2 with 8 mol% Y_2O_3, Tosoh corporation). This setup provided a reference atmosphere (air) and a sealed anode compartment with a controllable atmosphere. The working electrode of ~0.44 cm^2 was contacted with several mm of 0.3 mm diameter Pt wire pressed against the centre. The pellets were fabricated with a Pt-paste counter electrode, a Pt-ball reference electrode in the centre bore and two Pt leads in contact with the working electrode. The contacts for the working electrode and the reference electrode were pressed onto the surface of the electrolyte by means of a spring system providing a constant pressure to ensure adequate electrical contact. The two alumina tubes for supplying the fuel and oxidising gases were sealed to the YSZ electrolyte by means of gold and platinum seals. Gold and platinum were used

---

[a] A state-of-the-art anode is defined here as being fabricated to have a very low polarisation resistance.

due to the malleability and good sealing properties at the 1000 °C operating temperature of the fuel cell.

The electrolyte geometry used here was verified by finite element analysis[19] to have a stable frequency and a homogeneous current distribution, causing less than 3% error on a polarisation resistance as low as 0.16 Ωcm^2.

5.2.2 Sample Preparation

A Ni-based anode was applied to a sintered YSZ 3-electrode pellet. To ensure sufficient adhesion of the Ni-anode onto the YSZ pellet a $Ni(NO_3)_2$ solution (1 mmol/l in ethanol with 4 wt% Mowital B60H binder[20]) was painted onto the electrolyte pellet and decomposed in 3% H_2O + 9% H_2 in N_2 at 1420 °C.

5.2.2.1 Anode Paste Preparation

The anode paste was prepared as follows: YSZ (Tosoh TZ8Y with 8 mol% Y_2O_3) calcined at 1100 °C for two hours was ball milled in ethanol with a dispersant until an average diameter of 0.4 μm was reached for the monomodal particle size distribution.

Ni (Inco #255) with a particle size of 1-2 μm and a porous agglomerate structure in excess of 20 μm, was added to 10/90 vol% YSZ/Ni. The paste was milled until the bimodal particle size distribution contained 20% of particles of approximately 0.4 μm and 80% of approximately 8 μm diameter.

The paste was applied by brush in a layer of 10-50 μm without sintering. This anode was intended to have active sites on the interface of the electrode/electrolyte. The 10% YSZ was added only to restrain Ni agglomeration by sintering, and is not believed[21] to form percolation paths for ionic conduction.

5.2.3 Electrochemical Testing

Anodes were heated to 1000 °C in 9% H_2 + 3% H_2O before switching to an atmosphere of 97% H_2 + 3% H_2O with an open circuit voltage (OCV) against Pt in air of approximately -1070 mV ($pO_2 \sim 2\times10^{-18}$ atm). A total of 100 ml/min (at 25 °C) moist gas was passed over the anodes. Fuel composition was controlled by mixing nitrogen and hydrogen through thermal mass flowmeters and saturating this mixture with water at a controlled temperature.

pO_2 was determined by the Nernst expression from OCV vs. Pt/air. The accurate partial pressure pH_2O was determined from pO_2 and pH_2 by the following algorithm valid for 1000 K<T<1300 K[22]:

$$pH_2O = 10^{-(2.958-13022/T)}.pH_2.\sqrt{pO_2} \qquad \textbf{Equation 5.1}$$

Impedance spectroscopy was conducted with an applied amplitude of 20-30 mV. The frequency range used was 500 kHz to 0.01 Hz. At least 20 minutes was allowed for stabilization before recording each impedance spectrum. The equipment used for impedance spectroscopy was a Solartron 1260 or 1250 frequency response analyzer with a Solartron 1287 or 1286 electrochemical interface.

5.2.4 Experimental Design

Experiments performed on the anodes included impedance spectroscopy, chronoamperometry, cyclic voltammetry and also chronoamperometry under polarised conditions. Thermal activation data was obtained at temperatures varying from 700 °C to 1000 °C.

The fuel gas composition was also altered, by varying the partial pressure of H_2 and the partial pressure of H_2O in N_2. This gave information on reaction dependencies and provided data for the elucidation of the anode kinetics and mechanisms.

5.3 Results

5.3.1 Interpretation of Impedance Spectra

Impedance data obtained for the anodes contained up to two distinct arcs, and careful examination indicated that a minor arc is required in between the two major arcs to produce reasonable fits (see figure 5.1). Figure 5.1 describes a typical impedance spectrum obtained from a state-of-the-art anode fabricated at Risø National Laboratory, Roskilde, Denmark. Also superimposed on the graph is a high Ni (90% Ni) anode specifically fabricated to study the high frequency impedance arc. Marked on the graph are the three impedance arcs observed under the experimental conditions noted. The high frequency arc (I) is purported to be structure related, arc II is a diffusion related process and the third arc (III) is explained by a gas diffusion impedance based upon the geometry of the electrode testing facility.

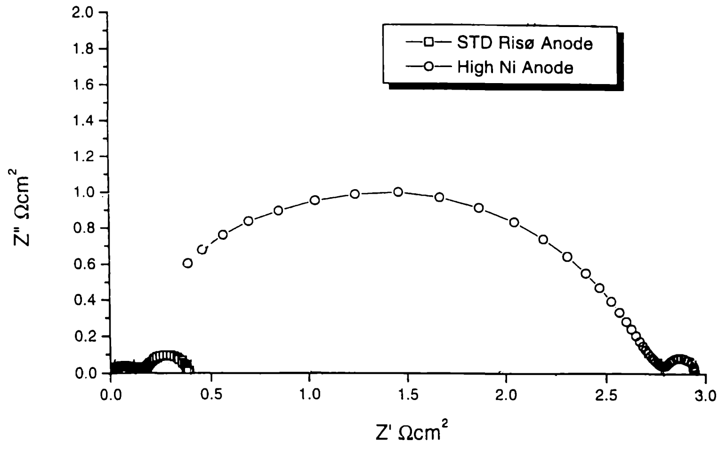

Figure 5.1 Impedance spectra of standard Risø anode and a high Ni anode at 1000 °C, at OCV in wet H_2, corrected for anode area and R_s subtracted.

In general, data were fitted with the software EQUIVCRT[23] using the equivalent circuit $LR_S(RQ)_I(RQ)_{II}(RQ)_{III}$ where L is an inductance, R a resistance and Q a constant phase element given as:

$$Q=Y_0(j\omega)^n \qquad \textbf{Equation 5.2}$$

Here Y_0 is an admittance, j the imaginary unit, ω the angular frequency and n is the frequency power.

Only arc I is reported in the following sections, since this is the arc that changes with structural alterations. With the n-values $(n_I,n_{II},n_{III})=(0.8, 0.75, 1.00)$ from the constant phase elements, derived previously[4] all obtained impedance spectra were fitted with less than 2% relative error at all frequencies.

Arcs II and III were attributed to diffusion above the anode[11] and gas conversion[9,10], respectively. When the ratio R_I/R_{II} or R_I/R_{III} was too high to yield a meaningful fit, the affected data points were omitted together with the relevant part of the equivalent circuit. For example, when arc II was very small, it was difficult to obtain a satisfactory fit, and the arc was ignored in the fitting procedure.

5.3.2 Anode Structure

The decomposition of $Ni(NO_3)_2$ on the electrolyte at 1420 °C left an even layer of Ni spheres (<1 µm) on the electrolyte surface. A scanning electron microscope (SEM) image of this layer is shown in figure 5.2, taken after electrochemical testing in an area where the overlying Ni-layer had detached, due to the current collecting wires. The spheres adhered well to the electrolyte and circular scars were seen on the electrolyte where a sphere had been removed.

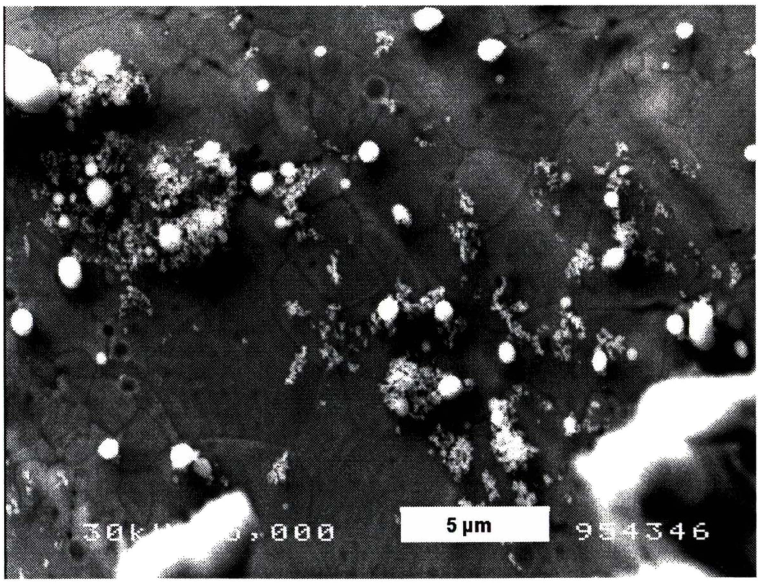

Figure 5.2 Microstructure of anode active layer, illustrating Ni balls produced from the decomposition of $Ni(NO_3)_2$ at 1420 °C in wet H_2.

In figure 5.3 the surface of the 90/10 vol% Ni/YSZ indicates a porous but well percolating Ni-structure. Figure 5.4 is a close-up of the 90/10 vol% Ni/YSZ structure detailing the extent of sintering (necking) of the Ni particles and the distribution of fine YSZ particles on the Ni-surface. A cross section of the anode is given in figure 5.5, showing an open Ni-structure with internal porosity, presumably due to YSZ-grains being trapped between sintering Ni grains.

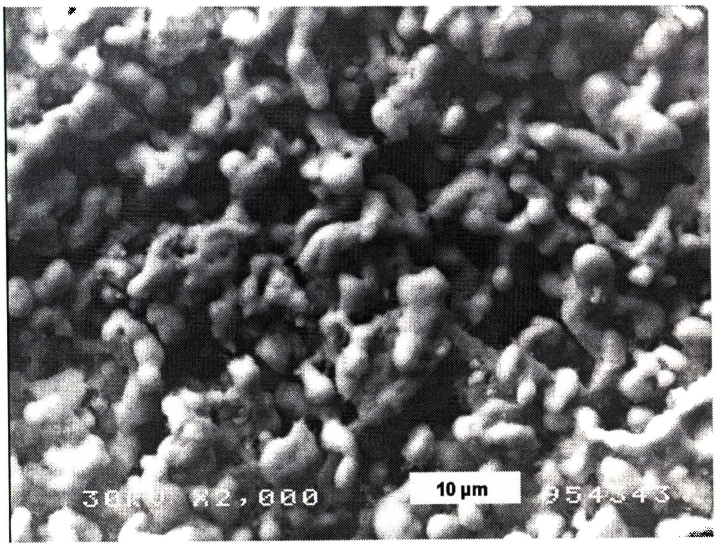

Figure 5.3 Surface of the current collecting layer containing 90 vol% Ni and 10 vol% YSZ as observed by SEM, illustrating the degree of Ni sintering.

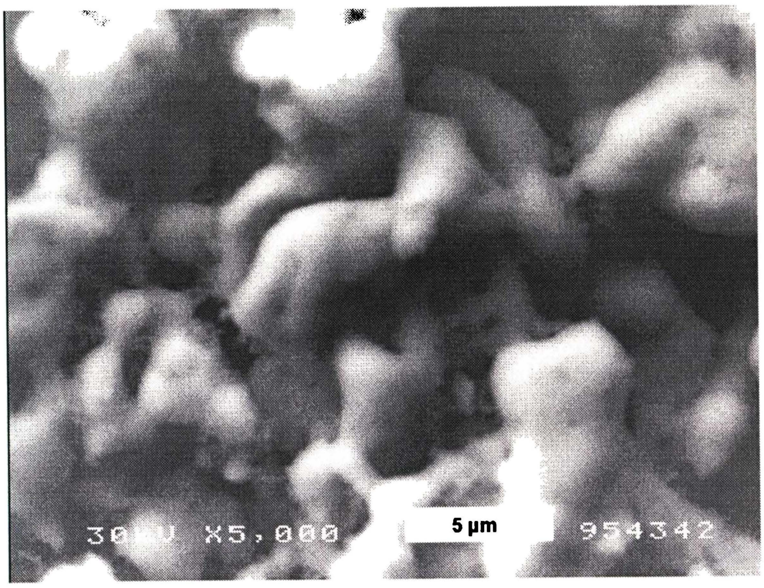

Figure 5.4 SEM image of the current collecting layer surface, indicating the purpose of the fine YSZ particles to inhibit the high degree of Ni particle sintering.

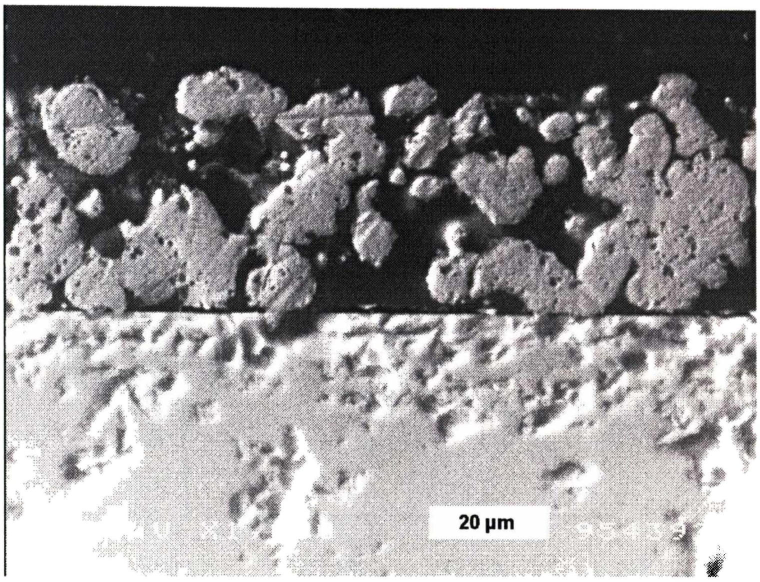

Figure 5.5 Structure of polished cross-section of the current collecting layer as observed by SEM.

5.3.3 Thermal Activation

Comparing two anodes (samples A527 and A528) in a temperature range of 700 °C to 1000 °C, an activation energy of Process I (high frequency arc) was in the range of 0.94 to 1.10 eV. The electrolyte (series resistance Rs) activation energy was between 0.80 and 0.86 eV.

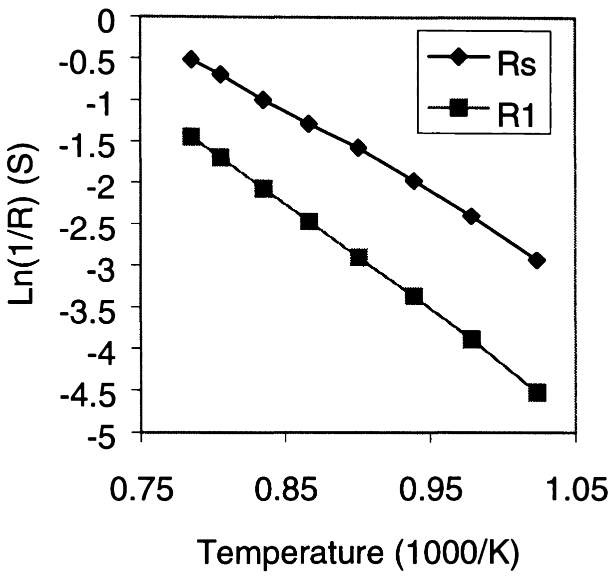

Figure 5.6 Thermal activation of processes in the range of 700 °C to 1000 °C.

5.3.4 Gas Composition

Experiments were conducted where the pH_2O was varied within the range of 0.035-0.37 atm. at fixed pH_2 of 0.25 and 0.50 atm. The resistance of process I is given in figure 5.7. The curves indicated a reduction in resistance when increasing pH_2O, possibly with a change to a more constant resistance above 0.2 atm.

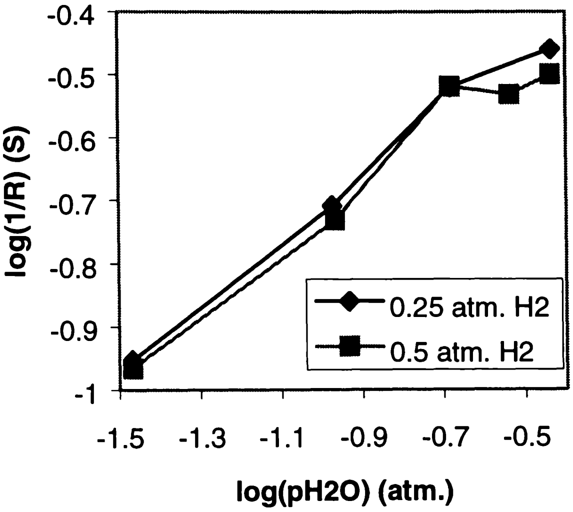

Figure 5.7 Inverse resistance of R_I as a function of steam partial pressure showing a dependence up to 0.2 atm.

Varying pH_2 in the range 0.01-0.97 atm., at constant pH_2O of 0.03 atm., indicated a constant resistance above a pH_2 of 0.4 atm., and a decreasing resistance with decreasing pH_2 below 0.4 atm., figure 5.8.

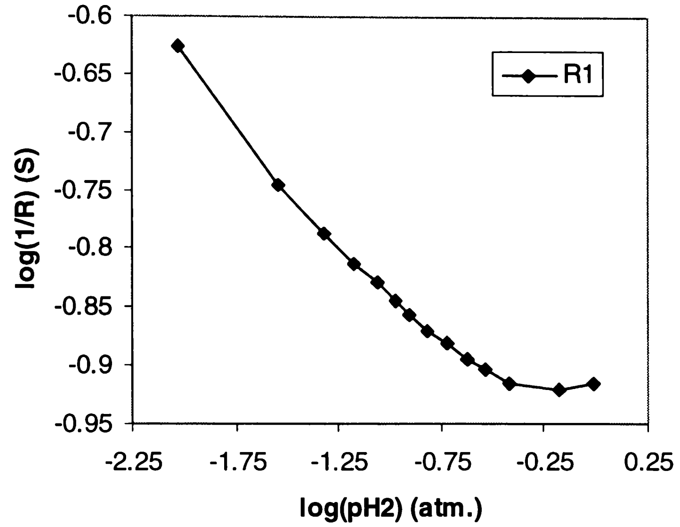

Figure 5.8 Inverse resistance of R_I as a function of H_2 partial pressure showing a dependence of R proportional to $pH_2^{-0.16}$, up to 0.2 atm.

5.3.5 Polarisation

The polarisation resistance for process I at 1000 °C in wet hydrogen decreased with anodic overpotential in the investigated range of 0-300 mV, figure 5.9. The i-η curve taken in 97% H_2 + 3% H_2O at 1000 °C, given in figure 5.10, indicated an exponential behaviour for anodic overpotentials and a more complex behavior at cathodic overpotentials. Anodic and cathodic sweeps taken from OCV gave inductive hysteresis in both directions. A Tafel type representation is given in figure 5.11 for increasing currents.

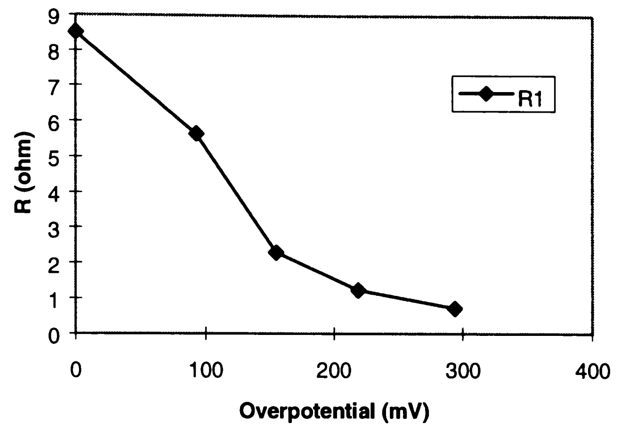

Figure 5.9 Contributions to the polarisation resistance Rp and the dependency on anodic overpotential at 1000 °C in H_2 + 3% H_2O.

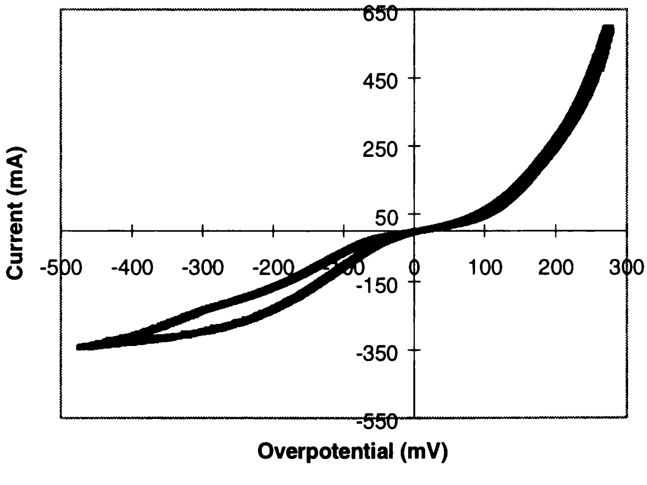

Figure 5.10. I-η characteristics after correction for iR losses. T=1000 °C in an atmosphere of 97% H_2 + 3% H_2O. The hysteresis is inductive.

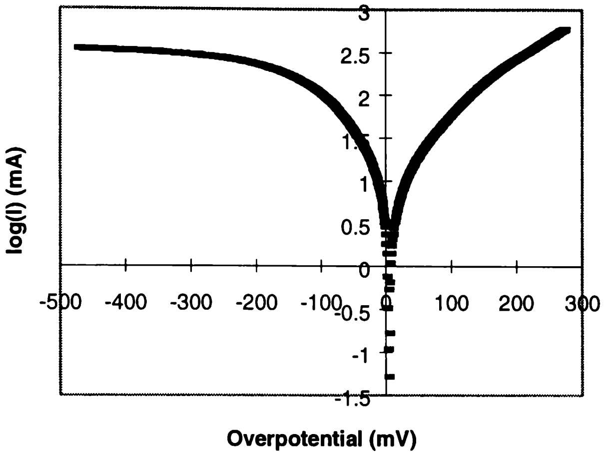

Figure 5.11. Tafel type plot of electrode overpotential as a function of log current. T=1000 °C in an atmosphere of 97% H_2 + 3% H_2O. Only increasing currents from OCV are given.

5.4 Discussion

5.4.1 Thermal Activation

The activation energy of process I was in the order of 0.9-1.1 eV. In the literature, quite a scatter was reported; 0.5 eV for a supposedly dense Ni-electrode[17], 0.8 eV[11] and 1.0 eV[7] for cermets, and 1.6 eV for single arc point electrodes[8]. A reappearing feature was a slight non-linearity of the Arrhenius plots[7,11] indicating a higher activation energy at lower temperatures. This has an obvious impact on the comparison of the reported values, depending on the temperature range investigated.

If process I had been a simple electrochemical process, the activation energy would be expected to be well defined and reported values should have agreed within the experimental error. Two potential explanations are suggested:

1) The impedance arc interpreted as process I could consist of two processes with similar time constants. These would be in series judging from the curvature of the Arrhenius plots.

2) Process I could be a transport process or a surface specific reaction, depending on the microstructure and level of impurities. In this way a variation in activation energy could be expected between anodes of different geometry/fabrication technique.

A simple difference in the geometry of anodes could be the decisive factor in determining which of two processes are rate limiting and whether their time constants are similar. There is a tendency in the literature towards the presence of high activation energies in point contacts (a coarse structure without sintering), and lower values in fine cermets. Coarse cermets tested in the three-electrode setup indicated the presence of both a high and a low activation energy process[24].

For comparison, the thermal activation of oxide ion conduction in YSZ was typically 0.8-0.9 eV[25,26] whereas hydrogen diffusion in YSZ (10 mol% Y_2O_3) has a thermal activation energy of approximately 0.75 eV at 900-1000 °C as calculated from published data[27].

5.4.2 Hydrogen Partial Pressure

Variation of the pH_2 from 0.01 to 0.97 atm., with a fixed pH_2O of 0.03 atm., indicated two intervals, one below 0.4 atm. where $R_I \propto pH_2^{0.16}$, and one above 0.4 atm. where R_I was independent of pH_2.

A change in the properties at pH_2 of approximately 0.4-0.5 atm. has also been observed elsewhere[28]. In earlier work[11] on state-of-the-art cermets with poorer resolution of the high frequency impedance arc, a dependency $R_I \propto pH_2^{-0.16}$ was found over the same full range of pH_2.

For a Ni point electrode[8] with a thermal activation energy of 1.6 eV, a dependency of $R_P \propto pH_2^{0.5}$ below a pH_2 of approximately 0.2 atm., and a dependency of $R_P \propto pH_2^{-0.5}$ for a pH_2 >0.3 atm, was reported.

5.4.3 Steam Partial Pressure

Varying the steam partial pressure from 0.03 to 0.37 atm., at a constant pH_2 of 0.25 and 0.50 atm., a $R_I \propto pH_2O^{-0.5}$ dependency was found. In earlier work[11] with state-of-the-art cermets, a dependency of $R_I \propto pH_2^{-0.16}$ was found over the same full range of pH_2O. Above 0.20 atm. of water, R_I tended to be less dependent on pH_2O, which has been observed under similar conditions for the high frequency arc shown elsewhere[11].

5.4.4 Polarisation

Due to the high R_I and thus high R_P (as compared to state-of-the-art cermet anodes), quite high overpotentials could be applied with the thick electrolyte pellet, without significant heating (5 °C) by the passage of current. Earlier measurements[29] indicated a heating of less than 5 °C at 1000 °C by passing less than 500 mA/cm^2. The inductive hysteresis observed in figure 5.11, was not expected to be associated with heating. On plotting log(i) vs. η, a linear region was observed at high anodic overpotentials, with a slope of 211 mV per decade, figure 5.12.

Assuming a Tafel behaviour according to equation 5.3, the slope of figure 5.12 at high anodic current transforms to RT/nF according to a Nernst interpretation, with a calculated n-value of approximately 1.2.

$$\eta = a + b \log I$$ **Equation 5-3**

$$b = 2.303RT / nF$$ **Equation 5-4**

Where a and b are constants, F is the Faraday constant, RT has the usual meaning and n is a coefficient that depends essentially upon the number of electrons taking part in the charge transfer reaction.

The cathodic current indicated a more complex behaviour of a limiting type. Calculating the maximum attainable current with the actual gas flow (100 ml/min over 0.44 cm^2 at 25 °C, 3% H_2O), a value of 1.3 A/cm^2 was found. It is thus unlikely that the cathodic limiting parameter is due to a high concentration of water.

Sufficient information was not present to conclude that the observed anodic rate-limiting step was a charge transfer reaction. Looking at the fundamentally different behaviour under cathodic polarisation, it was considered unreasonable to assume a Butler-Volmer type behaviour. This was due to the non-symmetry of figure 5.11, which is normally associated with Butler-Volmer type behaviour.

Guindet *et al.*[12] described the variation of the overvoltage versus current density as a Tafel-type equation:

$$i = i_o \exp(\frac{nF}{RT}\eta)$$ **Equation 5.5**

with an n-value of 2, using a point electrode. Kawada *et al.*[16] also found a value of 2 for hydrogen oxidation on a Ni/YSZ cermet electrode at 1000 °C, with the same Tafel relationship. Mohamedi-Boulenouar *et al.*[6] using a Butler-Volmer-type relation stated a value between 1.4 and 1.7 for a point electrode.

5.5 Conclusions

The present work confirmed that a high frequency arc in the impedance spectra obtained on Ni/YSZ cermet anodes was indeed related to the structure of the cermet. The activation energy of process I was in the order of 0.9-1.1 eV. A reappearing feature in the literature was a slight non-linearity of the Arrhenius plots, which could indicate a second high frequency impedance arc present. This could be a reason for the large variation of the activation energies calculated for process I between the literature.

A $R_I \propto pH_2^{0.16}$ dependency was found when varying the hydrogen partial pressure from 0.01 to 0.97 atm., with a fixed pH_2O of 0.03 atm.

A $R_I \propto pH_2O^{-0.5}$ dependency was found when varying the steam partial pressure from 0.03 to 0.37 atm., at a constant pH_2 of 0.25 and 0.50 atm.,

A Tafel type relation was used to describe the anodic polarisation results, but, does not conclusively imply that a charge transfer reaction was the rate-limiting step. On plotting log(I) vs. η, a linear region was observed at high anodic overpotentials, with a slope of 211 mV per decade. Using the slope of the Tafel plot, a value of $n = 1.2$ was calculated, indicating one electron taking part in the charge transfer reaction.

5.6 Acknowledgements

Research performed in collaboration with Søren Primdahl from Risø National Laboratory, Roskilde, Denmark.

5.7 References

---

[1] J.Divisek, A.Kornyshev, W.Lehnert, U.Stimming, I.C.Vinke, K.Wippermann. Advanced Characterisation techniques for Nickel-YSZ Cermet Electrodes Used in Solid Oxide Fuel Cells. 5th International Symposium on Solid Oxide Fuel Cells, SOFC V, June 2-5, 1997. Aachen, Germany.

[2] R.J.Aaberg, R.Tunold, R.Ødegård, S.Tjelle. A Possible Reaction Mechanism for the Oxidation of H_2 on Ni/YSZ Cermet Electrodes. . 5th International Symposium on Solid Oxide Fuel Cells, SOFC V, June 2-5, 1997. Aachen, Germany.

[3] R.Cunningham, C.Finnerty, K.Kendall, R.Ormerod. An In-situ Catalytic and Electrochemical Study of Working Ni/ZrO_2 Anodes in Tubular SOFCs. 5th International Symposium on Solid Oxide Fuel Cells, SOFC V, June 2-5, 1997. Aachen, Germany.

[4] J.Van herle, R.Ihringer, A.McEvoy. Development of a Standard Ni-YSZ Cermet Anode for Intermediate Temperatures. 5th International Symposium on Solid Oxide Fuel Cells, SOFC V, June 2-5, 1997. Aachen, Germany.

[5] C.Iwasawa, M.Nagata, N.Kaneta, Y.Seino, M.Ono. A Study of Anode Materials and Structures for SOFC. 5th International Symposium on Solid Oxide Fuel Cells, SOFC V, June 2-5, 1997. Aachen, Germany.

[6] F.Z. Mohamedi-Boulenouar, J. Guindet and A. Hammou, 5th International Symposium on Solid Oxide Fuel Cells, SOFC V, June 2-5, 1997. Aachen, Germany. U. Stimming, S. C. Singhal, H. Tagawa and W. Lehnert, Editors, **PV 97-40**, p.441, The Electrochemical Society Proceedings Series, Pennington, NJ (1997)

[7] J. Geyer, H. Kohlmüller, H. Landes, R. Stübner, Investigations into the Kinetics of the Ni-YSZ-Cermet-Anode of a Solid Oxide Fuel Cell. Proceedings of the 5th International Symposium on Solid Oxide Fuel Cells, SOFC V, June 2-5, 1997. Aachen, Germany.

[8] M. Mogensen, S. Primdahl, J.T. Rheinländer, S. Gormsen, S. Linderoth and M. Brown, Proceedings of the 4th International Symposium on Solid Oxide Fuel Cells SOFC IV, M. Dokiya, O. Yamamoto, H. Tagawa and S.C. Singhal, Editors, **PV 95-1**, p.657, The Electrochemical Society Proceedings Series, Pennington, NJ (1995).

[9] S. Primdahl, M. Mogensen, Gas Conversion Impedance: SOFC Anodes in H_2/H_2O Atmospheres. 5th International Symposium on Solid Oxide Fuel Cells, SOFC V, June 2-5, 1997. Aachen, Germany.

[10] S. Primdahl and M.Mogensen, Gas Diffusion Impedance in Characterisation of Solid Oxide Fuel Cell Anodes. Submitted to J.Electrochem. Soc.

[11] S. Primdahl and M. Mogensen, *Journal of the Electrochemical Society,* **144** 3409 (1997)

[12] J. Guindet, C. Roux and A. Hammou in Proceedings of the 2nd International Symposium on Solid Oxide Fuel Cells, F. Grosz, P. Zegers, S.C. Singhal and O. Yamamoto, Editors, p.553, Athens, Greece (1991) EUR-13564-EN.

[13] P.A. Osborg and T. Norby, in 7th SOFC WORKSHOP, Theory and measurement of Microscale Processes in Solid Oxide Fuel Cells, p.47, Wadahl, Norway, (1995). IEA report obtainable from H. Nabielek, KFA-ISR Forschungszentrum Jülich GmbH, D-52425 Jülich, Germany.

[14] J. Mizusaki, H. Tagawa, T. Saito, K. Kamitani, T. Yamamura, K. Hirano, S. Ehara, T. Takagi, T. Hikita, M. Ippommatsu, S. Nakagawa and K. Hashimoto, *Journal of the Electrochemical Society*, **141** 8 (1994)

[15] T. Norby, O.J. Velle, H. Leth-Olsen and R. Tunold.Proceeding of the 3rd International Symposium on Solid Oxide Fuel Cells, SOFC III, S.C. Singhal and H. Iwahara, Editors, **PV 93-4,** p.473, The Electrochemical Society Proceedings Series, Pennington, NJ, 1993.

[16] T.Kawada, N.Sakai, H.Yokokawa, M.Dokiya, M.Mori, T.Iwata, *Journal of the Electrochemical Society.*, **137**, 10, 3042 (1990)

[17] N. Nakagawa, H. Sakurai, K. Kondo, T. Morimoto, K. Hatanaka and K. Kato *Journal of the Electrochemical Society,* **142** 3474 (1995)

[18] D.W. Dees, U. Balachandran, S.E. Dorris, J.J. Heiberger, C.C. McPheeters and J.J. Picciolo, Proceedings of the First International Symposium on Solid Oxide Fuel Cells, S.C. Singhal, Editor, p.317, **PV 89-11** The Electrochemical Society Proceedings Series, Pennington, NJ,1989.

[19] J.Winkler, P.V.Hendriksen, N.Bonanos, M.Mogensen. *Journal of the Electrochemical Society.* **145** 4, 1184 (1998)

[20] K.R.Thampi, A.J.McEvoy. J.Van Herle. *Journal of the Electrochemical Society,* **142** 506 (1995)

[21] T.Kawashima, M.Hishinuma. *Materials Transactions*, JIM, **37** 7 (1996)

[22] R. Hartung and H.-H. Möbius, *Chemie-Ing. Techn.*, **40** 12 (1968)

[23] B.A. Boukamp, *Solid State Ionics*, **20** 31 (1986)

[24] Unpublished measurements on coarse Ni/YSZ cermets, courtesy of F. Tietz, Research centre Jülich.

[25] F.T. Ciacchi, K.M. Crane and S.P.S. Badwal, *Solid State Ionics*, **73** 49 (1994)

[26] S.P.S. Badwal *Solid State Ionics*, **52 No 1-3**, 23 (1992)

[27] C. Wagner, *Ber. Bunsenges. Physik. Chem.* **72** 7 (1968)

[28] K. Eguchi, T. Setoguchi, K. Okamoto and H. Arai. Proceedings of the 3rd International Symposium on SOFC, S.C. Singhal and H. Iwahara, Editors, **PV 93-4**, p.494, The Electrochemical Society Proceedings Series, Pennington, NJ,1993.

[29] S. Primdahl and P.V. Hendriksen. *High Temperature Electrochemistry: Ceramics and Metals.* F.W. Poulsen, N. Bonanos, S. Linderoth, M. Mogensen and B. Zachau-Christiansen, Editors, p.403, 17th Risø International Symposium on Materials Science, Denmark, 1996.

Chapter Six

To be submitted to The Journal of the Electrochemical Society.

6. Characterisation of Types of Ni/YSZ Anodes

6.1 Introduction

The performance of a solid oxide fuel cell (SOFC) anode is strongly dependent on the fabrication methods and resulting microstructure of the cermet. Since the polarisation characteristics of the anode are highly dependent on its morphology, it is necessary to investigate the correlations between anodes with different structures, including fine structured anodes, coarse anodes, Ni felt and Ni point electrodes.

A homogeneous or graded structure consisting of three phases, Ni, yttria stabilised zirconia (YSZ) and porosity should be obtained, providing percolation paths for electrons, oxide ions and gaseous hydrogen and water, respectively. This requirement originates in the poor conductivity of electrons in YSZ and oxide ions in Ni. The line where the three phases meet is referred to as the triple phase boundary (TPB) and is considered to be electrochemically active only if percolation paths for the active species are provided. The reaction rate for electrochemical oxidation of hydrogen has been demonstrated to correlate to the TPB on model Ni anodes[1,2], making the extension of the length a technology aim.

This aim can in theory be achieved by a finer structure, or by increasing the thickness of the cermet anode. In practice, however, both solutions are limited by the requirement for low resistivity and percolation of active species. As the characteristic dimensions of the structure decrease, and as the anode thickness increases, the transport resistivity increases.

It has been proposed that the observed reaction limitation cannot be related to the hydrogen oxidation process. This is judged from overpotentials obtained at lower temperatures and extrapolated to SOFC-relevant temperatures from the observed activation energy[3]. The bondbreaking reaction of H_2 on Ni has also been suggested not to be limiting, due to its high sticking coefficient[4]. Relying on these observations the cause for the observed anodic overpotential must be related to transport limitations.

As a general observation, the anodic reaction rate can be limited by steps in the electrochemical reaction at the TPB, by transport restrictions in the solid structure for electrons and oxide ions, by gas diffusion in the cermet structure, and by surface diffusion and adsorption on the cermet surface. However, not all measurable contributions to the electrode polarisation are related to the examined anodes.

Gas conversion, relating to the changes in the Nernst potential of the fuel gas (with respect to a stable reference electrode) by passing a current at finite fuel gas flowrate, has been shown to add significantly to the measured overpotential of state-of-the-art anodes[5,6].

Diffusion in the gas over the anode surface has been reported[7]. A model involving a 1 mm thick layer of stagnant gas over the anode surface has been verified with experiments[8]. According to the model, the diffusion limitation in the porous cermet is insignificant for anodes of about 50 μm thickness and with a porosity of about 50%. Diffusion in ceramic structures over anodes has been demonstrated to be significant when the porosity is extremely low[26].

Neither gas conversion nor diffusion over the anode has any relation to the anode itself. They are instead concentration polarisations depending on the apparatus design, placement of reference electrode and gas exchange rates, and can vary significantly with the test geometry. It is recognised that in studies of high-performance state-of-the-art anodes, or in low partial pressures of hydrogen or water, the electrochemical data can be affected by the presence of these concentration polarisations[26,9].

Both state-of-the-art anodes with high current densities and 'model' anodes with a simple geometry have been studied and reported. The overall outcome of these studies does not always agree. The number of distinct arcs in impedance spectra under similar experimental conditions can vary, and the apparent activation energy, and dependence on gas mixture, associated with these arcs is inconclusive.

On identifying the concentration polarisation effects in data reported in the literature, there are several indications that one or two arcs at high frequency in impedance spectra are related to the Ni/YSZ cermet anode microstructure[9]. Impedance measurements on point electrodes, Ni films and cermets can give a number of combinations of arcs. This can vary from one arc for certain point electrodes to three (or four) arcs for some cermets.

Micro-electrodes (point shaped contacts) are reported to give one[10] or two[2,11,12] arcs. Measurements on Ni pattern electrodes are reported to yield one[1] or two[13] arcs. Measurements on cermets are reported to contain one arc[14], one arc plus an arc from diffusion above the active anode[7,25], and one arc plus two arcs relating to diffusion over the anode and gas conversion[9,26].

Studies revealing how only the high frequency arc is affected by poisoning of the Ni surface by H_2S in the fuel, is taken as evidence of the rate limiting process involving, to some extent, the Ni surface or a species made available from this surface[7,15].

Furthermore, the impedance for a reaction expected to take place on or at the TPB, must be in parallel to the interface capacitance. This capacitance has been reported for

Pt/YSZ to be in the order of 10 μF/cm^2 at 800 to 1000 °C[16]. The capacitance associated with the Ni/YSZ interface (high frequency arc) was about 10 μF/cm^2 for both Ni-pattern[2] and cermet[26] anodes.

On summarising the literature, it has been suggested that Ni/YSZ anodes operated in H_2/H_2O atmospheres at 700-1000 °C, can be thought to exhibit one arc representing one significant rate limiting process, but in several cases a second arc has appeared[17]. The exact nature of these arcs is unclear, but the sintering of anodes has been demonstrated to affect the shape of the high frequency impedance for Ni/YSZ cermets.

In this study, four types of Ni/YSZ anodes have been characterised and compared to illustrate similarities and differences from state-of-the-art cermet anodes, to coarse structured cermets, to two-dimensional Ni anodes with significantly higher polarization resistance. The various anodes have been studied on well characterised electrolyte samples[18] in the same setup where the gas conversion[5,6] and diffusion[8] over the anode are well understood, and can be corrected where appropriate. The anode structure-dependent high frequency arc in the impedance spectrum has been studied.

The aim of this chapter is:

i) to demonstrate the electrochemically active thickness of a technological cermet anode,

ii) to illustrate how the structure-dependent part of impedance spectra in some cases is composed of more than one arc, and

iii) to discuss the nature of the limitation or limitations reflected in the impedance arc or arcs in terms of thermal activation and dependence on partial pressures of H_2 and H_2O.

6.2 Experimental

6.2.1 Sample Preparation

All electrochemical tests were carried out on a three-electrode pellet (chapter 2, figure 2.10), produced from YSZ (ZrO_2 doped with 8 mol% Y_2O_3, Tosoh corporation). The pellets, with circular working electrodes of about 0.44 cm^2 are fabricated with a Pt-paste counter electrode, a Pt-ball reference electrode in the centre bore and two Pt leads in contact with the working electrode. The electrolyte geometry used here is verified by finite element analysis to have a frequency-stable, homogeneous current distribution, causing less than 3% error on a polarisation resistance as low as 0.16 Ωcm^2[18].

Four types of anodes have been prepared:

(i) A state-of-the-art Ni/YSZ cermet anode was prepared by spray-painting. An ethanol-based slurry, composed of NiO (99% pure, Merck) and YSZ (ZrO_2 with 8 mol% Y_2O_3, Tosoh corporation), was suspended by a dispersant[19]. The Ni/YSZ volume ratio was 40/60 in the reduced cermet. After deagglomeration in a ball mill, the YSZ particle size was observed as being 0.4 μm. The NiO particle size distribution was bimodal with fractions of approximately 0.4 μm and 10 μm in the volume ratio 6:1. The slurry was sprayed onto sintered YSZ three-electrode pellets in layers of up to 20 μm and sintered for 2 hours at 1300 °C, after the application of each layer. The anodes were typically 40 to 50 μm thick after three layers were deposited.

Anodes of this type were prepared to an average thickness of about 3.5 μm. A current-collecting layer was applied on these thin anodes, consisting of a 20 to 50 μm thick, unfired layer of 90/10 vol% Ni/YSZ, as described below.

(ii) A Ni slurry-based anode was prepared without sintering before testing. To enhance adhesion of the Ni-based anode on the YSZ pellet a Ni solution containing 1 mmol/L $Ni(NO_3)_2$ in ethanol with 4 wt% binder, (B60H, Mowital) was painted on the electrolyte pellet and decomposed in moist 9% H_2 at 1420 °C.[20]

The anode paste was prepared as follows: YSZ (ZrO_2 with 8 mol% Y_2O_3, Tosoh corporation) calcined at 1100°C for two hours was ball milled in ethanol with a dispersant until an average diameter of 0.4 μm was reached for the monomodal particle size distribution. Ni (Ni #255, Inco) with a particle size of 1 to 2 μm was added and the viscous paste was milled until the bimodal particle size distribution contained about 20 vol% of 0.4 μm and 80 vol% of 8 μm diameter particles. The paste was applied by brush in a layer of 20 to 50 μm thick. The Ni/YSZ volume ratio was 90/10 in the anode.

(iii) Coarse cermet anodes were prepared by screen-printing. The waterbased screen print paste contained 57 wt% green NiO (Baker), 38 wt% YSZ (Tosoh, ZrO_2 with 8 mol% Y_2O_3) precalcined at 1300 °C for 2 hours and 5 wt% ethylcellulose. The samples were dried and sintered at 1500 °C for 4.5 hours.

(iv) A Ni-felt anode was constructed as follows. A 1 mm thick Ni-felt (Ni-fibremat, 80/20 fibres/particles, Fibrex) consisting of fibres of 25 μm diameter was pressed against the surface of a three-electrode pellet using a perforated Al_2O_3 disk.

6.2.2 Electrochemical Testing

The three-electrode pellets were mounted in a four-lead three-electrode setup (see section 2.7.2.2). This setup provided a reference atmosphere (air) and a sealed anode compartment with a controllable atmosphere.

Anodes were heated to 1000 °C in 9% H_2 + 3% H_2O before switching to an atmosphere of 97% H_2 + 3% H_2O with an open circuit voltage (OCV) against Pt in air of about -1070 mV ($pO_2 \sim 2 \times 10^{-18}$ atm.). A total of 100 ml/min (at 25 °C) gas was passed over the anodes. Fuel composition was controlled by mixing nitrogen and hydrogen through thermal mass flowmeters and saturating this mixture, or part of it, with water at a controlled temperature.

pO_2 was determined by the Nernst expression from OCV vs. Pt/air. The accurate partial pressure pH_2O is determined from pO_2 and pH_2 by the following algorithm valid for 1000 K<T<1300 K[21]:

$$pH_2O = 10^{-(2.958-13022/T)}.pH_2.\sqrt{pO_2} \qquad \textbf{Equation 6.1}$$

Impedance spectroscopy was conducted with an applied amplitude of 20 to 30 mV. The frequency range used was 500 kHz to 0.01 Hz, in some cases only 65 kHz to 0.1 Hz. The equipment used for impedance spectroscopy was a Solartron 1260 or 1250 frequency response analyzer with a Solartron 1287 or 1286 electrochemical interface.

6.3 Results

6.3.1 Anode Structure

The microstructure of the reduced anodes was examined on polished cross-sections using an SEM. By this method it is not possible to distinguish between Ni and YSZ due to the similar atomic weights. Optical microscopy with the inherent limitations in resolution was used as a supplement to identify the distribution of the solid phases.

The microstructure of the fine cermet anode is given in a cross section in figure 6.1. The particles were 0.5 to 3 μm, and the porosity was in the order of 50%. Using optical microscopy, the distribution of the two phases was verified to be fairly homogeneous. Furthermore, Ni was evaluated to constitute the larger fraction of particles, with YSZ particles typically in the range of 0.5 to 1 μm. The anode thickness was evaluated from an average of 10 images obtained over a 7 mm cross section of the anode.

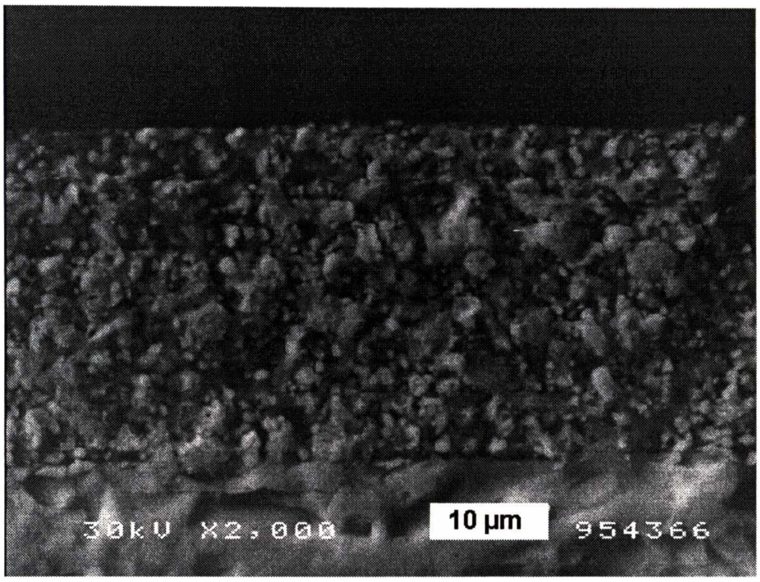

Figure 6.1 SEM micrograph showing structure of a fine cermet anode as observed by backscattered electrons on a polished cross section.

The Ni-slurry anodes with 90/10 vol% Ni/YSZ had a porous, well percolating Ni-structure, figure 6.2. In figure 6.3, a close-up of the surface structure is given, detailing the extent of Ni sintering and the distribution of 0.3 to 1 μm fine YSZ particles dispersed on the Ni-surface. The dispersion of YSZ particles was taken to indicate that all active TPB should be found on the 2D interface between the bulk electrolyte and the Ni anode. The characteristic size of the Ni particles touching the electrolyte was about 10 μm, and about 20% of the electrolyte surface was contacted by the Ni anode judging from 10 SEM images. This yielded a TPB of about 800 cm/cm^2.

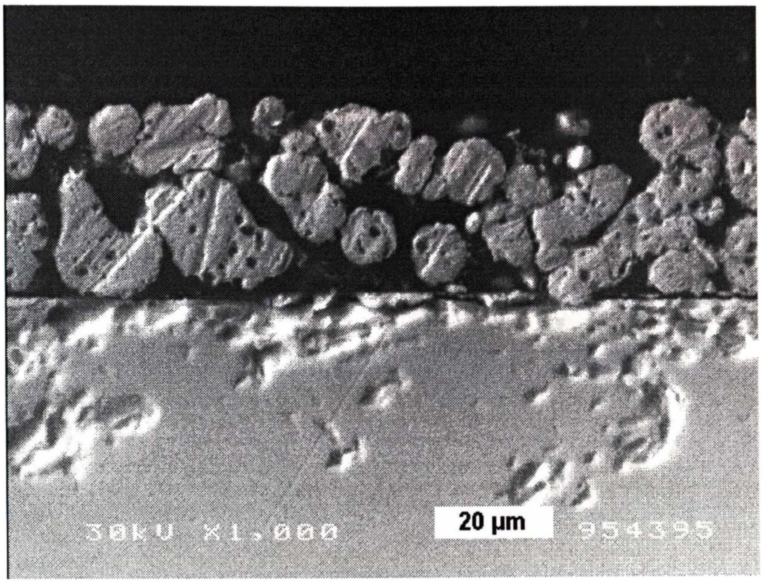

Figure 6.2 SEM micrograph showing structure of a Ni-paste anode as observed by backscattered electrons on a polished cross section.

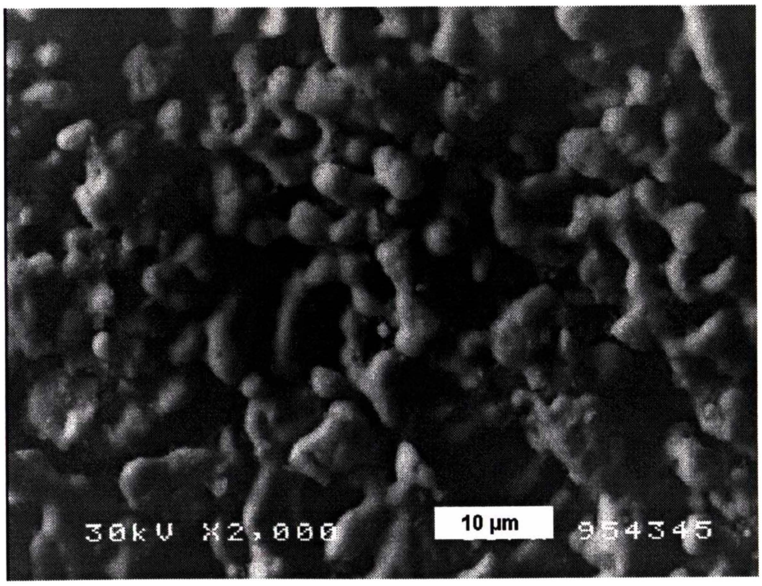

Figure 6.3 SEM micrograph showing structure of a Ni-paste anode as observed by backscattered electrons on the surface.

The structure of the coarse cermet anodes is indicated in a cross section in figure 6.4. The particle size was in the range of 3-5 μm for both phases with the Ni particles being clearly distinguishable from the YSZ particles by their morphology.

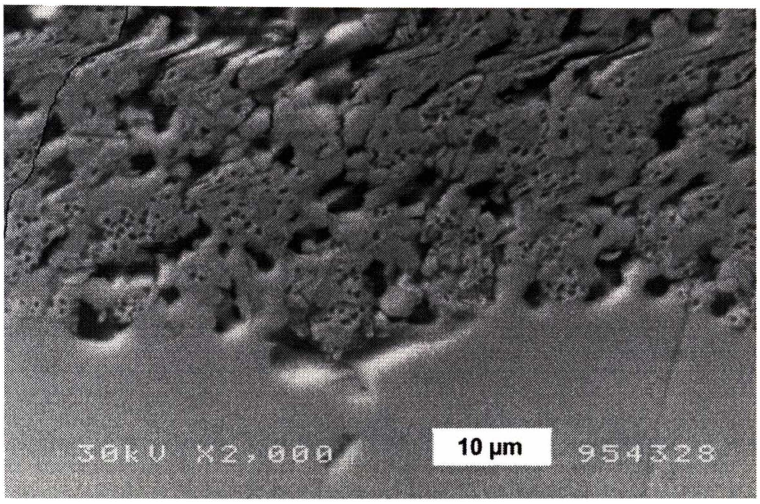

Figure 6.4 SEM micrograph showing structure of a coarse cermet anode as observed by backscattered electrons on a polished cross section.

The 25 μm Ni-felt anodes left a 20 μm wide Ni imprint on the YSZ surface. This imprint was taken to represent the TPB on the 2D interface and the estimated contact surface was 8% with a TPB length in the order of 90 cm/cm^2

6.3.2 Impedance Spectra

Impedance spectra obtained at the maximum temperature (1000 °C) were considered first, as the concentration overvoltages (gas conversion and diffusion) are most distinct at high temperatures. This is due to the processes being more or less unactivated by temperature, in contrast to the activated reaction impedance.

Area specific spectra obtained at OCV at 1000 °C in 97% H_2 + 3% H_2O are given in figures 6.5, 6.6, 6.7, and 6.8, after correction for a series resistance of 1 to 3 Ω, and a macroscopic anode area in the range of 0.4 to 0.45 cm^2. Characteristic frequencies are marked for ease of comparison. Firstly, gas conversion (marked III) was recognised in figures 6.5, 6.6 and 6.7, comprising of 0.12 to 0.15 Ωcm^2 at a characteristic frequency of 1 Hz[6]. The diffusion impedance relating to the gas over the anode was resolvable in figures 6.5 and 6.6 as an arc (marked II) of about 0.025 Ωcm^2 at an intermediate characteristic frequency of 10 to 100 Hz[8]. In figure 6.7, the diffusion impedance cannot be resolved and in figure 6.8 neither of the concentration polarisation processes are recognised, due to the relative magnitude of the reaction impedance.

The structure dependent part of the impedance spectrum (marked I) was seen to be describable by one arc in figures 6.5 and 6.6, but required two arcs in figures 6.7 and 6.8.

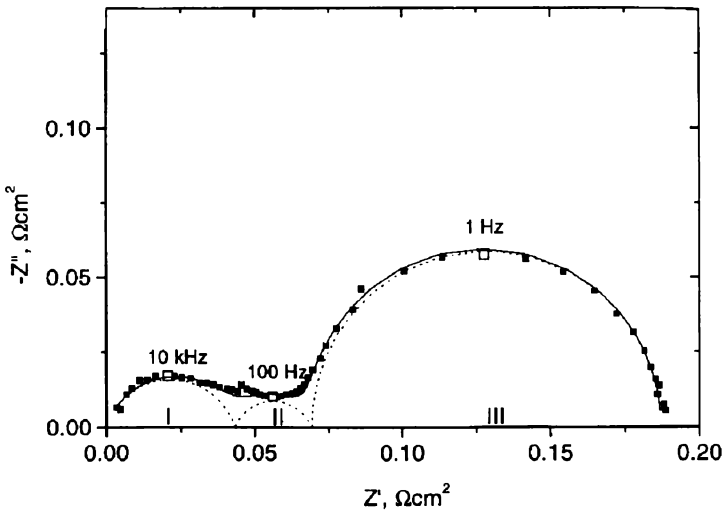

Figure 6.5 Area specific impedance spectra obtained at OCV at 1000°C in H_2 + 3% H_2O on a fine cermet anode. Points are experimental data, solid lines are total fit data and dashed lines indicate each impedance arc in the fit.

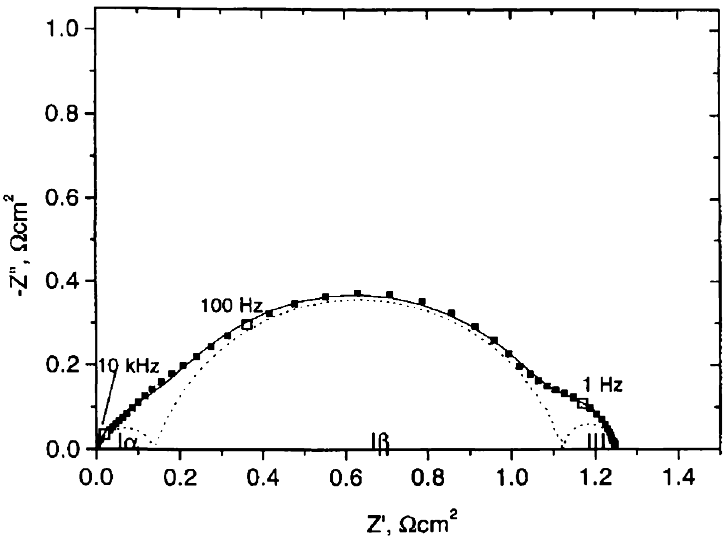

Figure 6.6 Area specific impedance spectra obtained at OCV at 1000°C in H_2 + 3% H_2O on a Ni-paste anode A528. Points are experimental data, solid lines are total fit data and dashed lines indicate each impedance arc in the fit.

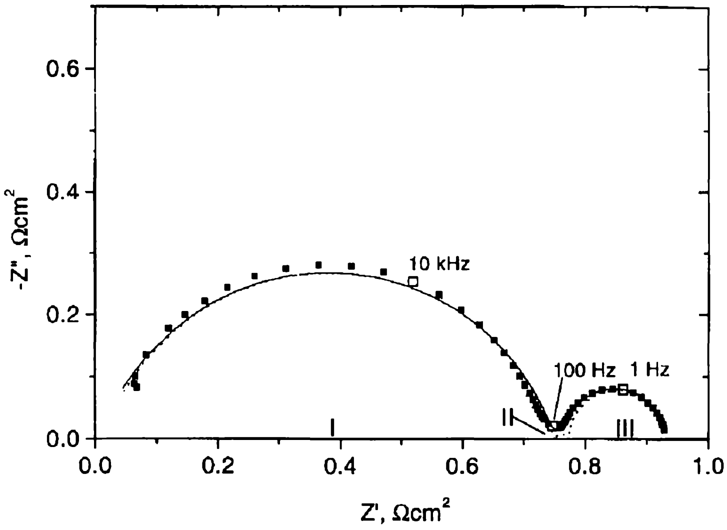

Figure 6.7 Area specific impedance spectra obtained at OCV at 1000°C in H_2 + 3% H_2O on a coarse cermet anode X133. Points are experimental data, solid lines are total fit data and dashed lines indicate each impedance arc in the fit.

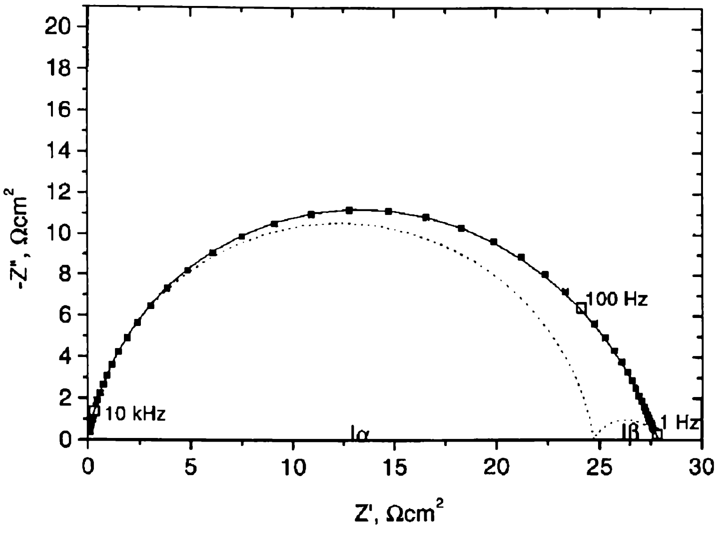

Figure 6.8 Area specific impedance spectra obtained at OCV at 1000°C in H_2 + 3% H_2O on a Ni-felt anode X73 Points are experimental data, solid lines are total fit data and dashed lines indicate each impedance arc in the fit.

The processes contributing to the impedance spectra were described by an equivalent circuit. This allowed the data to be condensed and provided the basis of a meaningful and comparable presentation. The selected equivalent circuit must be complex enough to account for the impedance spectra, within an accuracy of 1% for both real and imaginary parts under all experimental conditions. An accuracy of about 0.25% was obtainable for most spectra, except at the highest frequencies.

Impedance data were fitted with the software EQUIVCRT[22], using an equivalent circuit containing the elements L, R, C and Q, where L is an inductance, R a resistance, C a capacitance and Q a constant phase element given as $Q=Y_0(j\omega)^n$. Here Y_0 is an admittance, j the imaginary unit, ω the angular frequency and n is the frequency power.

The structure dependent part of the obtained impedance spectra was, in general, well described by one arc at lower temperatures, represented by an $(RQ)_1$ subcircuit with an n-value of 0.8 to 0.9. This is in agreement with reported impedance spectra on Ni/YSZ anodes for both cermet anodes[6,8,9,27] and for point electrodes.[10]

At higher temperature, two arcs were needed for coarse cermet anodes and Ni-felt anodes. The smaller of the two high frequency arcs was at the higher frequency for the coarse cermet anode, and the converse for the Ni-felt anode, figures 6.7 and 6.8. Two arcs denoted $(RQ)_{1\alpha}(RQ)_{1\beta}$ were used with fixed n-values selected as average values of what was obtained in unrestricted fits for these anodes. α and β refer to arcs with high and low relaxation frequencies recognised in impedance spectra from a given anode type rather than a distinct process. The use of such average values for these overlapping arcs (processes with similar time constants) is debatable. Nevertheless, this approach is considered the best option for impedance spectra where one arc is too simple for an interpretation. The major flaw with this interpretation is that in a fit of such overlapping arcs with a high correlation factor, changes in n-values can add a high degree of uncertainty to the data of the minor arc. A dominating arc is less sensitive to this uncertainty and the overall R_1 remains unaffected.

Homogeneous, one-dimensional finite length diffusion impedance can generally be handled as a finite length Warburg diffusion[22]. An $(RQ)_2$ subcircuit with an n-value of 0.75 was previously applied for this setup[6,8] and will be used here, accepting a broader time distribution of the process caused by the inhomogeneous gas flow pattern over the anode surface in the setup.[8]

Gas conversion is demonstrated to contribute a perfect semicircle at lower frequencies, and modelling predicts an $(RC)_3$ subcircuit.[5,6]

In general, impedance data were interpreted from the lowest obtainable frequencies, up to a vertical line at frequencies from 10 to 100 kHz. This vertical component was interpreted as a simple inductance, L, introduced by the measurement system. A series resistance, R_S, accounted for the electrolyte resistance between the working electrode and the reference electrode.

The above considerations, in conjunction with the obtained impedance spectra, led to the overall equivalent circuit $LR_S(RQ)_{1\alpha}(RQ)_{1\beta}(RQ)_2(RC)_3$. The equivalent circuits used, and selected n-values for each anode type, are listed in Table 6.1. In spectra where the ratio R_1/R_2 or R_1/R_3 was too high to yield reliable data for the minor arc, appropriate data points were omitted together with the relevant part of the equivalent circuit. In the following, the resistive parameters $R_{1\alpha}$, $R_{1\beta}$ and $R_1 = R_{1\alpha}+R_{1\beta}$ were studied and discussed.

Table 6.1 Appearance of the anode structure dependent section of the impedance spectra and selected equivalent circuits and n-values for each arc. α denotes the high frequency arc, where two arcs are required to obtain acceptable fits.

Anode Type	Appearance of Arc I	HighFrequency Circuit	n-values	Total Equivalent Circuit
Fine cermet	one arc	$(RQ)_I$	0.8	$LR_S(RQ)_I(RQ)_2(RC)_3$
Ni-slurry	one arc	$(RQ)_I$	0.8	$LR_S(RQ)_I(RC)_3$
Coarse cermet	two arcs	$(RQ)_{I\alpha}(RQ)_{I\beta}$	0.8 and 0.8	$LR_S(RQ)_{I\alpha}(RQ)_{I\beta}(RQ)_2(RC)_3$
Ni-felt	two arcs	$(RQ)_{I\alpha}(RQ)_{I\beta}$	0.9 and 0.7	$LR_S(RQ)_{I\alpha}(RQ)_{I\beta}$

6.3.3 Thickness

Fine cermet anodes with a thickness in the range of 3.5 μm to 54 μm were measured with an overlying current collector structure. A blank sample with only the current collector deposited on an electrolyte pellet was assigned the thickness 0 μm. R_1, R_2 and R_3 are given in figure 6.9 as function of anode thickness, after testing at 1000 °C in 97% H_2 + 3% H_2O, and fitted to the selected equivalent circuit. At a thickness of about 10 μm a pronounced change in R_1 was observed. At lower thickness' the values were about 0.7 Ωcm^2, at higher thickness R_1 was found to be an order of magnitude lower. The series resistance was scattered between 0.4 and 1.3 Ωcm^2, as expected for the electrolyte pellet at this temperature. This indicated good in-plane resistivity in the current collector. As expected, no variation was seen in R_2 and R_3 with thickness.

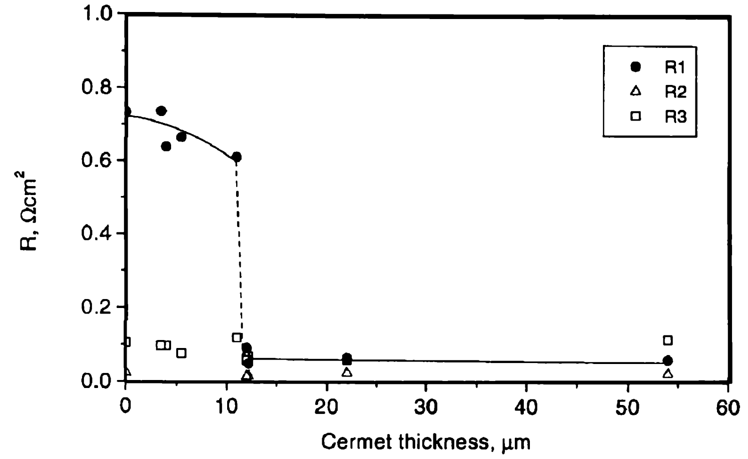

Figure 6.9 Dependence of anode thickness for contributions to the polarisation resistance for fine cermet anodes at 1000°C in 97% H_2 + 3% H_2O at OCV.

6.3.4 Thermal Activation

Impedance spectra at OCV were obtained in 97%H_2 + 3% H_2O, in the temperature range of 750 to 1000 °C, for the four types of anodes. After fitting with the appropriate equivalent circuits, (listed in Table 6.1) the resistive parameters $R_{1\alpha}$, $R_{1\beta}$, and R_1 were plotted with Arrhenius type plots, given in figures 6.10, 6.11 and 6.12. Approximation to straight lines (Arrhenius behaviour) was assumed and the activation energies are summarized in Table 6.2.

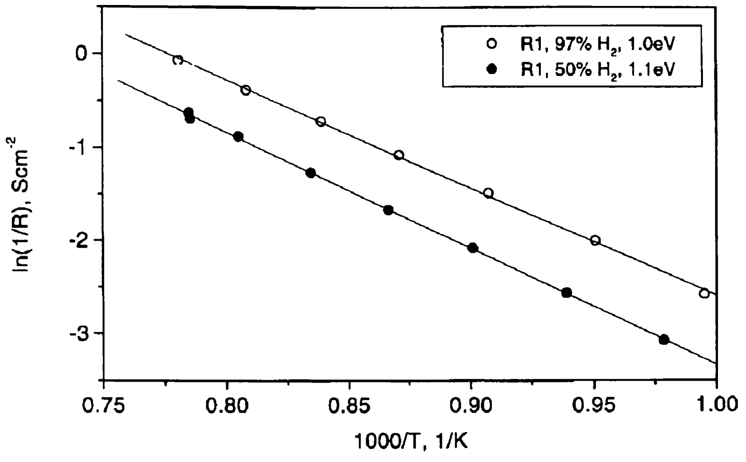

Figure 6.10 Arrhenius type plot wherefrom the apparent activation energy of $R_{1\alpha}$, $R_{1\beta}$, and R_1 can be estimated. Data obtained by fitting impedance spectra obtained at 700°C to 1000°C in H_2 + 3% H_2O at OCV. Ni-slurry anode , A528, in H_2 (open) and in 50/50 N_2/H_2.

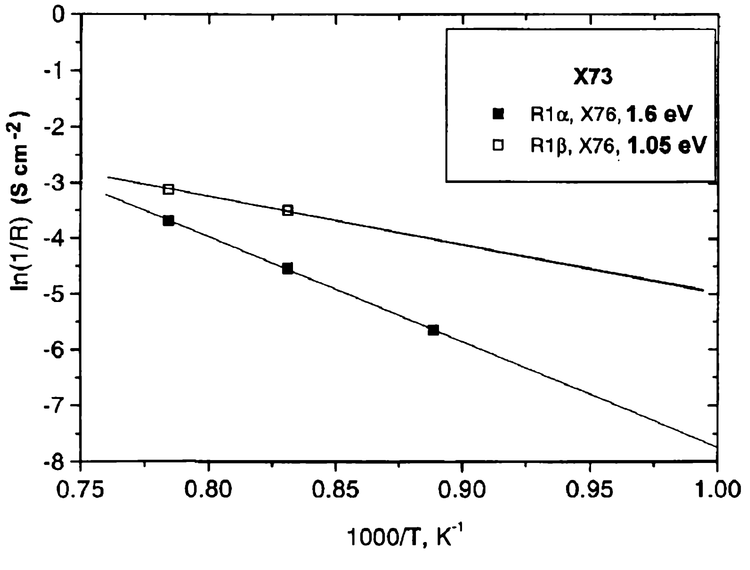

Figure 6.11 Arrhenius type plot where the apparent activation energy of $R_{1\alpha}$, $R_{1\beta}$, and R_1 can be estimated. Data obtained by fitting impedance spectra obtained at 700°C to 1000°C in H_2 + 3% H_2O at OCV. Ni-felt X73 (squares) and X76 (bullets).

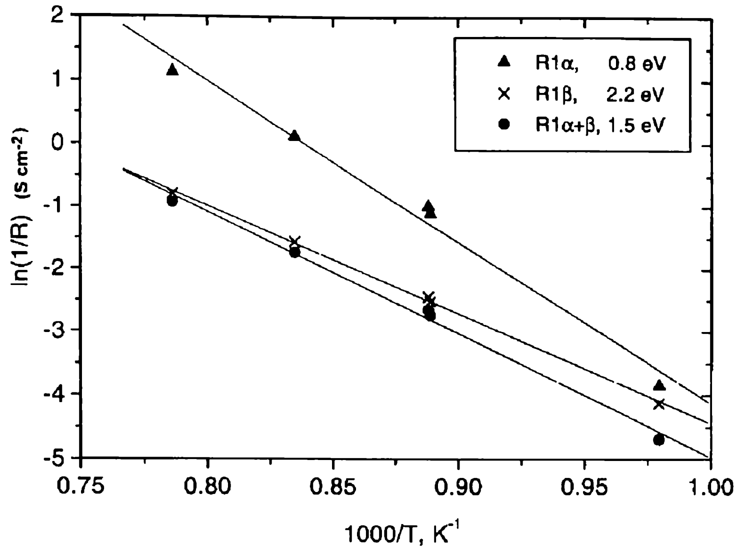

Figure 6.12 Arrhenius type plot where the apparent activation energy of $R_{1\alpha}$, $R_{1\beta}$, and R_1 can be estimated. Data obtained by fitting impedance spectra obtained at 700 °C to 1000 °C in H_2 + 3% H_2O at OCV. Coarse cermet anode, X133.

Table 6.2 Thermal activation energy, E, as evaluated from linear regression in an Arrhenius plot, E_l corresponds to R_l whereas E_α and E_β corresponds to the α and β arc, respectively.

Anode Type	Anode	E_l, eV	Temperature Interval, °C
Fine cermet[26]	A86,	E_l= 0.7	850-1000
	A92	E_l= 0.9	850-1000
Ni-slurry	A527,	E_l= 0.9	700-900
	A528	E_l= 1.1	750-1000
Coarse cermet	X132,	E_l= 1.6 E_α= 1.8 E_β= 1.1	750-1000
	X134	E_l= 1.2 E_α= 1.2 E_β= 0.9	770-1000
Ni-felt	X73	E_α= 1.6 $E\beta$=1.05	850-1000
Ni-point[23]	-[a]	E_l= 1.41	620-800
Ni-point[10]	-	E_l= 1.6	700-1000
Ni-wire[2]	-	E_α= 0.6 E_β=1.8	550-900
Cermet[7]	-	E_l= 1.01	700-1000
Ni-film[25]	-	E_l= 0.5	700-1000
Ni-pattern[13]	-	E_l= 1.6	700-950

---

[a] Sample anodes from the literature.

6.3.5 Gas Composition

Impedance spectra were obtained while varying the pH_2 at constant pH_2O at 1000 °C and fitted to the appropriate equivalent circuits. Reciprocal values of the resistive parameters $R_{1\alpha}$, $R_{1\beta}$, and R_1 are given as a function of pH_2 in a double logarithmic plot, figures 6.13, 6.14 and 6.15. The curves for R_1 indicated a fairly constant resistance, sometimes with a tendency to slight nonlinearity at a pH_2 of about 0.3 atm. The same tendency seems to hold for the dominant arc for coarse cermets and Ni-felt anodes. Linear slopes are summarized in Table 6.3

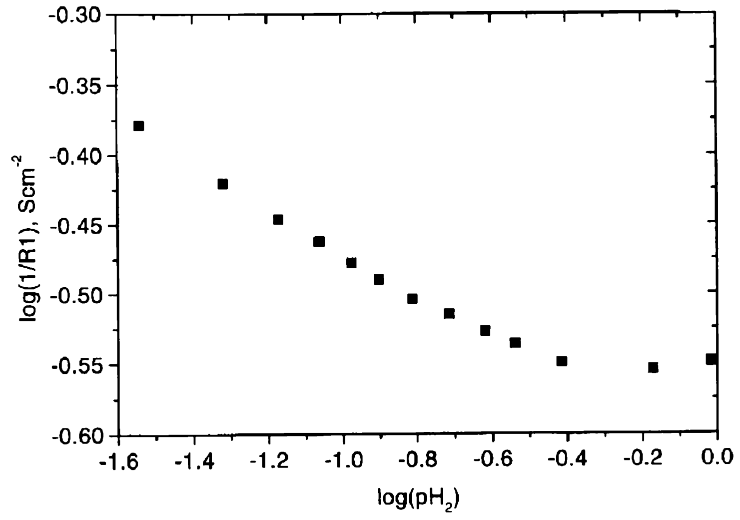

Figure 6.13 Dependence of $R_{1\alpha}$, $R_{1\beta}$ and R_1 on pH_2 at 1000°C in 3% H_2O at OCV, Ni-paste anode.

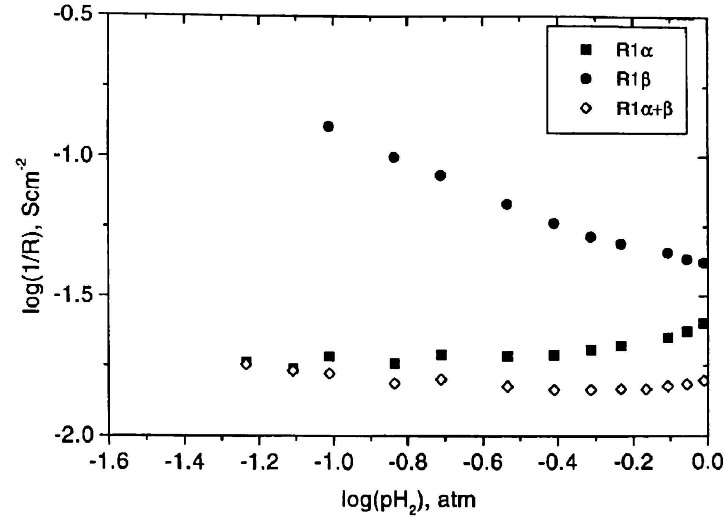

Figure 6.14 Dependence of $R_{1\alpha}$, $R_{1\beta}$ and R_1 on pH_2 at 1000°C in 3% H_2O at OCV. X134, Ni-felt X76.

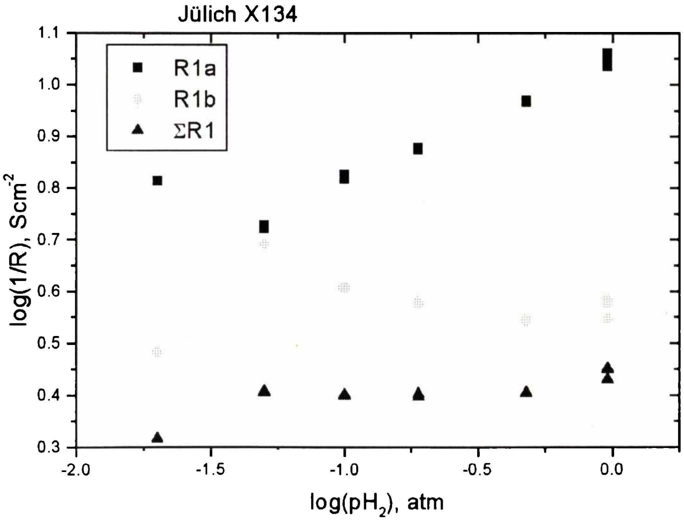

Figure 6.15 Dependence of $R_{1\alpha}$, $R_{1\beta}$ and R_1 on pH_2 at 1000°C in 3% H_2O at OCV.A528, coarse cermet.

Table 6.3 Hydrogen partial pressure dependence as evaluated from linear regression in a double logarithmic plots, figures 6.13, 6.14 and 6.15. m_l corresponds to R_l whereas m_α and m_β corresponds to the α and β arc, respectively.

Anode Type	Anode	$1/R_l \propto pH_2^m$	Range of pH_2, atm.	Constant pH_2O, atm.
Fine cermet[26]	A228	m_l= 0.15	$10^{-1.2}$-10^0	0.03
Ni-slurry	A528	m_l=-0.15 m_l= 0	$10^{-1.6}$-$10^{-0.5}$ $10^{-0.5}$-10^0	0.03 0.03
Coarse cermet	X134	m_l= 0.05 m_α=0.25 m_β= 0	$10^{-2.0}$-10^0	0.035
Ni-felt	X76	m_l=-0.15 m_α=0 m_β=-0.6 m_l= 0 m_α=0.3 m_β=-0.3	$10^{-1.3}$-$10^{-0.5}$ $10^{-0.5}$-10^0	0.035 0.035
Ni-point[10]	-[b]	m_l=-0.5 m_l= 0.5	$10^{-1.5}$-$10^{-0.66}$ $10^{-0.66}$-10^0	pH_2O= 0.055 and at 975°C
Ni-film[25]	-	m_l= 0	10^{-2}-10^0	pH_2O= 0.02

Impedance spectra were obtained while varying the pH_2O at constant pH_2 at 1000 °C and fitted to the appropriate equivalent circuits. Reciprocal values of the resistive parameters $R_{l\alpha}$, $R_{l\beta}$, and R_l are given as a function of pH_2O in a double logarithmic plot, figures 6.16, 6.17 and 6.18. The curves indicated a reduction in resistance with increasing pH_2O. There was a tendency for the cermet anodes to have a weaker dependence on pH_2O than the Ni-felt and Ni-paste anodes, when the slopes were in the range of 0.5. The results are summarized in Table 6.4.

---

[b] Sample anodes from the literature.

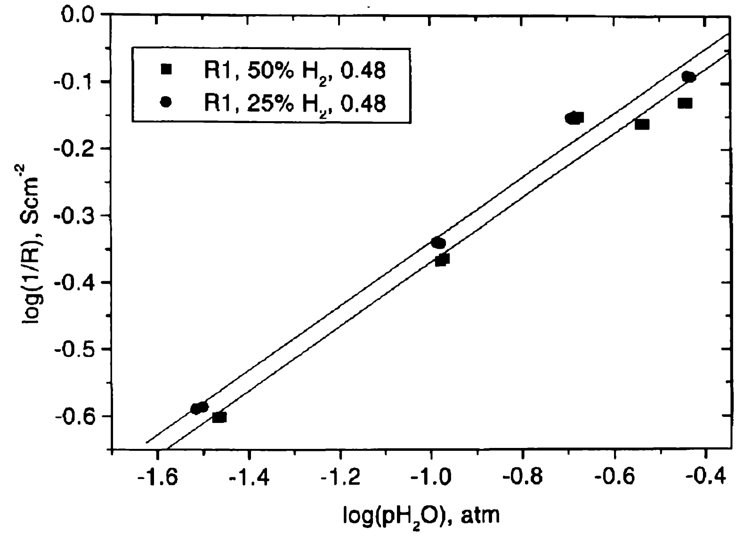

Figure 6.16 Dependence of $R_{1\alpha}$, $R_{1\beta}$ and R_1 on pH_2O at 1000°C in H_2 at OCV, Ni-paste anode A528, 50% H_2 (squares) and 25% H_2 (bullets).

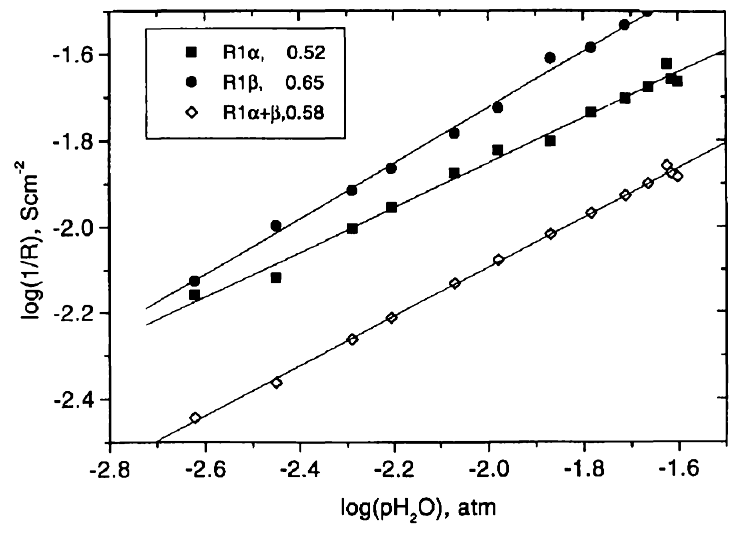

Figure 6.17 Dependence of $R_{1\alpha}$, $R_{1\beta}$ and R_1 on pH_2O at 1000°C in H_2 at OCV, Ni-felt anode X76 in 96-99.9% H_2.

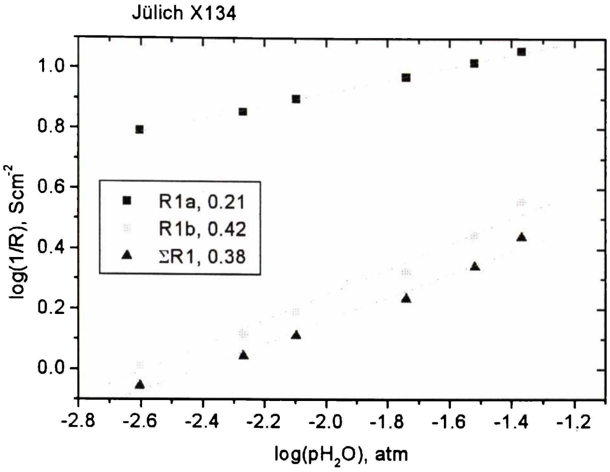

Figure 6.18 Dependence of $R_{1\alpha}$, $R_{1\beta}$ and R_1 on pH_2O at 1000°C in H_2 at OCV, Coarse cermet anode X134 in 96-99.9% H_2.

Table 6.4 Steam partial pressure dependence as evaluated from linear regression in a double logarithmic plots, figures 6.16, 6.17 and 6.18. m_l corresponds to R_l whereas m_α and m_β corresponds to the α and β arc, respectively.

Anode Type	Anode	$1/R_l \propto pH_2O^m$	Range of pH_2O, atm.	Constant pH_2, atm.
Fine cermet[26]	A51	m_l=0.3	$10^{-2.2}$-$10^{-1.4}$	0.97-0.99
		m_l=0.2	$10^{-1.6}$-$10^{-0.5}$	0.50
Ni-slurry	A528	m_l=0.6	$10^{-2.2}$-$10^{-0.5}$	0.965-0.99
		m_l=0.5	$10^{-1.5}$-$10^{-0.4}$	0.25 and 0.50
Coarse cermet	X134	m_l=0.4 m_α=0.2 m_β=0.4	$10^{-2.6}$-$10^{-1.4}$	0-965-0.99
Ni-felt	X76	m_l=0.6 m_α=0.5 m_β=0.65	$10^{-2.7}$-$10^{-1.5}$	0.97-0.99

6.4 Discussion

6.4.1 Active Thickness

As observed in figure 6.9, the active thickness of fine cermet anodes produced was about 10 μm when tested with a 90 vol% Ni/10 vol% YSZ current collector.

Analysis of experimental results on a two-dimensional Ni-pattern anode indicated a reaction zone extending about 1 μm from the TPB[24]. Dense Ni-anodes of various thickness were deposited on YSZ electrolytes and capped by a low-porosity ceramic layer. Impedance measurements suggested that the oxidation reaction takes place on a very thin zone of the Ni film within 1 μm of the TPB[25]. Assuming this reaction width along the TPB of a cermet, the active cermet thickness must be at least equal to 1 μm, as the reaction will reach this far into the cermet from TPB's on the anode/electrolyte interface.

An earlier study indicated no change in the polarisation resistance with thickness in the range of 20 μm to 70 μm, for fine cermet anodes[26]. In another study, the anode impedance had been demonstrated to decrease for thickness' up to about 10 μm, after which the impedance was constant[27]. Assuming adequate porosity (about 50%) the limitation for this active thickness was taken to be transport resistivity in the poorer solid conductor, presumably the YSZ structure. A fairly high resistivity in the YSZ structure of the cermet was measured after dissolving out the Ni, indicating a thin active anode layer near the electrolyte/anode interface[7].

6.4.2 Thermal Activation

The activation energy of structure related processes in the four anodes was between 0.8 and 1.8 eV. In the literature, a scatter was also reported, 0.5 eV for a dense Ni-electrode[25], 0.8 eV [26] and 1.0 eV [7] for cermets, 0.6 and 1.8 eV for two arcs on point electrodes[2], and 1.6 eV for one arc on a point electrode[10]. The published data suggested the presence of a high activation energy for point contacts, and coarse cermets, and lower values in fine cermets.

A reappearing feature is a non-linearity of reported Arrhenius plots, indicating a higher activation energy at lower temperatures. The impedance arc interpreted as one process could consist of two processes with similar time constants. These would operate in series, judging from the curvature of Arrhenius plots.

6.4.3 Hydrogen Partial Pressure

The results indicated a relatively constant resistance when increasing pH_2 from 0.03 atm. to 0.97 atm. The Ni slurry anode showed a very slight increase in resistance up to approximately 0.3 atm. pH_2. This was also mirrored by the Ni-felt anode with a very shallow minimum at a pH_2 of approximately 0.3 atm., whereas the coarse structured anode resistance was virtually constant over the pH_2 range of 0.01 atm. to 0.97 atm,. This is in agreement with Nakagawa *et al.*[25] who saw no dependence of pH_2 with conductivity at 1000 °C.

A three-electrode cell was used by Mohamedi-Boulenouar *et al.*[10] with a Ni point electrode. Measurements were carried out between 700 °C and 1000 °C and impedance spectroscopy was used to study the electrode, varying the hydrogen and water partial pressures. An impedance diagram with one arc was fitted to the experimental results. At 975 °C and fixed pH_2O, a minimum in conductivity was observed at a pH_2 of 0.2 atm. whereas Mizusaki *et al.*[1], using a Ni film electrode, showed that conductivity was at a minimum at 0.1 atm. and above, and independent of pH_2 below 850 °C. Above 850 °C, conductivity had a dependence of $p(H_2)^{-0.5}$, below 0.10 atm. pH_2, which was in agreement with Mohamedi-Boulenouar *et al.*[10]. These results also agree with Osborg *et al.*[2] who found that at 700 °C, pH_2 was independent of conductivity, but was contradictory at 900 °C, where conductivity increased with a $p(H_2)^{0.25}$ dependency until about 0.1 atm., after which it became independent.

6.4.4 Steam Partial Pressure

The results indicated a decrease in resistance with increasing pH_2O. There was a tendency of the cermet anodes to have less of a dependency on pH_20 than the Ni felt and Ni-paste anodes. A slope of approximately 0.5 for the Ni-paste and Ni-felt was observed which is in agreement with Mohamedi-Boulenouar *et al.*[10]. The authors showed a linear variation with a slope of 0.5 for conductivity with increasing pH_2O which was also observed by Nakagawa *et al.*[26] for a Ni film electrode measured at 1000 °C from a pH_2O of 0.01 atm. to 0.3 atm. This was also in agreement with Norby *et al.*[13] for a Ni wire electrode at 900 °C in a pH_2O of 0.06 atm.

The general trend of increasing conduction with increasing pH_2O has also been observed by Osborg *et al.*[2] when studying a nickel wire anode using impedance spectroscopy. The authors discovered two impedance arcs relating to the anode reaction (R3, R4). The R4 arc had a dependance of $p(H_2O)^1$ at high pH_2O (>0.01atm) and became independent of pH_2O at low pH_2O (<0.001 atm.). The activation energies were found to be 1.6 eV for the point electrode and 1.8 eV (R4) for the Ni wire (where R4 was proposed to be the high frequency structure related arc). Below 700 °C, Osborg *et al.*[2] found that the apparent activation energies for diffusion and charge transfer arcs changed and attained a common intermediate activation energy.

Mizusaki *et al.*[1], using impedance measurements at 700 °C to 850 °C in H_2/H_2O atmospheres on a Ni film electrode, showed that the reaction proceeds through the triple phase boundary. A pH_2O dependence was noted with a slope of 1 with increasing pH_2O from 0.003 atm. to 0.03 atm. H_2O.

Geyer *et al.*[7] investigated symmetrical Ni/YSZ cermet anodes between temperatures of 800 °C and 1000 °C with a varying feed gas composition of hydrogen with between 2% to 90% H_2O. Two well-separated impedance arcs were present, the high frequency arc was due to a combination of the charge transfer reaction and ionic resistance within the cermet. Varying the mole fraction of water vapour produced a broad conductance maximum around pH_20 = 0.5 atm. and an activation energy of 1.01 eV for the charge transfer process.

6.4.5 Possible Limiting Processes

The involved processes described above could be transport processes or surface specific reactions, depending on the microstructure and level of impurities. In this way a variation in activation energy could be accounted for between anodes of different geometry and those prepared from different raw materials sources.

NiO is to some extent soluble in YSZ, depending on sintering temperature and availability of NiO[28]. It has been shown[29] (section 3.4.4) that the sintering temperature controls the rate of NiO agglomeration and thus the morphology of the completed cermet layer. A sintering temperature of 1450 °C caused the NiO to agglomerate from a particle size of 1 μm to approximately 4 μm. Ultimately, this decreased the TPB and therefore severely affected the microstructure and the percolation paths of Ni in the reduced anode (see figures 3.15(a) and 3.15(b)). The 1300 °C sintering temperature was sufficient to sinter the active YSZ, producing an adhering anode layer, with no agglomeration of the NiO observed. Figures 3.14(a) and 3.14(b) show the particle size of the Ni after sintering and after reduction, with no significant increase.

It has been shown[30] that the anode microstructure and the subsequent microstructural degradation rate was sensitive to the reduction procedure. Attempts to reduce and operate anodes under various conditions indicated poor anode performance and stability when reduced in humidified 9% hydrogen in nitrogen, dry 9% hydrogen in nitrogen, or by applying a potential difference across the cell in nitrogen, compared to using short-time reduction in humidified pure hydrogen.

A possible transport difficulty could be caused by tortuous ionically conducting paths, created from the sintering of fine YSZ. This would cause a reduced electrochemically active layer due to the high overpotential needed to allow ionic conduction deep into the anode layer. A solution to this problem would be to include larger YSZ particles in the cermet slurry to provide more direct, ionically conducting paths, to the electrolyte substrate, thus reducing the overpotential needed to increase the electrochemically active anode thickness.

6.5 Conclusions

The performance of the anode is based on the particular microstructure formed during the fabrication process. Results can vary greatly when comparing anodes with various microstructures (cermets-(fine and coarse particle sizes), 2D nickel layers, and point electrodes).

The major difficulty with comparing impedance spectra obtained from anodes with substantially different microstructures is assigning the appropriate arcs. For example, an impedance spectrum obtained from a point electrode usually consists of one major arc, with the possibility of another suppressed arc. The arcs must be assigned as either structure-related, diffusion or gas conversion impedance. A cermet anode impedance spectrum might consist of three to four arcs, which must also be assigned correctly. Only then is it possible to satisfactorily compare results from various authors.

The activation energy of the structure-related processes for the four anodes was between 0.8 and 1.8 eV. This was quite a large range and seemed typical when comparing cermet anodes with point electrodes. The non-linearity of the Arrhenius plots had been noted in the literature, indicating a higher activation energy at lower temperatures. The structure related impedance arc interpreted as one process could consist of two processes with similar time constants, which has been observed for the Ni felt and the coarse structured cermet.

Increasing the pH_2O produced a decrease in resistance with a slope of approximately 0.5 for the Ni-paste and Ni-felt anodes. There was a tendency of the cermet anodes to have less of a dependency on pH_20 than the Ni felt and Ni-paste anodes.

Increasing pH_2 from 0.03 atm. to 0.97 atm. resulted in a relatively constant resistance. The Ni slurry anode showed a very slight increase in resistance up to approximately 0.3 atm. pH_2. This was also mirrored by the Ni felt anode with a very shallow minimum at a pH_2 of approximately 0.3 atm. However, the coarse structured anode resistance was virtually constant over the pH_2 range of 0.01 atm. to 0.97 atm,

6.6 Acknowledgements

Research performed in collaboration with Søren Primdahl from Risø National Laboratory, Roskilde, Denmark.

6.7 References

---

[1] J. Mizusaki, H. Tagawa, T. Saito, K. Kamitani, T. Yamamura, K. Hirano, S. Ehara, T. Takagi, T. Hikita, M. Ippommatsu, S. Nakagawa and K. Hashimoto, *Journal of the Electrochemical Society*, **141** 8 (1994)

[2] P.A. Osborg and T. Norby, in 7th SOFC WORKSHOP, Theory and measurement of Microscale Processes in Solid Oxide Fuel Cells, p.47, Wadahl, Norway, (1995). IEA report obtainable from H. Nabielek, KFA-ISR Forschungszentrum Jülich GmbH, D-52425 Jülich, Germany.

[3] M.Mogensen, S.Sunde, S.Primdahl. SOFC Anode Kinetics. Proceedings of the 17th Risø International Symposium on Material Science: High Temperature Electrochemistry: Ceramics and Metals. Editors: F.W.Poulsen, N.Bonanos, S.Linderoth, M.Mogensen, B.Zachau-Christiansen. Risø National Laboratory, Roskilde, Denmark, 1996.

[4] M.Mogensen, S.Skaarup. *Solid State Ionics*. **86-88** 1151 (1996)

[5] S. Primdahl, M. Mogensen, Gas Conversion Impedance: SOFC Anodes in H_2/H_2O Atmospheres. 5th International Symposium on Solid Oxide Fuel Cells, SOFC V, June 2-5, 1997. Aachen, Germany.

[6] S. Primdahl, M.Mogensen, *Journal of the Electrochemical Society*, **145** 7, 2431 (1998)

[7] J. Geyer, H. Kohlmüller, H. Landes, R. Stübner, Investigations into the Kinetics of the Ni-YSZ-Cermet-Anode of a Solid Oxide Fuel Cell. 5th International Symposium on Solid Oxide Fuel Cells, SOFC V, June 2-5, 1997. Aachen, Germany.

[8] S. Primdahl. M. Mogensen, Gas Diffusion Impedance in Characterisation of Solid Oxide Fuel Cell Anodes. Submitted to *Journal of the Electrochemical Society*, 1998.

[9] M. Mogensen, S. Primdahl, J.T. Rheinländer, S. Gormsen, S. Linderoth and M. Brown, In Proceedings of the 4th International Symposium on Solid Oxide Fuel Cells, M. Dokiya, O. Yamamoto, H. Tagawa and S.C. Singhal, Editors, **PV 95-1**, p.657, The Electrochemical Society Proceedings Series, Pennington, NJ (1995)

[10] F.Z. Mohamedi-Boulenouar, J. Guindet and A. Hammou, , U. Stimming, S. C. Singhal, H. Tagawa and W. Lehnert, Editors, 5th International Symposium on Solid Oxide Fuel Cells, SOFC V, June 2-5, 1997. Aachen, Germany. **PV 97-40**, p.441, The Electrochemical Society Proceedings Series, Pennington, NJ (1997)

[11] J. Guindet, C. Roux and A. Hammou in Proceedings of the 2nd International Symposium on Solid Oxide Fuel Cells, F. Grosz, P. Zegers, S.C. Singhal and O. Yamamoto, Editors, p.553, Athens, Greece (1991) EUR-13564-EN.

[12] J. Guindet, Thesis (in french), Institut National Polytechnique de Grenoble (1988)

[13] T. Norby, O.J. Velle, H. Leth-Olsen and R. Tunold Proceedings of the 3rd International Symposium on Solid Oxide Fuel Cells, S.C. Singhal and H. Iwahara, Editors, **PV 93-4,** p.473, The Electrochemical Society Proceedings Series, Pennington, NJ (1993)

[14] T. Kawada, N. Sakai, H. Yokokawa, M. Dokiya, M. Mori, T. Iwata, *Journal of the Electrochemical Society*, **137**, 10, 3042 (1990)

[15] D.W. Dees, U. Balachandran, S.E. Dorris, J.J. Heiberger, C.C. McPheeters and J.J. Picciolo, Proceedings of the 1st International Symposium on Solid Oxide Fuel Cells, S.C. Singhal, Editor, p.317, **PV 89-11** The Electrochemical Society Proceedings Series, Pennington, NJ, 1989.

[16] N.Robertson, J.Michaels, *Journal of the Electrochemical Society*. **138** 5, 1494 (1991)

[17] T.Kawada, N.Sakai, H.Yokokawa, M.Dokiya, M.Mori, T.Iwata. *Journal of the Electrochemical Society*. **137** 10, 3042 (1990)

---

[18] J. Winkler, P.V. Hendriksen, N. Bonanos M. Mogensen. *Journal of the Electrochemical Society.* **145** 4, 1184 (1998)

[19] C. Bagger, In *1992* Fuel Cell Seminar: Program and Abstracts, page 241, Nov. 29-Dec. 2, 1992, Tucson, AZ, Courtesy Associates, Inc. Washington, DC, 241 (1992)

[20] K.R. Thampi, A.J. McEvoy, J. Van Herle, *Journal of the Electrochemical Society,* **142**, 506 (1995)

[21] R. Hartung and H.-H. Möbius, *Chemie-Ing. Techn.,* **40** 12 (1968)

[22] B.A. Boukamp, *Solid State Ionics,* **20** 31 (1986)

[23] R.Baker, J.Guindet and M.Kleitz. *Journal of the Electrochemical Society,* **144** 2427 (1997)

[24] M.Kleitz, T.Kloidt, L.Desssemond. Conventional Oxygen Electrode Reaction: Facts and Models. Proceedings of the 13th Risø International Symposium: High Temperature Electrochemical Behaviour of Fast Ion and Mixed Conductors. Editors: F.W.Poulsen, J.J.Bentzen, T.Jacobsen, E.Skou, M.J.L.Østergård. Risø National Laboratory, Roskilde, Denmark, 1993.

[25] N. Nakagawa, H. Sakurai, K. Kondo, T. Morimoto, K. Hatanaka and K. Kato, *Journal of the Electrochemical Society* **142** 3474 (1995)

[26] S. Primdahl, M. Mogensen, *Journal of the Electrochemical Society,* **144** 3409 (1997)

[27] M.Brown, S.Primdahl, M.Mogensen, N.Sammes. Minimum Active Layer Thickness For a Ni/YSZ Cermet SOFC Anode. Submitted to the 18th Australasian Ceramics Conference, September, 1998.

[28] A. Kuzjukevics, S. Linderoth and J. Grabis, Proceedings of the 17th International Risø Symposium: High Temperature Electrochemistry: Ceramics and Metals, Editors: F. W. Poulsen, N. Bonanos, S. Linderoth, M. Mogensen and B. Zachau-Christiansen, Risø National Laboratory, Roskilde, Denmark, 319-324, 1996.

[29] S.Primdahl. Anode Sintering Temperature. Risø Internal Report. BC-322, March 1997. Materials Research Department, Risø National Laboratory, Denmark, 1997.

[30] S.Primdahl, M.Mogensen. Ni-YSZ-cermet anode behaviour studied in a 3-electrode test facility. DK-SOFC-BC-207, June 1994. Materials Research Department, Risø National Laboratory, Denmark, 1997.

Chapter Seven

7. Conclusions and Recommendations

7.1 Conclusions

Nickel/yttria stabilised zirconia (YSZ) cermet systems are employed as anode materials in high temperature solid oxide fuel cell (SOFC) applications. To summarise the literature, the Ni/YSZ anode is still the best system for the oxidation of H_2 in the SOFC. There is intensive research being performed to develop a mixed ionic/electronic conducting ceramic material. Unfortunately, no materials have performed satisfactorily over the entire oxygen partial pressure range that the anode is subjected to.

It is generally accepted that an efficient cermet anode for H_2 oxidation has the following requirements:

(i) Large triple phase boundary,
(ii) Good contact between the anode layer and the electrolyte,
(iii) Correct metal/ceramic particle size ratio,
(iv) Correct porosity,
(v) High ionic and electronic conductivity (percolation of both phases), and
(vi) Long term stability.

The composite Ni/YSZ cermet anode has been widely studied as an anode component for the SOFC. It consists of an intimate mixture of NiO and YSZ particles with a specific microstructure, optimised to enhance the TPB and percolation of the two phases.

The cermet is fabricated using a number of techniques, the most successful being a modified EVD process. Other satisfactory techniques being developed include wet powder spraying (WPS®) and slurry coating.

Recently, a number of different Ni/YSZ cermet anodes were studied using impedance spectroscopy and DC electrochemical methods. The electrode performance was correlated to the structure of the cermet as revealed by optical microscopy. Experiments were carried out on both very fine and coarse structures including the limiting case of a Ni point electrode. Three arcs were observed in the impedance spectra. The high frequency impedance arc was related to the cermet structure, the middle arc was related to a diffusion process occurring on the surface of the anode, while the low frequency impedance arc was related to a gas conversion impedance caused by the geometry of the electrode testing apparatus.

Chapter Three describes the preparation of the raw materials, including milling and sintering schedules, and particle size studies. Also covered, is the fabrication of the anode layers using a wet powder spraying (WPS®) process. The ionically conducting YSZ powder was modified, by sintering and milling, to vary the particle distribution. This allowed the fabrication of cermet powders with varying particle sizes and therefore microstructures. At a sintering temperature of 1100 °C, the YSZ was only partially sintered. The structure of the agglomerates showed YSZ balls (approximately 45-50 µm in diameter) made up of fine particles of YSZ, which could be easily milled. At a sintering temperature of 1400 °C, no porosity within the agglomerates was present. The average size (35-40 µm) of the agglomerates was smaller than the YSZ sintered at 1100 °C, indicating a dense structure. Bimodal particle distributions were present for the milled YSZ. The finest particles were approximately 0.4 μm, and represented the grinding limit, which was independent of calcining temperature. The agglomerate size decreased and the amount of fine YSZ increased as milling times were extended.

A 'paint' consisting of the cermet powder (NiO/YSZ), a solvent, and a binder was developed in order to use a wet powder spraying (WPS®) technique, to apply the electrode layer to the electrolyte substrate. By this method, reproducible anodes with good morphological properties were produced. The slurry was prepared with ethanol as the solvent and a PVP binder, to form a stable suspension. The ethanol provided a slow evaporation rate for the slurry and allowed the ceramic powders more time to densify. It also became clear that too much of a liquid phase on the substrate allowed separation of the NiO and YSZ to occur, causing a layering effect.

Anode sintering temperature was also studied indicating that a temperature of 1300 °C provided the optimum sintering effect. Agglomeration of the NiO in the anodes occurred at a high sintering temperature of 1450 °C. At this temperature the NiO was mobile enough to agglomerate from a particle size of approximately 1 μm to an average particle size of 4 μm. Upon reduction in hydrogen, the Ni formed 'islands' within the YSZ matrix and thus little percolation existed, causing very low electronic conduction. Anodes sintered at 1300 °C showed none of the agglomeration of NiO present in the samples sintered at higher temperatures. There was no discernable increase of Ni particle size after sintering and reducing in hydrogen.

The anodes fabricated for this research have followed some distinct trends. It has become evident that the anode slurry must contain fine (0.4 μm) YSZ to aid in the sintering of the YSZ matrix. It is also possible that a certain amount of coarse (5-10 μm) YSZ would be beneficial to shorten the ionically conducting paths, and also to stabilise the YSZ structure. The Ni must have a small particle size (approximately 1 μm) to ensure a large triple phase boundary (TPB), but only a sufficient amount to ensure the percolation of electrons. Electronic conductivity was improved with the increase in density of the anode.

In Chapter Four a number of Ni/YSZ cermet anodes consisting of 40 vol% nickel and 60 vol% YSZ were fabricated with varying thickness of the active layer. The anode materials were milled to the appropriate particle sizes, air-sprayed onto YSZ substrates and subsequently sintered to produce the anode component. The thickness' ranged from 3.5 µm to 54 µm in order to find the minimum thickness of active layer for a high performance anode using the least material. The anodes were studied in an atmosphere of hydrogen, water and nitrogen in a 3-electrode setup. Impedance spectroscopy was carried out at a temperature of 1000 °C.

It was found that approximately 12 µm was the limiting thickness for a low polarisation resistance. Below a thickness of 12 µm, the polarisation resistance increased in an erratic manner as the reaction zone was reduced. The area specific resistance of the porous nickel current collector was 0.80 Ωcm^2 at 1000 °C and 0.05 Ωcm^2 for a 12 µm thick Ni-YSZ-cermet.

Chapter Five discusses the development of Ni/YSZ cermet anodes with 90 vol% Ni and 10 vol% YSZ, fabricated in order to create an anode with significantly higher polarization resistance. Hereby a structure-related impedance arc at high frequencies could be examined in detail. The anode was studied in mixtures of hydrogen, water and nitrogen in a 3-electrode setup. Impedance measurements were carried out at temperatures ranging between 700 °C and 1000 °C. The activation energy was in the range of 0.94 to 1.10 eV. The rate limiting process appeared to be enhanced by increasing the water content up to 0.2 atm., thereafter no significant change took place, up to 0.37 atm. No marked effect of hydrogen partial pressure was noted above 0.4 atm.; below this value the resistance declined with decreasing pH_2. A Tafel type relation was used to describe the anodic polarization results but does not conclusively imply that a charge transfer reaction is the rate-limiting step. The present work confirmed that a high frequency arc from impedance spectroscopy data was indeed related to the structure of the cermet.

Characterisation of four different anodes was studied in Chapter Six to illustrate similarities and differences from state-of-the-art cermet anodes to coarse structured cermets to two-dimensional Ni anodes with significantly higher polarization resistance. The anode structure-dependent high frequency section of the impedance spectrum was studied. The activation energy of the structure-related processes for the four anodes was between 0.8 and 1.8 eV. This was quite a large range and seemed typical when comparing cermet anodes with point electrodes. The non-linearity of the Arrhenius plots was noted, indicating a higher activation energy at lower temperatures. The structure related impedance arc interpreted as one process could consist of two processes with similar time constants, which has been observed for the Ni felt and the coarse structured cermet. Increasing the pH_2O produced a decrease in resistance with a slope of approximately 0.5 for the Ni-paste and Ni-felt anodes. There was a tendency of the cermet anodes to have less of a dependency on pH_20 than the Ni felt and Ni-paste anodes. Increasing pH_2 from 0.03 atm. to 0.97 atm. resulted in a relatively constant resistance for all four anodes.

7.2 Recommendations for Future Work

7.2.1 General Comments

The Ni/YSZ cermet has been adopted as the anode material of choice by virtually all research teams. However, the performance of the cermet is highly dependent on the microstructure formed during fabrication of the anode. It is of utmost importance for the commercialisation of SOFCs that long-term stability be achieved for the cermet anode. The degradation of the cermet is related to Ni particle agglomeration at the operating temperature of 1000 °C.

The rate of degradation for the Ni/YSZ structure appears relatively small, using a modified electrochemical vapour deposition (EVD) fabrication process. This technique consists of forming a Ni matrix and then infusing YSZ into the porous structure. Due to the expense of the EVD process, commercialisation of SOFCs using this technique, will not be economically viable. More research needs to be performed on the basic techniques (slurry coating, wet powder spraying (WPS®), tape casting, callender rolling), to try and emulate the superior structure and low degradation rate produced by the EVD process.

When the Ni content is increased to provide better electronic conduction in the cermet, a problem can arise concerning the thermal expansion coefficient. The thermal expansion coefficient increases with increasing Ni content and over a certain volume percentage of Ni, the thermal mismatch between the anode layer and the electrolyte will be too great and the cell will crack under thermal gradients.

In conclusion, the author suggests that to solve the problems of anode degradation and poor microstructure, an anode consisting of YSZ powder with a bimodal particle size distribution must be fabricated. It has become evident during this research that the anode slurry must contain a certain amount of coarse (5-20 µm) YSZ to produce a matrix for long term stability and to shorten the ionically conducting paths. Fine YSZ (0.4 µm particle size) is also essential to act as a sintering aid to stabilise the anode structure, and to inhibit sintering/agglomeration of the fine Ni particles. The Ni must have a small particle size (approximately 1 µm) to ensure a large triple phase boundary (TPB), but only a sufficient quantity (40-50 vol%) to ensure the percolation of electrons.

7.2.2 Experimental Parameters

Discussed here is a schedule for proposed future experimental work to develop a Ni/YSZ cermet anode with long-term stability, using a bimodal YSZ particle size distribution.

7.2.2.1 Ni/YSZ Anodes

(i) Prepare coarse YSZ, sintered at 1400 °C and milled to the appropriate particle size.

(ii) Prepare fine YSZ with a article size of approximately 0.4 μm.

(iii) Prepare NiO with a particle size of approximately 1 μm.

(iv) Vary the Ni content from 20 to 40 vol% of total.

7.2.2.2 Experimental Matrix

(i) Coarse YSZ: 50 vol% of total volume.

(ii) Fine YSZ: 10 to 30 vol% of total volume.

(iii) Nickel: 20 to 40 vol% of total volume.

Table 7.1 Table of experimental matrix showing anode samples to be fabricated.

	Volume% Nickel		
Coarse YSZ (μm)	**20 vol% Ni**	**30 vol% Ni**	**40 vol% Ni**
5 μm (50 vol%)	30 vol% fine YSZ	20 vol% fine YSZ	10 vol% fine YSZ
10μm (50 vol%)	30 vol% fine YSZ	20 vol% fine YSZ	10 vol% fine YSZ
20 μm (50 vol%)	30 vol% fine YSZ	20 vol% fine YSZ	10 vol% fine YSZ

7.2.2.3 Fabrication

(i) Use a fabrication procedure based on the method described in section 3.2.3.

(ii) A total of 3 layers applied with the first layer being approximately 10 μm thick and subsequent layers of 20 μm, with a total layer thickness of 50 μm. Each layer is sintered at 1300 °C before the application of the next.

7.2.2.4 Electrochemical Characterisation

(i) Test in-plane DC conductivity.

(ii) Select a number of samples for impedance spectroscopy at OCV and polarisation experiments. Perform thermal activation (700 to 1000 °C at 50 °C intervals), gas composition (25% H_2 + 72% N_2 + 3%H_2O, 50% H_2 + 47% N_2 + 3% H_2O, 97% H_2 + 3% H_2O) and cyclic voltammetry experiments on 3-electrode YSZ pellets (section 2.7.2.2).

(iii) Long-term stability tests.

7.2.2.5 Microstructural Characterisation

(i) Particle size and particle size distribution experiments.

(ii) Optical Microscopy

(iii) Scanning Electron Microscopy (particle size study, elemental mapping, image analysis).

Appendix 1

Kröger-Vink Notation

The superscript symbols ‘x’, ‘˙˙‘and ‘–‘ represent a neutral, positive and negative charge respectively.

The subscript symbol denotes the lattice site label, that is, either a chemical symbol or the small letter ‘i’ for an interstitial site.

The main capitalised symbol denotes the species occupying the site, or the capitalised letter ‘V’ for a vacancy on the labelled site.

For example:

Y_{Zr}
represents a yttrium ion on a zirconium (Zr^{4+}) site with an effective charge of –1.

$V_o^{\cdot\cdot}$
implies an oxygen vacancy with an effective charge of +2.

O_o^x
indicates an occupied oxygen vacancy with no charge, that is, neutral.

Appendix 2

Particle Size Study

Particle size results for yttria stabilised zirconia (YSZ) sintered at 1100 °C and 1400 °C, and NiO, milled for various times.

Figure A2.1 Particles size of agglomerates of YSZ sintered at 1400 °C for 17 hours.

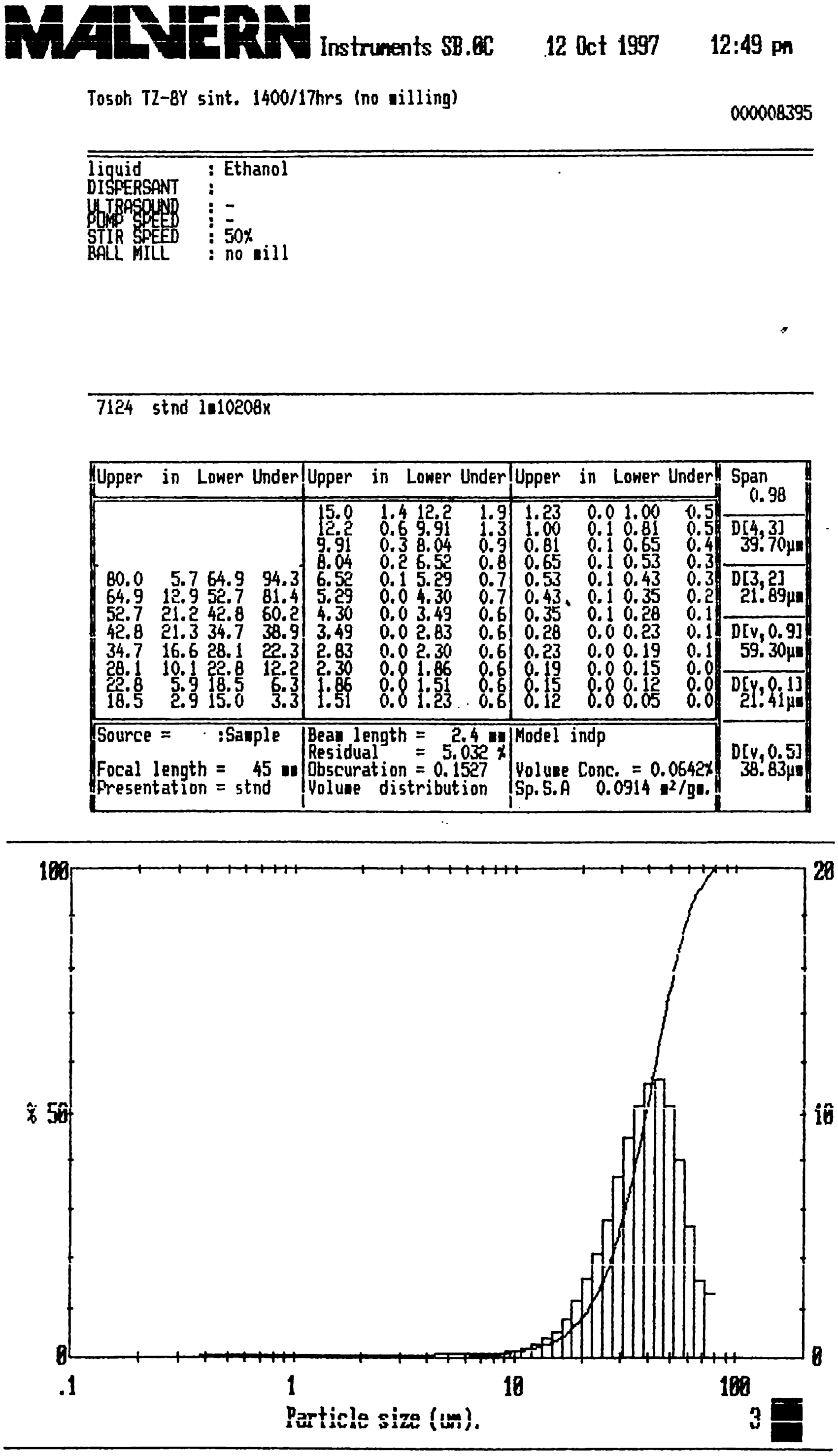

MALVERN Instruments SB.0C 12 Oct 1997 12:49 pm

Tosoh TZ-8Y sint. 1400/17hrs (no milling)

000008395

liquid : Ethanol
DISPERSANT :
ULTRASOUND : -
PUMP SPEED : -
STIR SPEED : 50%
BALL MILL : no mill

7124 stnd 1m10208x

Upper	in	Lower	Under	Upper	in	Lower	Under	Upper	in	Lower	Under
				15.0	1.4	12.2	1.9	1.23	0.0	1.00	0.5
				12.2	0.6	9.91	1.3	1.00	0.1	0.81	0.5
				9.91	0.3	8.04	0.9	0.81	0.1	0.65	0.4
				8.04	0.2	6.52	0.8	0.65	0.1	0.53	0.3
80.0	5.7	64.9	94.3	6.52	0.1	5.29	0.7	0.53	0.1	0.43	0.3
64.9	12.9	52.7	81.4	5.29	0.0	4.30	0.7	0.43	0.1	0.35	0.2
52.7	21.2	42.8	60.2	4.30	0.0	3.49	0.6	0.35	0.1	0.28	0.1
42.8	21.3	34.7	38.9	3.49	0.0	2.83	0.6	0.28	0.0	0.23	0.1
34.7	16.6	28.1	22.3	2.83	0.0	2.30	0.6	0.23	0.0	0.19	0.1
28.1	10.1	22.8	12.2	2.30	0.0	1.86	0.6	0.19	0.0	0.15	0.0
22.8	5.9	18.5	6.3	1.86	0.0	1.51	0.6	0.15	0.0	0.12	0.0
18.5	2.9	15.0	3.3	1.51	0.0	1.23	0.6	0.12	0.0	0.05	0.0

Span 0.98
D[4,3] 39.70μm
D[3,2] 21.89μm
D[v,0.9] 59.30μm
D[v,0.1] 21.41μm
D[v,0.5] 38.83μm

Source = :Sample
Focal length = 45 mm
Presentation = stnd

Beam length = 2.4 mm
Residual = 5.032 %
Obscuration = 0.1527
Volume distribution

Model indp
Volume Conc. = 0.0642%
Sp.S.A 0.0914 m²/gm.

Afdelingen for Materialeforskning

Figure A2.2 Particle size of YSZ after ball milling for 1 hour.

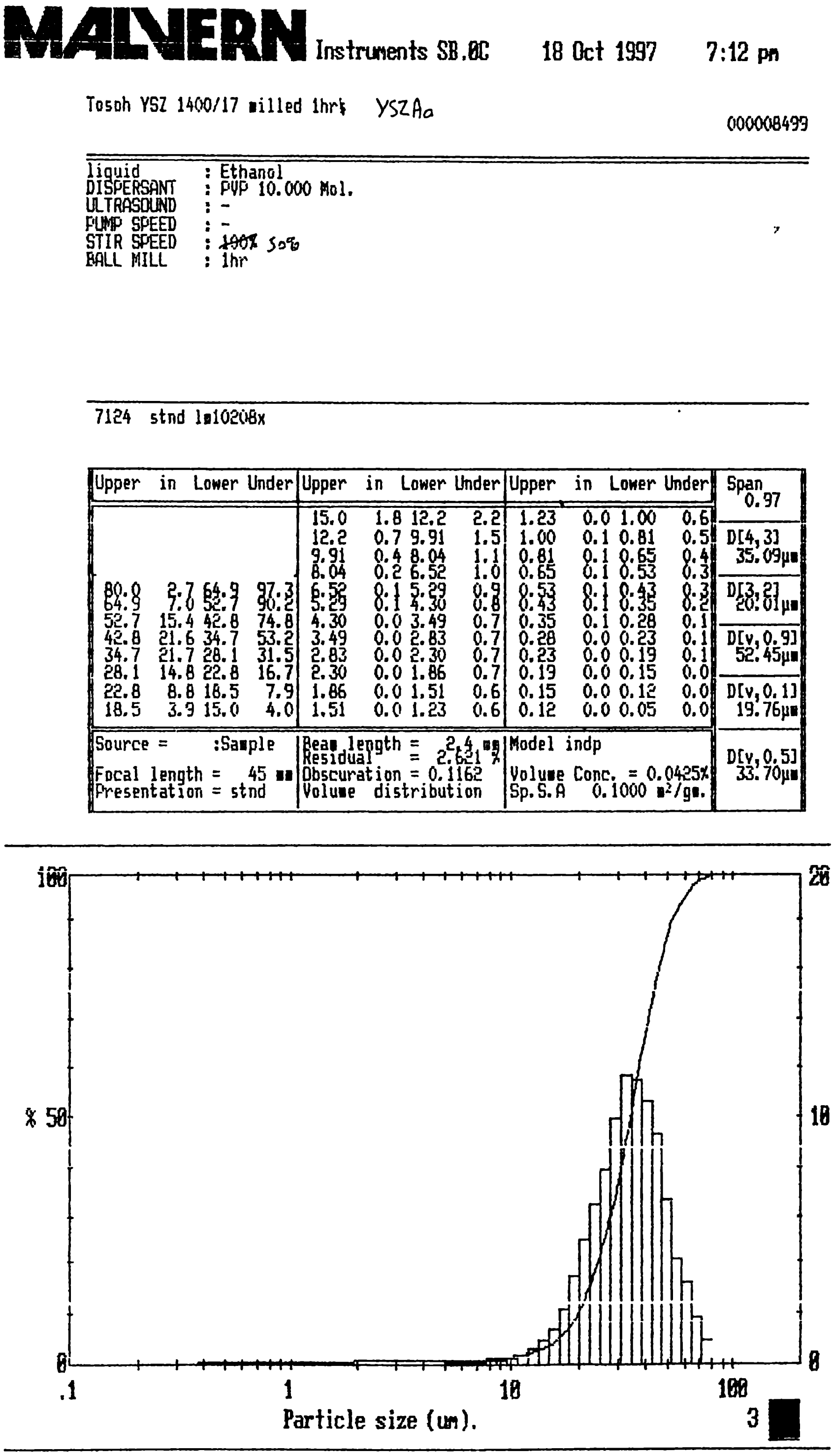

MALVERN Instruments SB.0C 18 Oct 1997 7:12 pm

Tosoh YSZ 1400/17 milled 1hr½ YSZAa

000008499

liquid : Ethanol
DISPERSANT : PVP 10.000 Mol.
ULTRASOUND : -
PUMP SPEED : -
STIR SPEED : ~~100%~~ 50%
BALL MILL : 1hr

7124 stnd 1m10208x

Upper	in	Lower	Under	Upper	in	Lower	Under	Upper	in	Lower	Under
				15.0	1.8	12.2	2.2	1.23	0.0	1.00	0.6
				12.2	0.7	9.91	1.5	1.00	0.1	0.81	0.5
				9.91	0.4	8.04	1.1	0.81	0.1	0.65	0.4
				8.04	0.2	6.52	1.0	0.65	0.1	0.53	0.3
80.0	2.7	64.9	97.3	6.52	0.1	5.29	0.9	0.53	0.1	0.43	0.3
64.9	7.0	52.7	90.2	5.29	0.1	4.30	0.8	0.43	0.1	0.35	0.2
52.7	15.4	42.8	74.8	4.30	0.0	3.49	0.7	0.35	0.1	0.28	0.1
42.8	21.6	34.7	53.2	3.49	0.0	2.83	0.7	0.28	0.0	0.23	0.1
34.7	21.7	28.1	31.5	2.83	0.0	2.30	0.7	0.23	0.0	0.19	0.1
28.1	14.8	22.8	16.7	2.30	0.0	1.86	0.7	0.19	0.0	0.15	0.0
22.8	8.8	18.5	7.9	1.86	0.0	1.51	0.6	0.15	0.0	0.12	0.0
18.5	3.9	15.0	4.0	1.51	0.0	1.23	0.6	0.12	0.0	0.05	0.0

Span 0.97
D[4,3] 35.09µm
D[3,2] 20.01µm
D[v,0.9] 52.45µm
D[v,0.1] 19.76µm
D[v,0.5] 33.70µm

Source = :Sample
Focal length = 45 mm
Presentation = stnd

Beam length = 2.4 mm
Residual = 2.621 %
Obscuration = 0.1162
Volume distribution

Model indp
Volume Conc. = 0.0425%
Sp.S.A 0.1000 m²/gm.

Afdelingen for Materialeforskning

Figure A2.3 Particle size of YSZ after ball milling for 2 hours.

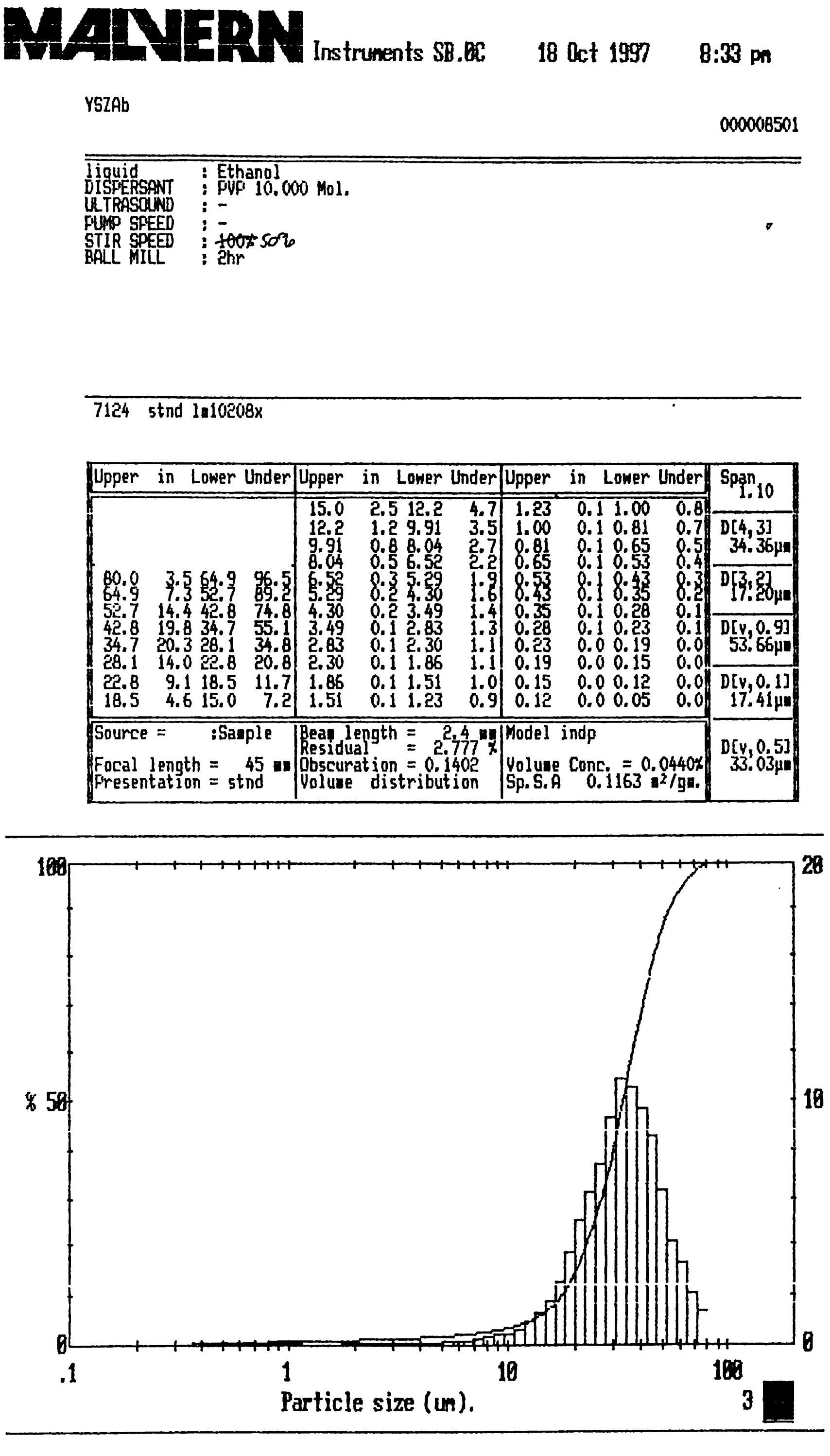

MALVERN Instruments SB.0C 18 Oct 1997 8:33 pm

YSZAb

000008501

liquid : Ethanol
DISPERSANT : PVP 10.000 Mol.
ULTRASOUND : -
PUMP SPEED : -
STIR SPEED : ~~100%~~ 50%
BALL MILL : 2hr

7124 stnd 1m10208x

Upper	in	Lower	Under	Upper	in	Lower	Under	Upper	in	Lower	Under
				15.0	2.5	12.2	4.7	1.23	0.1	1.00	0.8
				12.2	1.2	9.91	3.5	1.00	0.1	0.81	0.7
				9.91	0.8	8.04	2.7	0.81	0.1	0.65	0.5
				8.04	0.5	6.52	2.2	0.65	0.1	0.53	0.4
80.0	3.5	64.9	96.5	6.52	0.3	5.29	1.9	0.53	0.1	0.43	0.3
64.9	7.3	52.7	89.2	5.29	0.2	4.30	1.6	0.43	0.1	0.35	0.2
52.7	14.4	42.8	74.8	4.30	0.2	3.49	1.4	0.35	0.1	0.28	0.1
42.8	19.8	34.7	55.1	3.49	0.1	2.83	1.3	0.28	0.1	0.23	0.1
34.7	20.3	28.1	34.8	2.83	0.1	2.30	1.1	0.23	0.0	0.19	0.0
28.1	14.0	22.8	20.8	2.30	0.1	1.86	1.1	0.19	0.0	0.15	0.0
22.8	9.1	18.5	11.7	1.86	0.1	1.51	1.0	0.15	0.0	0.12	0.0
18.5	4.6	15.0	7.2	1.51	0.1	1.23	0.9	0.12	0.0	0.05	0.0

Source = :Sample
Focal length = 45 mm
Presentation = stnd

Beam length = 2.4 mm
Residual = 2.777 %
Obscuration = 0.1402
Volume distribution

Model indp
Volume Conc. = 0.0440%
Sp.S.A 0.1163 m²/gm.

Span 1.10
D[4,3] 34.36μm
D[3,2] 17.20μm
D[v,0.9] 53.66μm
D[v,0.1] 17.41μm
D[v,0.5] 33.03μm

Afdelingen for Materialeforskning

Figure A2.4 Particle size of YSZ after ball milling for 9 hours.

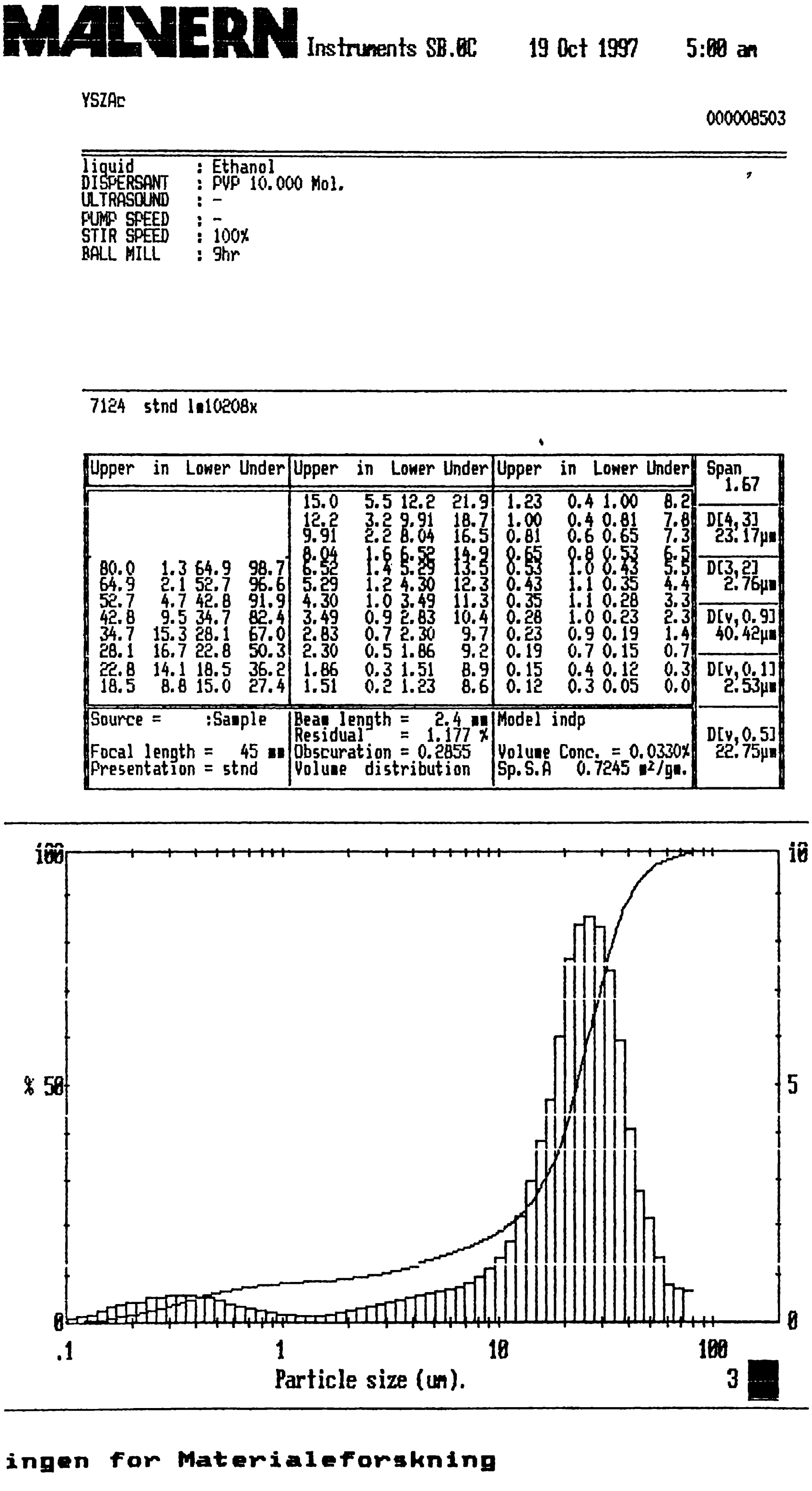

MALVERN Instruments SB.0C 19 Oct 1997 5:00 am

YSZAc

000008503

liquid : Ethanol
DISPERSANT : PVP 10.000 Mol.
ULTRASOUND : -
PUMP SPEED : -
STIR SPEED : 100%
BALL MILL : 9hr

7124 stnd 1m10208x

Upper	in	Lower	Under	Upper	in	Lower	Under	Upper	in	Lower	Under
				15.0	5.5	12.2	21.9	1.23	0.4	1.00	8.2
				12.2	3.2	9.91	18.7	1.00	0.4	0.81	7.8
				9.91	2.2	8.04	16.5	0.81	0.6	0.65	7.3
				8.04	1.6	6.52	14.9	0.65	0.8	0.53	6.5
80.0	1.3	64.9	98.7	6.52	1.4	5.29	13.5	0.53	1.0	0.43	5.5
64.9	2.1	52.7	96.6	5.29	1.2	4.30	12.3	0.43	1.1	0.35	4.4
52.7	4.7	42.8	91.9	4.30	1.0	3.49	11.3	0.35	1.1	0.28	3.3
42.8	9.5	34.7	82.4	3.49	0.9	2.83	10.4	0.28	1.0	0.23	2.3
34.7	15.3	28.1	67.0	2.83	0.7	2.30	9.7	0.23	0.9	0.19	1.4
28.1	16.7	22.8	50.3	2.30	0.5	1.86	9.2	0.19	0.7	0.15	0.7
22.8	14.1	18.5	36.2	1.86	0.3	1.51	8.9	0.15	0.4	0.12	0.3
18.5	8.8	15.0	27.4	1.51	0.2	1.23	8.6	0.12	0.3	0.05	0.0

Span 1.67
D[4,3] 23.17µm
D[3,2] 2.76µm
D[v,0.9] 40.42µm
D[v,0.1] 2.53µm
D[v,0.5] 22.75µm

Source = :Sample
Focal length = 45 mm
Presentation = stnd

Beam length = 2.4 mm
Residual = 1.177 %
Obscuration = 0.2855
Volume distribution

Model indp
Volume Conc. = 0.0330%
Sp.S.A 0.7245 m²/gm.

Afdelingen for Materialeforskning

Figure A2.5 Particle size of YSZ after ball milling for 21 hours.

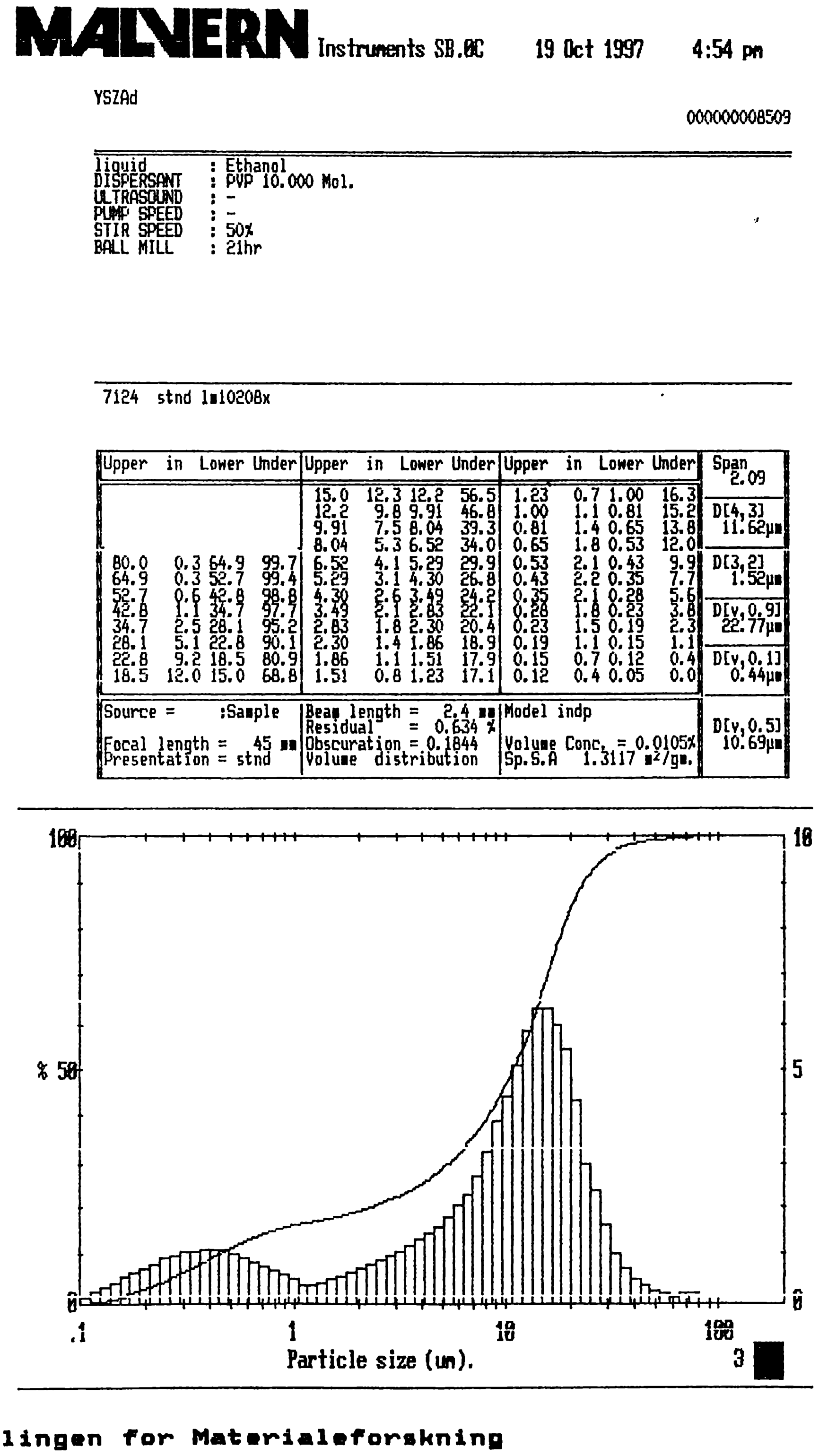

```
MALVERN Instruments SB.0C          19 Oct 1997        4:54 pm

YSZAd
                                                        000000008509

liquid          : Ethanol
DISPERSANT      : PVP 10.000 Mol.
ULTRASOUND      : -
PUMP SPEED      : -
STIR SPEED      : 50%
BALL MILL       : 21hr

7124  stnd 1■10208x

Upper   in  Lower Under|Upper   in  Lower Under|Upper   in  Lower Under| Span
                       |                       |                       |   2.09
                       | 15.0  12.3 12.2  56.5 | 1.23   0.7 1.00  16.3 |
                       | 12.2   9.8 9.91  46.8 | 1.00   1.1 0.81  15.2 | D[4,3]
                       | 9.91   7.5 8.04  39.3 | 0.81   1.4 0.65  13.8 |  11.62μ■
                       | 8.04   5.3 6.52  34.0 | 0.65   1.8 0.53  12.0 |
 80.0   0.3 64.9  99.7 | 6.52   4.1 5.29  29.9 | 0.53   2.1 0.43   9.9 | D[3,2]
 64.9   0.3 52.7  99.4 | 5.29   3.1 4.30  26.8 | 0.43   2.2 0.35   7.7 |   1.52μ■
 52.7   0.6 42.8  98.8 | 4.30   2.6 3.49  24.2 | 0.35   2.1 0.28   5.6 |
 42.8   1.1 34.7  97.7 | 3.49   2.1 2.83  22.1 | 0.28   1.8 0.23   3.8 | D[v,0.9]
 34.7   2.5 28.1  95.2 | 2.83   1.8 2.30  20.4 | 0.23   1.5 0.19   2.3 |  22.77μ■
 28.1   5.1 22.8  90.1 | 2.30   1.4 1.86  18.9 | 0.19   1.1 0.15   1.1 |
 22.8   9.2 18.5  80.9 | 1.86   1.1 1.51  17.9 | 0.15   0.7 0.12   0.4 | D[v,0.1]
 18.5  12.0 15.0  68.8 | 1.51   0.8 1.23  17.1 | 0.12   0.4 0.05   0.0 |   0.44μ■

Source =       :Sa■ple  |Bea■ length =   2.4 ■■|Model indp             |
                        |Residual    =  0.634 %|                       | D[v,0.5]
Focal length =    45 ■■ |Obscuration = 0.1844  |Volu■e Conc. = 0.0105% |  10.69μ■
Presentation = stnd     |Volu■e  distribution  |Sp.S.A   1.3117 ■²/g■. |
```

Afdelingen for Materialeforskning

Figure A2.6 Particle size of YSZ after ball milling for 33 hours.

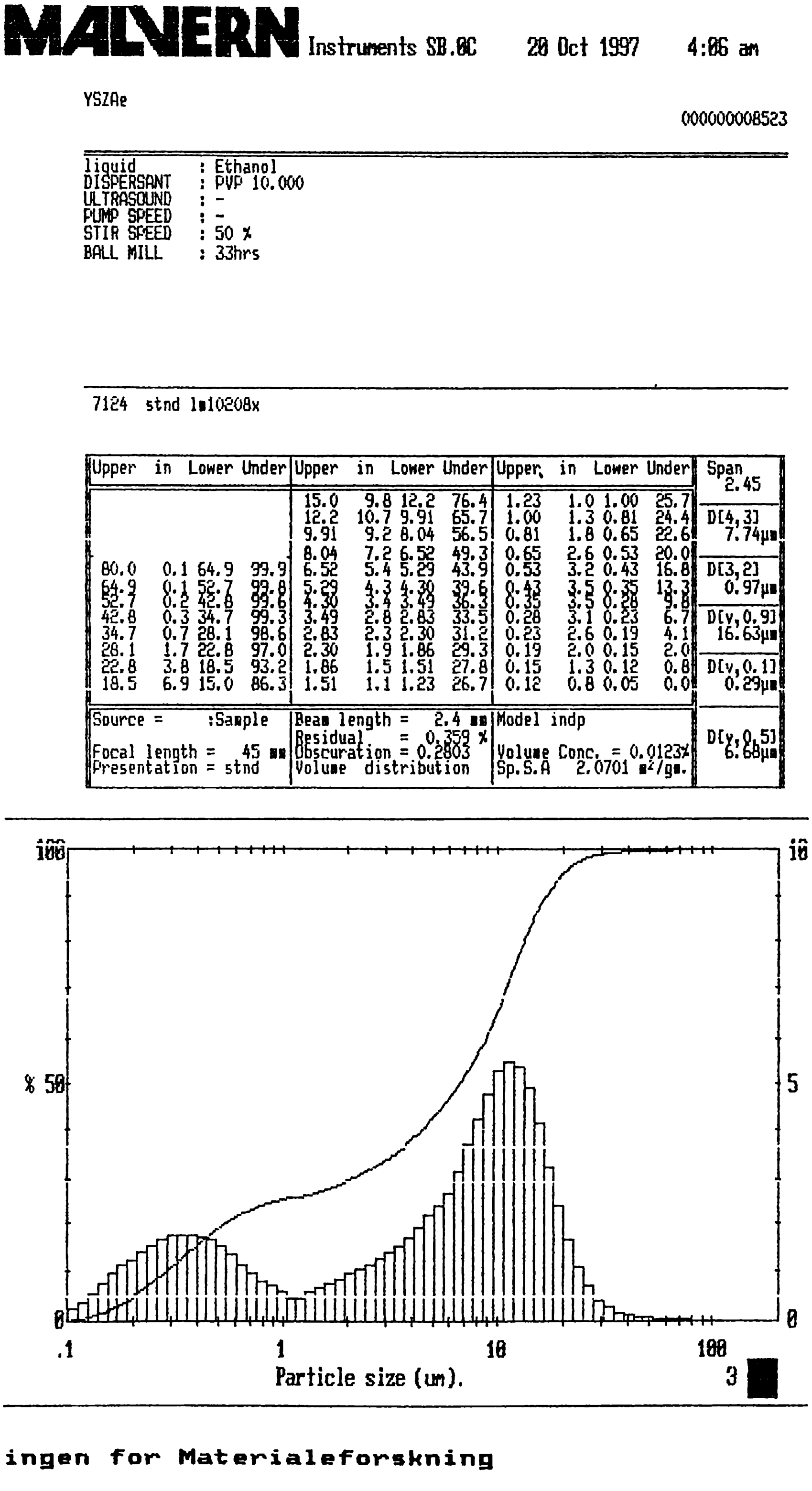

MALVERN Instruments SB.0C 20 Oct 1997 4:06 am

```
YSZAe
                                                        000000008523

liquid          : Ethanol
DISPERSANT      : PVP 10.000
ULTRASOUND      : -
PUMP SPEED      : -
STIR SPEED      : 50 %
BALL MILL       : 33hrs

 7124  stnd l■10208x

Upper  in  Lower Under|Upper  in  Lower Under|Upper  in  Lower Under| Span
                      | 15.0   9.8 12.2  76.4| 1.23   1.0 1.00  25.7|   2.45
                      | 12.2  10.7 9.91  65.7| 1.00   1.3 0.81  24.4| D[4,3]
                      | 9.91   9.2 8.04  56.5| 0.81   1.8 0.65  22.6|   7.74µ■
                      | 8.04   7.2 6.52  49.3| 0.65   2.6 0.53  20.0|
 80.0   0.1 64.9  99.9| 6.52   5.4 5.29  43.9| 0.53   3.2 0.43  16.8| D[3,2]
 64.9   0.1 52.7  99.8| 5.29   4.3 4.30  39.6| 0.43   3.5 0.35  13.3|   0.97µ■
 52.7   0.2 42.8  99.6| 4.30   3.4 3.49  36.3| 0.35   3.5 0.28   9.8| D[v,0.9]
 42.8   0.3 34.7  99.3| 3.49   2.8 2.83  33.5| 0.28   3.1 0.23   6.7|  16.63µ■
 34.7   0.7 28.1  98.6| 2.83   2.3 2.30  31.2| 0.23   2.6 0.19   4.1|
 28.1   1.7 22.8  97.0| 2.30   1.9 1.86  29.3| 0.19   2.0 0.15   2.0| D[v,0.1]
 22.8   3.8 18.5  93.2| 1.86   1.5 1.51  27.8| 0.15   1.3 0.12   0.8|   0.29µ■
 18.5   6.9 15.0  86.3| 1.51   1.1 1.23  26.7| 0.12   0.8 0.05   0.0|
Source =      :Sample |Bea■ length =   2.4 ■■|Model indp            | D[v,0.5]
                      |Residual     =  0.359 %|                      |   6.68µ■
Focal length =   45 ■■|Obscuration = 0.2803  |Volu■e Conc. = 0.0123%|
Presentation = stnd   |Volu■e  distribution  |Sp.S.A   2.0701 ■²/g■.|
```

Afdelingen for Materialeforskning

Figure A2.7 Particle size of YSZ after ball milling for 44 hours.

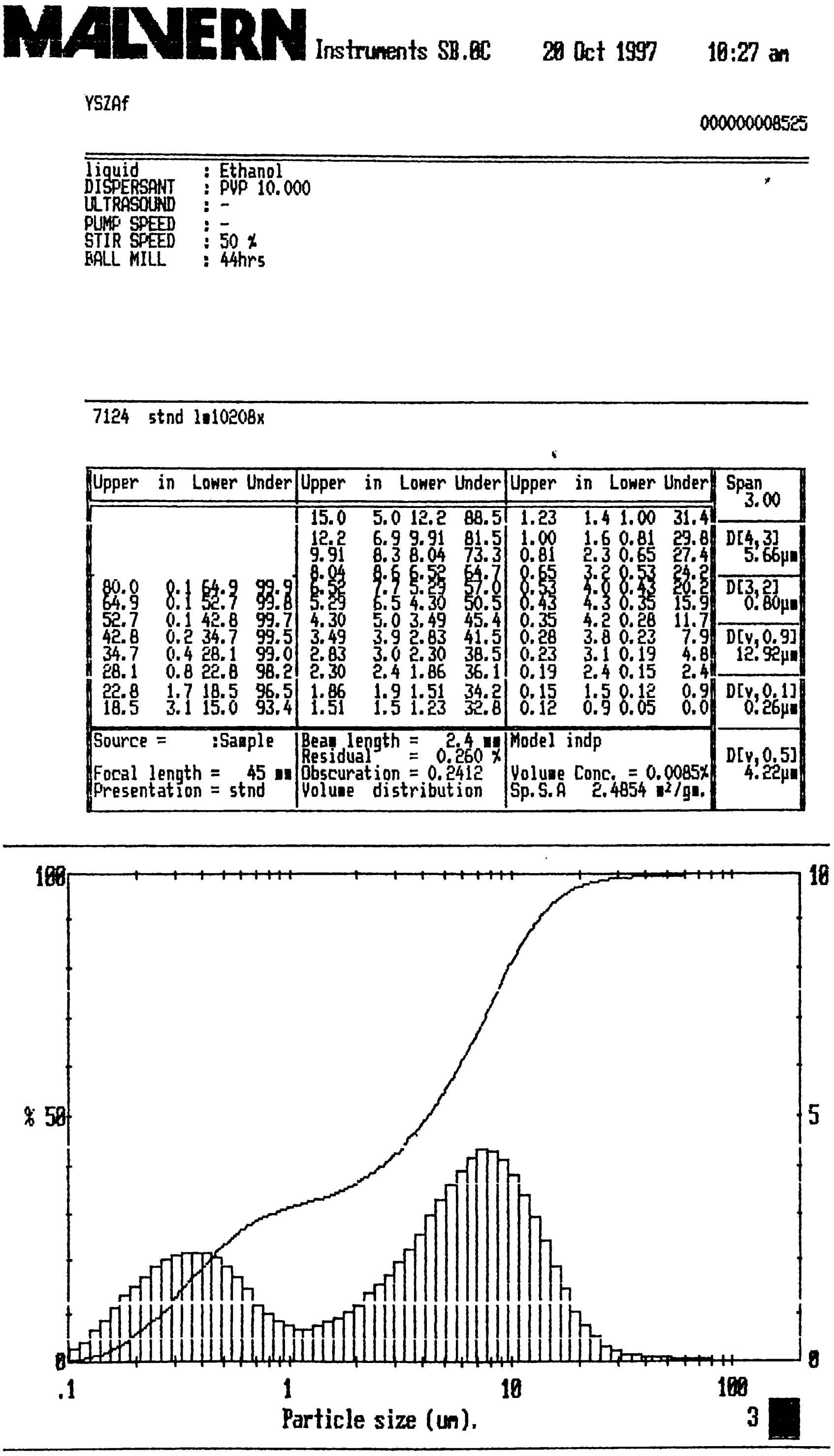

MALVERN Instruments SB.0C 20 Oct 1997 10:27 am

YSZAf

000000008525

liquid : Ethanol
DISPERSANT : PVP 10.000
ULTRASOUND : -
PUMP SPEED : -
STIR SPEED : 50 %
BALL MILL : 44hrs

7124 stnd 1■10208x

Upper	in	Lower	Under	Upper	in	Lower	Under	Upper	in	Lower	Under
				15.0	5.0	12.2	88.5	1.23	1.4	1.00	31.4
				12.2	6.9	9.91	81.5	1.00	1.6	0.81	29.8
				9.91	8.3	8.04	73.3	0.81	2.3	0.65	27.4
				8.04	8.6	6.52	64.7	0.65	3.2	0.53	24.2
80.0	0.1	64.9	99.9	6.52	7.7	5.29	57.0	0.53	4.0	0.43	20.2
64.9	0.1	52.7	99.8	5.29	6.5	4.30	50.5	0.43	4.3	0.35	15.9
52.7	0.1	42.8	99.7	4.30	5.0	3.49	45.4	0.35	4.2	0.28	11.7
42.8	0.2	34.7	99.5	3.49	3.9	2.83	41.5	0.28	3.8	0.23	7.9
34.7	0.4	28.1	99.0	2.83	3.0	2.30	38.5	0.23	3.1	0.19	4.8
28.1	0.8	22.8	98.2	2.30	2.4	1.86	36.1	0.19	2.4	0.15	2.4
22.8	1.7	18.5	96.5	1.86	1.9	1.51	34.2	0.15	1.5	0.12	0.9
18.5	3.1	15.0	93.4	1.51	1.5	1.23	32.8	0.12	0.9	0.05	0.0

Span 3.00
D[4,3] 5.66μm
D[3,2] 0.80μm
D[v,0.9] 12.92μm
D[v,0.1] 0.26μm
D[v,0.5] 4.22μm

Source = :Sample
Focal length = 45 mm
Presentation = stnd

Beam length = 2.4 mm
Residual = 0.260 %
Obscuration = 0.2412
Volume distribution

Model indp
Volume Conc. = 0.0085%
Sp.S.A 2.4854 m²/gm.

Figure A2.8 Particle size of YSZ after ball milling for 56 hours.

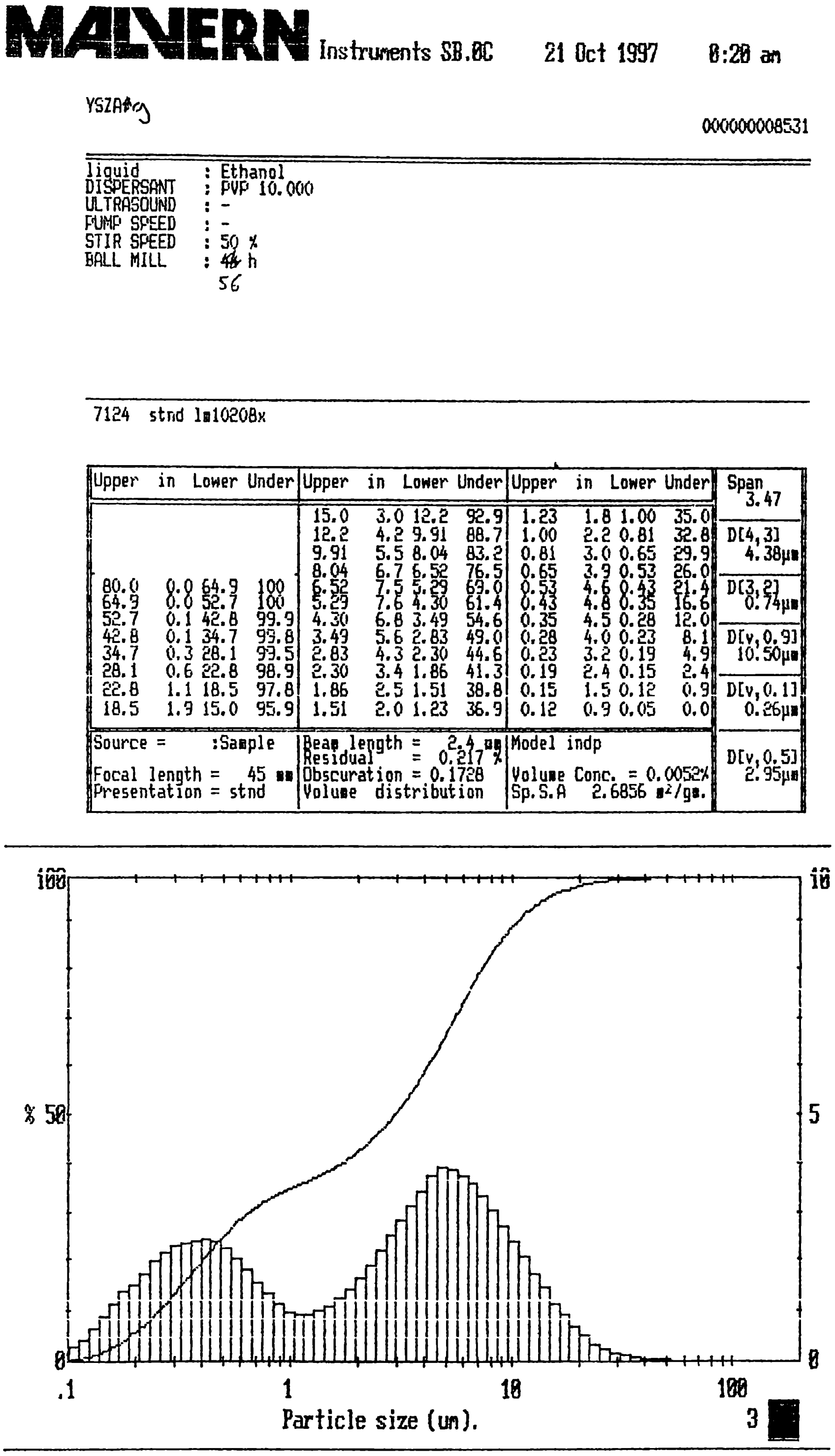

MALVERN Instruments SB.0C 21 Oct 1997 8:20 am

YSZA#6

000000008531

liquid : Ethanol
DISPERSANT : PVP 10.000
ULTRASOUND : -
PUMP SPEED : -
STIR SPEED : 50 %
BALL MILL : ~~48~~ h
56

7124 stnd 1■10208x

Upper	in	Lower	Under	Upper	in	Lower	Under	Upper	in	Lower	Under
				15.0	3.0	12.2	92.9	1.23	1.8	1.00	35.0
				12.2	4.2	9.91	88.7	1.00	2.2	0.81	32.8
				9.91	5.5	8.04	83.2	0.81	3.0	0.65	29.9
				8.04	6.7	6.52	76.5	0.65	3.9	0.53	26.0
80.0	0.0	64.9	100	6.52	7.5	5.29	69.0	0.53	4.6	0.43	21.4
64.9	0.0	52.7	100	5.29	7.6	4.30	61.4	0.43	4.8	0.35	16.6
52.7	0.1	42.8	99.9	4.30	6.8	3.49	54.6	0.35	4.5	0.28	12.0
42.8	0.1	34.7	99.8	3.49	5.6	2.83	49.0	0.28	4.0	0.23	8.1
34.7	0.3	28.1	99.5	2.83	4.3	2.30	44.6	0.23	3.2	0.19	4.9
28.1	0.6	22.8	98.9	2.30	3.4	1.86	41.3	0.19	2.4	0.15	2.4
22.8	1.1	18.5	97.8	1.86	2.5	1.51	38.8	0.15	1.5	0.12	0.9
18.5	1.9	15.0	95.9	1.51	2.0	1.23	36.9	0.12	0.9	0.05	0.0

Span 3.47
D[4,3] 4.38µm
D[3,2] 0.74µm
D[v,0.9] 10.50µm
D[v,0.1] 0.26µm
D[v,0.5] 2.95µm

Source = :Sample
Focal length = 45 mm
Presentation = stnd

Beam length = 2.4 mm
Residual = 0.217 %
Obscuration = 0.1728
Volume distribution

Model indp
Volume Conc. = 0.0052%
Sp.S.A 2.6856 m²/gm.

Figure A2.9 Particle size of YSZ after ball milling for 80 hours.

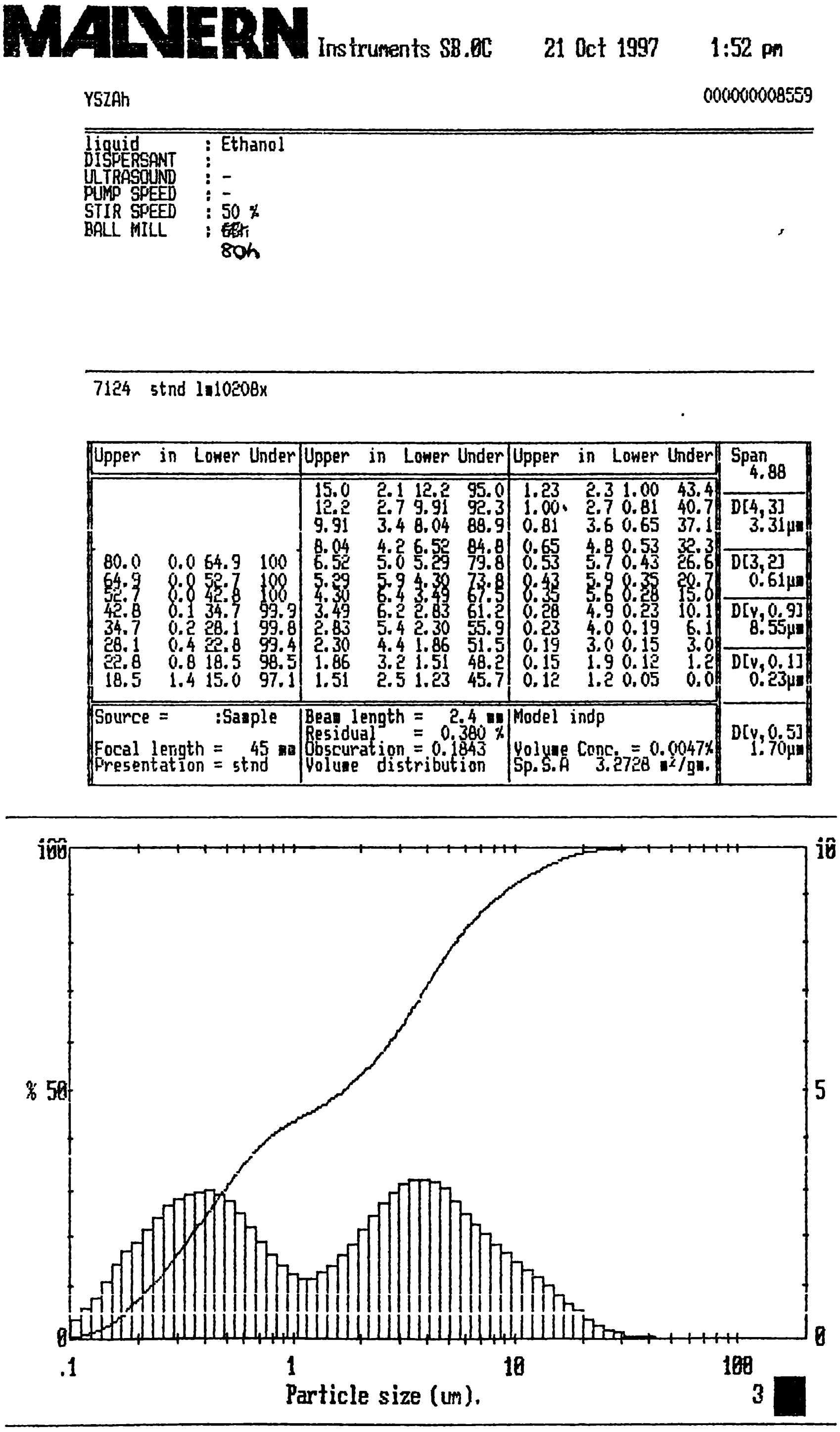

MALVERN Instruments SB.0C 21 Oct 1997 1:52 pm

YSZAh 000000008559

liquid : Ethanol
DISPERSANT :
ULTRASOUND : -
PUMP SPEED : -
STIR SPEED : 50 %
BALL MILL : ~~60h~~
80h

7124 stnd 1m10208x

Upper	in	Lower	Under	Upper	in	Lower	Under	Upper	in	Lower	Under
				15.0	2.1	12.2	95.0	1.23	2.3	1.00	43.4
				12.2	2.7	9.91	92.3	1.00	2.7	0.81	40.7
				9.91	3.4	8.04	88.9	0.81	3.6	0.65	37.1
				8.04	4.2	6.52	84.8	0.65	4.8	0.53	32.3
80.0	0.0	64.9	100	6.52	5.0	5.29	79.8	0.53	5.7	0.43	26.6
64.9	0.0	52.7	100	5.29	5.9	4.30	73.8	0.43	5.9	0.35	20.7
52.7	0.0	42.8	100	4.30	6.4	3.49	67.5	0.35	5.6	0.28	15.0
42.8	0.1	34.7	99.9	3.49	6.2	2.83	61.2	0.28	4.9	0.23	10.1
34.7	0.2	28.1	99.8	2.83	5.4	2.30	55.9	0.23	4.0	0.19	6.1
28.1	0.4	22.8	99.4	2.30	4.4	1.86	51.5	0.19	3.0	0.15	3.0
22.8	0.8	18.5	98.5	1.86	3.2	1.51	48.2	0.15	1.9	0.12	1.2
18.5	1.4	15.0	97.1	1.51	2.5	1.23	45.7	0.12	1.2	0.05	0.0

Span 4.88
D[4,3] 3.31µm
D[3,2] 0.61µm
D[v,0.9] 8.55µm
D[v,0.1] 0.23µm
D[v,0.5] 1.70µm

Source = :Sample
Focal length = 45 mm
Presentation = stnd

Beam length = 2.4 mm
Residual = 0.380 %
Obscuration = 0.1843
Volume distribution

Model indp
Volume Conc. = 0.0047%
Sp.S.A 3.2728 m²/gm.

Afdelingen for Materialeforskning

Figure A2.10 Particle size of YSZ after ball milling for 104 hours.

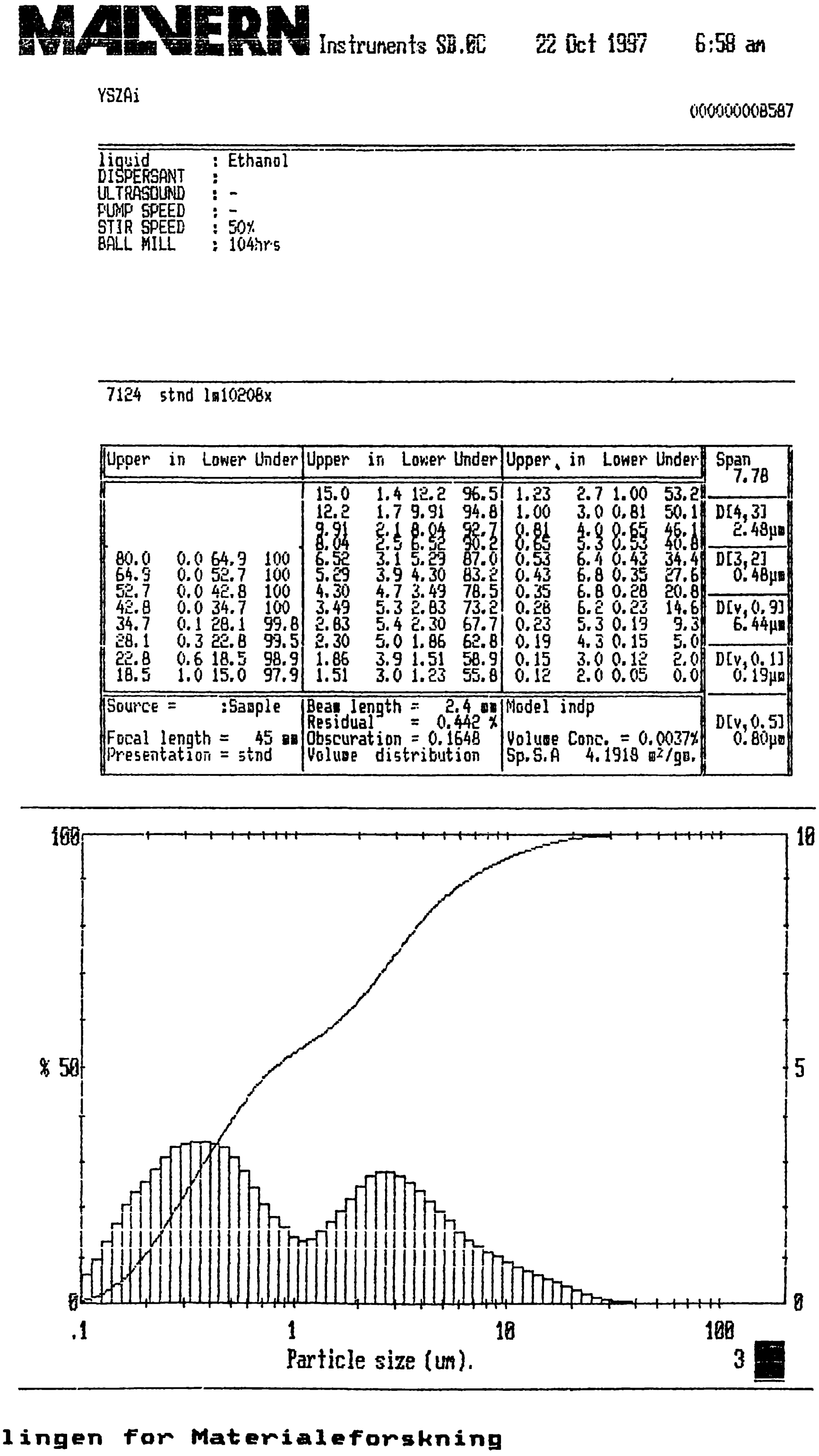

MALVERN Instruments SB.0C 22 Oct 1997 6:58 am

YSZAi

000000008587

liquid : Ethanol
DISPERSANT :
ULTRASOUND : -
PUMP SPEED : -
STIR SPEED : 50%
BALL MILL : 104hrs

7124 stnd lm10208x

Upper	in	Lower	Under	Upper	in	Lower	Under	Upper	in	Lower	Under	
				15.0	1.4	12.2	96.5	1.23	2.7	1.00	53.2	Span 7.78
				12.2	1.7	9.91	94.8	1.00	3.0	0.81	50.1	D[4,3] 2.48µm
				9.91	2.1	8.04	92.7	0.81	4.0	0.65	46.1	
				8.04	2.5	6.52	90.2	0.65	5.3	0.53	40.8	D[3,2] 0.48µm
80.0	0.0	64.9	100	6.52	3.1	5.29	87.0	0.53	6.4	0.43	34.4	
64.9	0.0	52.7	100	5.29	3.9	4.30	83.2	0.43	6.8	0.35	27.6	
52.7	0.0	42.8	100	4.30	4.7	3.49	78.5	0.35	6.8	0.28	20.8	D[v,0.9] 6.44µm
42.8	0.0	34.7	100	3.49	5.3	2.83	73.2	0.28	6.2	0.23	14.6	
34.7	0.1	28.1	99.8	2.83	5.4	2.30	67.7	0.23	5.3	0.19	9.3	
28.1	0.3	22.8	99.5	2.30	5.0	1.86	62.8	0.19	4.3	0.15	5.0	D[v,0.1] 0.19µm
22.8	0.6	18.5	98.9	1.86	3.9	1.51	58.9	0.15	3.0	0.12	2.0	
18.5	1.0	15.0	97.9	1.51	3.0	1.23	55.8	0.12	2.0	0.05	0.0	

Source = :Sample
Focal length = 45 mm
Presentation = stnd

Beam length = 2.4 mm
Residual = 0.442 %
Obscuration = 0.1648
Volume distribution

Model indp
Volume Conc. = 0.0037%
Sp.S.A 4.1918 m²/gm.

D[v,0.5] 0.80µm

Afdelingen for Materialeforskning

Figure A2.11 Particle size of YSZ after ball milling for 128 hours.

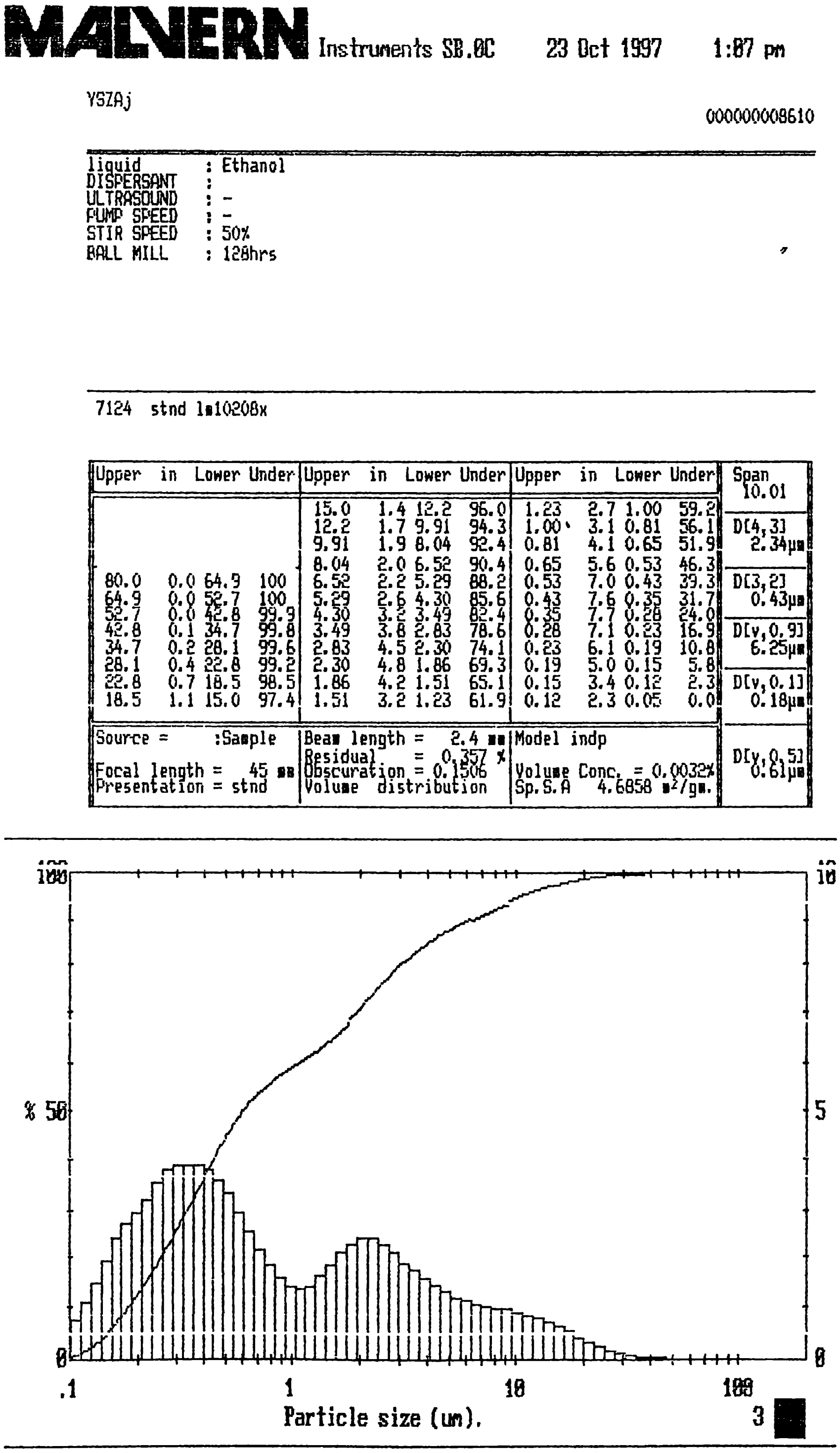

MALVERN Instruments SB.0C 23 Oct 1997 1:07 pm

YSZAj

000000008610

liquid : Ethanol
DISPERSANT :
ULTRASOUND : -
PUMP SPEED : -
STIR SPEED : 50%
BALL MILL : 128hrs

7124 stnd 1■10208x

Upper	in	Lower	Under	Upper	in	Lower	Under	Upper	in	Lower	Under
				15.0	1.4	12.2	96.0	1.23	2.7	1.00	59.2
				12.2	1.7	9.91	94.3	1.00	3.1	0.81	56.1
				9.91	1.9	8.04	92.4	0.81	4.1	0.65	51.9
				8.04	2.0	6.52	90.4	0.65	5.6	0.53	46.3
80.0	0.0	64.9	100	6.52	2.2	5.29	88.2	0.53	7.0	0.43	39.3
64.9	0.0	52.7	100	5.29	2.6	4.30	85.6	0.43	7.6	0.35	31.7
52.7	0.0	42.8	99.9	4.30	3.2	3.49	82.4	0.35	7.7	0.28	24.0
42.8	0.1	34.7	99.8	3.49	3.8	2.83	78.6	0.28	7.1	0.23	16.9
34.7	0.2	28.1	99.6	2.83	4.5	2.30	74.1	0.23	6.1	0.19	10.8
28.1	0.4	22.8	99.2	2.30	4.8	1.86	69.3	0.19	5.0	0.15	5.8
22.8	0.7	18.5	98.5	1.86	4.2	1.51	65.1	0.15	3.4	0.12	2.3
18.5	1.1	15.0	97.4	1.51	3.2	1.23	61.9	0.12	2.3	0.05	0.0

Span 10.01
D[4,3] 2.34µm
D[3,2] 0.43µm
D[v,0.9] 6.25µm
D[v,0.1] 0.18µm
D[v,0.5] 0.61µm

Source = :Sample
Focal length = 45 mm
Presentation = stnd

Beam length = 2.4 mm
Residual = 0.357 %
Obscuration = 0.1506
Volume distribution

Model indp
Volume Conc. = 0.0032%
Sp.S.A 4.6858 m²/gm.

Afdelingen for Materialeforskning

Figure A2.12 Particle size of YSZ after ball milling for 152 hours.

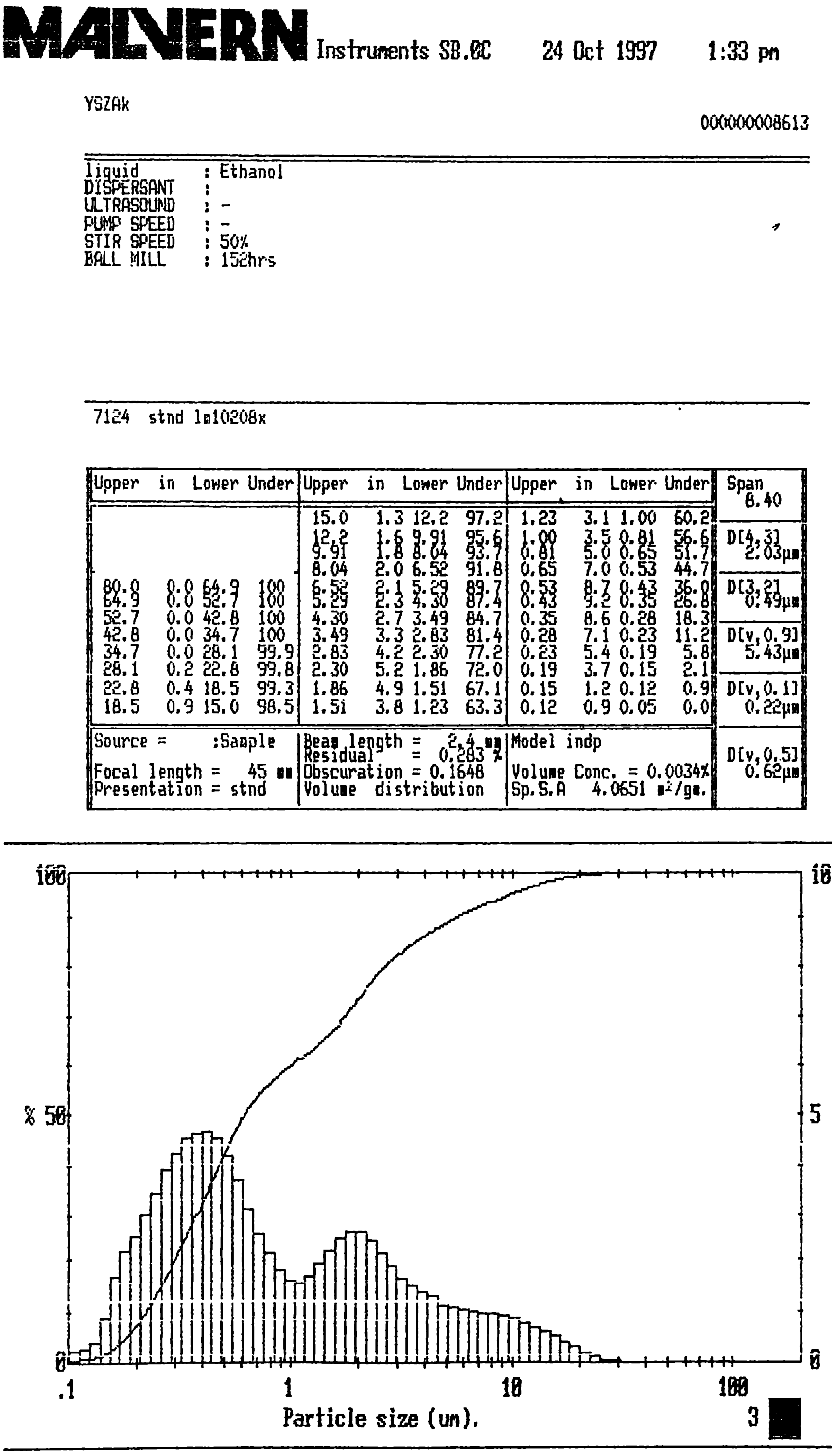

MALVERN Instruments SB.0C 24 Oct 1997 1:33 pm

YSZAk

00000008613

liquid : Ethanol
DISPERSANT :
ULTRASOUND : -
PUMP SPEED : -
STIR SPEED : 50%
BALL MILL : 152hrs

7124 stnd 1m10208x

Upper	in	Lower	Under	Upper	in	Lower	Under	Upper	in	Lower	Under	Span 8.40
				15.0	1.3	12.2	97.2	1.23	3.1	1.00	60.2	
				12.2	1.6	9.91	95.6	1.00	3.5	0.81	56.6	D[4,3] 2.03µm
				9.91	1.8	8.04	93.7	0.81	5.0	0.65	51.7	
				8.04	2.0	6.52	91.8	0.65	7.0	0.53	44.7	
80.0	0.0	64.9	100	6.52	2.1	5.29	89.7	0.53	8.7	0.43	36.0	D[3,2] 0.49µm
64.9	0.0	52.7	100	5.29	2.3	4.30	87.4	0.43	9.2	0.35	26.8	
52.7	0.0	42.8	100	4.30	2.7	3.49	84.7	0.35	8.6	0.28	18.3	
42.8	0.0	34.7	100	3.49	3.3	2.83	81.4	0.28	7.1	0.23	11.2	D[v,0.9] 5.43µm
34.7	0.0	28.1	99.9	2.83	4.2	2.30	77.2	0.23	5.4	0.19	5.8	
28.1	0.2	22.8	99.8	2.30	5.2	1.86	72.0	0.19	3.7	0.15	2.1	
22.8	0.4	18.5	99.3	1.86	4.9	1.51	67.1	0.15	1.2	0.12	0.9	D[v,0.1] 0.22µm
18.5	0.9	15.0	98.5	1.51	3.8	1.23	63.3	0.12	0.9	0.05	0.0	

Source = :Sample
Focal length = 45 mm
Presentation = stnd

Beam length = 2.4 mm
Residual = 0.283 %
Obscuration = 0.1648
Volume distribution

Model indp
Volume Conc. = 0.0034%
Sp.S.A 4.0651 m²/gm.

D[v,0.5]
0.62µm

Afdelingen for Materialeforskning

Figure A2.13 Particle size of YSZ after ball milling for 176 hours.

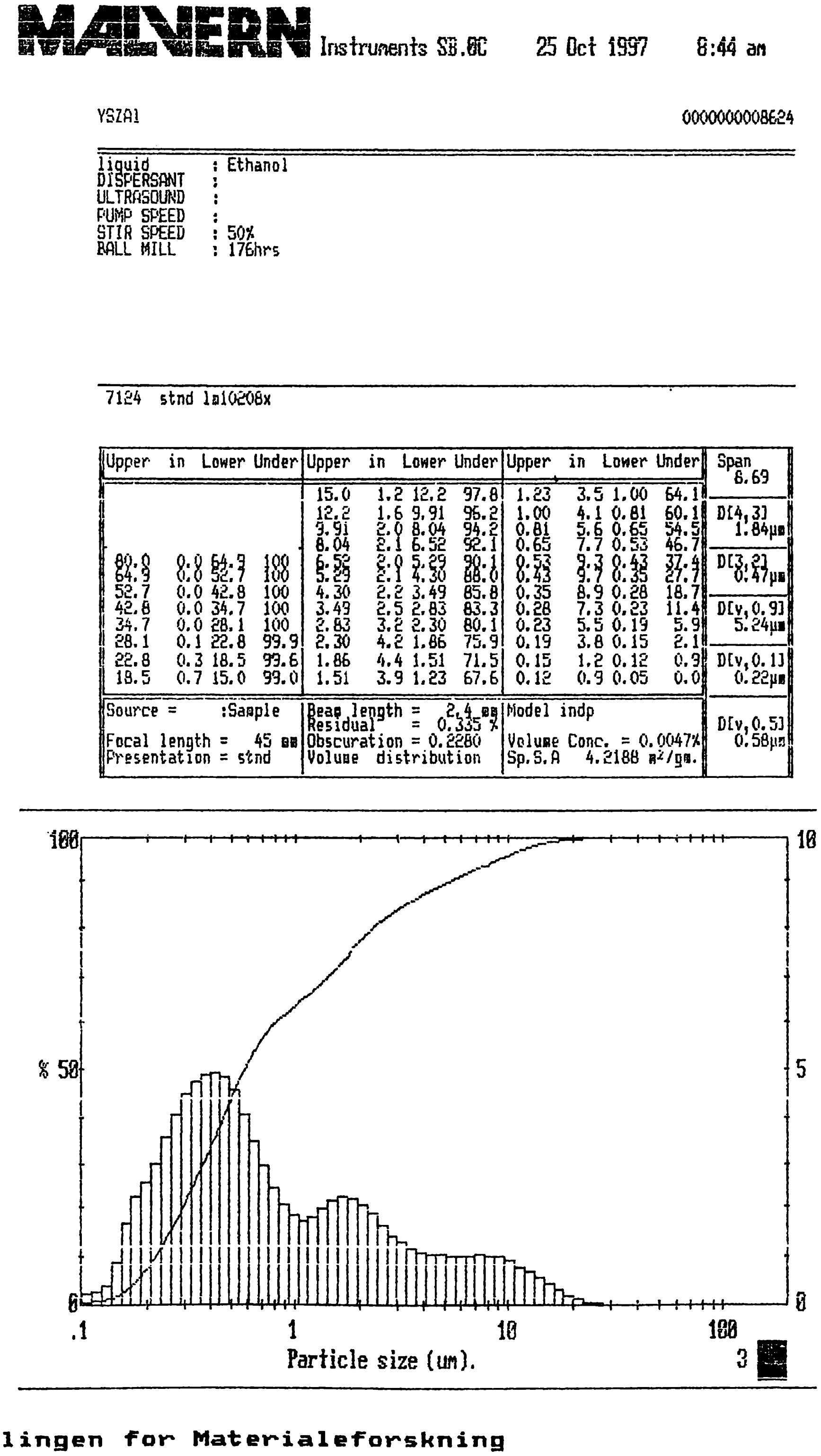

```
MALVERN Instruments SB.0C      25 Oct 1997      8:44 am

YSZA1                                          0000000008624

liquid        : Ethanol
DISPERSANT    :
ULTRASOUND    :
PUMP SPEED    :
STIR SPEED    : 50%
BALL MILL     : 176hrs

7124  stnd la10208x

Upper  in  Lower Under|Upper  in  Lower Under|Upper  in  Lower Under| Span
                      | 15.0   1.2 12.2  97.8| 1.23   3.5 1.00  64.1|   6.69
                      | 12.2   1.6 9.91  96.2| 1.00   4.1 0.81  60.1| D[4,3]
                      | 9.91   2.0 8.04  94.2| 0.81   5.6 0.65  54.5|   1.84µm
                      | 8.04   2.1 6.52  92.1| 0.65   7.7 0.53  46.7|
 80.0   0.0 64.9  100 | 6.52   2.0 5.29  90.1| 0.53   9.3 0.43  37.4| D[3,2]
 64.9   0.0 52.7  100 | 5.29   2.1 4.30  88.0| 0.43   9.7 0.35  27.7|   0.47µm
 52.7   0.0 42.8  100 | 4.30   2.2 3.49  85.8| 0.35   8.9 0.28  18.7|
 42.8   0.0 34.7  100 | 3.49   2.5 2.83  83.3| 0.28   7.3 0.23  11.4| D[v,0.9]
 34.7   0.0 28.1  100 | 2.83   3.2 2.30  80.1| 0.23   5.5 0.19   5.9|   5.24µm
 28.1   0.1 22.8  99.9| 2.30   4.2 1.86  75.9| 0.19   3.8 0.15   2.1|
 22.8   0.3 18.5  99.6| 1.86   4.4 1.51  71.5| 0.15   1.2 0.12   0.9| D[v,0.1]
 18.5   0.7 15.0  99.0| 1.51   3.9 1.23  67.6| 0.12   0.9 0.05   0.0|   0.22µm
Source =      :Sample |Beam length =  2.4 mm|Model indp             |
                      |Residual    =  0.335 %|                      | D[v,0.5]
Focal length =   45 mm|Obscuration = 0.2280 |Volume Conc. = 0.0047%|   0.58µm
Presentation = stnd   |Volume  distribution |Sp.S.A   4.2188 m²/gm.|

Afdelingen for Materialeforskning
```

Figure A2.14 Particle size of YSZ after ball milling for 197 hours.

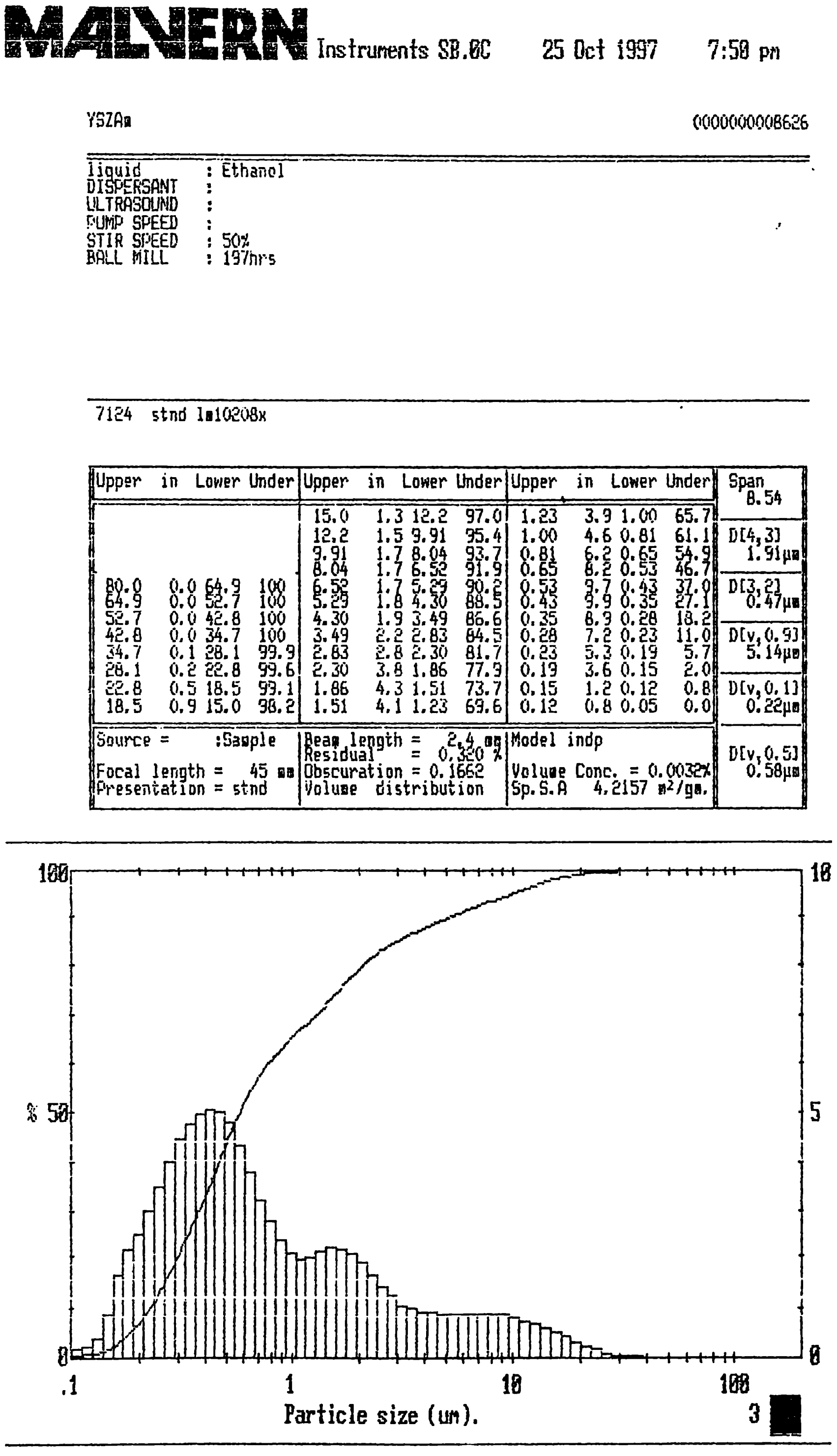

MALVERN Instruments SB.0C 25 Oct 1997 7:58 pm

YSZA■ 0000000008626

liquid : Ethanol
DISPERSANT :
ULTRASOUND :
PUMP SPEED :
STIR SPEED : 50%
BALL MILL : 197hrs

7124 stnd 1■10208x

Upper	in	Lower	Under	Upper	in	Lower	Under	Upper	in	Lower	Under
				15.0	1.3	12.2	97.0	1.23	3.9	1.00	65.7
				12.2	1.5	9.91	95.4	1.00	4.6	0.81	61.1
				9.91	1.7	8.04	93.7	0.81	6.2	0.65	54.9
				8.04	1.7	6.52	91.9	0.65	8.2	0.53	46.7
80.0	0.0	64.9	100	6.52	1.7	5.29	90.2	0.53	9.7	0.43	37.0
64.9	0.0	52.7	100	5.29	1.8	4.30	88.5	0.43	9.9	0.35	27.1
52.7	0.0	42.8	100	4.30	1.9	3.49	86.6	0.35	8.9	0.28	18.2
42.8	0.0	34.7	100	3.49	2.2	2.83	84.5	0.28	7.2	0.23	11.0
34.7	0.1	28.1	99.9	2.83	2.8	2.30	81.7	0.23	5.3	0.19	5.7
28.1	0.2	22.8	99.6	2.30	3.8	1.86	77.9	0.19	3.6	0.15	2.0
22.8	0.5	18.5	99.1	1.86	4.3	1.51	73.7	0.15	1.2	0.12	0.8
18.5	0.9	15.0	98.2	1.51	4.1	1.23	69.6	0.12	0.8	0.05	0.0

Span 8.54
D[4,3] 1.91µm
D[3,2] 0.47µm
D[v,0.9] 5.14µm
D[v,0.1] 0.22µm
D[v,0.5] 0.58µm

Source = :Sample
Focal length = 45 mm
Presentation = stnd

Beam length = 2.4 mm
Residual = 0.320 %
Obscuration = 0.1662
Volume distribution

Model indp
Volume Conc. = 0.0032%
Sp.S.A 4.2157 m²/gm.

Afdelingen for Materialeforskning

Figure A2.15 Particle size of YSZ after ball milling for 230 hours.

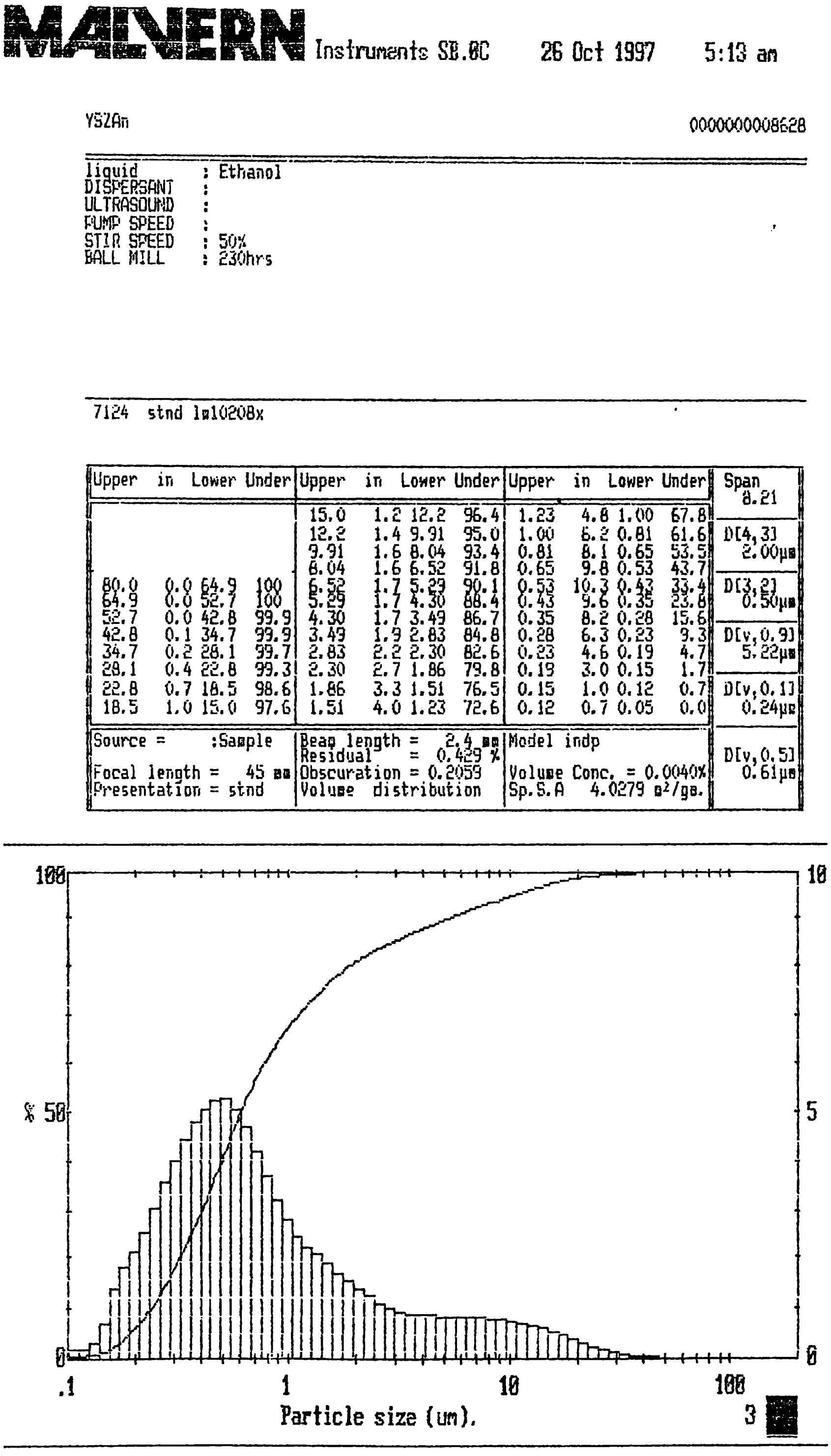

```
MALVERN Instruments SB.0C        26 Oct 1997       5:13 am

YSZAm                                                    000000008628

liquid          : Ethanol
DISPERSANT      :
ULTRASOUND      :
PUMP SPEED      :
STIR SPEED      : 50%
BALL MILL       : 230hrs


7124  stnd 1m10208x

Upper  in  Lower Under|Upper  in  Lower Under|Upper  in  Lower Under| Span
                      | 15.0   1.2 12.2  96.4| 1.23   4.8 1.00  67.8|   8.21
                      | 12.2   1.4 9.91  95.0| 1.00   6.2 0.81  61.6| D[4,3]
                      | 9.91   1.6 8.04  93.4| 0.81   8.1 0.65  53.5|  2.00µm
                      | 8.04   1.6 6.52  91.8| 0.65   9.8 0.53  43.7|
 80.0   0.0 64.9  100 | 6.52   1.7 5.29  90.1| 0.53  10.3 0.43  33.4| D[3,2]
 64.9   0.0 52.7  100 | 5.29   1.7 4.30  88.4| 0.43   9.6 0.35  23.8|  0.50µm
 52.7   0.0 42.8  99.9| 4.30   1.7 3.49  86.7| 0.35   8.2 0.28  15.6|
 42.8   0.1 34.7  99.9| 3.49   1.9 2.83  84.8| 0.28   6.3 0.23   9.3| D[v,0.9]
 34.7   0.2 28.1  99.7| 2.83   2.2 2.30  82.6| 0.23   4.6 0.19   4.7|  5.22µm
 28.1   0.4 22.8  99.3| 2.30   2.7 1.86  79.8| 0.19   3.0 0.15   1.7|
 22.8   0.7 18.5  98.6| 1.86   3.3 1.51  76.5| 0.15   1.0 0.12   0.7| D[v,0.1]
 18.5   1.0 15.0  97.6| 1.51   4.0 1.23  72.6| 0.12   0.7 0.05   0.0|  0.24µm
Source =      :Sample |Beam length =   2.4 mm|Model indp            |
                      |Residual    =  0.429 %|                      | D[v,0.5]
Focal length =   45 mm|Obscuration = 0.2059  |Volume Conc. = 0.0040%|  0.61µm
Presentation = stnd   |Volume  distribution  |Sp.S.A   4.0279 m²/gm.|
```

Afdelingen for Materialeforskning

Figure A2.16 Particle size of YSZ after ball milling for 267 hours.

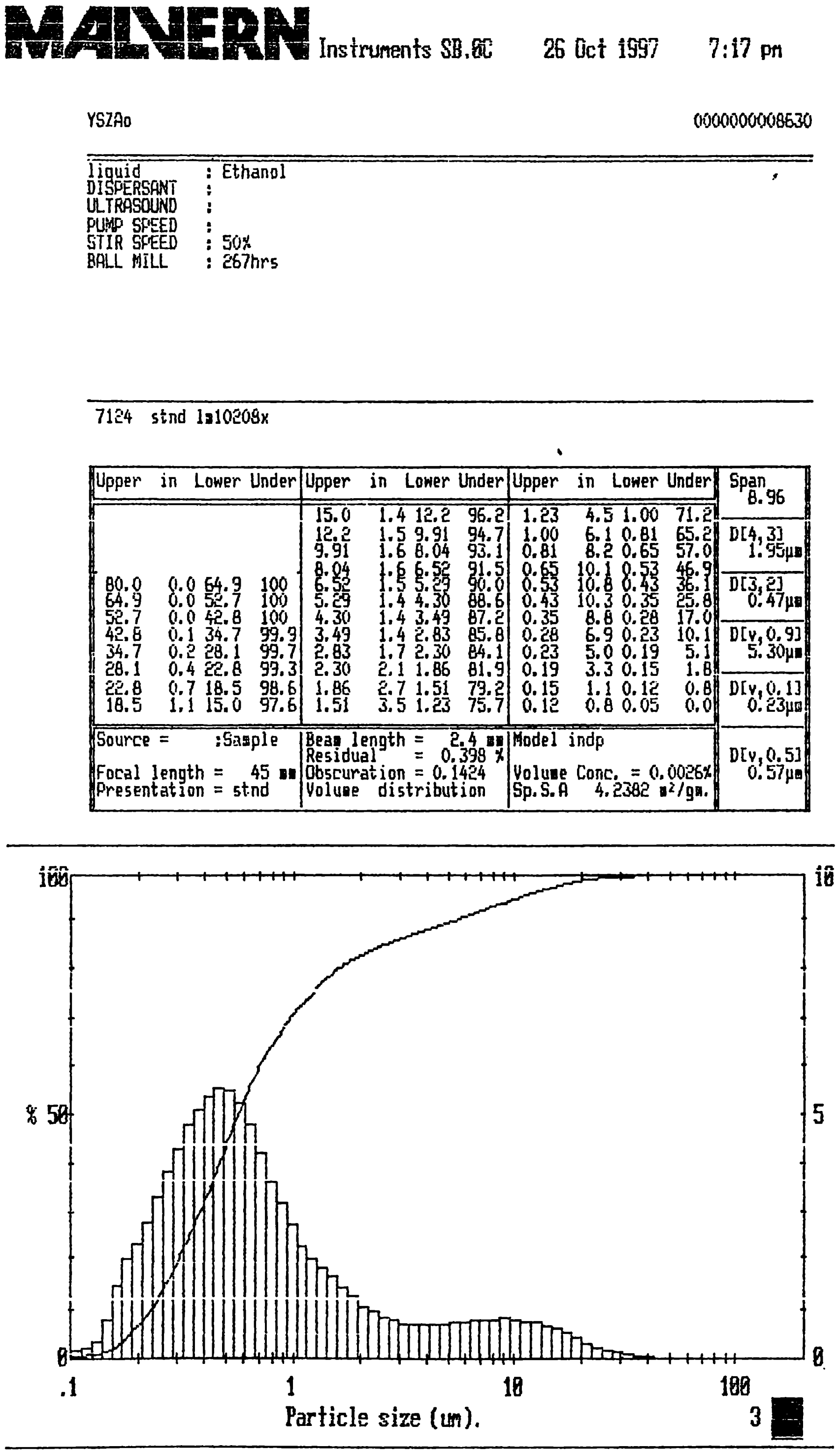

MALVERN Instruments SB.0C 26 Oct 1997 7:17 pm

YSZAo 0000000008630

liquid : Ethanol
DISPERSANT :
ULTRASOUND :
PUMP SPEED :
STIR SPEED : 50%
BALL MILL : 267hrs

7124 stnd 1a10208x

Upper	in	Lower	Under	Upper	in	Lower	Under	Upper	in	Lower	Under	Span 8.96
				15.0	1.4	12.2	96.2	1.23	4.5	1.00	71.2	
				12.2	1.5	9.91	94.7	1.00	6.1	0.81	65.2	D[4,3] 1.95µm
				9.91	1.6	8.04	93.1	0.81	8.2	0.65	57.0	
				8.04	1.6	6.52	91.5	0.65	10.1	0.53	46.9	
80.0	0.0	64.9	100	6.52	1.5	5.29	90.0	0.53	10.8	0.43	36.1	D[3,2] 0.47µm
64.9	0.0	52.7	100	5.29	1.4	4.30	88.6	0.43	10.3	0.35	25.8	
52.7	0.0	42.8	100	4.30	1.4	3.49	87.2	0.35	8.8	0.28	17.0	
42.8	0.1	34.7	99.9	3.49	1.4	2.83	85.8	0.28	6.9	0.23	10.1	D[v,0.9] 5.30µm
34.7	0.2	28.1	99.7	2.83	1.7	2.30	84.1	0.23	5.0	0.19	5.1	
28.1	0.4	22.8	99.3	2.30	2.1	1.86	81.9	0.19	3.3	0.15	1.8	
22.8	0.7	18.5	98.6	1.86	2.7	1.51	79.2	0.15	1.1	0.12	0.8	D[v,0.1] 0.23µm
18.5	1.1	15.0	97.6	1.51	3.5	1.23	75.7	0.12	0.8	0.05	0.0	

Source = :Sample Focal length = 45 mm Presentation = stnd	Beam length = 2.4 mm Residual = 0.398 % Obscuration = 0.1424 Volume distribution	Model indp Volume Conc. = 0.0026% Sp.S.A 4.2382 m²/gm.	D[v,0.5] 0.57µm

Afdelingen for Materialeforskning

Figure A2.17 Particle size of YSZ after ball milling for 291 hours.

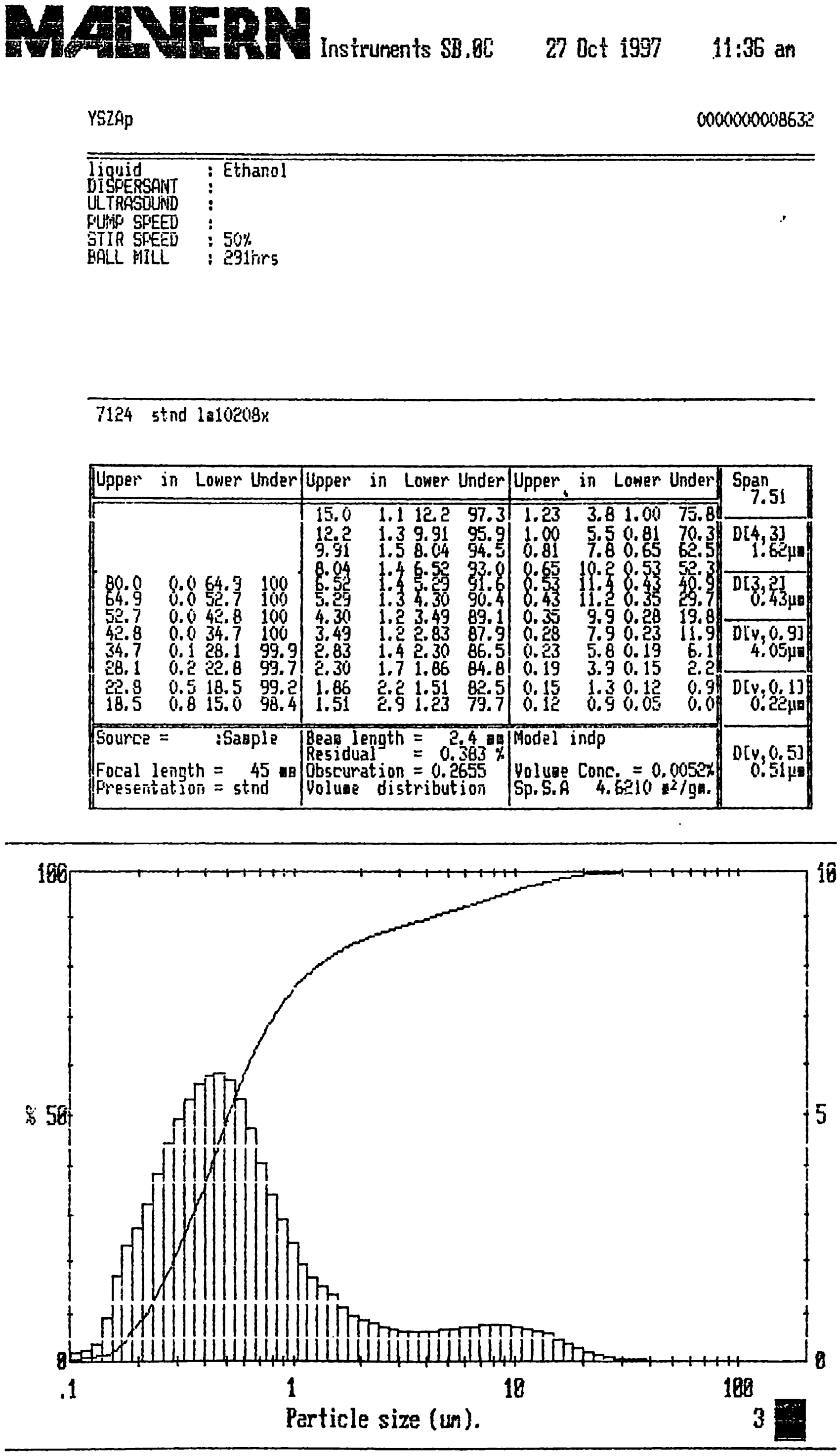

```
MALVERN Instruments SB.0C        27 Oct 1997      11:36 am

YSZAp                                              0000000008632

liquid         : Ethanol
DISPERSANT     :
ULTRASOUND     :
PUMP SPEED     :
STIR SPEED     : 50%
BALL MILL      : 291hrs

7124  stnd 1a10208x

Upper   in  Lower Under|Upper   in  Lower Under|Upper   in  Lower Under| Span
                       | 15.0   1.1 12.2   97.3| 1.23   3.8 1.00   75.8|  7.51
                       | 12.2   1.3 9.91   95.9| 1.00   5.5 0.81   70.3| D[4,3]
                       | 9.91   1.5 8.04   94.5| 0.81   7.8 0.65   62.5|  1.62µm
                       | 8.04   1.4 6.52   93.0| 0.65  10.2 0.53   52.3|
 80.0    0.0 64.9  100 | 6.52   1.4 5.29   91.6| 0.53  11.4 0.43   40.9| D[3,2]
 64.9    0.0 52.7  100 | 5.29   1.3 4.30   90.4| 0.43  11.2 0.35   29.7|  0.43µm
 52.7    0.0 42.8  100 | 4.30   1.2 3.49   89.1| 0.35   9.9 0.28   19.8|
 42.8    0.0 34.7  100 | 3.49   1.2 2.83   87.9| 0.28   7.9 0.23   11.9| D[v,0.9]
 34.7    0.1 28.1  99.9| 2.83   1.4 2.30   86.5| 0.23   5.8 0.19    6.1|  4.05µm
 28.1    0.2 22.8  99.7| 2.30   1.7 1.86   84.8| 0.19   3.9 0.15    2.2|
 22.8    0.5 18.5  99.2| 1.86   2.2 1.51   82.5| 0.15   1.3 0.12    0.9| D[v,0.1]
 18.5    0.8 15.0  98.4| 1.51   2.9 1.23   79.7| 0.12   0.9 0.05    0.0|  0.22µm
Source =       :Sample |Beam length =   2.4 mm |Model indp             |
                       |Residual    =  0.383 % |                       | D[v,0.5]
Focal length =    45 mm|Obscuration = 0.2655   |Volume Conc. = 0.0052% |  0.51µm
Presentation = stnd    |Volume  distribution   |Sp.S.A   4.6210 m²/gm. |
```

Afdelingen for Materialeforskning

Figure A2.18 Particle size of NiO before ball milling.

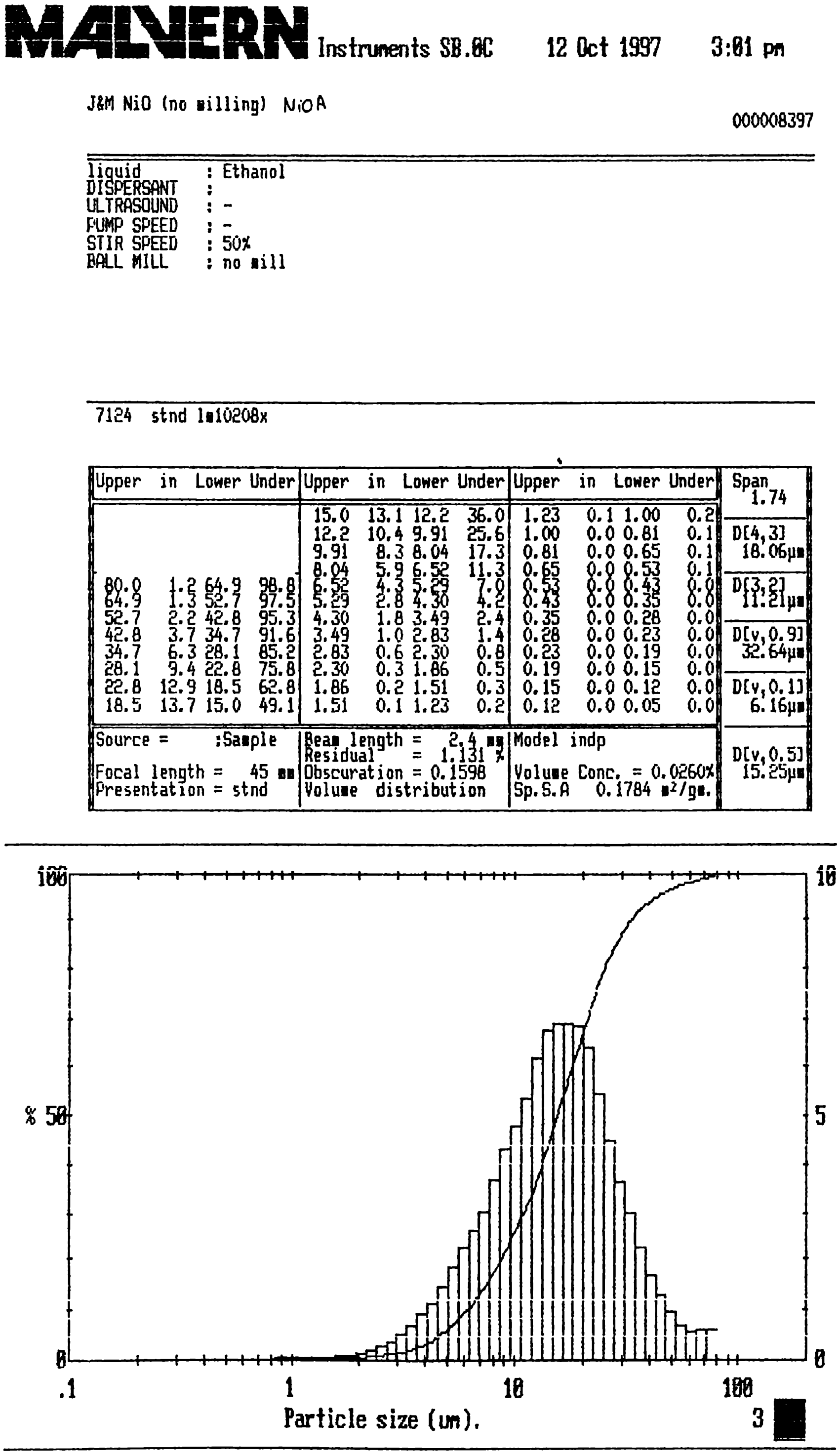

MALVERN Instruments SB.0C 12 Oct 1997 3:01 pm

J&M NiO (no milling) NiOA

000008397

liquid : Ethanol
DISPERSANT :
ULTRASOUND : -
PUMP SPEED : -
STIR SPEED : 50%
BALL MILL : no mill

7124 stnd 1m10208x

Upper	in	Lower	Under	Upper	in	Lower	Under	Upper	in	Lower	Under	Span 1.74
				15.0	13.1	12.2	36.0	1.23	0.1	1.00	0.2	
				12.2	10.4	9.91	25.6	1.00	0.0	0.81	0.1	D[4,3] 18.06µm
				9.91	8.3	8.04	17.3	0.81	0.0	0.65	0.1	
				8.04	5.9	6.52	11.3	0.65	0.0	0.53	0.1	
80.0	1.2	64.9	98.8	6.52	4.3	5.29	7.0	0.53	0.0	0.43	0.0	D[3,2] 11.21µm
64.9	1.3	52.7	97.5	5.29	2.8	4.30	4.2	0.43	0.0	0.35	0.0	
52.7	2.2	42.8	95.3	4.30	1.8	3.49	2.4	0.35	0.0	0.28	0.0	
42.8	3.7	34.7	91.6	3.49	1.0	2.83	1.4	0.28	0.0	0.23	0.0	D[v,0.9] 32.64µm
34.7	6.3	28.1	85.2	2.83	0.6	2.30	0.8	0.23	0.0	0.19	0.0	
28.1	9.4	22.8	75.8	2.30	0.3	1.86	0.5	0.19	0.0	0.15	0.0	
22.8	12.9	18.5	62.8	1.86	0.2	1.51	0.3	0.15	0.0	0.12	0.0	D[v,0.1] 6.16µm
18.5	13.7	15.0	49.1	1.51	0.1	1.23	0.2	0.12	0.0	0.05	0.0	

Source = :Sample
Focal length = 45 mm
Presentation = stnd

Beam length = 2.4 mm
Residual = 1.131 %
Obscuration = 0.1598
Volume distribution

Model indp
Volume Conc. = 0.0260%
Sp.S.A 0.1784 m²/gm.

D[v,0.5] 15.25µm

Afdelingen for Materialeforskning

Figure A2.19 Particle size of NiO after ball milling for 45 minutes.

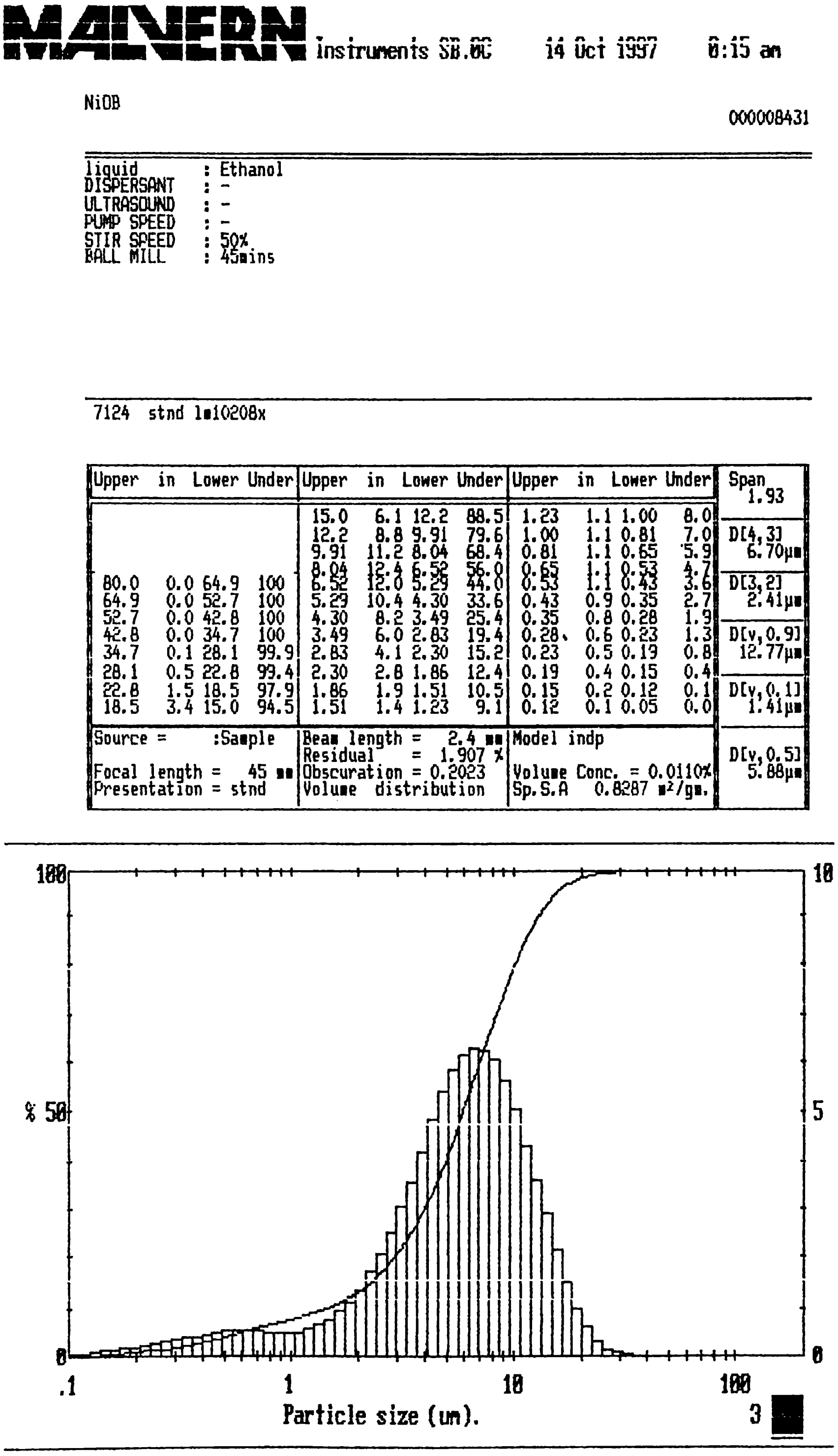

MALVERN Instruments SB.0C 14 Oct 1997 8:15 am

NiOB

000008431

liquid : Ethanol
DISPERSANT : -
ULTRASOUND : -
PUMP SPEED : -
STIR SPEED : 50%
BALL MILL : 45mins

7124 stnd 1m10208x

Upper	in	Lower	Under	Upper	in	Lower	Under	Upper	in	Lower	Under	
				15.0	6.1	12.2	88.5	1.23	1.1	1.00	8.0	Span 1.93
				12.2	8.8	9.91	79.6	1.00	1.1	0.81	7.0	D[4,3] 6.70µm
				9.91	11.2	8.04	68.4	0.81	1.1	0.65	5.9	
				8.04	12.4	6.52	56.0	0.65	1.1	0.53	4.7	D[3,2] 2.41µm
80.0	0.0	64.9	100	6.52	12.0	5.29	44.0	0.53	1.1	0.43	3.6	
64.9	0.0	52.7	100	5.29	10.4	4.30	33.6	0.43	0.9	0.35	2.7	
52.7	0.0	42.8	100	4.30	8.2	3.49	25.4	0.35	0.8	0.28	1.9	D[v,0.9] 12.77µm
42.8	0.0	34.7	100	3.49	6.0	2.83	19.4	0.28	0.6	0.23	1.3	
34.7	0.1	28.1	99.9	2.83	4.1	2.30	15.2	0.23	0.5	0.19	0.8	
28.1	0.5	22.8	99.4	2.30	2.8	1.86	12.4	0.19	0.4	0.15	0.4	D[v,0.1] 1.41µm
22.8	1.5	18.5	97.9	1.86	1.9	1.51	10.5	0.15	0.2	0.12	0.1	
18.5	3.4	15.0	94.5	1.51	1.4	1.23	9.1	0.12	0.1	0.05	0.0	

Source = :Sample Focal length = 45 mm Presentation = stnd	Beam length = 2.4 mm Residual = 1.907 % Obscuration = 0.2023 Volume distribution	Model indp Volume Conc. = 0.0110% Sp.S.A 0.8287 m²/gm.	D[v,0.5] 5.88µm

Afdelingen for Materialeforskning

Figure A2.20 Particle size of NiO after ball milling for 1 hour.

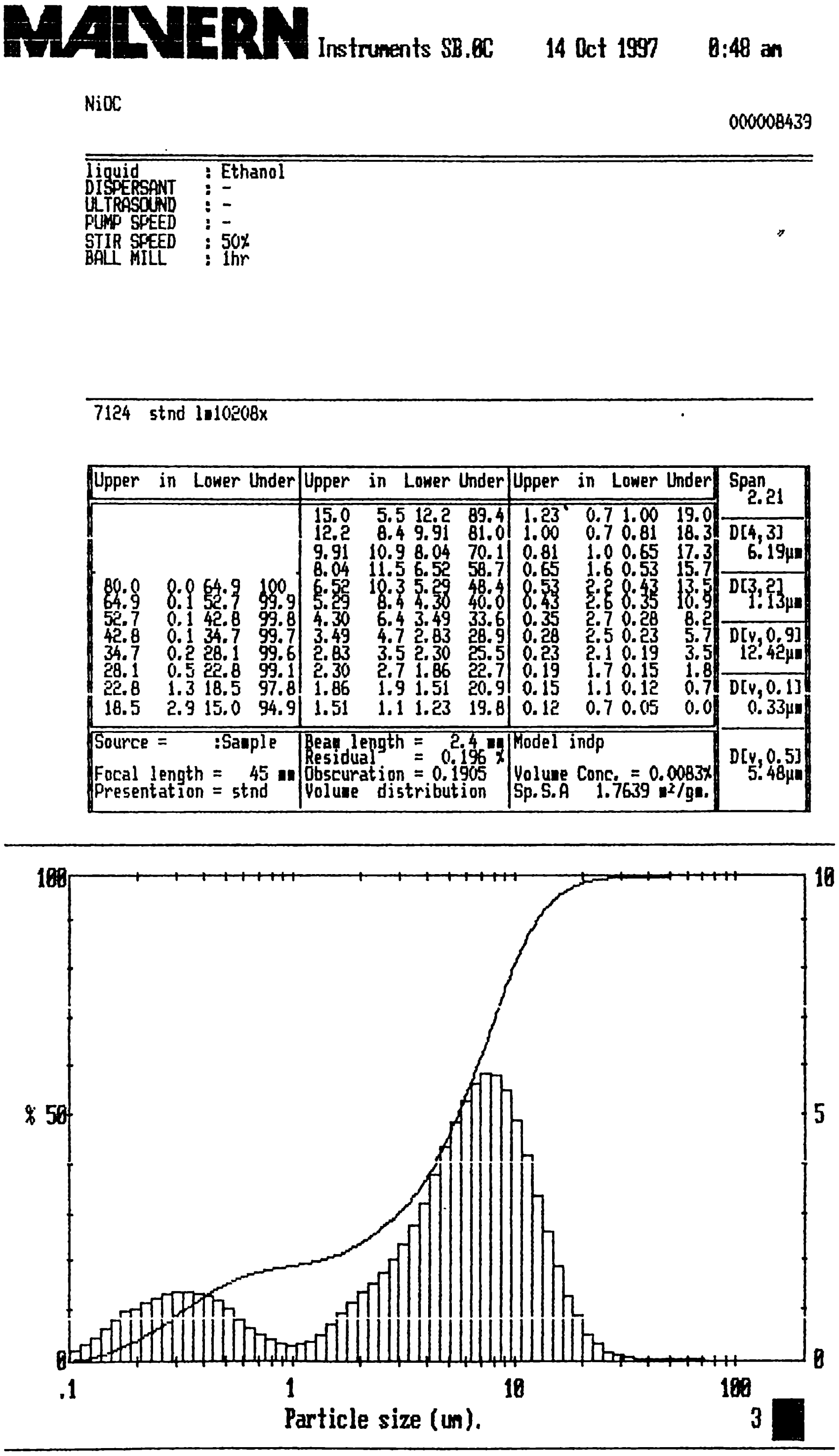

MALVERN Instruments SB.0C 14 Oct 1997 8:48 am

NiOC

000008439

liquid : Ethanol
DISPERSANT : -
ULTRASOUND : -
PUMP SPEED : -
STIR SPEED : 50%
BALL MILL : 1hr

7124 stnd 1m10208x

Upper	in	Lower	Under	Upper	in	Lower	Under	Upper	in	Lower	Under
				15.0	5.5	12.2	89.4	1.23	0.7	1.00	19.0
				12.2	8.4	9.91	81.0	1.00	0.7	0.81	18.3
				9.91	10.9	8.04	70.1	0.81	1.0	0.65	17.3
				8.04	11.5	6.52	58.7	0.65	1.6	0.53	15.7
80.0	0.0	64.9	100	6.52	10.3	5.29	48.4	0.53	2.2	0.43	13.5
64.9	0.1	52.7	99.9	5.29	8.4	4.30	40.0	0.43	2.6	0.35	10.9
52.7	0.1	42.8	99.8	4.30	6.4	3.49	33.6	0.35	2.7	0.28	8.2
42.8	0.1	34.7	99.7	3.49	4.7	2.83	28.9	0.28	2.5	0.23	5.7
34.7	0.2	28.1	99.6	2.83	3.5	2.30	25.5	0.23	2.1	0.19	3.5
28.1	0.5	22.8	99.1	2.30	2.7	1.86	22.7	0.19	1.7	0.15	1.8
22.8	1.3	18.5	97.8	1.86	1.9	1.51	20.9	0.15	1.1	0.12	0.7
18.5	2.9	15.0	94.9	1.51	1.1	1.23	19.8	0.12	0.7	0.05	0.0

Span 2.21
D[4,3] 6.19µm
D[3,2] 1.13µm
D[v,0.9] 12.42µm
D[v,0.1] 0.33µm
D[v,0.5] 5.48µm

Source = :Sample
Focal length = 45 mm
Presentation = stnd

Beam length = 2.4 mm
Residual = 0.196 %
Obscuration = 0.1905
Volume distribution

Model indp
Volume Conc. = 0.0083%
Sp.S.A 1.7639 m²/gm.

Afdelingen for Materialeforskning

Figure A2.21 Particle size of NiO after ball milling for 2 hours.

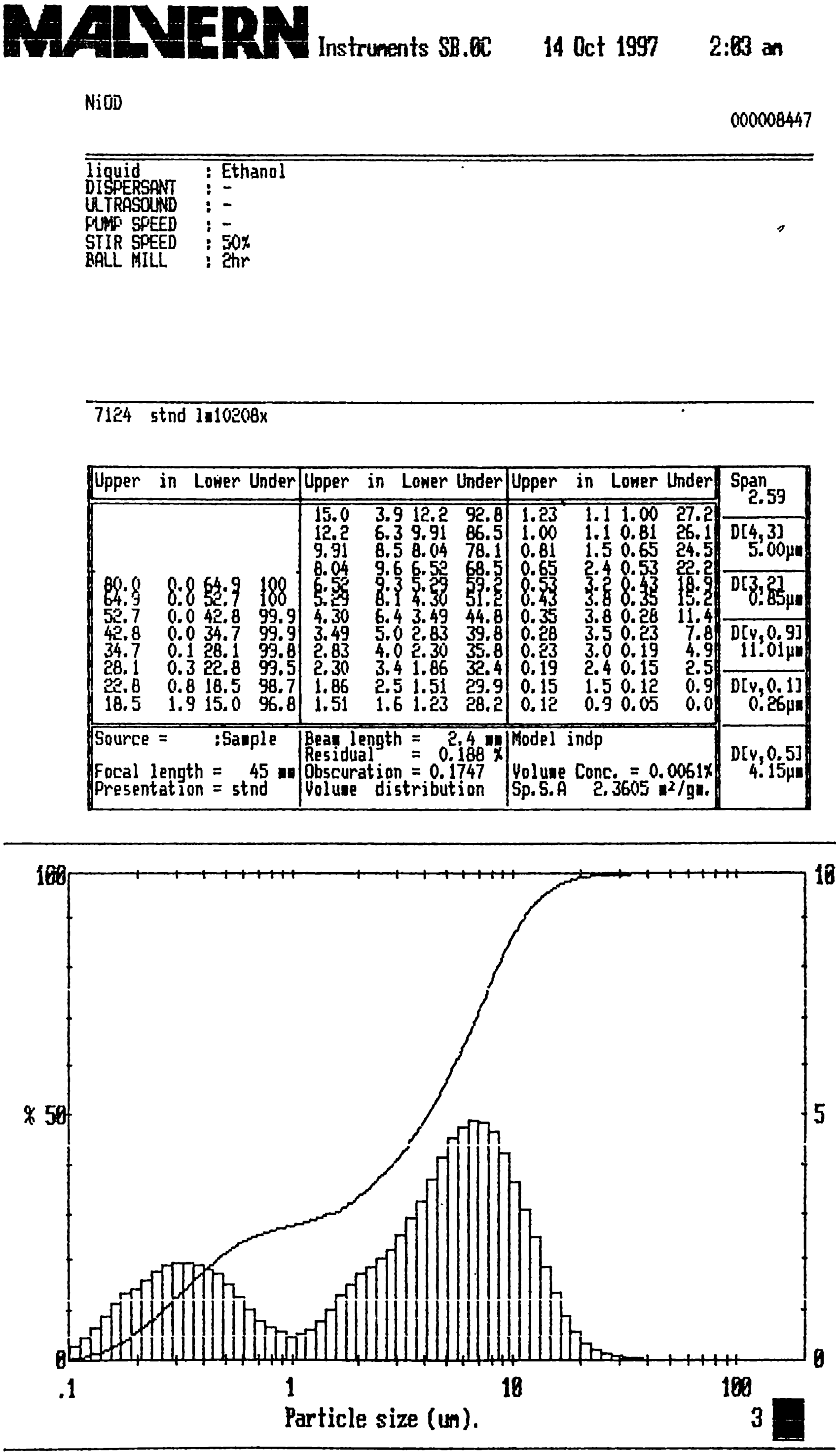

MALVERN Instruments SB.0C 14 Oct 1997 2:03 am

NiOD

000008447

liquid : Ethanol
DISPERSANT : -
ULTRASOUND : -
PUMP SPEED : -
STIR SPEED : 50%
BALL MILL : 2hr

7124 stnd 1m10208x

Upper	in	Lower	Under	Upper	in	Lower	Under	Upper	in	Lower	Under
				15.0	3.9	12.2	92.8	1.23	1.1	1.00	27.2
				12.2	6.3	9.91	86.5	1.00	1.1	0.81	26.1
				9.91	8.5	8.04	78.1	0.81	1.5	0.65	24.5
				8.04	9.6	6.52	68.5	0.65	2.4	0.53	22.2
80.0	0.0	64.9	100	6.52	9.3	5.29	59.2	0.53	3.2	0.43	18.9
64.9	0.0	52.7	100	5.29	8.1	4.30	51.2	0.43	3.8	0.35	15.2
52.7	0.0	42.8	99.9	4.30	6.4	3.49	44.8	0.35	3.8	0.28	11.4
42.8	0.0	34.7	99.9	3.49	5.0	2.83	39.8	0.28	3.5	0.23	7.8
34.7	0.1	28.1	99.8	2.83	4.0	2.30	35.8	0.23	3.0	0.19	4.9
28.1	0.3	22.8	99.5	2.30	3.4	1.86	32.4	0.19	2.4	0.15	2.5
22.8	0.8	18.5	98.7	1.86	2.5	1.51	29.9	0.15	1.5	0.12	0.9
18.5	1.9	15.0	96.8	1.51	1.6	1.23	28.2	0.12	0.9	0.05	0.0

Span 2.59
D[4,3] 5.00µm
D[3,2] 0.85µm
D[v,0.9] 11.01µm
D[v,0.1] 0.26µm

Source = :Sample
Focal length = 45 mm
Presentation = stnd

Beam length = 2.4 mm
Residual = 0.188 %
Obscuration = 0.1747
Volume distribution

Model indp
Volume Conc. = 0.0061%
Sp.S.A 2.3605 m²/gm.

D[v,0.5] 4.15µm

Afdelingen for Materialeforskning

Figure A2.21 Particle size of NiO after ball milling for 6 hours.

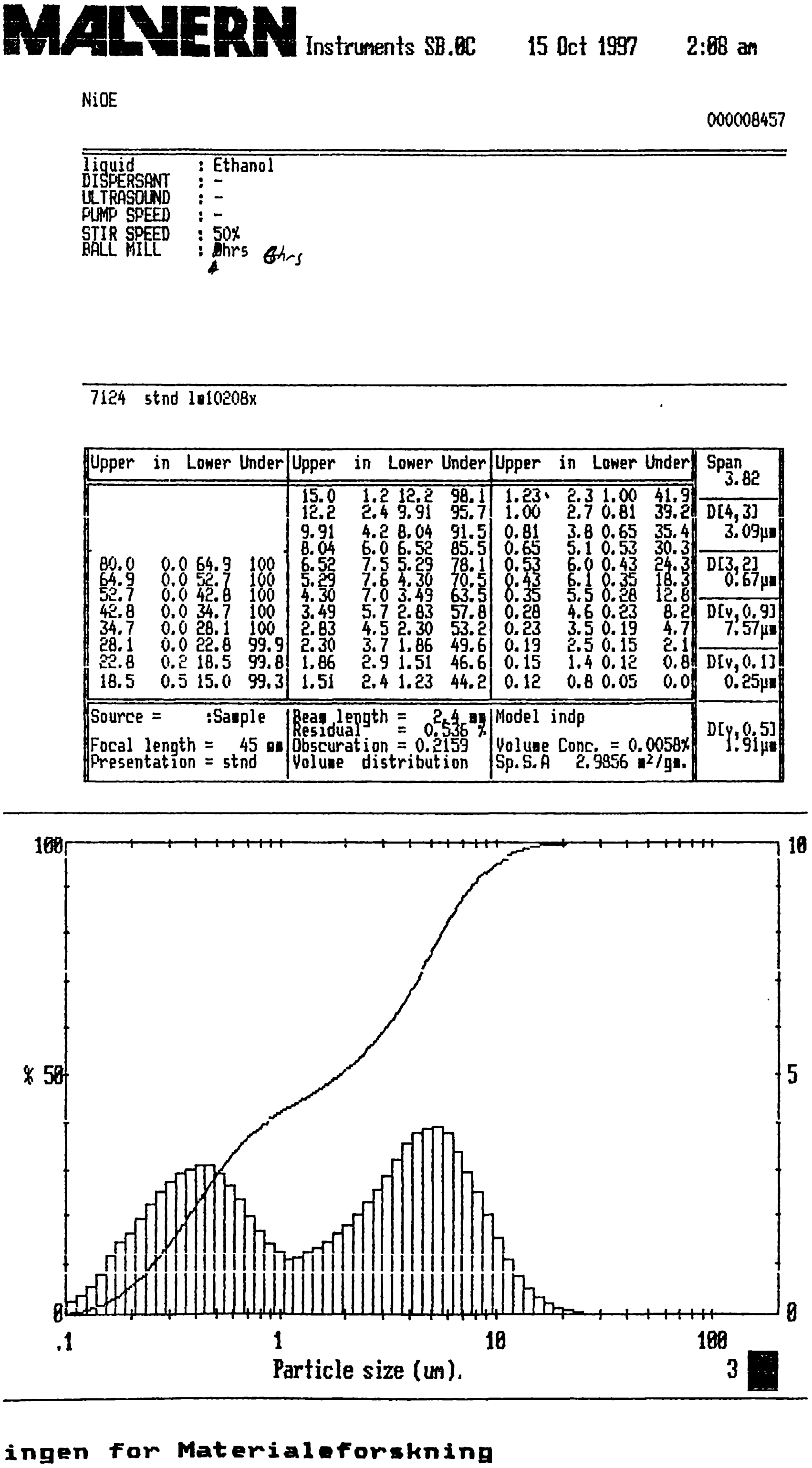

MALVERN Instruments SB.0C 15 Oct 1997 2:08 am

NiOE

000008457

liquid : Ethanol
DISPERSANT : -
ULTRASOUND : -
PUMP SPEED : -
STIR SPEED : 50%
BALL MILL : [illegible]hrs 6hrs
4

7124 stnd 1m10208x

Upper	in	Lower	Under	Upper	in	Lower	Under	Upper	in	Lower	Under
				15.0	1.2	12.2	98.1	1.23	2.3	1.00	41.9
				12.2	2.4	9.91	95.7	1.00	2.7	0.81	39.2
				9.91	4.2	8.04	91.5	0.81	3.8	0.65	35.4
				8.04	6.0	6.52	85.5	0.65	5.1	0.53	30.3
80.0	0.0	64.9	100	6.52	7.5	5.29	78.1	0.53	6.0	0.43	24.3
64.9	0.0	52.7	100	5.29	7.6	4.30	70.5	0.43	6.1	0.35	18.3
52.7	0.0	42.8	100	4.30	7.0	3.49	63.5	0.35	5.5	0.28	12.8
42.8	0.0	34.7	100	3.49	5.7	2.83	57.8	0.28	4.6	0.23	8.2
34.7	0.0	28.1	100	2.83	4.5	2.30	53.2	0.23	3.5	0.19	4.7
28.1	0.0	22.8	99.9	2.30	3.7	1.86	49.6	0.19	2.5	0.15	2.1
22.8	0.2	18.5	99.8	1.86	2.9	1.51	46.6	0.15	1.4	0.12	0.8
18.5	0.5	15.0	99.3	1.51	2.4	1.23	44.2	0.12	0.8	0.05	0.0

Source = :Sample
Focal length = 45 mm
Presentation = stnd

Beam length = 2.4 mm
Residual = 0.536 %
Obscuration = 0.2159
Volume distribution

Model indp
Volume Conc. = 0.0058%
Sp.S.A 2.9856 m²/gm.

Span 3.82
D[4,3] 3.09µm
D[3,2] 0.67µm
D[v,0.9] 7.57µm
D[v,0.1] 0.25µm
D[v,0.5] 1.91µm

Afdelingen for Materialeforskning

Figure A2.23 Particle size of NiO after ball milling for 11 hours.

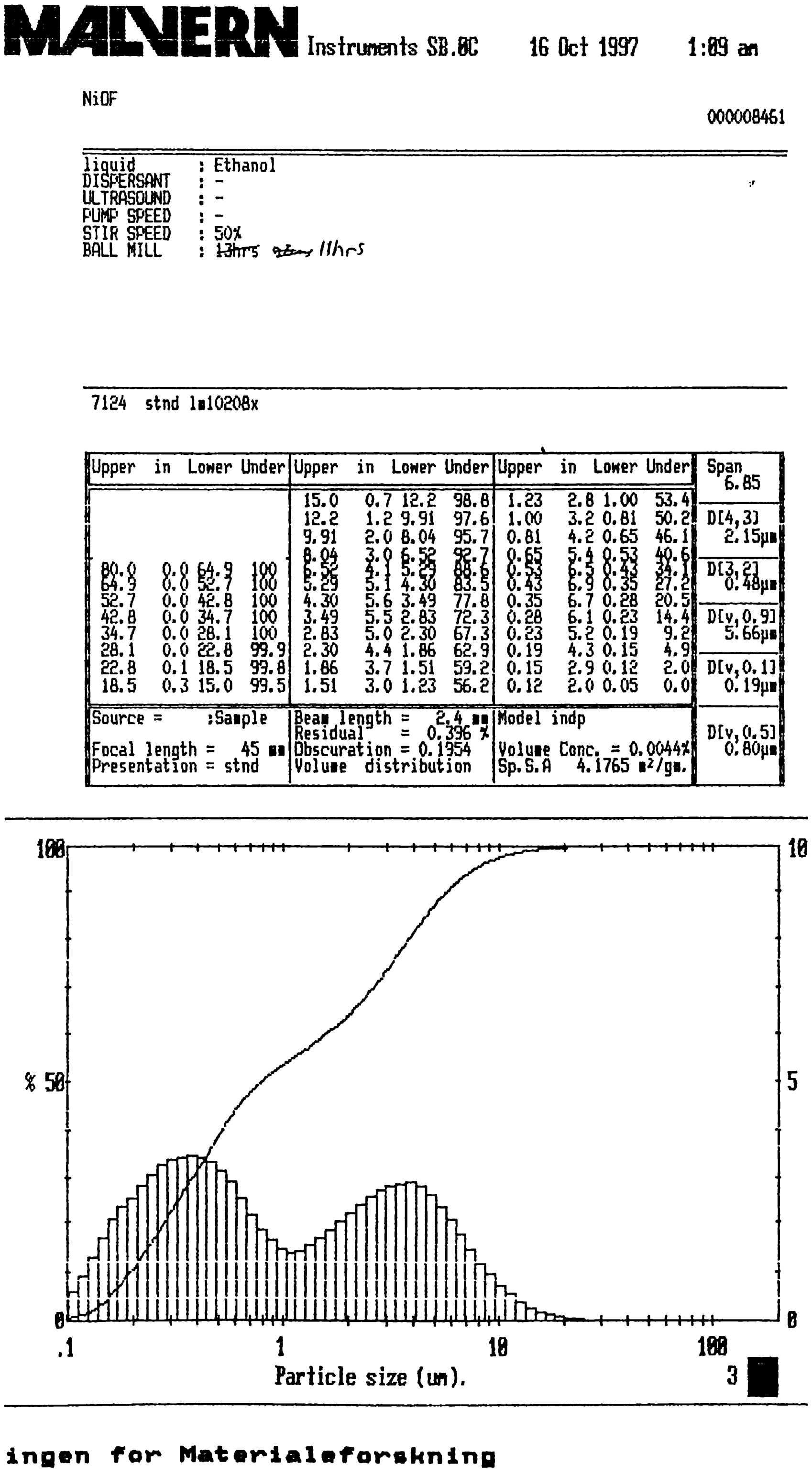

MALVERN Instruments SB.0C 16 Oct 1997 1:09 am

NiOF

000008461

liquid : Ethanol
DISPERSANT : -
ULTRASOUND : -
PUMP SPEED : -
STIR SPEED : 50%
BALL MILL : ~~13hrs~~ [illegible] 11hrs

7124 stnd 1■10208x

Upper	in	Lower	Under	Upper	in	Lower	Under	Upper	in	Lower	Under
				15.0	0.7	12.2	98.8	1.23	2.8	1.00	53.4
				12.2	1.2	9.91	97.6	1.00	3.2	0.81	50.2
				9.91	2.0	8.04	95.7	0.81	4.2	0.65	46.1
				8.04	3.0	6.52	92.7	0.65	5.4	0.53	40.6
80.0	0.0	64.9	100	6.52	4.1	5.29	88.6	0.53	6.5	0.43	34.1
64.9	0.0	52.7	100	5.29	5.1	4.30	83.5	0.43	6.9	0.35	27.2
52.7	0.0	42.8	100	4.30	5.6	3.49	77.8	0.35	6.7	0.28	20.5
42.8	0.0	34.7	100	3.49	5.5	2.83	72.3	0.28	6.1	0.23	14.4
34.7	0.0	28.1	100	2.83	5.0	2.30	67.3	0.23	5.2	0.19	9.2
28.1	0.0	22.8	99.9	2.30	4.4	1.86	62.9	0.19	4.3	0.15	4.9
22.8	0.1	18.5	99.8	1.86	3.7	1.51	59.2	0.15	2.9	0.12	2.0
18.5	0.3	15.0	99.5	1.51	3.0	1.23	56.2	0.12	2.0	0.05	0.0

Span 6.85
D[4,3] 2.15µm
D[3,2] 0.48µm
D[v,0.9] 5.66µm
D[v,0.1] 0.19µm
D[v,0.5] 0.80µm

Source = :Sample
Focal length = 45 mm
Presentation = stnd

Beam length = 2.4 mm
Residual = 0.396 %
Obscuration = 0.1954
Volume distribution

Model indp
Volume Conc. = 0.0044%
Sp.S.A 4.1765 m²/gm.

Afdelingen for Materialeforskning

Figure A2.24 Particle size of NiO after ball milling for 16 hours.

MALVERN Instruments SB.0C 16 Oct 1997 1:42 pm

NiOG

000008465

```
liquid        : Ethanol
DISPERSANT    : -
ULTRASOUND    : -
PUMP SPEED    : -
STIR SPEED    : 50%
BALL MILL     : 16hrs
```

7124 stnd 1m10208x

Upper	in	Lower	Under	Upper	in	Lower	Under	Upper	in	Lower	Under	Span 7.20
				15.0	0.6	12.2	98.7	1.23	3.1	1.00	58.7	
				12.2	0.9	9.91	97.8	1.00	3.5	0.81	55.3	D[4,3] 1.84μm
				9.91	1.4	8.04	96.4	0.81	4.5	0.65	50.7	
				8.04	2.0	6.52	94.5	0.65	5.9	0.53	44.8	
80.0	0.0	64.9	100	6.52	2.8	5.29	91.7	0.53	7.1	0.43	37.7	D[3,2] 0.44μm
64.9	0.0	52.7	100	5.29	3.6	4.30	88.0	0.43	7.6	0.35	30.1	
52.7	0.0	42.8	100	4.30	4.4	3.49	83.6	0.35	7.4	0.28	22.6	
42.8	0.0	34.7	100	3.49	4.8	2.83	78.8	0.28	6.8	0.23	15.9	D[v,0.9] 4.78μm
34.7	0.0	28.1	100	2.83	4.9	2.30	73.9	0.23	5.8	0.19	10.1	
28.1	0.1	22.8	99.9	2.30	4.7	1.86	69.2	0.19	4.7	0.15	5.4	
22.8	0.2	18.5	99.7	1.86	4.1	1.51	65.1	0.15	3.2	0.12	2.2	D[v,0.1] 0.19μm
18.5	0.4	15.0	99.3	1.51	3.4	1.23	61.8	0.12	2.2	0.05	0.0	

Source = :Sample Focal length = 45 mm Presentation = stnd	Beam length = 2.4 mm Residual = 0.360 % Obscuration = 0.1967 Volume distribution	Model indp Volume Conc. = 0.0042% Sp.S.A 4.5578 m²/gm.	D[v,0.5] 0.64μm

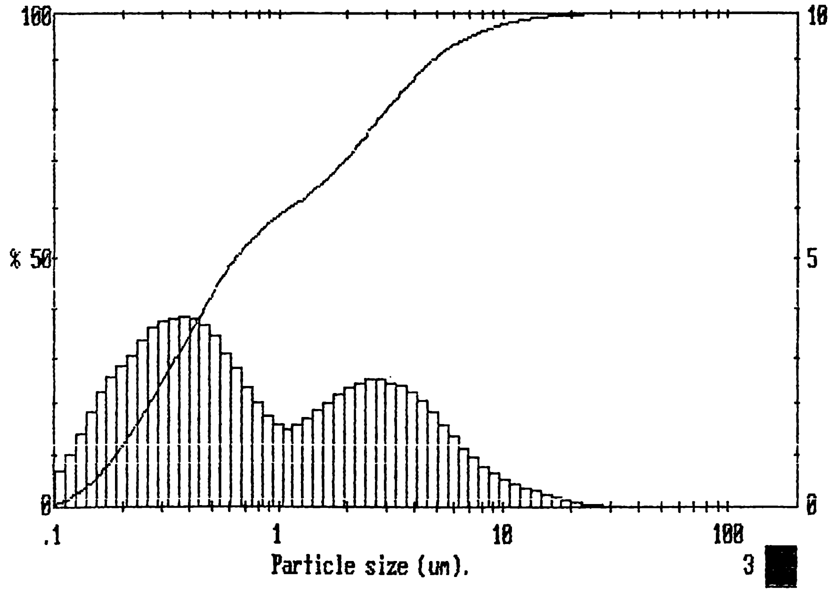

Afdelingen for Materialeforskning

Figure A2.25 Particle size of NiO after ball milling for 23 hours.

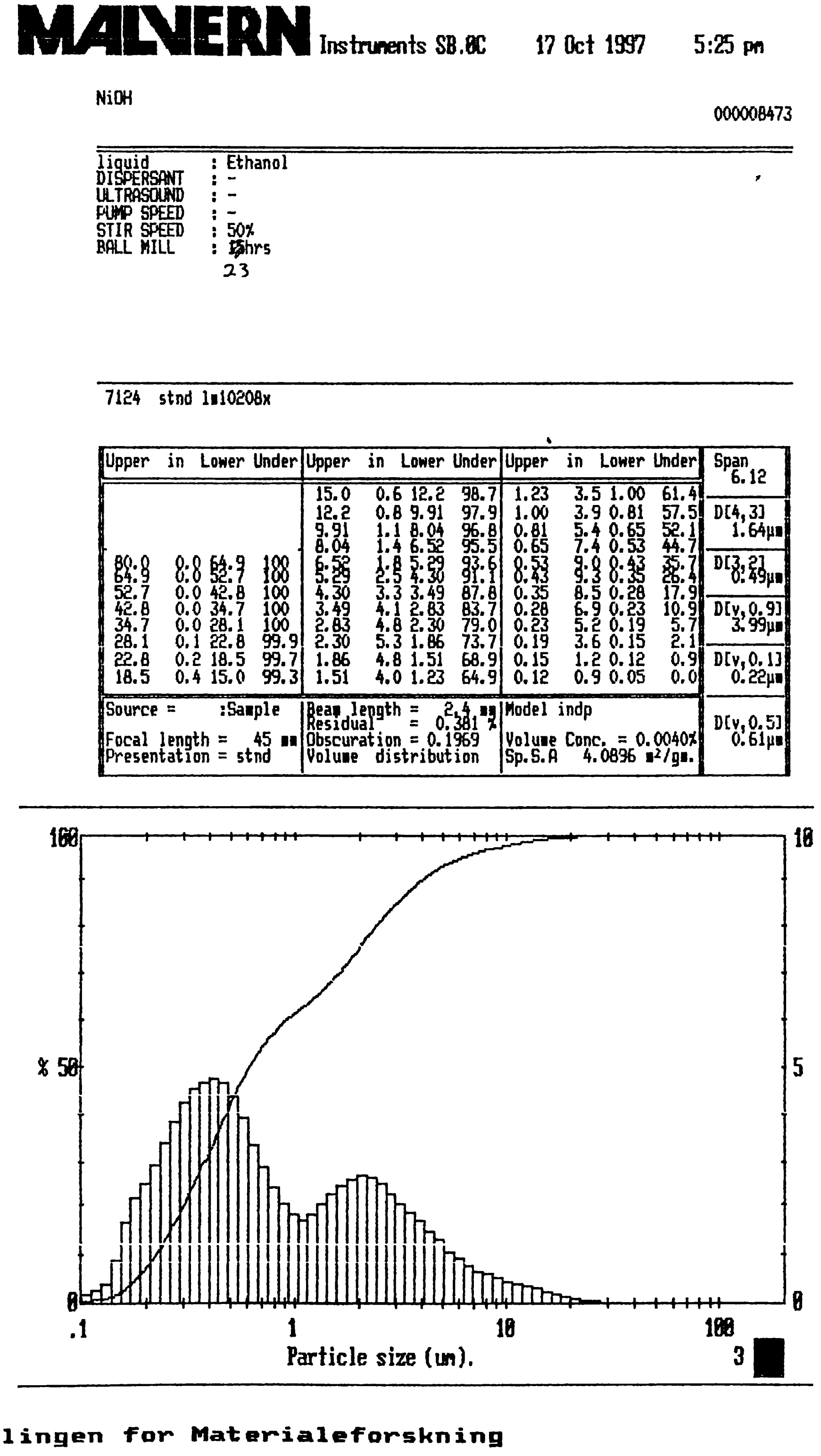

MALVERN Instruments SB.0C 17 Oct 1997 5:25 pm

NiOH

000008473

liquid : Ethanol
DISPERSANT : -
ULTRASOUND : -
PUMP SPEED : -
STIR SPEED : 50%
BALL MILL : ~~15~~hrs
23

7124 stnd 1m10208x

Upper	in	Lower	Under	Upper	in	Lower	Under	Upper	in	Lower	Under
				15.0	0.6	12.2	98.7	1.23	3.5	1.00	61.4
				12.2	0.8	9.91	97.9	1.00	3.9	0.81	57.5
				9.91	1.1	8.04	96.8	0.81	5.4	0.65	52.1
				8.04	1.4	6.52	95.5	0.65	7.4	0.53	44.7
80.0	0.0	64.9	100	6.52	1.8	5.29	93.6	0.53	9.0	0.43	35.7
64.9	0.0	52.7	100	5.29	2.5	4.30	91.1	0.43	9.3	0.35	26.4
52.7	0.0	42.8	100	4.30	3.3	3.49	87.8	0.35	8.5	0.28	17.9
42.8	0.0	34.7	100	3.49	4.1	2.83	83.7	0.28	6.9	0.23	10.9
34.7	0.0	28.1	100	2.83	4.8	2.30	79.0	0.23	5.2	0.19	5.7
28.1	0.1	22.8	99.9	2.30	5.3	1.86	73.7	0.19	3.6	0.15	2.1
22.8	0.2	18.5	99.7	1.86	4.8	1.51	68.9	0.15	1.2	0.12	0.9
18.5	0.4	15.0	99.3	1.51	4.0	1.23	64.9	0.12	0.9	0.05	0.0

Span 6.12
D[4,3] 1.64µm
D[3,2] 0.49µm
D[v,0.9] 3.99µm
D[v,0.1] 0.22µm
D[v,0.5] 0.61µm

Source = :Sample
Focal length = 45 mm
Presentation = stnd

Beam length = 2.4 mm
Residual = 0.381 %
Obscuration = 0.1969
Volume distribution

Model indp
Volume Conc. = 0.0040%
Sp.S.A 4.0896 m^2/gm.

Afdelingen for Materialeforskning

Figure A2.26 Particle size of NiO after ball milling for 40 hours.

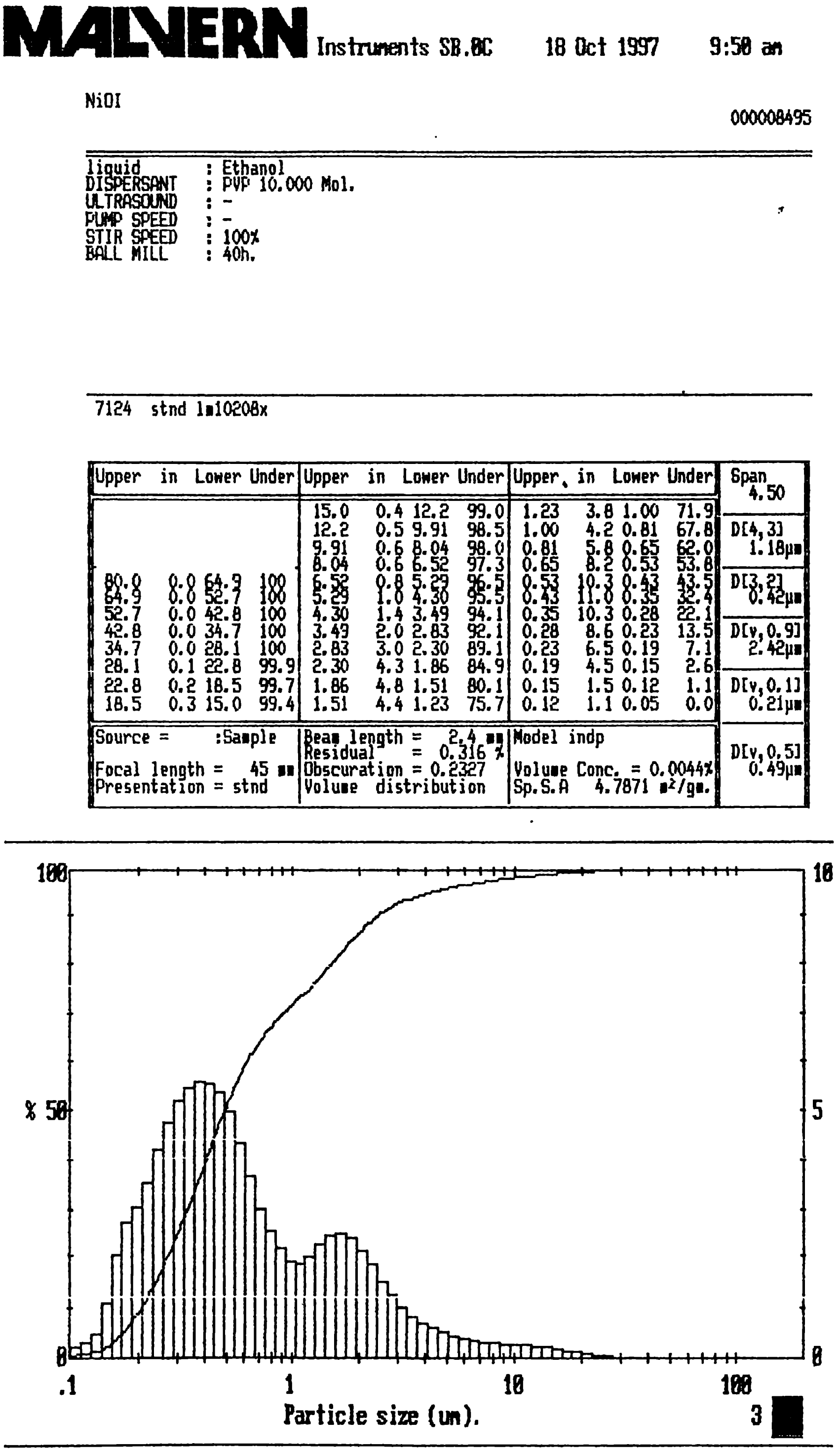

MALVERN Instruments SB.0C 18 Oct 1997 9:50 am

NiOI

000008495

liquid : Ethanol
DISPERSANT : PVP 10.000 Mol.
ULTRASOUND : -
PUMP SPEED : -
STIR SPEED : 100%
BALL MILL : 40h.

7124 stnd 1m10208x

Upper	in	Lower	Under	Upper	in	Lower	Under	Upper	in	Lower	Under
				15.0	0.4	12.2	99.0	1.23	3.8	1.00	71.9
				12.2	0.5	9.91	98.5	1.00	4.2	0.81	67.8
				9.91	0.6	8.04	98.0	0.81	5.8	0.65	62.0
				8.04	0.6	6.52	97.3	0.65	8.2	0.53	53.8
80.0	0.0	64.9	100	6.52	0.8	5.29	96.5	0.53	10.3	0.43	43.5
64.9	0.0	52.7	100	5.29	1.0	4.30	95.5	0.43	11.0	0.35	32.4
52.7	0.0	42.8	100	4.30	1.4	3.49	94.1	0.35	10.3	0.28	22.1
42.8	0.0	34.7	100	3.49	2.0	2.83	92.1	0.28	8.6	0.23	13.5
34.7	0.0	28.1	100	2.83	3.0	2.30	89.1	0.23	6.5	0.19	7.1
28.1	0.1	22.8	99.9	2.30	4.3	1.86	84.9	0.19	4.5	0.15	2.6
22.8	0.2	18.5	99.7	1.86	4.8	1.51	80.1	0.15	1.5	0.12	1.1
18.5	0.3	15.0	99.4	1.51	4.4	1.23	75.7	0.12	1.1	0.05	0.0

Span 4.50
D[4,3] 1.18µm
D[3,2] 0.42µm
D[v,0.9] 2.42µm
D[v,0.1] 0.21µm
D[v,0.5] 0.49µm

Source = :Sample
Focal length = 45 mm
Presentation = stnd

Beam length = 2.4 mm
Residual = 0.316 %
Obscuration = 0.2327
Volume distribution

Model indp
Volume Conc. = 0.0044%
Sp.S.A 4.7871 m²/gm.

Afdelingen for Materialeforskning

Figure A2.27 Particle size of NiO after ball milling for 52 hours.

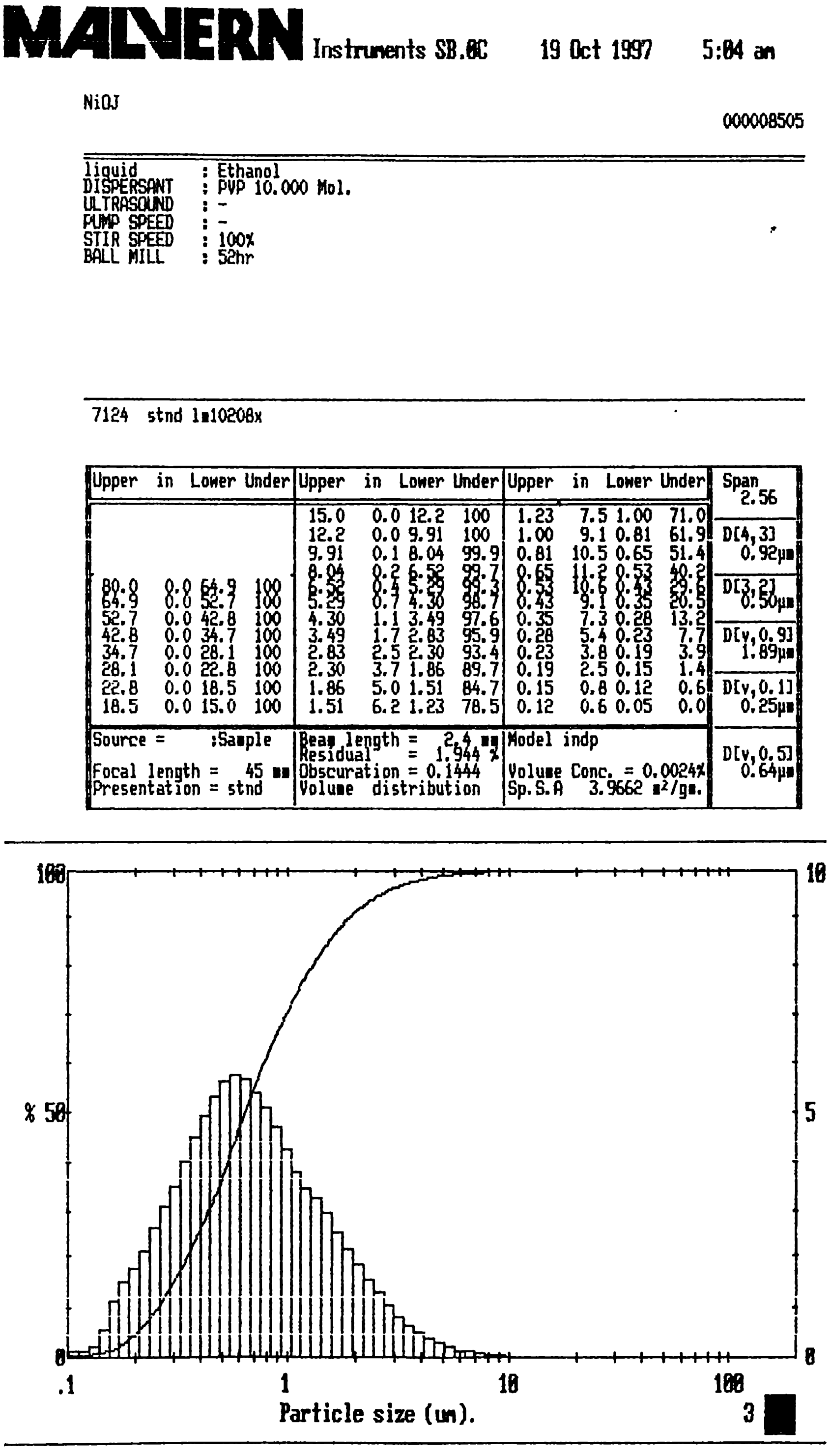

MALVERN Instruments SB.0C 19 Oct 1997 5:04 am

NiOJ

000008505

liquid : Ethanol
DISPERSANT : PVP 10.000 Mol.
ULTRASOUND : -
PUMP SPEED : -
STIR SPEED : 100%
BALL MILL : 52hr

7124 stnd 1m10208x

Upper	in	Lower	Under	Upper	in	Lower	Under	Upper	in	Lower	Under
				15.0	0.0	12.2	100	1.23	7.5	1.00	71.0
				12.2	0.0	9.91	100	1.00	9.1	0.81	61.9
				9.91	0.1	8.04	99.9	0.81	10.5	0.65	51.4
				8.04	0.2	6.52	99.7	0.65	11.2	0.53	40.2
80.0	0.0	64.9	100	6.52	0.4	5.29	99.3	0.53	10.6	0.43	29.6
64.9	0.0	52.7	100	5.29	0.7	4.30	98.7	0.43	9.1	0.35	20.5
52.7	0.0	42.8	100	4.30	1.1	3.49	97.6	0.35	7.3	0.28	13.2
42.8	0.0	34.7	100	3.49	1.7	2.83	95.9	0.28	5.4	0.23	7.7
34.7	0.0	28.1	100	2.83	2.5	2.30	93.4	0.23	3.8	0.19	3.9
28.1	0.0	22.8	100	2.30	3.7	1.86	89.7	0.19	2.5	0.15	1.4
22.8	0.0	18.5	100	1.86	5.0	1.51	84.7	0.15	0.8	0.12	0.6
18.5	0.0	15.0	100	1.51	6.2	1.23	78.5	0.12	0.6	0.05	0.0

Span 2.56
D[4,3] 0.92µm
D[3,2] 0.50µm
D[v,0.9] 1.89µm
D[v,0.1] 0.25µm
D[v,0.5] 0.64µm

Source = :Sample
Focal length = 45 mm
Presentation = stnd

Beam length = 2.4 mm
Residual = 1.944 %
Obscuration = 0.1444
Volume distribution

Model indp
Volume Conc. = 0.0024%
Sp.S.A 3.9662 m²/gm.

Afdelingen for Materialeforskning

Figure A2.28 Particle size of NiO after ball milling for 64 hours.

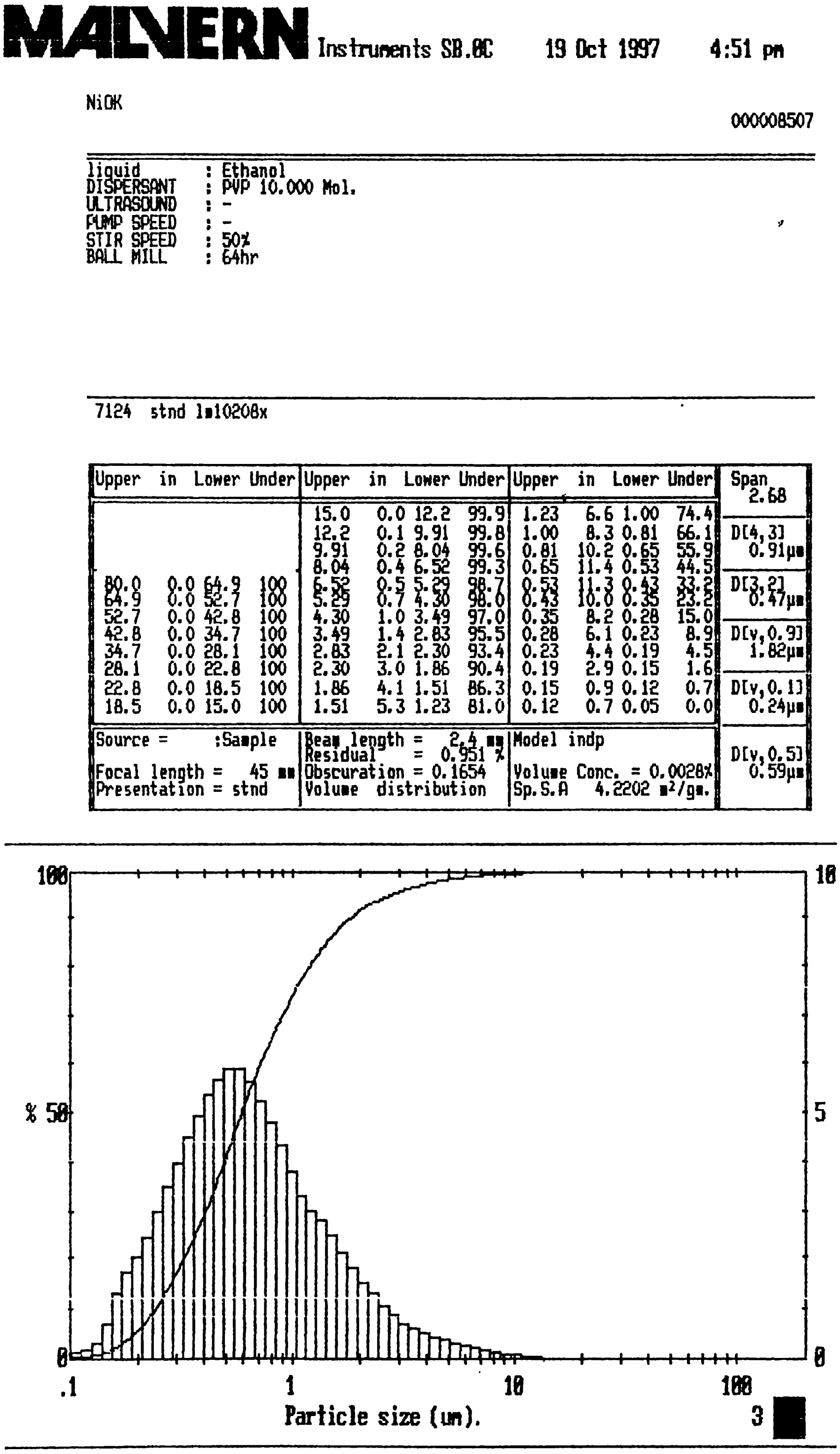

MALVERN Instruments SB.0C 19 Oct 1997 4:51 pm

NiOK

000008507

liquid : Ethanol
DISPERSANT : PVP 10.000 Mol.
ULTRASOUND : -
PUMP SPEED : -
STIR SPEED : 50%
BALL MILL : 64hr

7124 stnd 1m10208x

Upper	in	Lower	Under	Upper	in	Lower	Under	Upper	in	Lower	Under
				15.0	0.0	12.2	99.9	1.23	6.6	1.00	74.4
				12.2	0.1	9.91	99.8	1.00	8.3	0.81	66.1
				9.91	0.2	8.04	99.6	0.81	10.2	0.65	55.9
				8.04	0.4	6.52	99.3	0.65	11.4	0.53	44.5
80.0	0.0	64.9	100	6.52	0.5	5.29	98.7	0.53	11.3	0.43	33.2
64.9	0.0	52.7	100	5.29	0.7	4.30	98.0	0.43	10.0	0.35	23.2
52.7	0.0	42.8	100	4.30	1.0	3.49	97.0	0.35	8.2	0.28	15.0
42.8	0.0	34.7	100	3.49	1.4	2.83	95.5	0.28	6.1	0.23	8.9
34.7	0.0	28.1	100	2.83	2.1	2.30	93.4	0.23	4.4	0.19	4.5
28.1	0.0	22.8	100	2.30	3.0	1.86	90.4	0.19	2.9	0.15	1.6
22.8	0.0	18.5	100	1.86	4.1	1.51	86.3	0.15	0.9	0.12	0.7
18.5	0.0	15.0	100	1.51	5.3	1.23	81.0	0.12	0.7	0.05	0.0

Source = :Sample
Focal length = 45 mm
Presentation = stnd

Beam length = 2.4 mm
Residual = 0.951 %
Obscuration = 0.1654
Volume distribution

Model indp
Volume Conc. = 0.0028%
Sp.S.A 4.2202 m²/gm.

Span 2.68
D[4,3] 0.91μm
D[3,2] 0.47μm
D[v,0.9] 1.82μm
D[v,0.1] 0.24μm
D[v,0.5] 0.59μm

Afdelingen for Materialeforskning

Figure A2.29 Particle size of YSZ after ball milling for 10 hours.

Result. Analysis Table

ser Name: m Brown Security 2

D: YSZ10 Run No: 10 Measured: 7/19/98 4:36PM
ile: BROWN Rec. No: 17 Analysed: 7/19/98 4:37PM
ath: C:\SIZERS\DATA\TECHNOL\ Source: Analysed

ange: 300RF mm Beam: 2.40 mm Sampler: MS17 Obs': 24.5 %
resentation: 3RHA Analysis: Polydisperse Residual: 0.947 %
odifications: None

onc. = 0.0053 %Vol Density = 1.000 g/cm^3 S.S.A.= 5.3497 m^2/g
istribution: Volume D[4, 3] = 7.65 um D[3, 2] = 1.12 um
(v, 0.1) = 0.36 um D(v, 0.5) = 6.62 um D(v, 0.9) = 17.47 um
pan = 2.586E+00 Uniformity = 9.001E-01

Size (um)	Volume In %	Size (um)	Volume In %	Size (um)	Volume In %	Size (um)	Volume In %
0.05	0.00	0.58	2.30	6.63	4.23	76.32	0.00
0.06	0.00	0.67	1.48	7.72	5.47	88.91	0.00
0.07	0.00	0.78	1.33	9.00	6.72	103.58	0.00
0.08	0.00	0.91	1.34	10.48	7.50	120.67	0.00
0.09	0.00	1.06	1.60	12.21	7.49	140.58	0.00
0.11	0.02	1.24	1.54	14.22	6.61	163.77	0.00
0.13	0.05	1.44	1.49	16.57	5.07	190.80	0.00
0.15	0.14	1.68	1.45	19.31	3.61	222.28	0.00
0.17	0.32	1.95	1.39	22.49	2.24	258.95	0.00
0.20	0.69	2.28	1.34	26.20	1.01	301.68	0.00
0.23	1.47	2.65	1.03	30.53	0.00	351.46	0.00
0.27	3.00	3.09	1.07	35.56	0.00	409.45	0.00
0.31	5.11	3.60	1.28	41.43	0.00	477.01	0.00
0.36	6.02	4.19	1.69	48.27	0.00	555.71	0.00
0.42	4.53	4.88	2.31	56.23	0.00	647.41	0.00
0.49	2.91	5.69	3.16	65.51	0.00	754.23	0.00
0.58		6.63		76.32		878.67	

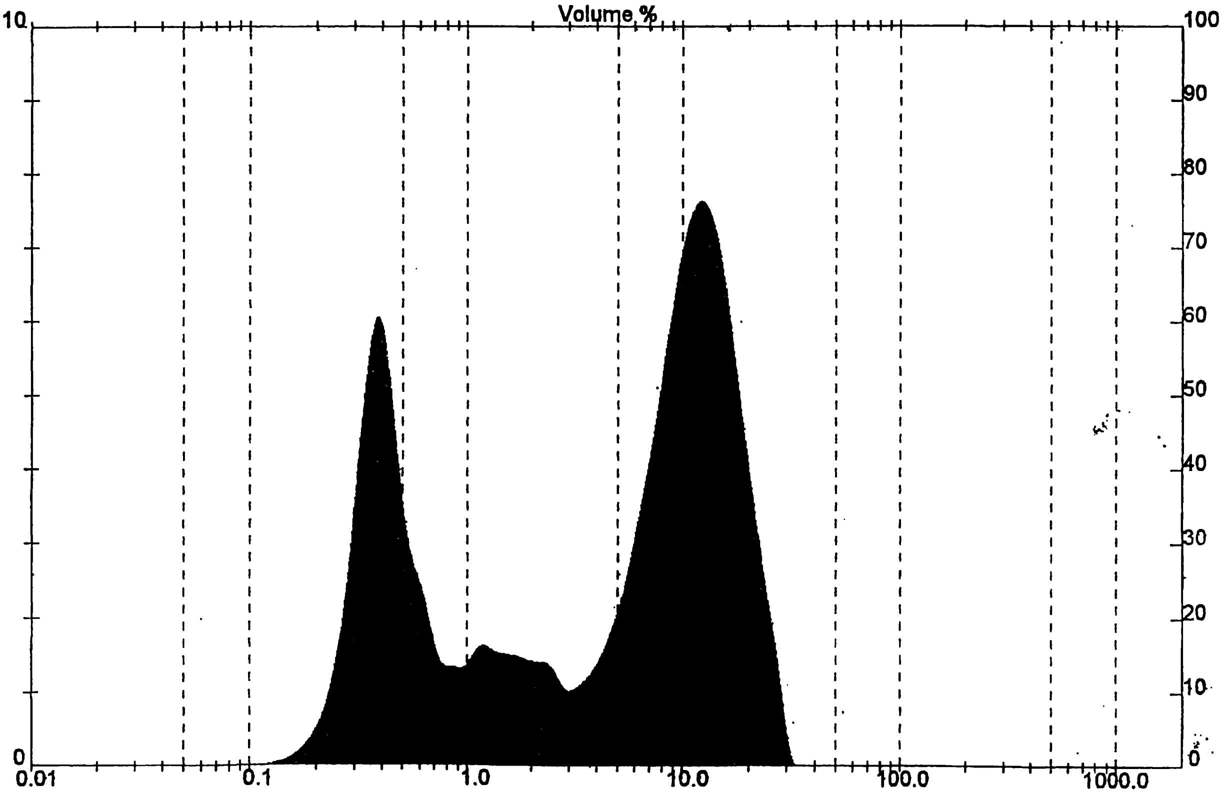

Figure A2.30 Particle size of YSZ after ball milling for 15 hours.

Result: Analysis Table

User Name: m Brown Security 2

ID: YSZ15 Run No: 8 Measured: 7/19/98 4:32PM
File: BROWN Rec. No: 16 Analysed: 7/19/98 4:32PM
Path: C:\SIZERS\DATA\TECHNOL\ Source: Analysed

Range: 300RF mm Beam: 2.40 mm Sampler: MS17 Obs': 17.5 %
Presentation: 3RHA Analysis: Polydisperse Residual: 0.984 %
Modifications: None

Conc. = 0.0031 %Vol Density = 1.000 g/cm^3 S.S.A.= 6.2180 m^2/g
Distribution: Volume D[4, 3] = 5.34 um D[3, 2] = 0.96 um
D(v, 0.1) = 0.35 um D(v, 0.5) = 3.98 um D(v, 0.9) = 13.05 um
Span = 3.193E+00 Uniformity = 1.096E+00

Size (um)	Volume In %	Size (um)	Volume In %	Size (um)	Volume In %	Size (um)	Volume In %
0.05	0.00	0.58	2.19	6.63	5.90	76.32	0.00
0.06	0.00	0.67	1.02	7.72	6.41	88.91	0.00
0.07	0.00	0.78	0.83	9.00	6.38	103.58	0.00
0.08	0.00	0.91	0.88	10.48	5.76	120.67	0.00
0.09	0.00	1.06	1.54	12.21	4.67	140.58	0.00
0.11	0.00	1.24	1.50	14.22	3.59	163.77	0.00
0.13	0.01	1.44	1.31	16.57	2.50	190.80	0.00
0.15	0.04	1.68	1.35	19.31	1.41	222.28	0.00
0.17	0.13	1.95	1.41	22.49	0.00	258.95	0.00
0.20	0.40	2.28	1.52	26.20	0.00	301.68	0.00
0.23	1.19	2.65	1.73	30.53	0.00	351.46	0.00
0.27	3.33	3.09	2.09	35.56	0.00	409.45	0.00
0.31	7.21	3.60	2.61	41.43	0.00	477.01	0.00
0.36	9.23	4.19	3.29	48.27	0.00	555.71	0.00
0.42	6.19	4.88	4.08	56.23	0.00	647.41	0.00
0.49	3.24	5.69	5.04	65.51	0.00	754.23	0.00
0.58		6.63		76.32		878.67	

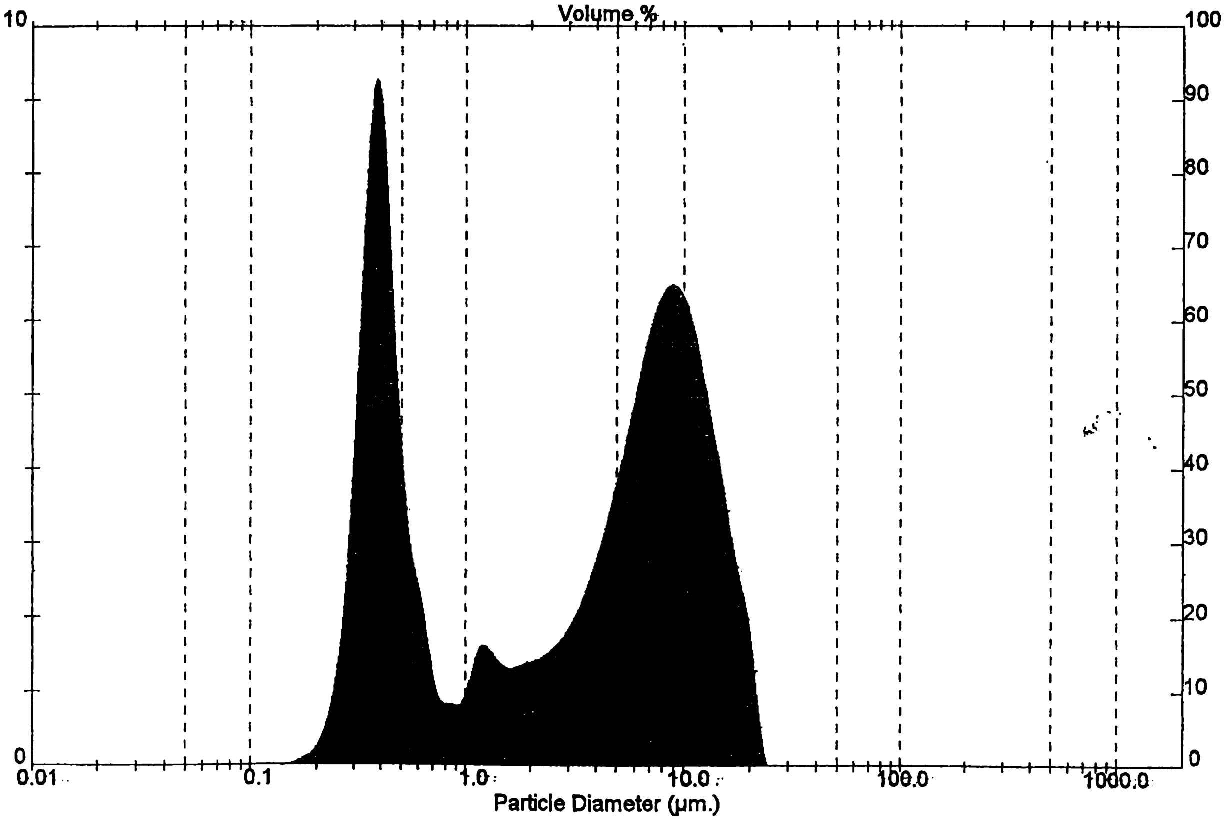

Figure A2.31 Particle size of NiO after ball milling for 26 hours.

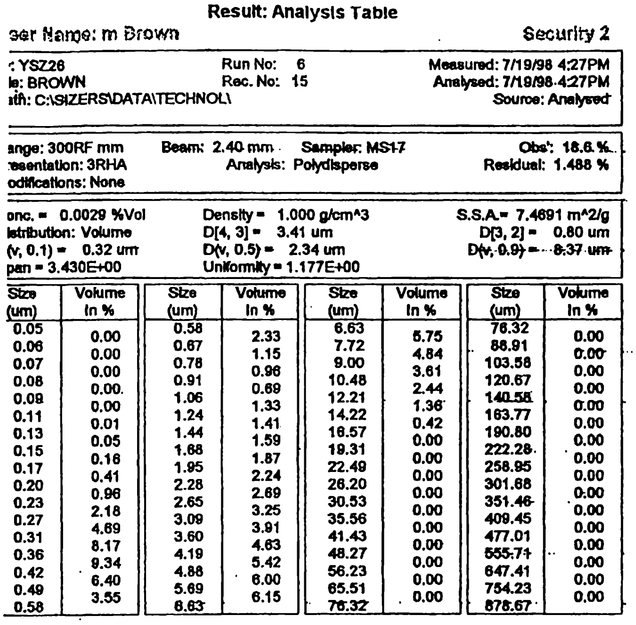

Result: Analysis Table

ser Name: m Brown		Security 2

: YSZ26	Run No: 6	Measured: 7/19/98 4:27PM
le: BROWN	Rec. No: 15	Analysed: 7/19/98 4:27PM
ath: C:\SIZERS\DATA\TECHNOL\	Source: Analysed

ange: 300RF mm	Beam: 2.40 mm	Sampler: MS17	Obs': 18.6 %
esentation: 3RHA	Analysis: Polydisperse	Residual: 1.488 %
odifications: None

onc. = 0.0029 %Vol	Density = 1.000 g/cm^3	S.S.A.= 7.4691 m^2/g
istribution: Volume	D[4, 3] = 3.41 um	D[3, 2] = 0.80 um
(v, 0.1) = 0.32 um	D(v, 0.5) = 2.34 um	D(v, 0.9) = 8.37 um
pan = 3.430E+00	Uniformity = 1.177E+00

Size (um)	Volume In %	Size (um)	Volume In %	Size (um)	Volume In %	Size (um)	Volume In %
0.05	0.00	0.58	2.33	6.63	5.75	76.32	0.00
0.06	0.00	0.67	1.15	7.72	4.84	88.91	0.00
0.07	0.00	0.78	0.96	9.00	3.61	103.58	0.00
0.08	0.00	0.91	0.69	10.48	2.44	120.67	0.00
0.09	0.00	1.06	1.33	12.21	1.36	140.58	0.00
0.11	0.01	1.24	1.41	14.22	0.42	163.77	0.00
0.13	0.05	1.44	1.59	16.57	0.00	190.80	0.00
0.15	0.16	1.68	1.87	19.31	0.00	222.28	0.00
0.17	0.41	1.95	2.24	22.49	0.00	258.95	0.00
0.20	0.96	2.28	2.69	26.20	0.00	301.68	0.00
0.23	2.18	2.65	3.25	30.53	0.00	351.46	0.00
0.27	4.69	3.09	3.91	35.56	0.00	409.45	0.00
0.31	8.17	3.60	4.63	41.43	0.00	477.01	0.00
0.36	9.34	4.19	5.42	48.27	0.00	555.71	0.00
0.42	6.40	4.88	6.00	56.23	0.00	647.41	0.00
0.49	3.55	5.69	6.15	65.51	0.00	754.23	0.00
0.58		6.63		76.32		878.67	

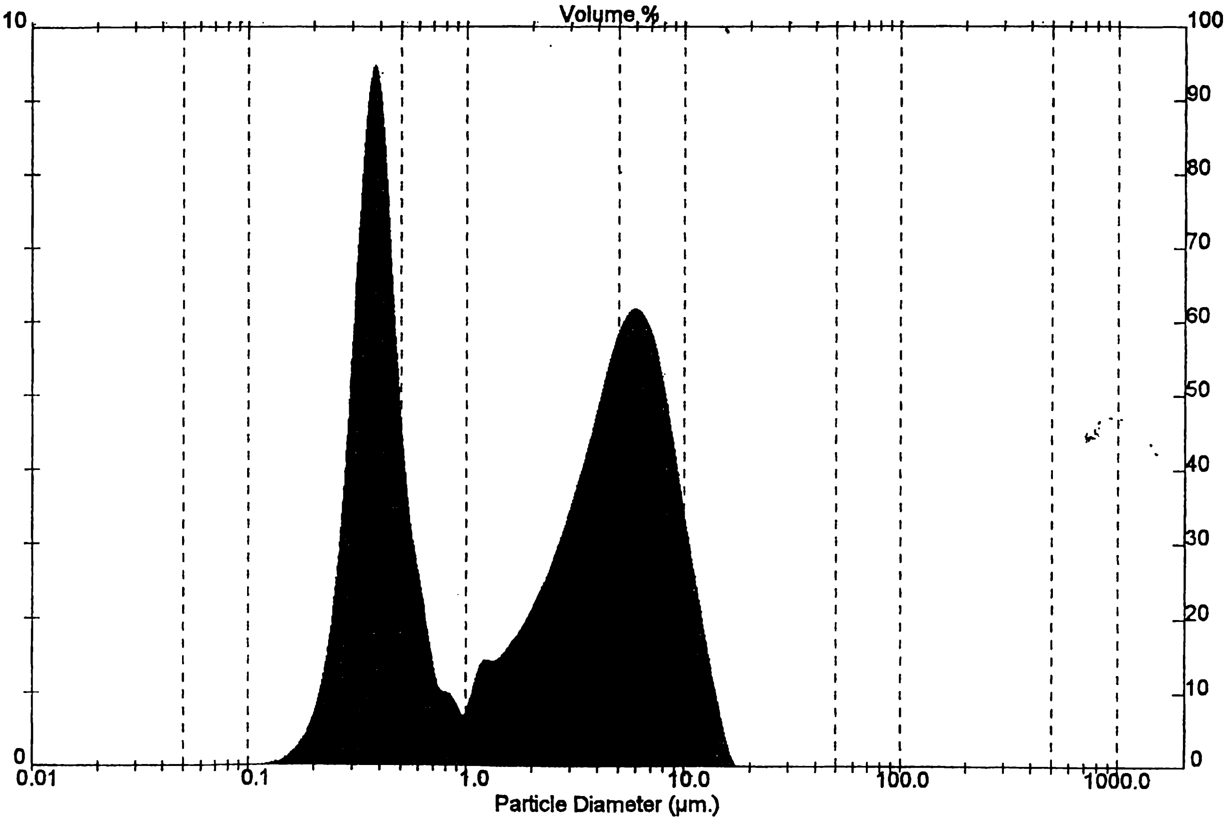

Figure A2.32 Particle size of YSZ after centrifugal milling for 45 minutes.

Result: Analysis Table

ID: 1400/17 3/4hr mill + Run No: 5 Measured: 20/9/96 12:53
File: CENTMILL Rec. No: 16 Analysed: 20/9/96 12:53
Path: A:\ Source: Analysed

Range: 300RF mm Beam: 2.40 mm Sampler: MS17 Obs': 16.6 %
Presentation: 3OHD Analysis: Polydisperse Residual: 2.016 %
Modifications: None

Conc. = 0.0099 %Vol Density = 1.000 g/cm^3 S.S.A.= 4.9442 m^2/g
Distribution: Volume D[4, 3] = 10.95 um D[3, 2] = 1.21 um
D(v, 0.1) = 0.30 um D(v, 0.5) = 10.44 um D(v, 0.9) = 21.83 um
Span = 2.062E+00 Uniformity = 6.264E-01

Size (um)	Volume In %	Size (um)	Volume In %	Size (um)	Volume In %	Size (um)	Volume In %
0.05	0.01	0.58	0.61	6.63	4.87	76.32	0.00
0.06	0.02	0.67	0.24	7.72	6.13	88.91	0.00
0.07	0.05	0.78	0.17	9.00	7.35	103.58	0.00
0.08	0.11	0.91	0.06	10.48	8.42	120.67	0.00
0.09	0.21	1.06	0.08	12.21	9.33	140.58	0.00
0.11	0.37	1.24	0.13	14.22	8.99	163.77	0.00
0.13	0.64	1.44	0.20	16.57	7.90	190.80	0.00
0.15	1.00	1.68	0.28	19.31	6.26	222.28	0.00
0.17	1.45	1.95	0.39	22.49	4.42	258.95	0.00
0.20	1.94	2.28	0.51	26.20	2.73	301.68	0.00
0.23	2.36	2.65	0.68	30.53	1.44	351.46	0.00
0.27	2.56	3.09	0.94	35.56	0.33	409.45	0.00
0.31	2.43	3.60	1.34	41.43	0.00	477.01	0.00
0.36	2.06	4.19	1.91	48.27	0.00	555.71	0.00
0.42	1.60	4.88	2.69	56.23	0.00	647.41	0.00
0.49	1.10	5.69	3.69	65.51	0.00	754.23	0.00
0.58		6.63		76.32		878.67	

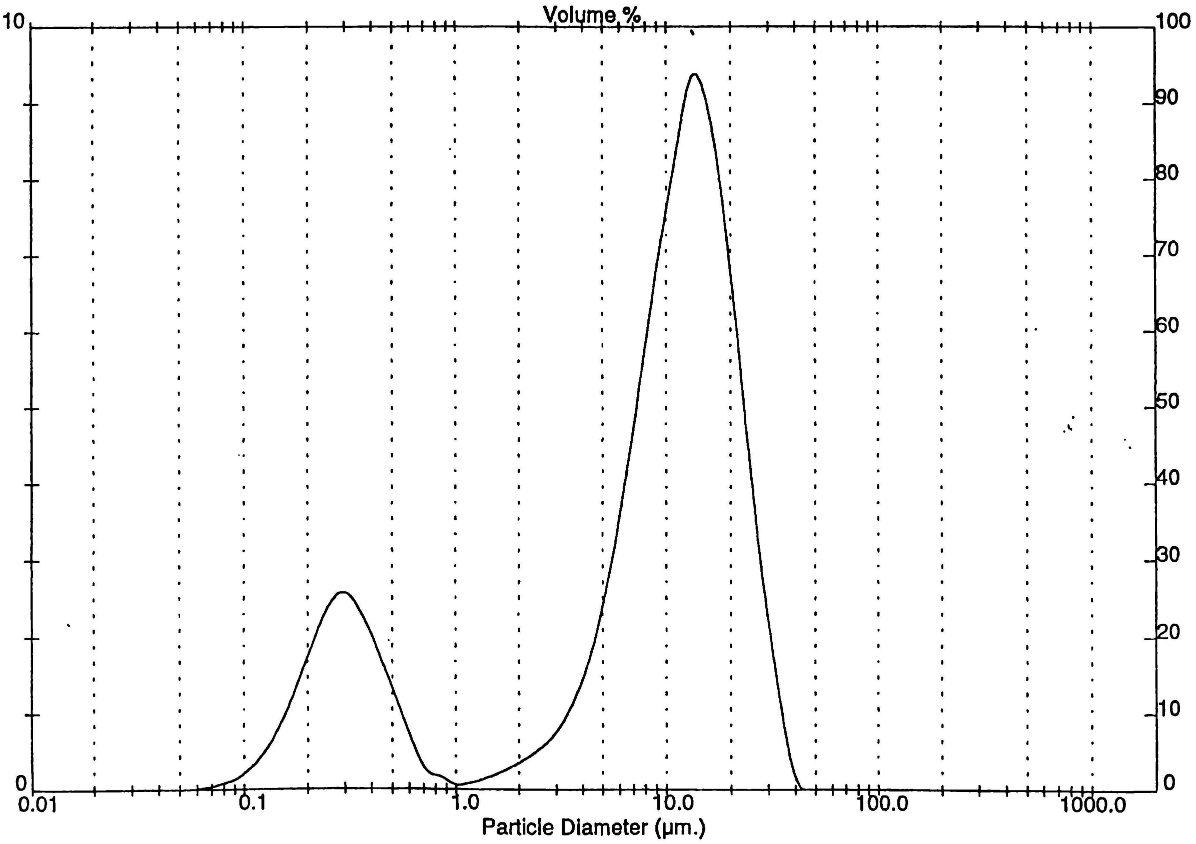

Figure A2.33 Particle size of YSZ after centrifugal milling for 1 hour.

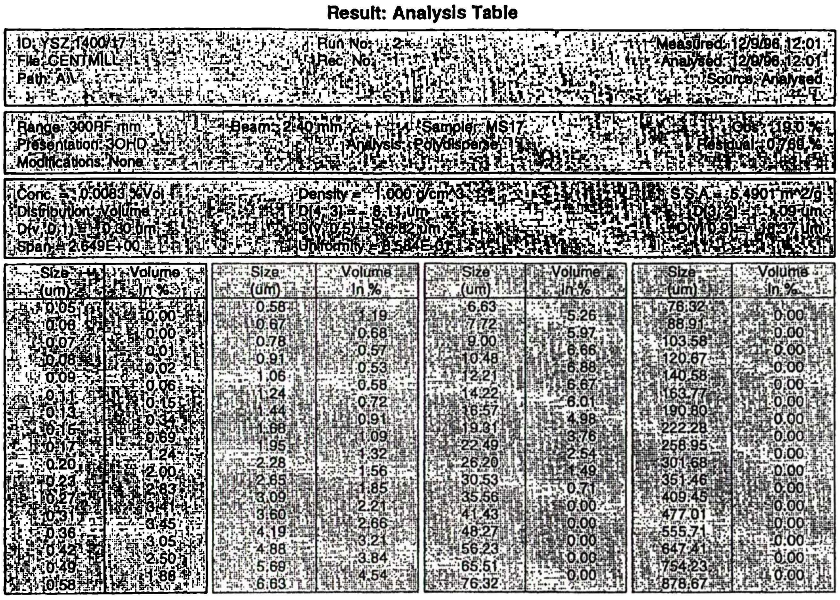

Result: Analysis Table

ID: YSZ 1400/17 Run No: 2 Measured: 12/9/96 12:01
File: CENTMILL Rec. No: 1 Analysed: 12/9/96 12:01
Path: A:\ Source: Analysed

Range: 300RF mm Beam: 2.40 mm Sampler: MS17 Obs': 19.0 %
Presentation: 3OHD Analysis: Polydisperse Residual: 0.769 %
Modifications: None

Conc. = 0.0083 %Vol Density = 1.000 g/cm^3 S.S.A.= 5.4901 m^2/g
Distribution: Volume D[4, 3] = 8.11 um D[3, 2] = 1.09 um
D(v, 0.1) = 0.30 um D(v, 0.5) = 6.82 um D(v, 0.9) = 18.37 um
Span = 2.649E+00 Uniformity = 8.584E-01

Size (um)	Volume In %	Size (um)	Volume In %	Size (um)	Volume In %	Size (um)	Volume In %
0.05	0.00	0.58	1.19	6.63	5.26	76.32	0.00
0.06	0.00	0.67	0.68	7.72	5.97	88.91	0.00
0.07	0.01	0.78	0.57	9.00	6.66	103.58	0.00
0.08	0.02	0.91	0.53	10.48	6.88	120.67	0.00
0.09	0.06	1.06	0.58	12.21	6.67	140.58	0.00
0.11	0.15	1.24	0.72	14.22	6.01	163.77	0.00
0.13	0.34	1.44	0.91	16.57	4.98	190.80	0.00
0.15	0.69	1.68	1.09	19.31	3.76	222.28	0.00
0.17	1.24	1.95	1.32	22.49	2.54	258.95	0.00
0.20	2.00	2.28	1.56	26.20	1.49	301.68	0.00
0.23	2.83	2.65	1.85	30.53	0.71	351.46	0.00
0.27	3.41	3.09	2.21	35.56	0.00	409.45	0.00
0.31	3.45	3.60	2.66	41.43	0.00	477.01	0.00
0.36	3.05	4.19	3.21	48.27	0.00	555.71	0.00
0.42	2.50	4.88	3.84	56.23	0.00	647.41	0.00
0.49	1.86	5.69	4.54	65.51	0.00	754.23	0.00
0.58		6.63		76.32		878.67	

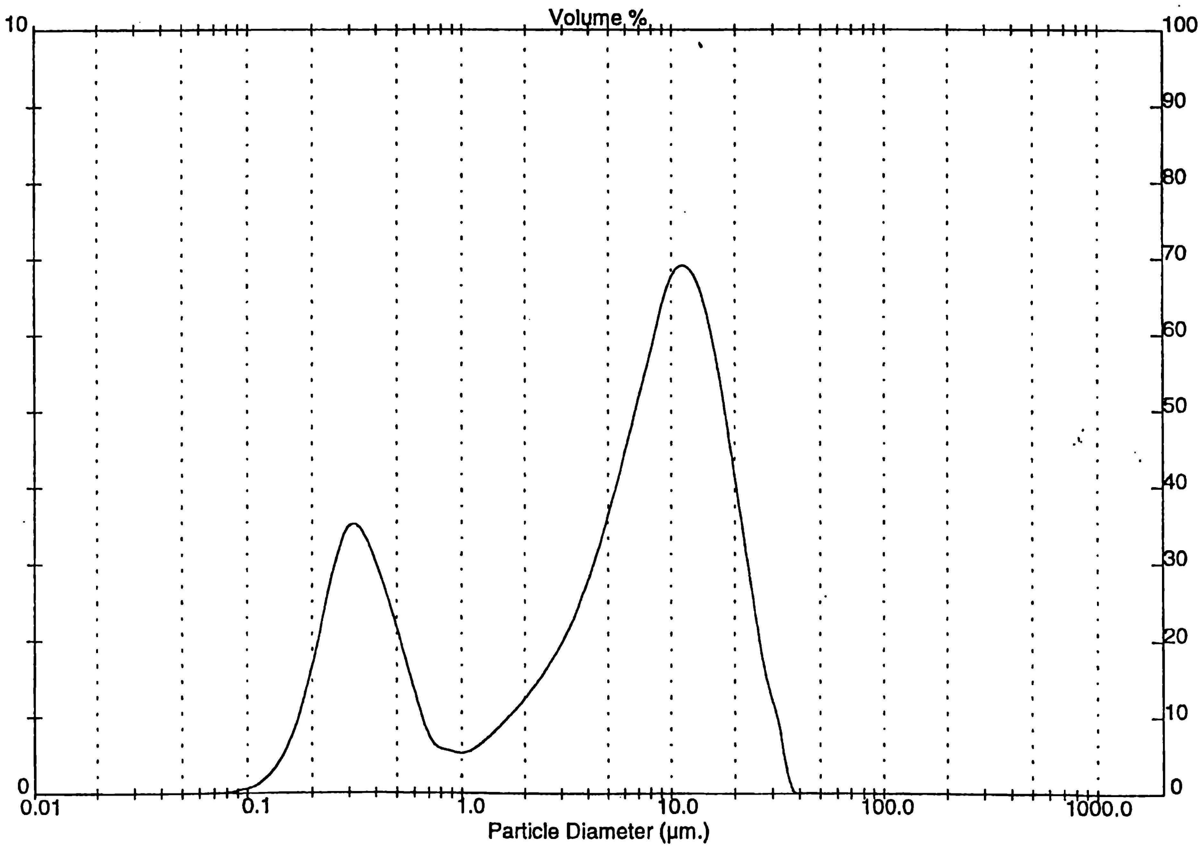

Figure A2.34 Particle size of YSZ after centrifugal milling for 3 hours.

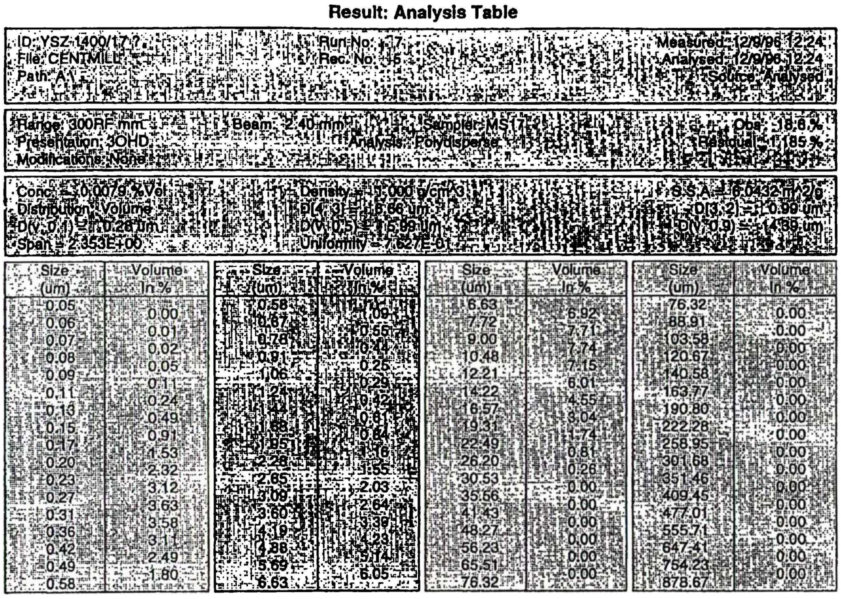

Result: Analysis Table

ID: YSZ 1400/17 ? Run No: 7 Measured: 12/9/96 12:24
File: CENTMILL Rec. No: 5 Analysed: 12/9/96 12:24
Path: A:\ Source: Analysed

Range: 300RF mm Beam: 2.40 mm Sampler: MS17 Obs': 18.6 %
Presentation: 3OHD Analysis: Polydisperse Residual: 1.185 %
Modifications: None

Conc. = 0.0079 %Vol Density = 1.000 g/cm^3 S.S.A.= 6.0432 m^2/g
Distribution: Volume D[4, 3] = 6.66 um D[3, 2] = 0.99 um
D(v, 0.1) = 0.28 um D(v, 0.5) = 5.99 um D(v, 0.9) = 14.39 um
Span = 2.353E+00 Uniformity = 7.627E-01

Size (um)	Volume In %	Size (um)	Volume In %	Size (um)	Volume In %	Size (um)	Volume In %
0.05	0.00	0.58	1.09	6.63	6.92	76.32	0.00
0.06	0.01	0.67	0.55	7.72	7.71	88.91	0.00
0.07	0.02	0.78	0.44	9.00	7.74	103.58	0.00
0.08	0.05	0.91	0.25	10.48	7.15	120.67	0.00
0.09	0.11	1.06	0.29	12.21	6.01	140.58	0.00
0.11	0.24	1.24	0.42	14.22	4.55	163.77	0.00
0.13	0.49	1.44	0.61	16.57	3.04	190.80	0.00
0.15	0.91	1.68	0.84	19.31	1.74	222.28	0.00
0.17	1.53	1.95	1.16	22.49	0.81	258.95	0.00
0.20	2.32	2.28	1.55	26.20	0.26	301.68	0.00
0.23	3.12	2.65	2.03	30.53	0.00	351.46	0.00
0.27	3.63	3.09	2.64	35.56	0.00	409.45	0.00
0.31	3.58	3.60	3.39	41.43	0.00	477.01	0.00
0.36	3.11	4.19	4.23	48.27	0.00	555.71	0.00
0.42	2.49	4.88	5.14	56.23	0.00	647.41	0.00
0.49	1.80	5.69	6.05	65.51	0.00	754.23	0.00
0.58		6.63		76.32		878.67	

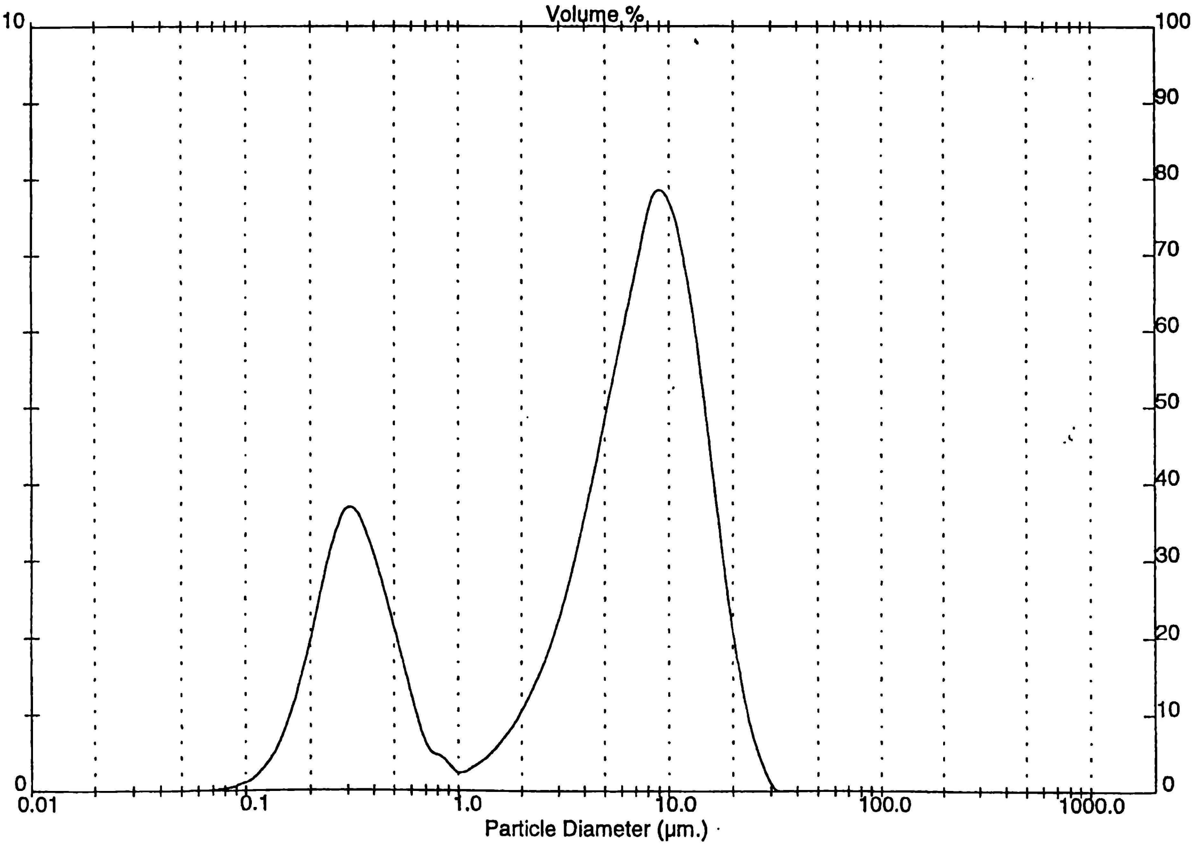

Figure A2.35 Particle size of YSZ after centrifugal milling for 5 hours.

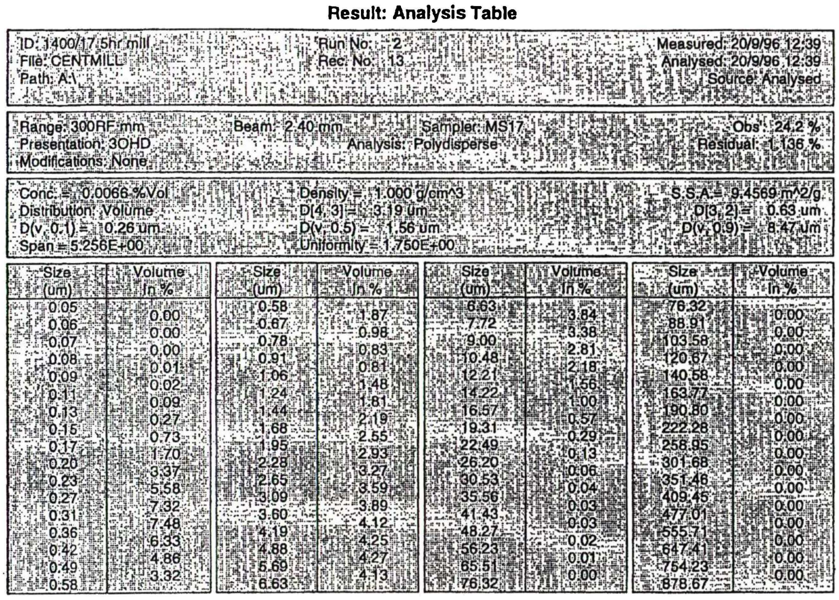

Result: Analysis Table

ID: 1400/17.5hr mill   Run No: 2   Measured: 20/9/96 12:39
File: CENTMILL   Rec. No: 13   Analysed: 20/9/96 12:39
Path: A:\   Source: Analysed

Range: 300RF mm   Beam: 2.40 mm   Sampler: MS17   Obs': 24.2 %
Presentation: 3OHD   Analysis: Polydisperse   Residual: 1.136 %
Modifications: None

Conc. = 0.0066 %Vol   Density = 1.000 g/cm^3   S.S.A.= 9.4569 m^2/g
Distribution: Volume   D[4, 3] = 3.19 um   D[3, 2] = 0.63 um
D(v, 0.1) = 0.26 um   D(v, 0.5) = 1.56 um   D(v, 0.9) = 8.47 um
Span = 5.256E+00   Uniformity = 1.750E+00

Size (um)	Volume In %	Size (um)	Volume In %	Size (um)	Volume In %	Size (um)	Volume In %
0.05	0.00	0.58	1.87	6.63	3.84	76.32	0.00
0.06	0.00	0.67	0.98	7.72	3.38	88.91	0.00
0.07	0.00	0.78	0.83	9.00	2.81	103.58	0.00
0.08	0.01	0.91	0.81	10.48	2.18	120.67	0.00
0.09	0.02	1.06	1.48	12.21	1.56	140.58	0.00
0.11	0.09	1.24	1.81	14.22	1.00	163.77	0.00
0.13	0.27	1.44	2.19	16.57	0.57	190.80	0.00
0.15	0.73	1.68	2.55	19.31	0.29	222.28	0.00
0.17	1.70	1.95	2.93	22.49	0.13	258.95	0.00
0.20	3.37	2.28	3.27	26.20	0.06	301.68	0.00
0.23	5.58	2.65	3.59	30.53	0.04	351.46	0.00
0.27	7.32	3.09	3.89	35.56	0.03	409.45	0.00
0.31	7.48	3.60	4.12	41.43	0.03	477.01	0.00
0.36	6.33	4.19	4.25	48.27	0.02	555.71	0.00
0.42	4.86	4.88	4.27	56.23	0.01	647.41	0.00
0.49	3.32	5.69	4.13	65.51	0.00	754.23	0.00
0.58		6.63		76.32		878.67	

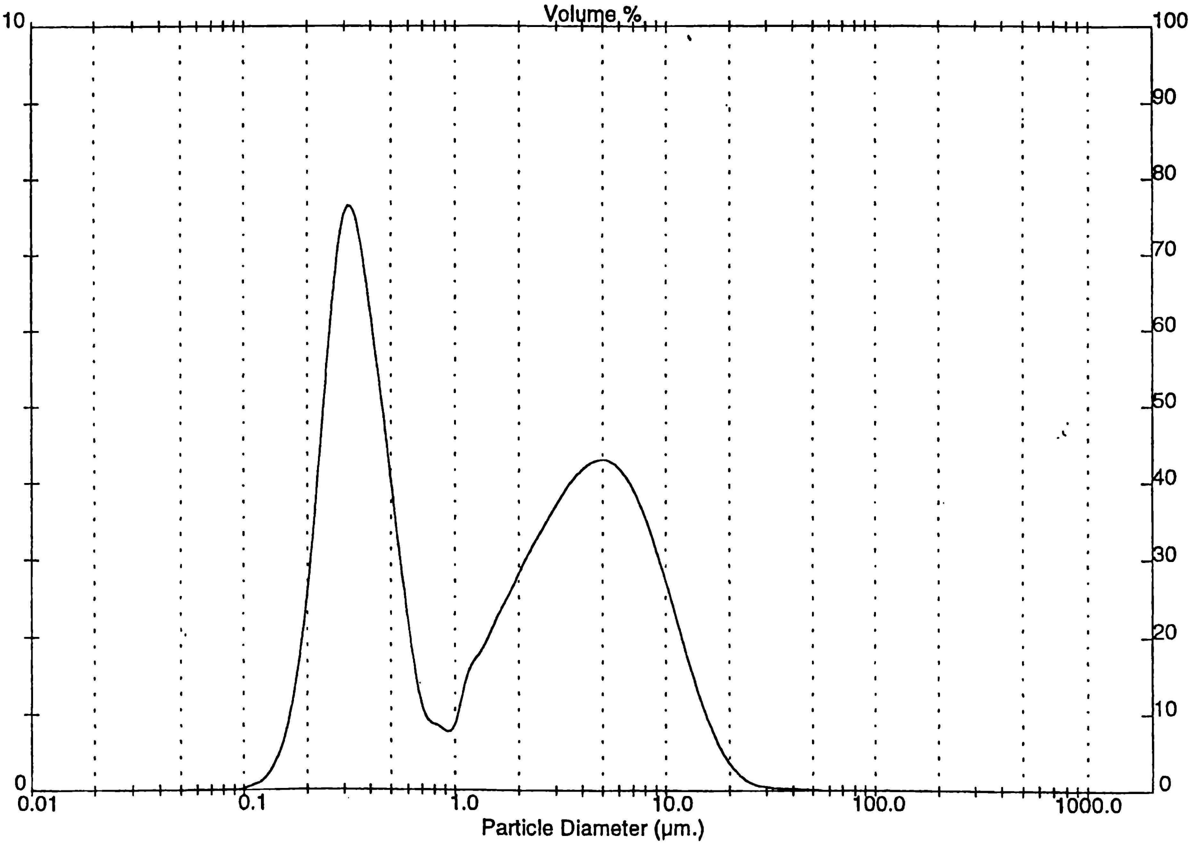

Figure A2.36 Particle size of YSZ after centrifugal milling for 7 hours.

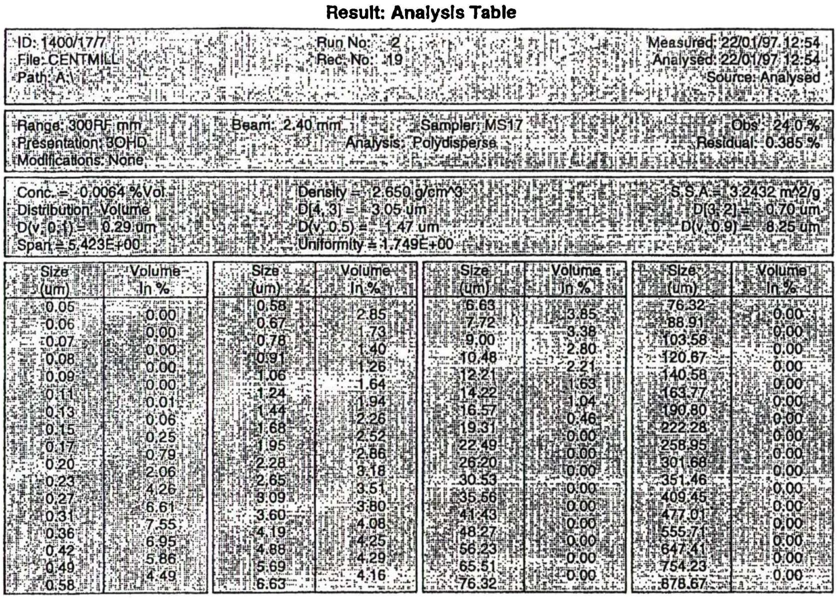

Result: Analysis Table

ID: 1400/17/7 Run No: 2 Measured: 22/01/97 12:54
File: CENTMILL Rec. No: 19 Analysed: 22/01/97 12:54
Path: A:\ Source: Analysed

Range: 300RF mm Beam: 2.40 mm Sampler: MS17 Obs': 24.0 %
Presentation: 3OHD Analysis: Polydisperse Residual: 0.385 %
Modifications: None

Conc. = 0.0064 %Vol Density = 2.650 g/cm^3 S.S.A.= 3.2432 m^2/g
Distribution: Volume D[4, 3] = 3.05 um D[3, 2] = 0.70 um
D(v, 0.1) = 0.29 um D(v, 0.5) = 1.47 um D(v, 0.9) = 8.25 um
Span = 5.423E+00 Uniformity = 1.749E+00

Size (um)	Volume In %	Size (um)	Volume In %	Size (um)	Volume In %	Size (um)	Volume In %
0.05	0.00	0.58	2.85	6.63	3.85	76.32	0.00
0.06	0.00	0.67	1.73	7.72	3.38	88.91	0.00
0.07	0.00	0.78	1.40	9.00	2.80	103.58	0.00
0.08	0.00	0.91	1.26	10.48	2.21	120.67	0.00
0.09	0.00	1.06	1.64	12.21	1.63	140.58	0.00
0.11	0.01	1.24	1.94	14.22	1.04	163.77	0.00
0.13	0.06	1.44	2.26	16.57	0.46	190.80	0.00
0.15	0.25	1.68	2.52	19.31	0.00	222.28	0.00
0.17	0.79	1.95	2.86	22.49	0.00	258.95	0.00
0.20	2.06	2.28	3.18	26.20	0.00	301.68	0.00
0.23	4.26	2.65	3.51	30.53	0.00	351.46	0.00
0.27	6.61	3.09	3.80	35.56	0.00	409.45	0.00
0.31	7.55	3.60	4.08	41.43	0.00	477.01	0.00
0.36	6.95	4.19	4.25	48.27	0.00	555.71	0.00
0.42	5.86	4.88	4.29	56.23	0.00	647.41	0.00
0.49	4.49	5.69	4.16	65.51	0.00	754.23	0.00
0.58		6.63		76.32		878.67	

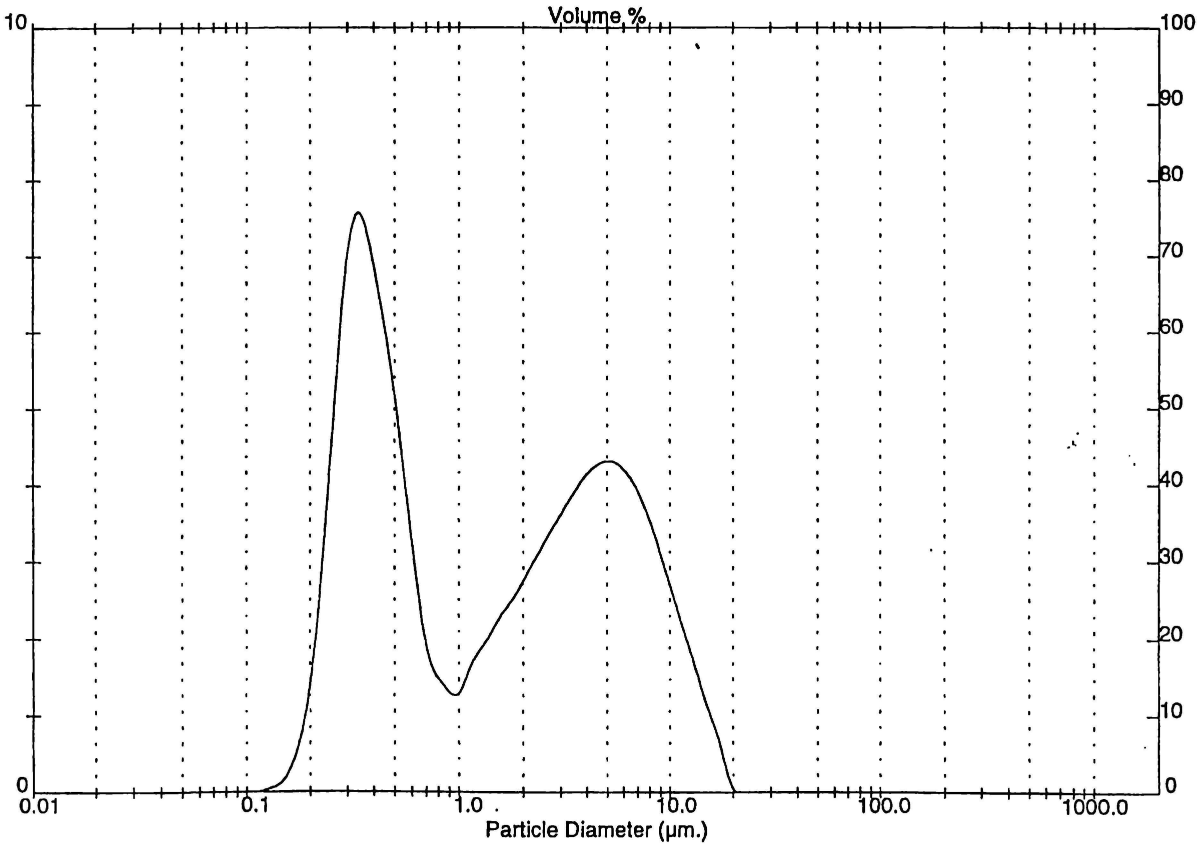

Appendix 3

Scanning Electron Microscopy Study

Scanning electron micrographs of YSZ and NiO after milling for various times, showing the structures encountered.

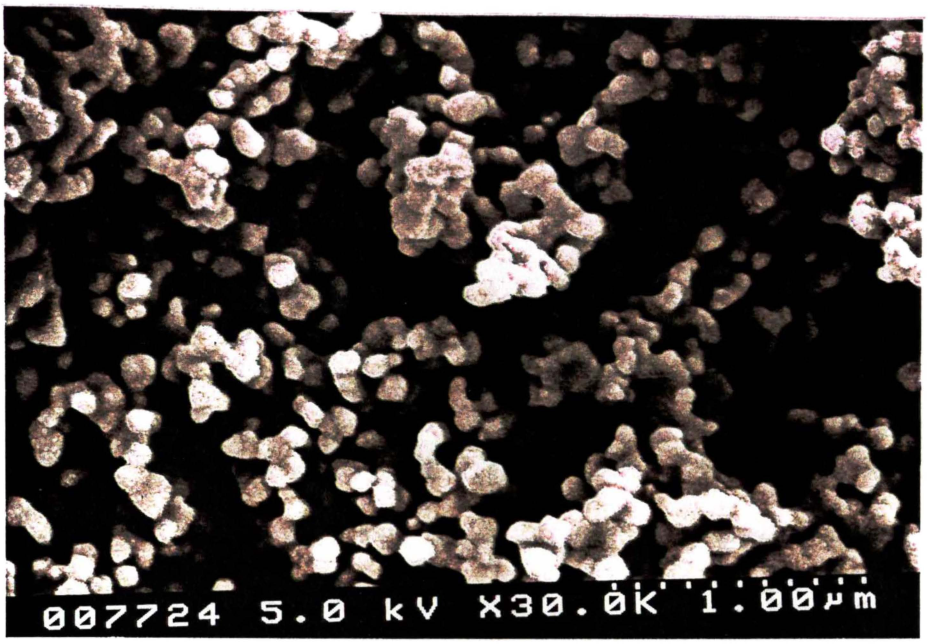

Figure A3.1 SEM Micrograph of individual YSZ particles.

Figure A3.2 SEM micrograph of YSZ sintered at 1400 °C after centrifugal milling for 45 mins.

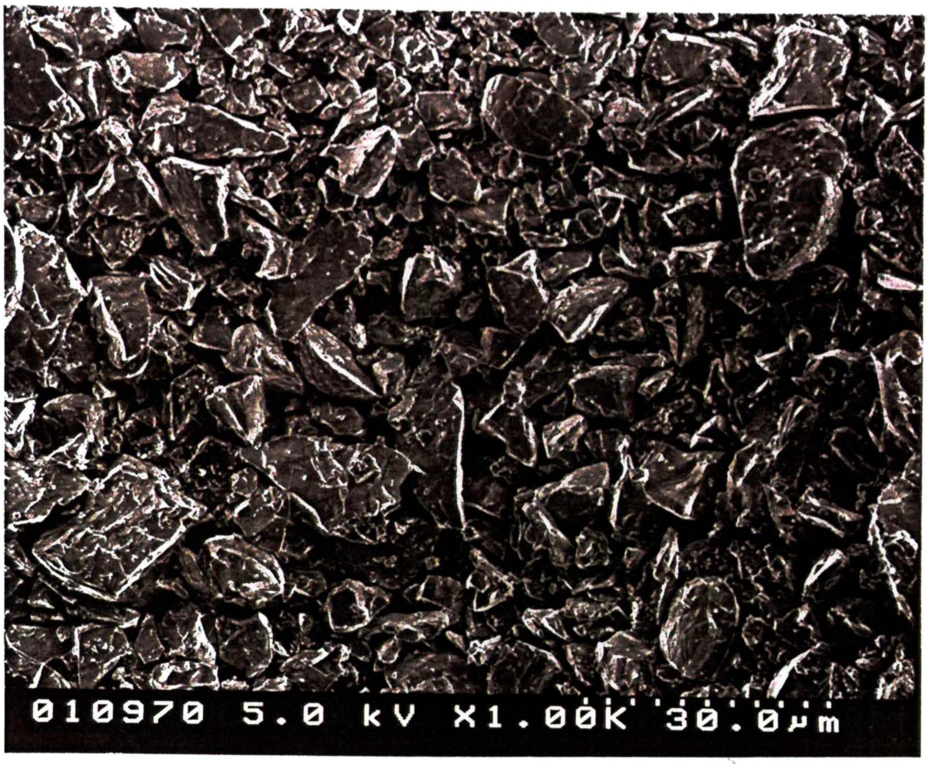

Figure A3.3 SEM micrograph of YSZ sintered at 1400 °C after centrifugal milling for 1 hour.

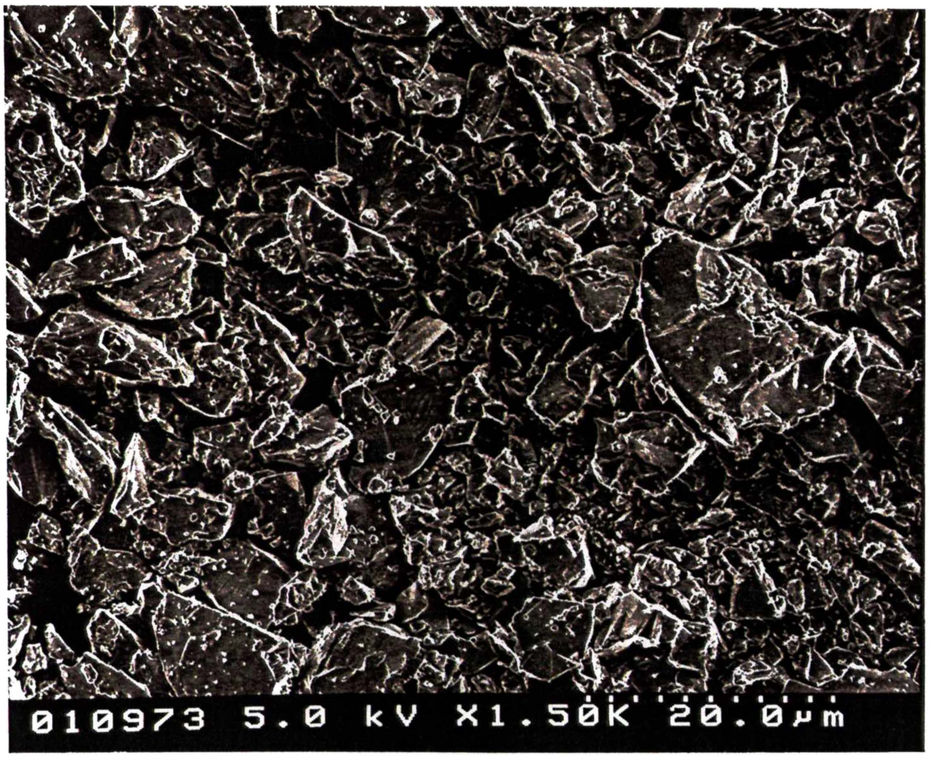

Figure A3.4 SEM micrograph of YSZ sintered at 1400 °C after centrifugal milling for 3 hours.

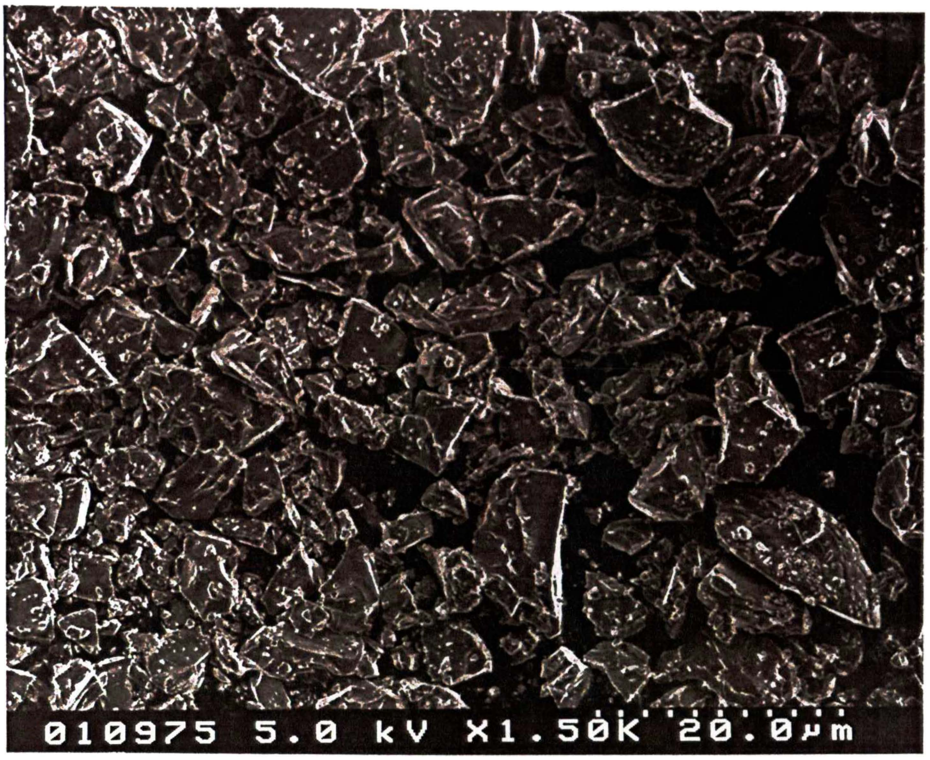

Figure A3.5 SEM micrograph of YSZ sintered at 1400 °C after centrifugal milling for 5 hours.

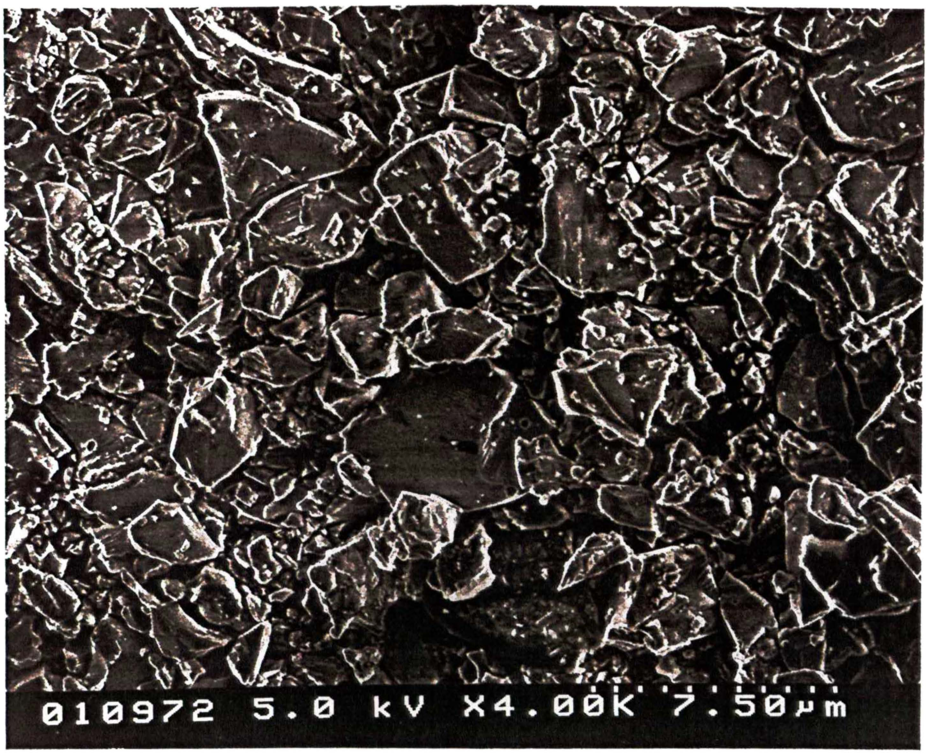

Figure A3.6 SEM micrograph of YSZ sintered at 1400 °C after centrifugal milling for 7 hours.

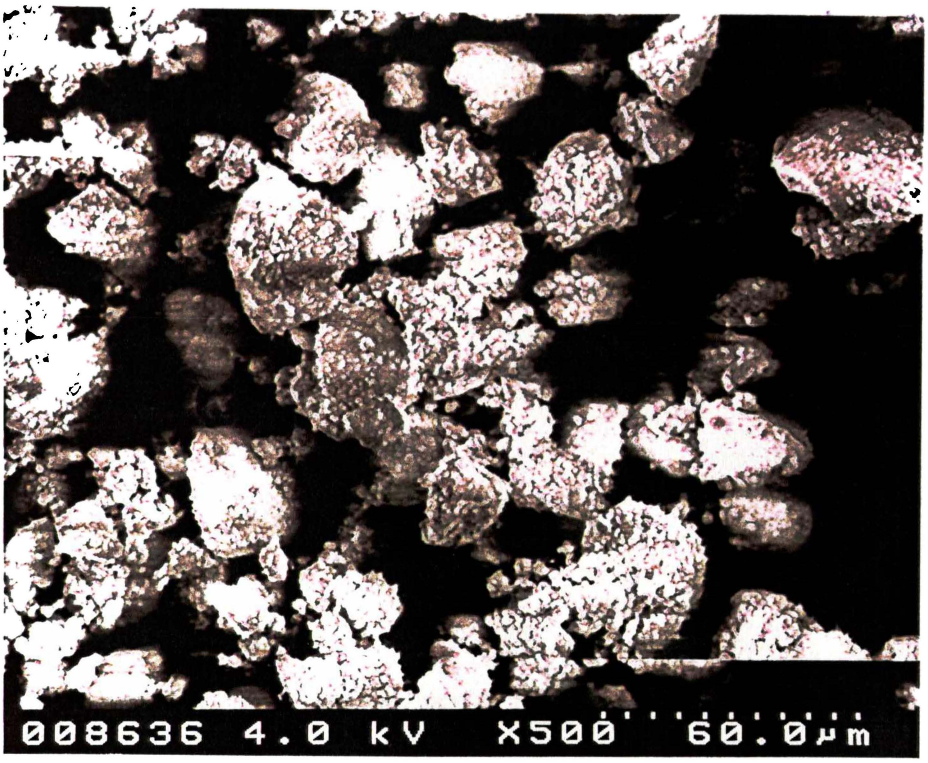

Figure A3.7 SEM micrograph of YSZ sintered at 1100 °C after ball milling for 4.5 hours.

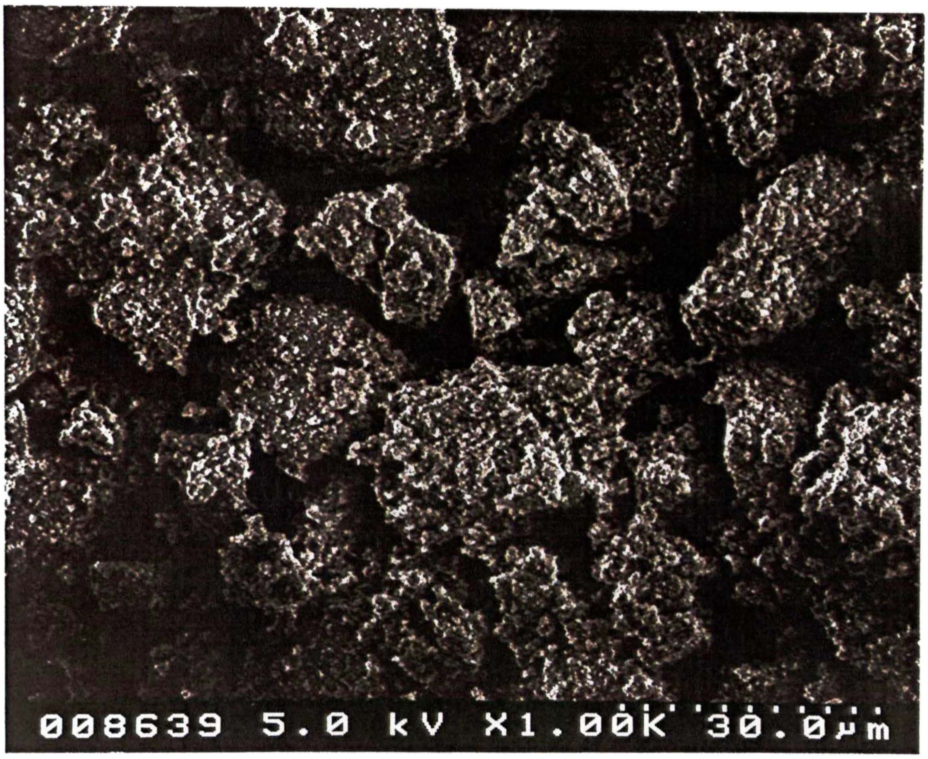

Figure A3.8 SEM micrograph of YSZ sintered at 1100 °C after ball milling for 6 hours.

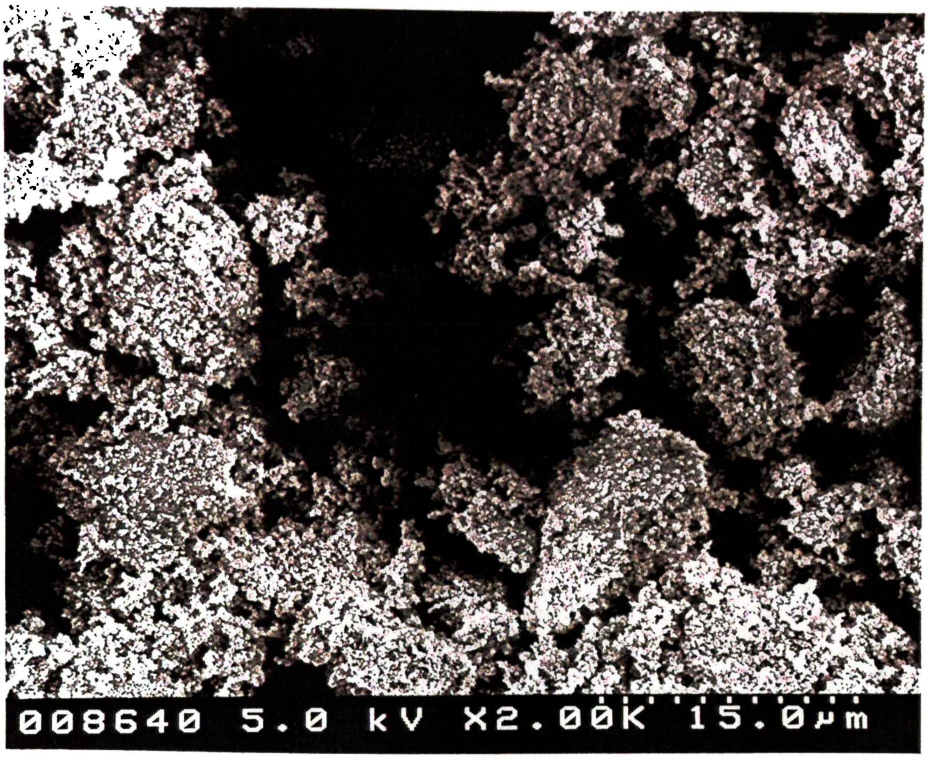

Figure A3.9 SEM micrograph of YSZ sintered at 1100 °C after ball milling for 10 hours.

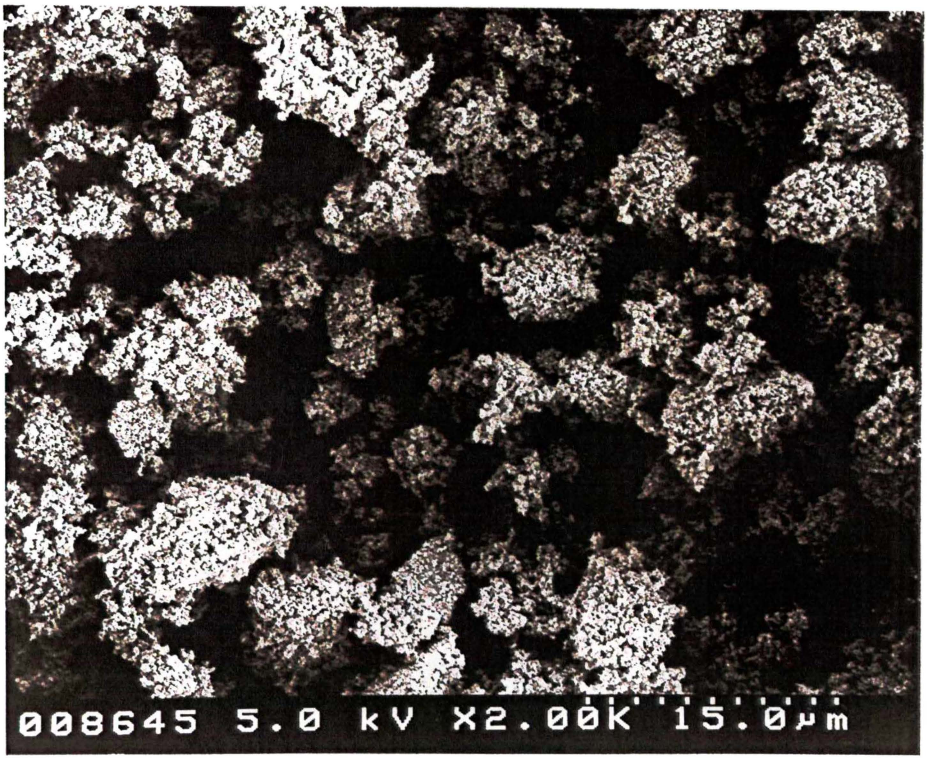

Figure A3.10 SEM micrograph of YSZ sintered at 1100 °C after ball milling for 15 hours.

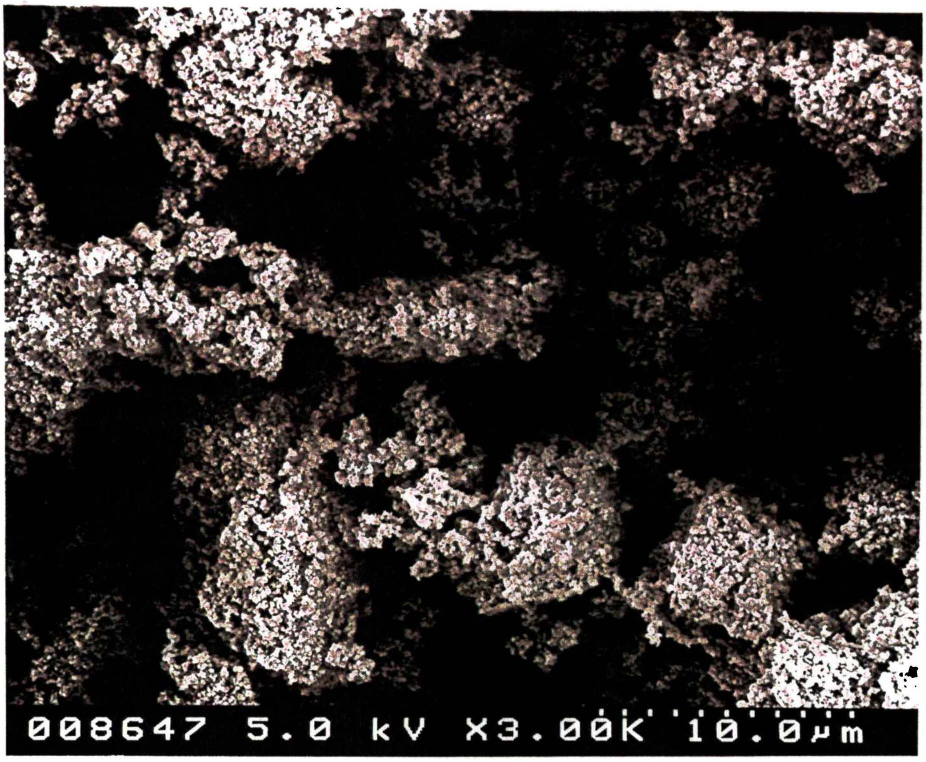

Figure A3.11 SEM micrograph of YSZ sintered at 1100 °C after ball milling for 22 hours.

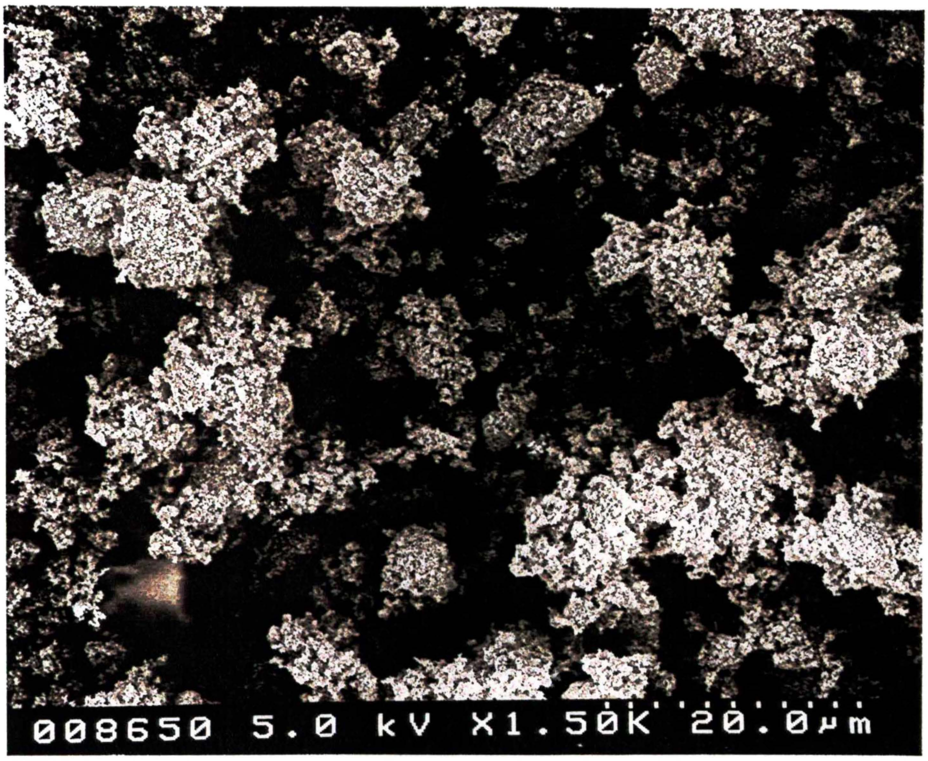

Figure A3.12 SEM micrograph of YSZ sintered at 1100 °C after ball milling for 26 hours.

Appendix 4

Optical Microscopy Study

Optical micrographs of the anodes fabricated illustrating morphological properties.

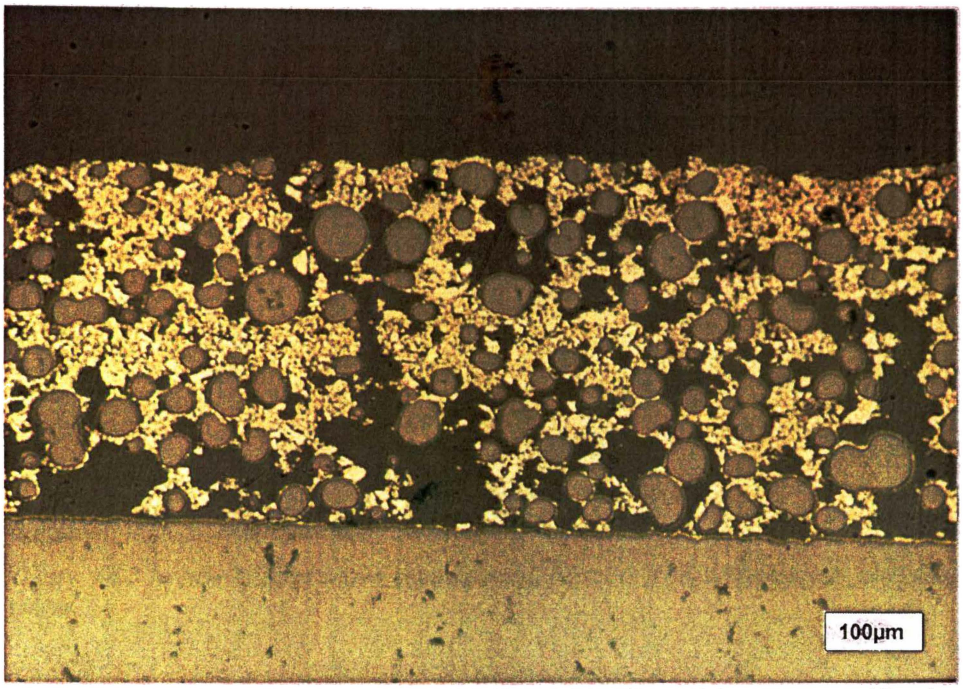

Figure A4.1 Anode #1 illustrating large YSZ and fine Ni particles at a magnification of 100x.

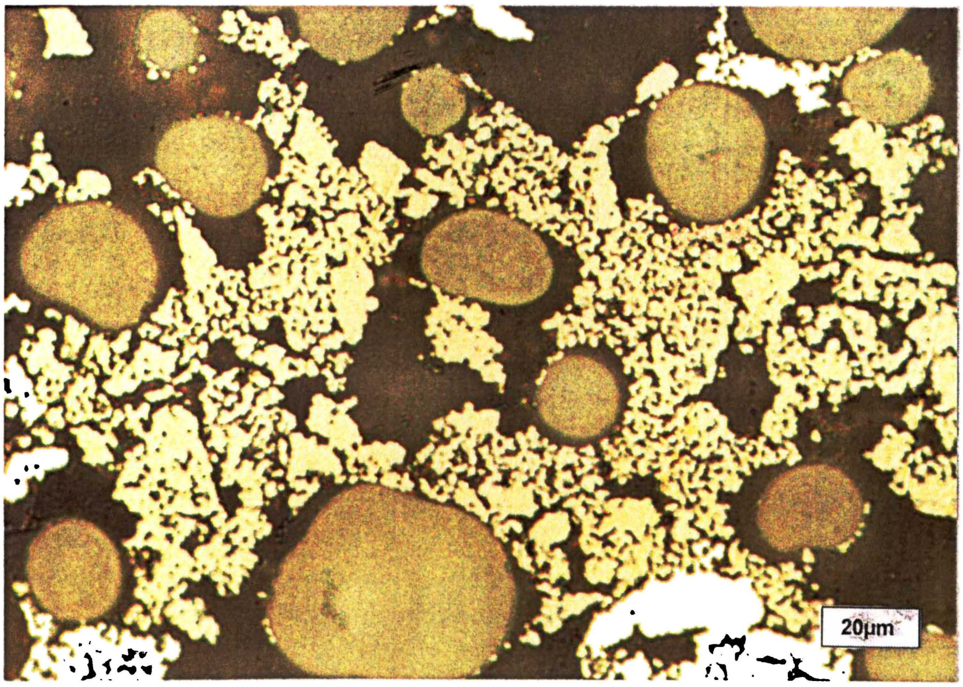

Figure A4.2 Anode #1 illustrating sintering of Ni particles around YSZ at a magnification of 500x.

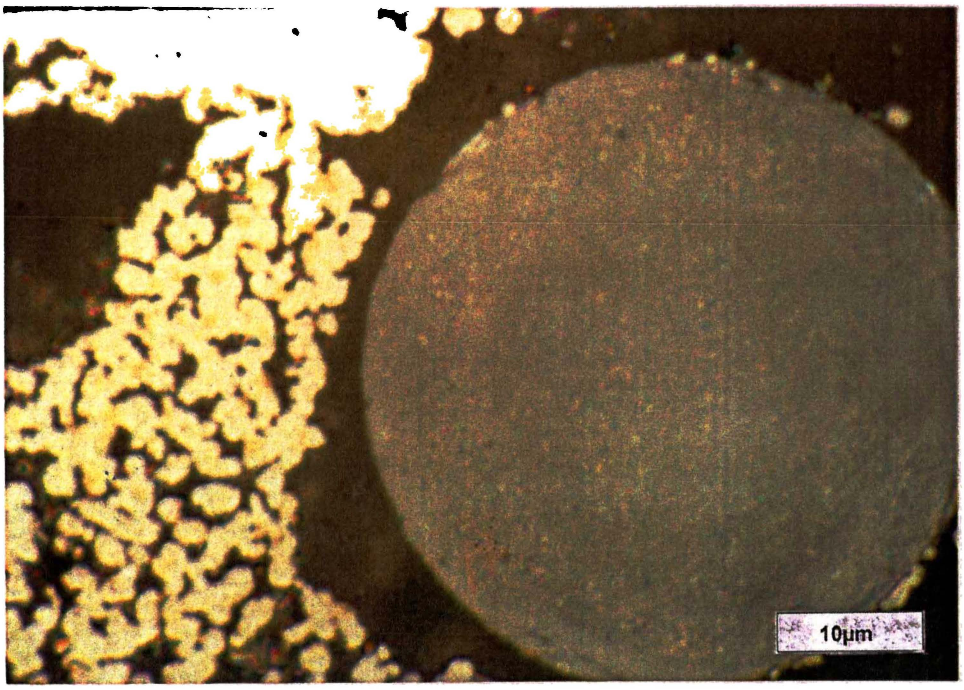

Figure A4.3 Anode #1 illustrating separation of Ni from YSZ agglomerate, magnification of 1500x.

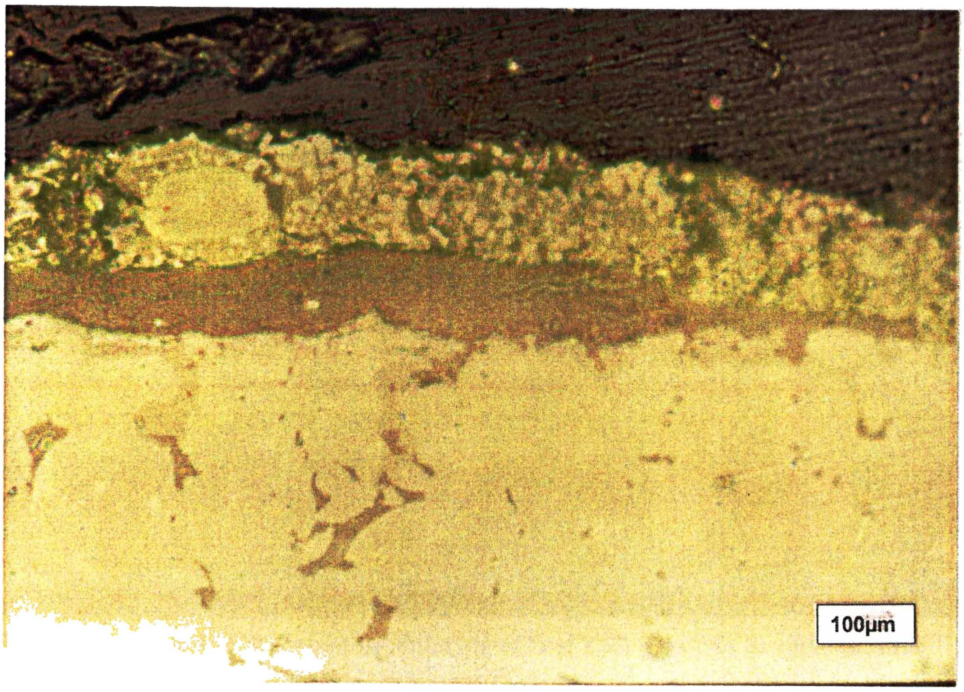

Figure A4.4 Illustration of spalling of the sintered anode layer at a magnification of 100x.

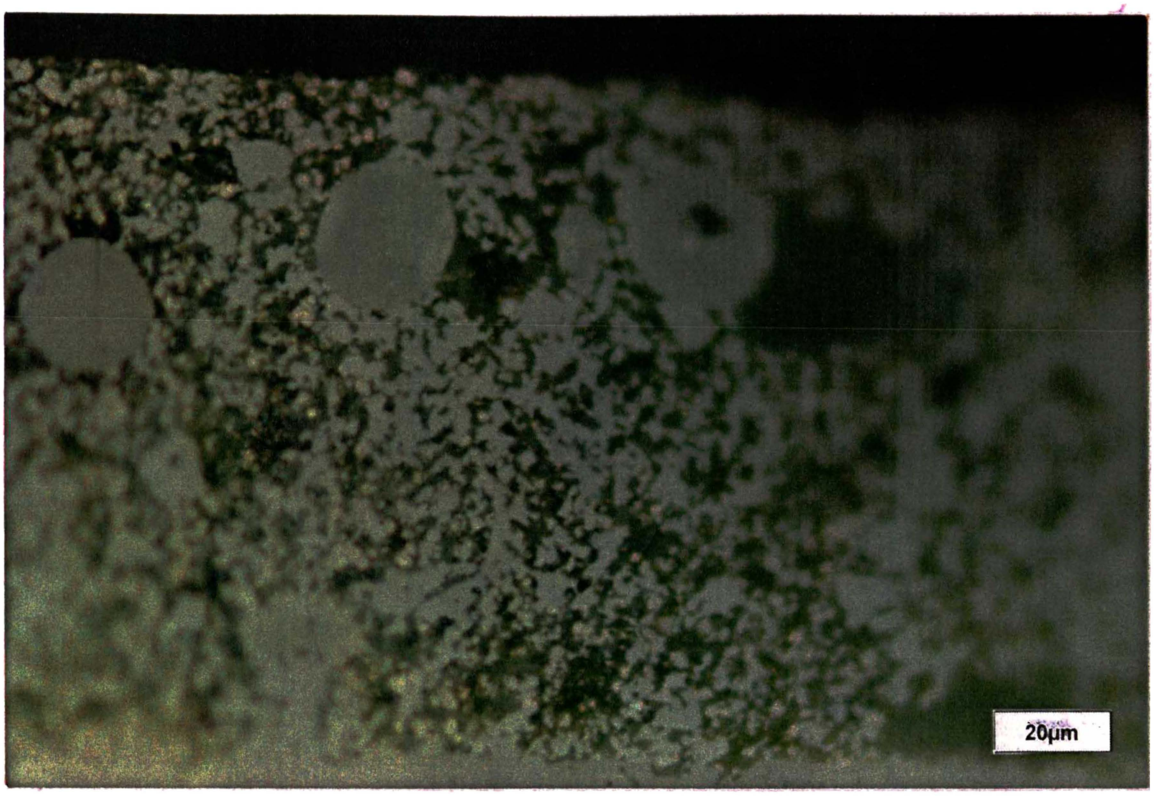

Figure A4.5 Anode #2 illustrating sintering of NiO and YSZ. Magnification of 500x.

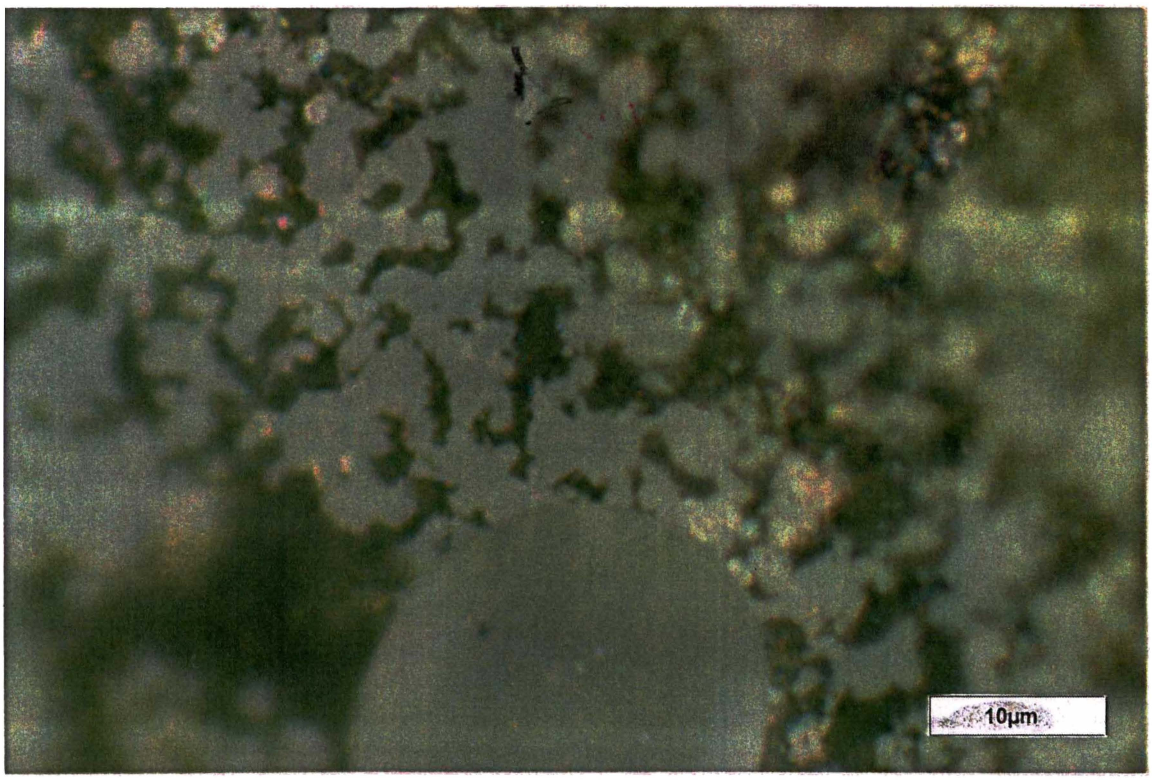

Figure A4.6 Anode #2 illustrating sintering of fine YSZ particles to agglomerates. Magnification of 1500x.

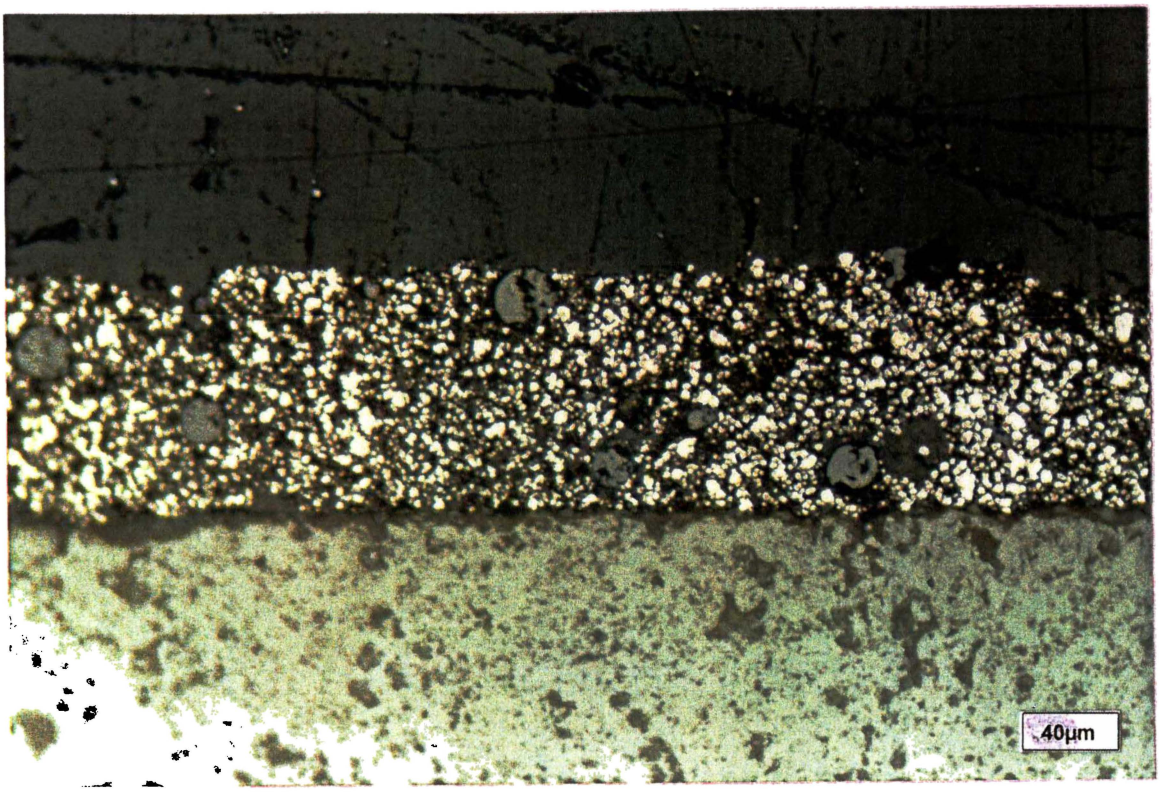

Figure A4.7 Anode #2 after reduction in H_2 at a magnification of 200x.

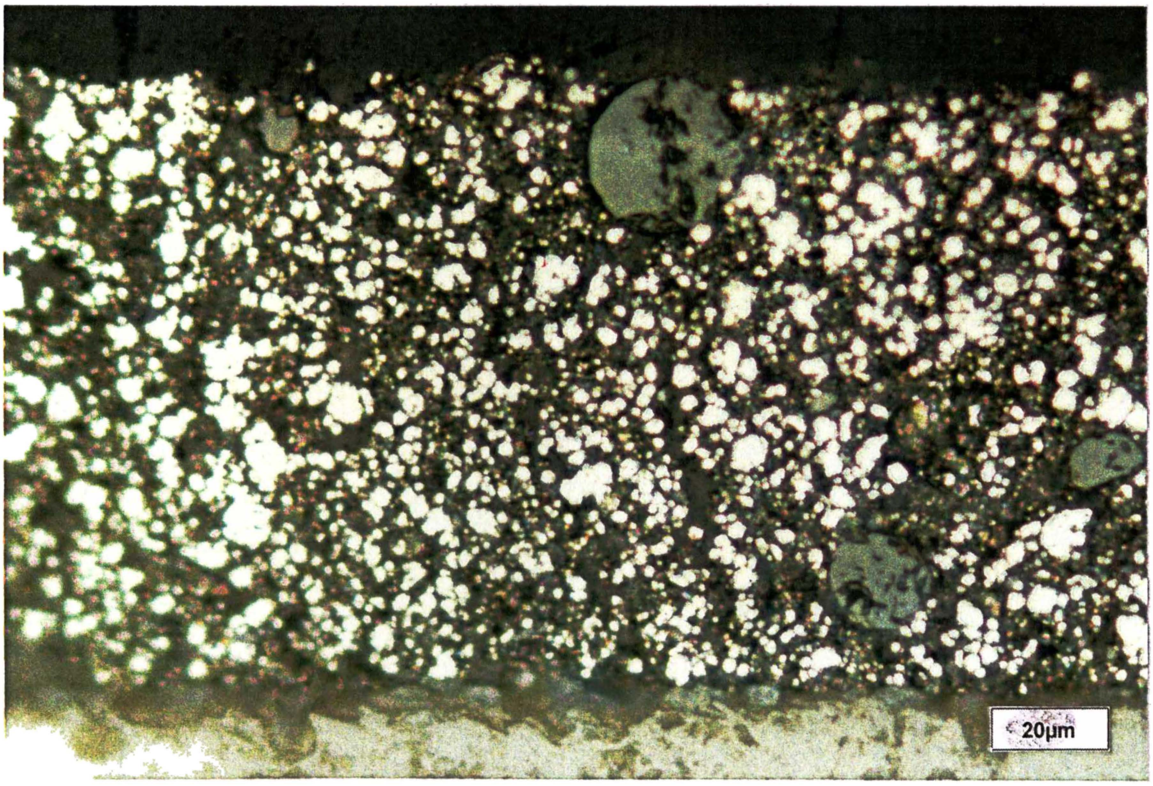

Figure A4.8 Anode #2 illustrating the Ni particle sintering at a magnification of 500x.

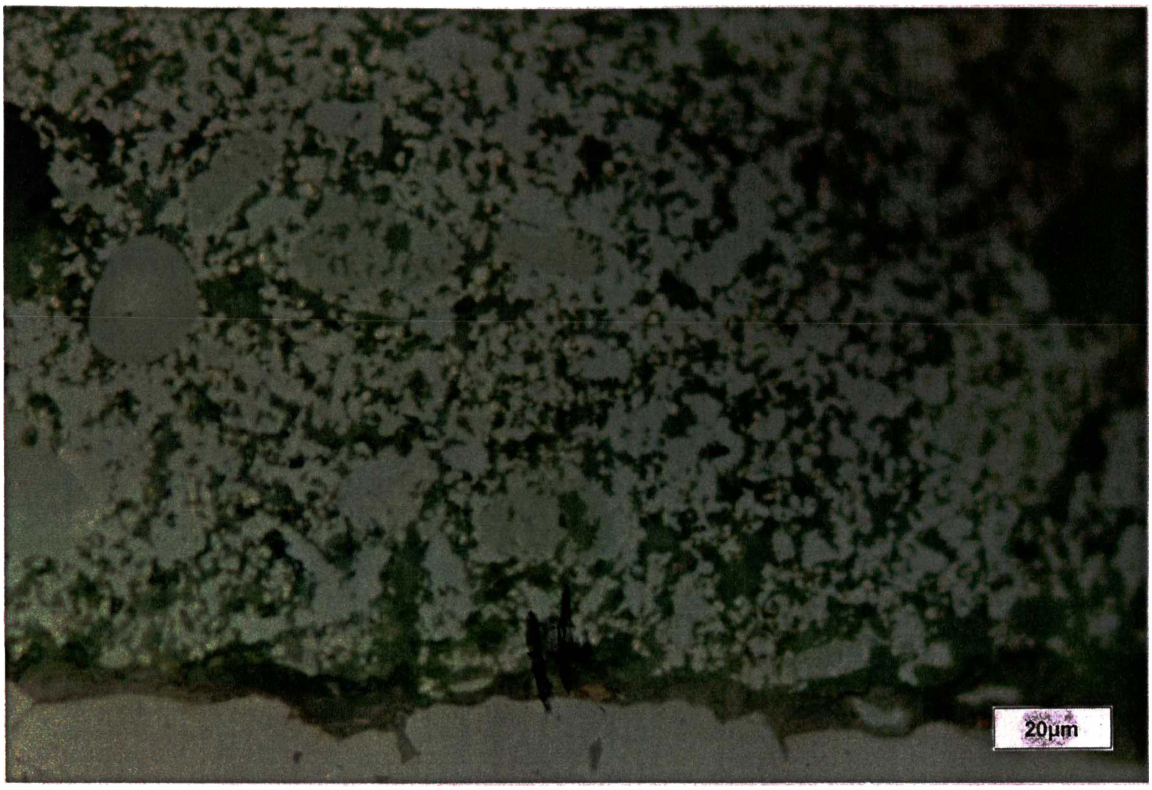

Figure A4.9 Anode #3 illustrating sintered layer at a magnification of 500x.

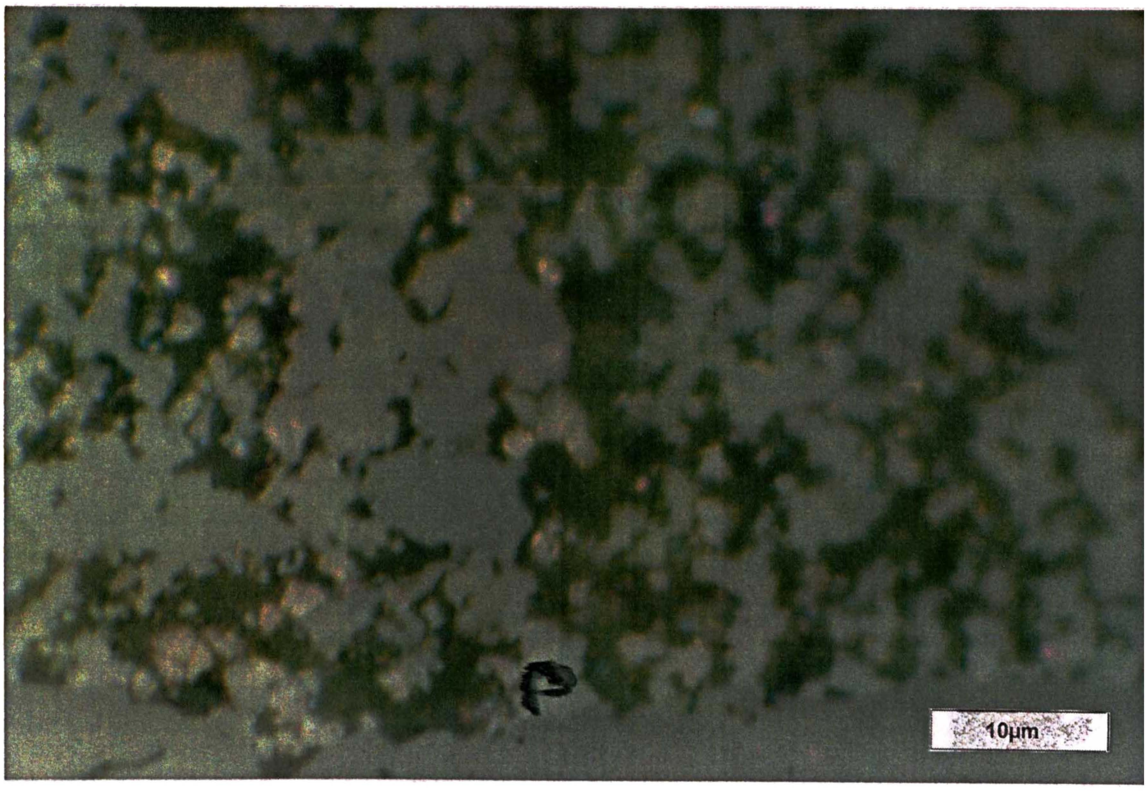

Figure A4.10 Anode #3 illustrating sintering of layer at a magnification of 1500x.

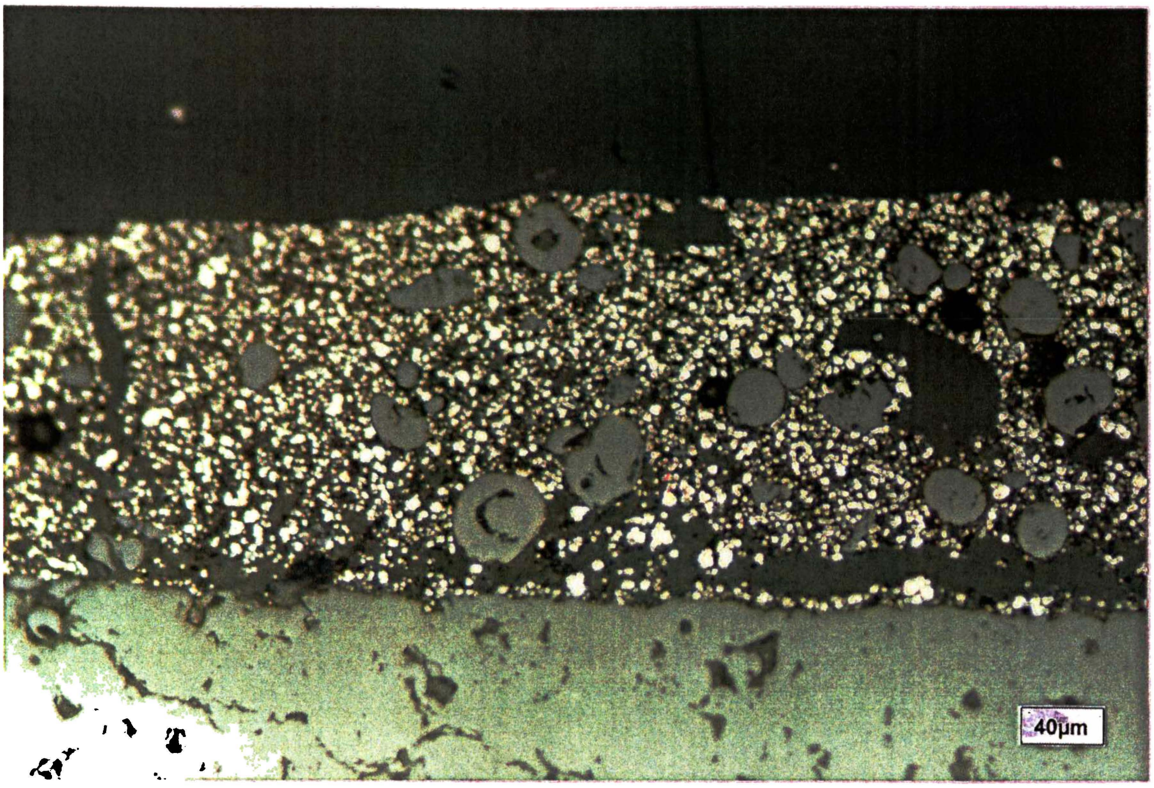

Figure A4.11 Anode #3 illustrating porosity of reduced layer at a magnification of 200x.

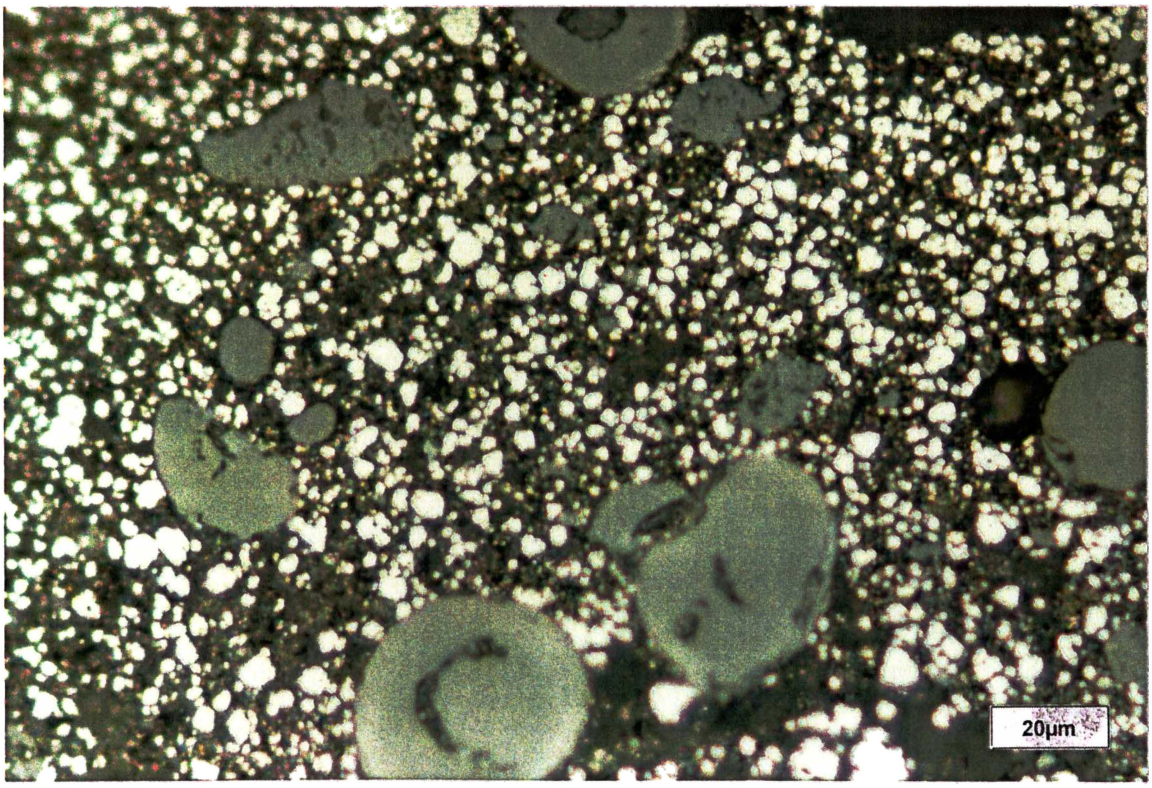

Figure A4.12 Anode #3 illustrating Ni and YSZ agglomerates at a magnification of 500x.

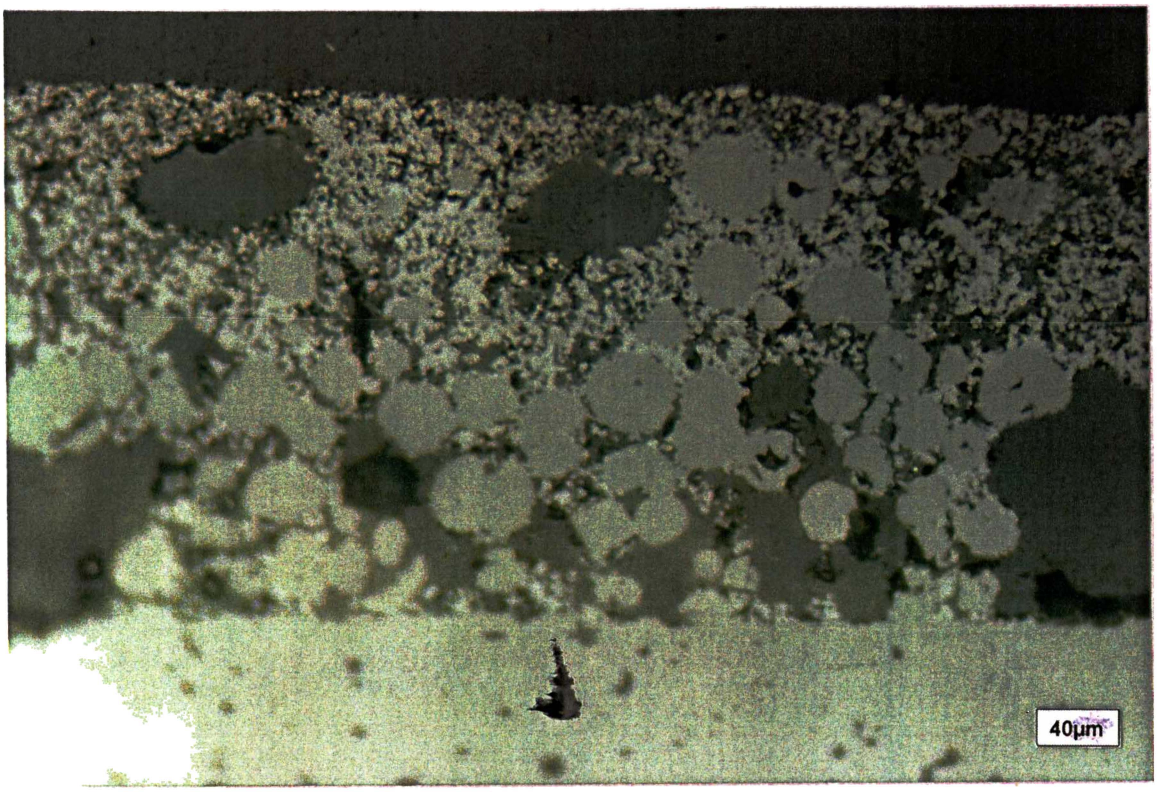

Figure A4.13 Anode #4 illustrating layering of YSZ agglomerates at a magnification of 200x.

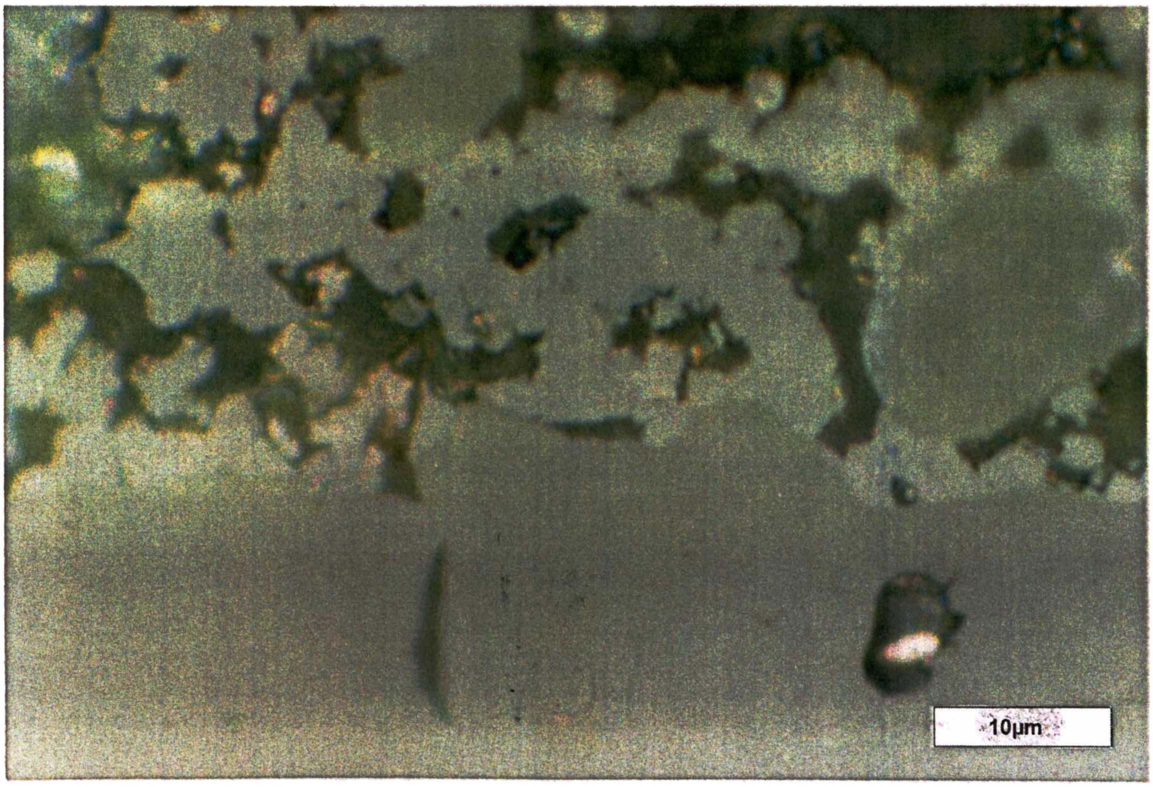

Figure A4.14 Anode #4 illustrating anode/electrolyte interface at a magnification of 1500x.

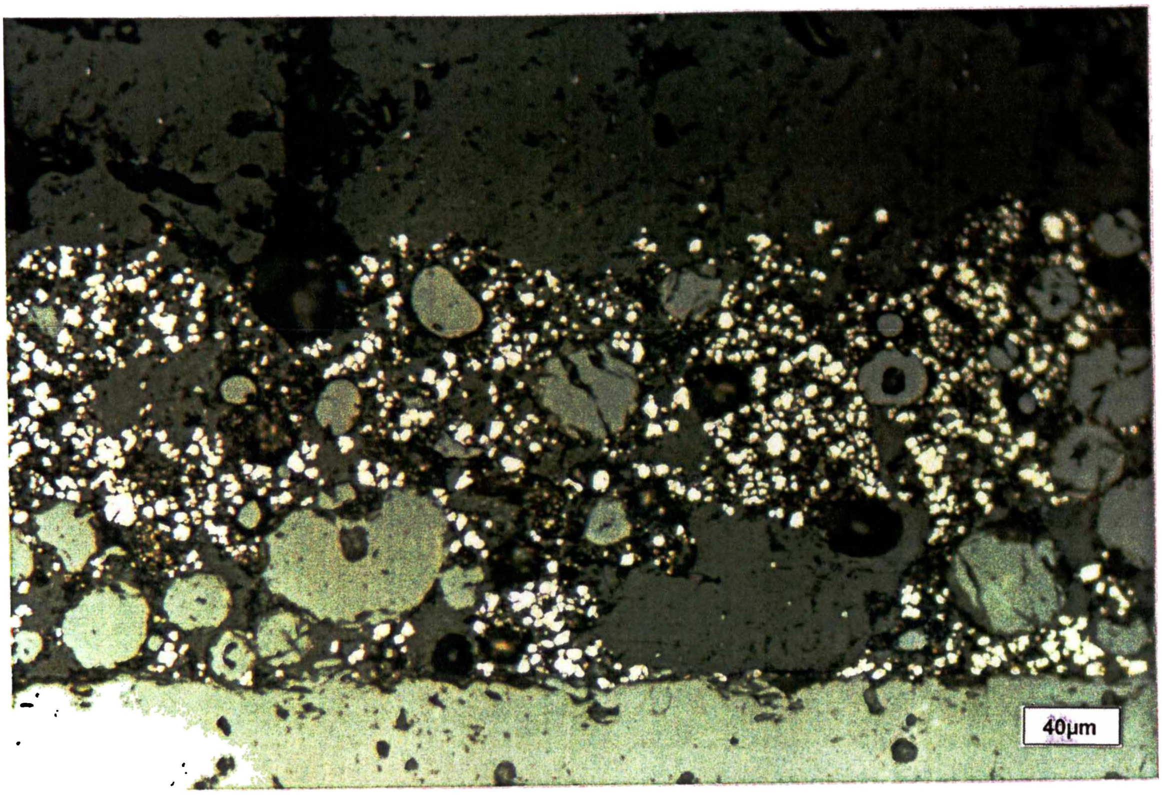

Figure A4.15 Anode #4 with high porosity of the reduced layer at a magnification of 200x.

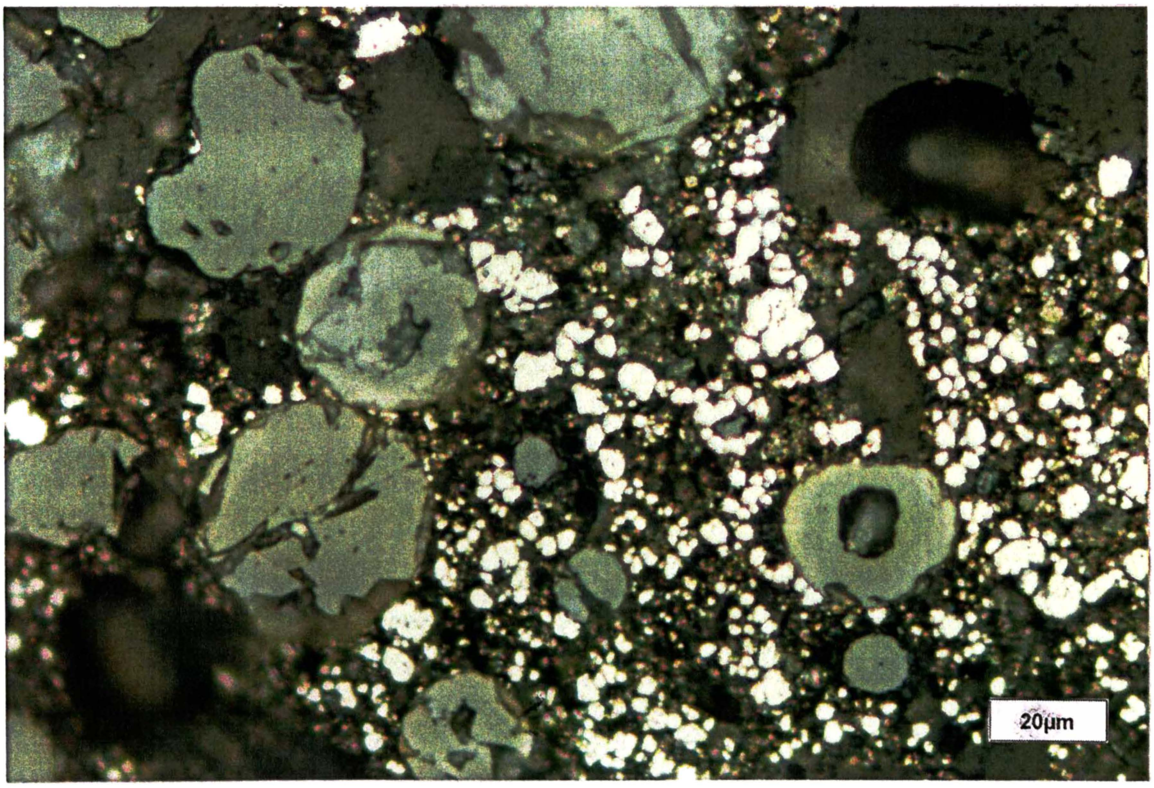

Figure A4.16 Anode #4 illustrating very high porosity at a magnification of 500x.

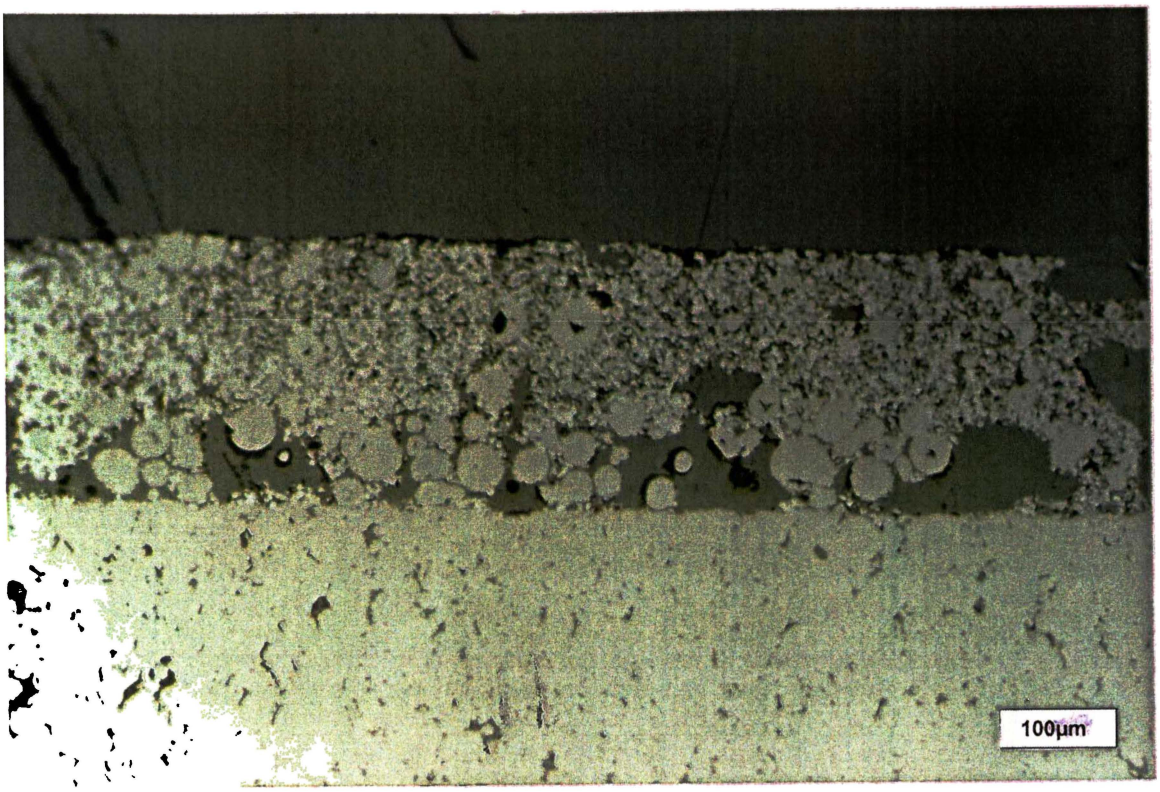

Figure A4.17 Anode #5 illustrating layering of YSZ agglomerates at a magnification of 100x.

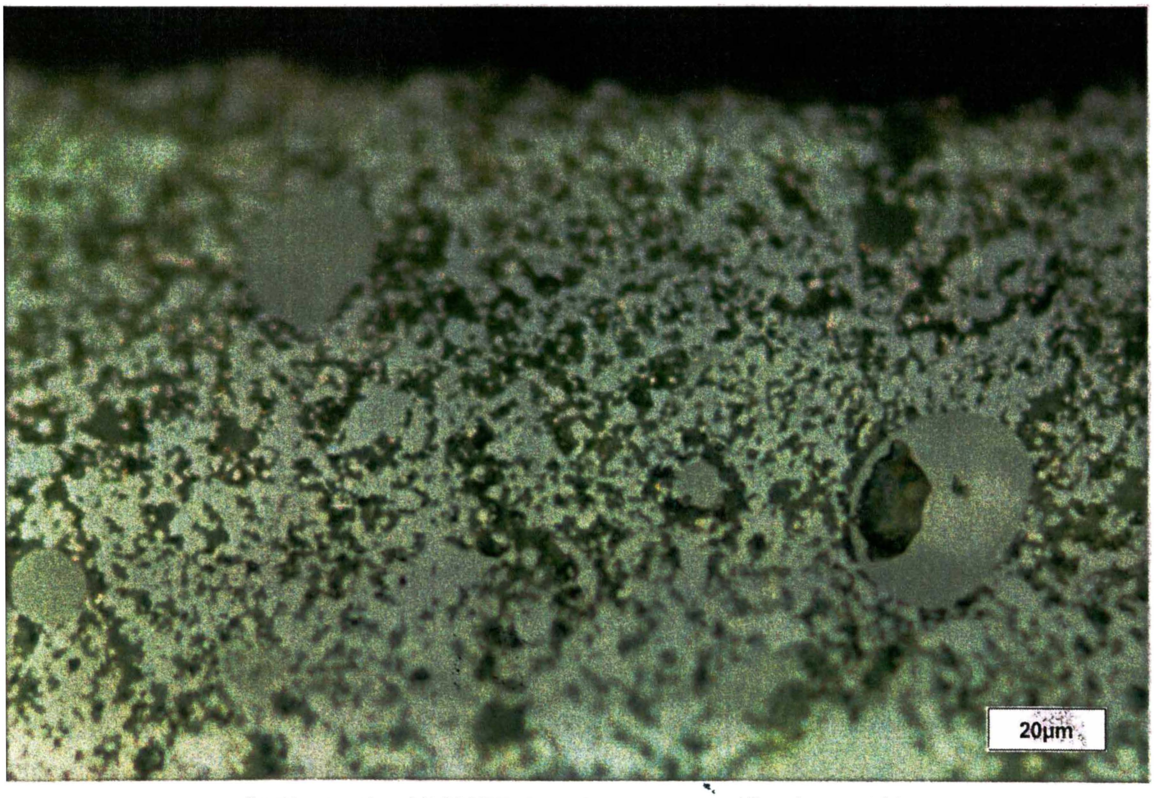

Figure A4.18 Anode #5 illustrating NiOYSZ sintering at a magnification of 500x.

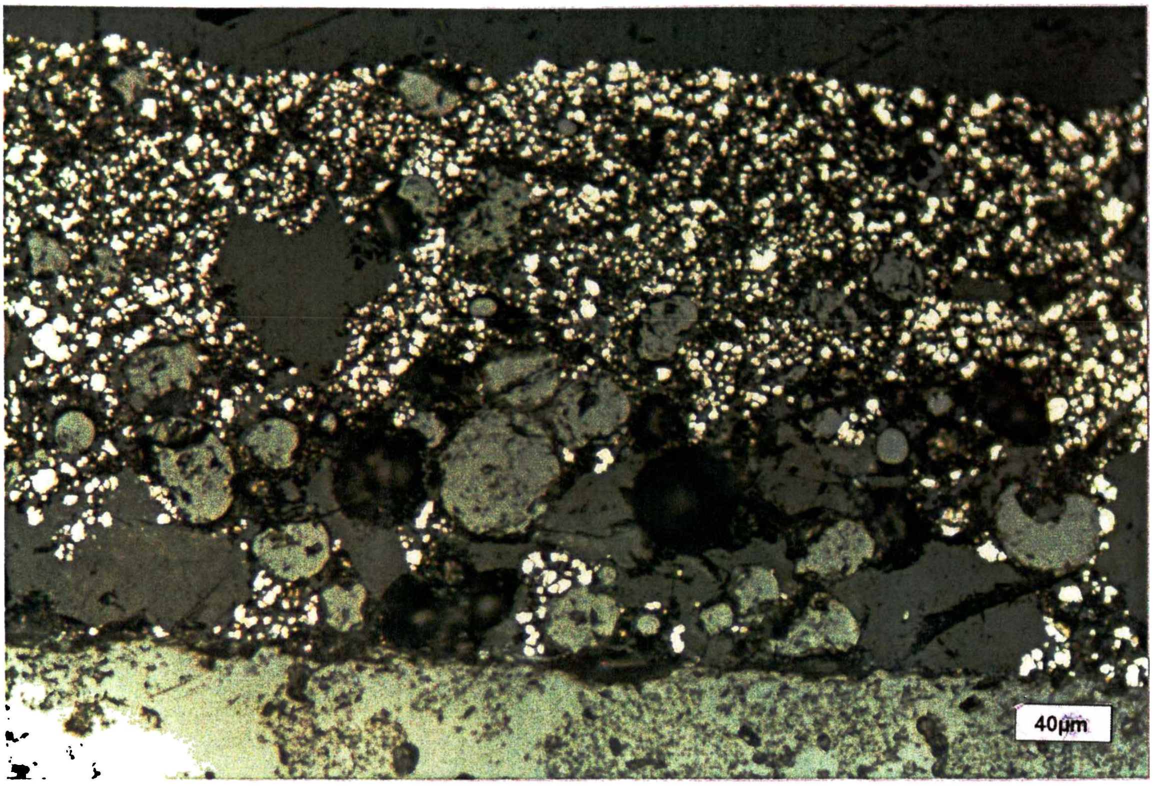

Figure A4.19 Anode #5 illustrating layering of YSZ agglomerates at a magnification of 200x.

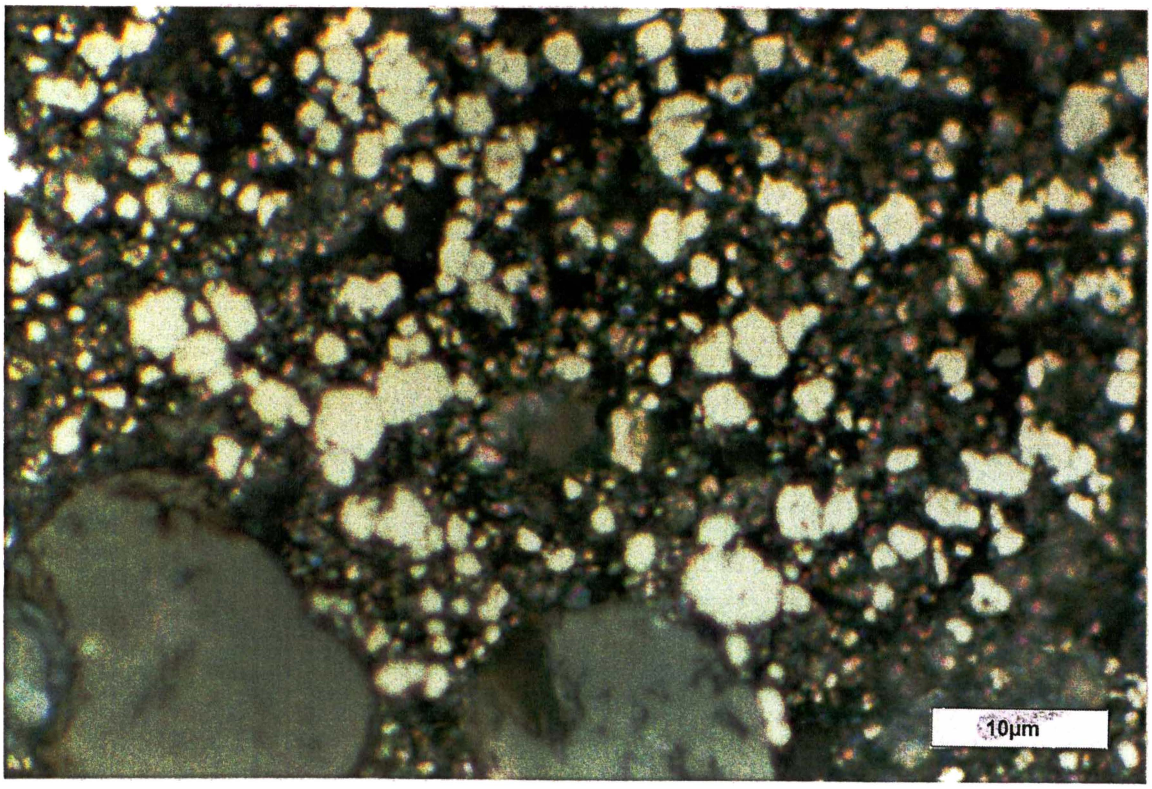

Figure A4.20 Anode #5 illustrating reduced layer with high porosity at a magnification of1500x.

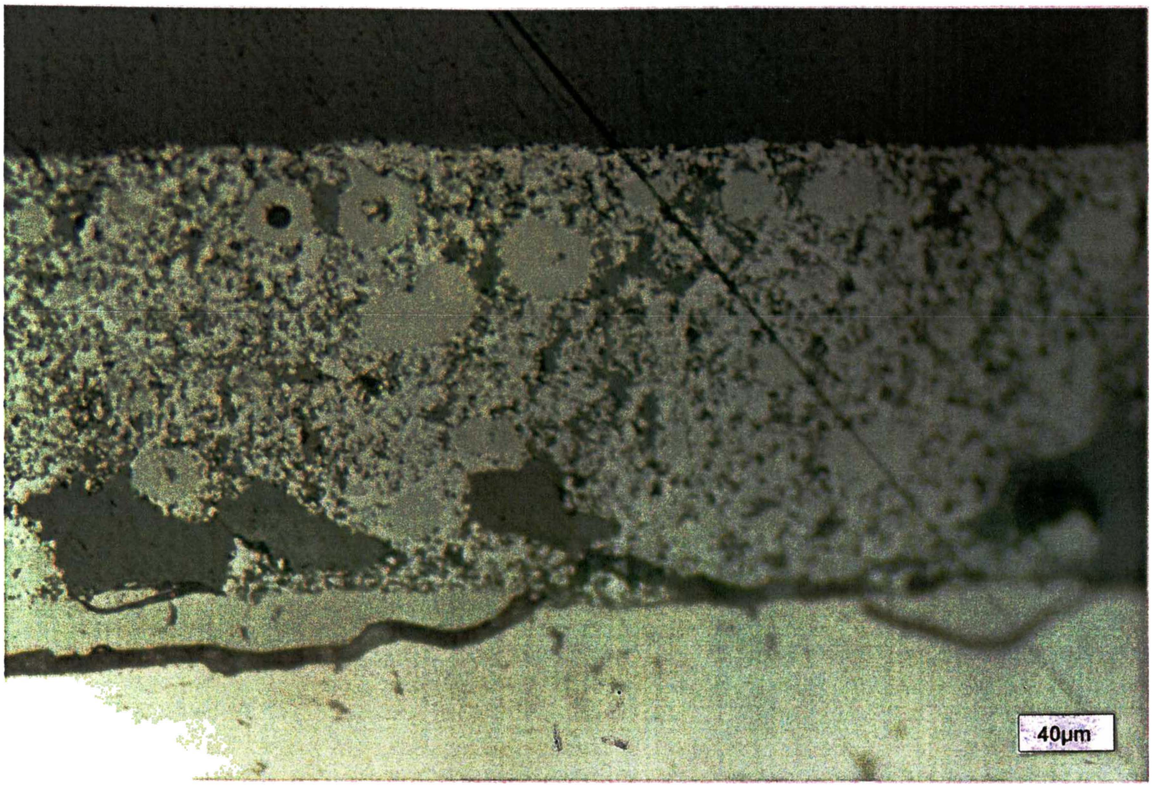

Figure A4.21 Anode #6 illustrating porosity at the interface, at a magnification of 200x.

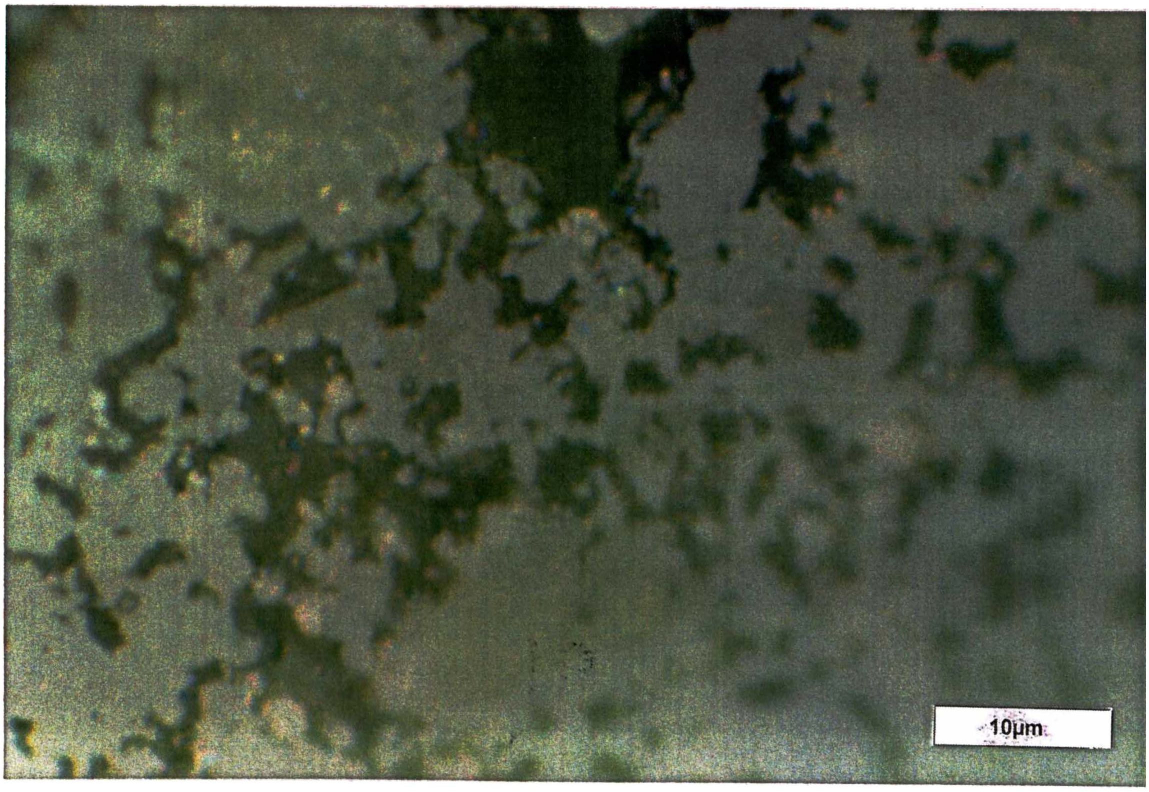

Figure A4.22 Anode #6 illustrating Nio/Ysz sintering at a magnification of 1500x.

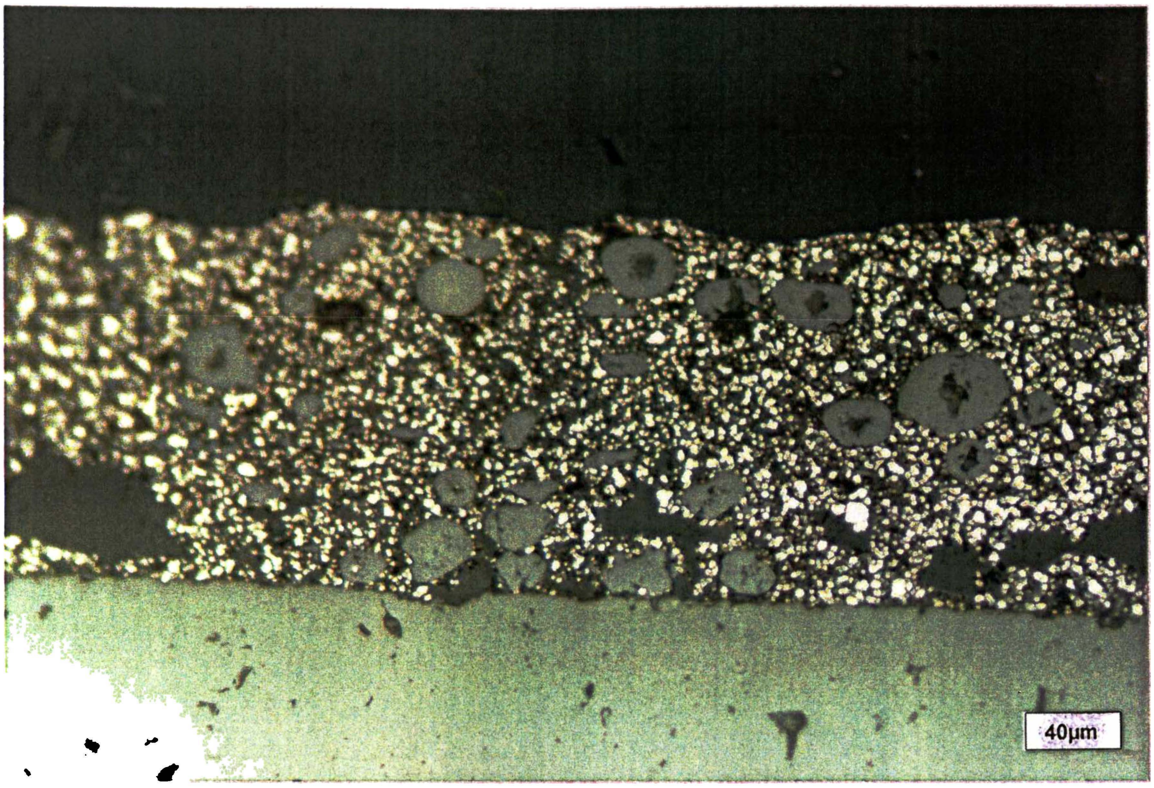

Figure A4.23 Anode #6 illustrating large voids at interface, at a magnification of 200x.

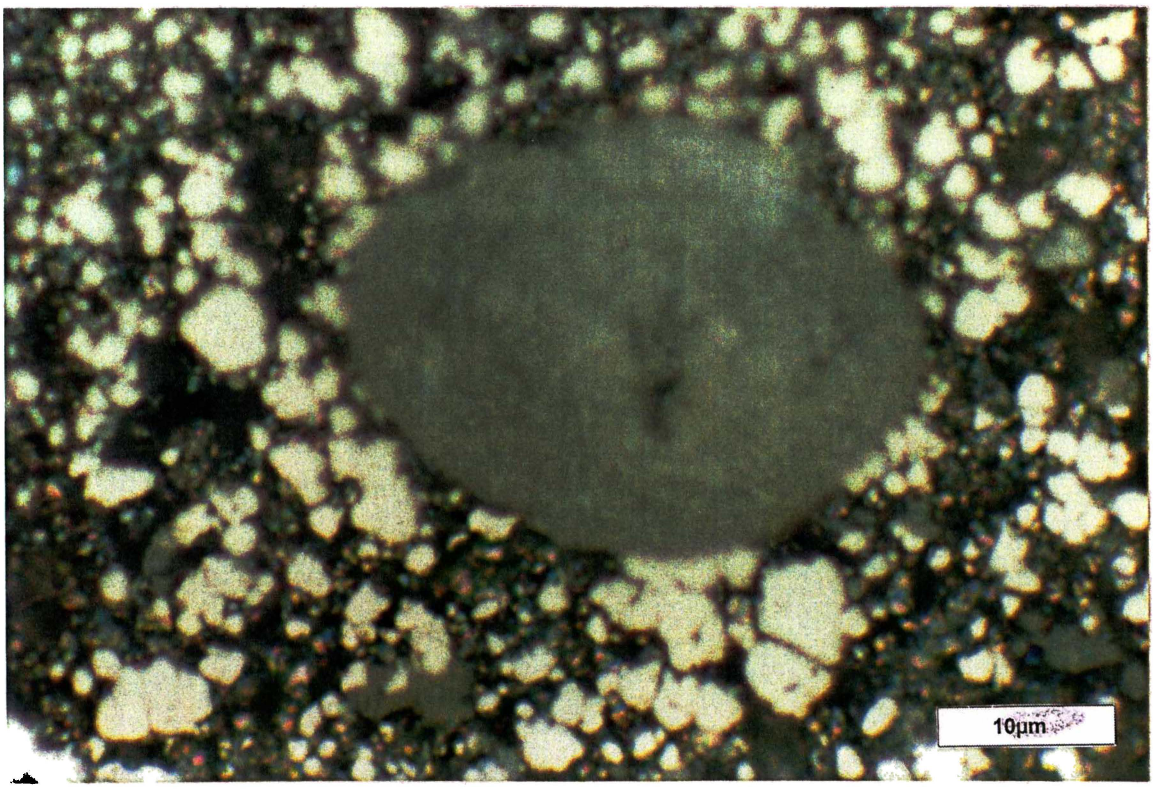

Figure A4.24 Anode #6 illustrating YSZ agglomerat at a magnification of 200x.

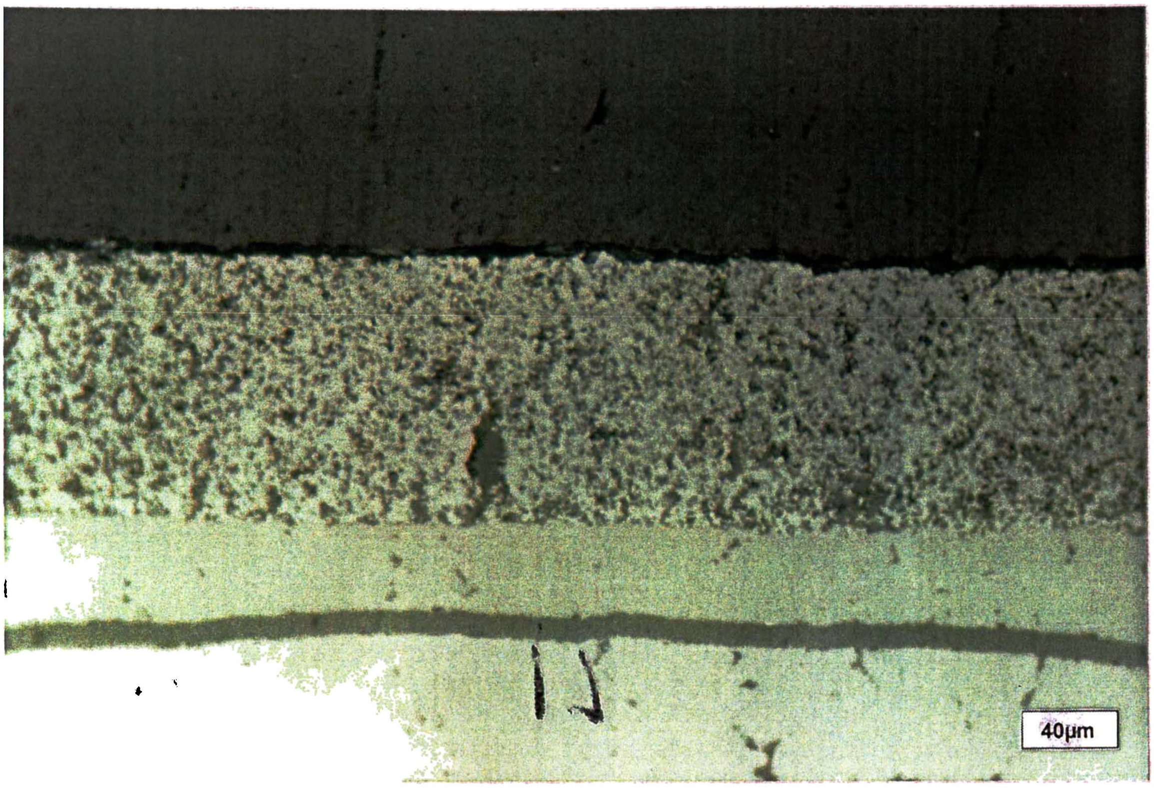

Figure A4.25 Anode #7 illustrating high percentage of YSZ, at a magnification of 200x.

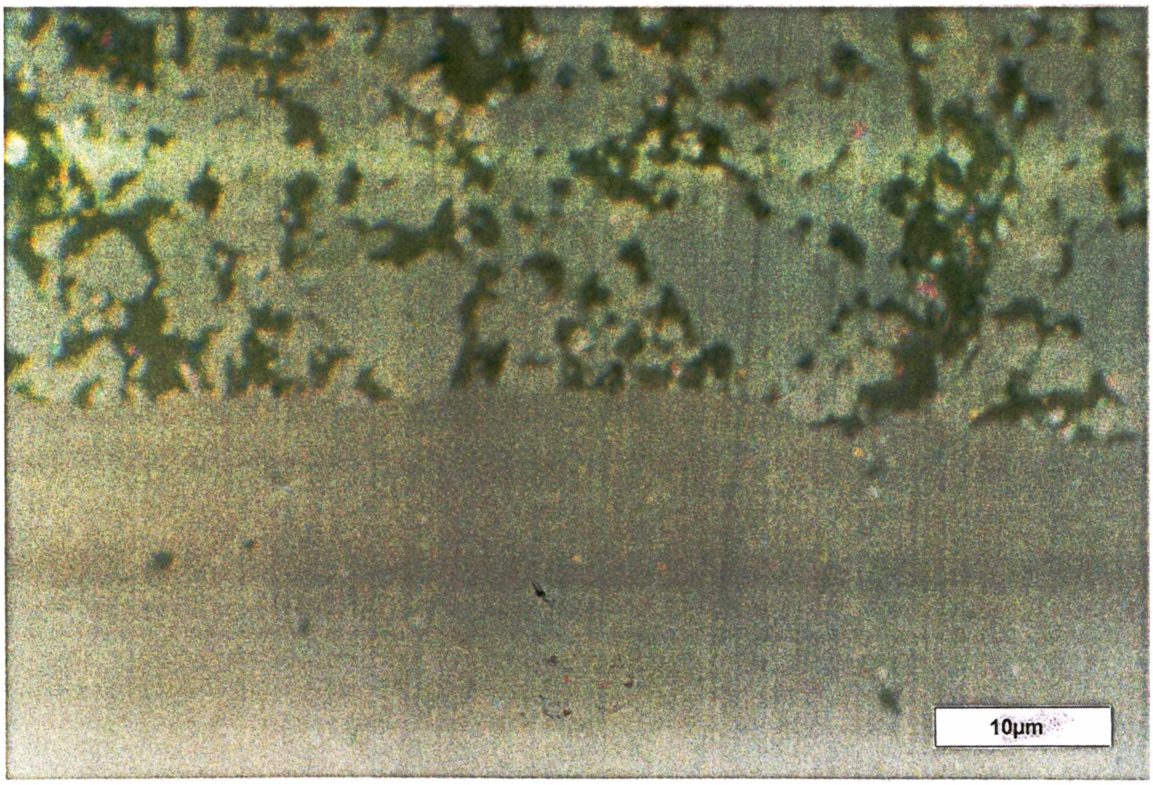

Figure A4.26 Anode #7 illustrating anode/interface, at a magnification of 1500x.

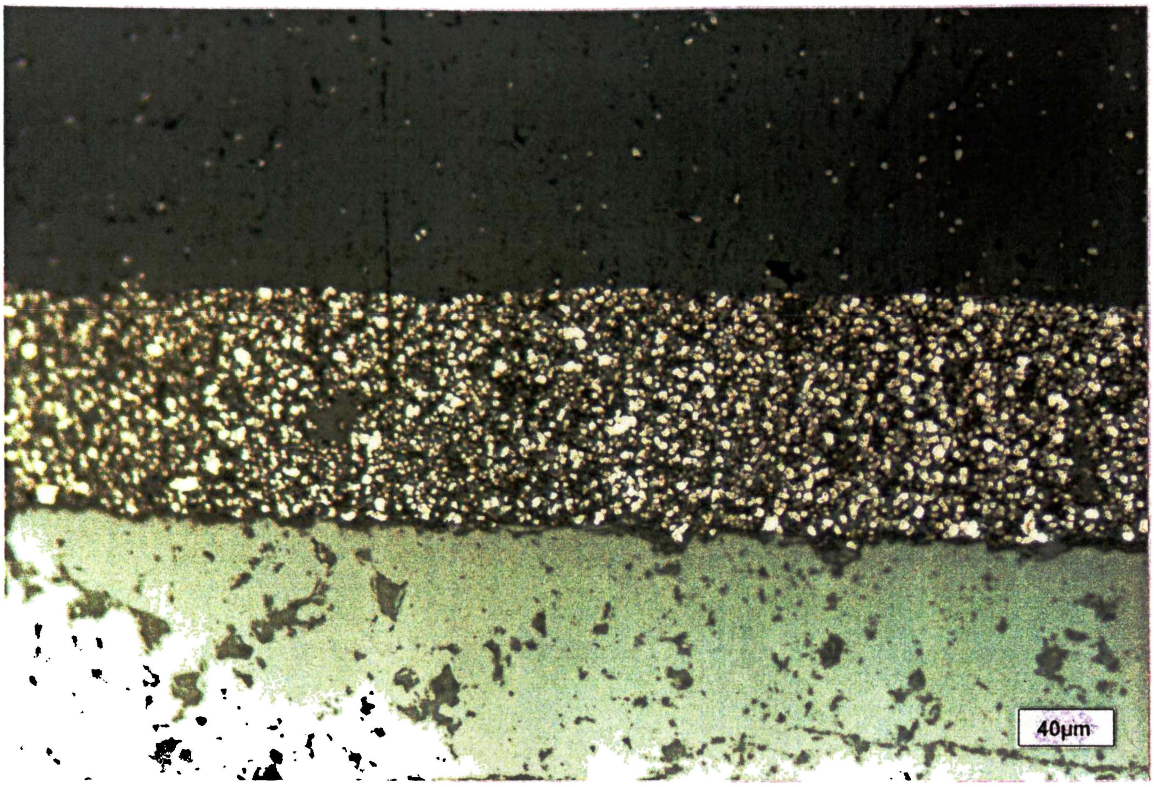

Figure A4.27 Anode #7 illustrating homogeneous layer at a magnification of 200x.

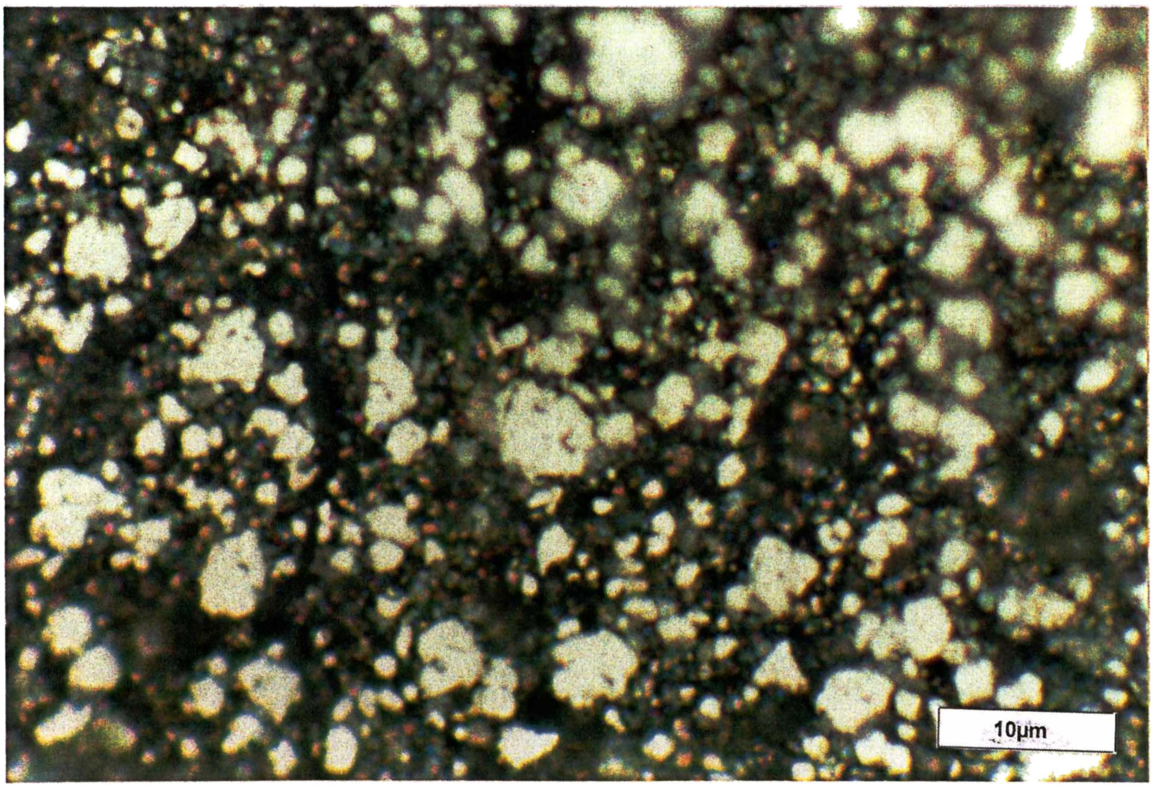

Figure A4.28 Anode #7 illustrating Ni dispersion at a magnification of 1500x.

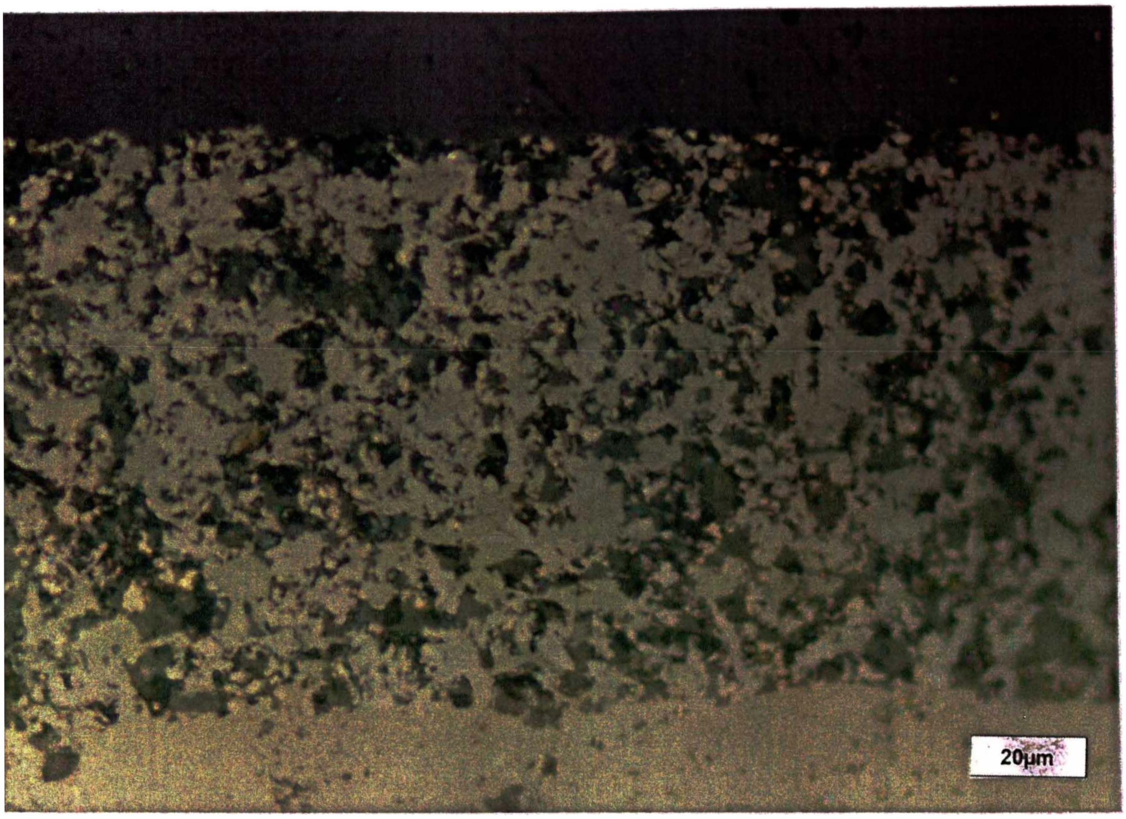

Figure A4.29 Anode #8 illustrating degree of sintering at a magnification of 500x.

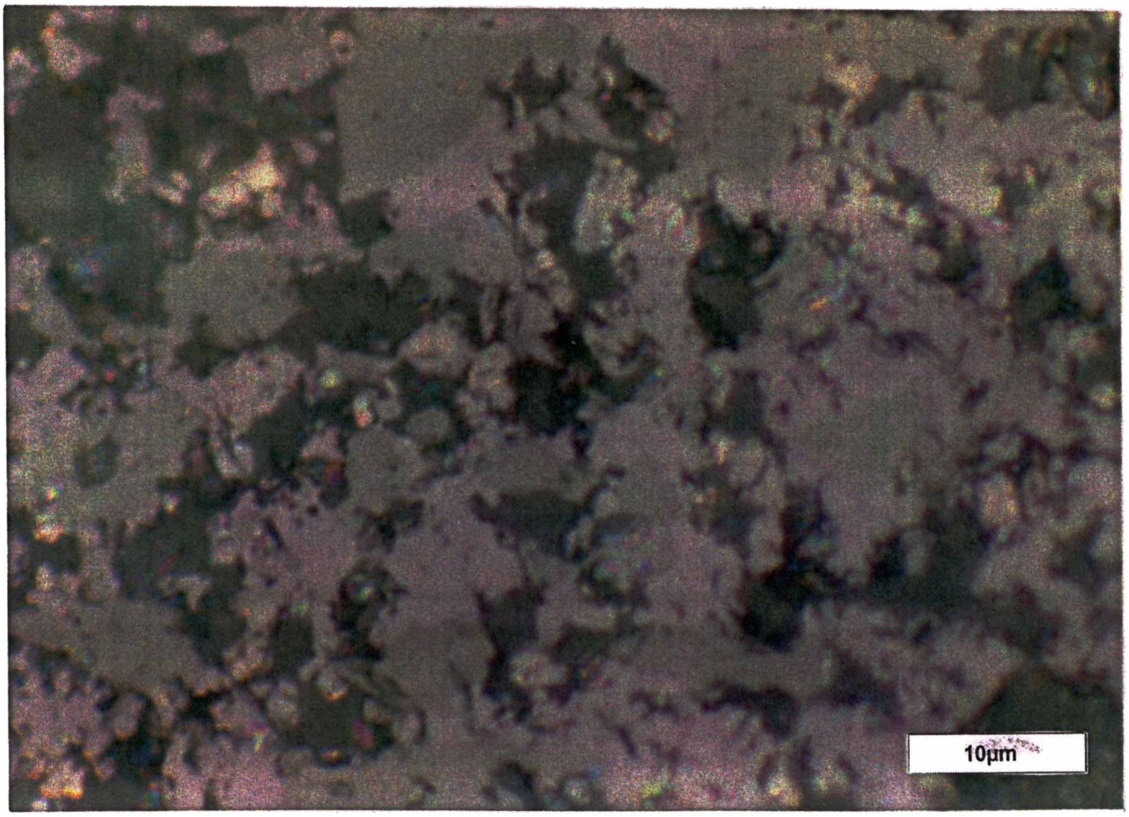

Figure A4.30 Anode #8 illustrating sintering of NiO/YSZ, at a magnification of 1500x.

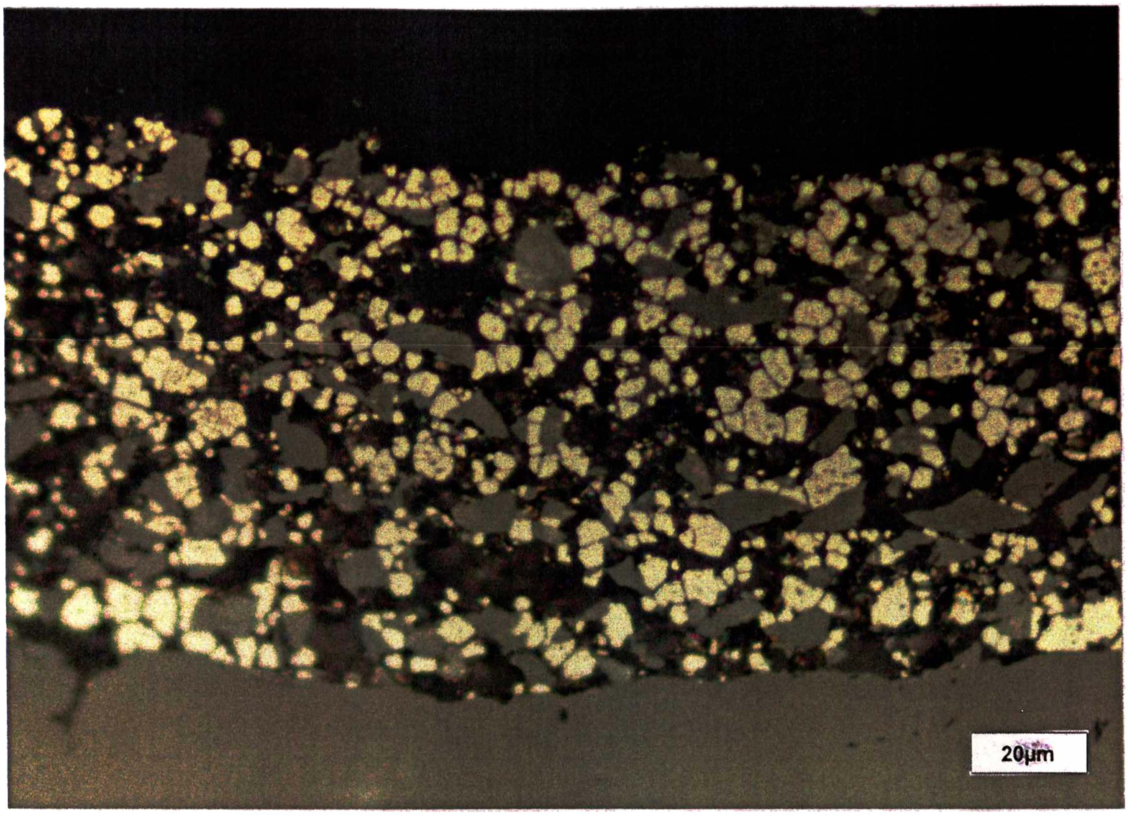

Figure A4.31 Anode #8 illustrating reduced layer, at a magnification of 500x.

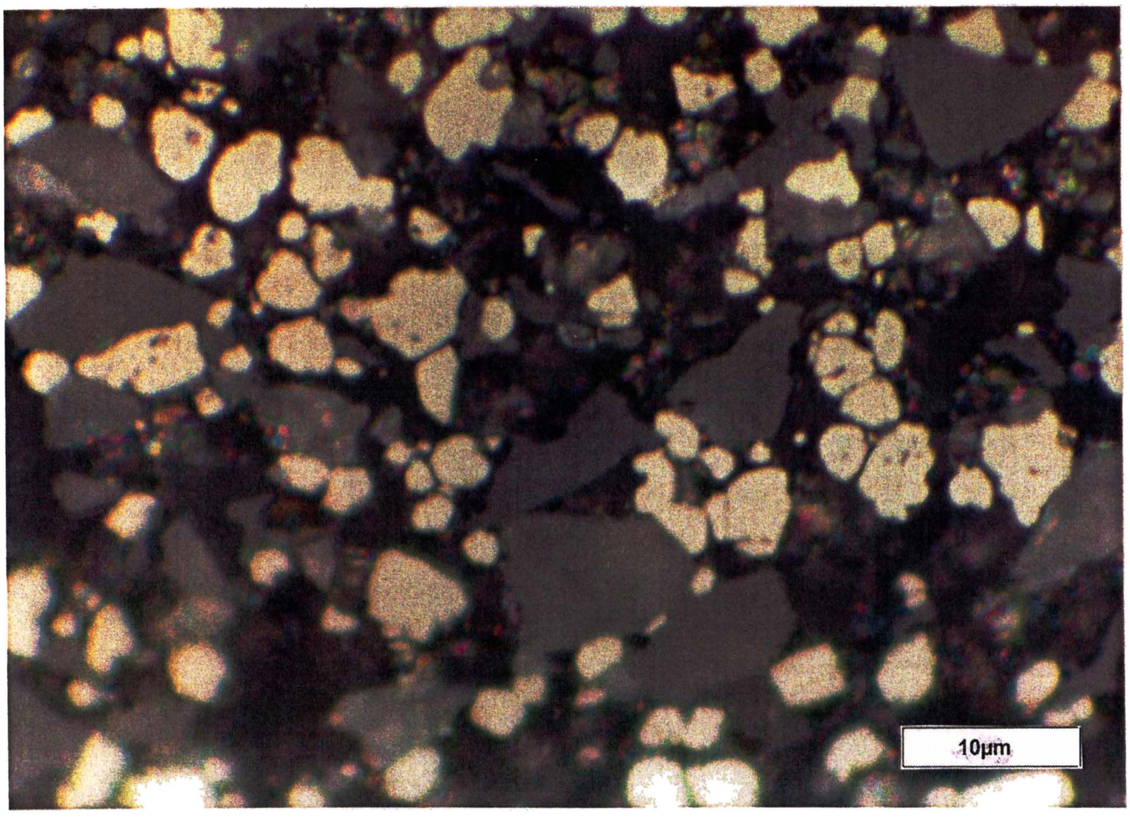

Figure A4.32 Anode #8 illustrating degree of Ni sintering, at a magnification of 1500x.

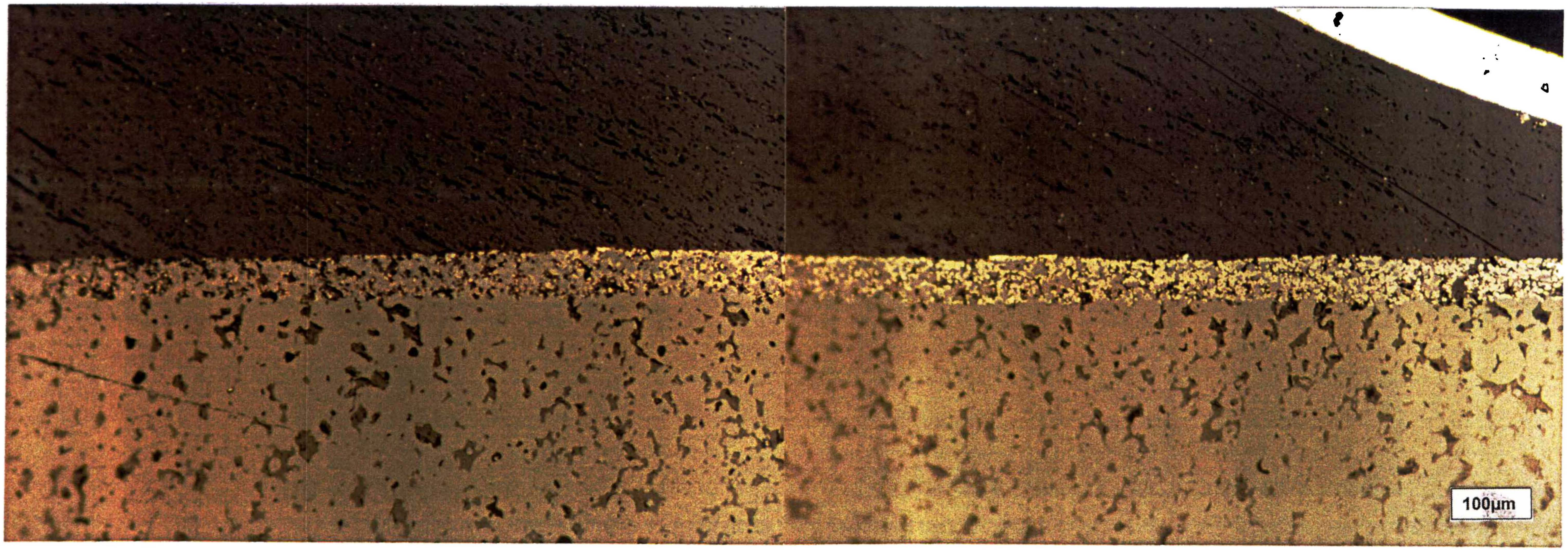

Figure A4.33 Anode #9 illustrating the inhomogeneous distribution of Ni particles across a section of the anode layer, at a magnification of 100x.

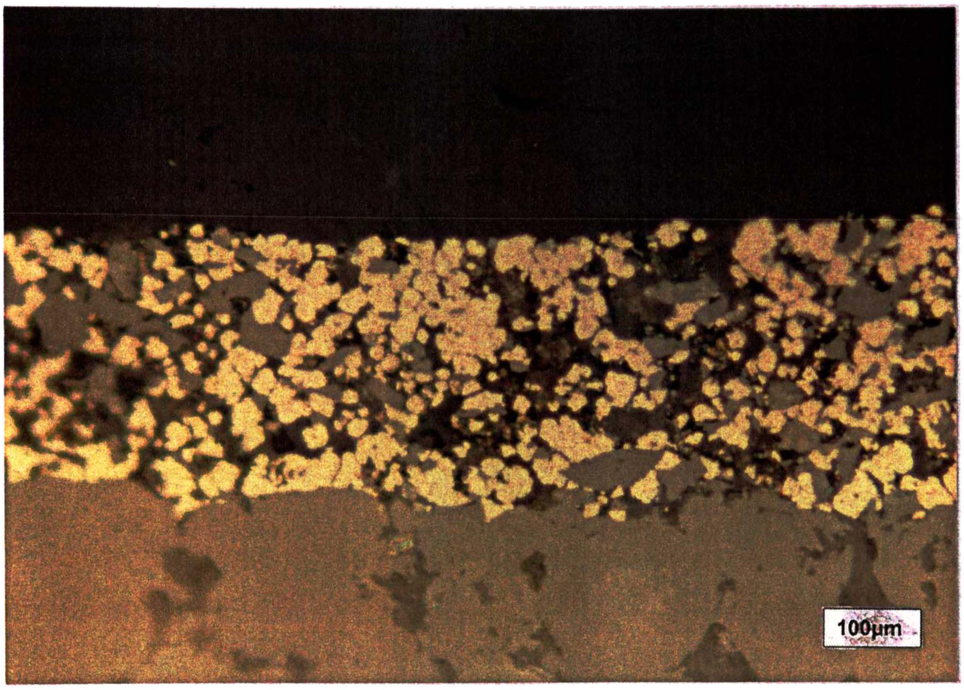

Figure A4.34 Anode #9 illustrating agglomeration of Ni at a magnification of 100x.

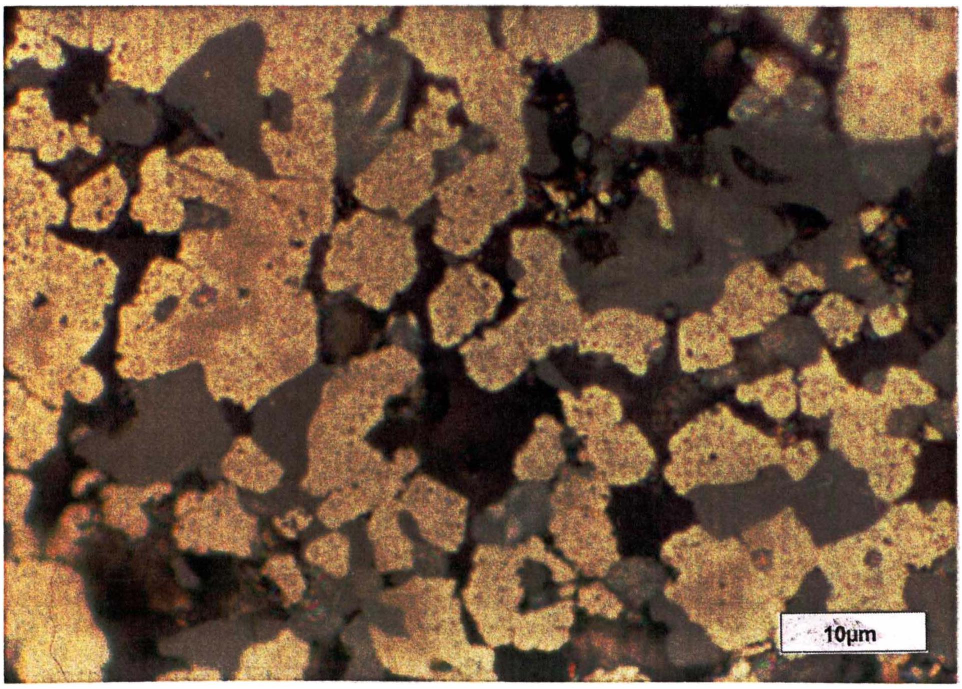

Figure A4.35 Anode #9 illustrating agglomeration of Ni at a magnification of 1500x.

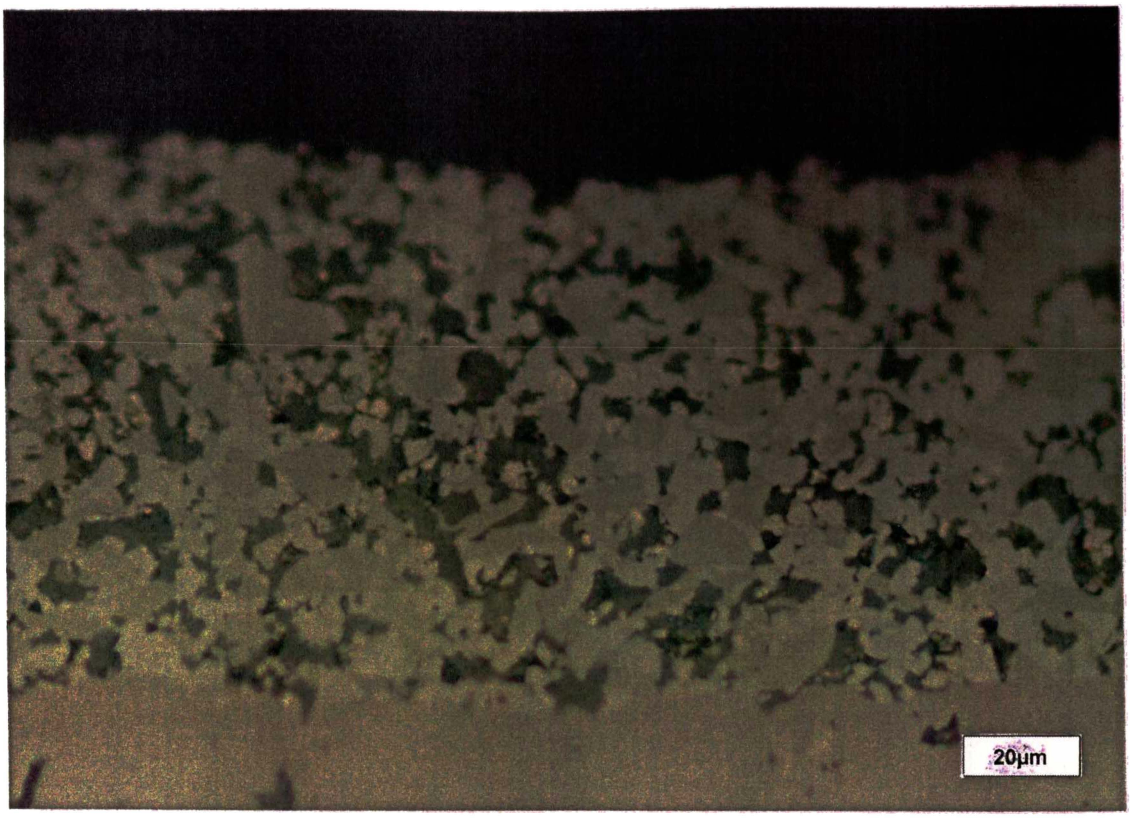

Figure A4.36 Anode #10 illustrating the sintering of NiO and YSZ at a magnification of 500x.

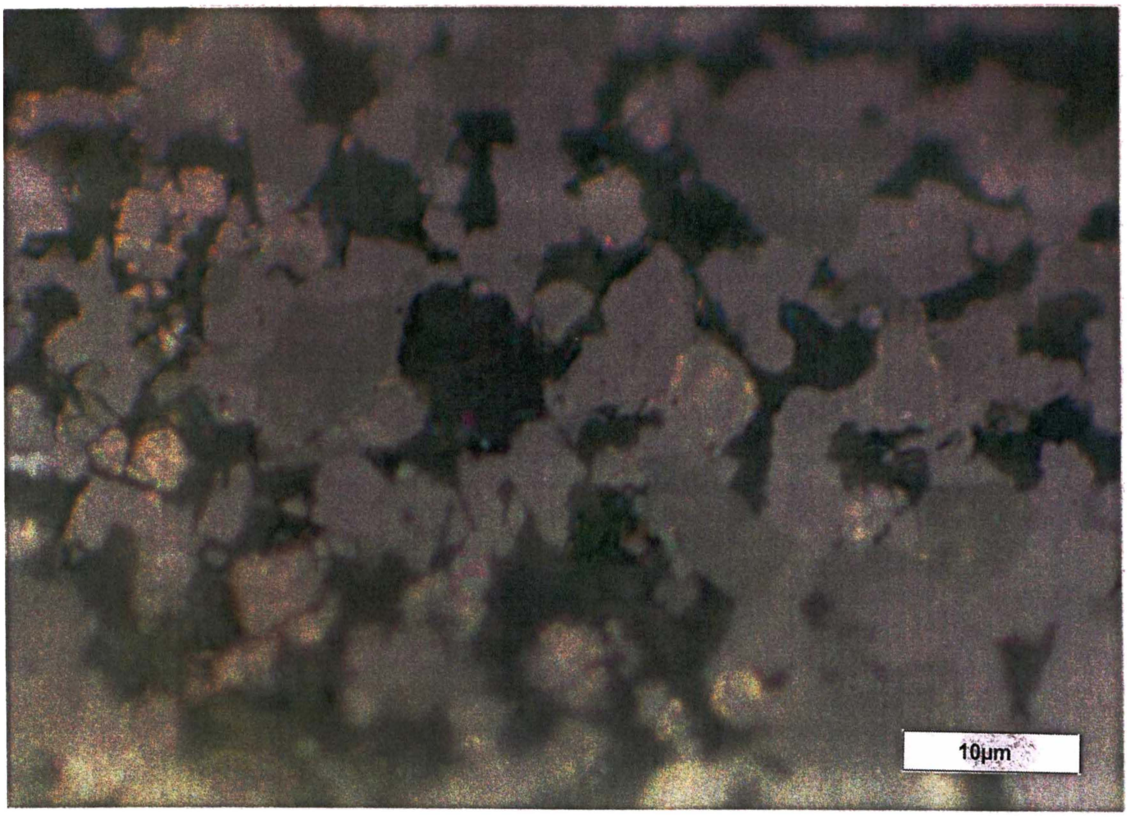

Figure A4.37 Anode #10 illustrating sintering of NiO and YSZ at a magnification of 1500x.

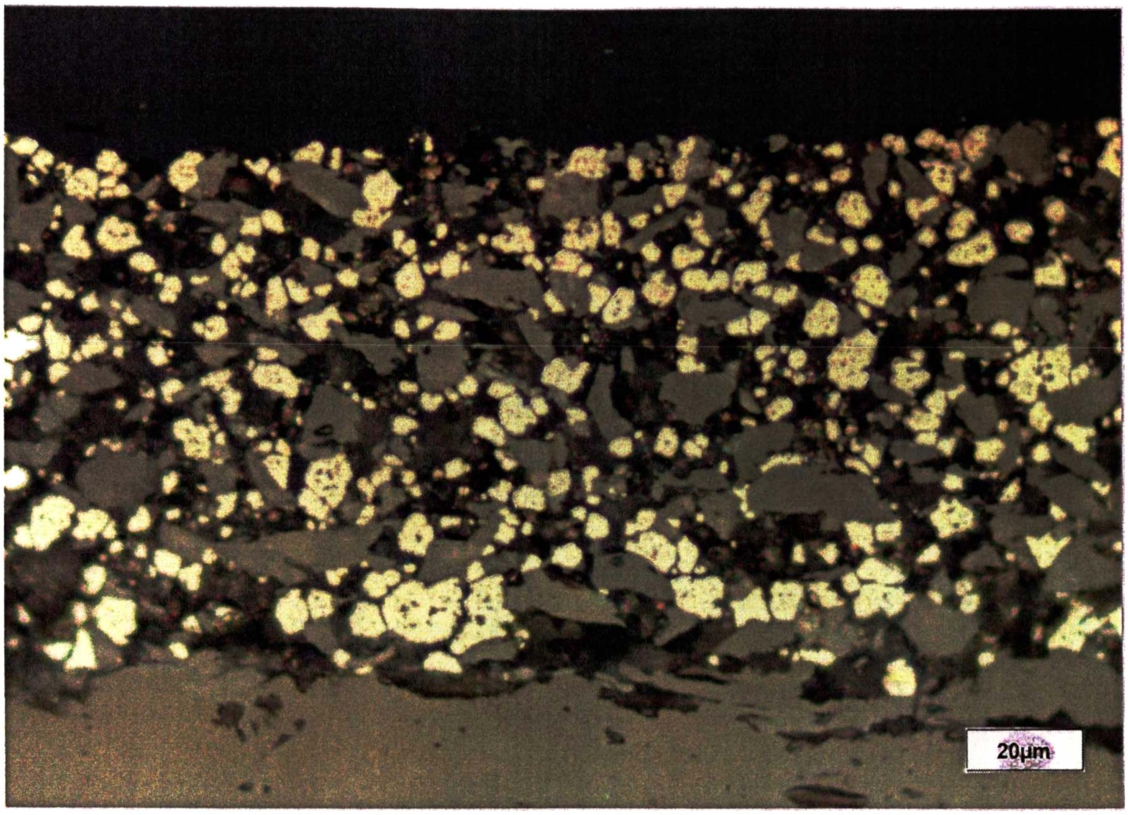

Figure A4.38 Anode #10 illustrating reduced layer at a magnification of 500x.

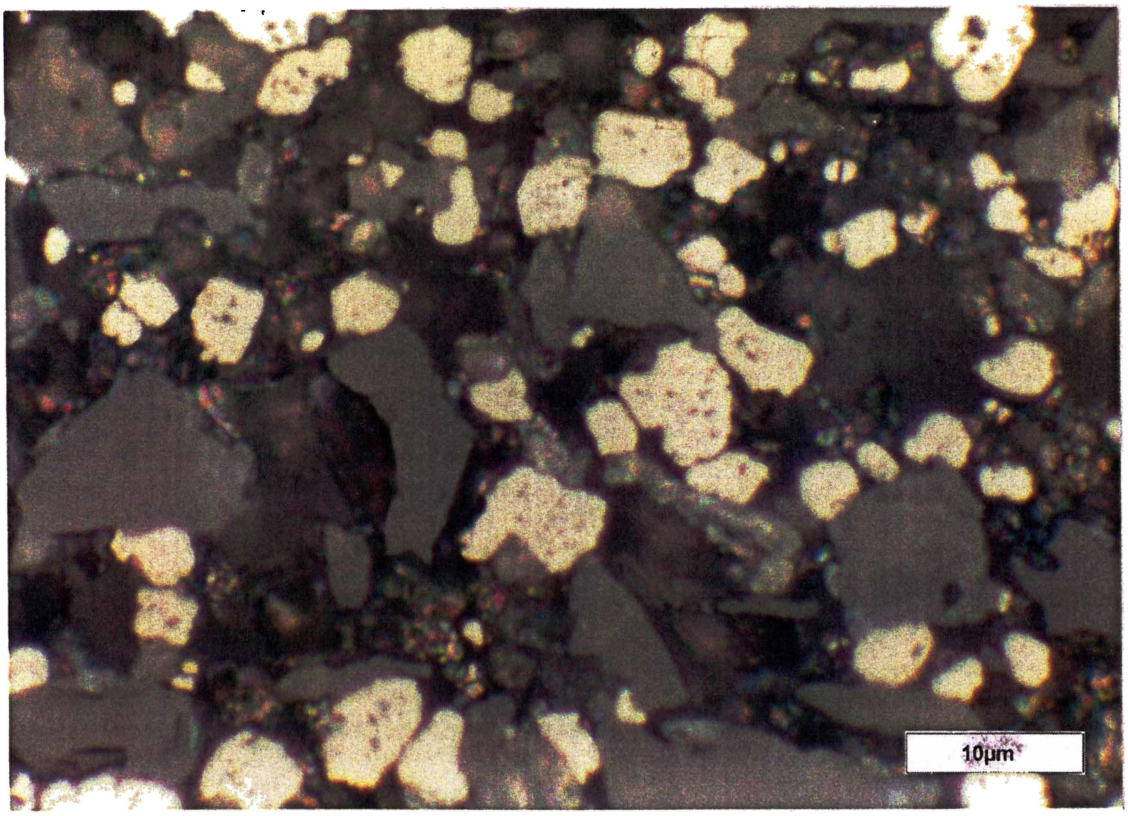

Figure A4.39 Anode #10 illustrating degree of Ni sintering at a magnification of 1500x.

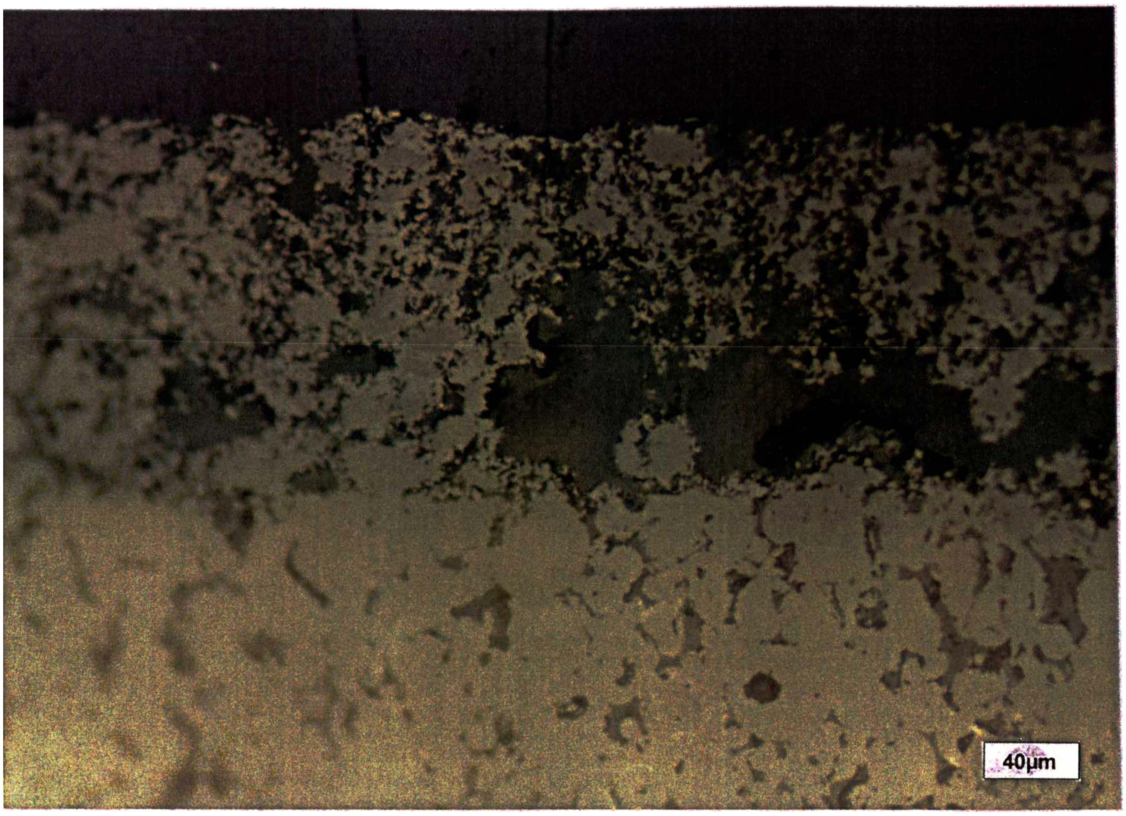

Figure A4.40 Anode #11 illustrating porosity at the interface at a magnification of 200x.

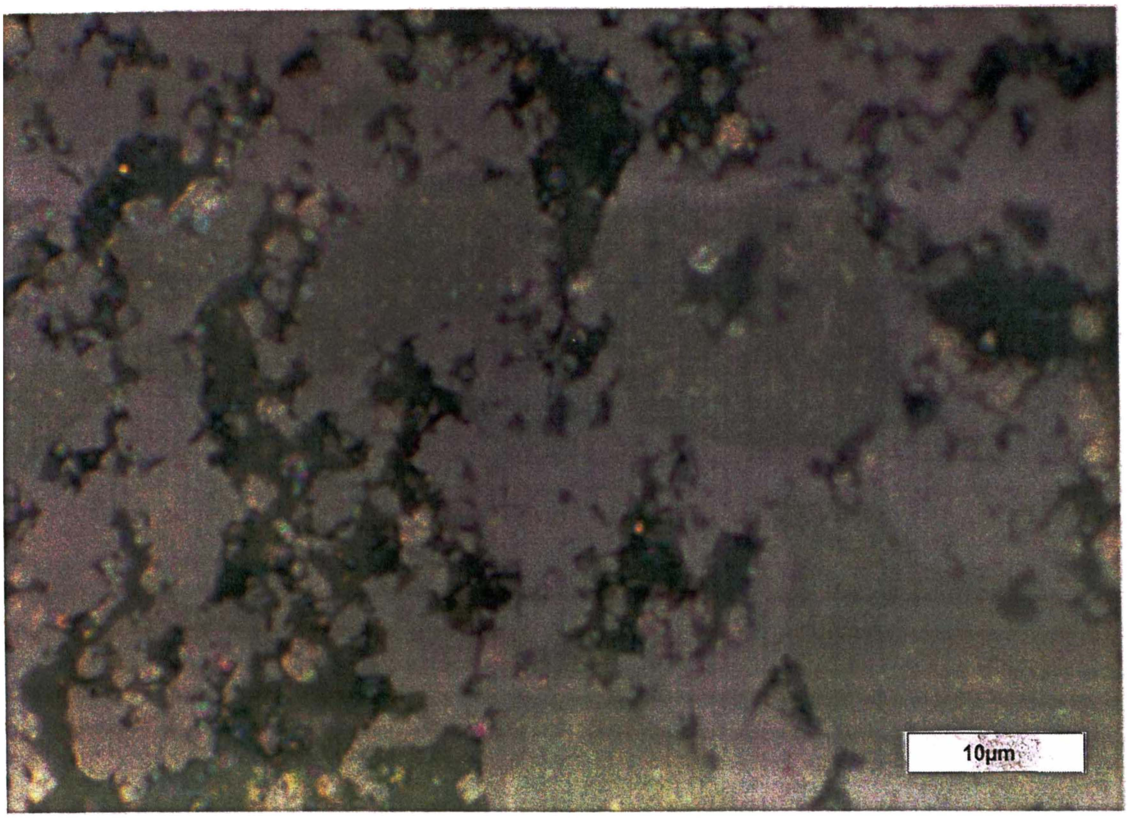

Figure A4.41 Anode #11 illustrating degree of YSZ sintering at a magnification of 1500x.

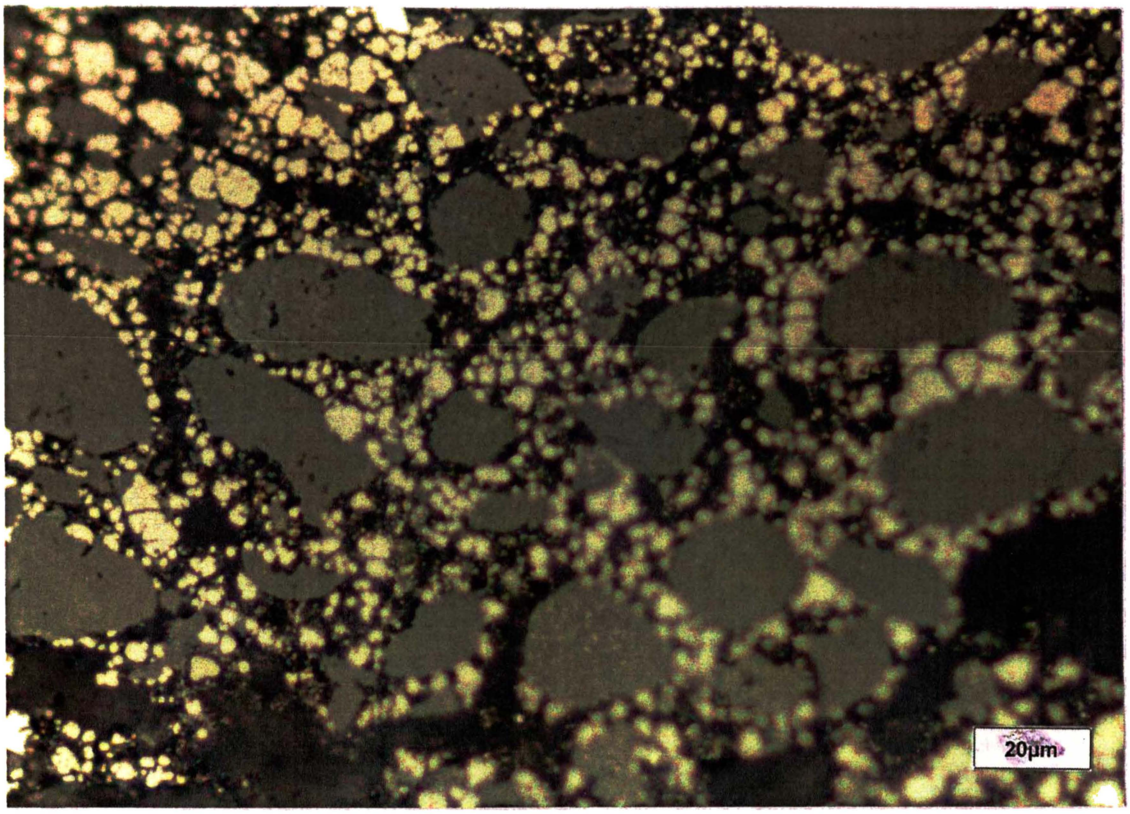

Figure A4.42 Anode #11 illustrating homogeneous distribution of YSZ. Magnification of 500x.

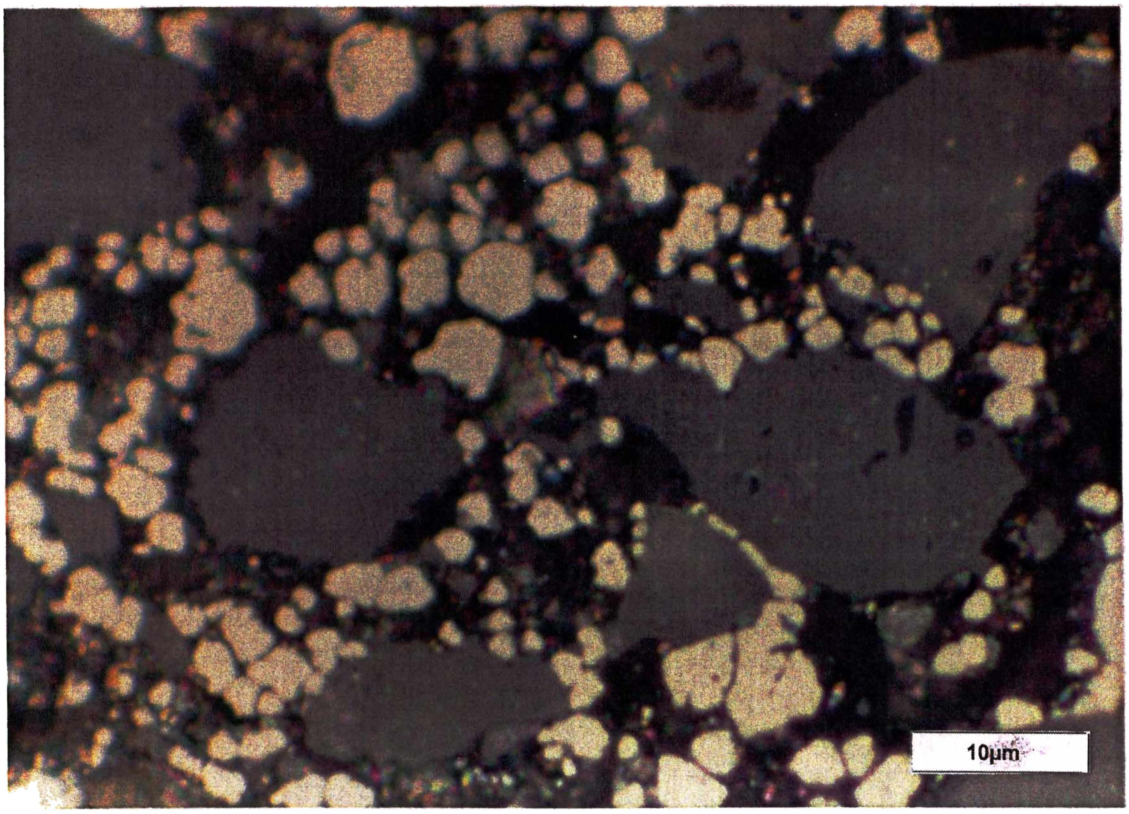

Figure A4.43 Anode #11 degree of Ni agglomeration at a magnification of 1500x.

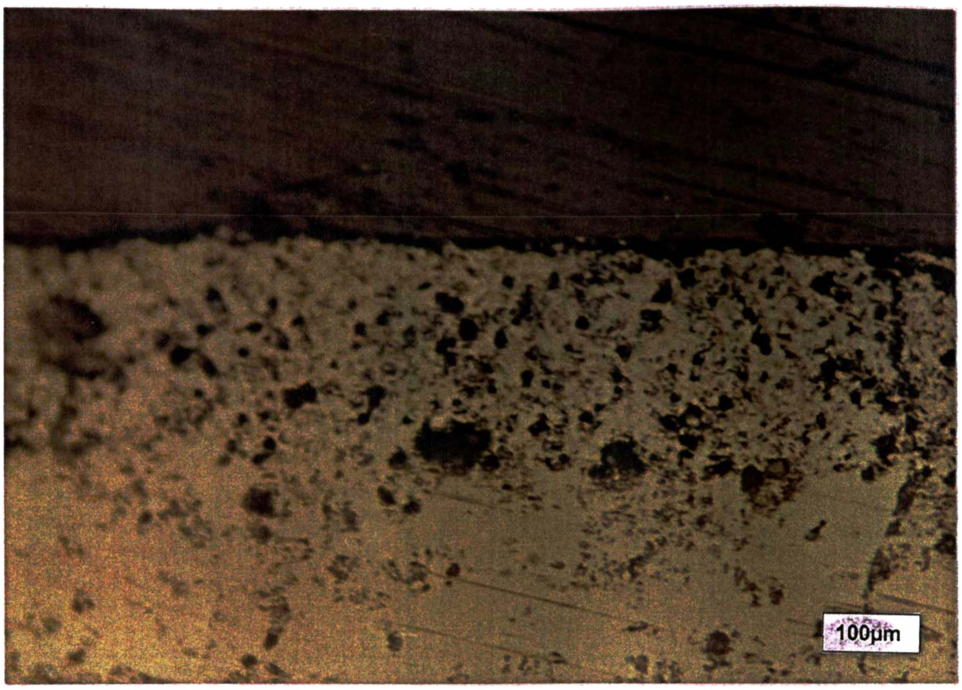

Figure A4.44 Anode #12 illustrating anode/interface, at a magnification of 100x.

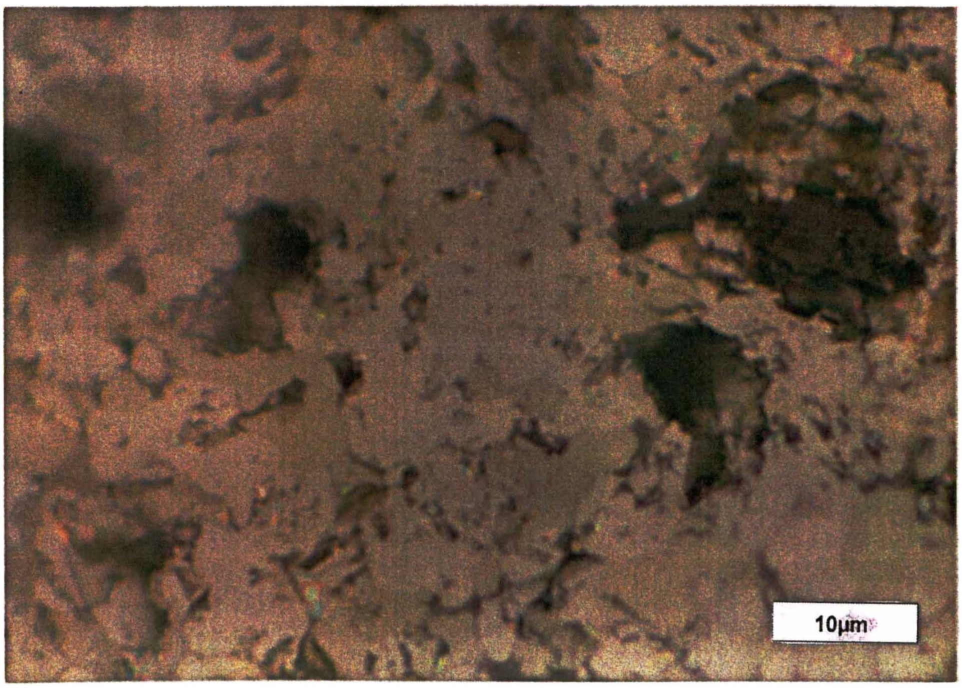

Figure A4.45 Anode #12 illustrating sintering of Nio and YSZ at a magnification of 1500x.

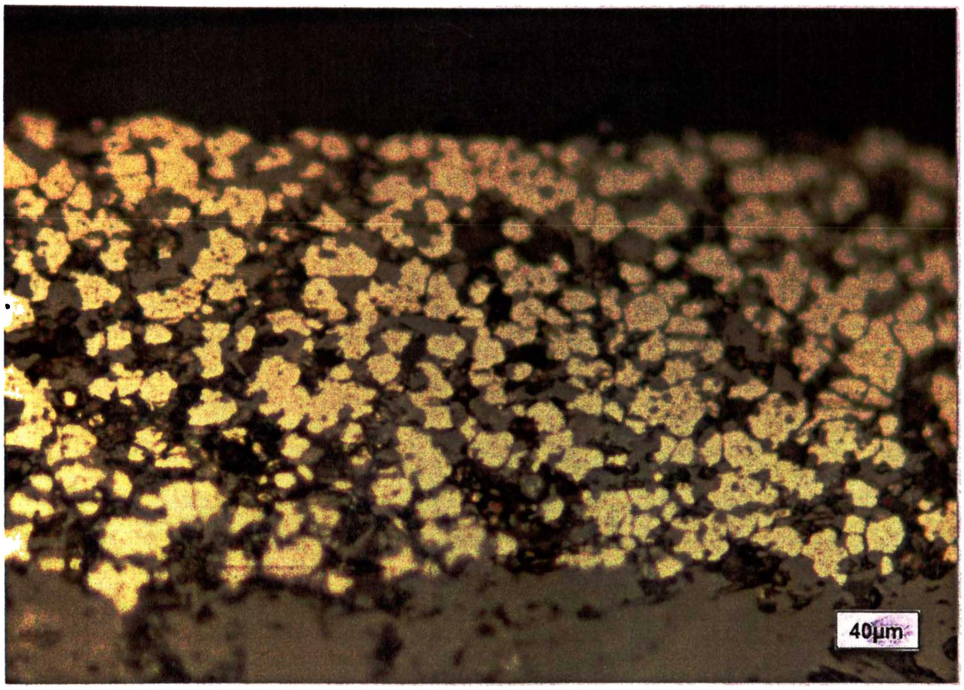

Figure A4.46 Anode #12 illustrating reduced anode at a magnification of 200x.

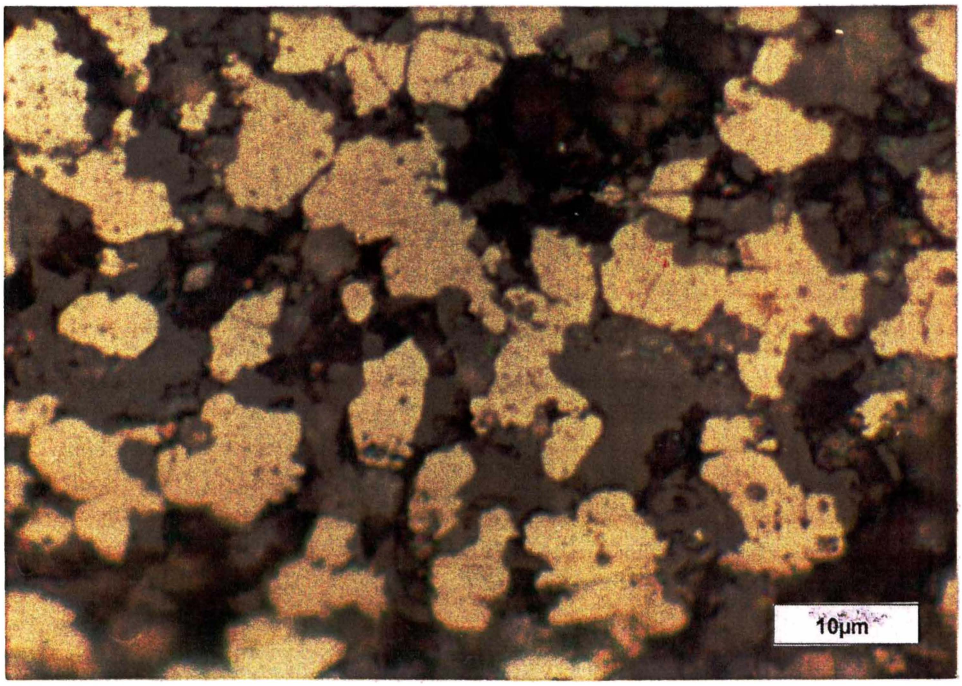

Figure A4.47 Anode #12 illustrating large particle size of Ni at a magnification of 1500x.

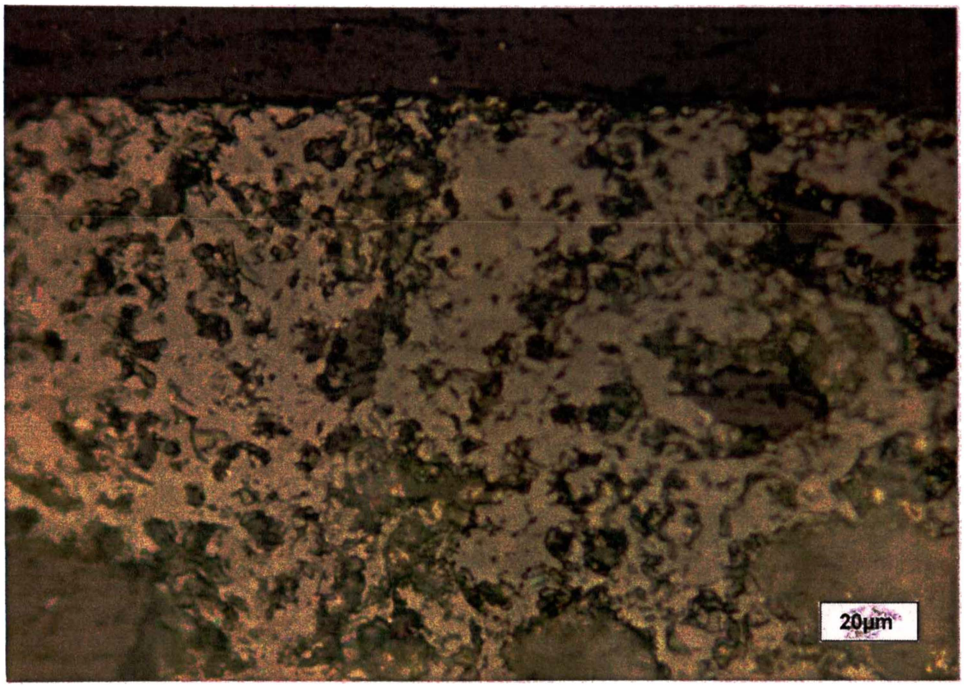

Figure A4.48 Anode #13 illustrating sintering of NiO/YSZ at a magnification of 500x.

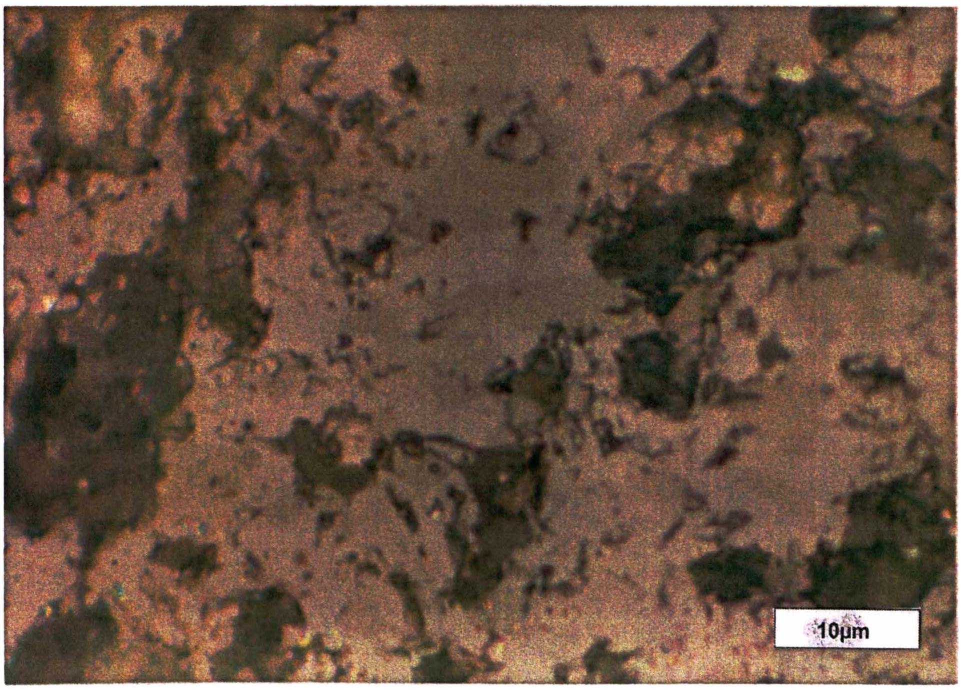

Figure A4.49 Anode #13 illustrating sintering of NiO and YSZ at a magnification of 1500x.

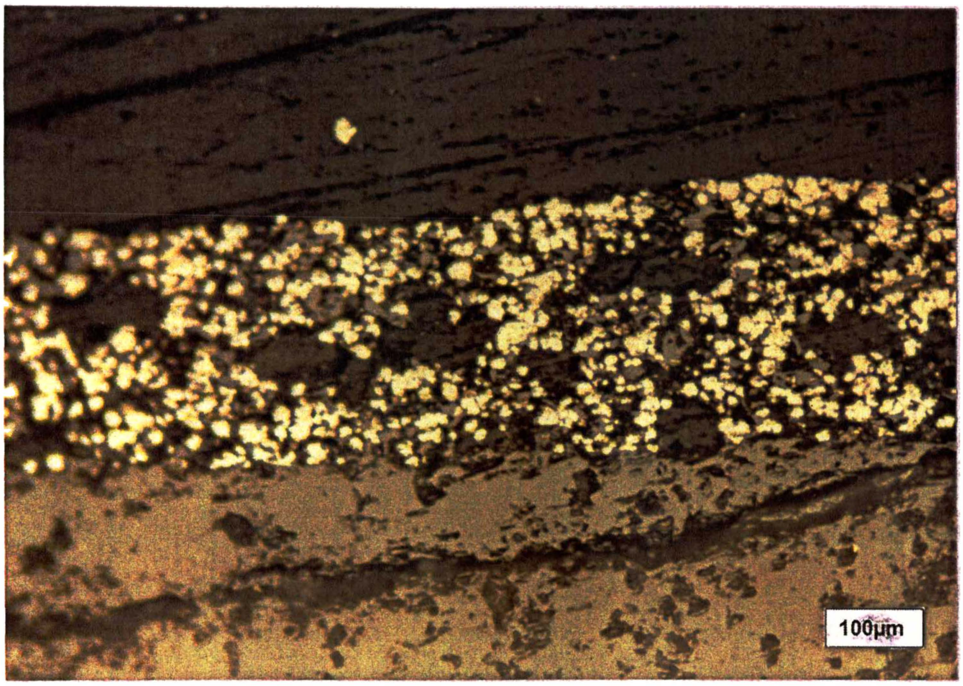

Figure A4.50 Anode #13 illustrating high percentage of voids at a magnification of 100x.

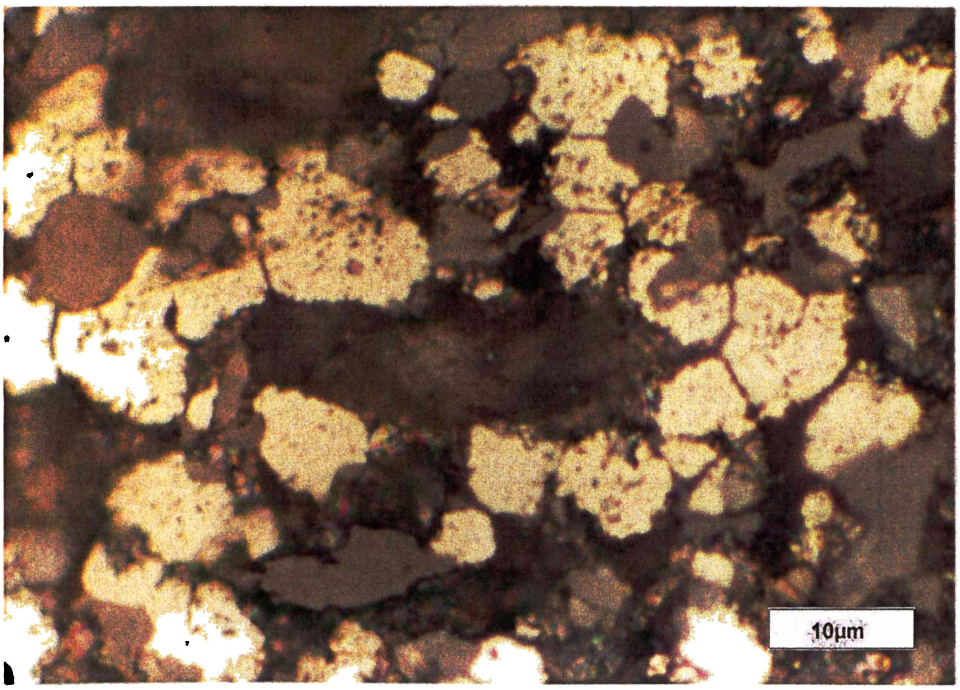

Figure A4.51 Anode #13 illustrating connecting paths of Ni at a magnification of 1500x.

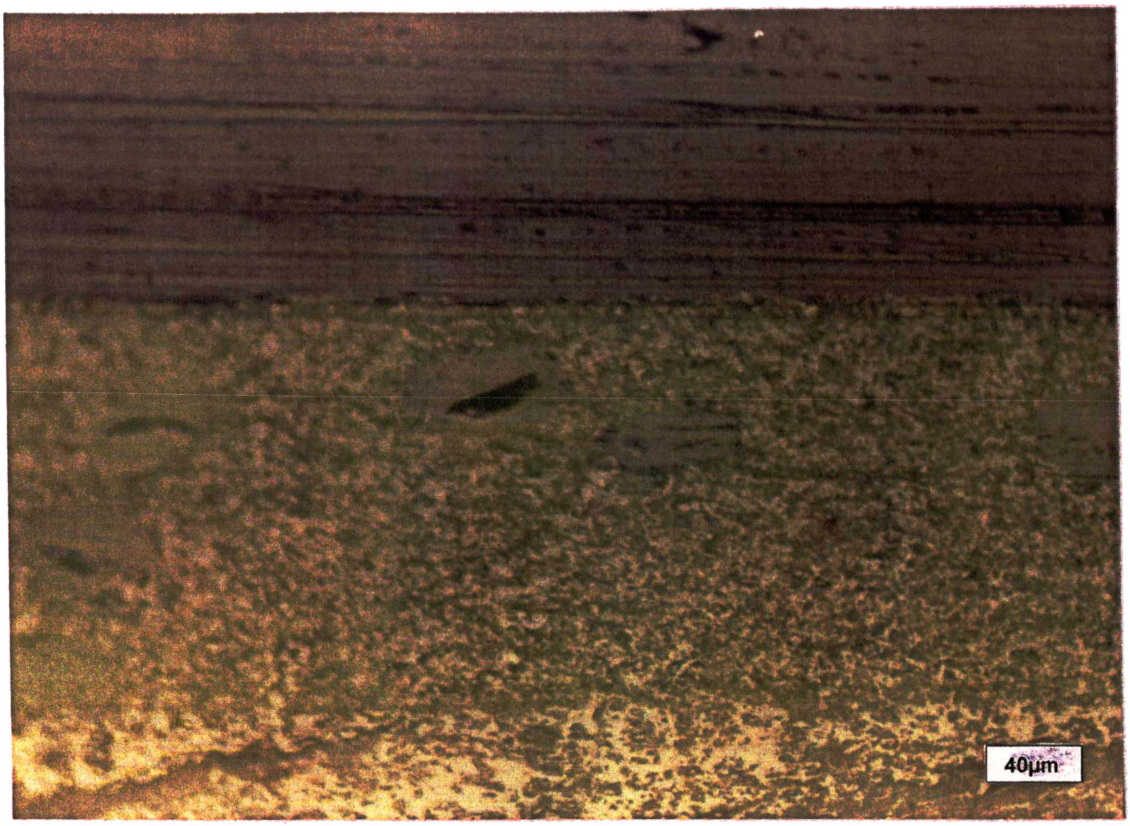

Figure A4.52 Anode #14 illustrating homogeneous NiO/YSZ distribution. Magnification of 200x.

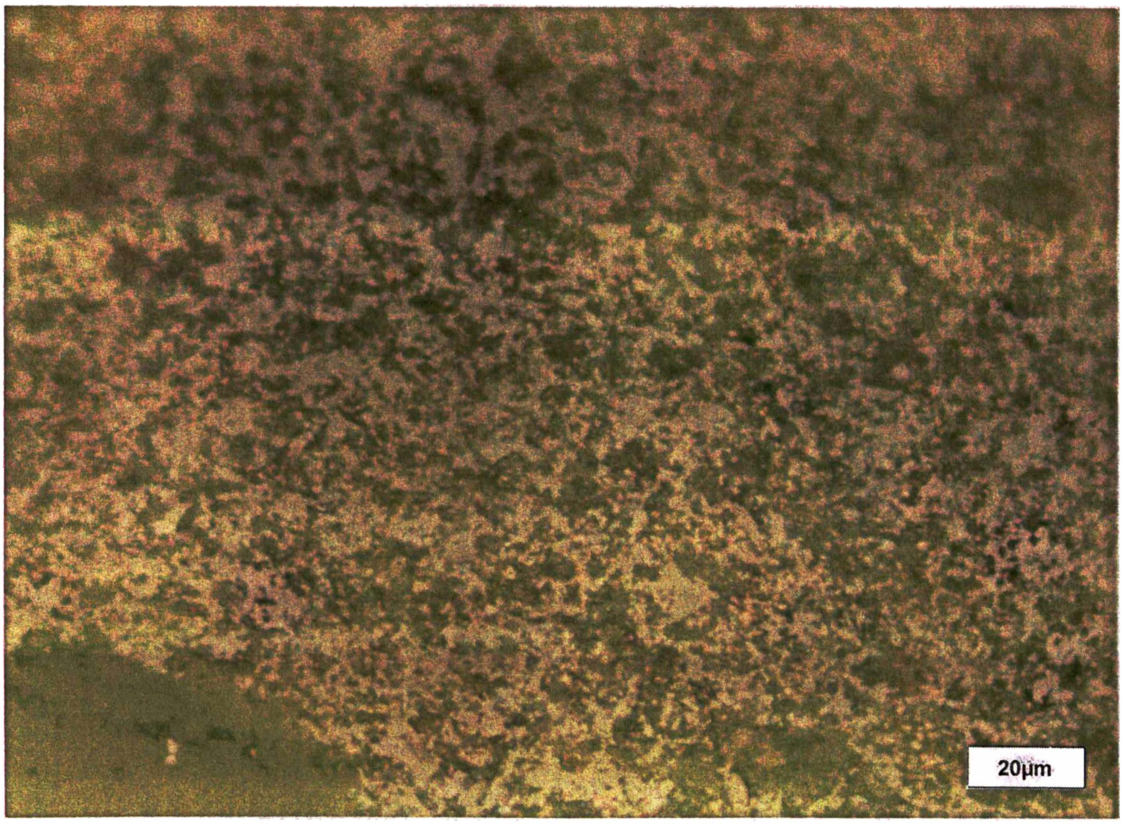

Figure A4.53 Anode #14 illustrating homogeneous NiO/YSZ distribution. Magnification of 500x.

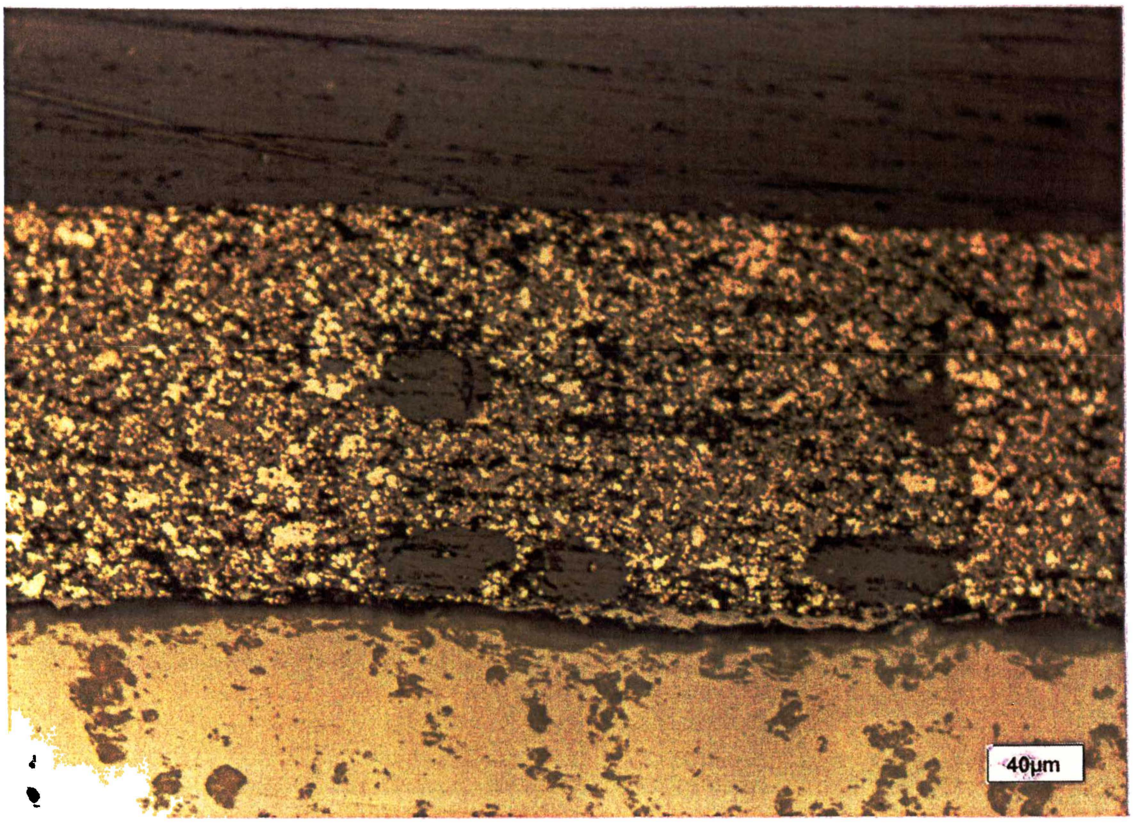

Figure A4.54 Anode #14 illustrating reduced layer with large voids at a magnification of 200x.

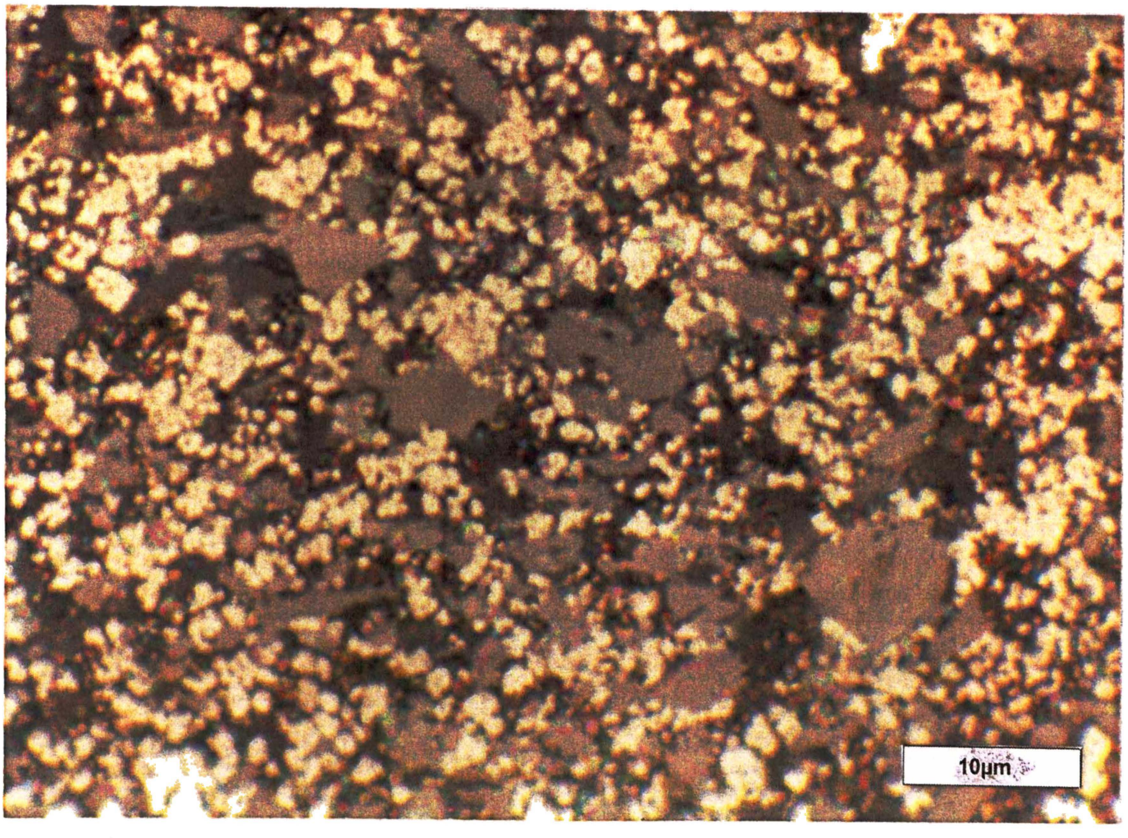

Figure A4.55 Anode #14 illustrating highly dispersed Ni at a magnification of 1500x.

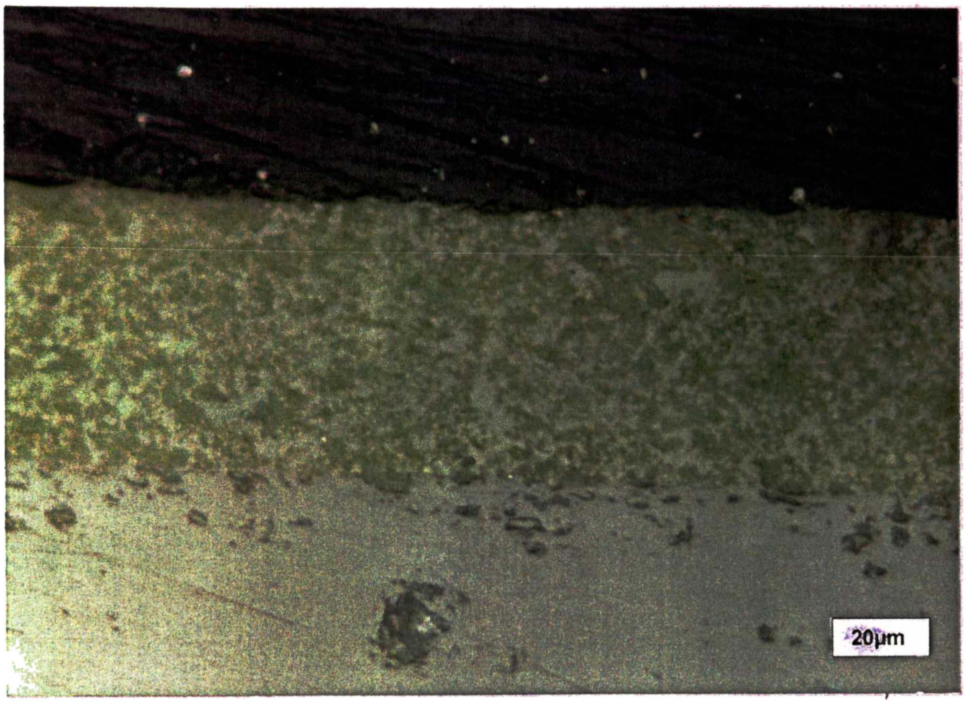

Figure A4.56 Anode #15 illustrating homogeneous NiO/YSZ distribution. Magnification of 500x.

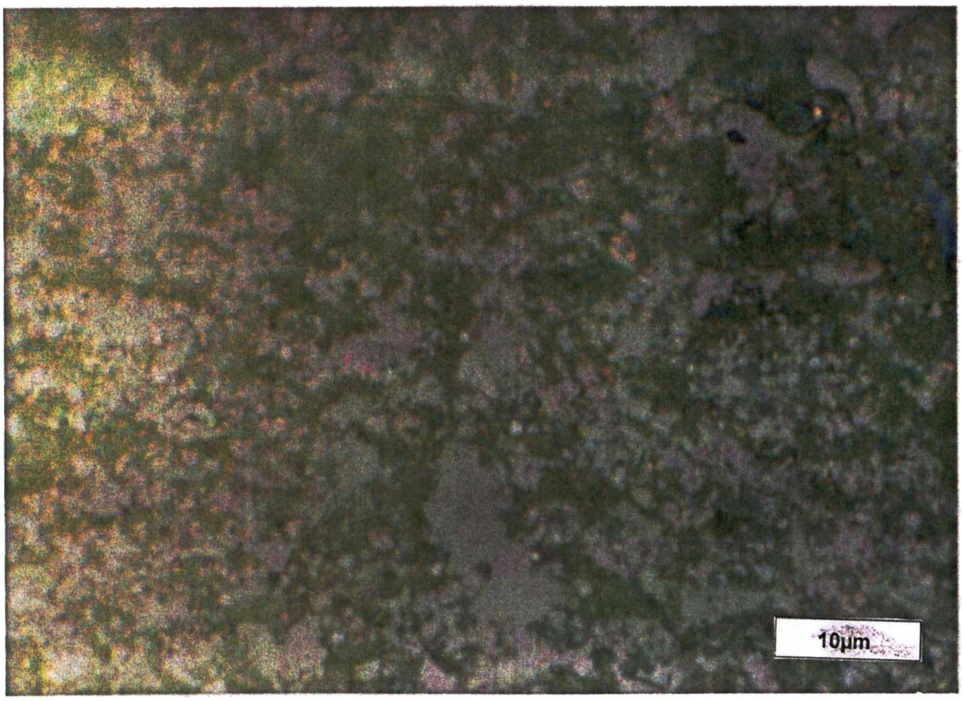

Figure A4.57 Anode #15 illustrating dispersion of Ni at a magnification of 1500x.

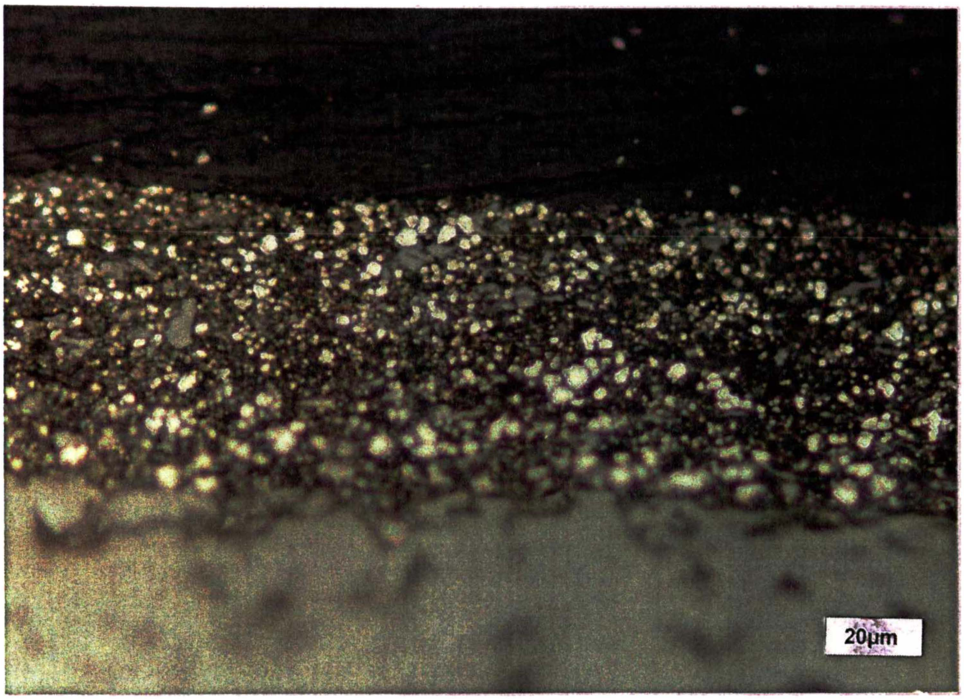

Figure A4.58 Anode #15 illustrating reduced layer at a magnification of 500x.

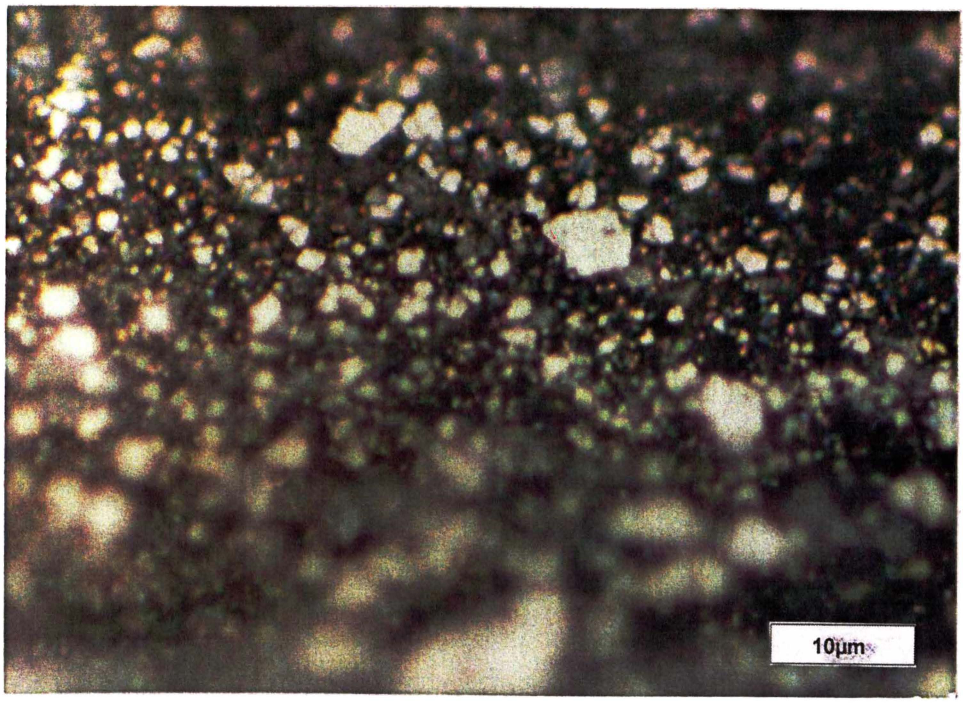

Figure A4.59 Anode #15 illustrating reduced layer at a magnification of 1500x.

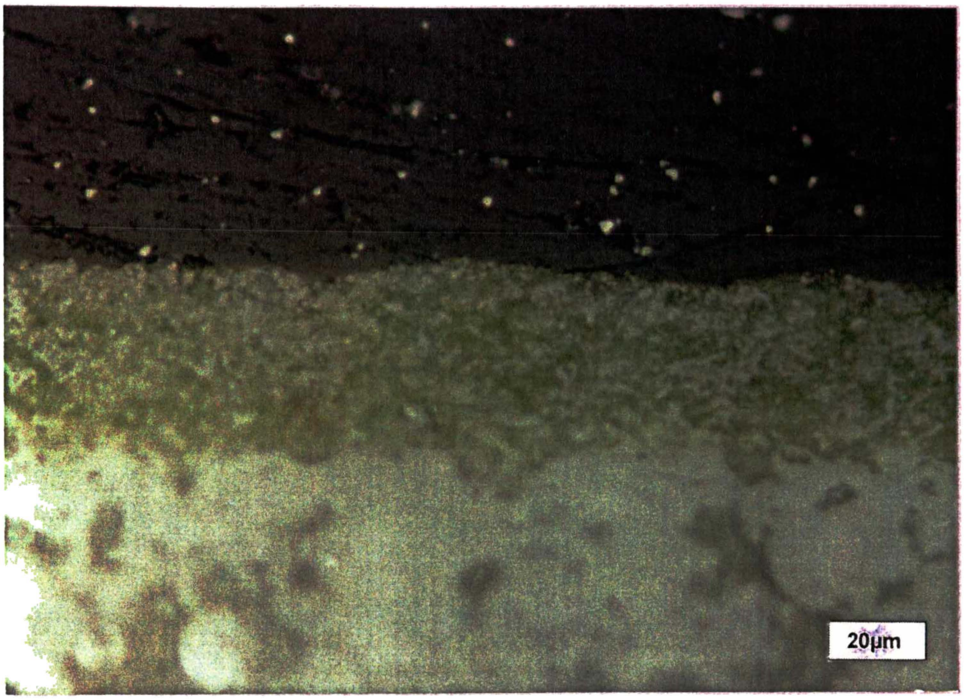

Figure A4.60 Anode #16 illustrating homogeneous NiO/YSZ distribution. Magnification of 500x.

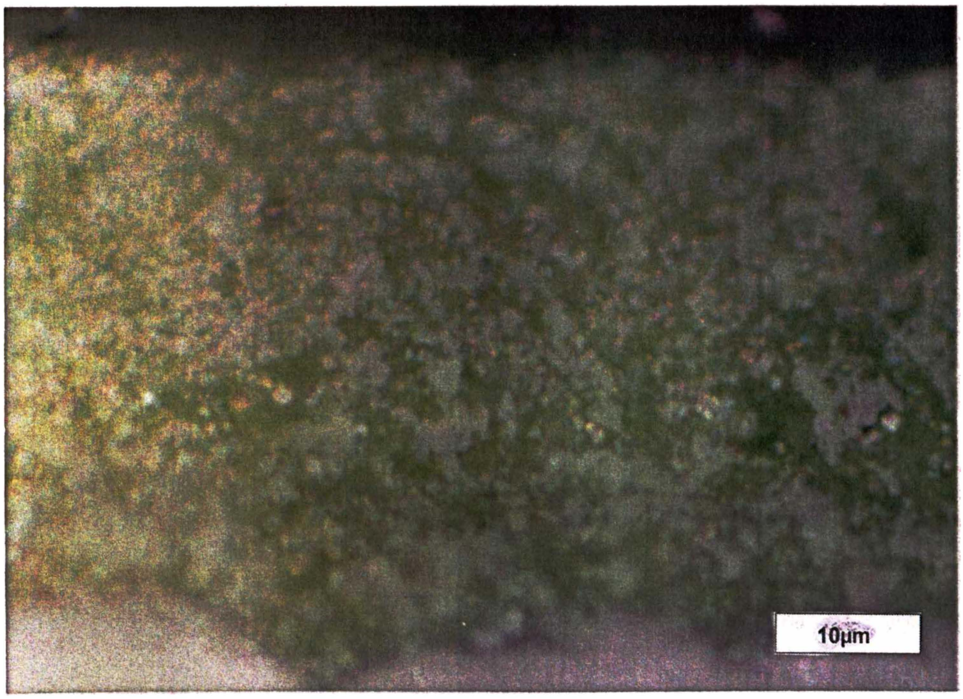

Figure A4.61 Anode #16 illustrating thickness of the layer at a magnification of 1500x.

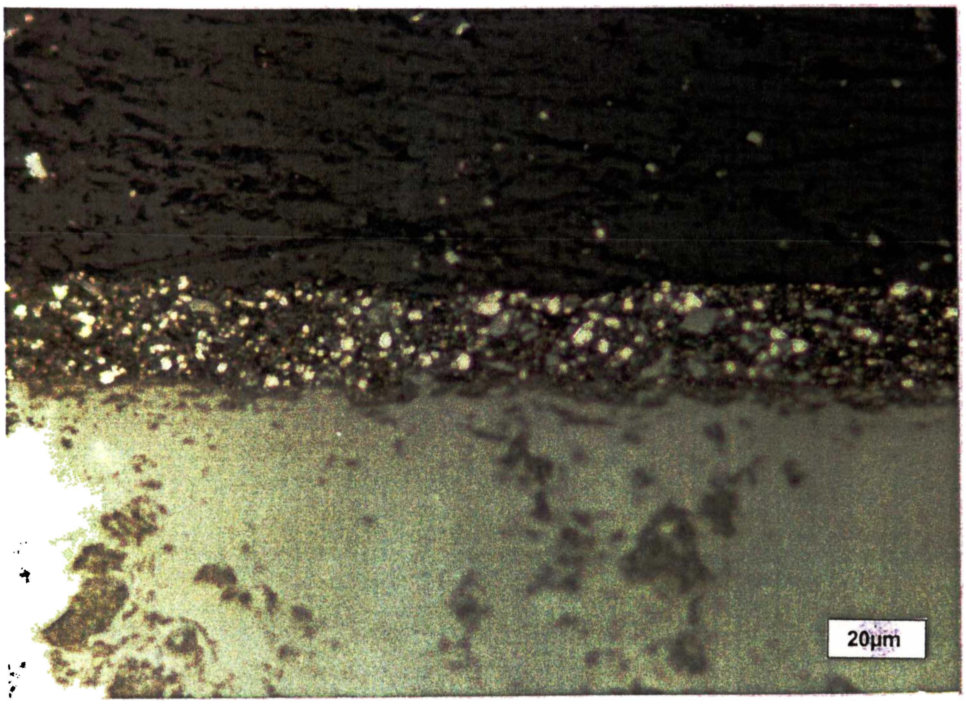

Figure A4.62 Anode #16 illustrating reduced layer at a magnification of 500x.

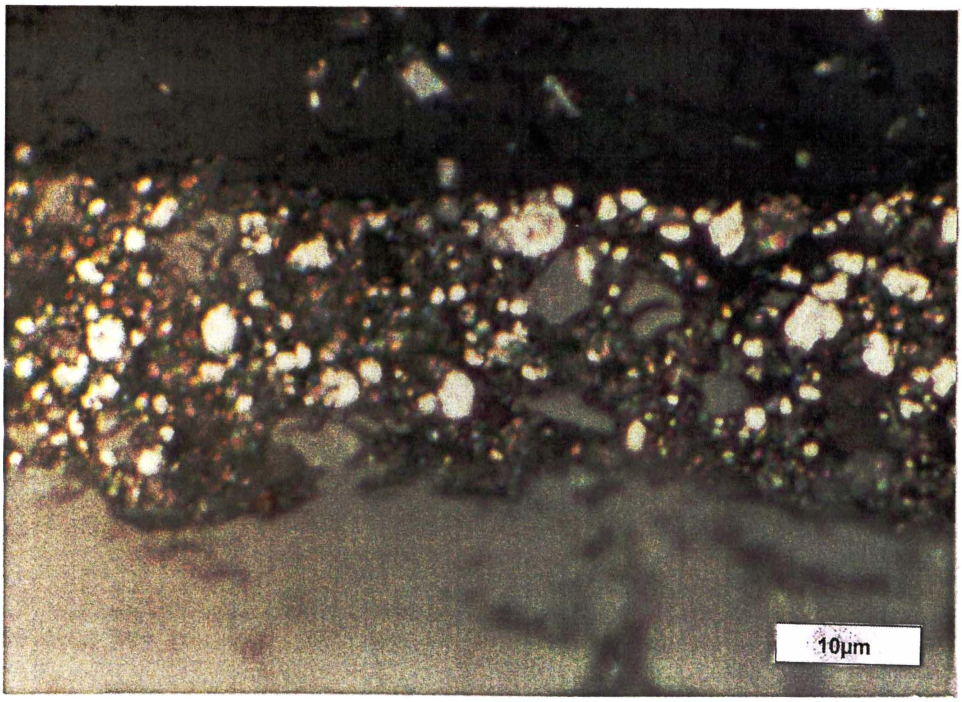

Figure A4.63 Anode #16 illustrating porosity of reduced layer at a magnification of 1500x.

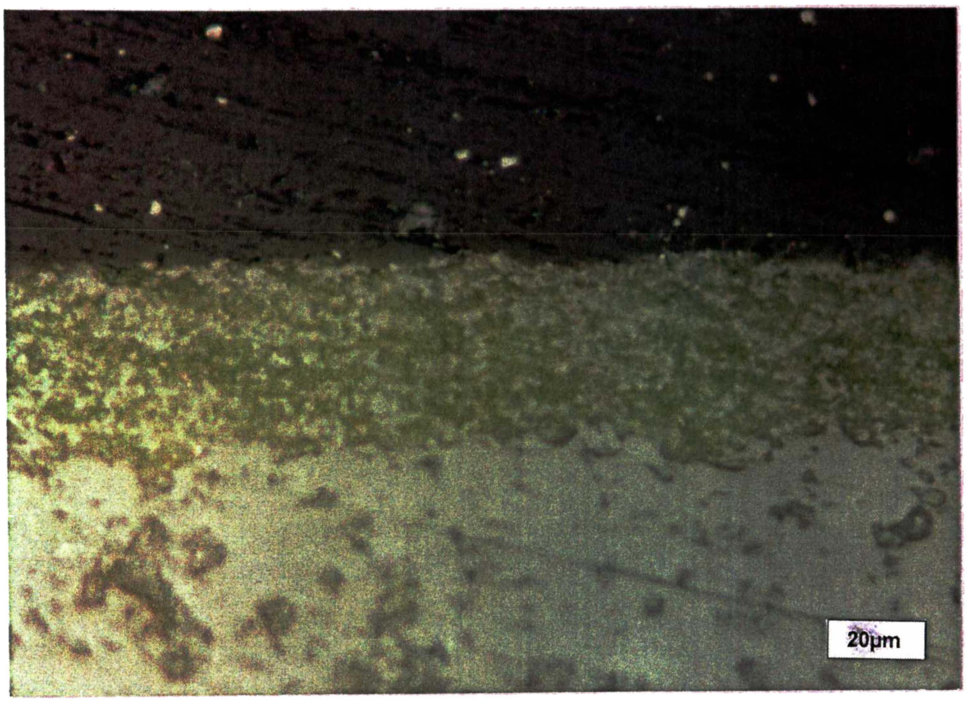

Figure A4.64 Anode #17 illustrating anode layer at a magnification of 500x.

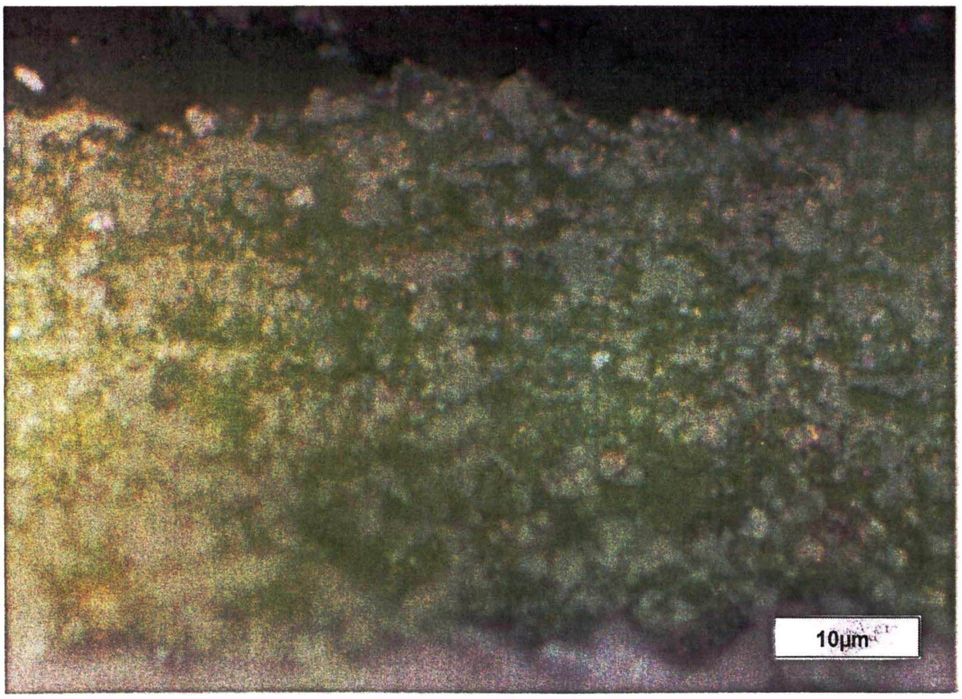

Figure A4.65 Anode #17 illustrating homogeneous NiO distribution at a magnification of 1500x.

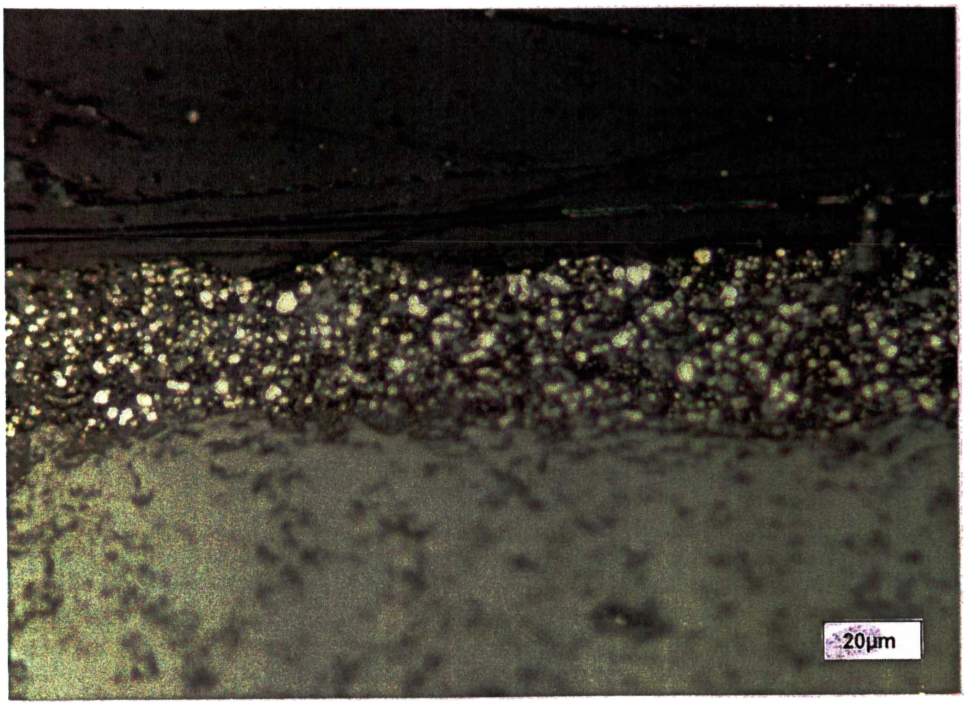

Figure A4.66 Anode #17 illustrating reduced layer at a magnification of 500x.

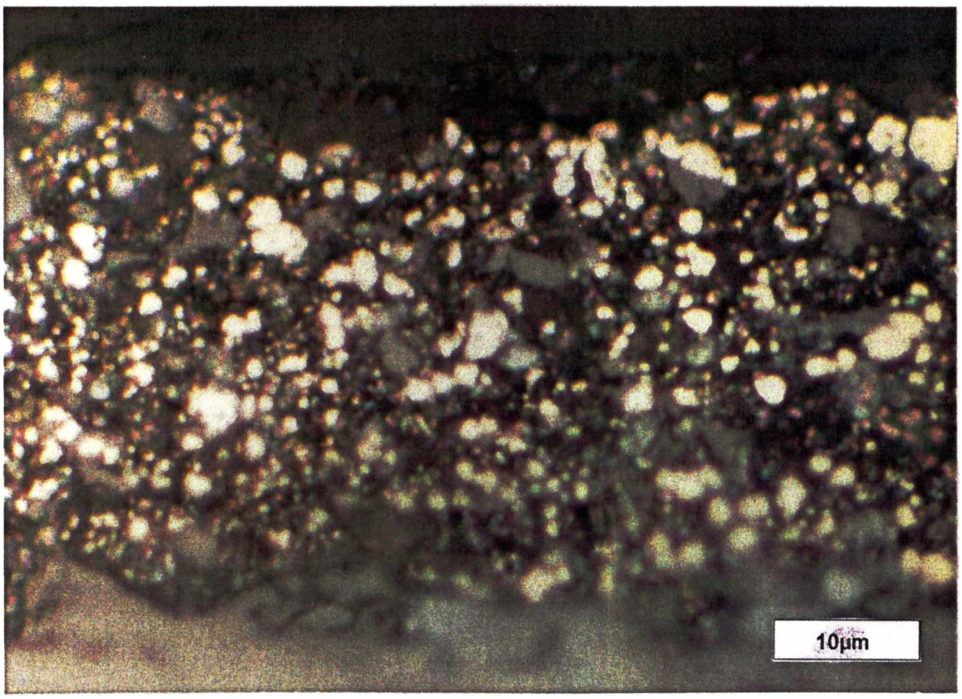

Figure A4.67 Anode #17 illustrating the high porosity of the layer at a magnification of 1500x.

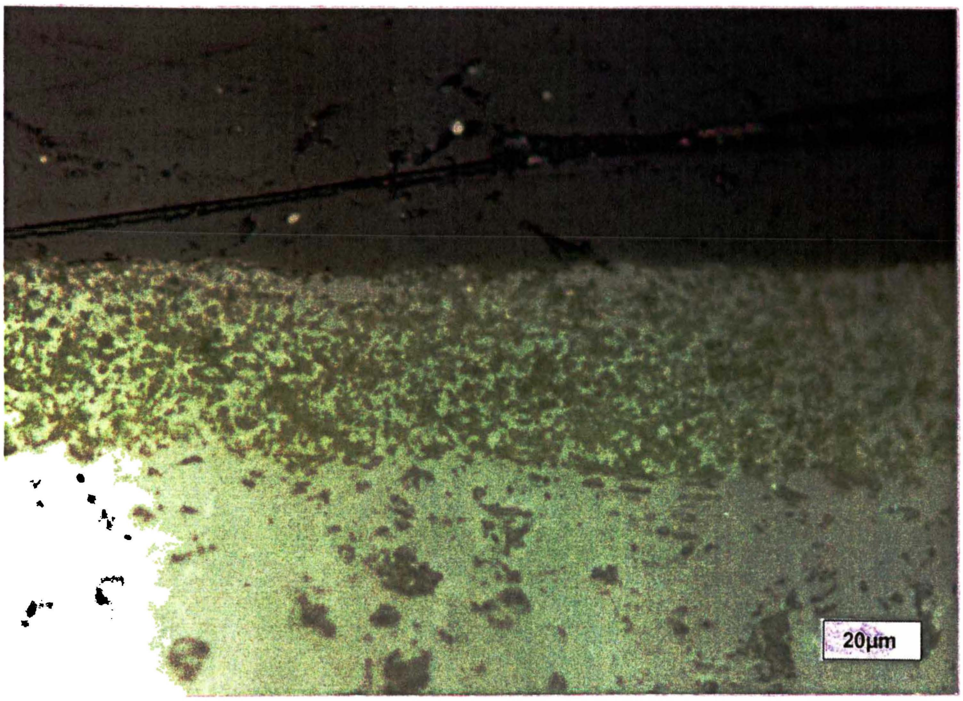

Figure A4.68 Anode #18 illustrating homogeneous NiO/YSZ distribution. Magnification of 500x.

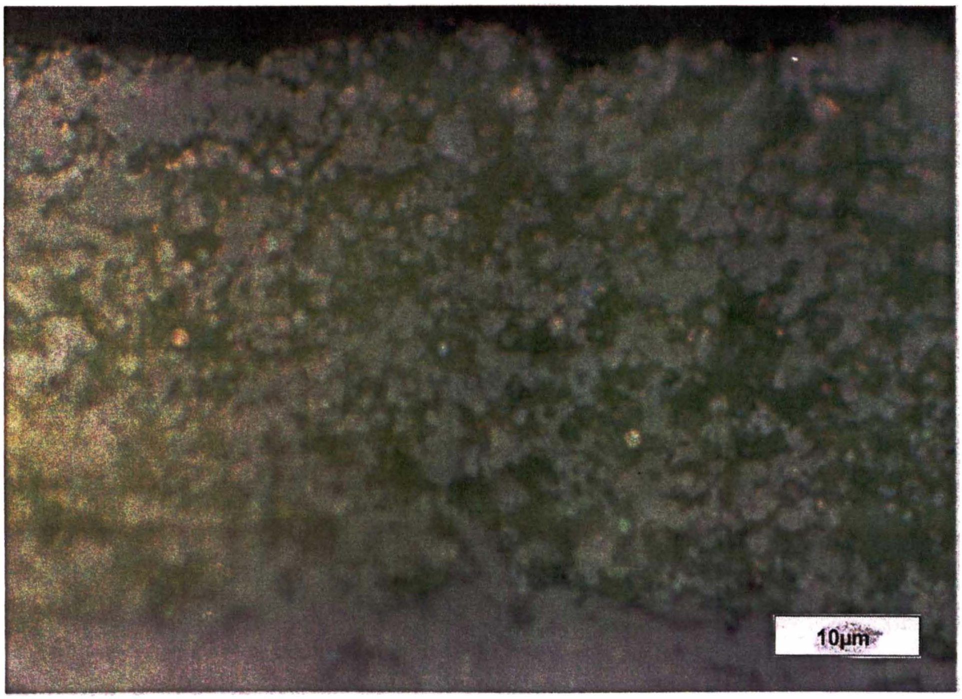

Figure A4.69 Anode #18 illustrating homogeneous dispersion of YSZ. Magnification of 1500x.

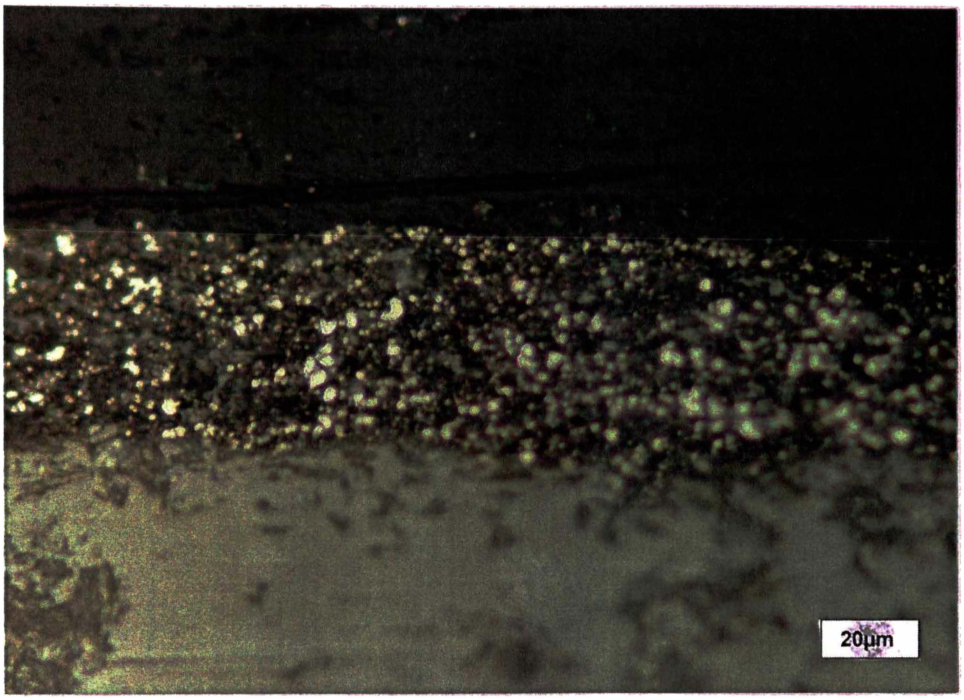

Figure A4.70 Anode #18 illustrating reduced layer at a magnification of 500x.

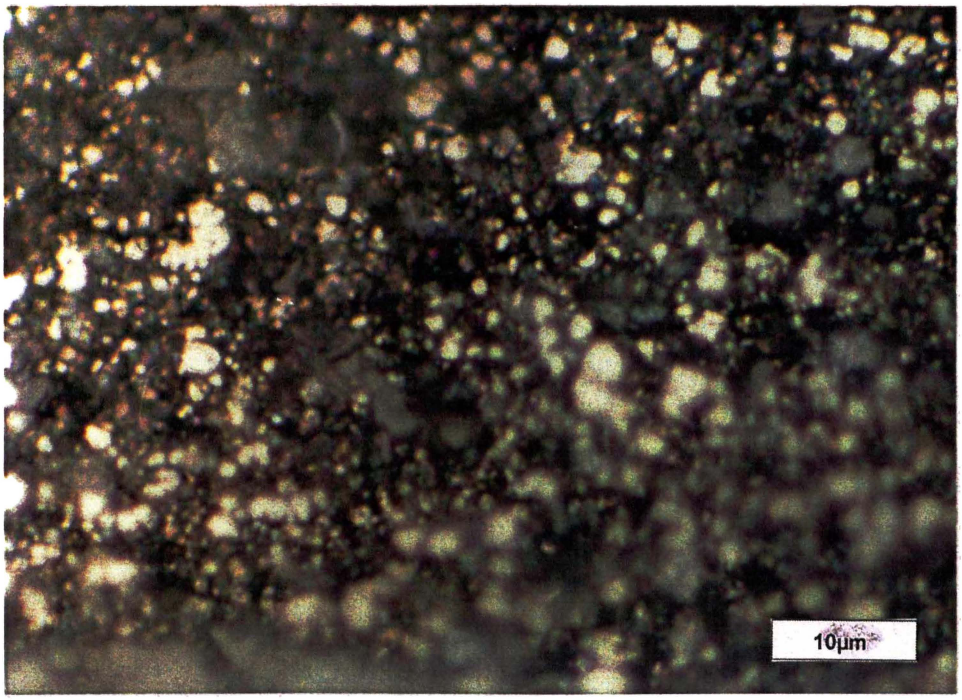

Figure A4.71 Anode #18 illustrating reduced layer at a magnification of 1500x.

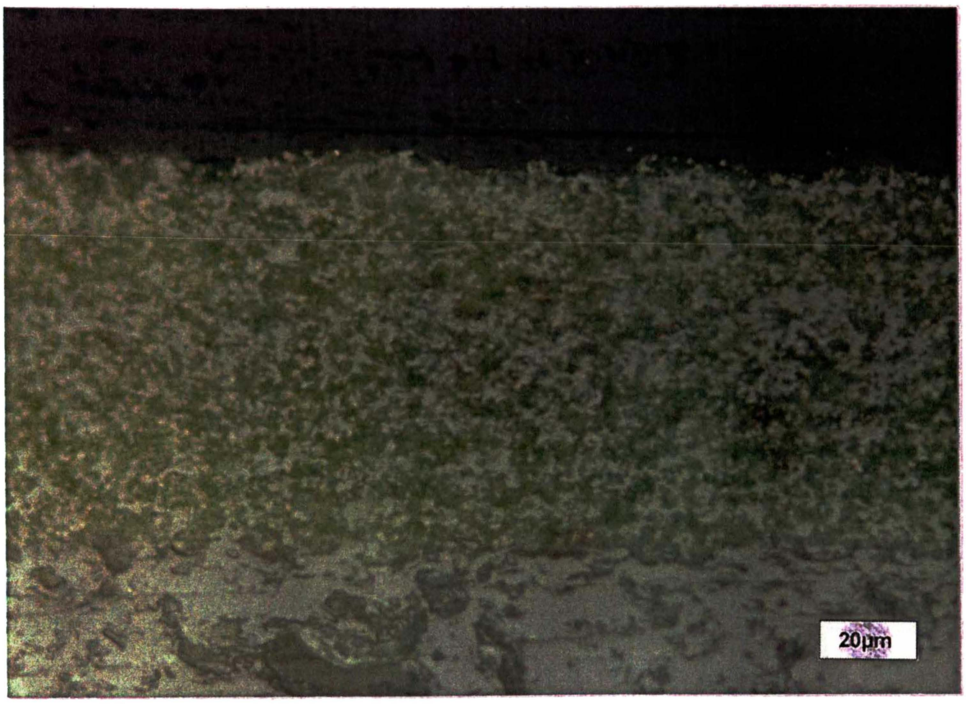

Figure A4.72 Anode #19 illustrating homogeneous NiO/YSZ distribution. Magnification of 500x.

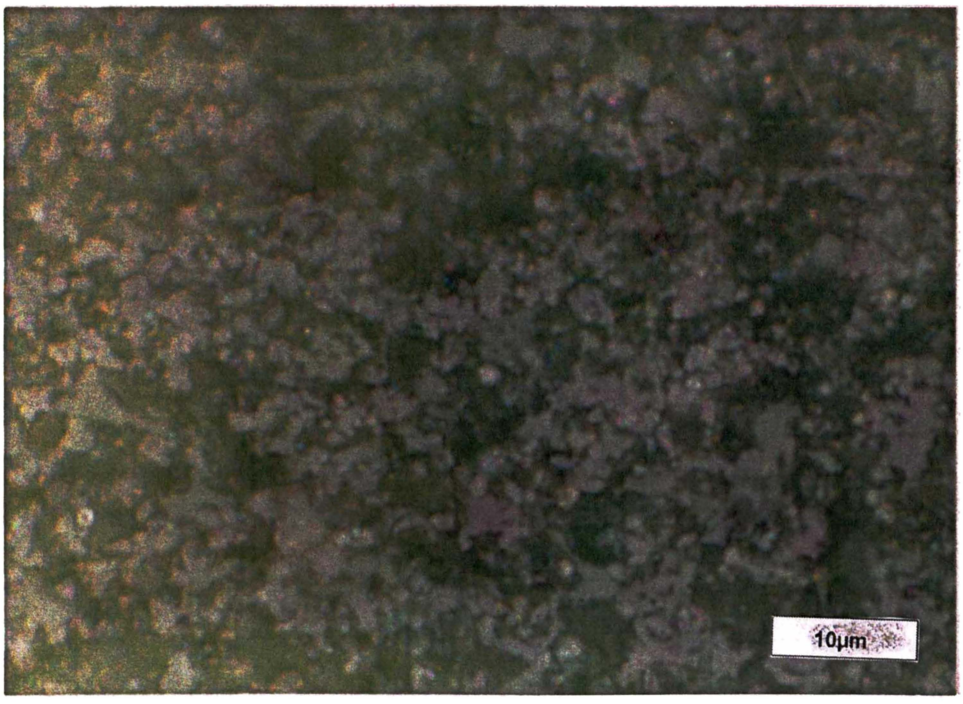

Figure A4.73 Anode #19 illustrating homogeneous NiO distribution. Magnification of 1500x.

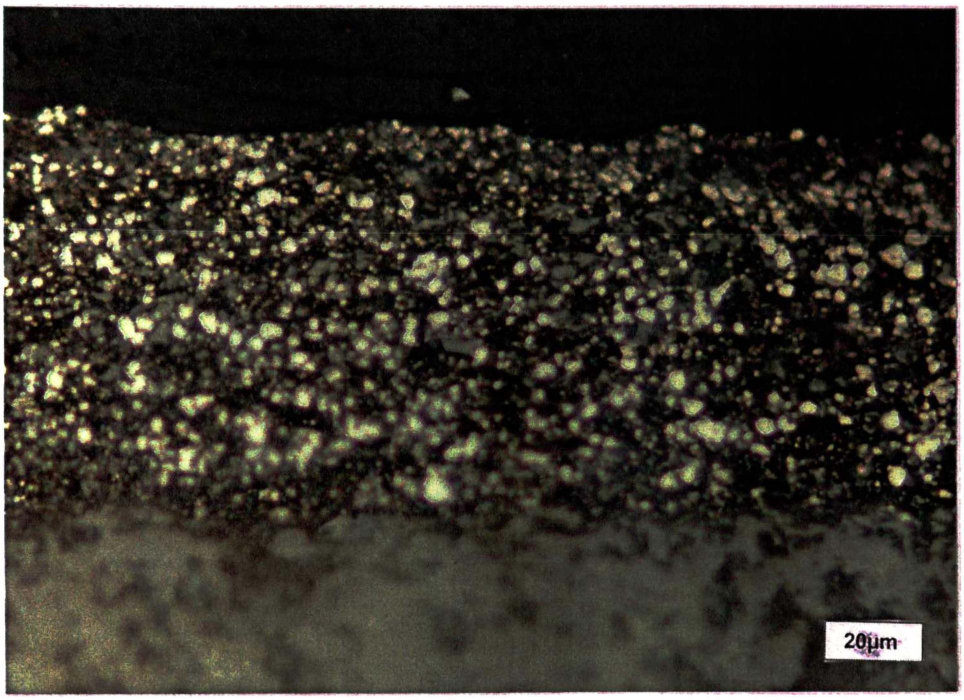

Figure A4.74 Anode #19 illustrating reduced anode layer at a magnification of 500x.

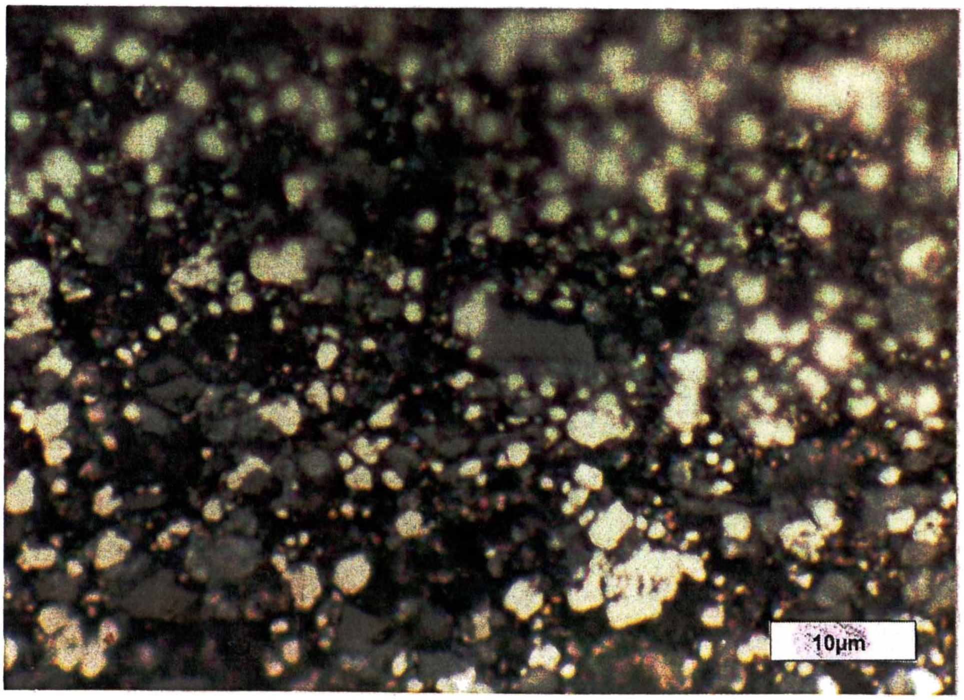

Figure A4.75 Anode #19 illustrating porosity of reduced layer at a magnification of 1500x.

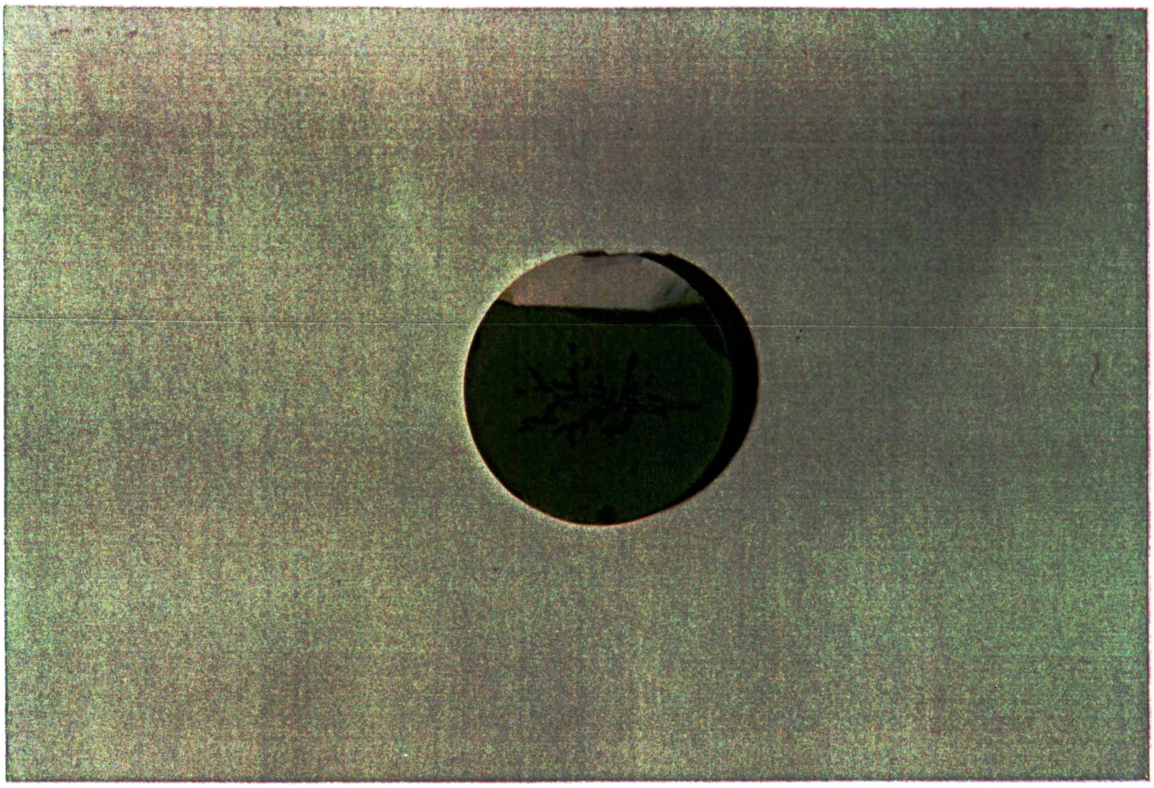

Figure A4.76 Anode #2 illustrating the surface, including defects present.

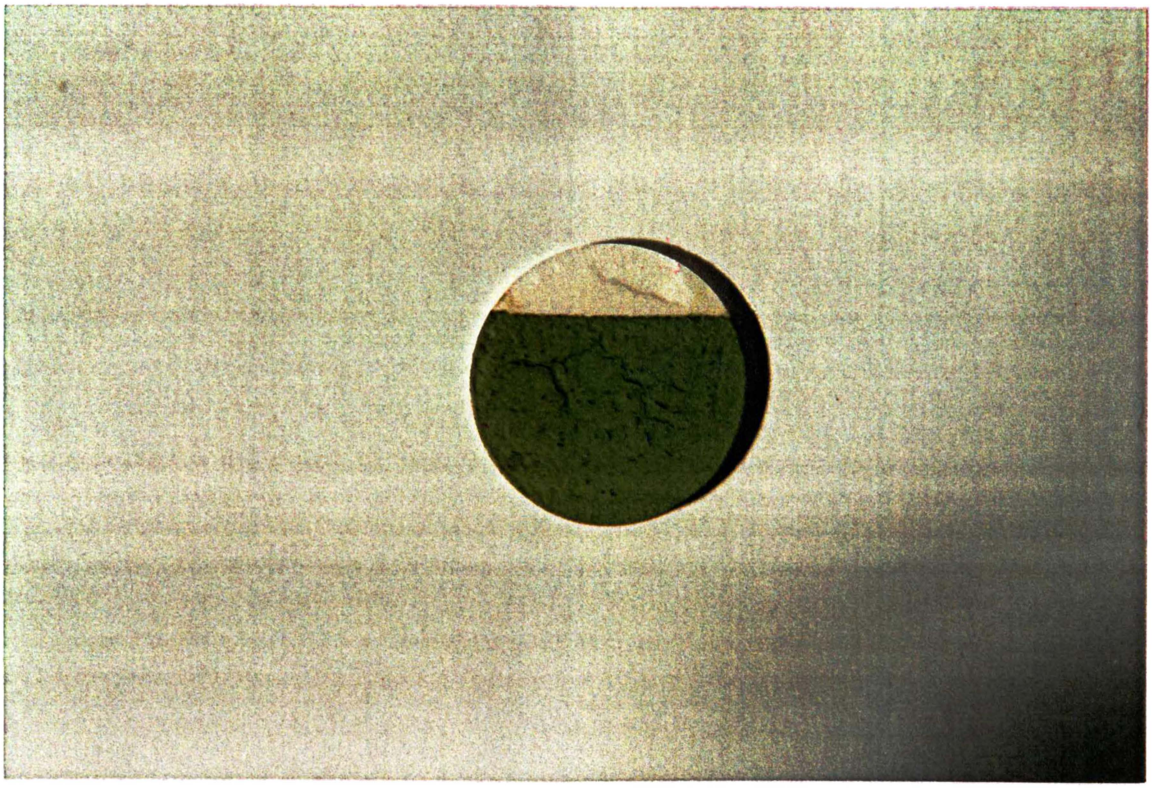

Figure A4.77 Anode #3 illustrating the surface, including defects present.

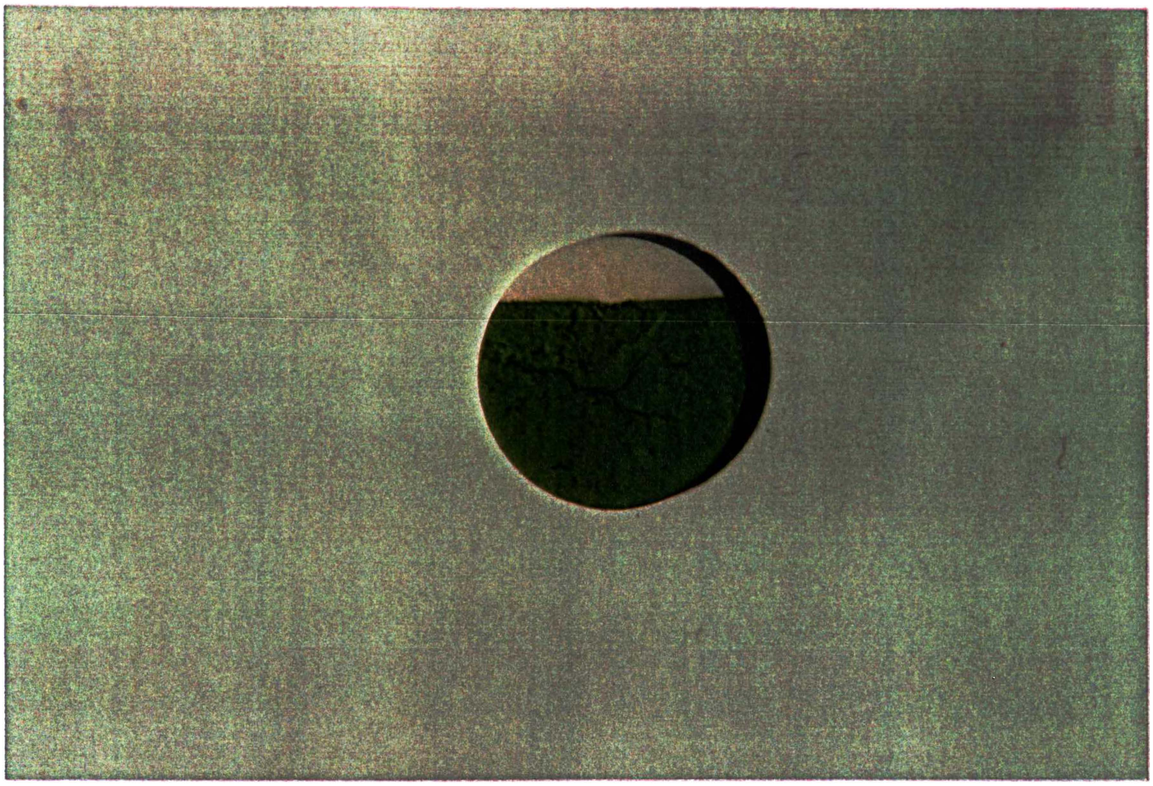

Figure A4.78 Anode #4 illustrating the surface, including defects present.

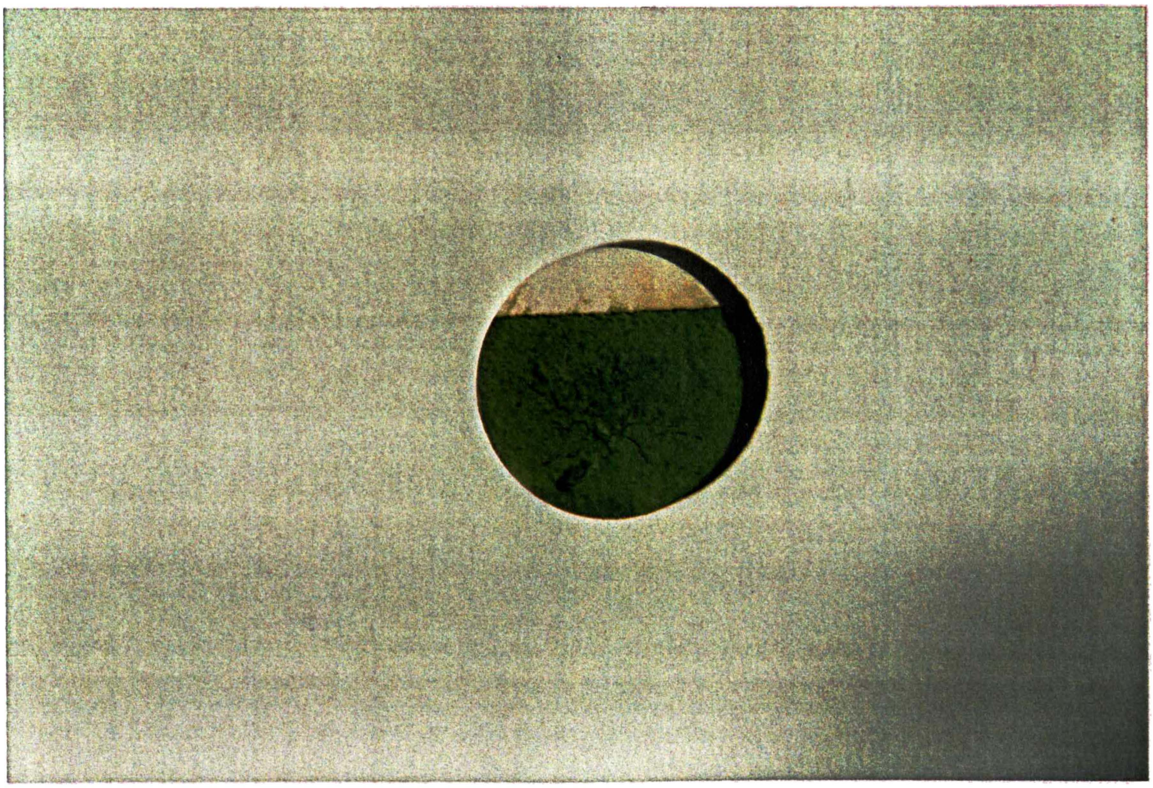

Figure A4.79 Anode #5 illustrating the surface, including defects present.

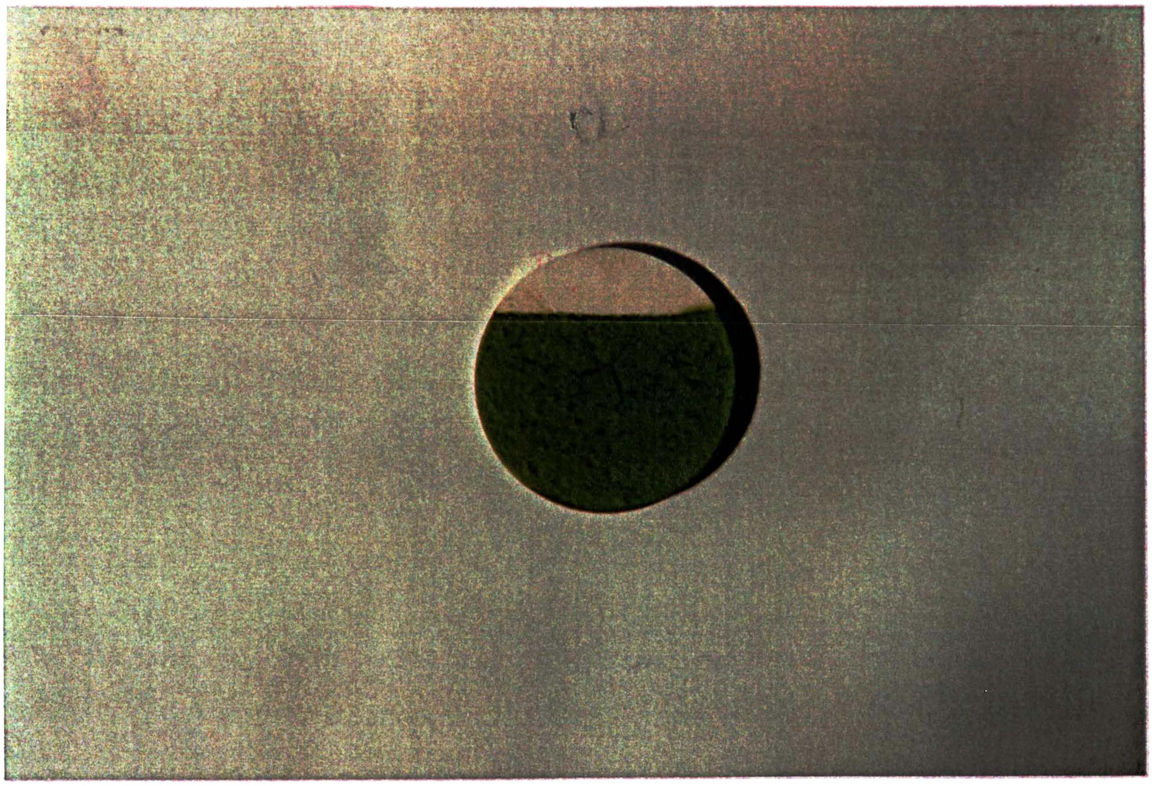

Figure A4.80 Anode #6 illustrating the surface, including defects present.

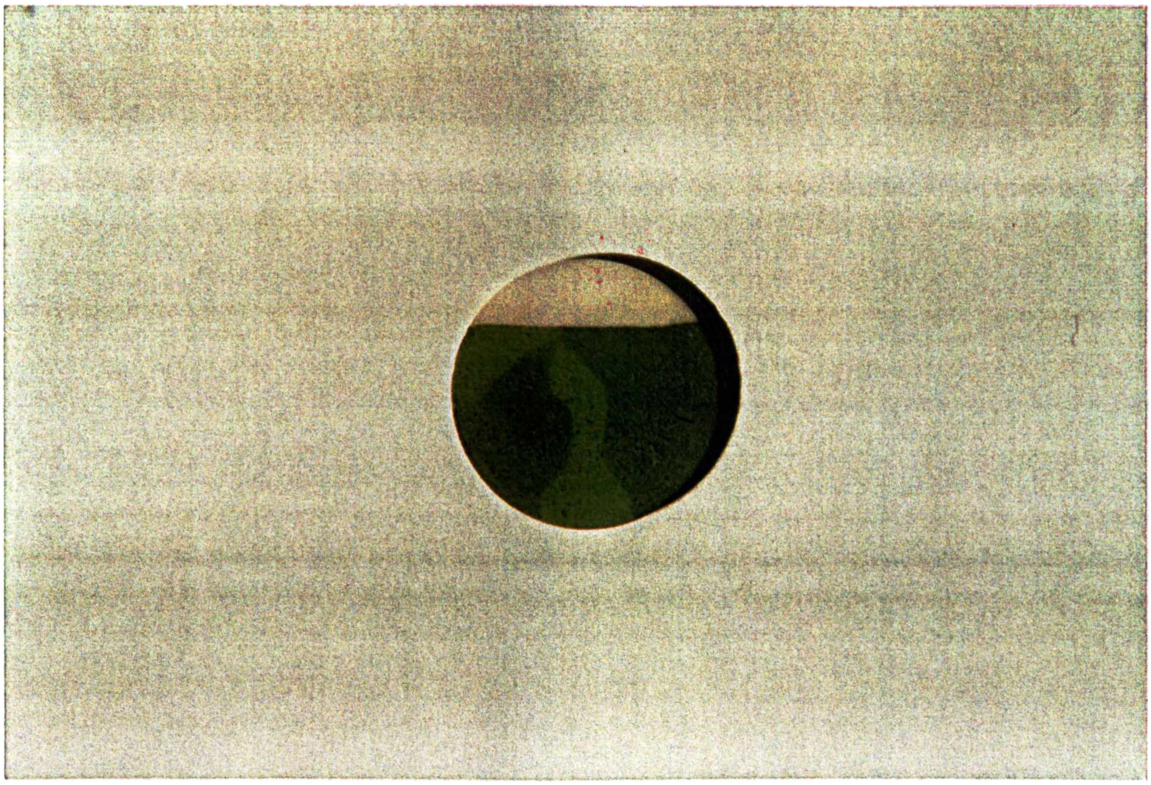

Figure A4.81 Anode #7 illustrating the surface, including defects present.

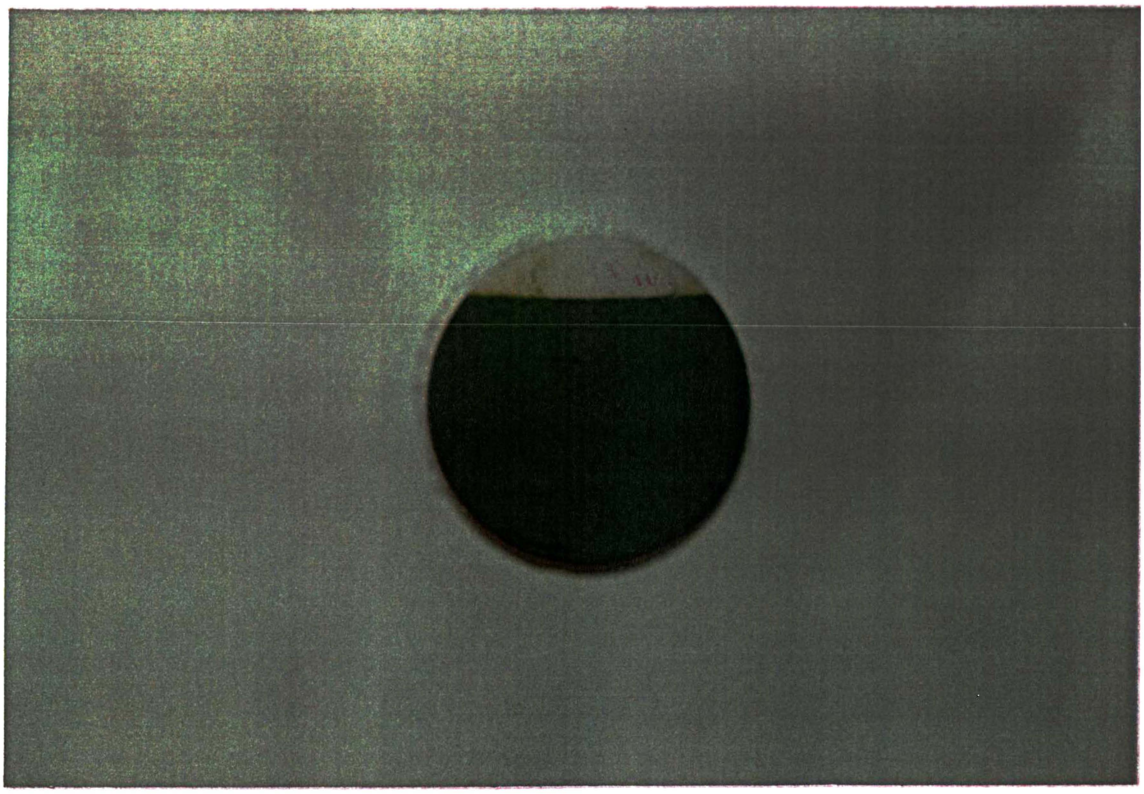

Figure A4.82 Anode #8 illustrating the surface, including defects present.

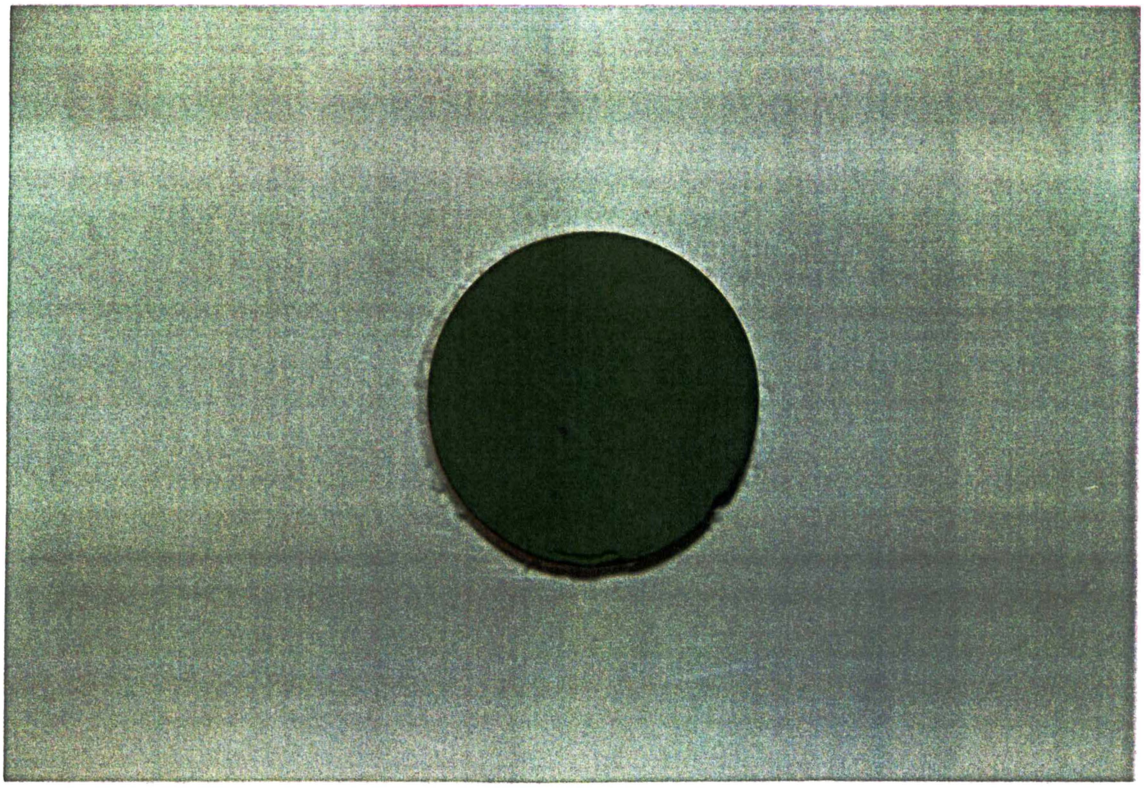

Figure A4.83 Anode #10 illustrating the surface, including defects present.

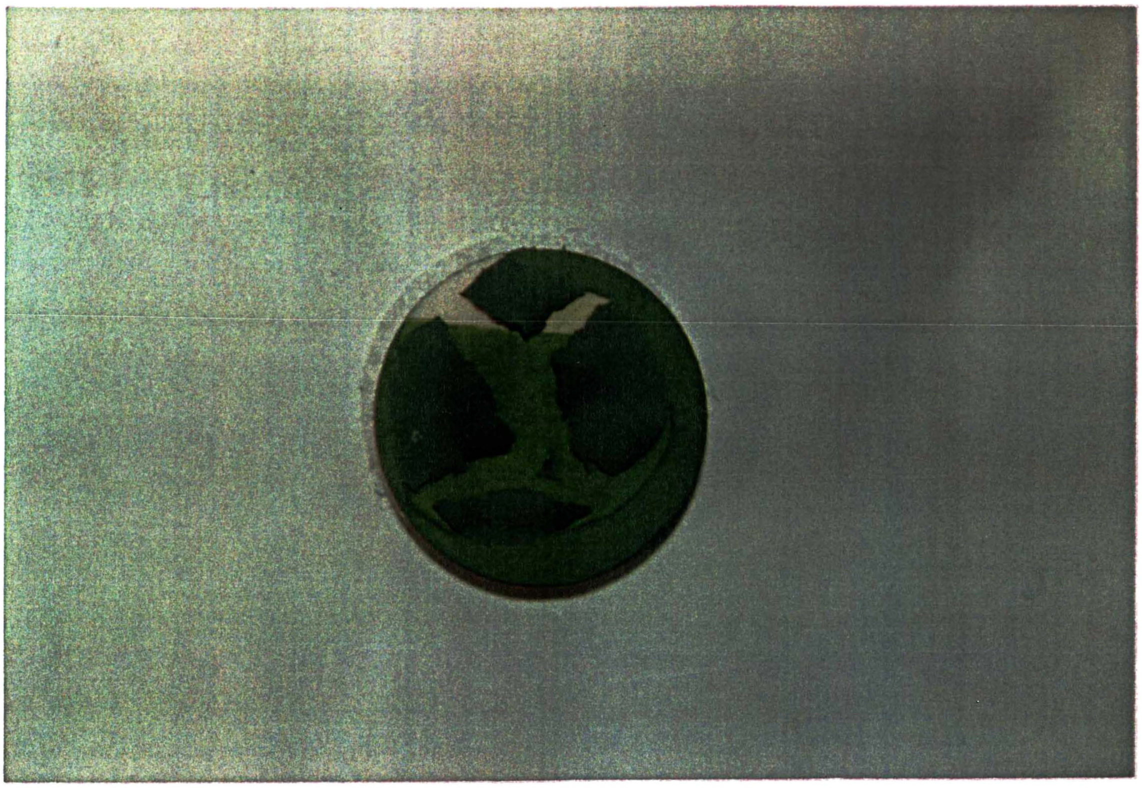

Figure A4.84 Anode #11 illustrating the surface, including defects present.

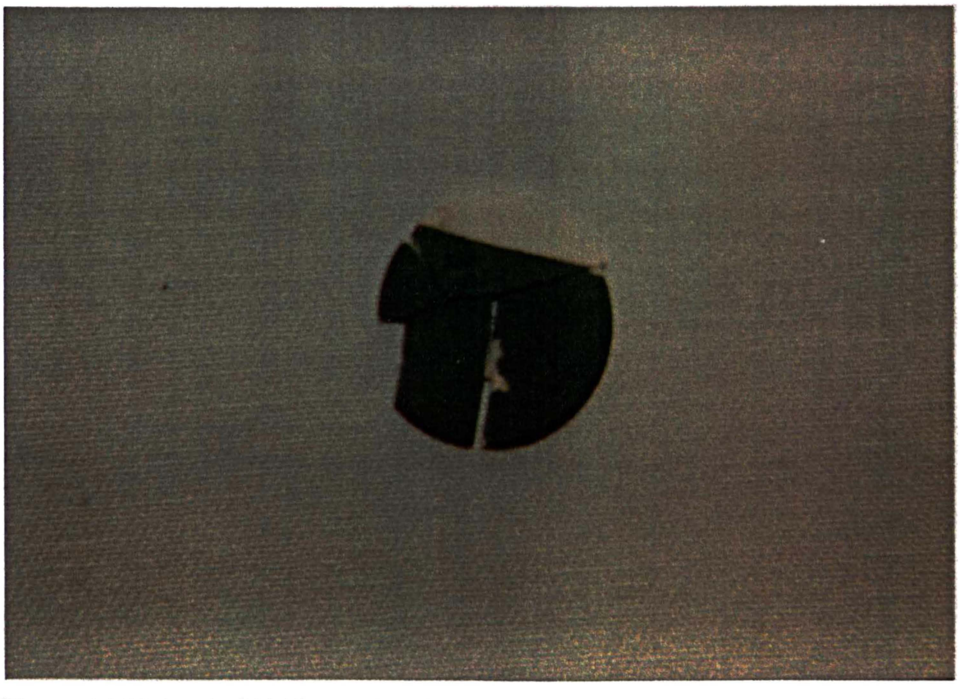

Figure A4.85 Anode #12 illustrating the surface, including defects present.

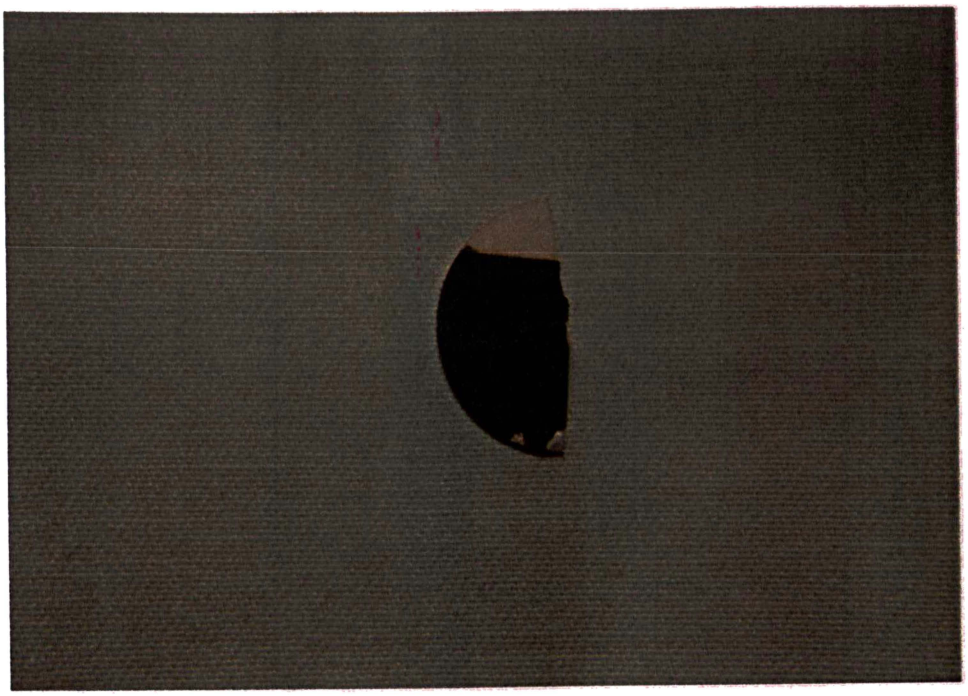

Figure A4.86 Anode #13 illustrating the surface, including defects present.

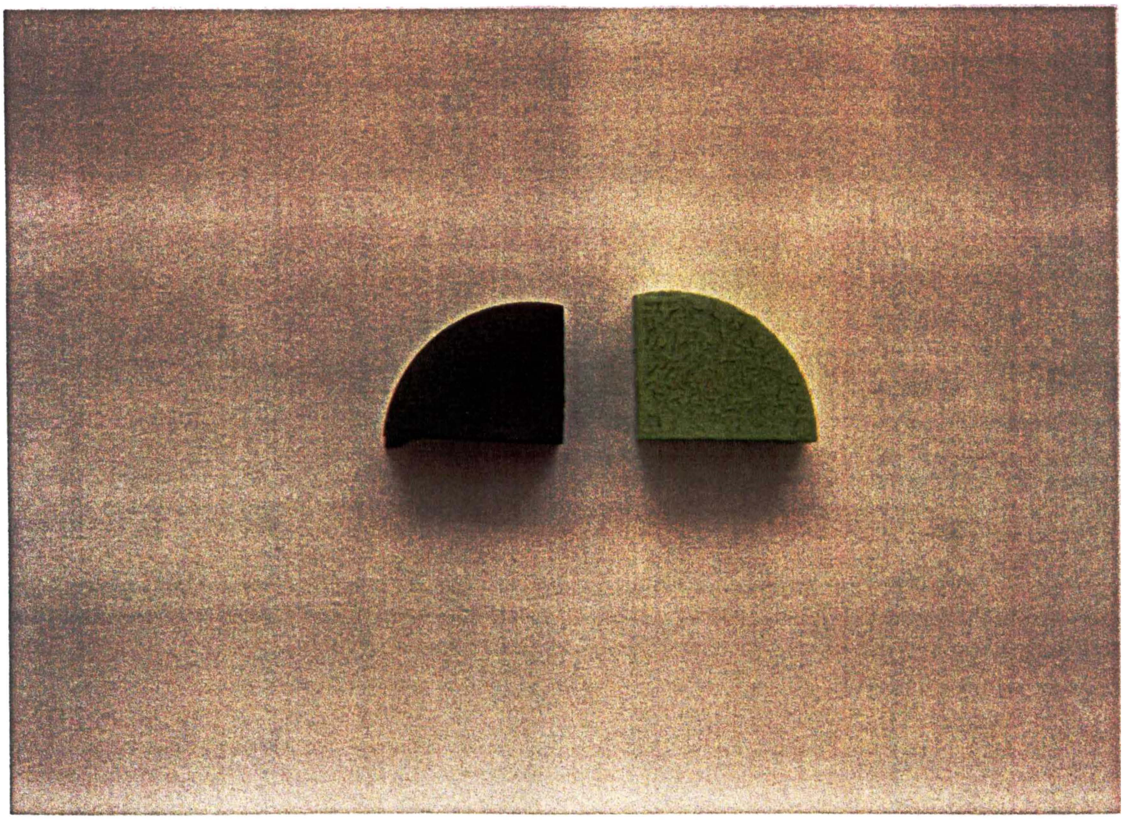

Figure A4.87 Anode #14 illustrating the surface, including defects present.